

UNIVERSITY OF CALIFORNIA
SANTA BARBARA

Modeling, Analysis, and Control of Spatially Distributed Systems

A Dissertation submitted in partial satisfaction
of the requirements for the degree of

Doctor of Philosophy

in

Mechanical Engineering

by

Mihailo R. Jovanović

Committee in charge:

Professor Bassam Bamieh, Chairperson

Professor George M. Homsy

Professor Igor Mezić

Professor Shiv Chandrasekaran

September 2004

The dissertation of Mihailo R. Jovanović is approved:

Professor George M. Homsy

Professor Igor Mezić

Professor Shiv Chandrasekaran

Professor Bassam Bamieh, Committee Chairperson

August 2004

Modeling, Analysis, and Control of Spatially Distributed Systems

Copyright © 2004

by

Mihailo R. Jovanović

To Aleksandra and my parents

Acknowledgements

First and foremost, I would like to express my deep gratitude to my graduate advisor Professor Bassam Bamieh for being an excellent teacher and mentor to me. His amazing knowledge, vision, flexibility, patience, and open-mindedness have inspired me to work hard. In my research, he gave me a lot of freedom and provided valuable advice, guidance, and critical remarks. Bassam, it has been a great honor and privilege to work with you!

Many thanks go to (late) Professor Mohammed Dahleh who recruited me to UCSB, suggested to me to work with Bassam, and served as my co-advisor until his untimely death in 2000.

I would like to thank Professors George M. Homsy, Igor Mezić, and Shiv Chandrasekaran for their time and effort to serve on my dissertation committee.

I am thankful to Professor Petar Kokotović for his support and constant encouragement in all aspects of my life from the beginning of my graduate school experience. He has created an outstanding research environment in the Center for Control Engineering and Computation (CCEC) at UCSB, and has been an inspiring role model.

It has been a privilege to get to know Professor Karl J. Åström. I would like to thank him for many fruitful discussions and his interest in my work. His positive attitude and enthusiasm had an enormous influence in both our department and CCEC.

All the faculty members of the CCEC are thankfully acknowledged. I have benefited immensely from my interactions with them and from the classes taught by them. Professor Bassam Bamieh's classes on Distributed Systems, Professor Petar Kokotović's classes on Adaptive Control, and Professor Andy Teel's classes on Nonlinear Systems helped me identify and solve many important research problems presented in this dissertation.

I have enjoyed the company of my office mates Aruna Ranaweera and Symeon Grivopoulos. Guys, I could not have asked for better office mates and friends. It has been fun sharing office with you, and I am going to miss you. I would also like to thank all other former and current members of the Dynamical Systems and Control Group in our department for their friendship, support, and valuable technical assistance during my stay at UCSB. It has been a genuine pleasure working and socializing with Mariateresa Napoli, Vasu Salapaka, Makan Fardad, Umesh Vaidya, Hana El-Samad, Yonggang Xu, Zoran Levnjajić, Sophie Loire, Niklas Karlsson, George Mathew, Thomas John, Greg Hagen, Jayati Ghosh, Erkut Aykutlug, Matthias Schibli, Michael Grebeck, Paul Cronin, Lasse Moklegaard, and Ove Storset.

It has been a lot of fun playing soccer (oops, excuse my language – football!) in Santa Barbara League with Aggressive Int., and in UCSB Intramurals with Damage Inc. This experience was really enjoyable thanks to my teammates from these two 'Santa Barbara Soccer Institutions'. It would be an overwhelming task to list all their names here.

I would like to acknowledge my friends from former Yugoslavia: Nebac, Doca, Škema, Draža, Nebojša, Vlada, Davor, Kiza, Alek, Dragiša, Dušan, Zoran, Saša, Aca, Edin, Jelena, Meri, Tanja, Una, Iva, Jovana, Biljana, Čika Mića, Čika Lale, and Tetka Lila. Guys, your friendship and our joint barbecues/parties made Santa Barbara feel like home.

Special thanks go to my granduncle Dragić Šević and his family for all of their help over the past six years. Deda, because of your hospitality, trips to Burbank appeared as trips to Arandjelovac. I appreciate everything you have done for Aleksandra and me.

Finally, my warmest thanks go to my wife Aleksandra and my parents. Aleksandra has been a perfect partner and my best friend throughout the years; my parents have always encouraged me to be independent

and to pursue my dreams even when they were driving me away from home. This dissertation would not have been possible without their continuous support, understanding, and endless love.

Curriculum Vitae of Mihailo R. Jovanović

Education

PhD in Mechanical Engineering. University of California at Santa Barbara, September 2004. **GPA:** 3.95/4.00.

MS in Mechanical Engineering. University of Belgrade, June 1998.

Dipl. Ing., Mechanical Engineering. University of Belgrade, July 1995.

Graduated with First Class Honors, **GPA:** 9.53/10.00.

Experience

Graduate Researcher. University of California at Santa Barbara, July 1999 – present.

Teaching Assistant. University of California at Santa Barbara, 1998 – present.

Staff Intern. Raytheon Co., Santa Barbara Remote Sensing, Summer 2001.

Assistant Lecturer. University of Belgrade, Dept. of Mech. Eng., 1995 – 1998.

Graduate Researcher. University of Belgrade, Dept. of Mech. Eng., 1995 – 1998.

Staff Intern. Siemens Co., Spring 1997.

Undergraduate Researcher. University of Belgrade, Dept. of Mech. Eng., Spring 1995.

Awards, Honors and Recognition

BEST SESSION PRESENTATION AWARD, American Control Conference, 2001, 2002, 2003, 2004.

INVITED SPEAKER, AMS–IMS–SIAM Joint Summer Conference on Hydrodynamic Stability and Flow Control, Snowbird, UT, July 2003.

THE NICOLITCH TRUST SCHOLARSHIP – "for a recipient with exemplary grades and leadership potential", 2002.

THE MECHANICAL & ENVIRONMENTAL ENGINEERING DEPARTMENT FELLOWSHIP, University of California at Santa Barbara, 1998.

THE BEST STUDENT OF THE CLASS AWARD (a class of approximately 500 students), Department of Mechanical Engineering, University of Belgrade, 1995.

Appeared on DEAN'S LIST each year during undergraduate studies, 1991 – 1995.

THE FUND FOR AN OPEN SOCIETY GRANT, to participate at the FLUCOME'97 conference in Japan, 1997.

THE MINISTRY OF SCIENCE & TECHNOLOGY OF THE REPUBLIC OF SERBIA FELLOWSHIP, Jan. 1996 – Jan. 1997.

THE FOUNDATION FOR DEVELOPMENT OF YOUNG RESEARCHERS OF THE REPUBLIC OF SERBIA FELLOWSHIP, Oct. 1995 – Oct. 1996.

ENERGOPROJECT, Co. FELLOWSHIP, Oct. 1994 – Oct. 1995.

Professional Activities

Member of IEEE, CONTROL SYSTEMS SOCIETY.

Referee for IEEE Transactions on Automatic Control, European Journal of Control, Journal of Fluid Mechanics, Journal of Atmospheric Sciences, IEEE Conference on Decision and Control, American Control Conference.

Additional Information

Male. Citizen of Serbia & Montenegro. Permanent resident of the United States.

Language skills: Serbian (native), English (fluent).

Selected Publications

Journals

1. M. R. JOVANOVIĆ & B. BAMIEH, *Unstable modes versus non-normal modes in supercritical channel flows*, submitted to J. Fluid Mech., 2004, <http://www.me.ucsb.edu/~jmihailo/publications/jfm04fh.html>.
2. M. R. JOVANOVIĆ & B. BAMIEH, *On the ill-posedness of certain vehicular platoon control problems*, submitted to IEEE Transactions on Automatic Control, 2003, <http://www.me.ucsb.edu/~jmihailo/publications/tac03-platoons.html>.
3. M. R. JOVANOVIĆ & B. BAMIEH, *Exact computation of frequency responses for a class of spatially distributed systems*, submitted to Systems & Control Letters, 2003, <http://www.me.ucsb.edu/~jmihailo/publications/scl03.html>.
4. M. R. JOVANOVIĆ & B. BAMIEH, *Componentwise energy amplification in channel flows*, to appear in J. Fluid Mech., 2003, <http://www.me.ucsb.edu/~jmihailo/publications/jfm03.html>.
5. M. R. JOVANOVIĆ & B. BAMIEH, *Lyapunov-based distributed control of systems on lattices*, to appear in IEEE Transactions on Automatic Control, 2003, <http://www.me.ucsb.edu/~jmihailo/publications/tac03-lattice.html>.

Refereed Proceedings

1. M. R. JOVANOVIĆ & B. BAMIEH, *On the ill-posedness of certain vehicular platoon control problems*, to appear in Proceedings of the 43rd IEEE Conference on Decision and Control, Paradise Island, Bahamas, 2004.
2. M. R. JOVANOVIĆ & B. BAMIEH, *Architecture induced by distributed backstepping design*, to appear in Proceedings of the 43rd IEEE Conference on Decision and Control, Paradise Island, Bahamas, 2004.
3. M. R. JOVANOVIĆ & B. BAMIEH, *Unstable modes versus non-normal modes in supercritical channel flows*, in Proceedings of the 2004 American Control Conference, Boston, MA, pp. 2245-2250, 2004.
4. M. R. JOVANOVIĆ, J. M. FOWLER, B. BAMIEH, & R. D'ANDREA, *On avoiding saturation in the control of vehicular platoons*, in Proceedings of the 2004 American Control Conference, Boston, MA, pp. 2257-2262, 2004.
5. M. R. JOVANOVIĆ & B. BAMIEH, *Exact computation of frequency responses for a class of infinite dimensional systems*, in Proceedings of the 42nd IEEE Conference on Decision and Control, Maui, HI, pp. 1339-1344, 2003.
6. M. R. JOVANOVIĆ & B. BAMIEH, *Lyapunov-based output-feedback distributed control of systems on lattices*, in Proceedings of the 42nd IEEE Conference on Decision and Control, Maui, HI, pp. 1333-1338, 2003.
7. M. R. JOVANOVIĆ & B. BAMIEH, *Lyapunov-based state-feedback distributed control of systems on lattices*, in Proceedings of the 2003 American Control Conference, Denver, CO, pp. 101-106, 2003.
8. M. R. JOVANOVIĆ, B. BAMIEH, & M. GREBECK, *Parametric resonance in spatially distributed systems*, in Proceedings of the 2003 American Control Conference, Denver, CO, pp. 119-124, 2003.
9. M. R. JOVANOVIĆ & B. BAMIEH, *Frequency domain analysis of the linearized Navier-Stokes equations*, in Proceedings of the 2003 American Control Conference, Denver, CO, pp. 3190-3195, 2003.
10. M. R. JOVANOVIĆ, *Nonlinear control of an electrohydraulic velocity servosystem*, in Proceedings of the 2002 American Control Conference, Anchorage, AL, pp. 588-593, 2002.
11. M. R. JOVANOVIĆ & B. BAMIEH, *Modelling flow statistics using the linearized Navier-Stokes equations*, in Proceedings of the 40th IEEE Conference on Decision and Control, Orlando, FL, pp. 4944-4949, 2001.

12. M. R. JOVANOVIĆ & B. BAMIEH, *The spatio-temporal impulse response of the linearized Navier-Stokes equations*, in Proceedings of the 2001 American Control Conference, Arlington, VA, pp. 1948-1953, 2001.

Unrefereed Proceedings

1. M. R. JOVANOVIĆ & B. BAMIEH, *Unstable modes versus non-normal modes in supercritical channel flows*, 56th Annual Meeting of the American Physical Society, Division for Fluid Dynamics, East Rutherford, NJ, 2003.
2. M. R. JOVANOVIĆ & B. BAMIEH, *The spatio-temporal frequency responses of the linearized Navier-Stokes equations*, 55th Annual Meeting of the American Physical Society, Division for Fluid Dynamics, Dallas, TX, 2002.
3. B. BAMIEH & M. R. JOVANOVIĆ, *Drag reduction/enhancement with riblets as parametric resonance*, 54th Annual Meeting of the American Physical Society, Division for Fluid Dynamics, San Diego, CA, 2001.
4. M. R. JOVANOVIĆ & B. BAMIEH, *The impulse response of the linearized Navier-Stokes equations*, 53rd Annual Meeting of the American Physical Society, Division for Fluid Dynamics, Washington, DC, 2000.
5. B. BAMIEH, M. R. JOVANOVIĆ, & M. DAHLEH, *A model for the effect of riblets on wall bounded shear flow transition*, 52nd Annual Meeting of the American Physical Society, Division for Fluid Dynamics, New Orleans, LA, 1999.

Abstract

Modeling, Analysis, and Control of Spatially Distributed Systems

by

Mihailo R. Jovanović

Spatially distributed dynamical systems arise in a variety of science and engineering problems. These systems are typically described by Partial Integro-Differential Equations (P(I)DEs), or by a finite or infinite number of coupled Ordinary Differential Equations (ODEs). In this dissertation, we model spatially distributed dynamical systems and present new tools for their analysis and design. All theoretical tools that we develop are applicable to classes of systems characterized by their structural properties. We exploit these structural properties and provide non-conservative results.

Part I of the dissertation is devoted to the distributed systems theory. We derive an explicit formula for the Hilbert–Schmidt norm of the frequency response operator for a class of P(I)DEs. Our method avoids the need for spatial discretization and provides an exact reduction of an infinite dimensional problem to a problem in which only matrices of finite dimensions are involved. We also develop tools for analysis of stability and input-output system norms of linear P(I)DEs with spatially periodic coefficients. We illustrate how stability properties and input-output norms of spatially invariant systems can be changed when a spatially periodic feedback is introduced.

In Part II, we use system theoretic approach to model and analyze the transition and turbulence in plane channel flows. We utilize a componentwise frequency response analysis to reveal distinct resonant mechanisms for subcritical transition. We further illustrate that the spatio-temporal impulse responses of the Linearized Navier-Stokes equations contain many qualitative features of early stages of turbulent spots.

Part III considers distributed control of systems on lattices. We utilize backstepping as a tool for distributed control of these systems. We discuss architecture induced by distributed backstepping design and demonstrate that backstepping yields controllers with inherent degree of spatial localization. Also, we revisit several widely cited results in the control of vehicular platoons and show that they are inherently ill-posed. Finally, we remark on phenomenon of peaking in the control of vehicular platoons and demonstrate how to avoid it.

Contents

Acknowledgements	v
Curriculum Vitae	vii
Abstract	x
List of Figures	xv
1 Introduction	1
1.1 Organization of the dissertation	2
1.2 Contributions of the dissertation	2
I Distributed systems theory	6
2 Control theoretic preliminaries	7
2.1 Equations in evolution form	9
2.2 Dynamical systems with input and system uncertainty	10
2.2.1 Spatio-temporal impulse and frequency responses	11
2.2.2 Input-output system gains	12
2.2.3 Finite horizon input-output gains	14
2.2.4 Exponentially discounted input-output gains	14
2.2.5 Input-output directions	16
2.2.6 Robustness analysis versus input-output analysis	16
Bibliography	19
3 Exact determination of frequency responses for a class of spatially distributed systems	20
3.1 Preliminaries	20
3.2 Determination of frequency responses from state-space realizations	21
3.2.1 State-space realizations of \mathcal{H} , \mathcal{H}^* , and \mathcal{HH}^*	22
3.2.2 Determination of traces from state-space realizations	23
3.2.3 Explicit formula for Hilbert–Schmidt norm	25
3.3 Examples	26
3.3.1 A one-dimensional diffusion equation	26
3.4 Summary	27
Bibliography	28

4 Stability and system norms of PDEs with periodic coefficients	29
4.1 Preliminaries	29
4.2 Representation of the lifted systems	31
4.2.1 Spatially invariant operators	33
4.2.2 Periodic gains	33
4.2.3 Feedback interconnections	35
4.3 Stability and input-output norms of spatially periodic systems	36
4.4 Examples of PDEs with periodic coefficients	38
4.5 Extensions	42
4.6 Summary	42
Bibliography	43
5 Conclusions and future directions	44
Bibliography	46
II Modeling and analysis of transition and turbulence in channel flows	47
6 Background	48
Bibliography	51
7 Dynamical description of flow fluctuations	54
7.1 Linearized Navier-Stokes equations	54
7.1.1 Externally excited LNS equations in the evolution form	56
7.1.2 The underlying operators	60
7.1.3 Spectral analysis of Squire and Orr-Sommerfeld operators at $k_x = 0$	62
7.2 Numerical method	63
Bibliography	64
8 Spatio-temporal frequency responses of the linearized Navier-Stokes equations in channel flows	65
8.1 Frequency responses in Poiseuille flow with $R = 2000$	66
8.1.1 Componentwise energy amplification	67
8.1.2 Maximal singular values	71
8.1.3 Dominant flow structures	72
8.2 Frequency responses in Couette flow with $R = 2000$	76
8.3 Frequency responses in turbulent mean velocity profile flow with $R_\tau = 590$	77
8.4 Frequency responses in Poiseuille flow with $R = 5700$	77
8.5 Unstable modes versus non-normal modes in supercritical channel flows	78
8.6 Summary	80
Bibliography	82
9 The cross sectional 2D/3C model: analytical results	84
9.1 Dependence of singular values on the Reynolds number	85
9.2 Dependence of Hilbert–Schmidt norms on the Reynolds number	88
9.3 Dependence of \mathcal{H}_∞ and \mathcal{H}_2 norms on the Reynolds number	92
9.4 Energy amplification of near-wall external excitations	97
9.5 Exact determination of Hilbert–Schmidt norms	100
9.5.1 State-space realizations of the linearized Navier-Stokes equations	101

9.5.2	Formulae for Hilbert–Schmidt norms at $\omega = 0$	103
9.6	Exact determination of \mathcal{H}_2 norms	104
9.6.1	Expressions for \mathcal{H}_2 norms via Lyapunov equations	105
9.6.2	Formulae for operator traces	108
9.7	Summary	117
Bibliography		118
10 Spatio-temporal impulse responses of the linearized Navier-Stokes equations in channel flows		119
10.1	Preliminaries	120
10.2	Spatio-temporal impulse responses in Poiseuille flow with $R = 2000$	122
10.2.1	Impulse responses for streamwise independent perturbations	122
10.2.2	Impulse responses for full three-dimensional perturbations	124
10.3	Summary	129
Bibliography		135
11 Conclusions and future directions		137
Bibliography		139
III Distributed control of systems on lattices		140
12 Distributed backstepping control of systems on lattices		141
12.1	Introduction	141
12.2	Systems on lattices	143
12.2.1	Notation	143
12.2.2	An example of systems on lattices: mass-spring system	143
12.2.3	Classes of systems	145
12.2.4	Well-posedness of open-loop systems	146
12.2.5	Distributed controller architectures	148
12.3	Nominal state-feedback distributed backstepping design	148
12.3.1	Global backstepping design	149
12.3.2	Individual cell backstepping design	151
12.3.3	Distributed integrator backstepping	152
12.4	Architecture induced by nominal distributed backstepping design	154
12.4.1	Design of controllers with less interactions	157
12.5	Adaptive state-feedback distributed backstepping design	161
12.5.1	Constant unknown parameters	161
12.5.2	Spatially varying unknown parameters	165
12.6	Dynamical order induced by adaptive distributed backstepping design	167
12.7	Output-feedback distributed backstepping design	168
12.7.1	Nominal output-feedback design	169
12.7.2	Adaptive output-feedback design	171
12.8	Well-posedness of closed-loop systems	174
12.9	An example of distributed backstepping design: mass-spring system	174
12.9.1	Nominal state-feedback design	174
12.9.2	Adaptive state-feedback design	176
12.9.3	Nominal output-feedback design	179
12.9.4	Adaptive output-feedback design	179
12.9.5	Fully decentralized state-feedback design	180
12.10	Summary	180

Bibliography	181
13 Distributed control of vehicular platoons	185
13.1 On the ill-posedness of certain vehicular platoon control problems	186
13.1.1 Optimal control of finite vehicular platoons	186
13.1.2 Optimal control of infinite vehicular platoons	191
13.1.3 Alternative problem formulations	194
13.2 Limitations and tradeoffs in the control of vehicular platoons	199
13.2.1 Lyapunov-based control of vehicular platoons	199
13.2.2 Issues arising in control strategies with uniform convergence rates	201
13.2.3 Design limitations and tradeoffs in vehicular platoons	205
13.2.4 Control without reaching saturation	208
13.3 Summary	209
Bibliography	211
14 Conclusions and future directions	213

List of Figures

2.1	One-dimensional array of identical masses and springs.	8
2.2	Block diagram of system (2.29) in a form suitable for the application of small gain theorem.	18
3.1	Boundary conditions with delta function as input.	24
4.1	Block diagram of system (4.15) with spatially invariant operators \mathcal{A}_1 , \mathcal{B}_1 , \mathcal{B}_2 , and \mathcal{C} , and an X -periodic matrix valued function f	35
4.2	Left plot: $\max(\operatorname{Re}\{\lambda(\mathcal{A})\})$ as a function of α and X for $f(x) := \alpha \cos(\frac{2\pi}{X}x)$, $c_0 = 0.4$, $\rho = 0.4$, and $\Omega = 5$. Right plot: $\max(\operatorname{Re}\{\lambda(\mathcal{A})\})$ as a function of α for $f(x) := \alpha \cos(\frac{2\pi}{X}x)$, $X \approx 1.31$, $c_0 = 0.4$, $\rho = 0.4$, and $\Omega = 5$	39
4.3	The dependence of the \mathcal{H}_∞ norm of system (4.27) with $\{c = 1, q = 0.5\}$ on amplitude and period of spatially periodic feedback (left plot), and period for $\alpha = 15$ (right plot).	42
7.1	Three dimensional plane Poiseuille flow.	55
8.1	Plots of $[\ \mathcal{H}_{rs}\ _2](k_x, k_z)$ in Poiseuille flow with $R = 2000$	68
8.2	Plots of $[\ \mathcal{H}_x\ _2](k_x, k_z)$, $[\ \mathcal{H}_y\ _2](k_x, k_z)$, and $[\ \mathcal{H}_z\ _2](k_x, k_z)$, in Poiseuille flow with $R = 2000$	69
8.3	Plots of $[\ \mathcal{H}_u\ _2](k_x, k_z)$, $[\ \mathcal{H}_v\ _2](k_x, k_z)$, and $[\ \mathcal{H}_w\ _2](k_x, k_z)$, in Poiseuille flow with $R = 2000$	70
8.4	Plot of $[\ \mathcal{H}\ _2](k_x, k_z)$ in Poiseuille flow with $R = 2000$	71
8.5	Plots of $[\ \mathcal{H}\ _\infty](k_x, k_z)$ in Poiseuille flow with $R = 2000$	71
8.6	Maximal singular values of operators $\mathcal{H}(k_x, k_z, \omega)$ (solid), $\mathcal{H}_x(k_x, k_z, \omega)$ (dash-dot), $\mathcal{H}_y(k_x, k_z, \omega)$ (dot), and $\mathcal{H}_z(k_x, k_z, \omega)$ (dash) in Poiseuille flow with $R = 2000$. In all three cases the dependence on the remaining two frequencies is taken away by determining a supremum over them.	72
8.7	Singular values of operator (8.2) at: $(k_x = 0, k_z = 1.62, \omega = 0)$ (left), $(k_x = 0.01, k_z = 1.67, \omega = -0.0066)$ (middle), and $(k_x = 0.1, k_z = 2.12, \omega = -0.066)$ (right), in Poiseuille flow with $R = 2000$	73
8.8	Streamwise velocity (pseudo-color plots), and stream-function (contour plots) perturbation development for largest singular value (left) and second largest singular value (right) of operator (8.2) at $(k_x = 0, k_z = 1.62, \omega = 0)$ (location where the global maximum of $\sigma_{\max}(\mathcal{H}(k_x, k_z, \omega))$ takes place), in Poiseuille flow with $R = 2000$. Red color represents high speed streaks, and blue color represents low speed streaks.	73
8.9	Streamwise velocity and vorticity perturbation development for largest singular value of operator \mathcal{H} at $(k_x = 0.01, k_z = 1.67, \omega = -0.0066)$, in Poiseuille flow with $R = 2000$. High (low) velocity and vorticity regions are respectively represented by red and yellow (green and blue) colors. Isosurfaces of u and ω_x are respectively taken at ± 0.5 and ± 0.1	74
8.10	Streamwise velocity and vorticity perturbation development for second largest singular value of operator \mathcal{H} at $(k_x = 0.01, k_z = 1.67, \omega = -0.0066)$, in Poiseuille flow with $R = 2000$. High (low) velocity and vorticity regions are respectively represented by red and yellow (green and blue) colors. Isosurfaces of both u and ω_x are taken at ± 0.5	75

8.11	Streamwise velocity perturbation development for largest singular value (first row) and second largest singular value (second row) of operator \mathcal{H} at $(k_x = 0.1, k_z = 2.12, \omega = -0.066)$, in Poiseuille flow with $R = 2000$. High speed streaks are represented by red color, and low speed streaks are represented by green color. Isosurfaces are taken at ± 0.5 .	75
8.12	Plots of $[\ \mathcal{H}_x\ _2](k_x, k_z)$, $[\ \mathcal{H}_y\ _2](k_x, k_z)$, and $[\ \mathcal{H}_z\ _2](k_x, k_z)$, in Couette flow with $R = 2000$.	76
8.13	Plots of $[\ \mathcal{H}_u\ _2](k_x, k_z)$, $[\ \mathcal{H}_v\ _2](k_x, k_z)$, and $[\ \mathcal{H}_w\ _2](k_x, k_z)$, in Couette flow with $R = 2000$.	76
8.14	Channel flow turbulent mean velocity profile with $R_\tau = 590$.	77
8.15	Plots of $[\ \mathcal{H}_x\ _2](k_x, k_z)$, $[\ \mathcal{H}_y\ _2](k_x, k_z)$, and $[\ \mathcal{H}_z\ _2](k_x, k_z)$, in turbulent mean velocity profile flow with $R_\tau = 590$.	78
8.16	Plots of $[\ \mathcal{H}_u\ _2](k_x, k_z)$, $[\ \mathcal{H}_v\ _2](k_x, k_z)$, and $[\ \mathcal{H}_w\ _2](k_x, k_z)$, in turbulent mean velocity profile flow with $R_\tau = 590$.	78
8.17	Plots of $[\ \mathcal{H}\ _\infty](k_x, k_z)$ and $[\ \mathcal{H}\ _2](k_x, k_z)$ in Poiseuille flow with $R = 5700$.	79
8.18	Plots of $[\ \mathcal{H}_\alpha\ _\infty](k_x, k_z)$ and $[\ \mathcal{H}_\alpha\ _2](k_x, k_z)$ in Poiseuille flow with $R = 10000$ and $\alpha = 0.0038$.	80
9.1	Block diagram of the streamwise constant LNS system (9.1) with $\Omega := \omega R$.	86
9.2	Plots of the maximal singular values of operators $\bar{\mathcal{H}}_{rs}(\Omega, k_z)$. Nominal-flow-dependent quantities $\varsigma_{uy,1}(\Omega, k_z)$ and $\varsigma_{uz,1}(\Omega, k_z)$ are determined for Couette flow.	87
9.3	Plots of the l and m functions in Theorem 7. Nominal-flow-dependent quantities $m_{uy}(\Omega, k_z)$ and $m_{uz}(\Omega, k_z)$ are determined for Couette flow.	89
9.4	Plots of the l and m functions in Theorem 7 at $\Omega = 0$. Nominal-flow-dependent quantities $m_{uy}(0, k_z)$ and $m_{uz}(0, k_z)$ are determined for Couette flow.	90
9.5	Plots of the l and m functions in Corollary 8. Nominal-flow-dependent quantities $m_y(\Omega, k_z)$ and $m_z(\Omega, k_z)$ are determined for Couette flow.	91
9.6	Plots of the l and m functions in Corollary 9. Nominal-flow-dependent quantity $m_u(\Omega, k_z)$ is determined for Couette flow.	92
9.7	Plots of the l and m functions in Corollary 10. Nominal-flow-dependent quantity $m(\Omega, k_z)$ is determined for Couette flow.	92
9.8	Plots of functions $h_{rs}(k_z)$, $\{r = u, v, w; s = x, y, z\}$, in Theorem 11.	94
9.9	Plots of $f_{rs}(k_z)$, $\{r = u, v, w; s = x, y, z\}$, $g_{uy}(k_z)$, and $g_{uz}(k_z)$. Functions $g_{uy}(k_z)$ and $g_{uz}(k_z)$ are determined for Couette flow.	95
9.10	The k_z -dependence of f_x , f_y , f_z , g_y , and g_z . Expressions for f_x , f_y , and f_z are the same for all channel flows, as demonstrated in § 9.6.2. The terms responsible for the $O(R^3)$ energy amplification are shown in the middle (Couette flow) and right (Poiseuille flow) plots.	96
9.11	The k_z -dependence of f_u , f_v , f_w , and g_u . Expressions for f_u , f_v , and f_w are the same for all channel flows, as demonstrated in § 9.6.2. The terms responsible for the $O(R^3)$ energy amplification are shown in the middle (Couette flow) and right (Poiseuille flow) plots.	97
9.12	The k_z -dependence of f_x , f_y , and f_z for different values of a .	99
9.13	Plots of $g_y(k_z, a)$, and $g_z(k_z, a)$ in Couette flow.	99
9.14	Plots of $\sup_{k_z} g_y(k_z, a)$, $\sup_{k_z} g_z(k_z, a)$, and $\sup_{k_z} g_z(k_z, a) / \sup_{k_z} g_y(k_z, a)$ in Couette flow.	100
10.1	Forcing distribution in the wall-normal direction for $y_0 = -0.9$, and $\varepsilon = 1/2000$.	122
10.2	Plots of $[\ \mathcal{G}_x\ _2](k_z)$, $[\ \mathcal{G}_y\ _2](k_z)$, and $[\ \mathcal{G}_z\ _2](k_z)$ for streamwise constant perturbations. Forcing of the form $d_s = f_{s0}(y)\delta(z, t)$ is introduced, where $f_{s0}(y)$, for every $s = x, y, z$, is shown in Figure 10.1.	123
10.3	Plots of $[\ \mathcal{G}_x\ _2](t)$ (blue), $[\ \mathcal{G}_y\ _2](t)$ (green), and $[\ \mathcal{G}_z\ _2](t)$ (red) for streamwise constant perturbations. Forcing of the form $d_s = f_{s0}(y)\delta(z, t)$ is introduced, where $f_{s0}(y)$, for every $s = x, y, z$, is shown in Figure 10.1.	123
10.4	Streamwise velocity (pseudo-color plots) and stream-function (contour plots) perturbation development for streamwise constant perturbations at: $t = 5\text{s}$ (top left), $t = 20\text{s}$ (top right), $t = 100\text{s}$ (bottom left), and $t = 200\text{s}$ (bottom right). Forcing of the form $d_x = d_y \equiv 0$, $d_z = f_{z0}(y)\delta(z, t)$ is introduced, where $f_{z0}(y)$ is shown in Figure 10.1. Red color represents high speed streak, and blue color represents low speed streak. The vortex between the streaks is counter clockwise rotating.	124

10.5	Plots of $\ \mathcal{G}_x\ _2(k_x, k_z)$, $\ \mathcal{G}_y\ _2(k_x, k_z)$, and $\ \mathcal{G}_z\ _2(k_x, k_z)$. Forcing of the form $d_s = f_{s0}(y)\delta(x, z, t)$ is introduced, where $f_{s0}(y)$, for every $s = x, y, z$, is shown in Figure 10.1.	125
10.6	Streamwise velocity perturbation isosurface plots at: $t = 5 s$ (first row left), $t = 10 s$ (first row right), $t = 15 s$ (second row left), $t = 20 s$ (second row right), $t = 40 s$ (third row left), $t = 80 s$ (third row right), $t = 120 s$ (fourth row left), and $t = 160 s$ (fourth row right). Forcing of the form $d_x = d_y \equiv 0$, $d_z = f_{z0}(y)\delta(x, z, t)$ is introduced, where $f_{z0}(y)$ is shown in Figure 10.1. Red color represents regions of high velocity, and green color represents regions of low velocity. Isosurfaces are taken at $\pm 10^{-3}$	126
10.7	Streamwise velocity perturbation pseudo-color plots in the horizontal plane $y \approx 0.68$ at: $t = 5 s$ (first row left), $t = 10 s$ (first row right), $t = 15 s$ (second row left), $t = 20 s$ (second row right), $t = 40 s$ (third row left), $t = 80 s$ (third row right), $t = 120 s$ (fourth row left), and $t = 160 s$ (fourth row right). Forcing of the form $d_x = d_y \equiv 0$, $d_z = f_{z0}(y)\delta(x, z, t)$ is introduced, where $f_{z0}(y)$ is shown in Figure 10.1. Hot colors represent regions of high velocity, and cold colors represent regions of low velocity.	127
10.8	Streamwise vorticity isosurface plots at: $t = 40 s$ (top left), $t = 80 s$ (top right), $t = 120 s$ (bottom left), and $t = 160 s$ (bottom right). Forcing of the form $d_x = d_y \equiv 0$, $d_z = f_{z0}(y)\delta(x, z, t)$ is introduced, where $f_{z0}(y)$ is shown in Figure 10.1. Yellow color represents regions of high vorticity, and blue color represents regions of low vorticity. Isosurfaces are taken at $\pm 10^{-2}$	128
10.9	Pseudo-color plots of the streamwise velocity (left) and vorticity (right) perturbation profiles in a cross section of the channel at $x \approx 56$ and $t = 160 s$. Forcing of the form $d_x = d_y \equiv 0$, $d_z = f_{z0}(y)\delta(x, z, t)$ is introduced, where $f_{z0}(y)$ is shown in Figure 10.1.	129
10.10	Streamwise velocity perturbation isosurface plot at: $t = 40 s$ (top left), $t = 80 s$ (top right), $t = 120 s$ (bottom left), and $t = 160 s$ (bottom right). Forcing of the form $d_x = d_z \equiv 0$, $d_y = f_{y0}(y)\delta(x, z, t)$ is introduced, where $f_{y0}(y)$ is shown in Figure 10.1. Red color represents regions of high velocity, and green color represents regions of low velocity. Isosurfaces are taken at $\pm 2 \times 10^{-4}$	130
10.11	Streamwise velocity perturbation pseudo-color plots in the horizontal plane $y \approx 0.68$ at: $t = 40 s$ (top left), $t = 80 s$ (top right), $t = 120 s$ (bottom left), and $t = 160 s$ (bottom right). Forcing of the form $d_x = d_z \equiv 0$, $d_y = f_{y0}(y)\delta(x, z, t)$ is introduced, where $f_{y0}(y)$ is shown in Figure 10.1. Hot colors represent regions of high velocity, and cold colors represent regions of low velocity.	131
10.12	Streamwise velocity perturbation isosurface plots at: $t = 40 s$ (top left), $t = 80 s$ (top right), $t = 120 s$ (bottom left), and $t = 160 s$ (bottom right). Forcing of the form $d_y = d_z \equiv 0$, $d_x = f_{x0}(y)\delta(x, z, t)$ is introduced, where $f_{x0}(y)$ is shown in Figure 10.1. Red color represents regions of high velocity, and green color represents regions of low velocity. Isosurfaces are taken at $\pm 2 \times 10^{-4}$	132
10.13	Streamwise velocity perturbation pseudo-color plots in the horizontal plane $y \approx 0.68$ at: $t = 40 s$ (top left), $t = 80 s$ (top right), $t = 120 s$ (bottom left), and $t = 160 s$ (bottom right). Forcing of the form $d_y = d_z \equiv 0$, $d_x = f_{x0}(y)\delta(x, z, t)$ is introduced, where $f_{x0}(y)$ is shown in Figure 10.1. Hot colors represent regions of high velocity, and cold colors represent regions of low velocity.	133
12.1	Mass-spring system.	143
12.2	Graphical illustration of function $f_{2n}(\Psi_1, \Psi_2)$, $n \in \mathbb{Z}$	147
12.3	Distributed controller architectures for centralized, localized (with nearest neighbor interactions), and fully decentralized control strategies.	149
12.4	Graphical illustration of function $p_n(\Psi_1) = p_n(\{\psi_{1,n+2j}\}_{j \in \mathbb{Z}_N})$, $n \in \mathbb{Z}$. The ‘worst case’ nominal distributed backstepping design for system (12.13) with at most $2N$ interactions per plant cell induces at most $4N$ interactions per controller cell.	156
12.5	The ‘worst case’ nominal distributed backstepping design for system (12.13) with at most $2N$ interactions per plant cell induces at most $2mN$ interactions per controller cell.	156

12.6	The architecture of the ‘worst case’ nominal distributed backstepping controller for system (12.30).	157
12.7	Control of system (12.30) with $M = 100$ cells using the ‘worst case’ nominal backstepping controller with $k_1 = k_2 = 1$	158
12.8	Control of system (12.30) with $M = 100$ cells using the nearest neighbor interaction backstepping controller (12.33,12.34,12.35) with $k_1 = k_2 = 1$ and $\kappa = 0.5$	160
12.9	Control of system (12.30) with $M = 100$ cells using the fully decentralized backstepping controller (12.36,12.37) with $k_0 = k_1 = k_2 = 1$ and $\kappa = 0.5$	161
12.10	Controller architectures of mass-spring system.	175
12.11	Finite dimensional mass-spring system.	176
12.12	Simulation results of uncontrolled (first row left) and controlled linear mass-spring system with $N = 100$ masses and $m = k = 1$. The initial state of the system is randomly selected. Control law (12.71) is used with $c_{1n} = c_{2n} = 1$, $\forall n = 1, \dots, N$	176
12.13	Simulation results of a linear mass-spring system with $N = 100$ masses and unknown parameters $m = k = 1$, using centralized controller (12.74) with $\gamma = \beta = c_{1n} = c_{2n} = 1$, $\forall n = 1, \dots, N$, and $\hat{\theta}(0) = \hat{\rho}(0) = 0.5$. The initial state of the mass-spring system is randomly selected.	178
12.14	Simulation results of linear mass-spring system with $N = 100$ masses and unknown parameters $m_n = k_n = 1$, $\forall n = 1, \dots, N$, using control law (12.76) with $\gamma_n = \beta_n = c_{1n} = c_{2n} = 1$, and $\hat{\theta}_n(0) = \hat{\rho}_n(0) = 0.5$, $\forall n = 1, \dots, N$. The initial state of the mass-spring system is randomly selected. We remark that x and v denote states of the error system, that is, $x := \psi_1$, $v := \psi_2$	179
12.15	Simulation results of linear mass-spring system with $N = 100$ masses and $m_n = k_n = 1$, $\forall n = 1, \dots, N$, using output-feedback control law (12.77) with $c_{1n} = c_{2n} = 1$, $d_{1n} = d_{2n} = 0.2$, $l_{1n} = 5$, $l_{2n} = 6$, and $\hat{\psi}_{1n}(0) = \hat{\psi}_{2n}(0) = 0$, $\forall n = 1, \dots, N$. The initial state of the mass-spring system is randomly selected.	180
13.1	Finite platoon of vehicles.	186
13.2	Finite platoon with fictitious lead and follow vehicles.	188
13.3	The minimal (left plot) and maximal eigenvalues (middle plot) of the ARE solution P_M for system (13.2) with performance objective (13.5), and the dominant poles of LQR controlled platoon (13.2,13.5) (right plot) as functions of the number of vehicles for $\{\kappa = 0, q_1 = q_3 = r = 1\}$	188
13.4	Absolute and relative position errors of an LQR controlled string (13.2,13.5) with 20 vehicles (left column) and 50 vehicles (right column), for $\{\kappa = 0, q_1 = q_3 = r = 1\}$. Simulation results are obtained for the following initial condition: $\{\xi_n(0) = \zeta_n(0) = 1, \forall n = \{1, \dots, M\}\}$	189
13.5	The minimal singular values of matrix $D_M(\lambda) := [A^T - \lambda I \ Q^T]^T$ at $\lambda = 0$ for system (13.2) with performance objectives: (13.5) (left plot), (13.6) (middle plot), and (13.7) (right plot) as functions of the number of vehicles for $\{\kappa = 0, q_1 = q_3 = r = 1\}$. These singular values are given in the logarithmic scale.	189
13.6	The minimal (left plot) and maximal eigenvalues (middle plot) of the ARE solution P_M for system (13.3) with performance objective (13.7), and the dominant poles of LQR controlled platoon (13.3,13.7) (right plot) as functions of the number of vehicles for $\kappa = q_1 = q_3 = r = 1$	190
13.7	Relative position errors of LQR controlled system (13.3,13.7) with 20 vehicles (left plot) and 50 vehicles (right plot), for $\kappa = q_1 = q_3 = r = 1$. Simulation results are obtained for the following initial condition: $\{\eta_n(0) = 1, \forall n = \{2, \dots, M\}; \zeta_n(0) = 1, \forall n = \{1, \dots, M\}\}$	190
13.8	Infinite platoon of vehicles.	191
13.9	The spectrum of the closed-loop generator in an LQR controlled spatially invariant string of vehicles (13.8) with performance objective (13.10) and $\{\kappa = 0, q_1 = q_3 = r = 1\}$	193
13.10	An example of a position initial condition for which there is at least one vehicle whose absolute position error does not asymptotically converge to zero when the control strategy of [2] is used.	193

13.11 An example of a position initial condition for which there is at least a pair of vehicles whose relative distance does not asymptotically converge to the desired inter-vehicular spacing L when a control strategy of [1] is used.	194
13.12 The spectrum of the closed-loop generator in an LQR controlled spatially invariant string of vehicles (13.8) with performance objective (13.15) and $\{\kappa = 0, q_1 = q_2 = q_3 = r = 1\}$	195
13.13 The minimal (left plot) and maximal eigenvalues (middle plot) of the ARE solution P_M for system (13.2) with performance objective (13.16), and the dominant poles of LQR controlled platoon (13.2,13.16) (right plot) as functions of the number of vehicles, for $\{\kappa = 0, q_1 = q_2 = q_3 = r = 1\}$	196
13.14 Absolute position errors of an LQR controlled string (13.2,13.16) with 20 vehicles (left plot) and 50 vehicles (right plot), for $\{\kappa = 0, q_1 = q_2 = q_3 = r = 1\}$. Simulation results are obtained for the following initial condition: $\{\xi_n(0) = \zeta_n(0) = 1, \forall n = \{1, \dots, M\}\}$	196
13.15 Semi-infinite platoon of vehicles. The lead vehicle is indexed by zero.	199
13.16 Simulation results of vehicular platoon using control law (13.26a,13.28) with $\alpha = \beta = a = 1$, and $b = 2$. The initial state of the platoon system is given by (13.31) with $N = 50$ and $S = 0.5$	202
13.17 Circular platoon of M vehicles.	203
13.18 Solution of system (13.37,13.38) for initial conditions determined by (13.45) with $N = 50$ and $S_n = 0.5$, for every $n \in \{1, \dots, N\}$. The control gains are determined using (13.46) with $v_{\max} = u_{\max} = 5$, and $\{\varrho_n = 1, \sigma_n = 0.8, \forall n \in \mathbb{N}\}$	207
13.19 Simulation results of platoon with 101 vehicles ($M = 100$) using controller (13.51) with $\alpha_0 = 1, \{\alpha_n = \beta_n = 1, \forall n \in \{1, \dots, M\}\}, \{a_n = 1, b_n = 2, \forall n \in \{0, \dots, M\}\}$. The measured initial condition is given by (13.45) with $N = 50$ and $S_n = 0.5$, for every $n \in \{1, \dots, N\}$, whereas the numbers μ_n and ν_n that determine the actual initial condition are randomly selected.	209

Chapter 1

Introduction

Spatially distributed dynamical systems are encountered in a variety of science and engineering problems. An appropriate framework for considering these systems is that of a spatio-temporal system in which all signals of interest are considered as functions of both temporal and spatial independent variables. Depending on the particular problem, the spatial domain can be either continuous or discrete. In the latter case, the systems under study are usually referred to as the systems on lattices. Typically, systems on continuous spatial domains are described by Partial Integro-Differential Equations (P(I)DEs), whereas systems on lattices can be modelled by a finite or infinite number of coupled Ordinary Differential Equations (ODEs). This coupling can be introduced by both physical interactions between different subsystems and by a particular control objective that the designer wants to accomplish. We will discuss both these situations in this dissertation. Moreover, systems on lattices can be obtained by the appropriate spatial discretization of P(I)DEs. Standard examples of systems on continuous spatial domains include: diffusion and wave equations, Maxwell equations, Euler and Navier-Stokes equations, Burgers equation, Korteweg-de Vries (KdV) equation, and Schrödinger equation. On the other hand, systems on lattices can range from the macroscopic—such as cross directional control in the process industry, vehicular platoons, Unmanned Aerial Vehicles (UAVs) formations, and satellite constellations—to the microscopic, such as arrays of micro-mirrors or micro-cantilevers.

Significant potential for research on spatially distributed systems is due to the field of Micro-Electro-Mechanical Systems (MEMS) where the fabrication of large arrays of sensors and actuators is now both feasible and economical. It is widely recognized that one of the next frontiers in this area is the system-level design of such MEMS, including the integration of distributed feedback control and estimation. The key design issues in the control of these systems are architectural such as the choice of localized versus centralized control.

The main topics of this dissertation are modeling, analysis, and control of spatially distributed dynamical systems. We are interested in the development of theoretical methods for the analysis and design of these systems, and the application of these methods to important physical and engineering problems. All theoretical tools that we develop are applicable to classes of systems characterized by their structural properties. We exploit these structural properties and provide non-conservative results.

Some of the problems that we consider are:

- Modeling and analysis of transition and turbulence in channel flows.
- Explicit determination of frequency responses for a class of spatially distributed systems.
- Internal and input-output properties of PDEs with periodic coefficients.
- Architectural issues in distributed control of nonlinear systems on lattices.
- Ill-posedness and peaking in the control of vehicular platoons.

The motivation for considering these problems stems from engineering practice. During my studies, I discovered that examining physical problems from different viewpoints often leads to new and exciting questions

regarding analysis and control. On the other hand, theoretical methods that we develop in this dissertation are used to provide guidelines for the design of simpler, more efficient, and more reliable systems.

1.1 Organization of the dissertation

This dissertation contains three parts. At the end of every part there is a chapter devoted to concluding remarks and open problems for future research. Each chapter contains Bibliography at its end.

Part I is devoted to the distributed systems theory, and it contains four chapters. In Chapter 2, we provide system theoretic preliminaries, and give a background material on analysis of spatially distributed linear systems with input and system uncertainty. In Chapter 3, instead of usual finite dimensional approximations of the underlying operators, we derive an explicit formula for the Hilbert–Schmidt norm of the frequency response operator for a class of P(I)DEs. The application of this formula is illustrated on two examples: a one-dimensional diffusion equation, and a system that describes the dynamics of velocity fluctuations in channel fluid flows. In Chapter 4, we develop tools for analysis of stability and input-output system norms of P(I)DEs with spatially periodic coefficients. For this class of systems, we introduce the notion of parametric resonance and provide examples of physical systems in which parametric resonance takes place. In Chapter 5, we give some concluding remarks on Part I, and discuss future research directions.

Part II contains six chapters. In these chapters we use system theoretic approach to model and analyze the transition and turbulence in plane channel flows. In Chapter 6, we provide a background material on the problem of transition to turbulence in wall bounded shear flows, and formulate basic theoretical problems. In Chapter 7, we develop an evolution model of the Linearized Navier-Stokes (LNS) equations subject to body forces that model external excitations. We also provide certain mathematical considerations required for the precise definition of the underlying operators in the LNS equations. In Chapter 8, we study the LNS equations in plane channel flows from an input-output point of view by analyzing their spatio-temporal frequency responses. We utilize componentwise input-output analysis to reveal distinct resonant mechanisms for subcritical transition. In Chapter 9, we derive several analytical expressions to clarify the relative rates of amplification from different forcing directions to velocity field components, as well as their dependence on the Reynolds number (R). These derivations are obtained for streamwise independent perturbations. In Chapter 10, we present various portions of the spatio-temporal impulse responses of the LNS equations in subcritical Poiseuille flow with $R = 2000$. We illustrate that the spatio-temporal impulse responses of the LNS equations contain many qualitative features of early stages of turbulent spots. Finally, in Chapter 11, we conclude Part II and remark on open research problems.

Part III considers distributed control of systems on lattices. This part contains three chapters. In Chapter 12, we first give a background material on systems on lattices and distributed control of thereof. We then utilize backstepping as a tool for nominal and adaptive, state and output-feedback distributed control of systems on lattices. We discuss architecture induced by distributed backstepping design and quantify the number of control induced interactions. We demonstrate that backstepping yields distributed controllers with inherent degree of spatial localization, and that there is a strong similarity between controller and plant architectures. In Chapter 13, we study distributed control of vehicular platoons. We revisit several widely cited results in this area and show that they are inherently ill-posed. We also remark on some fundamental limitations and tradeoffs in the control of vehicular platoons. In Chapter 14, we close Part III with a brief summary of our major results, and comment on the ongoing and future research directions.

1.2 Contributions of the dissertation

The most important contributions of this dissertation are given below.

Part I

Explicit formula for the Hilbert–Schmidt norm of the frequency response operator. Instead of usual finite dimensional approximations of spatial operators, we derived an *explicit formula* for the Hilbert–Schmidt norm (i.e., the power spectral density) of the frequency response operator. This is done for a class

of P(I)DEs in which a spatial independent variable belongs to a finite interval. The formula only involves finite dimensional computations with matrices whose dimension is at most four times larger than the order of the underlying generators. For example, for a heat equation, the largest matrix at any temporal frequency belongs to $\mathbb{C}^{8 \times 8}$. Thus, the developed procedure avoids the need for spatial discretization and provides an exact reduction of an infinite dimensional problem to a finite dimensional problem.

Stability and system norms of PDEs with periodic coefficients. We developed a spatio-temporal lifting technique similar to the temporal lifting technique for linear periodic ODEs. This technique provides for a strong equivalence between spatially periodic distributed systems defined on a continuous spatial domain with spatially invariant systems defined on a discrete lattice. For the purpose of stability characterization, the lifting technique is equivalent to the more widely used Floquet analysis of periodic PDEs. However, Floquet analysis does not easily lend itself to the computation of system norms and sensitivities. We showed how the lifting technique can be utilized to ascertain both the spectrum of the generating operator and the \mathcal{H}_∞ and \mathcal{H}_2 norms of spatially distributed systems.

Parametric resonance in PDEs with spatially periodic coefficients. Stability properties of certain Linear Time Invariant (LTI) systems can be changed by connecting them in feedback with temporally periodic gains. Depending on the relation between the period of the time varying gain and the dominant modes of the LTI system, the overall system may be stabilized or destabilized. This phenomenon is usually referred to as *parametric resonance*. An example of system in which parametric resonance takes place is given by the Mathieu equation. We investigated similar parametric resonance mechanisms for distributed systems described by PDEs with spatially periodic coefficients. Furthermore, we provided physically relevant examples that demonstrate how internal and input-output properties of spatially invariant PDEs can be altered in the presence of spatially periodic feedback terms.

Part II

Model that rigorously accounts for uncertain body forces. We developed an evolution model of the LNS equations subject to body forces that model external excitations in three spatial directions. The LNS equations with inputs were previously studied, but with an important difference: forcing was introduced directly in the evolution model. Thus, the interpretation of forcing in this formulation was not clear. In our setup, the forcing is first introduced in the basic LNS equations, and then the forced LNS equations are transformed to the evolution model. This results in a more transparent interpretation of the excitations as body forces, and allows for a detailed analysis of the relative effects of polarized forces.

Componentwise input-output analysis of transition and turbulence. The analysis of dynamical systems with inputs has a long history in circuit theory, controls, communications, and signal processing. In this analysis, it is convenient to express dynamical systems as input-output ‘blocks’ that can be connected together in a variety of cascade, series, and feedback arrangements. The utility of this approach is twofold. First, it greatly facilitates engineering analysis and design of complex systems made up of sub-blocks that are easier to characterize. Second, it allows for modeling dynamical inputs which are unmeasurable or uncertain. These include stochastic or deterministic uncertain signals such as noise or uncertain forcing that are inevitably present in most physical systems.

We initiated use of componentwise input-output framework for analysis of transition and turbulence. This framework uncovers several amplification mechanisms for subcritical transition. These mechanisms are responsible for creation of streamwise vortices and streaks, oblique waves, and Tollmien-Schlichting (TS) waves. Using componentwise spatio-temporal frequency responses we explained—for the first time—TS waves, oblique waves, and streamwise vortices and streaks as input-output resonances. For subcritical flows, we demonstrated that the streamwise elongated structures are most amplified by the system’s dynamics, followed by the oblique perturbations, followed by the TS waves.

Quantification of effectiveness (energy content) of forcing (velocity) components. We showed that for channel-wide external excitations, the spanwise (d_z) and wall-normal (d_y) forces have the strongest influence on the velocity field. The impact of these forces is most powerful on the streamwise velocity component (u). For the streamwise constant perturbations we demonstrated analytically that the frequency

responses from d_z and d_y to u scale *quadratically* with the Reynolds number. On the other hand, the frequency responses from all other inputs to other velocity outputs scale at most *linearly* with R (also demonstrated analytically). Furthermore, we analytically established that for near-wall external excitations, d_z has, by far, the strongest effect on the velocity field. This is consistent with recent *numerical* work on channel flow turbulence control using the Lorentz force, where it was concluded that the spanwise forcing confined within the viscous sub-layer had the strongest effect in suppressing turbulence.

Unstable vs. non-normal modes in supercritical flows. We demonstrated the importance of non-modal effects in supercritical channel flows. In these flows, unstable modes grow relatively slowly, and we showed that when compared over long but finite times, non-normal modes in the form of streamwise elongated structures prevail TS modes. Our analysis method is based on computing exponentially discounted input-output system gains. From a physical perspective this type of analysis amounts to accounting for the finite time phenomena rather than the asymptotic phenomena of infinite time limits. We illustrated many qualitative similarities between subcritical and supercritical channel flows when the latter are analyzed with the appropriate exponential discounts on their energies. If this type of analysis is performed than, effectively, it turns out that the streamwise elongated flow structures contribute most to the perturbation energy for both these flows.

Spatio-temporal impulse responses of the LNS equations. We determined the spatio-temporal impulse responses of the LNS equations in subcritical Poiseuille flow with $R = 2000$. We established that the LNS equations exhibit rich and complex structures hitherto unseen by other linear analysis methods. These structures are ubiquitous in both transitional channel and boundary layer flows. For example, the observed results bear remarkable qualitative resemblance to the early stages of turbulent spots, in terms of the ‘arrow-head’ shape, the streaky structures, and the cross-contamination phenomena as the spots grow. This resemblance is only qualitative, as other features of turbulent spots are not represented in the responses we compute. As an argument for this kind of impulse response analysis of the linearized equations, we note that such structures are practically impossible to observe from a purely modal analysis of the LNS equations.

Part III

Architecture induced by backstepping distributed design. An important problem in the distributed control of large-scale and infinite dimensional systems on lattices is related to the choice of the appropriate controller architecture. We utilized backstepping as a tool for distributed design, and demonstrated that nominal backstepping always yields localized distributed controllers whose architecture can be significantly altered by different choices of stabilizing functions during the recursive design. For the ‘worst case’ situation in which all interactions are cancelled at each step of backstepping we quantified the number of control induced interactions necessary to achieve the desired objective. This number is determined by two factors: the number of interactions per plant cell, and the largest number of integrators that separate interactions from control inputs. When the matching condition is satisfied the control problem can always be posed in such a way to yield controllers of the same architecture as the original plant. Furthermore, the global backstepping design can be utilized to obtain distributed controllers with less interactions. This is done by identification of beneficial interactions and feedback domination of harmful interaction.

The only situation which results in a centralized controller is for plants with constant parametric uncertainties when we started our design with one estimate per unknown parameter. We demonstrated that this can be overcome by the ‘over-parameterization’ of the unknown constant parameters. As a result, each control cell has its own dynamical estimator of unknown parameters which avoids the centralized architecture. The order of this estimator is equal to the number of unknown parameters. Similar ideas were also employed for adaptive control of systems with spatially varying parametric uncertainties. For this class of systems, we quantified the dynamical order of each control cell induced by backstepping design. In particular, for plants with interactions and unknown parameters ‘one integrator away’ from the control input, we showed that this dynamical order scales linearly with the number of interactions per plant cell.

Ill-posedness in vehicular platoons. We exhibited shortcomings of several widely cited solutions to the LQR problem for large scale vehicular platoons. By considering infinite platoons as the limit of the large-but-finite platoons, we employed spatially invariant theory to show *analytically* how these formulations lack

stabilizability or detectability. We argued that the infinite platoons represent useful abstractions of large-but-finite platoons: they explain the almost loss of stabilizability or detectability in the large-but-finite problems, and the arbitrarily slowing rate of convergence towards desired formation observed in numerical studies of finite platoons of increasing sizes. Furthermore, using the infinite platoon formulation, we demonstrated how incorporating absolute position errors in the performance objective alleviates these difficulties and provides uniformly bounded rates of convergence.

Peaking in vehicular platoons. We showed that imposing a uniform rate of convergence for all vehicles towards their desired trajectories may generate peaking in both velocity and control. In other words, we demonstrated that in very large platoons the initial deviations of vehicles from their desired trajectories should be considered when selecting control gains. We established explicit constraints on these gains—for any given set of initial conditions—to assure the desired quality of position transients without magnitude and rate peaking. These requirements were used to generate the trajectories around which the states of the platoon system were driven towards their desired values without the excessive use of control effort.

Part I

Distributed systems theory

Chapter 2

Control theoretic preliminaries

The so-called ‘evolution form’ of a linear spatially distributed system with inputs together with an output equation is given by

$$\partial_t \psi(t) = \mathcal{A}\psi(t) + \mathcal{B}\mathbf{d}(t), \quad (2.1a)$$

$$\phi(t) = \mathcal{C}\psi(t), \quad (2.1b)$$

where $\psi(t)$ and $\phi(t)$ are elements of a Hilbert (or Banach)¹ space, \mathcal{A} , \mathcal{B} , and \mathcal{C} are certain operators (for example, partial differential and/or integral operators), and $\mathbf{d}(t)$ is an excitation input. The reason for writing the equations in the above form is to regard the vector valued function ψ as the ‘state’ of the system (from which any other quantity can be computed at a given point in time), \mathbf{d} as an input, and ϕ as an output. This is the so-called *state-space* form of driven dynamical systems common in the Dynamics and Controls literature [2]. This ‘universal’ form is a useful framework for analyzing linear dynamical systems. For example, under suitable conditions, the stability properties of the above equation are determined by the spectrum of the operator \mathcal{A} , and input-output properties are determined by the ‘compressed resolvent’ or ‘transfer function’ $\mathcal{H}(s) := \mathcal{C}(sI - \mathcal{A})^{-1}\mathcal{B}$.

We illustrate with two examples how state-space representation of spatially distributed systems can be obtained. The externally excited wave equation

$$\partial_{tt}\phi(x,t) = \partial_{xx}\phi(x,t) + d(x,t),$$

can be put in form (2.1) with

$$\mathcal{A} := \begin{bmatrix} 0 & I \\ \partial_{xx} & 0 \end{bmatrix}, \quad \mathcal{B} := \begin{bmatrix} 0 \\ I \end{bmatrix}, \quad \mathcal{C} := \begin{bmatrix} I & 0 \end{bmatrix},$$

by defining $\psi_1 := \phi$, $\psi_2 := \partial_t\phi$, and $\psi := [\psi_1 \ \psi_2]^T$. In this case the underlying state-space is a space of spatially distributed functions, and operator \mathcal{A} represent a one-dimensional spatial differential operator that acts on ψ . To precisely characterize operator \mathcal{A} we need to incorporate the relevant boundary conditions (that we do not specify here) in the description of its domain. This point of view follows from treating the time axis in a fundamentally different manner than the spatial axes, and it implies temporal causality.

The second example is given by a one-dimensional array of identical masses and springs shown in Figure 2.1. For simplicity, all masses and spring constants are normalized to unity.

If the restoring forces are modelled as linear functions of displacements, the dynamics of the n -th mass are given by

$$\ddot{x}_n = x_{n-1} - 2x_n + x_{n+1} + d_n, \quad n \in \mathbb{Z}, \quad (2.2)$$

where x_n represents the displacement from a reference position of the n -th mass, and d_n is the external force

¹A Banach space is a complete vector space with a norm. A Hilbert space is a Banach space with an inner product.

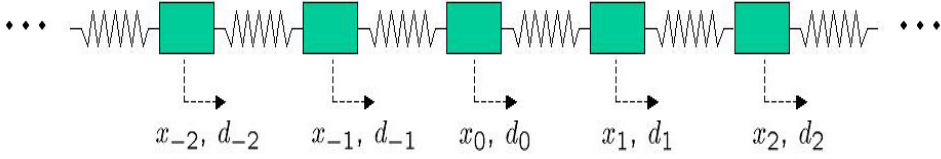


Figure 2.1: One-dimensional array of identical masses and springs.

(for example, control) applied on the n -th mass. This system represent an example of systems on lattices in which interactions between different subsystems originate because of physical interconnections between them. Its mathematical representation can be rewritten in form (2.1) with

$$\mathcal{A} := \begin{bmatrix} 0 & I \\ A_{21} & 0 \end{bmatrix}, \quad \mathcal{B} := \begin{bmatrix} 0 \\ I \end{bmatrix}, \quad \mathcal{C} := [I \ 0],$$

where A_{21} represents the bi-infinite Toeplitz matrix with the elements on the main diagonal equal to -2 , and the elements on the first upper and lower diagonals equal to 1 . The system's state, $\psi^T := [\psi_1^T \ \psi_2^T]$, consists of two parts: infinite vectors ψ_1 and ψ_2 respectively denote the positions and velocities of all masses, that is, $\psi_1 := \{x_n\}_{n \in \mathbb{Z}}$ and $\psi_2 := \{\dot{x}_n\}_{n \in \mathbb{Z}}$. Similarly, the input and output vectors are given by: $\mathbf{d} := \{d_n\}_{n \in \mathbb{Z}}$ and $\phi := \{x_n\}_{n \in \mathbb{Z}}$. Therefore, the dynamics of the entire mass-spring system can be considered as the abstract evolution equation either on a Hilbert space of square summable sequences $\mathbb{H} := l_2 \times l_2$, or on a Banach space of bounded sequences $\mathbb{B} := l_\infty \times l_\infty$.

At first the evolution form of the equations might seem as an unnecessarily abstract way of representing the dynamics of spatially distributed systems. It is however a very useful point of view that serves to unify results from a variety of disciplines. More importantly, one can leverage intuition gained from finite dimensional systems to understand the dynamics of infinite dimensional systems. For example, when \mathcal{A} is a matrix, asymptotic stability of (2.1a) is equivalent to all of its eigenvalues having negative real parts. Under some technical conditions in the infinite dimensional case, asymptotic stability is equivalent to the spectrum of \mathcal{A} being in the open left-half of the complex plane. There are examples where the latter statement is false. Such examples are sometimes used in the literature [2–5] to emphasize the distinction between finite and infinite dimensional systems. We instead choose to emphasize and leverage the similarities, rather than the differences. We will state conditions under which the analogies between finite and infinite dimensional systems hold, and we will see that for all the physical examples we consider in this dissertation, this analogy does indeed hold.

We note that we will often employ recently developed theory for spatially invariant linear systems to study the dynamical properties of spatially distributed systems. The spatial invariance should be regarded as the analogue to time invariance for spatio-temporal systems, and it implies that there is a notion of translation in some spatial coordinates, with respect to which the plant dynamics are invariant. For this class of problems, the properties (e.g., stabilizability, detectability, stability) of infinite dimensional systems are precisely determined by the respective properties of parameterized families of finite dimensional systems. A parameterized family of finite dimensional systems is obtained from an infinite dimensional spatially invariant system by the application of the appropriate general Fourier transform: classical Fourier transform, Fourier series, \mathcal{Z} -transform, and discrete Fourier transform. For example, an infinite dimensional spatially invariant system is stabilizable if and only if its finite dimensional counterpart is stabilizable for each value of frequency parameter κ . Furthermore, optimal controllers (in a variety of norms) for spatially invariant plants inherit this spatially invariant structure. It was also established that optimal controllers with quadratic performance objectives (such as LQR, \mathcal{H}_2 , and \mathcal{H}_∞) have an inherent degree of spatial localization. Without going into further detail, we refer the reader to [6] and references therein for a background material on analysis and design tools for spatially invariant systems.

Our presentation is organized as follows: in § 2.1, we describe a systematic procedure for obtaining equations in the evolution form from a linear system with static-in-time constraints. In § 2.2, we describe the tools for analysis of spatially distributed linear dynamical systems with input and system uncertainty.

2.1 Equations in evolution form

The evolution form of a linear spatially distributed system with inputs is given by (2.1a). In this section, we describe a systematic procedure for deriving equations in evolution form from linear systems with static-in-time constraints. This procedure is applied in § 7.1.1 to the linearized Navier-Stokes equations to point out the many possibilities for using different combinations of velocity and vorticity fields to encode the state of the system.

The general situation is as follows: consider an equation of the form

$$\partial_t \varphi = \bar{\mathcal{A}}\varphi - \bar{\mathcal{B}}p + \mathbf{d}, \quad (2.3)$$

subject to a static-in-time constraint

$$\bar{\mathcal{D}}\varphi = 0, \quad (2.4)$$

where $\bar{\mathcal{A}}$, $\bar{\mathcal{B}}$, and $\bar{\mathcal{D}}$ are linear time invariant operators between Hilbert (or Banach) spaces, \mathbf{d} is a given external excitation, and φ and p are the fields of interest determined from the solution of the above equations. Suppose that we initially regard the state of the system as determined by the vector field $[\varphi \ p]^T$. The constraint (2.4) means that the φ component of the state evolves in the linear subspace $\mathcal{N}(\bar{\mathcal{D}})$ (the null space of $\bar{\mathcal{D}}$), and that the field p has to adjust itself to insure that $\partial_t \varphi$ remains in that subspace. Hence, a minimal number of fields necessary for parameterization of the system's state is determined by the number of fields required to span the subspace $\mathcal{N}(\bar{\mathcal{D}})$. Typically, the number of fields for a minimal state is equal to the difference between the number of fields appearing in φ and the number of constraints in equation (2.4).

The field p is determined by the requirement that $\partial_t \varphi(t) \in \mathcal{N}(\bar{\mathcal{D}})$, i.e. for any t , $\bar{\mathcal{D}}\partial_t \varphi(t) = 0$. Using (2.3), this implies

$$\bar{\mathcal{D}}\partial_t \varphi = \bar{\mathcal{D}}\bar{\mathcal{A}}\varphi - \bar{\mathcal{D}}\bar{\mathcal{B}}p + \bar{\mathcal{D}}\mathbf{d} = 0 \quad \Rightarrow \quad \bar{\mathcal{D}}\bar{\mathcal{B}}p = \bar{\mathcal{D}}\bar{\mathcal{A}}\varphi + \bar{\mathcal{D}}\mathbf{d}.$$

If the operator $\bar{\mathcal{D}}\bar{\mathcal{B}}$ has a well-defined inverse, then there always exists field p that solves equations (2.3,2.4). Furthermore, p is uniquely determined from φ and \mathbf{d} by

$$p = (\bar{\mathcal{D}}\bar{\mathcal{B}})^{-1}\bar{\mathcal{D}}\bar{\mathcal{A}}\varphi + (\bar{\mathcal{D}}\bar{\mathcal{B}})^{-1}\bar{\mathcal{D}}\mathbf{d}. \quad (2.5)$$

Substitution of this expression in equation (2.3) yields

$$\partial_t \varphi = (I - \bar{\mathcal{B}}(\bar{\mathcal{D}}\bar{\mathcal{B}})^{-1}\bar{\mathcal{D}})\bar{\mathcal{A}}\varphi + (I - \bar{\mathcal{B}}(\bar{\mathcal{D}}\bar{\mathcal{B}})^{-1}\bar{\mathcal{D}})\mathbf{d}. \quad (2.6)$$

We note that in this last equation, if the initial condition is such that $\bar{\mathcal{D}}\varphi(0) = 0$, then by construction we are guaranteed that $\bar{\mathcal{D}}\varphi(t) = 0$ for all $t \geq 0$. Equation (2.6) is in evolution form. However, since the state φ evolves in a proper subspace $\mathcal{N}(\bar{\mathcal{D}})$, it is possible to define a state of lower ‘dimension’ than φ .

We now describe the general construction of a minimal state-space representation. This procedure requires finding an operator \mathcal{K} with the property that its range space $\mathcal{R}(\mathcal{K}) = \mathcal{N}(\bar{\mathcal{D}})$. In other words, for any φ such that $\bar{\mathcal{D}}\varphi = 0$, there exists a vector field ψ such that

$$\varphi = \mathcal{K}\psi, \quad (2.7)$$

which also implies $\bar{\mathcal{D}}\mathcal{K} = 0$. We then say that the subspace $\mathcal{N}(\bar{\mathcal{D}})$ is parameterized by field ψ . Furthermore, we demand that this parameterization be minimal in the sense that \mathcal{K} have a left inverse \mathcal{K}^{-L} , i.e. $\mathcal{K}^{-L}\mathcal{K} = I$. Thus, the parameterizing fields can be obtained by

$$\psi = \mathcal{K}^{-L}\varphi, \quad \text{if} \quad \bar{\mathcal{D}}\varphi = 0.$$

Substituting $\mathcal{K}\psi$ for φ in equation (2.6) and operating on both sides by \mathcal{K}^{-L} , we obtain the evolution

equation for ψ as

$$\begin{aligned}\partial_t \psi &= \mathcal{K}^{-L}(\bar{\mathcal{A}} - \bar{\mathcal{B}}(\bar{\mathcal{D}}\bar{\mathcal{B}})^{-1}\bar{\mathcal{D}}\bar{\mathcal{A}})\mathcal{K} \psi + \mathcal{K}^{-L}(I - \bar{\mathcal{B}}(\bar{\mathcal{D}}\bar{\mathcal{B}})^{-1}\bar{\mathcal{D}}) \mathbf{d} \\ &=: \mathcal{A} \psi + \mathcal{B} \mathbf{d}.\end{aligned}\quad (2.8)$$

Note that if this equation is solved forward in time, for any $t \geq 0$, the original fields $\varphi(t)$ and $p(t)$ can be found from $\psi(t)$ by solving equations (2.7) and (2.5). These equations involve only time-invariant operators.

Now, the construction of a \mathcal{K} that has a left inverse, and is such that $\bar{\mathcal{D}}\mathcal{K} = 0$, is not always obvious. However, a simple scheme can be devised by expressing these requirements in a ‘block operator’ decomposition as follows:

$$\begin{bmatrix} \bar{\mathcal{D}} \\ \mathcal{K}^{-L} \end{bmatrix} \mathcal{K} = \begin{bmatrix} 0 \\ I \end{bmatrix}.$$

In the typical case that $\bar{\mathcal{D}}$ has a right inverse $\bar{\mathcal{D}}^{-R}$, these requirements are equivalent to

$$\begin{bmatrix} \bar{\mathcal{D}} \\ \mathcal{K}^{-L} \end{bmatrix} \begin{bmatrix} \bar{\mathcal{D}}^{-R} & \mathcal{K} \end{bmatrix} = \begin{bmatrix} I & 0 \\ 0 & I \end{bmatrix}.$$

Thus given $\bar{\mathcal{D}}$, if one can find an operator \mathcal{K}^{-L} such that the operator $\begin{bmatrix} \bar{\mathcal{D}} \\ \mathcal{K}^{-L} \end{bmatrix}$ is invertible, then its inverse can be partitioned into $\begin{bmatrix} \bar{\mathcal{D}}^{-R} & \mathcal{K} \end{bmatrix}$, and both \mathcal{K} and \mathcal{K}^{-L} are obtained.

2.2 Dynamical systems with input and system uncertainty

In this section, we discuss the main features of the input-output analysis of spatially distributed linear dynamical systems. The results presented here have a fairly general character and can be applied to study the input-output properties of

$$\partial_t \psi(y, t, \kappa) = [\mathcal{A}(\kappa)\psi(y, t, \kappa)](y) + [\mathcal{B}(\kappa)\mathbf{d}(t, \kappa)](y), \quad (2.9a)$$

$$\phi(y, t, \kappa) = [\mathcal{C}(\kappa)\psi(y, t, \kappa)](y), \quad (2.9b)$$

where $\kappa := [\kappa_1 \cdots \kappa_d]^*$ represents the vector of frequencies corresponding to the spatial coordinates $\xi := [\xi_1 \cdots \xi_d]^*$ that belong to a certain group \mathbb{G} [6]. On the other hand, $y := [y_1 \cdots y_q]^*$ denotes the additional spatial coordinates varying in set \mathbb{P} without any group structure (that is, the spatial coordinates in which the underlying operators are not translation invariant). We note that system (2.9) represents the transformed version of

$$\partial_t \psi(y, t, \xi) = [\mathcal{A}\psi(t)](y, \xi) + [\mathcal{B}\mathbf{d}(t)](y, \xi), \quad (2.10a)$$

$$\phi(y, t, \xi) = [\mathcal{C}\psi(t)](y, \xi), \quad (2.10b)$$

obtained by the application of the Fourier transform in the spatially invariant directions. For notational convenience, we use the same notation to denote the field $\psi(y, t, \xi)$ and its spatial Fourier transform $\psi(y, t, \kappa)$. The distinction between the two should be clear from the context.

For example, a two-dimensional diffusion equation defined on the spatial domain $\mathbb{R} \times [-1, 1]$

$$\begin{aligned}\partial_t \phi(y, t, x) &= \partial_{xx}\phi(y, t, x) + \partial_{yy}\phi(y, t, x) + d(y, t, x), \\ \phi(\pm 1, t, x) &= 0, \quad t \geq 0, \quad x \in \mathbb{R}, \quad y \in [-1, 1],\end{aligned}$$

is translation invariant in the x direction, but it is not translation invariant in the y direction. The Fourier representation of this system is given by (2.9) with $\{\mathcal{A}(\kappa) := \partial_{yy} - \kappa^2, \mathcal{B}(\kappa) := I, \mathcal{C}(\kappa) := I, \kappa \in \mathbb{R}\}$. The underlying state-space is a Hilbert space of square integrable functions $L_2[-1, 1]$, and the domain of operator $\mathcal{A}(\kappa)$ for any given κ is readily determined from the Dirichlet boundary conditions on ϕ (see, for example, [2]).

Our presentation is organized as follows: in § 2.2.1, we introduce notions of *spatio-temporal impulse and*

frequency responses, and make some remarks about their utility in understanding behavior of linear systems. In § 2.2.2, we discuss different quantities that can be determined based on impulse and frequency responses, and define the notion of input-output system norms. In § 2.2.6, we illustrate that the problem of robust stability can be recast into the input-output framework and addressed using input-output tools.

2.2.1 Spatio-temporal impulse and frequency responses

We introduce the notion of the spatio-temporal frequency response as follows: let the input to (2.10) be a field that is harmonic in the t and ξ variables, that is of the form

$$\mathbf{d}(y, t, \xi) = \bar{\mathbf{d}}(y) e^{i(\bar{\kappa} \cdot \xi + \bar{\omega}t)},$$

where $\bar{\mathbf{d}}(y)$ is some function of y , and $\bar{\kappa} \cdot \xi := \bar{\kappa}^T \xi$. Assuming stability of the generator \mathcal{A} , it can then be shown that the output is also harmonic in the same variables and is determined by

$$\phi(y, t, \xi) = [\mathcal{H}(\bar{\omega}, \bar{\kappa}) \bar{\mathbf{d}}](y) e^{i(\bar{\kappa} \cdot \xi + \bar{\omega}t)}, \quad (2.11)$$

where the operator $\mathcal{H}(\omega, \kappa)$ is given by

$$\mathcal{H}(\omega, \kappa) = \mathcal{C}(\kappa)(i\omega I - \mathcal{A}(\kappa))^{-1} \mathcal{B}(\kappa). \quad (2.12)$$

There are two possible interpretations of this. If this harmonic input is assumed to act over the time interval $-\infty < t < \infty$, then initial states do not play a role, and the output is precisely given by (2.11). If on the other hand the harmonic input is assumed to act over $0 \leq t < \infty$ with zero initial state ($\psi(y, 0, \xi) = 0$), then the output limits to (2.11) as transients asymptotically die out (due to stability) in the ‘steady-state’ (that is, as $t \rightarrow \infty$).

Note that for each (ω, κ) , $\mathcal{H}(\omega, \kappa)$ is an operator in y . The operator-valued function $\mathcal{H}(\omega, \kappa)$ in (2.12) is called the spatio-temporal frequency response of system (2.9). It is a function of temporal frequency ω and vector of spatial frequencies κ . Another interpretation of this function is that it maps the Fourier transform of the input to the Fourier transform of the output, that is

$$\begin{aligned} \phi(y, \omega, \kappa) &= [\mathcal{H}(\omega, \kappa) \mathbf{d}(\omega, \kappa)](y) \\ &= \int_{\mathbb{P}} [\mathcal{H}(\omega, \kappa)](y, \eta) \mathbf{d}(\eta, \omega, \kappa) d\eta, \end{aligned} \quad (2.13)$$

where by an abuse of notation we use the symbol $[\mathcal{H}(\omega, \kappa)](y, \eta)$ to denote the kernel function representing the operator $\mathcal{H}(\omega, \kappa)$.

On the other hand, the spatio-temporal impulse response of system (2.9) is determined by

$$\mathcal{H}(t, \kappa) = \mathcal{C}(\kappa) e^{\mathcal{A}(\kappa)t} \mathcal{B}(\kappa), \quad (2.14)$$

where $e^{\mathcal{A}(\kappa)t}$ denotes the symbol for the operator semigroup generated by $\mathcal{A}(\kappa)$ [2]. Clearly, (2.14) represents an inverse temporal Fourier transform of (2.12). The terminology for the spatio-temporal impulse response is due to the fact that the kernel representation $[\mathcal{H}(t, \kappa)](y, y_0)$ of operator $\mathcal{H}(t, \kappa)$ represents the solution of system (2.9) to a spatio-temporal impulsive input function $\delta(y - y_0, t)$. The response to any other forcing field $\mathbf{d}(y, t, \kappa)$ is then given by

$$\phi(y, t, \kappa) = \int_{\mathbb{P}} \int_0^\infty [\mathcal{H}(t - \tau, \kappa)](y, \eta) \mathbf{d}(\eta, \tau, \kappa) d\tau d\eta. \quad (2.15)$$

The response in the physical space $\phi(y, t, \xi)$ can be obtained by applying the inverse spatial Fourier transform on (2.15), which results into

$$\phi(y, t, \xi) = \int_{\mathbb{G}} \int_{\mathbb{P}} \int_0^\infty \mathcal{H}(y, \eta, t - \tau, \xi - \zeta) \mathbf{d}(\eta, \tau, \zeta) d\tau d\eta d\zeta.$$

Clearly, function $\mathcal{H}(y, y_0, t, \xi)$ represents the solution of system (2.10) to $\mathbf{d}(y, t, \xi) := \delta(y - y_0, t, \xi)$. Thus, the response to any forcing function in the physical space can be obtained as the superposition of a spatially and temporally shifted family of impulse responses.

To recap: given a particular spatio-temporal frequency response, there is a unique corresponding spatio-temporal impulse response that can be derived from it. Therefore, the frequency and impulse responses contain the same information about the system's dynamics. However, features of these dynamics are more easily seen in one or the other response.

2.2.2 Input-output system gains

The frequency response (2.12) contains a large amount of information about the dynamical behavior of system (2.9). It is not always straightforward to visualize it since it is a function of temporal and spatial frequency variables, and is also operator valued (or matrix valued after a suitable discretization in y). Here, we will mainly be interested in the behavior of the response as a function of the spatial frequencies. Therefore, we will need to somehow aggregate the effects of dynamics in t and y . This can be done in a variety of ways. We choose here to use the so-called \mathcal{H}_2 and \mathcal{H}_∞ system norms [7]. These are input-output norms of dynamical systems of the type (2.9), and they quantify the ‘amplification’ or ‘gain’ of a system, or in other words, the relative size of the output to the input. We note that there is no general relationship between the \mathcal{H}_2 and \mathcal{H}_∞ norms.

- The \mathcal{H}_2 norm is defined by

$$[\|\mathcal{H}\|_2^2](\kappa) := \frac{1}{2\pi} \int_{-\infty}^{\infty} \|\mathcal{H}(\omega, \kappa)\|_{HS}^2 d\omega = \int_0^\infty \|\mathcal{H}(t, \kappa)\|_{HS}^2 dt, \quad (2.16)$$

where $\|\cdot\|_{HS}$ is the Hilbert-Schmidt norm of an operator defined by

$$\|\mathcal{H}\|_{HS}^2 := \text{trace}(\mathcal{H}\mathcal{H}^*) = \sum_{n=1}^{\infty} \sigma_n^2(\mathcal{H}). \quad (2.17)$$

The n -th singular value of operator \mathcal{H} is denoted by $\sigma_n(\mathcal{H})$. In the case when \mathcal{H} is a matrix, this is precisely the Frobenius norm.

- The \mathcal{H}_∞ norm is defined by

$$[\|\mathcal{H}\|_\infty](\kappa) := \sup_{\omega} \sigma_{\max}(\mathcal{H}(\omega, \kappa)), \quad (2.18)$$

where σ_{\max} is the maximum singular value.

These norms have interesting physical interpretations. We can regard \mathcal{H} in (2.13) as representing the ‘amplification’ or ‘gain’ from \mathbf{d} to ϕ at given frequencies. The quantity (2.18) represents a maximization of this gain over input temporal frequencies and spatial shapes (by this we mean the variation of the input as a function of y). The former is obtained by the maximization over ω and the latter by taking a maximum singular value. Thus, we can interpret the \mathcal{H}_∞ norm as the *worst case amplification* of inputs. Furthermore, we can find frequencies $\bar{\omega}$ (the frequency at which \sup_{ω} is achieved) and $\bar{\kappa}$, and input shape $\bar{\mathbf{d}}(y)$ (namely the right singular function corresponding to the maximum singular value) such that with input

$$\mathbf{d}(y, t, \xi) = \bar{\mathbf{d}}(y)e^{i(\bar{\kappa}\cdot\xi + \bar{\omega}t)},$$

the output ϕ has this worst case amplification, that is

$$\int_{\mathbb{P}} \int_0^\infty \phi^*(y, t, \bar{\kappa}) \phi(y, t, \bar{\kappa}) dy dt = \sup_{\kappa} [\|\mathcal{H}\|_\infty](\kappa).$$

On the other hand, the \mathcal{H}_2 norm has a stochastic interpretation: it quantifies the variance (energy) amplification of harmonic (in ξ) stochastic (in y and t) disturbances at any given κ . In the fluid mechanics

literature the \mathcal{H}_2 norm is also referred to as the *ensemble average energy density* of the statistical steady-state [8]. More generally, the frequency response operator captures the mapping of second order statistics from the input to the output random fields. Let the input \mathbf{d} be a zero-mean homogenous (in ξ and t) white random field, i.e. one whose auto-correlation is

$$\mathcal{E}\{\mathbf{d}(y_1, t_1, \xi_1)\mathbf{d}^*(y_2, t_2, \xi_2)\} = I\delta(y_1 - y_2, t_1 - t_2, \xi_1 - \xi_2),$$

where I is the identity matrix. The output random field will be stationary in ξ and t (but not in y), and will have correlations determined by system's dynamics. We define the auto-correlation function of ϕ after averaging in y by

$$R_\phi(t, \xi) := \int_{\mathbb{P}} \int_{\mathbb{P}} \mathcal{E}\{\phi(y_1, \tau + t, \zeta + \xi) \phi^*(y_2, \tau, \zeta)\} dy_1 dy_2.$$

Note that R_ϕ contains all the two-point correlation functions in ξ and t . Let W_ϕ be the Power Spectral Density (PSD) function of ϕ obtained by a Fourier transform of R_ϕ . It is then a standard fact [9] that the PSD is given from system's frequency response by

$$W_\phi(\omega, \kappa) := \text{trace}(\mathcal{H}(\omega, \kappa)\mathcal{H}^*(\omega, \kappa)) = \|\mathcal{H}(\omega, \kappa)\|_{HS}^2.$$

Comparing this last expression with (2.16), we see that the \mathcal{H}_2 norm at each κ captures the total PSD at this vector of spatial frequencies after integrating in temporal frequency.

We point out that for computing the \mathcal{H}_2 norm, the expression (2.16) can be determined without actually integrating in ω . It is a standard fact from linear systems theory [7] that this quantity can be computed using the solutions of the operator Lyapunov equations

$$\begin{aligned} \mathcal{A}(\kappa)\mathcal{X}_\infty(\kappa) + \mathcal{X}_\infty(\kappa)\mathcal{A}^*(\kappa) &= -\mathcal{B}(\kappa)\mathcal{B}^*(\kappa), \\ \mathcal{A}^*(\kappa)\mathcal{Y}_\infty(\kappa) + \mathcal{Y}_\infty(\kappa)\mathcal{A}(\kappa) &= -\mathcal{C}^*(\kappa)\mathcal{C}(\kappa), \end{aligned}$$

where \mathcal{A}^* , \mathcal{B}^* , and \mathcal{C}^* respectively represent adjoints of operators \mathcal{A} , \mathcal{B} , and \mathcal{C} . The \mathcal{H}_2 norm is then computed from either of the following two expressions

$$[\|\mathcal{H}\|_2^2](\kappa) = \text{trace}(\mathcal{X}_\infty(\kappa)\mathcal{C}^*(\kappa)\mathcal{C}(\kappa)) = \text{trace}(\mathcal{Y}_\infty(\kappa)\mathcal{B}(\kappa)\mathcal{B}^*(\kappa)).$$

In the controls literature, operators $\mathcal{X}_\infty(\kappa)$ and $\mathcal{Y}_\infty(\kappa)$ are respectively referred to as the controllability and observability Gramians [7].

The Hilbert-Schmidt norm of the impulse response operator can be also integrated over the finite time interval to yield:

$$[\|\mathcal{H}\|_2^2](t, \kappa) := \int_0^t \|\mathcal{H}(\tau, \kappa)\|_{HS}^2 d\tau.$$

The resulting measure of input-output amplification can be determined as

$$[\|\mathcal{H}\|_2^2](t, \kappa) = \text{trace}(\mathcal{X}_t(\kappa)\mathcal{C}^*(\kappa)\mathcal{C}(\kappa)) = \text{trace}(\mathcal{Y}_t(\kappa)\mathcal{B}(\kappa)\mathcal{B}^*(\kappa)),$$

where operators $\mathcal{X}_t(\kappa)$ and $\mathcal{Y}_t(\kappa)$ represent solutions of the following two differential Lyapunov equations

$$\begin{aligned} \frac{d\mathcal{X}_t(\kappa)}{dt} &= \mathcal{A}(\kappa)\mathcal{X}_t(\kappa) + \mathcal{X}_t(\kappa)\mathcal{A}^*(\kappa) + \mathcal{B}(\kappa)\mathcal{B}^*(\kappa), \\ \frac{d\mathcal{Y}_t(\kappa)}{dt} &= \mathcal{A}^*(\kappa)\mathcal{Y}_t(\kappa) + \mathcal{Y}_t(\kappa)\mathcal{A}(\kappa) + \mathcal{C}^*(\kappa)\mathcal{C}(\kappa), \end{aligned} \tag{2.19}$$

with the initial conditions $\mathcal{X}_0(\kappa) = 0$ and $\mathcal{Y}_0(\kappa) = 0$, for every κ . For stable systems, these two operators can be determined based on

$$\begin{aligned}\mathcal{X}_t(\kappa) &= \mathcal{X}_\infty(\kappa) - e^{\mathcal{A}(\kappa)t} \mathcal{X}_\infty(\kappa) e^{\mathcal{A}^*(\kappa)t}, \\ \mathcal{Y}_t(\kappa) &= \mathcal{Y}_\infty(\kappa) - e^{\mathcal{A}^*(\kappa)t} \mathcal{Y}_\infty(\kappa) e^{\mathcal{A}(\kappa)t}.\end{aligned}\quad (2.20)$$

It is a standard fact from control theory [7, 10] that both \mathcal{H}_∞ and \mathcal{H}_2 norms are finite for stable causal dynamical systems. However, for unstable systems these measures of input-output amplification can become infinitely large. Because of this, it is desirable to develop computationally efficient tools for determination of the finite-horizon input-output gains for spatially distributed systems with unstable dynamics. In § 2.2.3, we define these gains and argue that their analysis represents a non-trivial mathematical exercise. In § 2.2.4, we propose an intuitively equivalent measure of input-output amplification by introducing the ‘exponential discounting’ in signals appearing in (2.9).

2.2.3 Finite horizon input-output gains

In this subsection, we define the notion of finite horizon input-output system gains for system (2.9). In particular, we want to analyze the induced finite horizon 2 norm, that is, the induced norm of the so-called ‘state space compression operator’ [11]. The definition of this norm in the temporal domain is given by

$$[\|\mathcal{H}_T\|_\infty](\kappa) = \sup_{\|\mathbf{d}_T\|_2(\kappa) \leq 1} \frac{[\|\boldsymbol{\phi}_T\|_2](\kappa)}{[\|\mathbf{d}_T\|_2](\kappa)}, \quad (2.21)$$

where

$$[\|\mathbf{d}_T\|_2^2](\kappa) := \int_0^T [\|\mathbf{d}\|_2^2](\kappa, t) dt := \int_0^T \int_{\mathbb{P}} \mathbf{d}^*(y, t, \kappa) \mathbf{d}(y, t, \kappa) dy dt.$$

Clearly, the measure of input-output amplification defined by (2.21) represents a finite horizon equivalent of the previously defined \mathcal{H}_∞ norm. This quantity assumes finite values even for unstable systems, which is an appealing property. However, the computation of (2.21) is a non-trivial mathematical exercise (see, for example, [11]).

Also, for unstable systems we can study $[\|\mathcal{H}\|_2](t, \kappa)$. We note that for system (2.9) with unstable dynamics \mathcal{X}_t and \mathcal{Y}_t cannot be computed using (2.20) since both \mathcal{X}_∞ and \mathcal{Y}_∞ diverge in this case. Notwithstanding, $[\|\mathcal{H}\|_2](t, \kappa)$ can be determined by performing the direct numerical integration of the finite dimensional equivalent of either of the two equations in (2.19). This would typically require solving a very large number of ODEs which is computationally inefficient. For this reason, in § 2.2.4, we show how these finite horizon input-output gains can be approximately determined by considering the ‘exponentially discounted’ versions of signals in (2.9).

2.2.4 Exponentially discounted input-output gains

In this subsection, we define the input-output gains for unstable spatially distributed systems with ‘exponentially discounted’ inputs and outputs, that is $\mathbf{d}_\alpha := e^{-\alpha t} \mathbf{d}$, $\boldsymbol{\phi}_\alpha := e^{-\alpha t} \boldsymbol{\phi}$, with $\alpha > 0$. Transformation of this form renders (2.9) into

$$\partial_t \boldsymbol{\psi}_\alpha(y, t, \kappa) = [\mathcal{A}_\alpha(\kappa) \boldsymbol{\psi}_\alpha(t, \kappa)](y) + [\mathcal{B}(\kappa) \mathbf{d}_\alpha(t, \kappa)](y), \quad (2.22a)$$

$$\boldsymbol{\phi}_\alpha(y, t, \kappa) = [\mathcal{C}(\kappa) \boldsymbol{\psi}_\alpha(t, \kappa)](y), \quad (2.22b)$$

where $\boldsymbol{\psi}_\alpha := e^{-\alpha t} \boldsymbol{\psi}$ is the exponentially weighted state of (2.9). Input and output operators \mathcal{B} and \mathcal{C} have the same meaning as in (2.9), whereas the generator of (2.22) is obtained by shifting the generator of (2.9) by the amount proportional to the exponential discounting, i.e. $\mathcal{A}_\alpha(\kappa) := \mathcal{A}(\kappa) - \alpha I$. The frequency domain

description of (2.22) is clearly given by

$$\begin{aligned}\phi_\alpha(y, \omega, \kappa) &= [\mathcal{H}_\alpha(\omega, \kappa)\mathbf{d}_\alpha(\omega, \kappa)](y) \\ &= [\mathcal{C}(\kappa)(i\omega I - \mathcal{A}_\alpha(\kappa))^{-1}\mathcal{B}(\kappa)\mathbf{d}_\alpha(\omega, \kappa)](y) \\ &= [\mathcal{C}(\kappa)((i\omega + \alpha)I - \mathcal{A}(\kappa))^{-1}\mathcal{B}(\kappa)\mathbf{d}_\alpha(\omega, \kappa)](y).\end{aligned}$$

If parameter α is chosen so that $\alpha > \sup_\kappa \lambda_{\max}\{\mathcal{A}(\kappa)\}$, than $\mathcal{A}_\alpha(\kappa)$ represents an exponentially stable operator for any given κ . Therefore, the net effect of exponential discounting in this case is stabilization of (2.9) which implies that the \mathcal{H}_∞ and \mathcal{H}_2 norms of system (2.22) can be computed using the procedure outlined in § 2.2.2. In particular, the following interpretation can be given to the \mathcal{H}_∞ norm of (2.22) in the time domain

$$[\|\mathcal{H}_\alpha\|_\infty](\kappa) = \sup_{[\|\mathbf{d}_\alpha\|_2](\kappa) \leq 1} \frac{[\|\phi_\alpha\|_2](\kappa)}{[\|\mathbf{d}_\alpha\|_2](\kappa)},$$

where

$$\begin{aligned}[\|\mathbf{d}_\alpha\|_2^2](\kappa) &:= \int_0^\infty \int_{\mathbb{P}} \mathbf{d}_\alpha^*(y, t, \kappa) \mathbf{d}_\alpha(y, t, \kappa) dy dt \\ &= \int_0^\infty \int_{\mathbb{P}} e^{-2\alpha t} \mathbf{d}^*(y, t, \kappa) \mathbf{d}(y, t, \kappa) dy dt \\ &= \int_0^\infty e^{-2\alpha t} [\|\mathbf{d}\|_2^2](t, \kappa) dt.\end{aligned}$$

On the other hand, for a given κ and $t > 0$, the ‘finite horizon \mathcal{H}_2 norm’ of system (2.9) at time t can be determined by the \mathcal{H}_2 norm of system (2.22), provided that the design parameter α is appropriately selected. This is because $[\|\mathcal{H}\|_2](t, \kappa)$ represents a monotonically increasing function of time which is equal to zero at $t = 0$, and $[\|\mathcal{H}_\alpha\|_2](\kappa)$ is a finite number for any given κ . Unfortunately, in general, it is very difficult to establish the exact correspondence between $[\|\mathcal{H}\|_2](t, \kappa)$ and $[\|\mathcal{H}_\alpha\|_2](\kappa)$. In other words, it is very hard to determine pair (t, α) at which $[\|\mathcal{H}\|_2](t, \kappa) = [\|\mathcal{H}_\alpha\|_2](\kappa)$. However, some intuition can be gained by considering the following scalar example

$$\left. \begin{aligned}\dot{\psi} &= a\psi + d \\ \phi &= \psi\end{aligned}\right\}, \quad a > 0, \quad (2.23)$$

with its ‘exponentially discounted’ equivalent of the form

$$\left. \begin{aligned}\dot{\psi}_\alpha &= (a - \alpha)\psi_\alpha + d_\alpha \\ \phi_\alpha &= \psi_\alpha\end{aligned}\right\}, \quad \alpha > a. \quad (2.24)$$

The ‘finite horizon \mathcal{H}_2 norm’ of system (2.23) and the \mathcal{H}_2 norm of system (2.24) are respectively given by

$$\begin{aligned}[\|H\|_2^2](t) &= \frac{1}{2a}(e^{2at} - 1), \\ \|H_\alpha\|_2^2 &= \frac{1}{2a(\alpha - a)},\end{aligned}$$

which implies that, for a chosen $\alpha > a$, $[\|H\|_2](t) = \|H_\alpha\|_2$ at

$$t = \frac{1}{2a} \ln \frac{\alpha}{\alpha - a}.$$

Equivalently, for a given $t > 0$, these two quantities are equal if α satisfies

$$\alpha = \frac{ae^{2at}}{e^{2at} - 1}.$$

Therefore, both the location of the unstable pole and the desired time interval determine the value of parameter α for which the \mathcal{H}_2 norm of system (2.24) determines the ‘finite horizon \mathcal{H}_2 norm’ of system (2.23). Furthermore, the closer α to a and the smaller a , the larger time at which $[\|H\|_2](t) = \|H_\alpha\|_2$.

2.2.5 Input-output directions

As mentioned above, at fixed frequencies (ω, κ) , $\mathcal{H}(\omega, \kappa)$ represents an operator in y . Since this operator is compact [2], we can study its properties using the *singular value (Schmidt) decomposition*

$$[\mathcal{H}(\omega, \kappa) \mathbf{d}(\omega, \kappa)](y) = \sum_{m=1}^{\infty} \sigma_m(\omega, \kappa) \langle \mathbf{d}, \boldsymbol{\iota}_m \rangle \mathbf{o}_m(y, \omega, \kappa), \quad (2.25)$$

where $\{\sigma_m \geq 0\}_{m \in \mathbb{N}}$ are the singular values of \mathcal{H} arranged in descending order, and $\{\boldsymbol{\iota}_m\}_{m \in \mathbb{N}}$, $\{\mathbf{o}_m\}_{m \in \mathbb{N}}$ are respectively the right and the left singular functions, that is

$$\begin{aligned} [\mathcal{H}^*(\omega, \kappa) \mathcal{H}(\omega, \kappa) \boldsymbol{\iota}_m(\omega, \kappa)](y) &= \sigma_m^2(\omega, \kappa) \boldsymbol{\iota}_m(y, \omega, \kappa), \\ [\mathcal{H}(\omega, \kappa) \mathcal{H}^*(\omega, \kappa) \mathbf{o}_m(\omega, \kappa)](y) &= \sigma_m^2(\omega, \kappa) \mathbf{o}_m(y, \omega, \kappa). \end{aligned}$$

By substituting $\mathbf{d}(y, \omega, \kappa) := \boldsymbol{\iota}_n(y, \omega, \kappa)$, $n \in \mathbb{N}$, in (2.25) we obtain

$$[\mathcal{H}(\omega, \kappa) \boldsymbol{\iota}_n(\omega, \kappa)](y) = \sigma_n(\omega, \kappa) \mathbf{o}_n(y, \omega, \kappa).$$

This relationship illustrates that an input in the direction $\boldsymbol{\iota}_n(y, \omega, \kappa)$ produces the output in the direction $\mathbf{o}_n(y, \omega, \kappa)$. For this reason, functions $\boldsymbol{\iota}_n(y, \omega, \kappa)$ and $\mathbf{o}_n(y, \omega, \kappa)$ are respectively referred to as the *input* and *output directions*. On the other hand, $\sigma_n(\omega, \kappa)$ represents the input-output gain when the system is excited in the direction $\boldsymbol{\iota}_n(y, \omega, \kappa)$. Since the singular values of $\mathcal{H}(\omega, \kappa)$ are arranged in descending order, the largest gain in any input direction is determined by $\sigma_1(\omega, \kappa)$: the maximal singular value of the frequency response operator. The corresponding vectors $\boldsymbol{\iota}_1(y, \omega, \kappa)$ and $\mathbf{o}_1(y, \omega, \kappa)$ respectively represent the most amplified input direction and the output direction in which the inputs are most efficient. These directions are referred to as the *worst-case* input and output directions at any given (ω, κ) . The worst-case input and output directions over all frequencies are the ones that correspond to $\sup_{\kappa, \omega} \sigma_{\max}(\mathcal{H}(\omega, \kappa)) =: \sup_{\kappa} [\|\mathcal{H}\|_{\infty}](\kappa)$. Clearly, the notion of worst-case directions is well defined only for stable systems, since otherwise, there exist input directions that lead to *unbounded amplification* by the system’s dynamics.

2.2.6 Robustness analysis versus input-output analysis

In this subsection, we illustrate that the problem of robust stability can be addressed using input-output tools. In particular, we apply a *small gain theorem* to show that the robust stability analysis is equivalent to the input-output analysis for certain part of the system. In other words, we utilize input-output approach to cast the problem under study into a fairly general framework which allows for consideration of seemingly different issues.

Consider a system of the form

$$\partial_t \psi = \mathcal{A} \psi, \quad (2.26)$$

where, in general, \mathcal{A} is an operator. For example, the unforced evolution model (2.1a) can be represented by (2.26). Let us assume that operator \mathcal{A} generates the strongly continuous (C^0) semigroup $e^{\mathcal{A}t}$ on the underlying Hilbert space \mathbb{H} . To characterize the *exponential stability*² of $e^{\mathcal{A}t}$ we need to introduce the notion of *resolvent* of the operator \mathcal{A} . This quantity is the operator valued function defined on the *resolvent set* $\rho(\mathcal{A})$,

$$\rho(\mathcal{A}) := \{s \in \mathbb{C}; (sI - \mathcal{A})^{-1} \text{ exists } \& \| (sI - \mathcal{A})^{-1} \| < \infty \text{ on } \mathbb{H}\},$$

by

$$\mathcal{R} : \rho(\mathcal{A}) \rightarrow \mathcal{B}(\mathbb{H}, \mathbb{H}), \quad \mathcal{R}(\mathcal{A}) := (sI - \mathcal{A})^{-1},$$

² C^0 semigroup $e^{\mathcal{A}t}$ is exponentially stable if and only if $\|e^{\mathcal{A}t}\| \leq M e^{-\alpha t}$, $t \geq 0$, for some $M, \alpha > 0$.

where $\mathcal{B}(\mathbb{H}, \mathbb{H})$ denotes the space of all bounded linear operators from \mathbb{H} to \mathbb{H} .

It is a standard fact that $e^{\mathcal{A}t}$ is exponentially stable [2] if and only if the $\mathcal{R}(\mathcal{A})$ satisfies the following condition:

$$\sup_{Re(s)>0} \|\mathcal{R}(\mathcal{A})\| < \infty.$$

Clearly, if an additional term is added to the right-hand side of (2.26),

$$\partial_t \psi = \mathcal{A}\psi + \mathbf{d}, \quad (2.27)$$

then the resolvent can be determined as the transfer function from the input \mathbf{d} to the state ψ . Therefore, using the *maximum modulus principle*, it follows that the condition for the exponential stability of $e^{\mathcal{A}t}$ is precisely given in terms of the \mathcal{H}_∞ norm of system (2.27), with ψ being considered as the output. This is yet another interesting interpretation of the \mathcal{H}_∞ norm.

We note that, for all systems that we consider in this dissertation, the exponential stability of $e^{\mathcal{A}t}$ can be also characterized by the *spectrum* of the operator \mathcal{A} . In this case, the exponential stability of $e^{\mathcal{A}t}$ is equivalent to the requirement that the spectrum of \mathcal{A} belongs to the open left-half of the complex plane. The spectrum of \mathcal{A} is a closed subset of the complex plane defined by

$$\sigma(\mathcal{A}) := \mathbb{C} \setminus \rho(\mathcal{A}) = \{s \in \mathbb{C}, (sI - \mathcal{A}) \text{ is not 'boundedly invertible'}\}.$$

A certain operator is not '*boundedly invertible*' if it is either non-invertible (not one-to-one), or if its inverse represents an unbounded operator.

Also, we are interested in a problem of robust stability of $e^{\mathcal{A}t}$, which can be formulated as a stability problem for a system

$$\partial_t \psi = (\mathcal{A} + \Gamma)\psi, \quad (2.28)$$

where Γ is a bounded operator with $\|\Gamma\|_\infty \leq \varepsilon$. Consideration of this problem can be justified by a lack of complete knowledge of the elements of \mathcal{A} . Arguably, (2.26) is just a model of a physical system and, no matter how carefully the modeling has been performed, there will always be some discrepancies between the two. Modeling uncertainties can be rigorously accounted for by introducing operator Γ . This type of uncertainty is usually referred to as *unstructured uncertainty*, and it can be seen as ubiquitous errors which can be associated with all models [7]. However, this representation of uncertainty can be too conservative since some additional information about the structure of uncertainty is usually available. A more refined model can be obtained by considering a lower rank uncertainty problem

$$\partial_t \psi = (\mathcal{A} + \mathcal{B}\Gamma\mathcal{C})\psi, \quad (2.29)$$

where \mathcal{B} and \mathcal{C} are known operators of certain structure. The problem formulated in this fashion is more general than problem (2.28) since the latter can be recovered from the former by the appropriate choice of \mathcal{B} and \mathcal{C} ($\mathcal{B} = I$, $\mathcal{C} = I$). Because of this, we consider system (2.29) and study its stability properties.

Robust stability of (2.26) is guaranteed if and only if the resolvent of $\mathcal{A} + \mathcal{B}\Gamma\mathcal{C}$ satisfies

$$\sup_{Re(s)>0} \|\mathcal{R}(\mathcal{A} + \mathcal{B}\Gamma\mathcal{C})\| < \infty, \quad \forall \|\Gamma\|_\infty \leq \varepsilon. \quad (2.30)$$

For the systems under study in this dissertation, condition (2.30) is satisfied if the spectrum of $\mathcal{A} + \mathcal{B}\Gamma\mathcal{C}$ belongs to the open left-half of the complex plane for all $\|\Gamma\|_\infty \leq \varepsilon$. This requirement can be expressed in terms of the so-called *pseudo-spectra* [12–14], which is defined as

$$\sigma_\varepsilon(\mathcal{A}) := \{s \in \mathbb{C}, \exists \|\Gamma\|_\infty \leq \varepsilon \text{ s.t. } (sI - (\mathcal{A} + \mathcal{B}\Gamma\mathcal{C})) \text{ is not 'boundedly invertible'}\}. \quad (2.31)$$

The original definition of pseudo-spectra is given for $\mathcal{B} = I$, $\mathcal{C} = I$ and, thus, expression (2.31) is a slight generalization of this concept.

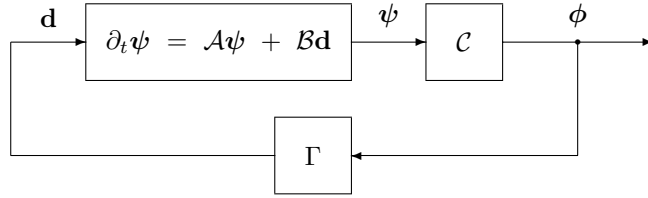


Figure 2.2: Block diagram of system (2.29) in a form suitable for the application of small gain theorem.

We now illustrate that system (2.29) can be represented by a feedback system of the form

$$\begin{aligned}\partial_t\psi &= \mathcal{A}\psi + \mathcal{B}\mathbf{d}, \\ \phi &= \mathcal{C}\psi,\end{aligned}\tag{2.32}$$

by the appropriate choice of input \mathbf{d} . Namely, by defining \mathbf{d} as $\mathbf{d} := \Gamma\phi$, we can readily recover (2.29) from (2.32). This representation is illustrated by a symbolic block diagram shown in Figure 2.2, where the known part of the system is separated from the uncertain part of the system. The system represented in this way is suitable for application of the small gain theorem. This theorem provides a test for stability of a nominally stable system with the *operator-valued* transfer function $\mathcal{H}(s) := \mathcal{C}(sI - \mathcal{A})^{-1}\mathcal{B}$ in the presence of unstructured uncertainty Γ .

Theorem 1 *The system shown in Figure 2.2 is internally stable for all $\|\Gamma\|_\infty \leq \varepsilon$ if and only if $\|\mathcal{H}\|_\infty < \frac{1}{\varepsilon}$.*

Hence, it has been established that the robust stability analysis is mathematically equivalent to the input-output analysis for a certain part of the system. Therefore, without loss of generality, input-output analysis can be performed with keeping in mind that, by doing so, the robust stability analysis can be captured as well.

Finally, we note that the pseudo-spectrum can be determined by computing the level sets of the function $\sigma_{\max}\{\mathcal{C}(sI - \mathcal{A})^{-1}\mathcal{B}\}$. In other words,

$$\sigma_\varepsilon(\mathcal{A}) = \left\{ s \in \mathbb{C}, \sigma_{\max}\{\mathcal{C}(sI - \mathcal{A})^{-1}\mathcal{B}\} \geq \frac{1}{\varepsilon} \right\}.$$

Thus, it has been illustrated that the input-output analysis has a very general character and that it can, in particular, be used for studying the problem of robust stability of dynamical systems.

Bibliography

- [1] E. W. Kamen, “Stabilization of linear spatially-distributed continuous-time and discrete-time systems,” in *Multidimensional Systems Theory*, N. K. Bose, Ed. Hingham, MA: Kluwer, 1985.
- [2] R. F. Curtain and H. J. Zwart, *An Introduction to Infinite-Dimensional Linear Systems Theory*. New York: Springer-Verlag, 1995.
- [3] J. L. Lions, *Optimal Control of Systems Governed by Partial Differential Equations*. New York: Springer-Verlag, 1971.
- [4] S. P. Banks, *State-Space and frequency-domain methods in the control of distributed parameter systems*. London, UK: Peter Peregrinus Ltd., 1983.
- [5] Z. Luo, B.Z.Guo, and O.Morgul, *Stability and Stabilization of Infinite Dimensional Systems with Applications*. London: Springer-Verlag, 1999.
- [6] B. Bamieh, F. Paganini, and M. A. Dahleh, “Distributed control of spatially invariant systems,” *IEEE Transactions on Automatic Control*, vol. 47, no. 7, pp. 1091–1107, July 2002.
- [7] K. Zhou, J. C. Doyle, and K. Glover, *Robust and Optimal Control*. Prentice Hall, 1996.
- [8] B. F. Farrell and P. J. Ioannou, “Stochastic forcing of the linearized Navier-Stokes equations,” *Physics of Fluids A*, vol. 5, no. 11, pp. 2600–2609, 1993.
- [9] E. VanMarcke, *Random Fields: Analysis and Synthesis*. MIT Press, 1983.
- [10] G. E. Dullerud and F. Paganini, *A course in robust control theory: a convex approach*. New York: Springer-Verlag, 2000.
- [11] G. E. Dullerud, “Computing the L_2 -induced norm of a compression operator,” *Systems and Control Letters*, vol. 37, pp. 87–91, 1999.
- [12] L. N. Trefethen, A. E. Trefethen, S. C. Reddy, and T. A. Driscoll, “Hydrodynamic stability without eigenvalues,” *Science*, vol. 261, pp. 578–584, 1993.
- [13] S. C. Reddy and D. S. Henningson, “Energy growth in viscous channel flows,” *J. Fluid Mech.*, vol. 252, pp. 209–238, 1993.
- [14] L. N. Trefethen, “Pseudospectra of linear operators,” *SIAM Rev.*, vol. 39, no. 3, pp. 383–406, 1997.

Chapter 3

Exact determination of frequency responses for a class of spatially distributed systems

In this chapter, we study frequency responses of the distributed systems in which a spatial independent variable belongs to a finite interval. Computation of frequency responses for this class of systems is usually done numerically by resorting to finite dimensional approximations of the underlying operators. We show that the spatial discretization can be circumvented and that frequency responses can be determined explicitly whenever the underlying operators can be represented by forced Two Point Boundary Value State-space Realizations (TPBVSR) which are well posed.

Our results build on the work presented in [1], where a formula for the trace of a class of differential operators defined by forced TPBVSR with constant coefficients was derived. This formula was used for computation of the \mathcal{H}_2 norm for a class of infinite dimensional systems in which the dynamical generators are normal (or self-adjoint). Here we study the *spatio-temporal frequency responses* of spatially distributed systems with, in general, non-normal dynamical generators and non-constant coefficients in a spatially independent variable. The fields of interest are assumed to satisfy the boundary conditions expressed in terms of a general linear homogeneous constraint. Our main result is an explicit formula for the *Hilbert–Schmidt norm* (that is, the power spectral density) of the frequency response operator. This formula involves only finite dimensional computations with matrices whose dimension is at most four times larger than the order of the underlying differential operator. In this way an exact reduction of an infinite dimensional problem to a finite dimensional problem is accomplished.

Our presentation is organized as follows: in § 3.1, we formulate the problem and briefly review the notion of frequency responses for spatially distributed systems. In § 3.2, we show how the frequency responses can be determined explicitly without resorting to the finite dimensional approximations. In § 3.3, we provide an example to illustrate the application of the developed procedure. An additional example, that shows how the Hilbert–Schmidt norms can be obtained explicitly for a system that describes the dynamics of velocity fluctuations in channel fluid flows, is given in § 9.5. We conclude by summarizing major contributions in § 3.4.

3.1 Preliminaries

We consider spatially distributed systems of the form

$$\partial_t \psi(y, t) = [\mathcal{A}\psi(t)](y) + [\mathcal{B}d(t)](y), \quad (3.1a)$$

$$\phi(y, t) = [\mathcal{C}\psi(t)](y), \quad (3.1b)$$

where \mathcal{A} , \mathcal{B} , and \mathcal{C} are linear operators, d is a forcing term, and ψ and ϕ are fields of interest determined by the solution of the above equation. The spatial independent variable y is assumed to belong to a finite interval $[a, b]$, with $a \in \mathbb{R}$, $b \in \mathbb{R}$, and $a < b$. We remark that (3.1) can be also used to describe multi-dimensional distributed systems that are spatially invariant in the remaining spatial directions [2]. In this case, the application of the spatial Fourier transform in these directions renders differential/integral operators into multiplication operators which results in a one-dimensional system parameterized by a vector of spatial frequencies κ

$$\partial_t \psi(y, t, \kappa) = [\mathcal{A}(\kappa)\psi(t, \kappa)](y) + [\mathcal{B}(\kappa)d(t, \kappa)](y), \quad (3.2a)$$

$$\phi(y, t, \kappa) = [\mathcal{C}(\kappa)\psi(t, \kappa)](y). \quad (3.2b)$$

Our objective is to investigate dynamical properties of system (3.1) or system (3.2) by computing their frequency responses. The frequency response of (3.1) is determined by [3]

$$\mathcal{H}(\omega) := \mathcal{C}(i\omega I - \mathcal{A})^{-1}\mathcal{B},$$

where ω denotes the temporal frequency. Similarly, the *spatio-temporal frequency response* of system (3.2) is given by

$$\mathcal{H}(\omega, \kappa) := \mathcal{C}(\kappa)(i\omega I - \mathcal{A}(\kappa))^{-1}\mathcal{B}(\kappa).$$

In the remainder of this chapter we discuss the latter notion, because it is more general.

We remark that for any given pair (ω, κ) , $\mathcal{H}(\omega, \kappa)$ represents an operator in y that maps $d(y, \omega, \kappa)$ into $\phi(y, \omega, \kappa)$ according to

$$\begin{aligned} \phi(y, \omega, \kappa) &= [\mathcal{H}(\omega, \kappa)d(\omega, \kappa)](y) \\ &= \int_a^b [\mathcal{H}(\omega, \kappa)](y, \eta)d(\eta, \omega, \kappa) d\eta, \end{aligned} \quad (3.3)$$

where by an abuse of notation we use the symbol $[\mathcal{H}(\omega, \kappa)](y, \eta)$ to denote the kernel function representing the operator $\mathcal{H}(\omega, \kappa)$. We assume that, for any given pair (ω, κ) , $[\mathcal{H}(\omega, \kappa)](y, \eta)$ represents a continuous matrix valued function on $[a, b] \times [a, b]$. It is a standard fact that under these conditions $\mathcal{H}(\omega, \kappa)$ is a Hilbert–Schmidt operator [4]. Thus, we can determine the Hilbert–Schmidt norm of $\mathcal{H}(\omega, \kappa)$ as

$$\|\mathcal{H}(\omega, \kappa)\|_{HS}^2 := \text{trace}(\mathcal{H}(\omega, \kappa)\mathcal{H}^*(\omega, \kappa)) = \int_a^b \text{tr}([\mathcal{F}(\omega, \kappa)](y, y)) dy,$$

where $[\mathcal{F}(\omega, \kappa)](y, \xi)$ denotes the kernel representation of the operator $\mathcal{F}(\omega, \kappa) := \mathcal{H}(\omega, \kappa)\mathcal{H}^*(\omega, \kappa)$, whereas $\text{trace}(\cdot)$ and $\text{tr}(\cdot)$ respectively denote the traces of the argument operator and the argument matrix.

Computation of $\|\mathcal{H}(\omega, \kappa)\|_{HS}$ is usually done numerically for any given pair (ω, κ) , after finite dimensional approximations of the underlying operators are determined by the appropriate spatial discretization. In § 3.2, we show that the Hilbert–Schmidt norm of $\mathcal{H}(\omega, \kappa)$ can be determined explicitly without resorting to the finite dimensional approximations, whenever $\mathcal{H}(\omega, \kappa)$ can be represented by a TPBVSR which is well posed.

3.2 Determination of frequency responses from state-space realizations

In this section, instead of usual finite dimensional approximations of the underlying operators, we derive an *explicit formula* for the Hilbert–Schmidt norm (i.e., the power spectral density) of the frequency response operator. This formula only involves finite dimensional computations with matrices whose dimension is at most four times larger than the order of the underlying differential operators. Before presenting the main result in § 3.2.3, we discuss state-space realizations of \mathcal{H} , \mathcal{H}^* , and $\mathcal{H}\mathcal{H}^*$ in § 3.2.1, and show how the trace of a certain differential operator can be determined from its TPBVSR in § 3.2.2.

3.2.1 State-space realizations of \mathcal{H} , \mathcal{H}^* , and \mathcal{HH}^*

We assume that the operator $\mathcal{H}(\omega, \kappa) : d(\omega, \kappa) \mapsto \phi(\omega, \kappa)$ in (3.3) can be represented by a well-posed TPBVSR of the following form¹

$$\mathcal{H} : \begin{cases} x'(y) = A_0(y)x(y) + B_0(y)d(y), \\ \phi(y) = C_0(y)x(y), \\ 0 = N_1x(a) + N_2x(b), \end{cases} \quad y \in [a, b], \quad (3.4)$$

where $x'(y) := dx(y)/dy$. The dependence on ω and κ is suppressed for notational convenience. Furthermore, for any given pair (ω, κ) , $A_0(y)$, $B_0(y)$, and $C_0(y)$ are matrix valued functions (with, in general, non-constant coefficients in y), defined on the interval $[a, b]$, of respective dimensions $n_0 \times n_0$, $n_0 \times p$, and $m \times n_0$. The boundary value matrices N_1 and N_2 are constant and have dimension $n_0 \times n_0$. These matrices have to be such that $[N_1 \ N_2]$ has a full row rank, to prevent a redundancy in boundary conditions. We remark that TPBVSR (3.4) is well-posed (that it, has a unique solution for any input $d(y)$) if and only if [5]

$$\det(N_1 + N_2\Phi_0(b, a)) \neq 0,$$

where $\Phi_0(y, \eta)$ denotes the state transition matrix of $A_0(y)$.

It can be shown that the adjoint of the operator $\mathcal{H}(\omega, \kappa)$, $\mathcal{H}^*(\omega, \kappa) : f(\omega, \kappa) \mapsto d(\omega, \kappa)$, can be represented by a well-posed TPBVSR of the following form

$$\mathcal{H}^* : \begin{cases} z'(y) = -A_0^*(y)z(y) - C_0^*(y)f(y), \\ d(y) = B_0^*(y)z(y), \\ 0 = M_1z(a) + M_2z(b), \end{cases} \quad y \in [a, b], \quad (3.5)$$

where A_0^* , B_0^* , and C_0^* respectively represent the adjoints (complex-conjugate-transpose matrices) of A_0 , B_0 , and C_0 . On the other hand, the constant boundary value matrices M_1 and M_2 are determined by

$$[M_1 \ M_2] \begin{bmatrix} N_1^* \\ -N_2^* \end{bmatrix} = 0. \quad (3.6)$$

We note that a variety of different M_1 and M_2 for which $[M_1 \ M_2]$ is a full row rank matrix can be chosen to satisfy (3.6). For example, a Singular Value Decomposition of a full column rank matrix $\begin{bmatrix} N_1^* \\ -N_2^* \end{bmatrix}$:

$$\begin{bmatrix} N_1^* \\ -N_2^* \end{bmatrix} = USV^* = [U_1 \ U_2] \begin{bmatrix} S_1 \\ 0 \end{bmatrix} V^* = U_1 S_1 V^*, \quad U_1, U_2 \in \mathbb{C}^{2n_0 \times n_0},$$

can be used to select these two matrices as

$$[M_1 \ M_2] = U_2^*.$$

Thus, a well-posed state-space realization of $\mathcal{H}(\omega, \kappa)\mathcal{H}^*(\omega, \kappa) : f(\omega, \kappa) \mapsto \phi(\omega, \kappa)$ can be obtained by combining (3.4) and (3.5)

$$\mathcal{HH}^* : \begin{cases} q'(y) = A(y)q(y) + B(y)f(y), \\ \phi(y) = C(y)q(y), \\ 0 = L_1q(a) + L_2q(b), \end{cases} \quad y \in [a, b], \quad (3.7)$$

¹In § 3.3 and § 9.5, we illustrate, by means of two examples, how this can be done.

where

$$\begin{aligned} q(y) &:= \begin{bmatrix} x(y) \\ z(y) \end{bmatrix} \in \mathbb{C}^{2n_0}, & L_1 &:= \begin{bmatrix} N_1 & 0 \\ 0 & M_1 \end{bmatrix}, & L_2 &:= \begin{bmatrix} N_2 & 0 \\ 0 & M_2 \end{bmatrix}, \\ A(y) &:= \begin{bmatrix} A_0(y) & B_0(y)B_0^*(y) \\ 0 & -A_0^*(y) \end{bmatrix}, & B(y) &:= \begin{bmatrix} 0 \\ -C_0^*(y) \end{bmatrix}, & C(y) &:= [C_0(y) \ 0]. \end{aligned}$$

In § 3.2.2, we show how $\text{trace}(\mathcal{H}\mathcal{H}^*)$ can be determined from the TPBVSR of $\mathcal{H}\mathcal{H}^*$ (3.7).

3.2.2 Determination of traces from state-space realizations

We study a well-posed TPBVSR of the form

$$\mathcal{F} : \begin{cases} q'(y) = A(y)q(y) + B(y)f(y), \\ \phi(y) = C(y)q(y), \\ 0 = L_1q(a) + L_2q(b), \end{cases} \quad y \in [a, b], \quad (3.8)$$

with $q(y) \in \mathbb{C}^n$, $f(y) \in \mathbb{C}^m$, $\phi(y) \in \mathbb{C}^m$, and derive an explicit formula for the trace of operator $\mathcal{F} : f \mapsto \phi$. This formula, as we will show, is expressed in terms of matrices $\{A(y), B(y), C(y), L_1, L_2\}$, and it only requires computation of two state transition matrices: the state transition matrix of $A(y)$, and the state transition matrix of a matrix that depends on $A(y)$, $B(y)$, and $C(y)$. The size of the latter matrix is $2n \times 2n$. Our results generalize the results of [1], where the trace formula for operators with constant coefficients and less general boundary conditions was derived. Here we study the problem with non-constant coefficients in y . In addition to that, the boundary conditions are given as a general linear homogeneous constraint on $q(y)$ at $y = a, b$.

We utilize the fact that the trace of an operator $\mathcal{F} : f \mapsto \phi$

$$\phi(y) = \int_a^b \mathcal{F}(y, \eta) f(\eta) d\eta, \quad (3.9)$$

with a continuous kernel $\mathcal{F}(y, \eta)$ is determined by

$$\text{trace}(\mathcal{F}) = \int_a^b \text{tr}(\mathcal{F}(y_o, y_o)) dy_o = \int_a^b \text{tr} \left(\sum_{k=1}^m \mathcal{F}(y_o, y_o) e_k e_k^T \right) dy_o,$$

where e_k denotes the k -th unit vector in \mathbb{R}^m . Clearly, each ‘column’ of the kernel can be obtained by forcing (3.9) with an impulsive function (that is, if $f(y) = \delta(y - y_o)e_k$ then $\mathcal{F}(y, y_o)e_k = \phi(y)$). Thus, for any given $y_o \in [a, b]$, $\mathcal{F}(y_o, y_o)e_k$ represents a response $\phi(y)$ evaluated at $y = y_o$ to input $f(y) = \delta(y - y_o)e_k$. The effect of forcing (3.8) with $f(y) = \delta(y - y_o)e_k$ is given by

$$q'(y) = A(y)q(y) + B(y)\delta(y - y_o)e_k \Rightarrow \begin{cases} q'(y) = A(y)q(y), \\ q(y_o^+) - q(y_o^-) = B(y_o)e_k, \end{cases}$$

where $q(y_o^+)$ and $q(y_o^-)$ respectively represent the limits of $q(y)$ as y_o is approached from above and below (see Figure 3.1). Hence,

$$\left. \begin{aligned} q'(y) &= A(y)q(y), \\ q(y_o^+) - q(y_o^-) &= B(y_o)e_k, \end{aligned} \right\} \Rightarrow \Phi(y_o, b)q(b) - \Phi(y_o, a)q(a) = B(y_o)e_k, \quad (3.10)$$

where $\Phi(y, \eta)$ denotes the state transition matrix of $A(y)$. By combining the boundary conditions from (3.9)

with (3.10) we obtain

$$\begin{bmatrix} L_1 & L_1 \\ -\Phi(y_o, a) & \Phi(y_o, b) \end{bmatrix} \begin{bmatrix} q(a) \\ q(b) \end{bmatrix} = \begin{bmatrix} 0 \\ B(y_o)e_k \end{bmatrix},$$

which yields

$$\begin{bmatrix} q(a) \\ q(b) \end{bmatrix} = \begin{bmatrix} -(L_1 + L_2\Phi(b, a))^{-1}L_2\Phi(b, y_o)B(y_o)e_k \\ (\Phi(b, y_o) - \Phi(b, a)(L_1 + L_2\Phi(b, a))^{-1}L_2\Phi(b, y_o))B(y_o)e_k \end{bmatrix}. \quad (3.11)$$

We note that the invertibility of matrix $L_1 + L_2\Phi(b, a)$ is equivalent to the well-posedness of the TPB-VSR (3.8) [5].

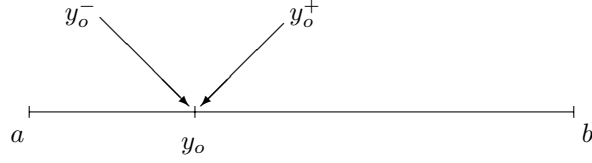


Figure 3.1: Boundary conditions with delta function as input.

Using (3.11), we express vector $\mathcal{F}(y_o, y_o)e_k$ as

$$\begin{aligned} \mathcal{F}(y_o, y_o)e_k &= \frac{1}{2}C(y_o)(q(y_o^-) + q(y_o^+)) \\ &= \frac{1}{2}C(y_o) \begin{bmatrix} \Phi(y_o, a) & \Phi(y_o, b) \end{bmatrix} \begin{bmatrix} q(a) \\ q(b) \end{bmatrix} \\ &= \frac{1}{2}C(y_o) (I - 2\Phi(y_o, a)(L_1 + L_2\Phi(b, a))^{-1}L_2\Phi(b, y_o)) B(y_o)e_k, \end{aligned}$$

which yields

$$\text{trace}(\mathcal{F}) = \text{tr}\left(\frac{1}{2} \int_a^b C(y)B(y) dy - (L_1 + L_2\Phi(b, a))^{-1}L_2 \int_a^b \Phi(b, y)B(y)C(y)\Phi(y, a) dy\right). \quad (3.12)$$

We have arrived at (3.12) using the commutativity property of the matrix trace.

We now exploit the fact that the integral in (3.12) can be evaluated in terms of the response of an unforced dynamical system of the form

$$\begin{cases} \begin{bmatrix} X'_1(y) \\ X'_2(y) \end{bmatrix} = \begin{bmatrix} A(y) & 0 \\ B(y)C(y) & A(y) \end{bmatrix} \begin{bmatrix} X_1(y) \\ X_2(y) \end{bmatrix}, \\ Y(y) = [0 \ I] \begin{bmatrix} X_1(y) \\ X_2(y) \end{bmatrix}, \\ \begin{bmatrix} X_1(a) \\ X_2(a) \end{bmatrix} = \begin{bmatrix} I \\ 0 \end{bmatrix}, \end{cases} \quad y \in [a, b], \quad (3.13)$$

as

$$Y(b) = \int_a^b \Phi(b, y)B(y)C(y)\Phi(y, a) dy = [0 \ I] \Psi(b, a) \begin{bmatrix} I \\ 0 \end{bmatrix}, \quad (3.14)$$

where $\Psi(y, \eta)$ denotes the state transition matrix of system (3.13). Therefore, we obtain an expression for

$\text{trace}(\mathcal{F})$ by combining (3.12) and (3.14)

$$\text{trace}(\mathcal{F}) = \text{tr}\left(\frac{1}{2} \int_a^b C(y)B(y) dy - (L_1 + L_2\Phi(b,a))^{-1}L_2 \begin{bmatrix} 0 & I \end{bmatrix} \Psi(b,a) \begin{bmatrix} I \\ 0 \end{bmatrix}\right). \quad (3.15)$$

In particular, for systems with constant coefficients in y formula (3.15) simplifies to

$$\text{trace}(\mathcal{F}) = \text{tr}\left(\frac{c}{2}CB - (L_1 + L_2e^{cA})^{-1}L_2 \begin{bmatrix} 0 & I \end{bmatrix} \exp\left\{c \begin{bmatrix} A & 0 \\ BC & A \end{bmatrix}\right\} \begin{bmatrix} I \\ 0 \end{bmatrix}\right), \quad (3.16)$$

where $c := b - a$. Furthermore, for operators \mathcal{F} with

$$A(y) := A, \quad B(y) := e^{-\alpha(y-a)}B, \quad C(y) := C,$$

formula (3.15) simplifies to

$$\begin{aligned} \text{trace}(\mathcal{F}) &= \frac{1 - e^{-\alpha c}}{2\alpha} \text{tr}(CB) - \\ &\quad \text{tr}\left((L_1 + L_2e^{cA})^{-1}L_2 \begin{bmatrix} 0 & I \end{bmatrix} \exp\left\{c \begin{bmatrix} A - \alpha I & 0 \\ BC & A \end{bmatrix}\right\} \begin{bmatrix} I \\ 0 \end{bmatrix}\right), \end{aligned} \quad (3.17)$$

Clearly, in the limit as $\alpha \rightarrow 0$, expression on the right-hand side of (3.17) approaches the expression on the right-hand side of (3.16). Trace formulae (3.16) and (3.17) are used in Chapter 9 to explicitly determine the \mathcal{H}_2 norms of the linearized Navier-Stokes equations in channel flows.

In § 3.2.3, we combine the results of § 3.2.1 and § 3.2.2 to provide an explicit formula for the Hilbert–Schmidt norm of the frequency response operator.

3.2.3 Explicit formula for Hilbert–Schmidt norm

The main result of this chapter is summarized in the following theorem.

Theorem 2 *The Hilbert–Schmidt norm of the frequency response operator $\mathcal{H}(\omega, \kappa) : d(\omega, \kappa) \mapsto \phi(\omega, \kappa)$, given by a well-posed TPBVSR (3.4), is determined by*

$$\|\mathcal{H}(\omega, \kappa)\|_{HS}^2 = -\text{tr}\left((L_1 + L_2\Phi(b,a))^{-1}L_2 \begin{bmatrix} 0 & I \end{bmatrix} \Psi(b,a) \begin{bmatrix} I \\ 0 \end{bmatrix}\right), \quad (3.18)$$

where

$$\begin{aligned} L_1 &:= \begin{bmatrix} N_1 & 0 \\ 0 & M_1 \end{bmatrix}, \quad L_2 := \begin{bmatrix} N_2 & 0 \\ 0 & M_2 \end{bmatrix}, \\ A(y) &:= \begin{bmatrix} A_0(y) & B_0(y)B_0^*(y) \\ 0 & -A_0^*(y) \end{bmatrix}, \quad B(y) := \begin{bmatrix} 0 \\ -C_0^*(y) \end{bmatrix}, \quad C(y) := [C_0(y) \ 0]. \end{aligned}$$

Matrices M_1 and M_2 are determined from the following Singular Value Decomposition

$$\begin{bmatrix} N_1^* \\ -N_2^* \end{bmatrix} = USV^* = [U_1 \ U_2] \begin{bmatrix} S_1 \\ 0 \end{bmatrix} V^* = U_1 S_1 V^*, \quad U_1, U_2 \in \mathbb{C}^{2n_0 \times n_0},$$

by

$$[M_1 \ M_2] = U_2^*.$$

On the other hand, $\Phi(y, \eta)$ and $\Psi(y, \eta)$ respectively denote the state transition matrices of $A(y)$ and

$$\begin{bmatrix} A(y) & 0 \\ B(y)C(y) & A(y) \end{bmatrix}.$$

For systems with constant coefficients in y formula (3.18) simplifies to

$$\|\mathcal{H}(\omega, \kappa)\|_{HS}^2 = -\text{tr}\left((L_1 + L_2 e^{cA})^{-1} L_2 \begin{bmatrix} 0 & I \end{bmatrix} \exp\left\{c \begin{bmatrix} A & 0 \\ BC & A \end{bmatrix}\right\} \begin{bmatrix} I \\ 0 \end{bmatrix}\right), \quad (3.19)$$

where $c := b - a$.

Hence, we have converted a problem of evaluating the Hilbert–Schmidt norm of an infinite dimensional object to computations with finite matrices. For systems with non-constant coefficients in y , at any given (ω, κ) , we need to solve a differential equation whose order is four times larger than the order of the original differential operator to obtain the state transition matrix $\Psi(b, a)$. On the other hand, for systems with constant coefficients in y this computation amounts to determination of the corresponding matrix exponential. Both computations can be easily performed using commercially available software such as MATLAB or MATHEMATICA.

In § 3.3 and § 9.5, we illustrate the application of this procedure and exactly determine the frequency responses of two systems: a one-dimensional diffusion equation, and a system that describes the dynamics of velocity fluctuations in channel fluid flows.

3.3 Examples

In this section, we illustrate how the frequency responses of a one-dimensional diffusion equation can be determined explicitly using the previously described procedure. In § 9.5, we also employ Theorem 2 to determine the Hilbert–Schmidt norms of the streamwise constant linearized Navier–Stokes equations in channel flows.

3.3.1 A one-dimensional diffusion equation

We consider a one-dimensional diffusion equation on $L^2[-1, 1]$ with Dirichlet boundary conditions

$$\begin{aligned} \partial_t \psi(y, t) &= [\partial_{yy} \psi(t)](y) + d(y, t), \\ \psi(\pm 1, t) &= 0. \end{aligned}$$

The application of the temporal Fourier transform yields

$$\psi(y, \omega) = [(i\omega I - \partial_{yy})^{-1} d(\omega)](y) =: [\mathcal{H}(\omega) d(\omega)](y).$$

Our objective is to compute the Hilbert–Schmidt norm of operator that maps d into ψ as a function of temporal frequency ω . A particular TPBVSR of $\mathcal{H}(\omega)$ is given by

$$\mathcal{H}(\omega) : \begin{cases} \begin{bmatrix} x'_1(y, \omega) \\ x'_2(y, \omega) \end{bmatrix} = \begin{bmatrix} 0 & 1 \\ i\omega & 0 \end{bmatrix} \begin{bmatrix} x_1(y, \omega) \\ x_2(y, \omega) \end{bmatrix} + \begin{bmatrix} 0 \\ -1 \end{bmatrix} d(y, \omega), \\ \psi(y, \omega) = [1 \ 0] \begin{bmatrix} x_1(y, \omega) \\ x_2(y, \omega) \end{bmatrix}, \\ 0 = \begin{bmatrix} 1 & 0 \\ 0 & 0 \end{bmatrix} \begin{bmatrix} x_1(-1, \omega) \\ x_2(-1, \omega) \end{bmatrix} + \begin{bmatrix} 0 & 0 \\ 1 & 0 \end{bmatrix} \begin{bmatrix} x_1(1, \omega) \\ x_2(1, \omega) \end{bmatrix}, \quad y \in [-1, 1]. \end{cases}$$

The application of procedure described in § 3.2.1 yields the realization of $\mathcal{H}(\omega)\mathcal{H}^*(\omega)$ in the form of (3.7) with

$$A = \begin{bmatrix} 0 & 1 & 0 & 0 \\ i\omega & 0 & 0 & 1 \\ 0 & 0 & 0 & i\omega \\ 0 & 0 & -1 & 0 \end{bmatrix}, \quad B = \begin{bmatrix} 0 \\ 0 \\ -1 \\ 0 \end{bmatrix}, \quad C = [1 \ 0 \ 0 \ 0],$$

$$L_1 = \begin{bmatrix} 1 & 0 & 0 & 0 \\ 0 & 0 & 0 & 0 \\ 0 & 0 & 0 & 1 \\ 0 & 0 & 0 & 0 \end{bmatrix}, \quad L_2 = \begin{bmatrix} 0 & 0 & 0 & 0 \\ 1 & 0 & 0 & 0 \\ 0 & 0 & 0 & 0 \\ 0 & 0 & 0 & 1 \end{bmatrix}.$$

The application of (3.19), with the help of MATHEMATICA, yields

$$\|\mathcal{H}(\omega)\|_{HS}^2 = \frac{1}{2\omega^2} \left\{ -1 + \frac{\sqrt{2\omega}(\sinh(\sqrt{8\omega}) + \sin(\sqrt{8\omega}))}{\cosh(\sqrt{8\omega}) - \cos(\sqrt{8\omega})} \right\}. \quad (3.20)$$

It is noteworthy that $\|\mathcal{H}(\omega)\|_{HS}^2$ can be also obtained by doing a spectral decomposition of the operator ∂_{yy} . It is well known (see, for example [3]) that this operator with Dirichlet boundary conditions has the following set of orthonormal eigenfunctions $\{\varphi_n\}_{n \in \mathbb{N}}$ with corresponding eigenvalues $\{\gamma_n\}_{n \in \mathbb{N}}$

$$\varphi_n(y) := \sin\left(\frac{n\pi}{2}(y+1)\right), \quad \gamma_n := -\frac{n^2\pi^2}{4}, \quad n \in \mathbb{N}.$$

It is easily shown that the eigenfunction expansion results into

$$\|\mathcal{H}(\omega)\|_{HS}^2 = \sum_{n \in \mathbb{N}} \frac{1}{\omega^2 + \left(\frac{n\pi}{2}\right)^4},$$

which can be summed to obtain (3.20). However, for operators that do not have explicit expressions for their eigenvalues, it is much easier to compute the trace explicitly as we illustrate in § 9.5.

3.4 Summary

We develop a procedure for the explicit determination of the frequency responses for a class of spatially distributed systems. This procedure avoids the need for spatial discretization and provides an exact reduction of an infinite dimensional problem to a problem in which only matrices of finite dimensions are involved. The order of these matrices is at most four times larger than the order of the differential operator at hand.

We also illustrate application of this technique by providing two examples: a one-dimensional diffusion equation (see § 3.3.1), and a system obtained by linearization of the Navier-Stokes equations in channel flows around a given nominal velocity profile (see § 9.5).

Bibliography

- [1] B. Bamieh and M. Dahleh, “Exact computation of traces and H^2 norms for a class of infinite dimensional problems,” *IEEE Transactions on Automatic Control*, vol. 48, no. 4, pp. 646–649, April 2003.
- [2] B. Bamieh, F. Paganini, and M. A. Dahleh, “Distributed control of spatially invariant systems,” *IEEE Transactions on Automatic Control*, vol. 47, no. 7, pp. 1091–1107, July 2002.
- [3] R. F. Curtain and H. J. Zwart, *An Introduction to Infinite-Dimensional Linear Systems Theory*. New York: Springer-Verlag, 1995.
- [4] N. Young, *An introduction to Hilbert spaces*. New York: Cambridge University Press, 1988.
- [5] I. Gohberg and M. A. Kaashoek, “Time varying linear systems with boundary conditions and integral operators, I. the transfer operator and its properties,” *Integral Equations and Operator Theory*, vol. 7, pp. 325–391, 1984.

Chapter 4

Stability and system norms of PDEs with periodic coefficients

It is well known that stability properties of certain Linear Time Invariant (LTI) systems can be altered by connecting them in feedback with temporally periodic gains. Depending on the relation between the period of the time varying gain and the dominant modes of the LTI system, the overall system may be stabilized or destabilized. This phenomenon is usually referred to as *parametric resonance* [1]. An example of system in which parametric resonance takes place is given by the Mathieu equation. In the controls literature, this phenomenon has been used in ‘sensorless control schemes’ to stabilize unstable systems, and is commonly referred to as *vibrational control*.

In this chapter, we investigate similar parametric resonance mechanisms for spatially distributed systems described by PDEs with periodic coefficients. Our objective is to characterize exponential stability and input-output norms of spatially periodic distributed systems. To this end, we develop a spatial lifting technique similar to the temporal lifting technique for linear periodic ODEs [2–8]. This technique provides for a strong equivalence between spatially periodic distributed systems defined on a continuous spatial domain with spatially invariant systems defined on a discrete lattice. Also, we show how lifting can be utilized for analysis of distributed system that are both spatially and temporally periodic.

For the purpose of stability characterization, the lifting technique is equivalent to the more widely used Floquet analysis of periodic PDEs. However, Floquet analysis does not easily lend itself to the computation of system norms and sensitivities. We show how the lifting technique can be used to compute both the spectrum of the generating operator and \mathcal{H}_∞ and \mathcal{H}_2 norms of distributed systems.

Our presentation is organized as follows: we begin next section with some mathematical preliminaries regarding the spatial lifting technique. We then present a convenient representation of lifted transfer functions using particular basis sets developed in [8] for use with periodic temporal systems. We then demonstrate how a representation of the lifted systems in the transformed domain can simply be determined from the Fourier symbol of the original PDE operator and the Fourier expansion series of the periodic gains. Finally, we present some examples of PDEs which exhibit parametric resonance, and use the lifting technique to calculate regions of stability and instability, and input-output norms as functions of the period and amplitude of the periodic gains.

4.1 Preliminaries

We consider spatially distributed systems of the form

$$\partial_t \psi(x, t) = \mathcal{A}\psi(x, t) + \mathcal{B}u(x, t), \quad (4.1a)$$

$$y(x, t) = \mathcal{C}\psi(x, t), \quad (4.1b)$$

where \mathcal{A} , \mathcal{B} , and \mathcal{C} are time invariant linear operators with spatially periodic coefficients, u is a forcing term, and ψ and y are state and output fields, respectively. The spatial independent variable x is assumed to belong to $(-\infty, \infty)$. Our objective is to investigate dynamical properties of system (4.1) by computing the operator \mathcal{A} eigenvalues and input-output system norms.

Input-output representation of (4.1) is given by

$$\begin{aligned} y(x, t) &= [\mathcal{H}u](x, t) \\ &= \int_0^\infty \int_{-\infty}^\infty \mathcal{H}(x, \xi, t - \tau) u(\xi, \tau) d\xi d\tau, \end{aligned} \quad (4.2)$$

where with a slight abuse of notation we use the same notation to denote an operator \mathcal{H} and its kernel $\mathcal{H}(x, \xi, t)$. For X -periodic system (4.1), the following properties of kernel function representing \mathcal{H} are readily established:

$$\begin{aligned} \mathcal{H}(x, \xi, t) &= \mathcal{H}(x + X, \xi + X, t), \\ \mathcal{H}(x, \xi, t) &= \mathcal{H}(x + nX, \xi + nX, t), \quad \forall n \in \mathbb{Z}, \\ \mathcal{H}(x + kX, \xi + nX, t) &= \mathcal{H}(x + (k - n)X, \xi, t), \quad \forall k, n \in \mathbb{Z}. \end{aligned}$$

One of the main difficulties in dealing with systems under study is the absence of spatial invariance. Linear spatially invariant systems are well studied [9] and convenient to work with. It is for this reason that we develop the appropriate tools that exploit the underlying periodicity and transform it into appropriate form of spatial invariance. In particular, we develop a spatial lifting technique similar to the temporal lifting technique for linear periodic ODEs [2].

The lifted signal of any $f \in L^2(-\infty, \infty)$ can be defined as $\bar{f}_k(\hat{x}) := f(kX + \hat{x})$, $k \in \mathbb{Z}$, $0 \leq \hat{x} \leq X$. The lifting can be visualized as a breaking a continuous-time signal up into a sequence of pieces which take their values in a function space of a length X . In other words, $\{\bar{f}_k\} \in l^2_{L^2[0, X]}$, that is for any given $k \in \mathbb{Z}$, $\bar{f}_k \in L^2[0, X]$. The lifting operator W_X is one-to-one and onto and thus has a well defined inverse given by $f = W_X^{-1}\bar{g}$, $f(x) = \bar{g}_k(x - kX)$, $k \in \mathbb{Z}$, $kX \leq x \leq (k + 1)X$. The action of the operator W_X^{-1} is exactly the opposite of the one caused by the lifting operator. Namely, W_X^{-1} puts together a sequence of function pieces whose value belongs to $L^2[0, X]$, giving a function $f \in L^2(-\infty, \infty)$. Furthermore, W_X represents an isometric isomorphism from $L^2[0, X]$ to $l^2_{L^2[0, X]}$. Additional properties of the lifting operator can be found in [2].

Using (4.2), the system's periodicity, and the definition of lifted signals, it is readily shown that $\bar{y}_k(\hat{x}, t) := y(kX + \hat{x}, t)$, for every $k \in \mathbb{Z}$ can be expressed as

$$\begin{aligned} \bar{y}_k(\hat{x}, t) &= \sum_{n \in \mathbb{Z}} \int_0^\infty \int_0^X \bar{\mathcal{H}}_{k-n}(\hat{x}, \eta, t - \tau) \bar{u}_n(\eta, \tau) d\eta d\tau \\ &=: \sum_{n \in \mathbb{Z}} [\bar{\mathcal{H}}_{k-n} \bar{u}_n](\hat{x}, t), \end{aligned} \quad (4.3)$$

which is the convolution representation of a system operating on the $L^2[0, X]$ valued signals (in \hat{x}) $\{\bar{y}_n\}_{n \in \mathbb{Z}}$ and $\{\bar{u}_n\}_{n \in \mathbb{Z}}$. Sequence $\{\bar{\mathcal{H}}_n\}_{n \in \mathbb{Z}}$ represents the operator-valued impulse response of the lifting of \mathcal{H} defined by

$$\bar{\mathcal{H}}_n(\hat{x}, \eta, t) := \mathcal{H}(nX + \hat{x}, \eta, t), \quad 0 \leq \hat{x} < X, \quad 0 \leq \eta < X, \quad t \geq 0, \quad n \in \mathbb{Z}.$$

Therefore, using lifting we have transformed spatially periodic system (4.2) defined on a continuous spatial domain $L^2(-\infty, \infty)$ to spatially invariant system (4.3) defined on a discrete spatial lattice \mathbb{Z} . This implies that the appropriate Fourier transform can be used to further simplify analysis [9]. In this particular situation, the appropriate Fourier transform is the bilateral \mathcal{Z} -transform evaluated on the unit circle ($z := e^{i\theta}$, with $0 \leq \theta < 2\pi$). We refer to this transform as \mathcal{Z}_θ -transform.

The \mathcal{Z}_θ -transform of the sequence of signals $\{\bar{f}_k\}$ is determined by $\hat{f}_\theta(\hat{x}) := \sum_{k \in \mathbb{Z}} \bar{f}_k(\hat{x}) e^{-i\theta k}$. Note that $\{\hat{f}_\theta\} : [0, 2\pi] \rightarrow L^2[0, X]$. In other words, $\{\hat{f}_\theta\}$ is an $L^2[0, X]$ -valued function defined on the unit circle, i.e.

$\{\hat{f}_\theta\} \in L^2_{L^2[0, X]}[0, 2\pi]$. Application of \mathcal{Z}_θ -transform on (4.3) yields

$$\begin{aligned}\hat{y}_\theta(\hat{x}, t) &= \int_0^\infty \int_0^X \hat{\mathcal{H}}_\theta(\hat{x}, \eta, t - \tau) \hat{u}_\theta(\eta, \tau) d\eta d\tau \\ &=: [\hat{\mathcal{H}}_\theta \hat{u}_\theta](\hat{x}, t),\end{aligned}\tag{4.4}$$

where

$$\begin{aligned}\hat{\mathcal{H}}_\theta(\hat{x}, \eta, t) &:= \sum_{n \in \mathbb{Z}} \bar{\mathcal{H}}_n(\hat{x}, \eta, t) e^{-i\theta n}, \\ \bar{\mathcal{H}}_n(\hat{x}, \eta, t) &= \frac{1}{2\pi} \int_0^{2\pi} \hat{\mathcal{H}}_\theta(\hat{x}, \eta, t) e^{i\theta n} d\theta.\end{aligned}$$

In particular, system (4.1) is transformed into

$$\partial_t \hat{\psi}_\theta(\hat{x}, t) = \hat{\mathcal{A}}_\theta \hat{\psi}_\theta(\hat{x}, t) + \hat{\mathcal{B}}_\theta \hat{u}_\theta(\hat{x}, t),\tag{4.5a}$$

$$\hat{y}_\theta(\hat{x}, t) = \hat{\mathcal{C}}_\theta \hat{\psi}_\theta(\hat{x}, t).\tag{4.5b}$$

Thus, a spatially distributed X -periodic system (4.1) defined over $L^2(-\infty, \infty)$ is transformed into a θ -parameterized family of spatially distributed systems (4.5) defined over $L^2[0, X]$ with $\theta \in [0, 2\pi]$, by combined application of the lifting and \mathcal{Z}_θ -transform.

In the next section, we illustrate that an appropriate basis representation of (4.5) can be determined explicitly for PDE operators with periodic coefficients.

4.2 Representation of the lifted systems

In this section, we first develop a convenient representation of the transforms of lifted signals, and then use it to obtain a representation of spatially periodic systems. To determine $\hat{f}_\theta(\hat{x})$ in terms of the original function $f(x)$, we need to find an appropriate way to represent $\hat{f}_\theta(\hat{x})$ for each fixed $\theta \in [0, 2\pi]$. Since for any given θ , \hat{f}_θ is a function (in \hat{x}) over $[0, X]$, we want to find a basis of $L^2[0, X]$ in which the representation of \hat{f}_θ is easily determined. The following Lemma from [8] shows that the θ -parameterized basis functions (4.6), for any given θ , represent an orthonormal basis of $L^2[0, X]$. This basis is most convenient for achieving our objective.

Lemma 3 *The θ -parameterized set of functions $\{\vartheta_{\theta,n}\}_{n \in \mathbb{Z}}$ of the form*

$$\vartheta_{\theta,n}(\hat{x}) := \frac{1}{\sqrt{X}} e^{i \frac{2\pi n + \theta}{X} \hat{x}},\tag{4.6}$$

for each $\theta \in [0, 2\pi]$ represents a complete orthonormal basis of $L^2[0, X]$.

The following Proposition shows that the coefficients in the $\vartheta_{\theta,n}(\hat{x})$ -basis expansion of $\hat{f}_\theta(\hat{x})$ can be determined from the Fourier transform of the original function $f(x)$.

Proposition 4 *Let $f(x) \in L^2(-\infty, \infty)$ have a Fourier transform $F(k_x)$*

$$F(k_x) := \int_{-\infty}^{\infty} f(x) e^{-ik_x x} dx.$$

Then $\hat{f}_\theta(\hat{x})$ can be represented as

$$\hat{f}_\theta(\hat{x}) = \frac{1}{\sqrt{X}} \sum_{n \in \mathbb{Z}} F\left(\frac{2\pi n + \theta}{X}\right) \vartheta_{\theta,n}(\hat{x}).\tag{4.7}$$

Proof: The Fourier transform of $f(x)$ can be expressed as

$$\begin{aligned}
F(k_x) &= \int_{-\infty}^{\infty} f(x) e^{-ik_x x} dx \\
&= \sum_{k \in \mathbb{Z}} \int_{kX}^{(k+1)X} f(x) e^{-ik_x x} dx \\
&= \sum_{k \in \mathbb{Z}} \int_{kX}^{(k+1)X} \bar{f}_k(x - kX) e^{-ik_x x} dx \\
&= \sum_{k \in \mathbb{Z}} \int_0^X \bar{f}_k(\hat{x}) e^{-ik_x(\hat{x} + kX)} d\hat{x} \\
&= \sum_{k \in \mathbb{Z}} e^{-ik_x X k} \int_0^X \bar{f}_k(\hat{x}) e^{-ik_x \hat{x}} d\hat{x}.
\end{aligned}$$

On the other hand, $\hat{f}_\theta(\hat{x})$ can be represented in terms of $L^2[0, X]$ basis functions in the following way

$$\hat{f}_\theta(\hat{x}) = \sum_{k \in \mathbb{Z}} \alpha_{\theta,k} \vartheta_{\theta,k}(\hat{x}), \quad (4.8)$$

where $\alpha_{\theta,k}$'s are coefficients to be determined. The definition of $\hat{f}_\theta(\hat{x})$ combined with the previous equation yields a relationship of the form

$$\sum_{k \in \mathbb{Z}} \alpha_{\theta,k} \vartheta_{\theta,k}(\hat{x}) = \sum_{k \in \mathbb{Z}} \bar{f}_k(\hat{x}) e^{-i\theta k}, \quad (4.9)$$

which allows us to find the unknown coefficients $\alpha_{\theta,n}$ by taking the $L^2[0, X]$ -inner product between $\vartheta_{\theta,n}(\hat{x})$ and (4.9). By doing so, one readily gets

$$\begin{aligned}
\alpha_{\theta,n} &= \left\langle \vartheta_{\theta,n}, \sum_{k \in \mathbb{Z}} \bar{f}_k e^{-i\theta k} \right\rangle_{L^2[0, X]} \\
&= \frac{1}{\sqrt{X}} \sum_{k \in \mathbb{Z}} e^{-i\theta k} \int_0^X \bar{f}_k(\hat{x}) e^{-i\frac{2\pi n + \theta}{X} \hat{x}} d\hat{x} \\
&= \frac{1}{\sqrt{X}} \sum_{k \in \mathbb{Z}} e^{-ik_x X k} \int_0^X \bar{f}_k(\hat{x}) e^{-ik_x \hat{x}} d\hat{x} \\
&= \frac{1}{\sqrt{X}} F\left(\frac{2\pi n + \theta}{X}\right),
\end{aligned}$$

which renders (4.8) into (4.7). ■

For notational convenience, we rewrite (4.7) as

$$\hat{f}_\theta(\hat{x}) = \mathcal{V}_\theta^{-1} F_\theta,$$

where F_θ is an infinite θ -parameterized vector determined by

$$F_\theta := \left[\dots \ F\left(\frac{-2\pi + \theta}{X}\right) \ F\left(\frac{\theta}{X}\right) \ F\left(\frac{2\pi + \theta}{X}\right) \ \dots \right]^T.$$

We refer to the operator that yields the coefficients in the $\{\vartheta_{\theta,n}(\hat{x})\}_{n \in \mathbb{Z}}$ -basis representation of $\hat{f}_\theta(\hat{x})$ as the \mathcal{V}_θ -transform. The action of this operator is clearly specified by

$$F_\theta = \mathcal{V}_\theta \hat{f}_\theta(\hat{x}) = \sqrt{X} \begin{bmatrix} \cdots & \langle \vartheta_{\theta,-1}, \hat{f}_\theta \rangle_{L^2[0,X]} & \langle \vartheta_{\theta,0}, \hat{f}_\theta \rangle_{L^2[0,X]} & \langle \vartheta_{\theta,1}, \hat{f}_\theta \rangle_{L^2[0,X]} & \cdots \end{bmatrix}^T.$$

We now apply these results to find the corresponding representations of the underlying operators in the $\vartheta_{\theta,n}(\hat{x})$ -basis.

4.2.1 Spatially invariant operators

Proposition 4 can be used to find the spectral coefficients in the $\vartheta_{\theta,n}(\hat{x})$ -basis expansion of $\hat{f}_\theta(\hat{x})$ as ‘samples’ of the Fourier transform $F(k_x)$. This implies that for a spatially invariant PDE [9] of the form

$$\partial_t \psi(x, t) = \mathcal{A}(\partial_x) \psi(x, t), \quad (4.10)$$

whose frequency domain equivalent is given by

$$\dot{\Psi}(k_x, t) = \mathcal{A}(ik_x) \Psi(k_x, t),$$

the representation of the transformed lifted system

$$\partial_t \hat{\psi}_\theta(\hat{x}, t) = \hat{\mathcal{A}}_\theta \hat{\psi}_\theta(\hat{x}, t),$$

in the basis $\{\vartheta_{\theta,n}(\hat{x})\}_{n \in \mathbb{Z}}$, is completely determined by

$$\dot{\Psi}_\theta(t) = A_\theta \Psi_\theta(t),$$

where $\Psi_\theta(t) := [\dots \Psi(\frac{\theta}{X}, t) \Psi(\frac{2\pi+\theta}{X}, t) \dots]^T$, and $A_\theta := \text{diag}\{\mathcal{A}(i\frac{2\pi n + \theta}{X})\}_{n \in \mathbb{Z}}$. In other words, the matrix representation of $\hat{\mathcal{A}}_\theta$ in the chosen basis is simply $\text{diag}\{\mathcal{A}(i\frac{2\pi n + \theta}{X})\}_{n \in \mathbb{Z}}$, where $\mathcal{A}(\cdot)$ is the symbol used for the original PDE operator. For example, for a heat equation on $L^2(-\infty, \infty)$, $\partial_t \psi(x, t) = \partial_x^2 \psi(x, t)$, the properties of our system are fully determined by $\text{diag}\{\dots, -(\frac{-2\pi+\theta}{X})^2, -(\frac{\theta}{X})^2, -(\frac{2\pi+\theta}{X})^2, \dots\}$, where parameter θ takes all values between 0 and 2π .

4.2.2 Periodic gains

To apply this theory to an arbitrary PDE with periodic coefficients we need a method for lifting the part of the system which contains the periodic terms. Suppose that we have a problem of the form (4.10) where the operator \mathcal{A} can be represented as $\mathcal{A}(\partial_x) := \mathcal{A}_1(\partial_x) + f(x)$, with \mathcal{A}_1 a spatially invariant operator and $f(x)$ an X -periodic function, $f(x) = f(x+X)$. Since we have shown in § 4.2.1 how to lift the spatially invariant part of our system, we now illustrate a way for lifting a periodic gain. Let

$$\phi(x, t) := f(x) \psi(x, t). \quad (4.11)$$

Due to X -periodicity of the function f , $\bar{f}_k(\hat{x}) := f(kX + \hat{x}) = f(\hat{x})$, $\forall k \in \mathbb{Z}$, the lifted signal is given by

$$\bar{\phi}_k(\hat{x}, t) := f(\hat{x}) \bar{\psi}_k(\hat{x}, t), \quad k \in \mathbb{Z}, \quad 0 \leq \hat{x} \leq X. \quad (4.12)$$

After applying the \mathcal{Z}_θ -transform (4.12) simplifies to

$$\hat{\phi}_\theta(\hat{x}, t) = f(\hat{x}) \hat{\psi}_\theta(\hat{x}, t), \quad \theta \in [0, 2\pi], \quad 0 \leq \hat{x} \leq X,$$

which means that the lifted operator is just multiplication by $f(\hat{x})$ and is constant in θ . Our objective is to find the representation of this operator in the $\{\vartheta_{\theta,n}(\hat{x})\}_{n \in \mathbb{Z}}$ -basis. Since $f(x)$ is a periodic function, it can be decomposed into its Fourier series, $f(x) = \sum_{m \in \mathbb{Z}} a_m e^{i\frac{2\pi m}{X}x}$. By applying the Fourier transform on (4.11)

we obtain

$$\begin{aligned}
\Phi(k_x, t) &= \int_{-\infty}^{\infty} f(x) \psi(x, t) e^{-ik_x x} dx \\
&= \sum_{m \in \mathbb{Z}} a_m \int_{-\infty}^{\infty} \psi(x, t) e^{-i(k_x - \frac{2\pi m}{X})x} dx \\
&= \sum_{m \in \mathbb{Z}} a_m \Psi(k_x - \frac{2\pi m}{X}, t).
\end{aligned} \tag{4.13}$$

Using Proposition 4, we express $\hat{\phi}_\theta(\hat{x}, t)$ as

$$\begin{aligned}
\hat{\phi}_\theta(\hat{x}, t) &= \frac{1}{\sqrt{X}} \sum_{n \in \mathbb{Z}} \Phi\left(\frac{2\pi n + \theta}{X}, t\right) \vartheta_{\theta, n}(\hat{x}) \\
&= \frac{1}{\sqrt{X}} \sum_{n, m \in \mathbb{Z}} a_m \Psi\left(\frac{2\pi(n-m)+\theta}{X}, t\right) \vartheta_{\theta, n}(\hat{x}),
\end{aligned}$$

where, based on (4.13), $\Phi\left(\frac{2\pi n + \theta}{X}, t\right)$ is determined by

$$\begin{aligned}
\Phi\left(\frac{2\pi n + \theta}{X}, t\right) &= \sum_{m \in \mathbb{Z}} a_m \Psi\left(\frac{2\pi(n-m)+\theta}{X}, t\right) \\
&= \sum_{k \in \mathbb{Z}} a_{n-k} \Psi\left(\frac{2\pi k + \theta}{X}, t\right),
\end{aligned}$$

or equivalently in the matrix form $\Phi_\theta(t) = \Gamma \Psi_\theta(t)$, where Γ is a bi-infinite Toeplitz matrix defined by

$$\Gamma := \begin{bmatrix} \ddots & \ddots & \ddots & & \\ \ddots & a_0 & a_{-1} & a_{-2} & \\ \ddots & a_1 & a_0 & a_{-1} & \ddots \\ a_2 & a_1 & a_0 & \ddots & \\ \ddots & \ddots & \ddots & \ddots & \end{bmatrix}. \tag{4.14}$$

Thus, we conclude that the matrix representation of a spatial-periodic gain in the $\{\vartheta_{\theta, n}(\hat{x})\}_{n \in \mathbb{Z}}$ -basis is completely determined by a Toeplitz matrix whose elements correspond to the Fourier coefficients

$$a_m := \frac{1}{X} \int_0^X f(x) e^{-i\frac{2\pi m}{X}x} dx.$$

For example,

$$f(x) = \alpha \sin\left(\frac{2\pi}{X}x\right) \Rightarrow a_m = \begin{cases} \frac{i\alpha}{2} & m = -1, \\ -\frac{i\alpha}{2} & m = 1, \\ 0 & \text{otherwise,} \end{cases}$$

and

$$f(x) = \alpha \cos\left(\frac{2\pi}{X}x\right) \Rightarrow a_m = \begin{cases} \frac{\alpha}{2} & m = \pm 1, \\ 0 & \text{otherwise.} \end{cases}$$

4.2.3 Feedback interconnections

The procedure described in § 4.2.1 and § 4.2.2 can be applied to obtain a representation of a system with spatially periodic coefficients on $L^2(-\infty, \infty)$ of the form

$$\partial_t \psi(x, t) = (\mathcal{A}_1 + \mathcal{B}_1 f \mathcal{C}) \psi(x, t) + \mathcal{B}_2 u(x, t) \quad (4.15a)$$

$$y(x, t) = \mathcal{C} \psi(x, t), \quad (4.15b)$$

where $\mathcal{A}_1, \mathcal{B}_1, \mathcal{B}_2$, and \mathcal{C} are spatially-invariant operators, f is a given X -periodic matrix valued function, u is a distributed input, y is a distributed output, and ψ is a distributed state. We can equivalently represent system (4.15) as shown in Figure 4.1.

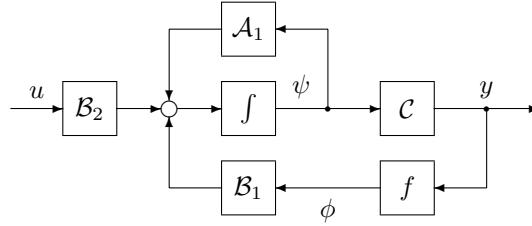


Figure 4.1: Block diagram of system (4.15) with spatially invariant operators $\mathcal{A}_1, \mathcal{B}_1, \mathcal{B}_2$, and \mathcal{C} , and an X -periodic matrix valued function f .

Since the lifting is invariant under feedback [2] the transformed lifted system can be rewritten as

$$\begin{aligned} \partial_t \hat{\psi}_\theta(\hat{x}, t) &= (\hat{\mathcal{A}}_{1\theta} + \hat{\mathcal{B}}_{1\theta} f(\hat{x}) \hat{\mathcal{C}}_\theta) \hat{\psi}_\theta(\hat{x}, t) + \hat{\mathcal{B}}_{2\theta} \hat{u}_\theta(\hat{x}, t) \\ &=: \hat{\mathcal{A}}_\theta \hat{\psi}_\theta(\hat{x}, t) + \hat{\mathcal{B}}_\theta \hat{u}_\theta(\hat{x}, t), \end{aligned} \quad (4.16a)$$

$$\hat{y}_\theta(\hat{x}, t) = \hat{\mathcal{C}}_\theta \hat{\psi}_\theta(\hat{x}, t), \quad (4.16b)$$

where $\{\hat{\mathcal{A}}_{1\theta}, \hat{\mathcal{B}}_{1\theta}, \hat{\mathcal{B}}_{2\theta}, \hat{\mathcal{C}}_\theta\}$ and $f(\hat{x})$ can be lifted according to the procedure described in § 4.2.1 and § 4.2.2. Thus, in the $\{\vartheta_{\theta,n}(\hat{x})\}_{n \in \mathbb{Z}}$ -basis system (4.16) is represented by

$$\begin{aligned} \dot{\Psi}_\theta(t) &= (A_{1\theta} + B_{1\theta} \Xi C_\theta) \Psi_\theta(t) + B_{2\theta} U_\theta(t) \\ &=: A_\theta \Psi_\theta(t) + B_\theta U_\theta(t), \end{aligned} \quad (4.17a)$$

$$Y_\theta(t) = C_\theta \Psi_\theta(t), \quad (4.17b)$$

where, for example, $A_{1\theta}$ is a bi-infinite block diagonal matrix determined by $\text{diag}\{\mathcal{A}_1(i \frac{2\pi n + \theta}{X})\}_{n \in \mathbb{Z}}$, and Ξ is a block Toeplitz matrix whose elements can be determined based on (4.14).

As an example, consider $\partial_t \psi = \partial_x^2 \psi + \cos(\frac{2\pi}{X}x) \partial_x^2 \psi + \partial_x u$. In this case, the operators on the right-hand side of (4.17a) respectively become $A_\theta = (I + \Gamma) \text{diag}\{-(\frac{2\pi n + \theta}{X})^2\}_{n \in \mathbb{Z}}$ and $B_\theta = \text{diag}\{i \frac{2\pi n + \theta}{X}\}_{n \in \mathbb{Z}}$.

In § 4.3, we show that stability properties and input-output system norms of spatially distributed systems with X -periodic coefficients can be determined by analyzing the representation of their \mathcal{Z}_θ -transformed lifted equivalents in the $\{\vartheta_{\theta,n}(\hat{x})\}_{n \in \mathbb{Z}}$ -basis.

4.3 Stability and input-output norms of spatially periodic systems

The commutative diagram below schematically illustrates combined action of the lifting, \mathcal{Z}_θ -transform, and \mathcal{V}_θ -transform on a spatially distributed X -periodic system:

$$\begin{array}{ccc}
 L_{l^2}^2[0, 2\pi) & \xrightarrow{H_\theta} & L_{l^2}^2[0, 2\pi) \\
 \downarrow \mathcal{V}_\theta^{-1} & & \uparrow \mathcal{V}_\theta \\
 L_{L^2[0, X]}^2[0, 2\pi) & \xrightarrow{\hat{\mathcal{H}}_\theta} & L_{L^2[0, X]}^2[0, 2\pi) \\
 \downarrow \mathcal{Z}_\theta^{-1} & & \uparrow \mathcal{Z}_\theta \\
 l_{L^2[0, X]}^2 & \xrightarrow{\bar{\mathcal{H}}} & l_{L^2[0, X]}^2 \\
 \downarrow W_X^{-1} & & \uparrow W_X \\
 L^2(-\infty, \infty) & \xrightarrow{\mathcal{H}} & L^2(-\infty, \infty)
 \end{array}$$

In other words, application of operator $\mathcal{T} := \mathcal{V}_\theta \mathcal{Z}_\theta W_X$ renders system (4.1) into a θ -parameterized time invariant family of systems of the form

$$\dot{\Psi}_\theta(t) = A_\theta \Psi_\theta(t) + B_\theta U_\theta(t), \quad (4.18a)$$

$$Y_\theta(t) = C_\theta \Psi_\theta(t), \quad (4.18b)$$

where A_θ , B_θ , and C_θ represent bi-infinite matrices that can be determined using the procedure developed in § 4.2. Therefore, the analysis of spatially distributed systems with periodic coefficients amounts to the analysis of their \mathcal{T} -transformed counterparts as parameter θ assumes all values in the interval $[0, 2\pi]$.

We point out that systems (4.1) and (4.18) have same stability properties. This follows from the fact that operator \mathcal{T} represents an isometric isomorphism from $L^2(-\infty, \infty)$ to $L_{l^2}^2[0, 2\pi)$ and Corollary 3 of [9]. Based on these, we conclude that system (4.1) is exponentially stable if and only if for each $\theta \in [0, 2\pi)$, A_θ in (4.18) is stable. Additionally, it can be shown that the spectrum of the generator of (4.1) is determined by

$$\sigma\{\mathcal{A}\} = \overline{\bigcup_{\theta \in [0, 2\pi)} \sigma\{A_\theta\}}.$$

Furthermore, since W_X , \mathcal{Z}_θ , and \mathcal{V}_θ represent bijective linear isometries it follows that the \mathcal{T} -transform preserves system norms [2]. To illustrate this, we apply the temporal Fourier transform on (4.1) and (4.18) to obtain

$$\begin{aligned}
 y(x, \omega) &= [\mathcal{C}(i\omega I - \mathcal{A})^{-1} \mathcal{B} u(\omega)](x) \\
 &=: [\mathcal{H}(\omega) u(\omega)](x) \\
 &= \int_{-\infty}^{\infty} \mathcal{H}(x, \xi, \omega) u(\xi, \omega) d\xi,
 \end{aligned}$$

and

$$\begin{aligned}
 Y_\theta(\omega) &= C_\theta(i\omega I - A_\theta)^{-1} B_\theta U_\theta(\omega) \\
 &=: H_\theta(\omega) U_\theta(\omega),
 \end{aligned}$$

respectively. We remark that for any given ω , $\mathcal{H}(\omega)$ represents a spatial operator that maps $u(\omega)$ into $y(\omega)$. On the other hand, $H_\theta(\omega)$ is a multiplication operator parameterized by two frequencies: $\omega \in \mathbb{R}$ and $\theta \in [0, 2\pi)$. Properties of these two operators are closely related. For example, the \mathcal{H}_∞ norm of operator \mathcal{H}

is determined by

$$\begin{aligned}\|\mathcal{H}\|_\infty &:= \sup_{\omega \in \mathbb{R}} \sigma_{\max}\{\mathcal{H}(\omega)\} \\ &= \sup_{\theta \in [0, 2\pi)} \sup_{\omega \in \mathbb{R}} \sigma_{\max}\{H_\theta(\omega)\}.\end{aligned}$$

On the other hand, following [3] we define the \mathcal{H}_2 norm of system (4.1) as

$$\|\mathcal{H}\|_2^2 := \frac{1}{2\pi} \int_{-\infty}^{\infty} \frac{1}{X} \int_0^X \text{trace} \left\{ \int_{-\infty}^{\infty} \mathcal{H}^*(x, \eta, \omega) \mathcal{H}(x, \eta, \omega) dx \right\} d\eta d\omega.$$

As shown at the end of this section, this quantity is determined by

$$\|\mathcal{H}\|_2^2 = \frac{1}{(2\pi)^2 X} \int_0^{2\pi} \int_{-\infty}^{\infty} \text{trace} \{ H_\theta^*(\omega) H_\theta(\omega) \} d\omega d\theta.$$

The \mathcal{H}_2 norm of stable systems can be obtained based on solutions of the algebraic Lyapunov equations of the form

$$\begin{aligned}A_\theta P_\theta + P_\theta A_\theta^* &= -B_\theta B_\theta^*, \\ A_\theta^* Q_\theta + Q_\theta A_\theta &= -C_\theta^* C_\theta,\end{aligned}$$

using either of the following two expressions:

$$\begin{aligned}\|\mathcal{H}\|_2^2 &= \frac{1}{2\pi X} \int_0^{2\pi} \text{trace} \{ P_\theta C_\theta^* C_\theta \} d\theta \\ &= \frac{1}{2\pi X} \int_0^{2\pi} \text{trace} \{ Q_\theta B_\theta B_\theta^* \} d\theta,\end{aligned}$$

Results of this section are summarized in the following theorem.

Theorem 5 *The feedback stability and the system norms are preserved under the transformation $\mathcal{T} := \mathcal{V}_\theta \mathcal{Z}_\theta W_X$. In particular, the spectrum of the generator of (4.1) is equal the spectrum of the generator of (4.18) as θ ranges over all possible values, that is*

$$\sigma\{\mathcal{A}\} = \overline{\bigcup_{\theta \in [0, 2\pi)} \sigma\{A_\theta\}}.$$

Furthermore, the \mathcal{H}_∞ and \mathcal{H}_2 norms of operator mapping input u into output y are determined by

$$\begin{aligned}\|\mathcal{H}\|_\infty &= \sup_{\theta \in [0, 2\pi)} \sup_{\omega \in \mathbb{R}} \sigma_{\max}\{H_\theta(\omega)\}, \\ \|\mathcal{H}\|_2^2 &= \frac{1}{(2\pi)^2 X} \int_0^{2\pi} \int_{-\infty}^{\infty} \text{trace} \{ H_\theta^*(\omega) H_\theta(\omega) \} d\omega d\theta.\end{aligned}$$

In § 4.4, we illustrate how stability properties and system norms of spatially invariant systems can be altered by connecting them in feedback with spatially periodic functions.

\mathcal{H}_2 norm of spatially periodic systems

Next, we derive the expression for \mathcal{H}_2 norm of system (4.1).

$$\begin{aligned}
\|\mathcal{H}\|_2^2 &:= \frac{1}{2\pi} \int_{-\infty}^{\infty} \frac{1}{X} \int_0^X \text{trace} \left\{ \int_{-\infty}^{\infty} \mathcal{H}^*(x, \eta, \omega) \mathcal{H}(x, \eta, \omega) dx \right\} d\eta d\omega \\
&= \frac{1}{2\pi} \int_{-\infty}^{\infty} \frac{1}{X} \int_0^X \text{trace} \left\{ \sum_{n \in \mathbb{Z}} \int_{nX}^{(n+1)X} \mathcal{H}^*(x, \eta, \omega) \mathcal{H}(x, \eta, \omega) dx \right\} d\eta d\omega \\
&= \frac{1}{2\pi} \int_{-\infty}^{\infty} \frac{1}{X} \int_0^X \text{trace} \left\{ \sum_{n \in \mathbb{Z}} \int_0^X \mathcal{H}^*(nX + \hat{x}, \eta, \omega) \mathcal{H}(nX + \hat{x}, \eta, \omega) d\hat{x} \right\} d\eta d\omega \\
&= \frac{1}{2\pi} \int_{-\infty}^{\infty} \frac{1}{X} \int_0^X \text{trace} \left\{ \sum_{n \in \mathbb{Z}} \int_0^X \bar{\mathcal{H}}_n^*(\hat{x}, \eta, \omega) \bar{\mathcal{H}}_n(\hat{x}, \eta, \omega) d\hat{x} \right\} d\eta d\omega \\
&= \frac{1}{2\pi} \int_{-\infty}^{\infty} \frac{1}{X} \int_0^X \text{trace} \left\{ \sum_{n \in \mathbb{Z}} \int_0^X \bar{\mathcal{H}}_n^*(\hat{x}, \eta, \omega) \frac{1}{2\pi} \int_0^{2\pi} \hat{\mathcal{H}}_\theta(\hat{x}, \eta, \omega) e^{i\theta n} d\theta d\hat{x} \right\} d\eta d\omega \\
&= \frac{1}{(2\pi)^2 X} \int_0^{2\pi} \int_{-\infty}^{\infty} \text{trace} \left\{ \int_0^X \int_0^X \left(\sum_{n \in \mathbb{Z}} \bar{\mathcal{H}}_n(\hat{x}, \eta, \omega) e^{-i\theta n} \right)^* \hat{\mathcal{H}}_\theta(\hat{x}, \eta, \omega) d\hat{x} d\eta \right\} d\omega d\theta \\
&= \frac{1}{(2\pi)^2 X} \int_0^{2\pi} \int_{-\infty}^{\infty} \text{trace} \left\{ \int_0^X \int_0^X \hat{\mathcal{H}}_\theta^*(\hat{x}, \eta, \omega) \hat{\mathcal{H}}_\theta(\hat{x}, \eta, \omega) d\hat{x} d\eta \right\} d\omega d\theta \\
&=: \frac{1}{(2\pi)^2 X} \int_0^{2\pi} \int_{-\infty}^{\infty} \|\hat{\mathcal{H}}_\theta(\omega)\|_{HS}^2 d\omega d\theta \\
&= \frac{1}{(2\pi)^2 X} \int_0^{2\pi} \int_{-\infty}^{\infty} \|\mathcal{V}_\theta^{-1} H_\theta(\omega) \mathcal{V}_\theta\|_{HS}^2 d\omega d\theta \\
&= \frac{1}{(2\pi)^2 X} \int_0^{2\pi} \int_{-\infty}^{\infty} \|H_\theta(\omega)\|_{HS}^2 d\omega d\theta \\
&= \frac{1}{(2\pi)^2 X} \int_0^{2\pi} \int_{-\infty}^{\infty} \text{trace} \{H_\theta^*(\omega) H_\theta(\omega)\} d\omega d\theta.
\end{aligned}$$

4.4 Examples of PDEs with periodic coefficients

In this section, we illustrate how stability properties and system norms of PDEs can be changed by introducing feedback terms with spatially periodic coefficients. Our results reveal that, depending on the values of amplitude and frequency of a periodic gain, both stability and input-output gains of the original equation can be modified. This phenomenon is referred to as ‘parametric resonance’ and is encountered in many problems of physical significance. Furthermore, we show how our results can lead to an *analytic expression* for the eigenvalues of the underlying operators, for a special class of PDEs with periodic coefficients.

First example

In [10], the periodic solutions of the Ginzburg-Landau (GL) equation are studied. This equation results from nonlinear stability theory and appears in the analysis of many relevant fluid mechanics problems: the Bénard problem, the Taylor problem, Tollmien-Schlichting waves, gravity waves, etc. (for more details see [10] and references therein). It is worth mentioning that the GL equation describes the evolution of a slowly varying complex amplitude of a neutral plane wave.

The linearization of this equation around its limit cycle solution $\phi_0 := f(x) \exp(i\Omega t)$, $f(x) = f(x + X)$, results in a PDE with periodic coefficients of the form

$$\partial_t \phi = z_1 \phi + z_2 \partial_x^2 \phi + z_3 (2|f|^2 \phi + f^2 \phi^*), \quad (4.19)$$

where ϕ^* is the complex-conjugate of a field ϕ , and $z_1 := \rho - i\Omega$, $z_2 := c_0 + i$, $z_3 := i - \rho$, with c_0 , Ω , and ρ

being real valued parameters. Furthermore, $\rho := c_0/c_1$, $0 \leq c_0^2 \leq c_1$.

If we introduce the following notation

$$\psi := \begin{bmatrix} \phi \\ \phi^* \end{bmatrix}, \quad (4.20)$$

we can rewrite (4.19) as

$$\partial_t \psi := \mathcal{A}(\partial_x) \psi, \quad (4.21)$$

where the operator \mathcal{A} is given by

$$\mathcal{A} := \begin{bmatrix} z_1 + z_2 \partial_x^2 + 2z_3|f|^2 & z_3 f^2 \\ (z_3 f^2)^* & z_1^* + z_2^* \partial_x^2 + 2z_3^*|f|^2 \end{bmatrix}.$$

Clearly, \mathcal{A} can be separated into a sum of a spatially invariant operator and a matrix-valued periodic function, which lends itself to the application of the results derived in § 4.2. We use these results for a numerical approximation of \mathcal{A} and investigate its eigenvalues. In particular, we assume $f(x) := \alpha \cos(\frac{2\pi}{X}x)$ and consider a problem of the stability of system (4.19). We note that in this case (4.19) cannot be interpreted as the linearized GL equation since ϕ_0 , for the above given $f(x)$, is no longer a limit cycle solution of the nonlinear GL equation. Nevertheless, this problem is worth investigating because it represents an example of a system whose stability can be changed by feedback terms with spatially periodic gains.

Figure 4.2 illustrates the maximal real part of the operator \mathcal{A} eigenvalues, $\lambda(\mathcal{A})$, as a function of α and X , for $c_0 = 0.4$, $\rho = 0.4$, and $\Omega = 5$. It can be readily shown that for $\alpha = 0$, $\max(\operatorname{Re}\{\lambda(\mathcal{A})\}) = \rho = 0.4$, which means that system (4.19) is open-loop unstable. Clearly, ‘closing a loop’, by introducing the spatially periodic gains in feedback, changes the value of $\max(\operatorname{Re}\{\lambda(\mathcal{A})\})$ significantly, as illustrated in the left plot of Figure 4.2.

Figure 4.2 also shows $\max(\operatorname{Re}\{\lambda(\mathcal{A})\})$ as a function of α for $X \approx 1.31$. The right plot in this figure further illustrates the previously mentioned changes in $\max(\operatorname{Re}\{\lambda(\mathcal{A})\})$, and reveals an interesting feature of this example. Namely, the regions of instability and stability repeat in an alternating arrangement for certain values of the amplitude α .

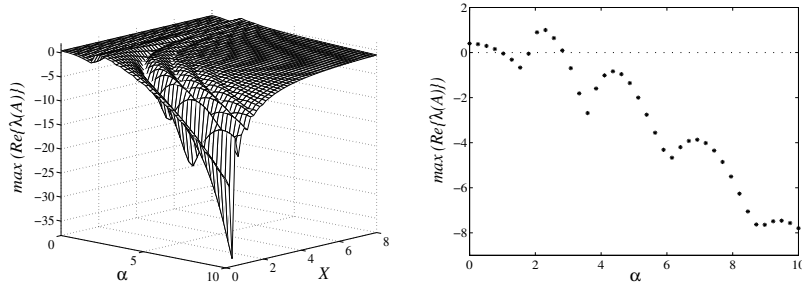


Figure 4.2: Left plot: $\max(\operatorname{Re}\{\lambda(\mathcal{A})\})$ as a function of α and X for $f(x) := \alpha \cos(\frac{2\pi}{X}x)$, $c_0 = 0.4$, $\rho = 0.4$, and $\Omega = 5$. Right plot: $\max(\operatorname{Re}\{\lambda(\mathcal{A})\})$ as a function of α for $f(x) := \alpha \cos(\frac{2\pi}{X}x)$, $X \approx 1.31$, $c_0 = 0.4$, $\rho = 0.4$, and $\Omega = 5$.

Second example

In [11], a class of nonlinear PDEs with periodic plane wave solutions including forms of the Schrödinger and generalized KdV equations is considered. The linearization of these equations around a plane wave yields

the following PDE with periodic coefficients:

$$\partial_t \phi(x, t) = p(\partial_x) \phi(x, t) + \alpha e^{2i\frac{2\pi}{X}x} \phi^*(x, t), \quad (4.22)$$

where p is a polynomial with complex coefficients, and α is a complex scalar. We can define the state by (4.20), which transforms (4.22) into (4.21), with

$$\mathcal{A} := \begin{bmatrix} \mathcal{A}_{11} & \mathcal{A}_{12} \\ \mathcal{A}_{21} & \mathcal{A}_{22} \end{bmatrix} := \begin{bmatrix} p(\partial_x) & \alpha e^{2i(\frac{2\pi}{X})x} \\ \alpha^* e^{-2i(\frac{2\pi}{X})x} & p^*(\partial_x) \end{bmatrix}.$$

Operator \mathcal{A} can be separated into a sum of a spatially invariant operator and a matrix-valued periodic function, and the previously described procedure transforms (4.21) into

$$\dot{\Psi}_\theta(t) = A_\theta \dot{\Psi}_\theta(t). \quad (4.23)$$

Bi-infinite Toeplitz matrices $A_{\theta 12}$ and $A_{\theta 21}$ are defined in (4.14) with the elements of $A_{\theta 12}$ given by

$$a_m = \begin{cases} \alpha & m = 2, \\ 0 & \text{otherwise,} \end{cases} \quad (4.24)$$

and the elements of $A_{\theta 21}$ given by

$$a_m = \begin{cases} \alpha^* & m = -2, \\ 0 & \text{otherwise.} \end{cases} \quad (4.25)$$

Furthermore, if we define $p_n(\theta) := p(i\frac{2\pi n + \theta}{X})$, then

$$A_{\theta 11} = \text{diag}\{p_n(\theta)\}_{n \in \mathbb{Z}}, \quad A_{\theta 22} = \text{diag}\{p_n^*(\theta)\}_{n \in \mathbb{Z}}.$$

The eigenvalues of A_θ are computed by defining $G_\theta := \lambda I - A_\theta$ and using the formula

$$\det(G_\theta) = \det(G_{\theta 11}) \det(G_{\theta 22} - G_{\theta 21} G_{\theta 11}^{-1} G_{\theta 12}).$$

Noting that $G_{\theta 12}$ and $G_{\theta 21}$ are just scaled backward and forward shift operators, respectively, then $\det(\lambda I - A_\theta)$ is computed to be

$$\begin{aligned} \prod_{n \in \mathbb{Z}} (\lambda - p_n(\theta)) \prod_{n \in \mathbb{Z}} (\lambda - p_n^*(\theta)) - \frac{|\alpha|^2}{\lambda - p_{n-2}(\theta)} &= \\ \prod_{n \in \mathbb{Z}} \{(\lambda - p_{n-2}(\theta))(\lambda - p_n^*(\theta)) - |\alpha|^2\}, \end{aligned}$$

which yields the eigenvalues $\lambda_n(\theta)$ of A_θ equal to

$$\frac{1}{2} \{p_{n-2}(\theta) + p_n^*(\theta) \pm \sqrt{4|\alpha|^2 + (p_{n-2}(\theta) - p_n^*(\theta))^2}\}.$$

This result can be applied to the nonlinear Schrödinger equation

$$i \partial_t \varphi(z, t) = - \partial_z^2 \varphi(z, t) - V(\varphi \varphi^*) \varphi(z, t), \quad (4.26)$$

with potential $V(\phi \phi^*)$ that satisfies the dispersion equation $V(a^2) = (\frac{2\pi}{X})^2 - (\frac{2\pi}{T})^2$. As illustrated in [11], (4.26) exhibits a periodic plane wave solution $a e^{i(\frac{2\pi}{X}z - \frac{2\pi}{T}t)}$. The linearization of (4.26) around this solution, together with a coordinate transformation of the form $x := z - \frac{X}{T}t$, yields (4.22) with

$$\begin{aligned} p(\partial_x) &:= \frac{X}{T} \partial_x + i(\partial_x^2 + V(a^2) + a^2 V'(a^2)), \\ \alpha &:= ia^2 V'(a^2). \end{aligned}$$

It is readily shown, using the previously derived formula for $\lambda_n(\theta)$, that the generator of (4.22) has purely imaginary eigenvalues if and only if $V'(a^2) \leq 0$. On the other hand, if $V'(a^2) > 0$ then there exist an eigenvalue of \mathcal{A} with a positive real part. The same conclusion has been derived in [11] using the technique which is well-suited for systems that can be represented by (4.22). It is worth noting that the spatio-temporal lifting can be used for analysis of stability and input-output norms of general linear PDEs with periodic coefficients on $L^2(-\infty, \infty)$.

Third example

In this subsection, by means of an example, we illustrate how system norms of spatially invariant systems can be changed by combining them in feedback with spatially periodic gains. In particular, we consider a system of the form

$$\partial_t \begin{bmatrix} \psi_1(x, t) \\ \psi_2(x, t) \end{bmatrix} = \begin{bmatrix} -c + \partial_{xx} & -f(x) \\ q + f(x) & -c + \partial_{xx} \end{bmatrix} \begin{bmatrix} \psi_1(x, t) \\ \psi_2(x, t) \end{bmatrix} + \begin{bmatrix} I & 0 \\ 0 & I \end{bmatrix} \begin{bmatrix} u_1(x, t) \\ u_2(x, t) \end{bmatrix}, \quad (4.27a)$$

$$\begin{bmatrix} y_1(x, t) \\ y_2(x, t) \end{bmatrix} = \begin{bmatrix} I & 0 \\ 0 & I \end{bmatrix} \begin{bmatrix} \psi_1(x, t) \\ \psi_2(x, t) \end{bmatrix}, \quad (4.27b)$$

where c and q are positive and non-negative real numbers, respectively, $f(x) := \alpha \cos(\frac{2\pi}{X}x)$, $\alpha \in \mathbb{R}$, and $x \in \mathbb{R}$. If $\alpha \equiv 0$, system (4.27) represent a linear spatially invariant system. In this case, using the tools of [9] it can be easily established that system (4.27) is exponentially stable with \mathcal{H}_∞ norm given by

$$\|\mathcal{H}\|_\infty^2 = \frac{1}{c^2 + 0.5(q^2 - q\sqrt{q^2 + 4c^2})}.$$

Our objective is to investigate the dynamical properties of system (4.27) for $\alpha \neq 0$.

The derivative of the following Lyapunov function candidate along the solutions of unforced system (4.27a)

$$V(\psi_1, \psi_2) := \frac{1}{2} \langle \psi_1, \psi_1 \rangle + \frac{1}{2} \langle \psi_2, \psi_2 \rangle,$$

is determined by

$$\begin{aligned} \dot{V}(\psi_1, \psi_2) &= \langle \psi_1, \partial_t \psi_1 \rangle + \langle \psi_2, \partial_t \psi_2 \rangle \\ &= \langle \psi_1, -c\psi_1 + \partial_{xx}\psi_1 - f\psi_2 \rangle + \langle \psi_2, q\psi_1 + f\psi_1 - c\psi_2 + \partial_{xx}\psi_2 \rangle \\ &= -c \langle \psi_1, \psi_1 \rangle - c \langle \psi_2, \psi_2 \rangle - \langle \partial_x \psi_1, \partial_x \psi_1 \rangle - \langle \partial_x \psi_2, \partial_x \psi_2 \rangle + q \langle \psi_2, \psi_1 \rangle \\ &\leq -(c - \frac{q}{2}) \langle \psi_1, \psi_1 \rangle - (c - \frac{q}{2}) \langle \psi_2, \psi_2 \rangle - \langle \partial_x \psi_1, \partial_x \psi_1 \rangle - \langle \partial_x \psi_2, \partial_x \psi_2 \rangle, \end{aligned}$$

which implies the negative definiteness of \dot{V} along the solutions of unforced system (4.27a) as long as parameters c and q are such that $q < 2c$. Therefore, the stability properties of the original spatially invariant system are not influenced by the periodic feedback if the coupling between the two subsystems in (4.27a) is small enough (that is, $q < 2c$). This estimate may be very conservative but it is important that we have established stability for certain values of parameters q and c irrespective of the values that period and amplitude of the periodic gain assume. This allows us to select the pair (q, c) to guarantee stability of (4.27a) and investigate the dependence of the input-output norms of (4.27) on both α and X .

The left plot in Figure 4.3 illustrates the dependence of the \mathcal{H}_∞ norm of system (4.27) on both amplitude and period of spatially periodic gain for $c = 1$ and $q = 0.5$. The right plot in the same figure shows how \mathcal{H}_∞ norm of (4.27) changes with X at $\alpha = 15$. We note that at $\alpha = 0$ \mathcal{H}_∞ norm is equal to 1.28 which corresponds to the value determined for the spatially invariant system. As our results indicate, even though the stability properties of system (4.27) are not changed by introducing the spatially periodic feedback, its presence has a beneficial influence on the input-output system gains. We remark that this fact cannot be established by the existing tools, e.g. Floquet analysis of periodic PDEs, because this type of analysis does

not easily lend itself to the computation of system norms. To this end, we have developed the procedure that can be used to compute both the spectrum of the generating operator and \mathcal{H}_2 and \mathcal{H}_∞ norms of spatially distributed systems with periodic coefficients.

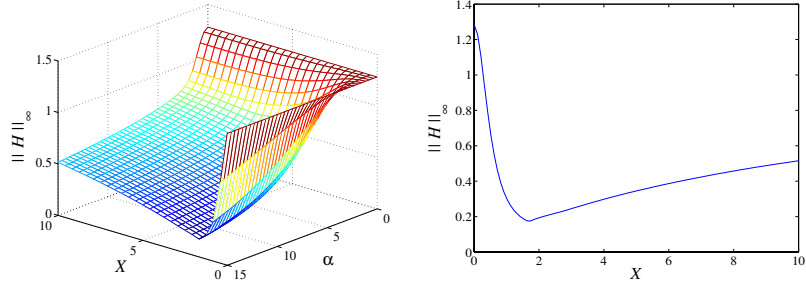


Figure 4.3: The dependence of the \mathcal{H}_∞ norm of system (4.27) with $\{c = 1, q = 0.5\}$ on amplitude and period of spatially periodic feedback (left plot), and period for $\alpha = 15$ (right plot).

4.5 Extensions

The developed procedure can be also used to investigate dynamical properties of systems of the form

$$\begin{aligned}\partial_t \psi(x, z, t) &= \mathcal{A}\psi(x, z, t) + \mathcal{B}u(x, z, t), \\ y(x, z, t) &= \mathcal{C}\psi(x, z, t),\end{aligned}$$

where \mathcal{A} , \mathcal{B} , and \mathcal{C} are time invariant linear operators with spatially periodic coefficients in $x \in \mathbb{R}$, whereas z belongs to a set of indices with no predefined structure. As an example, consider the following equation

$$\begin{aligned}\partial_t \psi(x, z, t) &= (\partial_{zz} + \partial_{xx} + f(x))\psi(x, z, t) + u(x, z, t), \\ y(x, z, t) &= \psi(x, z, t),\end{aligned}\tag{4.29}$$

with $z \in [-1, 1]$, $\psi(x, \pm 1, t) = 0$, and $f(x) = f(x + X)$. Using the results of § 4.2, system (4.29) can be transformed into a θ -parameterized family of PDEs of the form

$$\begin{aligned}\partial_t \Psi_\theta(z, t) &= (\partial_{zz} + D_\theta + \Gamma)\Psi_\theta(z, t) + U_\theta(z, t), \\ Y_\theta(z, t) &= \Psi_\theta(z, t),\end{aligned}\tag{4.30}$$

where $\theta \in [0, 2\pi)$, $D_\theta := \text{diag}\{-(\frac{2\pi n + \theta}{X})^2\}_{n \in \mathbb{Z}}$, and Γ is a Toeplitz matrix determined by (4.14). It is not difficult to show that systems (4.29) and (4.30) have equivalent stability properties and input-output norms.

4.6 Summary

We develop a framework for analysis of stability and input-output norms of distributed systems with spatially periodic coefficients. It is shown that the main ideas of a well known temporal lifting technique for linear periodic ODEs are readily extendable to PDEs in which certain coefficients are spatially periodic functions. A particular basis set is used to obtain convenient representations of transformed lifted signals and spatially periodic systems. It is also illustrated, by means of three examples, how stability properties and input-output norms of spatially invariant PDEs can be changed when a spatially periodic feedback is introduced.

Bibliography

- [1] V. I. Arnold, *Mathematical Methods of Classical Mechanics*. Springer-Verlag, 1989.
- [2] B. Bamieh and J. B. Pearson, “A general framework for linear periodic systems with applications to H^∞ sampled-data control,” *IEEE Transactions on Automatic Control*, vol. 37, no. 4, pp. 418–435, April 1992.
- [3] ——, “The H^2 problem for sampled-data systems,” *Systems and Control Letters*, vol. 19, no. 1, pp. 1–12, July 1992.
- [4] B. Bamieh, M. A. Dahleh, and J. B. Pearson, “Minimization of the L_∞ -induced norm for sampled-data systems,” *IEEE Transactions on Automatic Control*, vol. 38, no. 5, pp. 717–732, May 1993.
- [5] Y. Yamamoto, “A function space approach to sampled data control systems and tracking problems,” *IEEE Transactions on Automatic Control*, vol. 39, no. 4, pp. 703–713, April 1994.
- [6] T. Hagiwara and M. Araki, “FR-operator approach to the H_2 analysis and synthesis of sampled-data systems,” *IEEE Transactions on Automatic Control*, vol. 40, no. 8, pp. 1411–1421, August 1995.
- [7] T. Chen and B. Francis, *Optimal Sampled-Data Control Systems*. Springer, 1995.
- [8] G. E. Dullerud, *Control of Uncertain Sampled-Data Systems*. Birkhauser, 1996.
- [9] B. Bamieh, F. Paganini, and M. A. Dahleh, “Distributed control of spatially invariant systems,” *IEEE Transactions on Automatic Control*, vol. 47, no. 7, pp. 1091–1107, July 2002.
- [10] L. Sirovich and P. K. Newton, “Periodic solutions of the Ginzburg-Landau equation,” *Physica 21D*, pp. 115–125, 1986.
- [11] P. K. Newton and J. B. Keller, “Stability of periodic plane waves,” *SIAM J. Appl. Math.*, vol. 47, no. 5, pp. 959–964, October 1987.

Chapter 5

Conclusions and future directions

Conclusions

We introduce an explicit procedure for determination of the frequency responses for a class of P(I)DEs with, in general, non-normal dynamical generators and non-constant coefficients in the spatially independent variable. The motivation for this problem arises from the observation that the eigenvalue-based stability analysis of non-normal dynamical systems often leads to erroneous conclusions. Namely, these systems can exhibit large transient responses (i.e., behave as unstable on finite time intervals) even in the absence of exponentially growing system modes. In view of this, it is relevant to develop efficient schemes for determining appropriately defined measures of transient amplification.

Instead of usual finite dimensional approximations of the underlying operators, we derive an explicit formula for the power spectral density of the frequency response operator. This formula only involves finite dimensional computations with matrices whose dimension is at most four times larger than the order of the underlying generators. Thus, we perform an exact reduction of an infinite dimensional problem to a finite dimensional problem.

We also develop a framework for analysis of internal and input-output properties of PDEs with spatially periodic coefficients. We demonstrate that the main ideas of a well known temporal lifting technique for linear periodic ODEs can be extended to PDEs in which certain coefficients are spatially periodic functions. A particular basis set is used to obtain convenient representations of transformed lifted signals and spatially periodic systems. We also illustrate how stability and input-output norms of spatially invariant PDEs can be modified when a spatially periodic feedback is introduced.

Several open research problems are given below.

Future directions

Application of the exact formula for Hilbert–Schmidt norm of frequency response operator to problems with non-constant coefficients. All examples in this dissertation illustrate explicit determination of frequency responses for problems with constant coefficients in the spatially independent variable. We also plan to apply the formula for Hilbert–Schmidt norm of frequency response operator to problems with non-constant coefficients. This will require determination of the state transition matrices in (3.18), which necessitates solving certain differential equations. In particular, frequency response operator of a system that describes the dynamics of velocity fluctuations in channel fluid flows linearized around velocity profile $U(y) = 1 - y^2$ has a TPBVSR with non-constant coefficients in y .

Exact determination of maximal singular values of the frequency response operator. We intend to determine maximal singular values of the frequency response operator from its TPBVSR. These singular values, at any frequency, quantify the largest amplification of deterministic disturbances.

Identification of classes of PDEs in which parametric resonance can occurs. Recently, Fardad &

Bamieh [1] employed methodology developed in this dissertation and perturbation analysis to show how to design a spatially periodic perturbation to stabilize a marginally stable PDE. It was established that, up to first order in the perturbation parameter, parametric resonance can only occur at the isolated frequency twice larger than the frequency of the marginally-stable mode of the unperturbed system. Investigations along these lines will elucidate classes of spatially distributed systems in which parametric resonance can take place.

Bibliography

- [1] M. Fardad and B. Bamieh, “A perturbation analysis of parametric resonance and periodic control in spatially distributed systems,” 2004, submitted to the 43rd IEEE Control and Decision Conference.

Part II

Modeling and analysis of transition and turbulence in channel flows

Chapter 6

Background

The basic theoretical issues related to the study of transition to turbulence can be divided into two categories:

- **Explaining why the laminar-turbulent transition takes place.**
- **Determining the dominant structures of flow perturbations that lead to the transition.**

The classical approach to this problem involves the spectral (that is, normal mode) analysis of the NS equations linearized around certain laminar flow condition. For low Reynolds numbers all flows are stable [1–3], and classical analysis is thus concerned with finding the critical Reynolds numbers at which exponentially growing normal modes appear, or equivalently, identifying when the generator of the evolution equation becomes unstable. The predictions of these investigations agree fairly well with the experimental results in many relevant flows: e.g., those driven mainly by centrifugal and thermal forces [4]. However, in the very important case of shear flows in streamlined geometries, classical theory fails to predict both the transition Reynolds numbers and the dominant flow structures that accompany the transition. For example, plane Couette flow is stable for all values of the Reynolds number [5], and plane Poiseuille flow losses stability only if the Reynolds number becomes larger than approximately 5772 [6]. However, the experiments tell different story: the transition is observed to take place as early as $R \approx 350$ in Couette flow [7, 8], and as early as $R \approx 1000$ in Poiseuille flow [9]. Furthermore, the transition Reynolds numbers strongly depend on the experimental conditions. By comparing different experimental results for plane Poiseuille flow, the wide variation in transition Reynolds numbers from 266 [10] to 8000 [11] was observed in [9]. In the former case, the early transition was due to a noisy environment created by a non-smooth inlet contraction. On the other hand, the latter example demonstrates that under carefully controlled experiments the transition may not take place even for flows that are unstable according to the classical hydrodynamic stability theory. This indicates that the concept of stability/instability in the classical sense may be too narrow to capture the notion of transition.

For wall bounded shear flows, the classical hydrodynamic stability analysis leads to transition theories based on the well known Tollmien-Schlichting (TS) waves, which have long been considered to be the primary mechanism of instability leading to transition. TS waves represent the eigenfunctions corresponding to the ‘poorly damped’ system modes (that is, the eigenvalues in the immediate vicinity of the imaginary axis), and they can only be observed in carefully controlled experiments with very little background noise. Also, TS waves have been considered to be the first step in a transition scenario that leads to three-dimensional ‘secondary’ instabilities [12–14]. This scenario leaves many unanswered questions, as Herbert [13] observed:

‘In noisy environments, however, the TS mechanism is no longer needed and may be bypassed; preexisting vorticity concentration of irregular spacing and orientation combined with the mean shear directly activate the process of vortex tilting and stretching [14] that lead to transition.’

Indeed, the secondary instability theory is quite unsatisfactory for describing experimentally observed phenomena in so-called *natural transition* [15]. Unless in carefully controlled experiments, the transition Reynolds numbers, as well as the dominant flow structures, are not related to TS waves [9, 11, 15–19].

We approach this problem by analyzing the dynamical properties of the Navier-Stokes (NS) equations with spatially distributed and temporally varying body force fields. These fields are considered as inputs, and various combinations of the resulting velocity and vorticity fields are considered as outputs. This input-output analysis can in principle be done in any geometry and for the full nonlinear NS equations. In such generality however, it is difficult to obtain useful results. We therefore concentrate on the geometry of channel flows, and the input-output dynamics of the LNS equations.

The analysis of dynamical systems with inputs has a long history in circuit theory, controls, communications, and signal processing. In this analysis, it is convenient to express dynamical systems as input-output ‘blocks’ that can be connected together in a variety of cascade, series, and feedback arrangements. The utility of this approach is twofold. First, it greatly facilitates engineering analysis and design of complex systems made up of sub-blocks that are easier to characterize. Second, it allows for modeling dynamical inputs which are unmeasurable or uncertain. These include stochastic or deterministic uncertain signals such as noise or uncertain forcing that are inevitably present in most physical systems.

The terminology here might be a little confusing. While we are concerned with the dynamical behavior of the *linearized* NS equations, input-output analysis of the LNS is related but not equivalent to linear hydrodynamic stability analysis. As already mentioned, in the latter, the objective is to characterize exponentially growing (unstable) normal modes. As we will illustrate, input-output analysis reveals unstable normal modes, as well as transient growth, disturbance amplification, and so-called pseudo-spectral modes. This analysis has very close mathematical connections with work on transient energy growth (also known as non-normal growth) [20–22], pseudo-spectral analysis [4], and amplification of stochastic excitations [23, 24]. In some sense, it can also be considered as a type of receptivity analysis, though this connection is more qualitative in nature. Rather than study the receptivity of a boundary layer to upstream or free stream disturbances as is commonly done [25–27], our input-output analysis is the receptivity of channel flows to spatially and temporally distributed body forces. The latter is mathematically and computationally more tractable, yet appears to have many of the qualitative features of boundary layer receptivity analysis.

Our work is greatly influenced by recent research in what has become known as transient growth mechanisms for bypass transitions [4, 20–24, 28–33]. We will only briefly outline some of the more closely related work here, and refer the reader to the recent monograph [3] and the references therein for a fuller discussion. The main point of departure of this work from classical linear hydrodynamic stability is the fact that the latter is concerned solely with the existence of exponentially growing modes. In other words, it is essentially an asymptotic analysis of infinite time limits. In certain flows however, transient (that is, finite-time) phenomena appear to play a significant role. While the possibility of transient growth has long been recognized [34], it is only in the past two decades that effective mathematical methods have been used to analyze it. In [21, 22] initial states with the largest transient energy growth in subcritical flows were discovered using a singular value analysis. These ‘worst case’ initial states lead to flow structures that resemble streamwise vortices and streaks. A somewhat different analysis is done by computing the pseudo-spectrum rather than the spectrum of the generating dynamics [4], and the most unstable pseudo-spectral modes turn out to be related to streamwise vortices and streaks. A third analysis method [23, 24] studies the most energetic response of the linearized Navier-Stokes equations to stochastic excitation. Yet again, the most energetically excited flow structures appear to resemble streamwise vortices and streaks. The common theme between the three methods is that a certain norm of the perturbed flow state is used (namely kinetic energy density), and the responses with respect to various types of *uncertainties* are analyzed.

A streamwise vortex represents an elongated region of vorticity, and a streamwise streak represents an elongated region of high and low velocity perturbations. Both these structures are approximately aligned with the direction of nominal flow $U(y)$, and they are commonly observed in experimental investigations related to transition in channel and boundary layer flows [9, 15, 18, 19, 35].

Previous work on ‘non-normal growth’ has tended to emphasize transient energy growth as a mechanism that might lead to exiting a region of attraction of the full nonlinear Navier-Stokes equations. In this thesis however (and similarly in [23, 24]), we adopt a different perspective in which the LNS are considered with uncertain body forces, initial conditions are zero, and thus flow field perturbations are solely due to excitation by body forces. We show that the effects of these body forces on flow perturbations scale badly with the Reynolds number. Depending on the polarization of the force and how flow perturbations are measured, these effects scale with R , R^2 , R^3 , or R^4 . Thus, for large enough Reynolds numbers, the effects of even tiny

body forces will become appreciable. It is not difficult to argue that any flow condition has some degree of uncertainty in either flow geometry, base profile, and/or non-flat walls. In carefully controlled experiments, these uncertainties may be very small. However, it appears that the NS equations (both the linearized and full versions) in wall-bounded shear flows are exceedingly sensitive to small amounts of such uncertainty. It is thus important to analyze the equations while taking such uncertainties into account. We borrow heavily from the field of Robust Control theory [36], where mathematical tools for the analysis and control of uncertain dynamical systems have been developed. Indeed, several researches [37–41] have been successful in designing linear controllers based on these methods either for the LNS or nonlinear flow dynamics in Direct Numerical Simulations (DNS).

This part of the thesis is organized as follows: in Chapter 7, we discuss externally excited LNS equations in channel flows. These equations determine a dynamical description of flow fluctuations subject to spatially distributed and temporally varying body force fields. In Chapter 8, we present the spatio-temporal frequency responses in Poiseuille, Couette, and a turbulent mean flow profile. One of our main objectives is to illustrate the input-output resonances from forcing inputs in different directions to different components of the velocity field. The most amplified input-output resonances turn out to resemble streamwise vortices and streaks and oblique waves. A comparison between them and internal resonances (TS waves) is given using the frequency response. This is done for both subcritical and supercritical flows, where the latter are analyzed with the appropriate exponential discounts on their energies. One of our other conclusions is that the spanwise and wall-normal forces are much more influential on flow perturbations than the streamwise force. Furthermore, the impact of these forces is most powerful on the streamwise velocity component. Analytical explanations for these observations as well as formulae for the dependence of these influences on the Reynolds number are given in Chapter 9, where we also study the effectiveness of the near-wall inputs for streamwise constant three-dimensional perturbations. We *analytically* demonstrate that the spanwise direction force has, by far, the biggest impact on the evolution of the velocity field components. These facts were recently observed in experimental and numerical studies of flow control using the Lorentz force [42–46]. In Chapter 10, we study the spatio-temporal impulse responses of the LNS in subcritical Poiseuille flow with $R = 2000$. The first motivation for this problem comes from experimental work, where transition is observed to occur either naturally, with so-called ‘turbulent spots’, or when these spots are intentionally induced in the flow by deliberate external excitation, which can be modelled as a spatio-temporal impulse body force in the NS equations. We show that the impulse responses of the LNS system display some of the qualitative features of early stages of turbulent spots observed in experiments and full direct numerical simulations. Another motivation is to fully probe the dynamics of the linearized equations. We find that these equations exhibit rich and complex structures hitherto unseen by other linear analysis methods.

Bibliography

- [1] D. D. Joseph, *Stability of Fluid Motions I.* Springer-Verlag, 1976.
- [2] P. G. Drazin and W. H. Reid, *Hydrodynamic Stability.* Cambridge University Press, 1981.
- [3] P. J. Schmid and D. S. Henningson, *Stability and Transition in Shear Flows.* New York: Springer-Verlag, 2001.
- [4] L. N. Trefethen, A. E. Trefethen, S. C. Reddy, and T. A. Driscoll, “Hydrodynamic stability without eigenvalues,” *Science*, vol. 261, pp. 578–584, 1993.
- [5] V. A. Romanov, “Stability of plane-parallel Couette flow,” *Funct. Anal. Applics.*, vol. 7, pp. 137–146, 1973.
- [6] S. A. Orszag, “Accurate solution of the Orr-Sommerfeld equation,” *J. Fluid Mech.*, vol. 50, pp. 689–703, 1971.
- [7] N. Tillmark and P. H. Alfredsson, “Experiments on transition in plane Couette flow,” *J. Fluid Mech.*, vol. 235, pp. 89–102, 1992.
- [8] O. Dauchot and F. Daviaud, “Finite amplitude perturbation and spots growth mechanism in plane Couette flow,” *Physics of Fluids*, vol. 7, no. 2, pp. 335–343, 1995.
- [9] D. R. Carlson, S. E. Widnall, and M. F. Peeters, “A flow-visualization study of transition in plane Poiseuille flow,” *J. Fluid Mech.*, vol. 121, pp. 487–505, 1982.
- [10] S. J. Davies and C. M. White, “An experimental study of the flow of water in pipes of rectangular section,” *Proc. R. Soc. Lond. A*, vol. 119, no. 781, pp. 92–107, 1928.
- [11] M. Nishioka, S. Iida, and Y. Ichikawa, “An experimental investigation of the stability of plane Poiseuille flow,” *J. Fluid Mech.*, vol. 72, pp. 731–751, 1975.
- [12] S. A. Orszag and A. T. Patera, “Secondary instability of wall-bounded shear flows,” *J. Fluid Mech.*, vol. 128, pp. 347–385, 1983.
- [13] T. Herbert, “Secondary instability of boundary layers,” *Ann. Rev. Fluid Mech.*, vol. 20, pp. 487–526, 1988.
- [14] B. J. Bayly, S. A. Orszag, and T. Herbert, “Instability mechanisms in shear flow transition,” *Ann. Rev. Fluid Mech.*, vol. 20, pp. 359–391, 1988.
- [15] B. G. B. Klingmann, “On transition due to three-dimensional disturbances in plane Poiseuille flow,” *J. Fluid Mech.*, vol. 240, pp. 167–195, 1992.
- [16] P. S. Klebanoff, K. D. Tidstrom, and L. M. Sargent, “The three-dimensional nature of boundary-layer instability,” *J. Fluid Mech.*, vol. 12, pp. 1–34, 1962.
- [17] F. W. Chambers and A. S. W. Thomas, “Turbulent spots, wave packets, and growth,” *Physics of Fluids*, vol. 26, no. 5, pp. 1160–1162, 1983.

- [18] F. Alavyoon, D. S. Henningson, and P. H. Alfredsson, “Turbulent spots in plane Poiseuille flow - flow visualization,” *Physics of Fluids*, vol. 29, no. 4, pp. 1328–1331, 1986.
- [19] M. Matsubara and P. H. Alfredsson, “Disturbance growth in boundary layers subjected to free-stream turbulence,” *J. Fluid Mech.*, vol. 430, pp. 149–168, 2001.
- [20] L. H. Gustavsson, “Energy growth of three-dimensional disturbances in plane Poiseuille flow,” *J. Fluid Mech.*, vol. 98, p. 149, 1991.
- [21] K. M. Butler and B. F. Farrell, “Three-dimensional optimal perturbations in viscous shear flow,” *Physics of Fluids A*, vol. 4, p. 1637, 1992.
- [22] S. C. Reddy and D. S. Henningson, “Energy growth in viscous channel flows,” *J. Fluid Mech.*, vol. 252, pp. 209–238, 1993.
- [23] B. F. Farrell and P. J. Ioannou, “Stochastic forcing of the linearized Navier-Stokes equations,” *Physics of Fluids A*, vol. 5, no. 11, pp. 2600–2609, 1993.
- [24] B. Bamieh and M. Dahleh, “Energy amplification in channel flows with stochastic excitation,” *Physics of Fluids*, vol. 13, no. 11, pp. 3258–3269, 2001.
- [25] M. E. Goldstein and L. S. Hultgren, “Boundary-layer receptivity to long-wave free-stream disturbances,” *Annual Review of Fluid Mechanics*, vol. 21, pp. 137–166, 1989.
- [26] D. C. Hill, “Adjoint systems and their role in the receptivity problem for boundary layers,” *J. Fluid Mech.*, vol. 292, pp. 183–204, 1995.
- [27] P. Luchini and A. Bottaro, “Görtler vortices: a backward-in-time approach to the receptivity problem,” *J. Fluid Mech.*, vol. 363, pp. 1–23, 1998.
- [28] B. F. Farrell and P. J. Ioannou, “Perturbation growth in shear flow exhibits universality,” *Physics of Fluids A*, vol. 5, no. 9, pp. 2298–2300, 1993.
- [29] ——, “Variance maintained by stochastic forcing of non-normal dynamical systems associated with linearly stable flows,” *Physical Review Letters*, vol. 72, no. 8, pp. 1188–1191, 1994.
- [30] S. C. Reddy, P. J. Schmid, J. S. Baggett, and D. S. Henningson, “On stability of streamwise streaks and transition thresholds in plane channel flows,” *J. Fluid Mech.*, vol. 365, pp. 269–303, 1998.
- [31] P. Luchini, “Reynolds-number-independent instability of the boundary layer over a flat surface: optimal perturbations,” *J. Fluid Mech.*, vol. 404, pp. 289–309, 2000.
- [32] S. J. Chapman, “Subcritical transition in channel flows,” *J. Fluid Mech.*, vol. 451, pp. 35–97, 2002.
- [33] A. Bottaro, P. Corbett, and P. Luchini, “The effect of base flow variation on flow stability,” *J. Fluid Mech.*, vol. 476, pp. 293–302, 2003.
- [34] W. M. F. Orr, “The stability or instability of the steady motions of a perfect liquid and of a viscous liquid. Part I: A perfect liquid. Part II: A viscous liquid,” *Proc. R. Irish Acad. A*, vol. 27, pp. 9–138, 1907.
- [35] M. Asai and M. Nishioka, “Origin of the peak-valley wave structure leading to wall turbulence,” *J. Fluid Mech.*, vol. 208, pp. 1–23, 1989.
- [36] K. Zhou, J. C. Doyle, and K. Glover, *Robust and Optimal Control*. Prentice Hall, 1996.
- [37] T. R. Bewley and S. Liu, “Optimal and robust control and estimation of linear paths to transition,” *J. Fluid Mech.*, vol. 365, pp. 305–349, 1998.

- [38] K. H. Lee, L. Corteletti, J. Kim, and J. Speyer, “Application of reduced-order controller to turbulent flows for drag reduction,” *Physics of Fluids*, vol. 13, no. 5, pp. 1321–1330, 2001.
- [39] J. Kim, “Control of turbulent boundary layers,” *Physics of Fluids*, vol. 15, no. 5, pp. 1093–1105, 2003.
- [40] M. Höglberg, T. R. Bewley, and D. S. Henningson, “Linear feedback control and estimation of transition in plane channel flow,” *J. Fluid Mech.*, vol. 481, pp. 149–175, 2003.
- [41] ———, “Relaminarization of $R_{e\tau} = 100$ turbulence using linear state-feedback control,” *Physics of Fluids*, vol. 15, no. 11, pp. 3572–3575, 2003.
- [42] C. Henoch and J. Stace, “Experimental investigation of a salt water turbulent boundary layer modified by an applied streamwise magnetohydrodynamic body force,” *Physics of Fluids*, vol. 7, no. 6, pp. 1371–1383, 1995.
- [43] C. H. Crawford and G. E. Karniadakis, “Reynolds stress analysis of EMHD-controlled wall turbulence. Part I. Streamwise forcing,” *Physics of Fluids*, vol. 9, no. 3, pp. 788–806, 1997.
- [44] T. W. Berger, J. Kim, C. Lee, and J. Lim, “Turbulent boundary layer control utilizing the Lorentz force,” *Physics of Fluids*, vol. 12, no. 3, pp. 631–649, 2000.
- [45] Y. Du and G. E. Karniadakis, “Suppressing wall turbulence by means of a transverse traveling wave,” *Science*, vol. 288, pp. 1230–1234, 2000.
- [46] Y. Du, V. Symeonidis, and G. E. Karniadakis, “Drag reduction in wall-bounded turbulence via a transverse travelling wave,” *J. Fluid Mech.*, vol. 457, pp. 1–34, 2002.

Chapter 7

Dynamical description of flow fluctuations

Any real fluid flow is accompanied with certain imperfections that cause the velocity and pressure fields to deviate from their nominal values. These imperfections are typically difficult to model, and they may arise due to, for example, surface roughness or incoming stream irregularities. The purpose of this chapter is to develop the appropriate mathematical framework for studying the dynamics of flow fluctuations around certain nominal flow conditions. We confine our attention to the incompressible shear flows through plane channels with unidirectional parallel nominal velocity profiles that depend only on the wall-normal coordinate. The typical examples of these flows are given by plane Poiseuille flow (flow with a parabolic nominal velocity profile; this flow is also referred to as the plane channel flow), and plane Couette flow (flow with a linear nominal velocity profile; this flow is also referred to as the linear shear flow).

The problem of transition to turbulence in these particular flow geometries is central to the technologically important problem of skin friction drag reduction. Despite fairly simple geometrical configurations, the problem of transition in these flows has historically been most difficult to model. We approach this problem by accounting explicitly for signal uncertainty in the NS equations. Namely, we model the fluid flow in the presence of body force fields which we consider to be ‘external’ inputs or excitations in these equations. The sources of these additional ingredients in the NS equations can be the aforementioned imperfections in the geometry and/or incoming stream. In this framework, spatially distributed and temporally varying body force fields are considered as inputs, whereas various combinations of the resulting velocity and/or vorticity fields are considered as outputs.

7.1 Linearized Navier-Stokes equations

We consider three-dimensional flow between two parallel infinite plates. Figure 7.1 illustrates geometry in plane Poiseuille flow. Incompressible flow of a viscous Newtonian fluid satisfies the NS equations and the continuity equation given in their non-dimensional form by

$$\partial_t \mathbf{u} = -\nabla_{\mathbf{u}} \mathbf{u} - \nabla p + \frac{1}{R} \Delta \mathbf{u}, \quad (7.1a)$$

$$0 = \nabla \cdot \mathbf{u}, \quad (7.1b)$$

where \mathbf{u} is the velocity vector, p is pressure, R the Reynolds number, ∇ is the gradient, $\Delta := \nabla^2$ is the Laplacian, and the operator $\nabla_{\mathbf{u}}$ is given by $\nabla_{\mathbf{u}} := \mathbf{u} \cdot \nabla$. Each field is assumed to vary both temporally and spatially, e.g. $p = p(x, y, z, t)$.

The dynamics of fluctuations around a certain (not necessarily laminar) nominal flow condition $(\bar{\mathbf{u}}, \bar{p})$ are

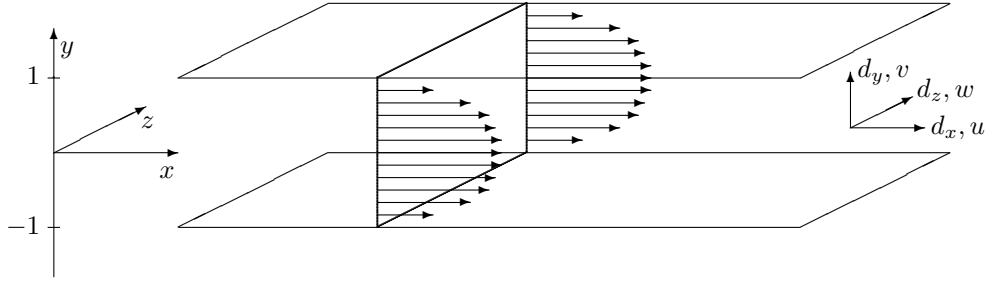


Figure 7.1: Three dimensional plane Poiseuille flow.

derived by expressing the fields as the sum of nominal and fluctuation terms

$$\mathbf{u} := \bar{\mathbf{u}} + \tilde{\mathbf{u}}, \quad p := \bar{p} + \tilde{p}.$$

By observing that the operator $\nabla_{\mathbf{u}}\mathbf{v}$ is bilinear in its arguments \mathbf{u} and \mathbf{v} , equation (7.1a) can now be rewritten as

$$\partial_t \tilde{\mathbf{u}} = -\nabla_{\bar{\mathbf{u}}} \tilde{\mathbf{u}} - \nabla_{\tilde{\mathbf{u}}} \bar{\mathbf{u}} - \nabla \tilde{p} + \frac{1}{R} \Delta \tilde{\mathbf{u}} - \{\partial_t \bar{\mathbf{u}} + \nabla_{\bar{\mathbf{u}}} \bar{\mathbf{u}} + \nabla \bar{p} - \frac{1}{R} \Delta \bar{\mathbf{u}}\} - \nabla_{\bar{\mathbf{u}}} \tilde{\mathbf{u}}, \quad (7.2)$$

together with $\nabla \cdot \tilde{\mathbf{u}} = -\nabla \cdot \bar{\mathbf{u}}$. These equations are PDEs with non-constant coefficients determined by $\bar{\mathbf{u}}$, and a forcing term given by the terms in the curly brackets. The latter terms sum to zero when the nominal fields are laminar (that is, satisfy the NS equations in the steady-state), where in addition we have $\nabla \cdot \tilde{\mathbf{u}} = 0$.

The LNS equations describe the dynamics of fluctuations up to first order, and are obtained by neglecting the second order term $\nabla_{\tilde{\mathbf{u}}} \tilde{\mathbf{u}}$. If the linearization of (7.1) is done around laminar flow, the linearized model simplifies to

$$\partial_t \tilde{\mathbf{u}} = -\nabla_{\bar{\mathbf{u}}} \tilde{\mathbf{u}} - \nabla_{\tilde{\mathbf{u}}} \bar{\mathbf{u}} - \nabla \tilde{p} + \frac{1}{R} \Delta \tilde{\mathbf{u}}, \quad (7.3a)$$

$$0 = \nabla \cdot \tilde{\mathbf{u}}. \quad (7.3b)$$

In the sequel we will return to the LNS in the more general situation when $(\bar{\mathbf{u}}, \bar{p})$ is not laminar.

We also consider the NS equations in the presence of external forces or excitations. One way of introducing external excitations into (7.1a) is by adding body forces $\mathbf{d}(x, y, z, t)$ to obtain

$$\partial_t \mathbf{u} = -\nabla_{\mathbf{u}} \mathbf{u} - \nabla p + \frac{1}{R} \Delta \mathbf{u} + \mathbf{d}.$$

Another interpretation of the forcing term \mathbf{d} is based on a robustness analysis and is outlined in § 2.2. The effect of this term on the linearized equations is easy to obtain, and by repeating the linearization procedure we obtain the equivalent of system (7.3) as

$$\begin{aligned} \partial_t \tilde{\mathbf{u}} &= -\nabla_{\bar{\mathbf{u}}} \tilde{\mathbf{u}} - \nabla_{\tilde{\mathbf{u}}} \bar{\mathbf{u}} - \nabla \tilde{p} + \frac{1}{R} \Delta \tilde{\mathbf{u}} + \mathbf{d}, \\ 0 &= \nabla \cdot \tilde{\mathbf{u}}. \end{aligned} \quad (7.4)$$

Let us assume that the only nonzero component of the steady state velocity field is velocity in the streamwise direction, $\bar{\mathbf{u}} := [U \ V \ W]^* = [U(y) \ 0 \ 0]^*$ ¹, and that the nominal pressure depends only on the streamwise coordinate, $\bar{p} = \bar{p}(x)$. Then, $\frac{1}{R} \Delta \bar{\mathbf{u}} - \nabla_{\bar{\mathbf{u}}} \bar{\mathbf{u}} - \nabla \bar{p}$ becomes equal to $[\frac{1}{R} \partial_{yy} U - \partial_x \bar{p} \ 0 \ 0]^*$

¹The same notation '*' is used to denote complex conjugate of a scalar, complex conjugate transpose of a matrix, and adjoint of an operator.

and we can rewrite the externally excited LNS system (7.4) as

$$\begin{aligned}\partial_t u + U \partial_x u + U' v &= -\partial_x p + \frac{1}{R} \Delta u + d_x, \\ \partial_t v + U \partial_x v &= -\partial_y p + \frac{1}{R} \Delta v + d_y, \\ \partial_t w + U \partial_x w &= -\partial_z p + \frac{1}{R} \Delta w + d_z, \\ \partial_x u + \partial_y v + \partial_z w &= 0,\end{aligned}\tag{7.5}$$

where $\tilde{\mathbf{u}} := [u \ v \ w]^*$, $\mathbf{d} := [d_x \ d_y \ d_z]^*$, and $U' := dU/dy$. An appropriate definition of the forcing term \mathbf{d} can be used to recover linearized version of (7.2) from (7.5).

In § 7.1.1, we apply the procedure described in § 2.1 to derive the evolution form of the LNS equations (7.4). Also, we point out the many possibilities for using different combinations of velocity and vorticity fields to encode the state of the LNS system.

7.1.1 Externally excited LNS equations in the evolution form

The externally excited LNS equations (7.4) are clearly not in the evolution form since this form does not allow for constraints like $\nabla \cdot \tilde{\mathbf{u}} = 0$. Furthermore, by definition, the ‘state’ of the system is a vector valued field such that at any point in time, this field completely determines the evolution of the system for the remainder of time. In (7.4), it is possible to use a smaller number of fields than $\tilde{\mathbf{u}}$ to encode the state of the system. An example of this is the well known technique of using normal velocity and vorticity equations to solve for plane channel flows [1].

We now illustrate the procedure developed in § 2.1 on the externally excited LNS system (7.5). The constraint $\bar{\mathcal{D}}\varphi = 0$ in this case is the zero divergence constraint, i.e. $\bar{\mathcal{D}} = [\partial_x \ \partial_y \ \partial_z]$. This one-by-three operator can be completed to an invertible three-by-three operator in many ways, one of which is

$$\begin{bmatrix} \partial_x & \partial_y & \partial_z \\ 0 & I & 0 \\ \partial_z & 0 & -\partial_x \end{bmatrix} =: \mathcal{T}.$$

Since \mathcal{T} is a three-by-three block operator with entries that mutually commute, its invertibility can be checked by computing the determinant $|\mathcal{T}| = -(\partial_{xx} + \partial_{zz})$. The last two rows of \mathcal{T} , which correspond to \mathcal{K}^{-L} , imply that ψ is the wall-normal velocity and vorticity fields

$$\psi = \begin{bmatrix} v \\ \omega_y \end{bmatrix} = \begin{bmatrix} 0 & I & 0 \\ \partial_z & 0 & -\partial_x \end{bmatrix} \begin{bmatrix} u \\ v \\ w \end{bmatrix}.$$

Clearly, there are many other possible completions of $\bar{\mathcal{D}}$ such that the resulting \mathcal{T} operator is invertible. Many different combinations of velocity and vorticity fields can thus be used to parameterize the state. The operator \mathcal{K} can be obtained from the last two columns of \mathcal{T}^{-1} , which can be calculated by the usual formulae for the inverse of a 3×3 matrix (since the entries of \mathcal{T} are mutually commutative). Following this procedure, \mathcal{K} is computed according to

$$\begin{bmatrix} u \\ v \\ w \end{bmatrix} = - \begin{bmatrix} \partial_{xy} & -\partial_z \\ -(\partial_{xx} + \partial_{zz}) & 0 \\ \partial_{yz} & \partial_x \end{bmatrix} (\partial_{xx} + \partial_{zz})^{-1} \begin{bmatrix} v \\ \omega_y \end{bmatrix} =: \mathcal{K} \begin{bmatrix} v \\ \omega_y \end{bmatrix}.\tag{7.6}$$

Now that we have identified a state parameterization $\psi := [v \ \omega_y]^*$, and the corresponding operators

\mathcal{K} and \mathcal{K}^{-L} for the LNS, the evolution form for the LNS is given by

$$\partial_t \psi = \mathcal{A}\psi + \mathcal{B}\mathbf{d}, \quad (7.7)$$

where

$$\begin{aligned} \mathcal{A} &:= \begin{bmatrix} \mathcal{A}_{11} & 0 \\ \mathcal{A}_{21} & \mathcal{A}_{22} \end{bmatrix} = \begin{bmatrix} -\Delta^{-1}U\partial_x\Delta + \Delta^{-1}U''\partial_x + \frac{1}{R}\Delta^{-1}\Delta^2 & 0 \\ -U'\partial_z & -U\partial_x + \frac{1}{R}\Delta \end{bmatrix}, \\ \mathcal{B} &:= [\mathcal{B}_x \ \mathcal{B}_y \ \mathcal{B}_z] = \begin{bmatrix} -\Delta^{-1}\partial_{xy} & \Delta^{-1}(\partial_{xx} + \partial_{zz}) & -\Delta^{-1}\partial_{yz} \\ \partial_z & 0 & -\partial_x \end{bmatrix}. \end{aligned}$$

We note that \mathcal{A}_{11} , \mathcal{A}_{22} , and \mathcal{A}_{21} are respectively referred to as the *Orr-Sommerfeld operator*, the *Squire operator*, and the *coupling operator*, whereas \mathcal{B}_x , \mathcal{B}_y , and \mathcal{B}_z denote the components of operator \mathcal{B} that act on d_x , d_y , and d_z . These operators represent Integro-Differential operators in three spatial directions: x , y , and z . We next utilize translation invariance of \mathcal{A} and \mathcal{B} in the horizontal directions to transform them into a parameterized family of one-dimensional operators in the wall-normal direction.

Translation invariance in horizontal directions

The basis behind a normal mode analysis of (7.7) is the fact that the operators \mathcal{A} and \mathcal{B} are translation invariant in the x and z directions. The dynamical system then has a much simpler description in terms of the evolution of the transformed velocity and vorticity fields

$$\hat{\psi}(k_x, y, k_z, t) := \int_{-\infty}^{\infty} \int_{-\infty}^{\infty} \psi(x, y, z, t) e^{-i(xk_x + zk_z)} dx dz,$$

where i is the imaginary unit, and k_x and k_z are the wave-numbers in the streamwise and spanwise directions. The evolution equations for the transformed fields become

$$\partial_t \hat{\psi} = \hat{\mathcal{A}}\hat{\psi} + \hat{\mathcal{B}}\hat{\mathbf{d}}, \quad (7.8)$$

with $\hat{\Delta} = \partial_{yy} - k_x^2 - k_z^2$, and

$$\begin{aligned} \hat{\mathcal{A}} &:= \begin{bmatrix} \hat{\mathcal{A}}_{11} & 0 \\ \hat{\mathcal{A}}_{21} & \hat{\mathcal{A}}_{22} \end{bmatrix} = \begin{bmatrix} -ik_x\hat{\Delta}^{-1}U\hat{\Delta} + ik_x\hat{\Delta}^{-1}U'' + \frac{1}{R}\hat{\Delta}^{-1}\hat{\Delta}^2 & 0 \\ -ik_zU' & -ik_xU + \frac{1}{R}\hat{\Delta} \end{bmatrix}, \\ \hat{\mathcal{B}} &:= [\hat{\mathcal{B}}_x \ \hat{\mathcal{B}}_y \ \hat{\mathcal{B}}_z] = \begin{bmatrix} -ik_x\hat{\Delta}^{-1}\partial_y & -(k_x^2 + k_z^2)\hat{\Delta}^{-1} & -ik_z\hat{\Delta}^{-1}\partial_y \\ ik_z & 0 & -ik_x \end{bmatrix}. \end{aligned}$$

Clearly, for any wave-number pair (k_x, k_z) , $\hat{\mathcal{A}}$ and $\hat{\mathcal{B}}$ represent one-dimensional operators in the wall-normal direction.

The boundary conditions on \hat{v} and $\hat{\omega}_y$ are derived from the original no-slip boundary conditions

$$\hat{v}(k_x, \pm 1, k_z, t) = \partial_y \hat{v}(k_x, \pm 1, k_z, t) = \hat{\omega}_y(k_x, \pm 1, k_z, t) = 0, \quad \forall k_x, k_z \in \mathbb{R}, \quad \forall t \geq 0. \quad (7.9)$$

On the other hand, from expression (2.5) in § 2.1 it follows that the pressure field is determined from $\hat{\psi}$ and $\hat{\mathbf{d}}$ by

$$\hat{\Delta}\hat{p} = -2ik_xU'\hat{v} + ik_x\hat{d}_x + \partial_y\hat{d}_y + ik_z\hat{d}_z.$$

Furthermore, from (7.6) it follows that streamwise and spanwise velocity perturbations can be computed from \hat{v} and $\hat{\omega}_y$ by

$$\hat{u} = \frac{i}{k_x^2 + k_z^2} (k_x \partial_y \hat{v} - k_z \hat{\omega}_y), \quad \hat{w} = \frac{i}{k_x^2 + k_z^2} (k_z \partial_y \hat{v} + k_x \hat{\omega}_y). \quad (7.10)$$

Similarly, the streamwise and spanwise vorticity fields are given by

$$\hat{\omega}_x = \frac{i}{k_x^2 + k_z^2} (k_z \hat{\Delta} \hat{v} + k_x \partial_y \hat{\omega}_y), \quad \hat{\omega}_z = \frac{i}{k_x^2 + k_z^2} (-k_x \hat{\Delta} \hat{v} + k_z \partial_y \hat{\omega}_y). \quad (7.11)$$

Output selection

Since one of our main objectives is to study input-output properties of the LNS equations, the appropriate output variable ϕ has to be selected. The choice of output should be motivated by the physics of the problem and can be made in a number of different ways. For example, an appropriately defined measure of the magnitude of velocity and/or vorticity field perturbations can be used to define the output variable. We choose the *kinetic energy density* of a harmonic perturbation to measure the size of the velocity field components. This quantity is defined for any given pairs of spatial wave-numbers in the streamwise and spanwise directions and at any given time as

$$E := \frac{k_x k_z}{16\pi^2} \int_{-1}^1 \int_0^{2\pi/k_x} \int_0^{2\pi/k_z} (u^2 + v^2 + w^2) dz dx dy, \quad (7.12)$$

where u , v , and w represent components of the velocity field in the physical space. When purely harmonic (in the horizontal directions) perturbations are considered, these velocities can be determined as [2]

$$\begin{aligned} u &= \operatorname{Re} \{ \hat{u} e^{i(k_x x + k_z z)} \} = \frac{1}{2} \{ \hat{u} e^{i(k_x x + k_z z)} + \hat{u}^* e^{-i(k_x x + k_z z)} \}, \\ v &= \operatorname{Re} \{ \hat{v} e^{i(k_x x + k_z z)} \} = \frac{1}{2} \{ \hat{v} e^{i(k_x x + k_z z)} + \hat{v}^* e^{-i(k_x x + k_z z)} \}, \\ w &= \operatorname{Re} \{ \hat{w} e^{i(k_x x + k_z z)} \} = \frac{1}{2} \{ \hat{w} e^{i(k_x x + k_z z)} + \hat{w}^* e^{-i(k_x x + k_z z)} \}. \end{aligned} \quad (7.13)$$

Substitution of (7.13) into (7.12) and integration over streamwise and spanwise directions yields

$$E = \frac{1}{8} \int_{-1}^1 (\hat{u}^* \hat{u} + \hat{v}^* \hat{v} + \hat{w}^* \hat{w}) dy. \quad (7.14)$$

Therefore, if the output of system (7.8) is defined as

$$\hat{\phi} := \begin{bmatrix} \hat{u} \\ \hat{v} \\ \hat{w} \end{bmatrix}, \quad (7.15)$$

then the kinetic energy density is completely determined by the $L^2[-1, 1]$ -norm of this output variable. In other words,

$$E = \langle \hat{\phi}, \hat{\phi} \rangle = \|\hat{\phi}\|^2,$$

where $\langle \cdot, \cdot \rangle$ denotes the $L^2[-1, 1]$ inner product, which is for our purposes defined as

$$\langle \hat{\phi}_1, \hat{\phi}_2 \rangle := \frac{1}{8} \int_{-1}^1 \hat{\phi}_1^* \hat{\phi}_2 dy. \quad (7.16)$$

Combining (7.10) and (7.15) the operator that maps the state of (7.8) into $\hat{\phi}$ can be expressed as

$$\hat{\phi} = \frac{1}{k_x^2 + k_z^2} \begin{bmatrix} ik_x \partial_y & -ik_z \\ k_x^2 + k_z^2 & 0 \\ ik_z \partial_y & ik_x \end{bmatrix} \hat{\psi} =: \hat{\mathcal{C}} \hat{\psi} = \begin{bmatrix} \hat{\mathcal{C}}_u \\ \hat{\mathcal{C}}_v \\ \hat{\mathcal{C}}_w \end{bmatrix} \hat{\psi} \quad (7.17)$$

Hence, system (7.8,7.17) can be abstractly rewritten as a one dimensional P(I)DE in the wall-normal direction parameterized by k_x and k_z

$$\partial_t \hat{\psi}(k_x, y, k_z, t) = [\hat{\mathcal{A}}(k_x, k_z) \hat{\psi}(k_x, k_z, t)](y) + [\hat{\mathcal{B}}(k_x, k_z) \hat{\mathbf{d}}(k_x, k_z, t)](y), \quad (7.18a)$$

$$\hat{\phi}(k_x, y, k_z, t) = [\hat{\mathcal{C}}(k_x, k_z) \hat{\psi}(k_x, k_z, t)](y), \quad (7.18b)$$

where $\hat{\mathcal{A}}(k_x, k_z)$, $\hat{\mathcal{B}}(k_x, k_z)$, and $\hat{\mathcal{C}}(k_x, k_z)$ represent the previously defined one dimensional operators in the wall-normal direction.

We note here that the LNS equations with input (7.18) that we use are qualitatively similar to those used by Farrell & Ioannou [3], but with an important difference. In [3], forcing was introduced directly in the right hand side of the $(\hat{v}, \hat{\omega}_y)$ equations. In our setup, the forcing is introduced in the more basic LNS equations, which results in a more transparent interpretation of the excitation as body forces, and allows for a detailed analysis of the relative effect of polarized forces. The mathematical difference is that the forcing in [3] has only two components and enters the equations through a different operator \mathcal{B} .

LNS equations with ‘structured’ external excitations

In the sequel, we will also analyze the situation in which the external excitation \mathbf{d} has an intensity that varies with the wall-normal direction. This is used to model the situation where the forcing fields have higher intensity near walls, as might be the case in certain flow control problems. A more general form for the forcing fields is

$$\mathbf{d}(x, y, z, t) := \begin{bmatrix} \gamma_x(y) & 0 & 0 \\ 0 & \gamma_y(y) & 0 \\ 0 & 0 & \gamma_z(y) \end{bmatrix} \mathbf{d}_0(x, y, z, t) = \begin{bmatrix} \gamma_x(y) d_{x0}(x, y, z, t) \\ \gamma_y(y) d_{y0}(x, y, z, t) \\ \gamma_z(y) d_{z0}(x, y, z, t) \end{bmatrix}, \quad (7.19)$$

where $\gamma_s(y)$ ($s = x, y$, or z) are certain *pre-specified* functions of y representing the relative intensities of the forcing fields in the wall-normal direction, $\mathbf{d}_0(x, y, z, t)$ is an *arbitrary* function of x, y, z , and t with a spatial Fourier transform $\hat{\mathbf{d}}_0(k_x, y, k_z, t)$. Note that \mathbf{d}_0 is considered ‘uniformly’ distributed in the wall-normal direction in a sense to be described in the sequel. It is convenient to incorporate the functions γ_s in the operator \mathcal{B} by defining

$$\mathcal{B}_0 := \mathcal{B} \begin{bmatrix} \gamma_x & 0 & 0 \\ 0 & \gamma_y & 0 \\ 0 & 0 & \gamma_z \end{bmatrix} = [\mathcal{B}_x \gamma_x \quad \mathcal{B}_y \gamma_y \quad \mathcal{B}_z \gamma_z] =: [\mathcal{B}_{x0} \quad \mathcal{B}_{y0} \quad \mathcal{B}_{z0}],$$

and then the system (7.18) can be rewritten as

$$\partial_t \hat{\psi}(k_x, y, k_z, t) = [\hat{\mathcal{A}}(k_x, k_z) \hat{\psi}(k_x, k_z, t)](y) + [\hat{\mathcal{B}}_0(k_x, k_z) \hat{\mathbf{d}}_0(k_x, k_z, t)](y), \quad (7.20a)$$

$$\hat{\phi}(k_x, y, k_z, t) = [\hat{\mathcal{C}}(k_x, k_z) \hat{\psi}(k_x, k_z, t)](y). \quad (7.20b)$$

Note that the equations are again in the state-space form but with a different operator acting on the input. We refer to systems (7.18) and (7.20) as the LNS systems with ‘unstructured’ and ‘structured’ external excitations, respectively. This reflects the fact that in the latter, the ‘ \mathcal{B} ’ operator has the wall-normal intensity profile of the forcing field built into it.

LNS equations with impulsive external excitations

In Chapter 10, we will compute and analyze the response of system (7.18) to the following forcing

$$\mathbf{d}(x, y, z, t) := \mathbf{f}_0(y) \delta(x, z, t) = \begin{bmatrix} f_{x0}(y) \\ f_{y0}(y) \\ f_{z0}(y) \end{bmatrix} \delta(x, z, t), \quad (7.21)$$

where $\delta(x, z, t)$ is the Dirac delta function in x , z , and t , and $\mathbf{f}_0(y)$ is an *arbitrary* forcing distribution in the wall-normal direction. Clearly, application of the spatial Fourier transform simplifies (7.21) to $\hat{\mathbf{d}}(k_x, y, k_z, t) = \mathbf{f}_0(y)\delta(t)$, which implies that the action of operator $\hat{\mathcal{B}}$ is completely determined by

$$\begin{aligned}\hat{\mathbf{F}}(k_x, y, k_z) &:= [\hat{\mathcal{B}}(k_x, k_z)\mathbf{f}_0](y) \\ &= [\hat{\mathcal{B}}_x(k_x, k_z)f_{x0}](y) + [\hat{\mathcal{B}}_y(k_x, k_z)f_{y0}](y) + [\hat{\mathcal{B}}_z(k_x, k_z)f_{z0}](y) \\ &= \hat{\mathbf{F}}_x(k_x, y, k_z) + \hat{\mathbf{F}}_y(k_x, y, k_z) + \hat{\mathbf{F}}_z(k_x, y, k_z),\end{aligned}$$

where

$$\hat{\mathbf{F}}_x = \begin{bmatrix} -ik_x\hat{\Delta}^{-1}f'_{x0} \\ ik_zf_{x0} \end{bmatrix}, \quad \hat{\mathbf{F}}_y = \begin{bmatrix} -(k_x^2 + k_z^2)\hat{\Delta}^{-1}f_{y0} \\ 0 \end{bmatrix}, \quad \hat{\mathbf{F}}_z = \begin{bmatrix} -ik_z\hat{\Delta}^{-1}f'_{z0} \\ -ik_xf_{z0} \end{bmatrix},$$

with $f'_{x0}(y) := df_{x0}(y)/dy$, and $f'_{z0}(y) := df_{z0}(y)/dy$. Therefore, in this particular case we can rewrite system (7.18) as

$$\partial_t \hat{\psi}(k_x, y, k_z, t) = [\hat{\mathcal{A}}(k_x, k_z)\hat{\psi}(k_x, k_z, t)](y) + \hat{\mathbf{F}}(k_x, y, k_z)\delta(t), \quad (7.22a)$$

$$\hat{\phi}(k_x, y, k_z, t) = [\hat{\mathcal{C}}(k_x, k_z)\hat{\psi}(k_x, k_z, t)](y), \quad (7.22b)$$

We note that, for any pair (k_x, k_z) , $\hat{\mathbf{F}}(k_x, y, k_z)$ represents a multiplication operator in y .

Certain mathematical considerations are required for a precise description of the above operators. They are included in § 7.1.2 and § 7.1.3. In § 7.2, we briefly describe the procedure used for numerical approximation of the forced evolution model (7.8).

7.1.2 The underlying operators

The underlying Hilbert space for operator $\hat{\mathcal{A}}$ is $\mathbb{H}_{os} \times L^2[-1, 1]$, where [4]

$$\mathbb{H}_{os} := \left\{ g \in L^2[-1, 1]; \quad g^{(2)} \in L^2[-1, 1], \quad g(\pm 1) = 0 \right\}.$$

This operator is an unbounded operator defined on a domain $\mathcal{D}(\hat{\mathcal{A}}) := \mathcal{D}(\hat{\mathcal{A}}_{11}) \times \mathcal{D}(\hat{\mathcal{A}}_{22})$. The domain of *Squire operator* $\hat{\mathcal{A}}_{22}$ is equal to \mathbb{H}_{os} , and the domain of *Orr-Sommerfeld operator* $\hat{\mathcal{A}}_{11}$ is defined by

$$\mathcal{D}(\hat{\mathcal{L}}) := \left\{ g \in \mathbb{H}_{os}; \quad g^{(4)} \in L^2[-1, 1], \quad g'(\pm 1) = 0 \right\}.$$

We endow the *state space* $\mathbb{H}_{os} \times L^2[-1, 1]$ with an *inner product* of the form

$$\langle \hat{\psi}_1, \hat{\psi}_2 \rangle_e := \langle \hat{\psi}_1, \hat{\mathcal{Q}}\hat{\psi}_2 \rangle, \quad (7.23)$$

where $\hat{\mathcal{Q}}$ is a block diagonal linear operator given by

$$\hat{\mathcal{Q}} := \frac{1}{k_x^2 + k_z^2} \begin{bmatrix} -\hat{\Delta} & 0 \\ 0 & I \end{bmatrix}. \quad (7.24)$$

The inner product on the right hand side of equation (7.23) is the standard $L^2[-1, 1]$ inner product. The inner product $\langle \cdot, \cdot \rangle_e$ determines then the kinetic energy density of a harmonic perturbation, which is a quadratic form of \hat{v} and $\hat{\omega}_y$ as follows [2]

$$E = \langle \hat{\psi}, \hat{\psi} \rangle_e = \frac{1}{8} \int_{-1}^1 \hat{\psi}^* \hat{\mathcal{Q}} \hat{\psi} dy =: \langle \hat{\psi}, \hat{\mathcal{Q}} \hat{\psi} \rangle.$$

For the purposes of norm computations, it is important to identify the adjoints of the relevant operators. The adjoint of an operator $\hat{\mathcal{G}}$ on a Hilbert space with an inner product $\langle \cdot, \cdot \rangle_e$, is defined by

$$\langle \hat{\psi}_1, \hat{\mathcal{G}}\hat{\psi}_2 \rangle_e = \langle \hat{\mathcal{G}}^*\hat{\psi}_1, \hat{\psi}_2 \rangle_e, \quad (7.25)$$

which must hold for all $\hat{\psi}_1, \hat{\psi}_2$ in the Hilbert space $\mathbb{H}_{os} \times L^2[-1, 1]$. Operator $\hat{\mathcal{A}}^*$ can be determined using (7.25), whereas the adjoints of operators $\hat{\mathcal{B}}, \hat{\mathcal{C}}$, and $\hat{\mathbf{F}}_s$ are respectively given by

$$\langle \hat{\psi}, \hat{\mathcal{B}}\hat{\mathbf{d}} \rangle_e = \langle \hat{\mathcal{B}}^*\hat{\psi}, \hat{\mathbf{d}} \rangle, \quad (7.26a)$$

$$\langle \hat{\phi}, \hat{\mathcal{C}}\hat{\psi} \rangle = \langle \hat{\mathcal{C}}^*\hat{\phi}, \hat{\psi} \rangle_e, \quad (7.26b)$$

$$\langle \hat{\psi}, \hat{\mathbf{F}}_s g(t) \rangle_e = \langle \hat{\mathbf{F}}_s^*\hat{\psi}, g(t) \rangle_{\mathbb{C}}. \quad (7.26c)$$

The inner products on the right-hand-side of (7.26a) and the left-hand-side of (7.26b) are the standard $L^2[-1, 1]$ inner products. The inner product on the right-hand-side of (7.26c) is the standard Euclidean inner product. Using (7.25) and (7.26) we determine $\hat{\mathcal{A}}^*, \hat{\mathcal{B}}^*, \hat{\mathcal{C}}^*$, and $\hat{\mathbf{F}}^*$ as

$$\hat{\mathcal{A}}^* = \begin{bmatrix} \hat{\mathcal{A}}_{11}^* & \hat{\mathcal{A}}_{21}^* \\ 0 & \hat{\mathcal{A}}_{22}^* \end{bmatrix}, \quad \hat{\mathcal{B}}^* = \begin{bmatrix} \hat{\mathcal{B}}_u^* \\ \hat{\mathcal{B}}_v^* \\ \hat{\mathcal{B}}_w^* \end{bmatrix}, \quad \hat{\mathcal{C}}^* = [\hat{\mathcal{C}}_u^* \quad \hat{\mathcal{C}}_v^* \quad \hat{\mathcal{C}}_w^*], \quad \hat{\mathbf{F}}^* = \hat{\mathbf{F}}_x^* + \hat{\mathbf{F}}_y^* + \hat{\mathbf{F}}_z^*, \quad (7.27)$$

where

$$\{\hat{\mathcal{A}}_{11}^* = ik_x U - ik_x \hat{\Delta}^{-1} U'' + \frac{1}{R} \Delta^{-1} \hat{\Delta}^2, \quad \hat{\mathcal{A}}_{22}^* = ik_x U + \frac{1}{R} \hat{\Delta}, \quad \hat{\mathcal{A}}_{21}^* = -ik_z \hat{\Delta}^{-1} U'\}, \quad (7.28)$$

and

$$\{\hat{\mathcal{B}}_x^* = \hat{\mathcal{C}}_u, \quad \hat{\mathcal{B}}_y^* = \hat{\mathcal{C}}_v, \quad \hat{\mathcal{B}}_z^* = \hat{\mathcal{C}}_w\}, \quad \{\hat{\mathcal{C}}_u^* = \hat{\mathcal{B}}_x, \quad \hat{\mathcal{C}}_v^* = \hat{\mathcal{B}}_y, \quad \hat{\mathcal{C}}_w^* = \hat{\mathcal{B}}_z\}. \quad (7.29)$$

On the other hand, the action of operators $\hat{\mathbf{F}}_s^*$ is determined by

$$\begin{aligned} \hat{\mathbf{F}}_x^* \hat{\psi} &= \frac{1}{k_x^2 + k_z^2} \int_{-1}^1 [-ik_x d'_{x0}(y) \quad -ik_z d_{x0}(y)] \begin{bmatrix} \hat{\psi}_1(y) \\ \hat{\psi}_2(y) \end{bmatrix} dy, \\ \hat{\mathbf{F}}_y^* \hat{\psi} &= \int_{-1}^1 [d_{y0}(y) \quad 0] \begin{bmatrix} \hat{\psi}_1(y) \\ \hat{\psi}_2(y) \end{bmatrix} dy, \\ \hat{\mathbf{F}}_z^* \hat{\psi} &= \frac{1}{k_x^2 + k_z^2} \int_{-1}^1 [-ik_z d'_{z0}(y) \quad ik_x d_{z0}(y)] \begin{bmatrix} \hat{\psi}_1(y) \\ \hat{\psi}_2(y) \end{bmatrix} dy. \end{aligned} \quad (7.30)$$

We remark that

$$\begin{aligned} \hat{\mathcal{B}}_u \hat{\mathcal{B}}_u^* &= \hat{\mathcal{C}}_u^* \hat{\mathcal{C}}_u = \frac{1}{k_x^2 + k_z^2} \begin{bmatrix} k_x^2 \hat{\Delta}^{-1} \partial_y^2 & -k_x k_z \hat{\Delta}^{-1} \partial_y \\ -k_x k_z \partial_y & k_z^2 \end{bmatrix}, \\ \hat{\mathcal{B}}_v \hat{\mathcal{B}}_v^* &= \hat{\mathcal{C}}_v^* \hat{\mathcal{C}}_v = \begin{bmatrix} -(k_x^2 + k_z^2) \hat{\Delta}^{-1} & 0 \\ 0 & 0 \end{bmatrix}, \\ \hat{\mathcal{B}}_w \hat{\mathcal{B}}_w^* &= \hat{\mathcal{C}}_w^* \hat{\mathcal{C}}_w = \frac{1}{k_x^2 + k_z^2} \begin{bmatrix} k_z^2 \hat{\Delta}^{-1} \partial_y^2 & k_x k_z \hat{\Delta}^{-1} \partial_y \\ k_x k_z \partial_y & k_x^2 \end{bmatrix}, \end{aligned} \quad (7.31)$$

which in turn implies

$$\hat{\mathcal{B}}\hat{\mathcal{B}}^* = \hat{\mathcal{C}}^*\hat{\mathcal{C}} = \begin{bmatrix} I & 0 \\ 0 & I \end{bmatrix}. \quad (7.32)$$

For ‘structured’ external excitations (7.19) we have

$$\begin{aligned} \hat{\mathcal{B}}_{x0}\hat{\mathcal{B}}_{x0}^* &:= \hat{\mathcal{B}}_x\gamma_x^2\hat{\mathcal{B}}_x^* = \frac{1}{k_x^2+k_z^2} \begin{bmatrix} k_x^2\hat{\Delta}^{-1}(2\gamma_x\gamma'_x\partial_y + \gamma_x^2\partial_{yy}) & -2k_xk_z\hat{\Delta}^{-1}\gamma_x\gamma'_x \\ -k_xk_z\gamma_x^2\partial_y & k_z^2\gamma_x^2 \end{bmatrix}, \\ \hat{\mathcal{B}}_{y0}\hat{\mathcal{B}}_{y0}^* &:= \hat{\mathcal{B}}_y\gamma_y^2\hat{\mathcal{B}}_y^* = \begin{bmatrix} -(k_x^2+k_z^2)\hat{\Delta}^{-1}\gamma_y^2 & 0 \\ 0 & 0 \end{bmatrix}, \\ \hat{\mathcal{B}}_{z0}\hat{\mathcal{B}}_{z0}^* &:= \hat{\mathcal{B}}_z\gamma_z^2\hat{\mathcal{B}}_z^* = \frac{1}{k_x^2+k_z^2} \begin{bmatrix} k_z^2\hat{\Delta}^{-1}(2\gamma_z\gamma'_z\partial_y + \gamma_z^2\partial_{yy}) & 2k_xk_z\hat{\Delta}^{-1}\gamma_z\gamma'_z \\ k_xk_z\gamma_z^2\partial_y & k_x^2\gamma_z^2 \end{bmatrix}, \end{aligned} \quad (7.33)$$

where $\gamma'_s := d\gamma_s(y)/dy$, for $s = x, y$, or z . The expressions (7.27-7.33) are utilized for norm computations of the spatio-temporal frequency and impulse responses.

7.1.3 Spectral analysis of Squire and Orr-Sommerfeld operators at $k_x = 0$

In this subsection, we perform spectral analysis of the Reynolds number independent, normalized Squire and Orr-Sommerfeld operators at $k_x = 0$. These two operators are denoted by $\hat{\mathcal{S}} := \hat{\Delta}$ and $\hat{\mathcal{L}} := \hat{\Delta}^{-1}\hat{\Delta}^2$, and their domains are determined by \mathbb{H}_{os} and $\mathcal{D}(\hat{\mathcal{A}}_{11})$, respectively. At any fixed k_z both $\hat{\mathcal{S}}$ and $\hat{\mathcal{L}}$ are self-adjoint (with respect to the inner products of $L^2[-1, 1]$ and \mathbb{H}_{os} , respectively) with discrete spectra, and they are negative definite (with respect to the aforementioned inner products). Thus, these two operators have only negative eigenvalues and generate stable evolutions. We note that the \mathbb{H}_{os} inner product is given by [4]

$$\langle g_1, g_2 \rangle_{os} := \langle g'_1, g'_2 \rangle_2 + k_z^2 \langle g_1, g_2 \rangle_2 = - \left\langle g_1, \hat{\Delta}g_2 \right\rangle_2.$$

It is well known that $\hat{\mathcal{S}}$ has the following set of orthonormal eigenfunctions $\{\varphi_n\}_{n \in \mathbb{N}}$ with corresponding eigenvalues $\{\gamma_n\}_{n \in \mathbb{N}}$

$$\varphi_n(y) := \sin\left(\frac{n\pi}{2}(y+1)\right), \quad \gamma_n(k_z) := -\left(\frac{n^2\pi^2}{4} + k_z^2\right), \quad n \in \mathbb{N}.$$

The spectral analysis of $\hat{\mathcal{L}}$ was performed in [5]. It was shown that $\hat{\mathcal{L}}$ has the set of eigenfunctions $\{\sigma_k\}_{k \in \mathbb{N}}$

$$\begin{aligned} \sigma_k(y, k_z, \lambda_k) &= A_k(\cos(p_k y) - \frac{\cos(p_k)}{\cosh(k_z)} \cosh(k_z y)) + B_k(\sin(p_k y) - \frac{\sin(p_k)}{\sinh(k_z)} \sinh(k_z y)) \\ &=: \sigma_{1k}(y, k_z, \lambda_k) + \sigma_{2k}(y, k_z, \lambda_k), \end{aligned}$$

with corresponding eigenvalues $\{\lambda_k\}_{k \in \mathbb{N}}$

$$\lambda_k := -(p_k^2 + k_z^2),$$

where p_k is obtained as a solution to either

$$p_k \tan(p_k) = -k_z \tanh(k_z), \quad (7.34)$$

or

$$p_k \cot(p_k) = k_z \coth(k_z). \quad (7.35)$$

It can be readily shown [5] that (7.34) and (7.35) cannot be satisfied simultaneously. In other words, if \bar{p}_k is obtained as a solution to (7.34) then \bar{p}_k does not satisfy (7.35), and vice versa. Furthermore, if (7.34) is satisfied then $\{A_k \neq 0, B_k \equiv 0\}$, and if (7.35) is satisfied then $\{A_k \equiv 0, B_k \neq 0\}$ [5], that is

$$\begin{aligned} p_k \tan(p_k) &= -k_z \tanh(k_z) \Rightarrow \{A_k \neq 0, B_k \equiv 0\}, \\ p_k \cot(p_k) &= k_z \coth(k_z) \Rightarrow \{A_k \equiv 0, B_k \neq 0\}. \end{aligned}$$

This implies that we can consider separately the spectral decompositions of $\hat{\mathcal{L}}$ in terms of $\{\sigma_{1k}\}_{k \in \mathbb{N}}$ and $\{\sigma_{2k}\}_{k \in \mathbb{N}}$ and combine them to determine the overall solution. In particular, the following choices of $\{A_k\}_{k \in \mathbb{N}}$ and $\{B_k\}_{k \in \mathbb{N}}$

$$\begin{aligned} A_k &:= \left\{ (p_{1k}^2 + k_z^2) \left(1 + \frac{\sin(2p_{1k})}{2p_{1k}} \right) \right\}^{-\frac{1}{2}}, \quad B_k \equiv 0, \quad p_{1k} \tan(p_{1k}) = -k_z \tanh(k_z), \\ A_k &\equiv 0, \quad B_k := \left\{ (p_{2k}^2 + k_z^2) \left(1 - \frac{\sin(2p_{2k})}{2p_{2k}} \right) \right\}^{-\frac{1}{2}}, \quad p_{2k} \cot(p_{2k}) = k_z \coth(k_z), \end{aligned}$$

respectively give the orthonormal sets of eigenfunctions $\{\sigma_{1k}\}_{k \in \mathbb{N}}$ and $\{\sigma_{2k}\}_{k \in \mathbb{N}}$.

7.2 Numerical method

In this section, we briefly describe the numerical method used for approximating the LNS equations. In the x and z directions, both frequency and impulse response calculations are done by ‘gridding’ in the wave-number space (k_x, k_z) . In the latter case, an inverse Fourier Transform is used to obtain the solutions in physical space (x, z) . In the wall-normal direction y , a Galerkin scheme [6] is used based on expansion using a set of basis functions that satisfy the appropriate boundary conditions [7].

We denote the basis functions we use for wall-normal velocity (\hat{v}) and vorticity ($\hat{\omega}_y$) by $\alpha_n(y)$ and $\beta_n(y)$ respectively. They are defined in terms of Chebyshev polynomials [6] as follows:

$$\alpha_n(y) := (1 - y^2)^2 T_n(y), \quad \beta_n(y) := (1 - y^2) T_n(y).$$

Clearly, these basis functions satisfy boundary conditions given by (7.9). If we assume that the number of \hat{v} and $\hat{\omega}_y$ basis functions is equal to N and M , respectively, we can express \hat{v} and $\hat{\omega}_y$ as

$$\hat{v}(k_x, y, k_z, t) \approx \sum_{n=0}^N a_n(k_x, k_z, t) \alpha_n(y), \quad \hat{\omega}_y(k_x, y, k_z, t) \approx \sum_{n=0}^M b_n(k_x, k_z, t) \beta_n(y),$$

where $a_n(k_x, k_z, t)$ and $b_n(k_x, k_z, t)$ are the so-called *spectral coefficients*. These coefficients are computed as a solution of a first order ODE obtained as a result of applying the Galerkin scheme to equation (7.8).

To obtain the corresponding ODE, one must find matrix representations of all operators in equation (7.8), and express external excitation in terms of basis functions. We note that these matrix entries can be calculated without numerical integration by exploiting the recursive relations between Chebyshev polynomials and their derivatives [6]. These matrix representations were developed for the case of a channel flow linearized around a nominal velocity profile of the form $\bar{\mathbf{u}} = [U(y) \ 0 \ 0]^*$. All numerical computations in this dissertation were performed using MATLAB.

Bibliography

- [1] J. Kim, P. Moin, and R. Moser, “Turbulence statistics in fully developed channel flow at low Reynolds number,” *J. Fluid Mech.*, vol. 177, pp. 133–166, 1987.
- [2] K. M. Butler and B. F. Farrell, “Three-dimensional optimal perturbations in viscous shear flow,” *Physics of Fluids A*, vol. 4, p. 1637, 1992.
- [3] B. F. Farrell and P. J. Ioannou, “Stochastic forcing of the linearized Navier-Stokes equations,” *Physics of Fluids A*, vol. 5, no. 11, pp. 2600–2609, 1993.
- [4] S. C. Reddy and D. S. Henningson, “Energy growth in viscous channel flows,” *J. Fluid Mech.*, vol. 252, pp. 209–238, 1993.
- [5] C. L. Dolph and D. C. Lewis, “On the application of infinite systems of ordinary differential equations to perturbations of plane Poiseuille flow,” *Quarterly of Applied Mathematics*, vol. XVI, no. 2, pp. 97–110, 1958.
- [6] J. P. Boyd, *Chebyshev and Fourier Spectral Methods*. Berlin, Heidelberg: Springer-Verlag, 1989.
- [7] A. Leonard, 1999, private communication.

Chapter 8

Spatio-temporal frequency responses of the linearized Navier-Stokes equations in channel flows

In this chapter, we study the LNS equations in plane channel flows from an input-output point of view by analyzing their spatio-temporal frequency responses. Spatially distributed and temporally varying body force fields are considered as inputs, while various combinations of the resulting velocity fields are considered as outputs. We show how the relative roles of TS waves, oblique waves, and streamwise vortices and streaks can be explained as input-output resonances of the spatio-temporal frequency responses. On the one hand, we study the effectiveness of input field components, and on the other, the energy content of the streamwise, wall-normal, and spanwise velocity perturbations. Our computations indicate that wall-normal and spanwise forces have much stronger influence on the velocity field than streamwise force, and that the impact of these forces is most powerful on the streamwise velocity.

We also demonstrate the significance of non-modal effects in supercritical channel flows. In these flows, unstable modes grow relatively slowly, and we show that when compared over long but finite times, non-normal modes in the form of streamwise elongated structures prevail TS modes. Our analysis method is based on computing exponentially discounted input-output system gains introduced in § 2.2.4. From a physical perspective this type of analysis amounts to accounting for the finite time phenomena rather than the asymptotic phenomena of infinite time limits. We illustrate many qualitative similarities between subcritical and supercritical channel flows when the latter are analyzed on finite time intervals. If this type of analysis is performed than, effectively, it turns out that the streamwise elongated flow structures contribute most to the perturbation energy for both these flows.

We recall that the LNS system with ‘unstructured’ external excitations (7.18) is given by

$$\begin{aligned}\partial_t \psi(k_x, y, k_z, t) &= [\mathcal{A}(k_x, k_z)\psi(k_x, k_z, t)](y) + [\mathcal{B}(k_x, k_z)\mathbf{d}(k_x, k_z, t)](y), \\ \phi(k_x, y, k_z, t) &= [\mathcal{C}(k_x, k_z)\psi(k_x, k_z, t)](y),\end{aligned}$$

where we no longer use the ‘caret symbol’ to denote Fourier transformed signals and operators. The spatio-temporal frequency response of this system is determined by

$$\mathcal{H}(k_x, k_z, \omega) = \mathcal{C}(k_x, k_z)(i\omega I - \mathcal{A}(k_x, k_z))^{-1}\mathcal{B}(k_x, k_z). \quad (8.2)$$

One of our main aims in this chapter is to perform a comparative analysis of the effects of forcing in the three different spatial directions on each of the three velocity fields. We thus need a more detailed analysis of the frequency response from each input to each output. Note that the input and output operators in the LNS system (7.18) have three subcomponents corresponding to each of the inputs and outputs respectively.

This induces a 3×3 matrix decomposition of the frequency response operator as follows

$$\begin{aligned} \mathcal{H}(k_x, k_z, \omega) &= \begin{bmatrix} \mathcal{C}_u \\ \mathcal{C}_v \\ \mathcal{C}_w \end{bmatrix} (\mathrm{i}\omega I - \mathcal{A}(k_x, k_z))^{-1} \begin{bmatrix} \mathcal{B}_x & \mathcal{B}_y & \mathcal{B}_z \end{bmatrix} \\ &=: \begin{bmatrix} \mathcal{H}_{ux}(k_x, k_z, \omega) & \mathcal{H}_{uy}(k_x, k_z, \omega) & \mathcal{H}_{uz}(k_x, k_z, \omega) \\ \mathcal{H}_{vx}(k_x, k_z, \omega) & \mathcal{H}_{vy}(k_x, k_z, \omega) & \mathcal{H}_{vz}(k_x, k_z, \omega) \\ \mathcal{H}_{wx}(k_x, k_z, \omega) & \mathcal{H}_{wy}(k_x, k_z, \omega) & \mathcal{H}_{wz}(k_x, k_z, \omega) \end{bmatrix}, \end{aligned} \quad (8.3)$$

where for example \mathcal{H}_{vz} is the response from the forcing d_z to the v velocity field, and similarly for the other 8 responses. By combining the rows and columns of this 3×3 matrix, we get another decomposition as follows

$$\begin{aligned} \mathcal{H}(k_x, k_z, \omega) &= \mathcal{C}(\mathrm{i}\omega I - \mathcal{A})^{-1} \begin{bmatrix} \mathcal{B}_x & \mathcal{B}_y & \mathcal{B}_z \end{bmatrix} \\ &=: \begin{bmatrix} \mathcal{H}_x(k_x, k_z, \omega) & \mathcal{H}_y(k_x, k_z, \omega) & \mathcal{H}_z(k_x, k_z, \omega) \end{bmatrix} \end{aligned} \quad (8.4)$$

$$= \begin{bmatrix} \mathcal{C}_u \\ \mathcal{C}_v \\ \mathcal{C}_w \end{bmatrix} (\mathrm{i}\omega I - \mathcal{A})^{-1} \mathcal{B} =: \begin{bmatrix} \mathcal{H}_u(k_x, k_z, \omega) \\ \mathcal{H}_v(k_x, k_z, \omega) \\ \mathcal{H}_w(k_x, k_z, \omega) \end{bmatrix}, \quad (8.5)$$

where, for example, \mathcal{H}_v is the response from all three inputs to the v field, and \mathcal{H}_x is the response from d_x to all three velocity fields.

All results presented here are obtained numerically using the scheme described in § 7.2, with 30 v and ω_y basis functions ($N = M = 29$). By increasing the number of basis functions it is confirmed that this resolution is high enough¹. The \mathcal{H}_2 -norm-like quantities are determined based on solutions of the corresponding Lyapunov equations, with 50×90 grid points in the wave-number space (k_x, k_z) . These points are chosen in the logarithmic scale with $\{k_{xmin} := 10^{-4}, k_{xmax} := 3.02\}$ and $\{k_{zmin} := 10^{-2}, k_{zmax} := 15.84\}$. On the other hand, the maximal singular values of the frequency response operator are calculated with $101 \times 90 \times 89$ grid points in the (k_x, k_z, ω) space. The frequency vectors in this case are given by: $\mathbf{k}_x := [-\mathbf{k}_{x1} \ 0 \ \mathbf{k}_{x1}]$, $\mathbf{k}_z := \mathbf{k}_{z1}$, and $\boldsymbol{\omega} := [-\boldsymbol{\omega}_1 \ 0 \ \boldsymbol{\omega}_1]$, where \mathbf{k}_{x1} , \mathbf{k}_{z1} , and $\boldsymbol{\omega}_1$ respectively denote the vectors with 50, 90, and 44 logarithmically spaced points between $\{k_{xmin} := 10^{-4}, k_{xmax} := 3.02\}$, $\{k_{zmin} := 10^{-2}, k_{zmax} := 15.85\}$, and $\{\omega_{min} := 10^{-3}, \omega_{max} := 2\}$.

This chapter is organized as follows: § 8.1 discusses componentwise energy amplification, maximal singular values of the frequency response operator, and dominant flow structures in subcritical Poiseuille flow with $R = 2000$. Sections 8.2, 8.3, and 8.4 are respectively devoted to the spatio-temporal frequency responses in Couette flow with $R = 2000$, turbulent mean velocity profile flow with $R_\tau = 590$, and Poiseuille flow with $R = 5700$. Finally, § 8.5 considers the relative importance of unstable modes and non-normal modes in supercritical Poiseuille flow with $R = 10000$.

8.1 Frequency responses in Poiseuille flow with $R = 2000$

In this section, we consider the NS equations linearized around a nominal velocity profile of the form $U(y) = 1 - y^2$ at $R = 2000$ ². We calculate the \mathcal{H}_2 and \mathcal{H}_∞ norms from different body force inputs to different velocity outputs as functions of spatial frequencies, and discuss the corresponding three-dimensional flow structures that are most amplified. These turn out to be typically streamwise elongated/spanwise periodic and oblique. We show how the relative roles of TS waves, oblique waves, and streamwise vortices and streaks can be explained as input-output resonances of the spatio-temporal frequency responses. We further analyze

¹We observe that in contrast to eigenvalue computations for the generator \mathcal{A} (which are used in stability calculations), much less resolution is required for computing system norms. While typically about 100 points might be required in a collocation scheme for stability calculations in channel flows, about 20-30 points are adequate to compute norms with very good accuracy. This is perhaps a reflection of the fact that norms are more ‘robust’ quantities than eigenvalues in channel flow problems.

²For this value of Reynolds number transition to turbulence has been observed in many experiments, despite the fact that the LNS equations are stable.

the effectiveness of input field components, and the energy content of u , v , and w . Also, we demonstrate that the wall-normal and spanwise forces have much stronger influence on the velocity field than the streamwise force, and that the impact of these forces is most powerful on the streamwise velocity component.

8.1.1 Componentwise energy amplification

We first study the frequency responses (as a function of k_x and k_z) of each of the components (subsystems) of the transfer function (8.3). We do this using the \mathcal{H}_2 norm, that is

$$[\|\mathcal{H}_{rs}\|_2^2](k_x, k_z) := \frac{1}{2\pi} \int_{-\infty}^{\infty} \|\mathcal{H}_{rs}(k_x, k_z, \omega)\|_{HS}^2 d\omega, \quad \text{for } r = u, v, w, \text{ and } s = x, y, z.$$

From Chapter 2, we recall that the \mathcal{H}_2 norm has an interesting stochastic interpretation: it quantifies the variance (energy) amplification of harmonic (in x and z) stochastic (in y and t) disturbances at any given wave-number pair (k_x, k_z) . In the fluid mechanics literature this measure of input-output amplification is also referred to as the *ensemble average energy density* of the statistical steady-state [1].

The (k_x, k_z) -parameterized \mathcal{H}_2 norms of all components of the frequency response operator are illustrated in Figure 8.1. Different plots correspond to the different elements of the operator valued matrix on the right-hand side of (8.3). All plots are given in the log–log–linear scale. We make the following observations:

- **Input-output amplifications from d_y and d_z to u attain the largest values.** Clearly, both $[\|\mathcal{H}_{uy}\|_2](k_x, k_z)$ and $[\|\mathcal{H}_{uz}\|_2](k_x, k_z)$ have fairly similar shapes with distinctive peaks whose values are at least one order of magnitude larger than the peak values of all other quantities shown in Figure 8.1. This illustrates that the wall-normal and spanwise forces have much stronger influence on the velocity field than the streamwise force, and that the impact of these forces is most powerful on the streamwise velocity component.
- **Different components of frequency response peak at different locations in the (k_x, k_z) -plane.** Hence, the componentwise input-output analysis uncovers *several distinct amplification mechanisms*. These mechanisms are responsible for creation of streamwise vortices and streaks (peak values at $k_x \approx 0$, $k_z \approx O(1)$), oblique waves (peak values at $k_x \approx O(1)$, $k_z \approx O(1)$), and TS waves (peak values at $k_x \approx O(1)$, $k_z \approx 0$).
- **The streamwise elongated structures are most amplified by system's dynamics, followed by the oblique perturbations, followed by the TS waves.** Clearly, there is about an order of magnitude difference between the largest peak values taking place at $(k_x \approx 0, k_z \approx O(1))$ and at $(k_x \approx O(1), k_z \approx O(1))$. On the other hand, in Poiseuille flow with $R = 2000$ the oblique waves are approximately four times more amplified than the least-stable LNS modes (TS waves). However, this is not to say that the TS waves and especially the oblique waves should be neglected in studies of transition. Either of them can trigger nonlinear terms in the full NS equations. Moreover, the phase of these perturbations can play an important role when the flow is connected in feedback with, for example, a controller for drag reduction.

We note that the importance of the streamwise vortices and streaks was thoroughly studied by [1–5], among others. The fact that the oblique waves often produce the greatest transient amplification was recognized by Farrell and Ioannou [6] in the study of the three-dimensional perturbations to viscous constant shear flow that give the largest energy growth on a selected time interval. Also, a Karhunen–Loëve analysis of a direct numerical simulation of turbulent channel flow at $R_\tau = 80$ revealed the presence of energetic oblique waves [7]. Oblique wave transition scenario was introduced in [8]. This transition scenario was studied experimentally in Poiseuille flow [9], and both experimentally and numerically in boundary layers [10]. The transition thresholds in oblique plane channel flow transition were examined in [11], and recently in [12]. The identification of the oblique waves as the input-output resonances of the LNS equations illustrates usefulness of the input-output approach to the analysis of the problem at hand.

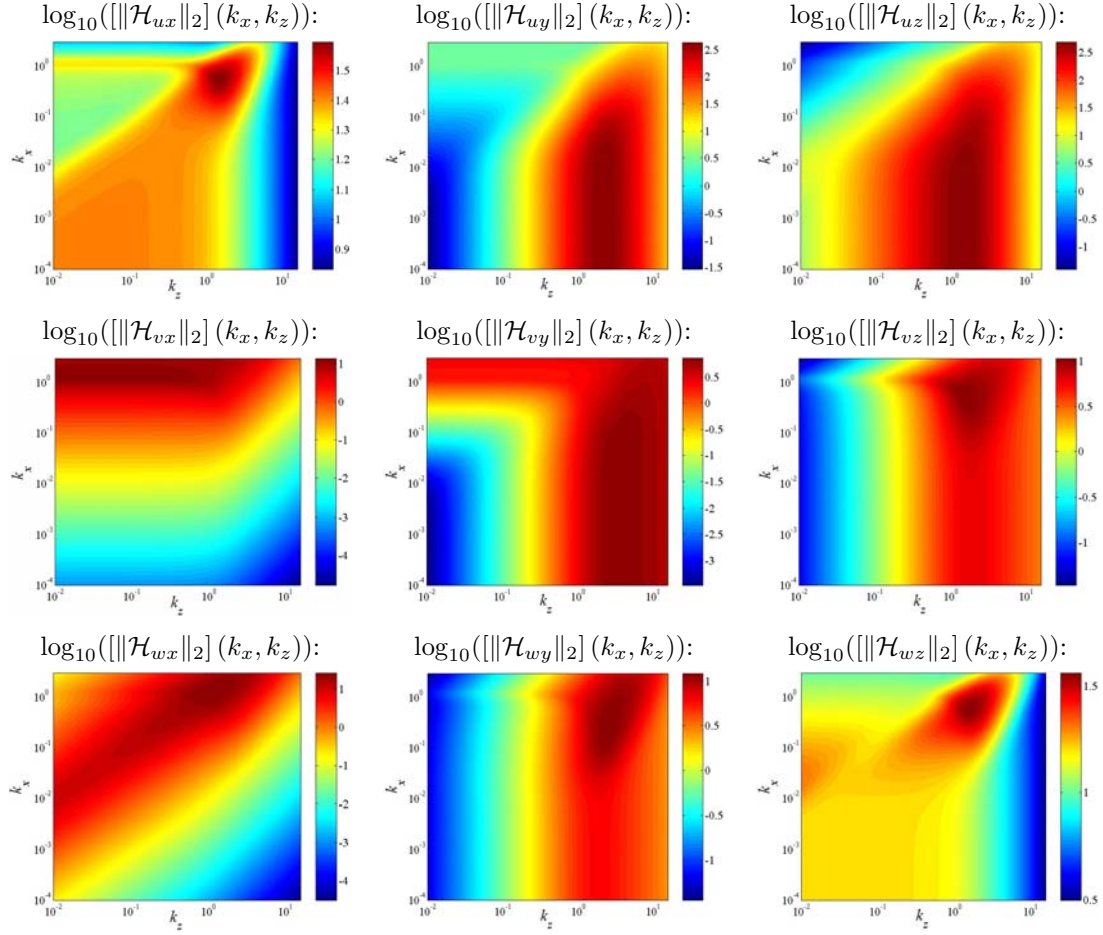


Figure 8.1: Plots of $\|\mathcal{H}_{rs}\|_2$ (k_x, k_z) in Poiseuille flow with $R = 2000$.

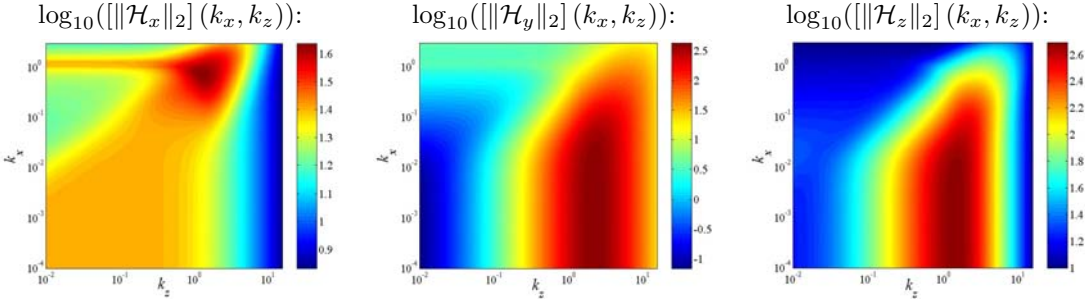


Figure 8.2: Plots of $\|\mathcal{H}_x\|_2(k_x, k_z)$, $\|\mathcal{H}_y\|_2(k_x, k_z)$, and $\|\mathcal{H}_z\|_2(k_x, k_z)$, in Poiseuille flow with $R = 2000$.

Figure 8.2 shows the \mathcal{H}_2 norms of different components of frequency response operator (8.4), that is

$$[\|\mathcal{H}_s\|_2^2](k_x, k_z) := \frac{1}{2\pi} \int_{-\infty}^{\infty} \|\mathcal{H}_s(k_x, k_z, \omega)\|_{HS}^2 d\omega, \quad \text{for } s = x, y, z.$$

These plots quantify the amplification from inputs in the three spatial directions to the velocity vector $\phi = [u \ v \ w]^T$. The square additive property of the \mathcal{H}_2 norm implies that these plots can be obtained by summing the rows in Figure 8.1. We note that:

- **The external excitations applied in the wall-normal and spanwise directions have much bigger impact on the velocity field than the streamwise direction forcing.** The analytical explanation for this observation is given in § 9.3, where we show that the energy of three-dimensional streamwise constant perturbations in the presence of either d_y or d_z achieves $O(R^3)$ amplification. On the other hand, only amplification proportional to the Reynolds number is achievable when external force in the streamwise direction is applied, as illustrated in § 9.3.
- **Functions $\|\mathcal{H}_y\|_2(k_x, k_z)$ and $\|\mathcal{H}_z\|_2(k_x, k_z)$ achieve their largest values at the different locations in the (k_x, k_z) -plane than function $\|\mathcal{H}_x\|_2(k_x, k_z)$.** Clearly, the former two quantities peak at $k_x = 0$ for certain $O(1)$ value of k_z . These input-output resonances correspond to the streamwise vortices and streaks. On the other hand, the latter quantity attains the global maximum at the location where both spatial wave-numbers have $O(1)$ values. We also observe a local peak at the streamwise wave-number axis in the left plot. This peak is caused by the least-stable modes of \mathcal{A} (TS waves). Even though the presence of the least-stable modes in the left plot is more prominent than in the middle and right plots, the structures that are more amplified by the system's dynamics are still three-dimensional. These structures correspond to the oblique waves.

Figure 8.3 illustrates the energy content of different velocity components by showing the k_x - k_z dependence of the \mathcal{H}_2 norm of frequency response operator (8.5), that is

$$[\|\mathcal{H}_r\|_2^2](k_x, k_z) := \frac{1}{2\pi} \int_{-\infty}^{\infty} \|\mathcal{H}_r(k_x, k_z, \omega)\|_{HS}^2 d\omega, \quad \text{for } r = u, v, w.$$

These plots quantify the respective amplification from input vector $\mathbf{d} := [d_x \ d_y \ d_z]^T$ to velocity perturbations u , v , and w . The square additive property of the \mathcal{H}_2 norm implies that these plots can be obtained by summing the columns in Figure 8.1. We remark that:

- **The energy content of the streamwise velocity is much bigger than the energy content of the other two velocity components.** The analytical explanation for this observation is given in § 9.3, where we explicitly show that the variance of three-dimensional streamwise velocity perturbations at $k_x = 0$ scales as R^3 . This is in sharp contrast with the amplification that v and w experience. Namely,

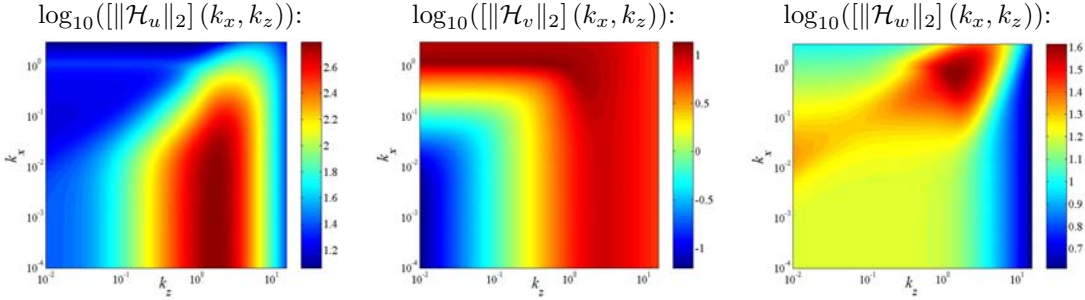


Figure 8.3: Plots of $\log_{10}(\|\mathcal{H}_u\|_2)(k_x, k_z)$, $\log_{10}(\|\mathcal{H}_v\|_2)(k_x, k_z)$, and $\log_{10}(\|\mathcal{H}_w\|_2)(k_x, k_z)$, in Poiseuille flow with $R = 2000$.

our derivations of § 9.3 prove that the variance of streamwise constant wall-normal and spanwise velocity perturbations is only proportional to the Reynolds number.

- **Functions $\|\mathcal{H}_u\|_2(k_x, k_z)$, $\|\mathcal{H}_v\|_2(k_x, k_z)$, and $\|\mathcal{H}_w\|_2(k_x, k_z)$ respectively achieve their largest values on the k_z -axis, k_x -axis, and at $(k_x \approx O(1), k_z \approx O(1))$.** These peaks correspond to the streamwise vortices and streaks (left plot), the least-stable system modes (middle plot), and the oblique waves (right plot). Since the evolution of the wall-normal velocity is governed by the stable Orr-Sommerfeld equation, it is not surprising that $\|\mathcal{H}_v\|_2(k_x, k_z)$ achieves its largest values in the immediate vicinity of the least-stable modes. The local peak at $(k_x = 0, k_z \approx O(1))$ in the middle plot signalizes a potential for the transient amplification in the Orr-Sommerfeld equation. However, this amplification is significantly weaker compared to the amplification of streamwise elongated structures in the left plot and oblique perturbations in the right plot. We further note that, since both u and w depend on ω_y (cf. (7.10)) they experience transient amplification due to a coupling between wall-normal velocity and vorticity perturbations. Physically, this coupling is due to a vortex stretching (vortex tilting) mechanism [13, 14]. Namely, the nominal spanwise vorticity (that is, $-U'$) is tilted in the wall-normal direction by the spanwise changes in v which leads to a transient growth of ω_y . Since for streamwise constant perturbations w depends only on v (cf. (7.10)), the amplification of w at $k_x = 0$ is limited to $O(R)$, as shown in § 9.3. Clearly, this amplification becomes larger when non-zero streamwise wave-numbers are considered. This can be attributed to the fact that away from k_z -axis w is a function of both v and ω_y (cf. (7.10)). The latter quantity achieves much bigger magnitudes than the former due to the aforementioned vortex tilting mechanism which is responsible for the input-output resonances observed in the right plot. We note that this mechanism does not take place whenever the nominal shear is zero (that is, $U' = 0$), or when there is no spanwise variations in the velocity perturbations (that is, $k_z = 0$).

In Figure 8.4, we show the \mathcal{H}_2 norm of frequency response operator (8.2). This plot quantifies the aggregate effect of forces in all three spatial directions to all three velocity components. Clearly, it is very difficult to notice different amplification mechanisms here, because of the dominance of the streamwise elongated structures. We remark that the TS waves generate a local peak at $(k_x \approx 1, k_z = 0)$, with a magnitude significantly lower than the one achieved by these prevailing streamwise elongated flow structures. On the other hand, the previously discussed peaks created by the oblique perturbations are inconspicuous in Figure 8.4. This demonstrates *utility of componentwise analysis over the analysis that only accounts for the aggregate effects*.

The numerical computations of this section are strengthened by a rigorous analysis of the various \mathcal{H}_2 norms of the streamwise constant three-dimensional channel flow perturbations. These analytical consideration are presented in § 9.3.

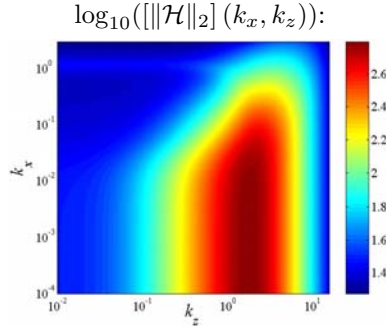


Figure 8.4: Plot of $[\|\mathcal{H}\|_2](k_x, k_z)$ in Poiseuille flow with $R = 2000$.

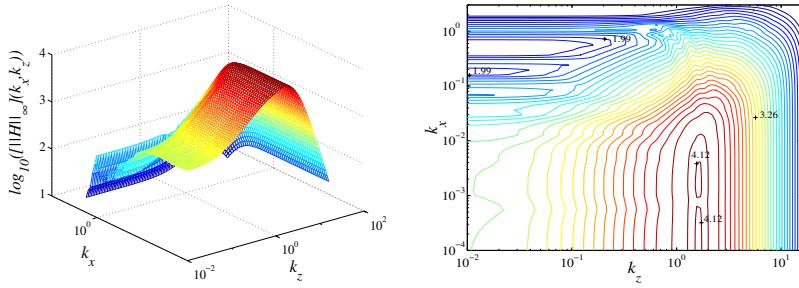


Figure 8.5: Plots of $[\|\mathcal{H}\|_\infty](k_x, k_z)$ in Poiseuille flow with $R = 2000$.

8.1.2 Maximal singular values

In this subsection, we study the \mathcal{H}_∞ -norm-like quantities of the transfer function (8.3). These quantities are obtained by taking suprema of $\sigma_{\max}(\mathcal{H}(k_x, k_z, \omega))$ over different frequencies. For example, from § 2.2.2 we recall that, the \mathcal{H}_∞ norm of system (7.18) with a frequency response (8.2) represents a (k_x, k_z) -parameterized function given by

$$[\|\mathcal{H}\|_\infty](k_x, k_z) := \sup_{\omega} \sigma_{\max}(\mathcal{H}(k_x, k_z, \omega)).$$

Suprema over spatial wave-numbers can be determined in a similar fashion.

We remind the reader that $[\|\mathcal{H}\|_\infty](k_x, k_z)$ has an interesting physical interpretation: at any pair (k_x, k_z) it quantifies the *worst case amplification* of deterministic inputs. In other words, $[\|\mathcal{H}\|_\infty](k_x, k_z)$ represent a maximization of the gain from \mathbf{d} to ϕ over input temporal frequencies and wall-normal shapes at given spatial wave-numbers. The former is obtained by the maximization over ω and the latter by taking a maximum singular value. Also, from § 2.2.6 we recall that $[\|\mathcal{H}\|_\infty](k_x, k_z)$ can be used to asses the stability margin of the LNS system (7.18) at any pair (k_x, k_z) . Namely, the \mathcal{H}_∞ norm precisely determines the ‘size’ of unstructured uncertainty that can be used to destabilize the system: the larger $[\|\mathcal{H}\|_\infty](k_x, k_z)$ the smaller stability margin of the LNS equations.

Figure 8.5 reveals the dependence of the \mathcal{H}_∞ norm of system (8.2) on both k_x and k_z in Poiseuille flow with $R = 2000$. The global maximum occurs at $(k_x = 0, k_z \approx 1.62)$. Based on contour plots, we also notice a local peak at $(k_x \approx 0.0015, k_z \approx 1.62)$. This local maximum has a value very close to the value of the global maximum. Under-damped system modes create a local peak at $(k_x \approx 1, k_z = 0)$, with a magnitude significantly lower than the magnitude achieved by dominant streamwise constant flow structures.

Figure 8.6 illustrates the maximal singular value plots of the operators \mathcal{H} , \mathcal{H}_x , \mathcal{H}_y , and \mathcal{H}_z in Poiseuille flow with $R = 2000$. For example, the left plot shows the k_x -dependence of $\sup_{k_z, \omega} \sigma_{\max}(\mathcal{H}(k_x, k_z, \omega))$ for these four operators. We make the following observations:

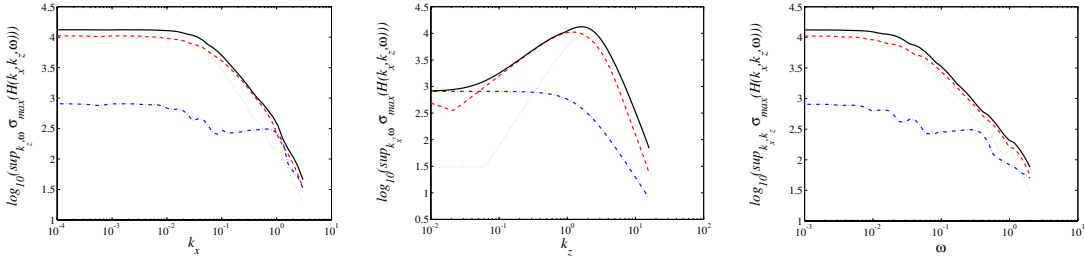


Figure 8.6: Maximal singular values of operators $\mathcal{H}(k_x, k_z, \omega)$ (solid), $\mathcal{H}_x(k_x, k_z, \omega)$ (dash-dot), $\mathcal{H}_y(k_x, k_z, \omega)$ (dot), and $\mathcal{H}_z(k_x, k_z, \omega)$ (dash) in Poiseuille flow with $R = 2000$. In all three cases the dependence on the remaining two frequencies is taken away by determining a supremum over them.

- **Streamwise elongated effects with large time constants dominate the evolution of the velocity perturbations.** Since all curves in the left and right plots achieve their peak values at $(k_x = 0, \omega = 0)$, this statement holds irrespective of spatial direction in which external excitation is applied. The results of § 8.1.1 do not contain any information about the temporal evolution of perturbations due to integration in time. On the other hand, the right plot in Figure 8.6 illustrates prevalence of perturbations that change slowly with time.
- **It appears that system acts as a low pass filter in both x and t .** When only forcing in the streamwise direction is applied, the LNS system behaves as a low pass filter in z as well. In this case, the spanwise elongated structures are most amplified by system's dynamics. However, this amplification is approximately two orders of magnitude smaller than the amplification achieved in the presence of either d_y or d_z .
- **Dominant spanwise length scale is much smaller than the dominant streamwise length scale when either d_y or d_z acts.** This is a direct consequence of the fact that the most amplified region of spanwise wave-numbers takes place away from $k_z = 0$, at $k_z = O(1)$.

Moreover, we note that even after taking suprema over two frequencies the dominance of streamwise elongated/spanwise periodic structures with long time constants is still identified using our approach. These structures are ubiquitous in experimental investigations related to transition in both channel and boundary layer flows [15–18]. This further exemplifies the power of the input-output approach to the analysis of the LNS equations.

8.1.3 Dominant flow structures

The left plot in Figure 8.7 shows the singular values of operator (8.2), arranged in descending order, at the location in the frequency space where $\sigma_{\max}(\mathcal{H}(k_x, k_z, \omega))$ achieves global maximum. This plot illustrates the existence of two strongly amplified perturbation types at $(k_x = 0, k_z = 1.62, \omega = 0)$.

The flow structures corresponding to the two largest singular values of operator $\mathcal{H}(0, 1.62, 0)$ are shown in Figure 8.8. The development of streamwise velocity (pseudo-color plots), and stream-function (contour plots) perturbations in the channel's cross-section is given. These perturbations are streamwise constant and, as such, they do not vary in the direction of the nominal flow. Several comments are in order:

- **The most amplified set of perturbations results in pairs of counter rotating streamwise vortices that generate high and low speed streaks symmetric with respect to the channel's centerline.** These perturbations have striking resemblance to the ‘Poiseuille flow symmetric global optima’ determined by Butler & Farrell [2] in their analysis of the most energetic initial conditions. We note that these perturbations experience energy growth that is approximately twice smaller than the energy growth of ‘antisymmetric global optima’ [2]. As remarked by Butler & Farrell [2], the experimental conditions, such as surface roughness or level of background noise, ‘may select perturbations

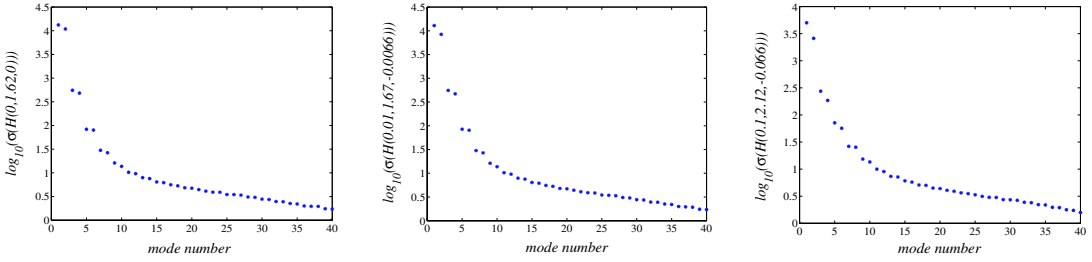


Figure 8.7: Singular values of operator (8.2) at: $(k_x = 0, k_z = 1.62, \omega = 0)$ (left), $(k_x = 0.01, k_z = 1.67, \omega = -0.0066)$ (middle), and $(k_x = 0.1, k_z = 2.12, \omega = -0.066)$ (right), in Poiseuille flow with $R = 2000$.

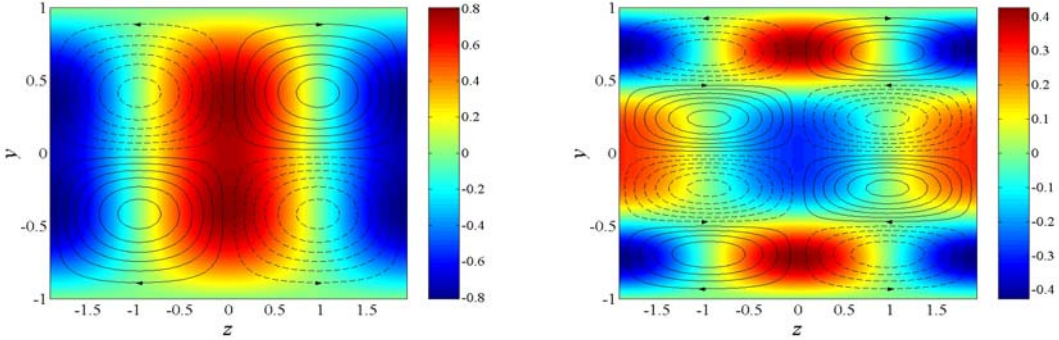


Figure 8.8: Streamwise velocity (pseudo-color plots), and stream-function (contour plots) perturbation development for largest singular value (left) and second largest singular value (right) of operator (8.2) at $(k_x = 0, k_z = 1.62, \omega = 0)$ (location where the global maximum of $\sigma_{\max}(\mathcal{H}(k_x, k_z, \omega))$ takes place), in Poiseuille flow with $R = 2000$. Red color represents high speed streaks, and blue color represents low speed streaks.

that grow robustly but not necessarily optimally³. Our results indicate that symmetric perturbations are most amplified by the system's dynamics in the presence of unstructured spatially distributed and temporally varying external excitations.

- **There exists no general relationship between transient growth and input-output analyses.** As already mentioned, the former focuses on the search for initial perturbations that gain the most energy on a certain time interval. On the other hand, the latter studies the LNS system in the presence of body forces. One of the goals of the input-output analysis may be determination of flow structures that are strongly amplified by the externally excited LNS dynamics. The results presented here establish that, in Poiseuille flow, the transient growth global optima do not correspond to the flow perturbations most amplified by the forced LNS equations. In § 8.2, we will illustrate that this is also the situation in Couette flow. Namely, it turns out that the dominant input-output resonances in Couette flow are streamwise constant. On the other hand, the flow perturbations with very slow streamwise variations and $k_z \approx 1.60$ have the strongest transient growth potential [2, 4].
- **The second set of strongly amplified perturbations results in four streamwise vortices occupying the channel width.** These counter-rotating vortices generate strong high (low) speed streaks in the near wall regions and a slightly weaker low (high) speed streak that fills the middle of the channel.

³Word optimal is used to denote initial perturbations that are capable of most energetic transient growth [2].

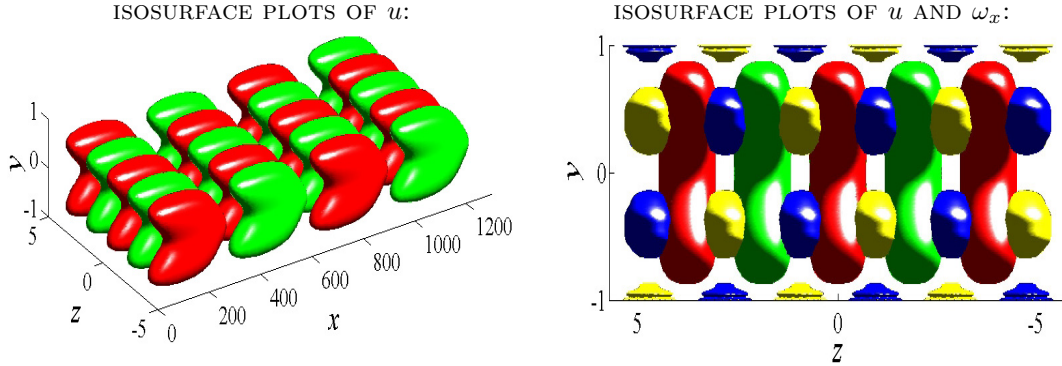


Figure 8.9: Streamwise velocity and vorticity perturbation development for largest singular value of operator \mathcal{H} at $(k_x = 0.01, k_z = 1.67, \omega = -0.0066)$, in Poiseuille flow with $R = 2000$. High (low) velocity and vorticity regions are respectively represented by red and yellow (green and blue) colors. Isosurfaces of u and ω_x are respectively taken at ± 0.5 and ± 0.1 .

The results shown in Figures 8.5 and 8.6 indicate that $\sigma_{\max}(\mathcal{H}(k_x, k_z, \omega))$ has a fairly uniform value in the region of k_z 's where this quantity peaks so long as (approximately) $|k_x| < 0.1$ and $|\omega| < 0.1$. This is further illustrated in the middle and right plots in Figure 8.7, where we respectively show the singular values of \mathcal{H} at $(k_x = 0.01, k_z = 1.67, \omega = -0.0066)$, and $(k_x = 0.1, k_z = 2.12, \omega = -0.066)$. We still observe presence of two strongly amplified perturbations.

The streamwise velocity and vorticity perturbation developments for these two cases are shown in Figures 8.9, 8.10, and 8.11. We remark that:

- **The plots are characterized by the alternating regions of high and low velocities that are elongated in the streamwise directions.** Some of the plots have the form of downstream oriented arrowhead-shaped structures. This rather characteristic shape is observed experimentally in laminar-turbulent transition studies in both channel [15–17] and boundary layer flows [18, 19].
- **The velocity (vorticity) perturbations develop symmetrically (antisymmetrically) about the channel's centerline.**
- **The vortices are positioned between the high and low velocity regions.**
- **There is a large concentration of arrays of counter rotating streamwise vortices in the vicinity of the lower and upper walls.** These streamwise vortices transport low-velocity fluid away from the walls towards the channel centerline and redistribute it in the spanwise direction.
- **Experimental and DNS results are characterized by the interaction of different modes rather than by a dominance of one particular mode.** Thus, the real flow is going to be much more complicated than the structures shown here. Nevertheless, the performed analysis serves as an indication of structures that can be expected to be seen in both experimental and numerical transition investigations. In Chapter 10, we will illustrate that the results presented here exhibit some qualitative similarities with the spatio-temporal impulse responses of the LNS equations.

To illustrate that most results of this section represent universal properties of the wall-bounded shear flows rather than just distinctive features of the plane Poiseuille flow, in § 8.2 and § 8.3, we respectively discuss frequency responses of the plane Couette flow with $R = 2000$ and turbulent mean velocity profile flow with $R_\tau = 590$.

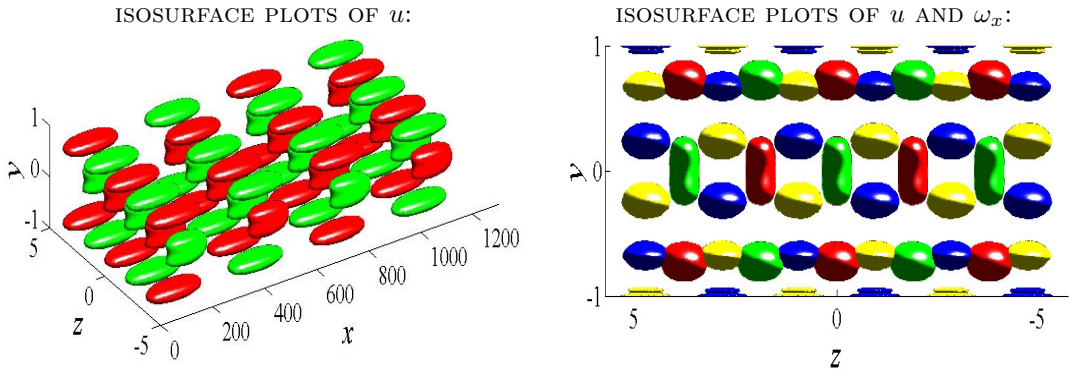


Figure 8.10: Streamwise velocity and vorticity perturbation development for second largest singular value of operator \mathcal{H} at $(k_x = 0.01, k_z = 1.67, \omega = -0.0066)$, in Poiseuille flow with $R = 2000$. High (low) velocity and vorticity regions are respectively represented by red and yellow (green and blue) colors. Isosurfaces of both u and ω_x are taken at ± 0.5 .

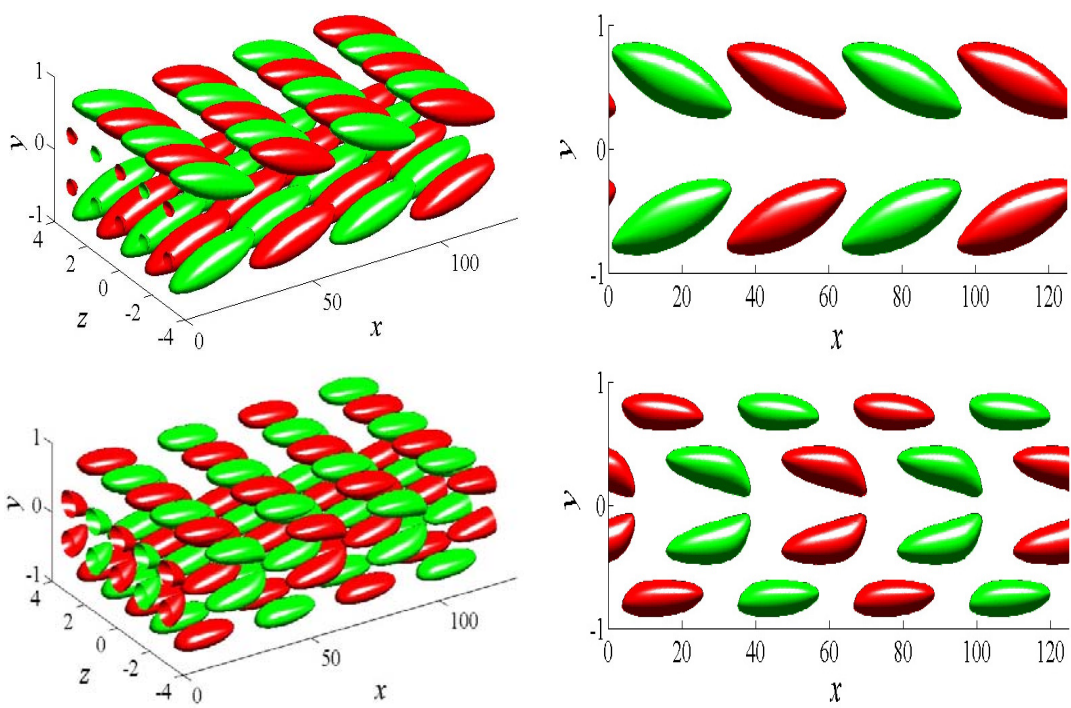


Figure 8.11: Streamwise velocity perturbation development for largest singular value (first row) and second largest singular value (second row) of operator \mathcal{H} at $(k_x = 0.1, k_z = 2.12, \omega = -0.066)$, in Poiseuille flow with $R = 2000$. High speed streaks are represented by red color, and low speed streaks are represented by green color. Isosurfaces are taken at ± 0.5 .

8.2 Frequency responses in Couette flow with $R = 2000$

In this section, we present different portions of the spatio-temporal frequency responses for the NS equations linearized around a nominal velocity profile of the form $U(y) = y$ at $R = 2000$. We compare the results presented here with the results presented in § 8.1 and find many qualitative similarities.

Figure 8.12 illustrates the effectiveness of input field components by showing the (k_x, k_z) -dependence of the \mathcal{H}_2 norm for all subsystems in (8.4). As in Poiseuille flow, excitations in the spanwise and wall-normal directions have much bigger influence on flow perturbations than the streamwise excitation. Furthermore, the peaks in the middle and right plots take place on the k_z -axis, whereas the peak in the left plot is moved to the location where both $k_x \neq 0$ and $k_z \neq 0$. The absence of the streamwise forcing in the equation that governs the evolution of the wall-normal velocity at $k_x = 0$ prevents large amplification in the latter case (see § 9.3 for analytical explanation). This amplification becomes bigger for non-zero values of k_x , but clearly, it never reaches values achieved by $\|\mathcal{H}_y\|_2(k_x, k_z)$ and $\|\mathcal{H}_z\|_2(k_x, k_z)$.

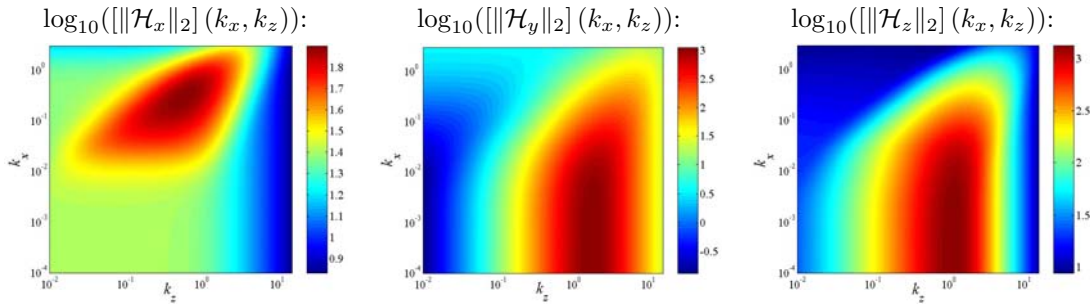


Figure 8.12: Plots of $\|\mathcal{H}_x\|_2(k_x, k_z)$, $\|\mathcal{H}_y\|_2(k_x, k_z)$, and $\|\mathcal{H}_z\|_2(k_x, k_z)$, in Couette flow with $R = 2000$.

Energy content of streamwise, wall-normal, and spanwise velocity components in Couette flow with $R = 2000$ is shown in Figure 8.13. By comparing these plots with their Poiseuille flow counterparts we conclude that they have fairly similar features. Furthermore, as in § 8.1, we note the dominance of the streamwise velocity perturbations.

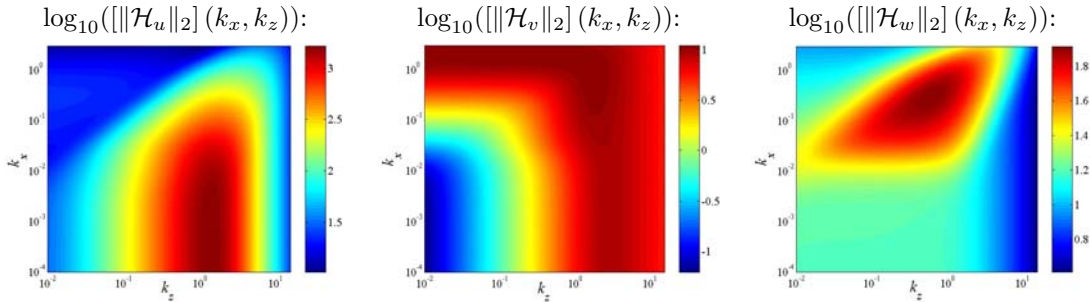


Figure 8.13: Plots of $\|\mathcal{H}_u\|_2(k_x, k_z)$, $\|\mathcal{H}_v\|_2(k_x, k_z)$, and $\|\mathcal{H}_w\|_2(k_x, k_z)$, in Couette flow with $R = 2000$.

Our computations show that the largest input-output gains in Couette flow are achieved at $(k_x = 0, k_z \approx O(1))$. This may seem to be at odds with [2,4], where it was established that, in Couette flow, the spanwise periodic perturbations with very slow streamwise variations generate the largest transient growth. We remark again that *there is no general relationship between transient growth and input-output analyses* (see § 8.1.3 for additional discussions). In view of this, both these results are correct and they are not in disagreement with each other. Not only does our analysis uncover the streamwise constant/spanwise periodic structures as the most amplified input-output resonances, but it also reveals that the spanwise periodic structures with

slow streamwise variations are strongly amplified by the LNS dynamics. Thus, in experimental or numerical investigations one should expect to observe both these effects.

We note that the spectral analysis of Couette and Poiseuille flows indicates that these two flows are quite different. Namely, the former is stable for all values of R [20], and the latter loses stability when R achieves values greater than 5772 [21]. However, according to the results of § 8.1 and § 8.2 these two flows have fairly similar qualitative features when analyzed from an input-output point of view.

8.3 Frequency responses in turbulent mean velocity profile flow with $R_\tau = 590$

In this section, we study the frequency responses for the flow that satisfies the NS equations linearized around turbulent mean velocity profile with $R_\tau = 590$. This velocity profile is shown in Figure 8.14, and it was obtained by direct numerical simulations of the channel flow at $R_\tau = 590$ [22]. This section illustrates that our methodology can be applied to study input-output properties of the system linearized around a velocity profile that is not a steady-state solution of the NS equations. Also, we compare the results presented here with the results obtained in subcritical Poiseuille (cf. § 8.1) and Couette (cf. § 8.2) flows with $R = 2000$.

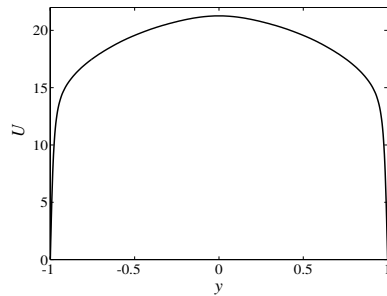


Figure 8.14: Channel flow turbulent mean velocity profile with $R_\tau = 590$.

The (k_x, k_z) -parameterized \mathcal{H}_2 norms of each component of operators (8.4) and (8.5) are respectively shown in Figures 8.15 and 8.16. Qualitatively, these plots resemble their analogues of § 8.1 and § 8.2. The strongly amplified resonances still have long streamwise length scales and certain spanwise periodicity.

Therefore, the frequency domain input-output analysis reveals that all channel flows with a streamwise direction mean velocity profile that depends only on the wall-normal coordinate are almost alike. This is an important discovery which, for example, indicates that the perturbations around laminar and turbulent channel flows should act in a similar way. However, the interpretation for these two cases is different. While the laminar flow perturbations initiate transition and consequently lead to turbulence, their turbulent flow counterparts are primarily responsible for maintenance of the turbulent state. Regardless of the interpretation, our results underscore the importance of non-modal effects in both transitional and fully turbulent channel flows.

8.4 Frequency responses in Poiseuille flow with $R = 5700$

In this section, we study the frequency responses in subcritical Poiseuille flow with $R = 5700$. We consider this problem for two reasons. First, we want to identify the dominant input-output resonances in the flow that is about to become unstable if the Reynolds number is increased by less than 1.25% (critical value of Reynolds number is approximately equal to 5772 [21]). Second, in § 8.5 we will compare results presented here with the results obtained in supercritical Poiseuille flow with $R = 10000$ in the presence of exponentially discounted input and output signals. Our main conclusions are:

- The dominant input-output resonances are still streamwise vortices and streaks.

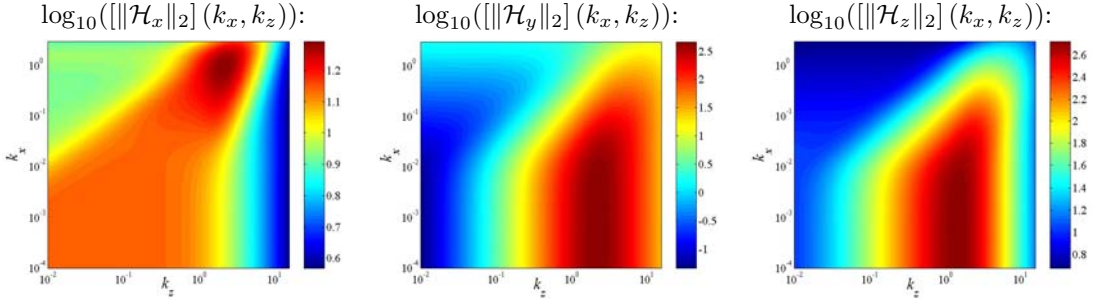


Figure 8.15: Plots of $\log_{10}(\|\mathcal{H}_x\|_2)(k_x, k_z)$, $\log_{10}(\|\mathcal{H}_y\|_2)(k_x, k_z)$, and $\log_{10}(\|\mathcal{H}_z\|_2)(k_x, k_z)$, in turbulent mean velocity profile flow with $R_\tau = 590$.

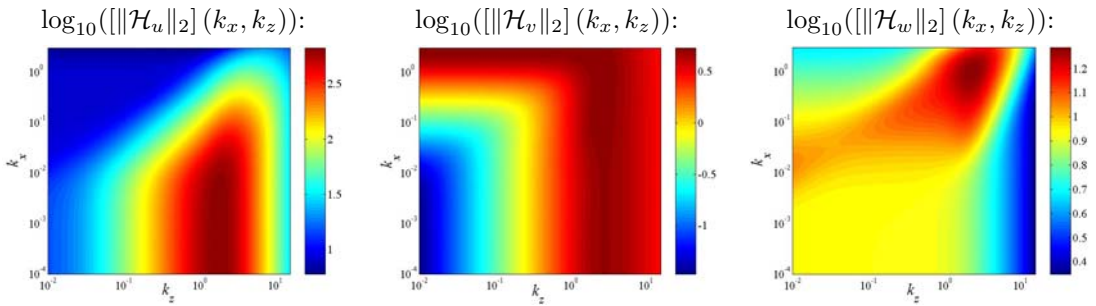


Figure 8.16: Plots of $\log_{10}(\|\mathcal{H}_u\|_2)(k_x, k_z)$, $\log_{10}(\|\mathcal{H}_v\|_2)(k_x, k_z)$, and $\log_{10}(\|\mathcal{H}_w\|_2)(k_x, k_z)$, in turbulent mean velocity profile flow with $R_\tau = 590$.

- Subcritical and supercritical flows have many qualitative similarities when the latter are analyzed on finite time intervals.

Figure 8.17 shows the \mathcal{H}_∞ and \mathcal{H}_2 norms of operator \mathcal{H} as functions of k_x and k_z . Despite the fact that the LNS equations are about to become unstable if the Reynolds number is slightly increased, the least-stable modes of generator \mathcal{A} are not most amplified by the system's dynamics. Rather, the largest input-output gains are attained for small streamwise wave-numbers at $O(1)$ value of k_z . As already discussed, this implies that the most amplified structures have very large streamwise elongation and spanwise periodicity determined by the value of k_z at which maximum happens to be. We note that the peaks corresponding to the least-stable modes have much bigger values here than, for example, at $R = 2000$ (cf. § 8.1). These peaks would go to infinity if the Reynolds number is increased above its critical value. However, this is an artifact of the definition of the \mathcal{H}_∞ and \mathcal{H}_2 norms rather than something that would play a dominant role in the initial stages of laminar-turbulent transition in flows that have some amount of background disturbances in them. This is further illustrated in § 8.5 where we analyze the exponentially discounted input-output gains in supercritical Poiseuille flow with $R = 10000$.

8.5 Unstable modes versus non-normal modes in supercritical channel flows

In this section, we demonstrate the significance of non-modal effects in supercritical channel flows. We utilize the fact that the input-output method can be generalized to supercritical flows by measuring the size of perturbations with appropriate exponential discounts on their energies (see § 2.2.4 for background material). Since the unstable modes of the LNS equations in, for example, Poiseuille flow have very slow

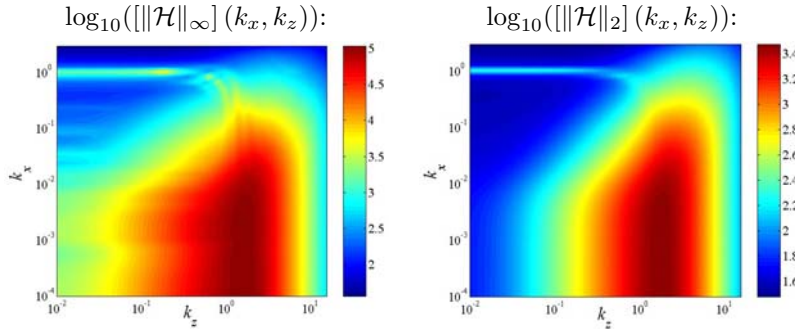


Figure 8.17: Plots of $\log_{10}(\|\mathcal{H}\|_\infty)(k_x, k_z)$ and $\log_{10}(\|\mathcal{H}\|_2)(k_x, k_z)$ in Poiseuille flow with $R = 5700$.

growth rates, it is relevant to investigate whether dominant supercritical flow structures on finite time intervals correspond to the structures generated by these exponentially growing modes or by something else. We illustrate that even a small amount of background disturbance in these flows yields completely different flow patterns from the ones corresponding to the exponentially growing system modes when finite time phenomena are considered. In particular, our results underscore the importance of the streamwise elongated flow structures (that is, streamwise vortices and streaks) not only in the subcritical channel flows, but also in the channel flows occurring in the supercritical regimes.

We study the exponentially discounted input-output gains in supercritical Poiseuille flow with $R = 10000$ and $\alpha := 0.0038$. This particular choice of parameter α is made because the LNS equations have an unstable mode with a real part approximately equal to 0.0037 at $R = 10000$, $k_x = 1$, and $k_z = 0$ [21]. Furthermore, we compare the subcritical result of § 8.4 and supercritical results presented here and show that they exhibit many qualitative similarities.

The left plot in Figure 8.18 illustrates the dependence of the exponentially discounted \mathcal{H}_∞ norm on both streamwise and spanwise wave-numbers. We make the following observations:

- **Even though the flow is supercritical, the dominant input-output resonances do not correspond to the unstable modes.** Rather, as in the subcritical case, they arise because of the vortex tilting mechanism [13, 14], that is, the coupling from v to ω_y in the LNS equations. Clearly, the global maximum of $\|\mathcal{H}_\alpha\|_\infty(k_x, k_z)$ occurs at $k_x = 0$ and $O(1)$ value of k_z .
- **Amplification achieved by 2D unstable modes is much lower than amplification achieved by streamwise constant flow structures.** These unstable modes create a local peak at $(k_x \approx 1, k_z = 0)$.
- **3D TS waves induce larger input-output gains than 2D TS waves.** These 3D exponentially growing modes create a local peak at $(k_x \approx 0.85, k_z \approx 0.38)$. This further exemplifies the importance of the three-dimensional analysis which has traditionally been neglected owing to the misinterpretation of the Squire theorem (for more detail see, for example, [23] and discussions therein).

The exponentially discounted \mathcal{H}_2 norm is shown in the right plot of Figure 8.18. We note that:

- **As for $\|\mathcal{H}_\alpha\|_\infty(k_x, k_z)$, the global maximum of $\|\mathcal{H}_\alpha\|_2(k_x, k_z)$ takes place at $(k_x = 0, k_z = O(1))$.**
- **The peaks arising due to the exponentially growing eigenvalues of \mathcal{A} are not as pronounced as their equivalents in $\|\mathcal{H}_\alpha\|_\infty(k_x, k_z)$.** Thus, the analysis of the variance accumulated on finite horizons indicates that in stochastically excited supercritical channel flows the most amplified input-output resonances (over long, but finite times) assume the form of streamwise vortices and streaks.

By comparing the results of this sections with the results of § 8.4, we observe a striking similarity between the frequency responses in Poiseuille flows with $R = 5700$ and $R = 10000$ (cf. Figures 8.17 and 8.18). Hence,

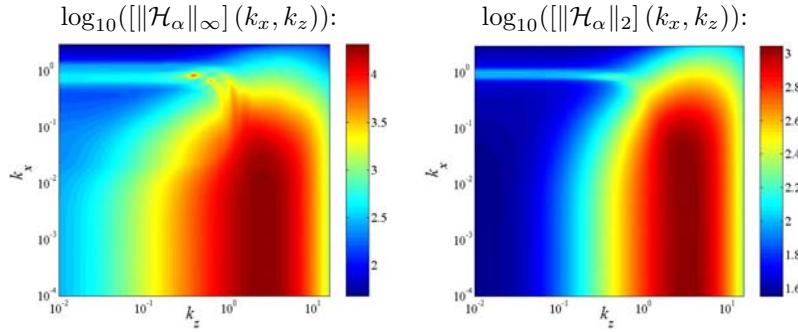


Figure 8.18: Plots of $\log_{10}(\|\mathcal{H}_\alpha\|_\infty)(k_x, k_z)$ and $\log_{10}(\|\mathcal{H}_\alpha\|_2)(k_x, k_z)$ in Poiseuille flow with $R = 10000$ and $\alpha = 0.0038$.

we conclude that subcritical and supercritical channel flows are qualitatively similar to each other provided that the latter are analyzed on finite time intervals.

The results of this section illustrate that even a small amount of external excitation in supercritical flows yields completely different flow patterns from the ones corresponding to the exponentially growing system modes when finite time phenomena are considered. In particular, we have established importance of the streamwise vortices and streaks in both subcritical and supercritical channel flows. We have also demonstrated the striking similarity between the supercritical and subcritical flows when the former are analyzed using the exponentially discounted system gains. The fact that the frequency response peaks produced by the TS waves (especially the three-dimensional ones) achieve much higher magnitudes than the corresponding peaks in subcritical channel flows at moderate Reynolds numbers (e.g. $R = 2000$) suggests that most turbulent flows probably have both instabilities and high amplification of background disturbances.

8.6 Summary

We consider the NS equations linearized around some parallel channel flow $U(y)$ (e.g., Poiseuille, Couette, and turbulent mean velocity profile), in the presence of spatially distributed and temporally varying three-dimensional body forces viewed as inputs. We carry out an input-output analysis in the frequency domain to investigate the dependence of different velocity ‘outputs’ (u, v, w) on the different body force ‘inputs’ (d_x, d_y, d_z) . We show how the relative roles of TS waves, oblique waves, and streamwise vortices and streaks can be explained as input-output resonances of the spatio-temporal frequency responses.

The effects of the inputs (d_x, d_y, d_z) on velocity fields are dependent on various parameters. We carry out a detailed study of these effects by quantifying them using system norms (also known as gains or amplifications), namely the so-called \mathcal{H}_∞ and \mathcal{H}_2 norms. We investigate the dependence of these norms on spatial frequencies, as well as the Reynolds number R . This frequency response analysis yields several conclusions, one of which is the dominance of streamwise elongated–spanwise periodic ($k_x \approx 0, k_z \approx O(1)$) and oblique ($k_x \approx O(1), k_z \approx O(1)$) effects. We also perform a detailed analysis of the effect of individual inputs on individual outputs. It turns out that the spanwise and wall-normal forces have the strongest influence on the velocity field. In particular, the impact of these forces is most powerful on the streamwise velocity component. Also, we calculate system norms as functions of spatial frequencies, and discuss the corresponding three-dimensional flow structures that are most amplified. These turn out to be typically streamwise elongated–spanwise periodic and sometimes oblique, which corresponds to structures commonly observed in experimental studies and fully nonlinear initial value simulations in channel flows.

The significance of non-modal effects in supercritical channel flows is also demonstrated. This is done by analyzing the LNS equations from an input-output point of view in the presence of exponentially discounted input and output signals. From a physical perspective this type of analysis amounts to accounting for the finite time phenomena rather than the asymptotic phenomena of infinite time limits. In particular, our results underscore the importance of the streamwise elongated flow effects not only in the subcritical channel

flows, but also in the channel flows taking place in the supercritical regimes.

It is quite compelling to argue that long-but-finite time analysis is relevant when considering linearized models. These models are not expected to be valid for infinite time in any case, as when perturbations grow, the linearized dynamics are altered. In the supercritical channel flow case, we see that the main features of the model (i.e., the modes contributing the most to perturbation energy) are very dependent on whether we take an infinite time limit or a large-but-finite time limit. The latter is arguably the more reasonable of the two, and when viewed this way, we have shown that aside from the energy of the perturbation, the spectral content of subcritical and supercritical channel flows is qualitatively very similar.

Bibliography

- [1] B. F. Farrell and P. J. Ioannou, “Stochastic forcing of the linearized Navier-Stokes equations,” *Physics of Fluids A*, vol. 5, no. 11, pp. 2600–2609, 1993.
- [2] K. M. Butler and B. F. Farrell, “Three-dimensional optimal perturbations in viscous shear flow,” *Physics of Fluids A*, vol. 4, p. 1637, 1992.
- [3] S. C. Reddy and D. S. Henningson, “Energy growth in viscous channel flows,” *J. Fluid Mech.*, vol. 252, pp. 209–238, 1993.
- [4] L. N. Trefethen, A. E. Trefethen, S. C. Reddy, and T. A. Driscoll, “Hydrodynamic stability without eigenvalues,” *Science*, vol. 261, pp. 578–584, 1993.
- [5] B. Bamieh and M. Dahleh, “Energy amplification in channel flows with stochastic excitation,” *Physics of Fluids*, vol. 13, no. 11, pp. 3258–3269, 2001.
- [6] B. F. Farrell and P. J. Ioannou, “Optimal excitation of three-dimensional perturbations in viscous constant shear flow,” *Physics of Fluids A*, vol. 5, no. 6, pp. 1390–1400, 1993.
- [7] L. Sirovich, K. S. Ball, and L. R. Keefe, “Plane waves and structures in turbulent channel flow,” *Physics of Fluids A*, vol. 2, pp. 2217–2226, 1990.
- [8] P. J. Schmid and D. S. Henningson, “A new mechanism for rapid transition involving a pair of oblique waves,” *Physics of Fluids A*, vol. 4, no. 9, pp. 1986–1989, 1992.
- [9] P. A. Elofsson and P. H. Alfredsson, “An experimental study of oblique transition in plane Poiseuille flow,” *J. Fluid Mech.*, vol. 358, pp. 177–202, 1998.
- [10] S. Berlin, M. Wiegel, and D. S. Henningson, “Numerical and experimental investigations of oblique boundary layer transition,” *J. Fluid Mech.*, vol. 393, pp. 23–57, 1999.
- [11] S. C. Reddy, P. J. Schmid, J. S. Baggett, and D. S. Henningson, “On stability of streamwise streaks and transition thresholds in plane channel flows,” *J. Fluid Mech.*, vol. 365, pp. 269–303, 1998.
- [12] S. J. Chapman, “Subcritical transition in channel flows,” *J. Fluid Mech.*, vol. 451, pp. 35–97, 2002.
- [13] M. T. Landahl, “Wave breakdown and turbulence,” *SIAM J. Appl. Math.*, vol. 28, pp. 735–756, 1975.
- [14] ——, “A note on an algebraic instability of inviscid parallel shear flows,” *J. Fluid Mech.*, vol. 98, pp. 243–251, 1980.
- [15] D. R. Carlson, S. E. Widnall, and M. F. Peeters, “A flow-visualization study of transition in plane Poiseuille flow,” *J. Fluid Mech.*, vol. 121, pp. 487–505, 1982.
- [16] F. Alavyoon, D. S. Henningson, and P. H. Alfredsson, “Turbulent spots in plane Poiseuille flow - flow visualization,” *Physics of Fluids*, vol. 29, no. 4, pp. 1328–1331, 1986.
- [17] B. G. B. Klingmann, “On transition due to three-dimensional disturbances in plane Poiseuille flow,” *J. Fluid Mech.*, vol. 240, pp. 167–195, 1992.

- [18] M. Matsubara and P. H. Alfredsson, “Disturbance growth in boundary layers subjected to free-stream turbulence,” *J. Fluid Mech.*, vol. 430, pp. 149–168, 2001.
- [19] F. W. Chambers and A. S. W. Thomas, “Turbulent spots, wave packets, and growth,” *Physics of Fluids*, vol. 26, no. 5, pp. 1160–1162, 1983.
- [20] V. A. Romanov, “Stability of plane-parallel Couette flow,” *Funct. Anal. Applics.*, vol. 7, pp. 137–146, 1973.
- [21] S. A. Orszag, “Accurate solution of the Orr-Sommerfeld equation,” *J. Fluid Mech.*, vol. 50, pp. 689–703, 1971.
- [22] R. D. Moser, J. Kim, and N. N. Mansour, “DNS of turbulent channel flow up to $Re_\tau = 590$,” *Physics of Fluids*, vol. 11, no. 4, pp. 943–945, 1999.
- [23] P. J. Schmid and D. S. Henningson, *Stability and Transition in Shear Flows*. New York: Springer-Verlag, 2001.

Chapter 9

The cross sectional 2D/3C model: analytical results

In this chapter, we study the forced LNS equations for streamwise constant three-dimensional perturbations. In this special case, the model for velocity perturbations is usually referred to as the two-dimensional, three component (2D/3C) model [1]. The motivation for analysis of this particular model is twofold. First, from numerical computations presented in Chapter 8, one observes that the streamwise constant perturbations experience utmost amplification rates. Second, this model is amenable to a thorough analysis which clarifies the relative strengths of amplification mechanisms from various forcing directions to velocity field components, as well as their dependence on the Reynolds number.

The governing dynamics of streamwise constant 3D perturbations are given by setting $k_x = 0$ in (7.18) which yields

$$\partial_t \begin{bmatrix} \psi_1 \\ \psi_2 \end{bmatrix} = \begin{bmatrix} \frac{1}{R}\mathcal{L} & 0 \\ \mathcal{C}_p & \frac{1}{R}\mathcal{S} \end{bmatrix} \begin{bmatrix} \psi_1 \\ \psi_2 \end{bmatrix} + \begin{bmatrix} 0 & \mathcal{B}_{y1} & \mathcal{B}_{z1} \\ \mathcal{B}_{x2} & 0 & 0 \end{bmatrix} \begin{bmatrix} d_x \\ d_y \\ d_z \end{bmatrix}, \quad (9.1a)$$

$$\begin{bmatrix} u \\ v \\ w \end{bmatrix} = \begin{bmatrix} 0 & \mathcal{C}_{u2} \\ \mathcal{C}_{v1} & 0 \\ \mathcal{C}_{w1} & 0 \end{bmatrix} \begin{bmatrix} \psi_1 \\ \psi_2 \end{bmatrix}, \quad (9.1b)$$

with

$$\begin{aligned} \mathcal{L} &:= \Delta^{-1}\Delta^2, & \mathcal{S} &:= \Delta, & \mathcal{C}_p &:= -ik_z U'(y), \\ \mathcal{B}_{x2} &:= ik_z, & \mathcal{B}_{y1} &:= -k_z^2\Delta^{-1}, & \mathcal{B}_{z1} &:= -ik_z\Delta^{-1}\partial_y, \\ \mathcal{C}_{u2} &:= -\frac{i}{k_z}, & \mathcal{C}_{v1} &:= I, & \mathcal{C}_{w1} &:= \frac{i}{k_z}\partial_y. \end{aligned}$$

These equations are parameterized by two important parameters: the spanwise wave number k_z , and the Reynolds number R . The wall-normal velocity and vorticity fields are in this chapter respectively denoted by $\psi_1(y, t, k_z)$ and $\psi_2(y, t, k_z)$, with the boundary conditions

$$\psi_1(\pm 1, t, k_z) = \partial_y \psi_1(\pm 1, t, k_z) = \psi_2(\pm 1, t, k_z) = 0.$$

We note that the lower-block-triangular generator in (9.1a) is exponentially stable for any finite R and any parallel flow $U(y)$. This follows from § 7.1.3, where the spectral analysis of the Reynolds number/nominal-velocity independent, normalized Squire and Orr-Sommerfeld operators \mathcal{S} and \mathcal{L} was performed. Thus, the expressions for input-output gains that we derive in this chapter are valid for all Reynolds numbers and all nominal velocity profiles $U(y)$.

Our presentation is organized as follows: in § 9.1 we determine the explicit dependence of singular values for each subsystem in (8.3) on the Reynolds number. These relationships are utilized to show how the

Hilbert–Schmidt (§ 9.2), \mathcal{H}_∞ and \mathcal{H}_2 (§ 9.3) norms scale with R for each of the components of the frequency response (8.3). Furthermore, the square additive property of the Hilbert–Schmidt and \mathcal{H}_2 norms is used to quantify:

- **Amplification from inputs in different spatial directions (d_x, d_y, d_z) to the velocity vector ϕ .**
- **Energy content of different velocity components (u, v, w).**
- **Aggregate effect of forces in all three spatial directions d to all three velocity components ϕ .**

We reinforce the numerical computations of Chapter 8 by explicit analytical derivations to demonstrate that:

- **The spanwise and wall-normal forces are much more influential on flow perturbations than the streamwise force.**
- **The impact of these forces is most powerful on the streamwise velocity.**

In § 9.4, we study the effectiveness of the near-wall inputs for streamwise constant three dimensional perturbations. We *analytically* establish that:

- **For near-wall inputs, the spanwise forcing has, by far, the biggest impact on the evolution of the velocity field components.**

These facts were recently observed in experimental and numerical studies of flow control using the Lorentz force [2–6]. In § 9.5, we employ the procedure developed in Chapter 3 to explicitly determine the Hilbert–Schmidt norms of each element in (8.3) as functions of spanwise wave-number and the appropriately scaled temporal frequency. In § 9.6, we perform a detailed analysis to show how the \mathcal{H}_2 norms of different subsystems depend on k_z for both ‘unstructured’ and ‘structured’ external excitations. This is done by employing the formula derived in § 3.2.2 to determine operator traces of the solutions of the corresponding Lyapunov equations. We close our presentation in § 9.7 with some concluding remarks.

9.1 Dependence of singular values on the Reynolds number

We first study the dependence of singular values on the Reynolds number for each of the components of the transfer function (8.3). As illustrated in Chapter 2, singular values of operators that map external excitations to the relevant physical quantities (in this case, velocity field components) can be used to quantify different measures of input amplification by system’s dynamics (e.g., Hilbert–Schmidt, \mathcal{H}_2 , and \mathcal{H}_∞ norms). We analytically establish that the singular values of frequency response operators from both spanwise and wall-normal forcing to streamwise velocity scale as R^2 , while the singular values of all other components in (8.3) scale at most as R . We also analyze the maximal singular values of each of the components in (8.3) as functions of k_z and the appropriately scaled temporal frequency.

Application of the temporal Fourier transform allows us to represent system (9.1) in terms of its block diagram shown in Figure 9.1 with $\Omega := \omega R$. We note that the same temporal scaling was previously employed by Gustavsson [7] in his undertaking to determine the transient growth of the wall-normal vorticity. From this block diagram it follows that operator $\mathcal{H}(\omega, k_z, R)$ that maps $[d_x \ d_y \ d_z]^T$ into $[u \ v \ w]^T$ can be expressed as

$$\begin{aligned} \begin{bmatrix} u \\ v \\ w \end{bmatrix} &= \begin{bmatrix} \mathcal{H}_{ux}(\omega, k_z, R) & \mathcal{H}_{uy}(\omega, k_z, R) & \mathcal{H}_{uz}(\omega, k_z, R) \\ \mathcal{H}_{vx}(\omega, k_z, R) & \mathcal{H}_{vy}(\omega, k_z, R) & \mathcal{H}_{vz}(\omega, k_z, R) \\ \mathcal{H}_{wx}(\omega, k_z, R) & \mathcal{H}_{wy}(\omega, k_z, R) & \mathcal{H}_{wz}(\omega, k_z, R) \end{bmatrix} \begin{bmatrix} d_x \\ d_y \\ d_z \end{bmatrix} \\ &:= \begin{bmatrix} R\bar{\mathcal{H}}_{ux}(\Omega, k_z) & R^2\bar{\mathcal{H}}_{uy}(\Omega, k_z) & R^2\bar{\mathcal{H}}_{uz}(\Omega, k_z) \\ 0 & R\bar{\mathcal{H}}_{vy}(\Omega, k_z) & R\bar{\mathcal{H}}_{vz}(\Omega, k_z) \\ 0 & R\bar{\mathcal{H}}_{wy}(\Omega, k_z) & R\bar{\mathcal{H}}_{wz}(\Omega, k_z) \end{bmatrix} \begin{bmatrix} d_x \\ d_y \\ d_z \end{bmatrix}, \end{aligned} \quad (9.2)$$

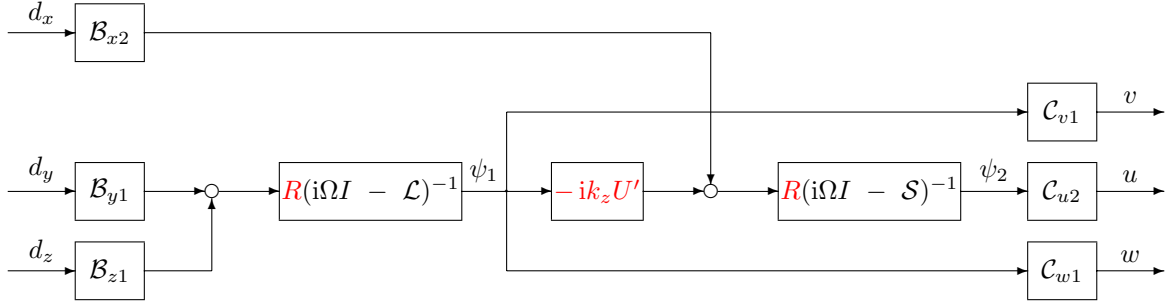


Figure 9.1: Block diagram of the streamwise constant LNS system (9.1) with $\Omega := \omega R$.

where

$$\begin{aligned}\bar{\mathcal{H}}_{ux}(\Omega, k_z) &:= \mathcal{C}_{u2}(i\Omega I - \mathcal{S})^{-1}\mathcal{B}_{x2}, \\ \bar{\mathcal{H}}_{uy}(\Omega, k_z) &:= \mathcal{C}_{u2}(i\Omega I - \mathcal{S})^{-1}\mathcal{C}_p(i\Omega I - \mathcal{L})^{-1}\mathcal{B}_{y1}, \\ \bar{\mathcal{H}}_{uz}(\Omega, k_z) &:= \mathcal{C}_{u2}(i\Omega I - \mathcal{S})^{-1}\mathcal{C}_p(i\Omega I - \mathcal{L})^{-1}\mathcal{B}_{z1}, \\ \bar{\mathcal{H}}_{rs}(\Omega, k_z) &:= \mathcal{C}_{r1}(i\Omega I - \mathcal{L})^{-1}\mathcal{B}_{s1}, \quad \{r = v, w; s = y, z\},\end{aligned}$$

represent the Reynolds number independent operators parameterized only by Ω and k_z . Thus, for the streamwise constant perturbations the frequency responses from d_y and d_z to u scale as R^2 , whereas the responses from all other inputs to other velocity outputs scale linearly with R . In particular, at $k_x = 0$ the streamwise forcing does not influence the wall-normal and the spanwise velocity components. It is noteworthy that the coupling term $\mathcal{C}_p := -ik_z U'$ is crucial for providing this R^2 -scaling. Namely, one can observe from Figure 9.1 that in the absence of shear or spanwise variations in the wall-normal velocity perturbation all components of operator $\mathcal{H}(0, k_z, \omega)$ in (8.3) are at most proportional to R . This further exemplifies the importance of the vortex stretching mechanism [8] in the wall-bounded shear flows. We remark that the numerical experiments of [9] indicated that without the coupling from v to ω_y the near-wall turbulence decays in a fully turbulent channel flow.

The following theorem follows directly from (9.2) and the fact that each operator in (9.2) is compact.

Theorem 6 *For any streamwise constant channel flow with nominal velocity $U(y)$, the singular values of operators $\mathcal{H}_{rs}(\omega, k_z, R)$ that map d_s into r , $\{r = u, v, w; s = x, y, z\}$, are given by*

$$\begin{aligned}&\begin{bmatrix} \sigma_{ux,n}(\omega, k_z, R) & \sigma_{uy,n}(\omega, k_z, R) & \sigma_{uz,n}(\omega, k_z, R) \\ \sigma_{vx,n}(\omega, k_z, R) & \sigma_{vy,n}(\omega, k_z, R) & \sigma_{vz,n}(\omega, k_z, R) \\ \sigma_{wx,n}(\omega, k_z, R) & \sigma_{wy,n}(\omega, k_z, R) & \sigma_{wz,n}(\omega, k_z, R) \end{bmatrix} \\&= \begin{bmatrix} \varsigma_{ux,n}(\Omega, k_z)R & \varsigma_{uy,n}(\Omega, k_z)R^2 & \varsigma_{uz,n}(\Omega, k_z)R^2 \\ 0 & \varsigma_{vy,n}(\Omega, k_z)R & \varsigma_{vz,n}(\Omega, k_z)R \\ 0 & \varsigma_{wy,n}(\Omega, k_z)R & \varsigma_{wz,n}(\Omega, k_z)R \end{bmatrix},\end{aligned}\tag{9.3}$$

where $\sigma_{rs,n}(\omega, k_z, R)$ and $\varsigma_{rs,n}(\Omega, k_z)$ respectively denote the n -th singular values of operators $\mathcal{H}_{rs}(\omega, k_z, R)$ and $\bar{\mathcal{H}}_{rs}(\Omega, k_z)$, with $\Omega := \omega R$ and $n \in \mathbb{N}$.

Several remarks are in order.

Remark 1 *For the streamwise constant perturbations, the singular values of the frequency response operators from the forces in the wall-normal and the spanwise directions to the streamwise velocity scale as R^2 . In all other cases they scale as R . In particular, at $k_x = 0$ the streamwise forcing does not influence the wall-normal and the spanwise velocity components. This illustrates the dominance of the streamwise velocity perturbations and the forces in the remaining two spatial directions in high Reynolds number channel flows.*

Remark 2 The expressions for the terms that multiply R on the right-hand side of (9.3) are the same for all channel flows, because these terms depend only on nominal-velocity independent operators \mathcal{L} and \mathcal{S} . On the other hand, the expressions for $\varsigma_{uy,n}(\Omega, k_z)$ and $\varsigma_{uz,n}(\Omega, k_z)$ depend on the coupling operator $\mathcal{C}_p := -ik_z U'(y)$, and therefore these singular values are nominal-velocity dependent.

Remark 3 Functions $\varsigma_{rs,n}(\Omega, k_z)$, for every $n \in \mathbb{N}$ and every $\{r = u, v, w; s = x, y, z\}$, depend only on two parameters: the spanwise wave number, and the product between temporal frequency ω and the Reynolds number R . Thus, $\sigma_{rs,n}(\omega, k_z, R)$ have the same dependence on k_z and $\Omega := \omega R$ for all R 's; only magnitudes of these singular values and regions of temporal frequencies ω where they achieve large values will change with R . As R increases, these regions of ω shrink as $1/R$. Therefore, for high Reynolds number channel flows the influence of small temporal frequencies dominates the evolution of the velocity perturbations. In view of this, one should expect preeminence of the effects with large time constants in channel flows with large R 's.

Figure 9.2 shows the dependence of the maximal singular values of operators $\bar{\mathcal{H}}_{rs}$ on Ω and k_z , for every $\{r = u, v, w; s = x, y, z\}$. These maximal singular values are determined, for any given pair (Ω, k_z) , numerically in MATLAB, and they quantify the largest amplification of deterministic disturbances for any input wall-normal shape. The nominal-flow-dependent quantities $\varsigma_{uy,1} := \varsigma_{uy,\max}$ and $\varsigma_{uz,1} := \varsigma_{uz,\max}$ are determined for Couette flow. Similar (Ω, k_z) -dependence of these two functions is observed in Poiseuille flow. Note that all quantities in Figure 9.2 achieve their respective maxima at $\Omega = 0$.

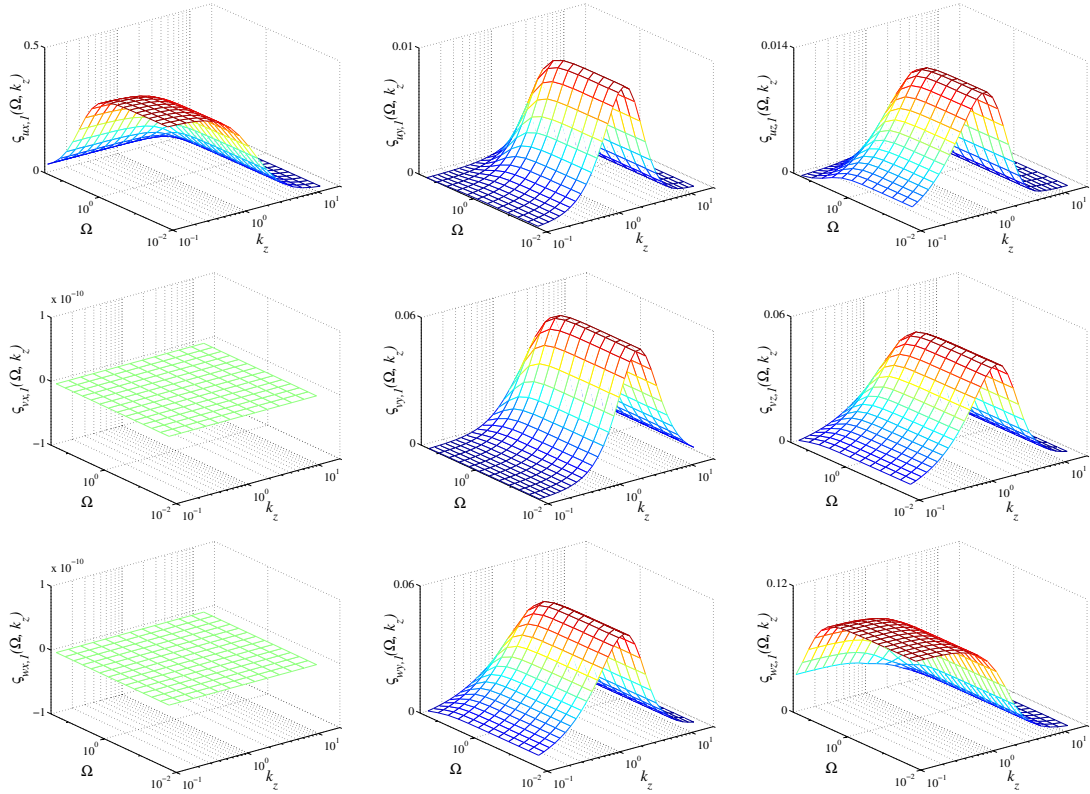


Figure 9.2: Plots of the maximal singular values of operators $\bar{\mathcal{H}}_{rs}(\Omega, k_z)$. Nominal-flow-dependent quantities $\varsigma_{uy,1}(\Omega, k_z)$ and $\varsigma_{uz,1}(\Omega, k_z)$ are determined for Couette flow.

Theorem 6 can be utilized to derive several important results: in § 9.2, and § 9.3, we respectively study the Reynolds number dependence of the Hilbert–Schmidt, \mathcal{H}_∞ and \mathcal{H}_2 norms for each of the components of the frequency response (8.3).

9.2 Dependence of Hilbert–Schmidt norms on the Reynolds number

The following theorem follows directly from Theorem 6 by exploiting the fact that the Hilbert–Schmidt norm (i.e., the power spectral density) of a certain operator can be obtained as a sum of squares of its singular values (cf. § 2.2.2). For example, the Hilbert–Schmidt norm of operator $\mathcal{H}_{ux}(\omega, k_z, R)$ that maps d_x into u is determined by

$$\begin{aligned}\|\mathcal{H}_{ux}(\omega, k_z, R)\|_{HS}^2 &= \sum_{n=1}^{\infty} \sigma_{ux,n}^2(\omega, k_z, R) = R^2 \sum_{n=1}^{\infty} \varsigma_{ux,n}^2(\Omega, k_z) \\ &= R^2 \|\bar{\mathcal{H}}_{ux}(\Omega, k_z)\|_{HS}^2 =: R^2 l_{ux}(\Omega, k_z).\end{aligned}$$

Similar exercise can be repeated to determine the power spectral densities of all other components of operator \mathcal{H} in (8.3). We conclude that the Hilbert–Schmidt norms of operators from both d_y and d_z to u scale as R^4 , while the Hilbert–Schmidt norms of all other operators in (8.3) scale as R^2 .

Theorem 7 *For any streamwise constant channel flow with nominal velocity $U(y)$, the Hilbert–Schmidt norms of operators $\mathcal{H}_{rs}(\omega, k_z, R)$ that map d_s into r , $\{r = u, v, w; s = x, y, z\}$, are given by*

$$\begin{aligned}&\left[\begin{array}{ccc} \|\mathcal{H}_{ux}(\omega, k_z, R)\|_{HS}^2 & \|\mathcal{H}_{uy}(\omega, k_z, R)\|_{HS}^2 & \|\mathcal{H}_{uz}(\omega, k_z, R)\|_{HS}^2 \\ \|\mathcal{H}_{vx}(\omega, k_z, R)\|_{HS}^2 & \|\mathcal{H}_{vy}(\omega, k_z, R)\|_{HS}^2 & \|\mathcal{H}_{vz}(\omega, k_z, R)\|_{HS}^2 \\ \|\mathcal{H}_{wx}(\omega, k_z, R)\|_{HS}^2 & \|\mathcal{H}_{wy}(\omega, k_z, R)\|_{HS}^2 & \|\mathcal{H}_{wz}(\omega, k_z, R)\|_{HS}^2 \end{array} \right] \\ &= \left[\begin{array}{ccc} l_{ux}(\Omega, k_z)R^2 & m_{uy}(\Omega, k_z)R^4 & m_{uz}(\Omega, k_z)R^4 \\ 0 & l_{vy}(\Omega, k_z)R^2 & l_{vz}(\Omega, k_z)R^2 \\ 0 & l_{wy}(\Omega, k_z)R^2 & l_{wz}(\Omega, k_z)R^2 \end{array} \right],\end{aligned}\tag{9.4}$$

where the l and m functions are independent of R , and $\Omega := \omega R$.

Figure 9.3 illustrates the plots of $\|\bar{\mathcal{H}}_{rs}(\Omega, k_z)\|_{HS}^2$, for every $\{r = u, v, w; s = x, y, z\}$. These computations are performed in MATLAB for any given pair (Ω, k_z) using the procedure developed in Chapter 3. Section 9.5 describes how this procedure can be employed to determine the Hilbert–Schmidt norms of the Reynolds number independent operators $\bar{\mathcal{H}}_{rs}(\Omega, k_z)$. The nominal-flow-dependent quantities m_{uy} and m_{uz} are determined for Couette flow.

Based on the discussion presented in Remark 3, and the importance of low temporal frequency effects (all quantities in Figure 9.3 peak at $\Omega = 0$), we also consider the LNS equations in the steady-state. Figure 9.4 shows the dependence of the l and m functions in Theorem 7 on k_z at $\omega = 0$. The explicit analytical formulae for these quantities are determined using expression (3.16), and they are given in § 9.5.2. The underlying matrix exponentials are evaluated symbolically in MATHEMATICA.

The following corollary of Theorem 7 is obtained by exploiting the definition of operators $\mathcal{H}_s(\omega, k_z, R)$ that map d_s into $\phi := [u \ v \ w]^T$, $\{s = x, y, z\}$, and linearity of the trace(\cdot) operator. For example, the Hilbert–Schmidt norm of operator $\mathcal{H}_y(\omega, k_z, R)$ is determined by

$$\begin{aligned}\|\mathcal{H}_y(\omega, k_z, R)\|_{HS}^2 &= \text{trace}(\mathcal{H}_y^* \mathcal{H}_y) = \text{trace}(\mathcal{H}_{uy}^* \mathcal{H}_{uy}) + \text{trace}(\mathcal{H}_{vy}^* \mathcal{H}_{vy}) + \text{trace}(\mathcal{H}_{wy}^* \mathcal{H}_{wy}) \\ &= \|\mathcal{H}_{uy}(\omega, k_z, R)\|_{HS}^2 + \|\mathcal{H}_{vy}(\omega, k_z, R)\|_{HS}^2 + \|\mathcal{H}_{wy}(\omega, k_z, R)\|_{HS}^2 \\ &= R^4 \|\bar{\mathcal{H}}_{uy}(\Omega, k_z)\|_{HS}^2 + R^2 \|\bar{\mathcal{H}}_{vy}(\Omega, k_z)\|_{HS}^2 + R^2 \|\bar{\mathcal{H}}_{wy}(\Omega, k_z)\|_{HS}^2 \\ &= R^4 m_{uy}(\Omega, k_z) + R^2 (l_{vy}(\Omega, k_z) + l_{wy}(\Omega, k_z)) \\ &=: R^4 m_y(\Omega, k_z) + R^2 l_y(\Omega, k_z).\end{aligned}$$

Similar procedure can be used to determine the Hilbert–Schmidt norms of all other components of operator \mathcal{H} in (8.4).

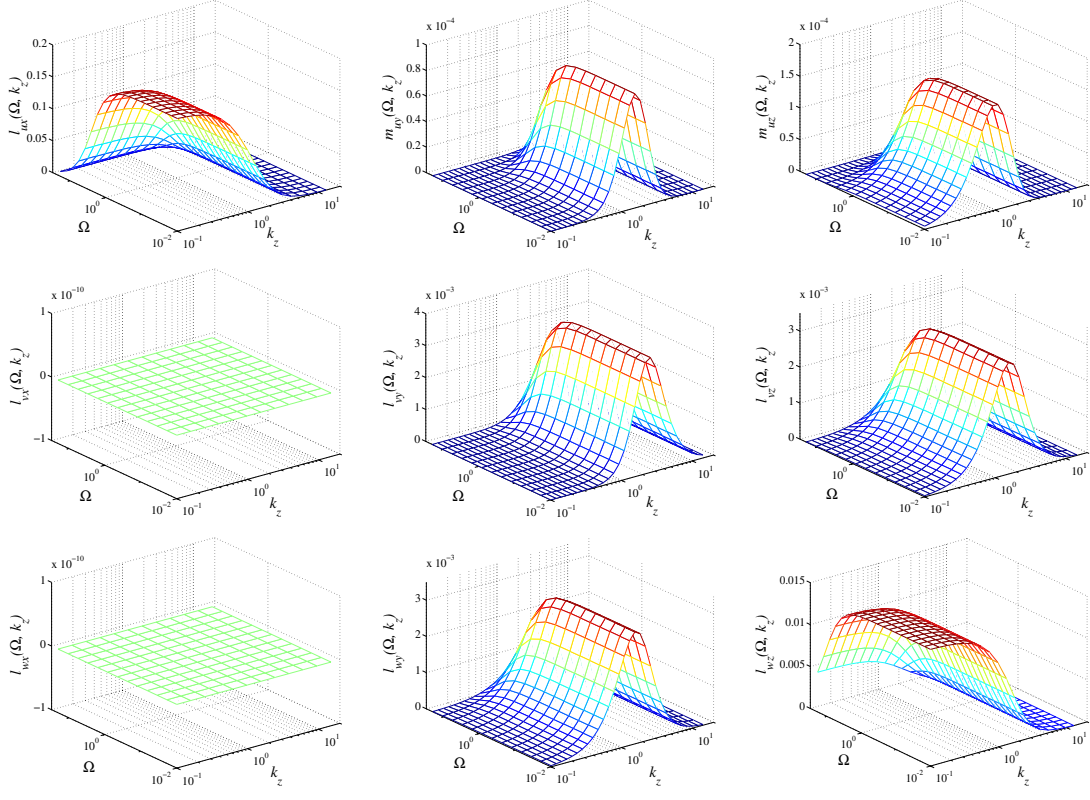


Figure 9.3: Plots of the l and m functions in Theorem 7. Nominal-flow-dependent quantities $m_{uy}(\Omega, k_z)$ and $m_{uz}(\Omega, k_z)$ are determined for Couette flow.

Corollary 8 For any streamwise constant channel flow with nominal velocity $U(y)$, the Hilbert–Schmidt norms of operators $\mathcal{H}_s(\omega, k_z, R)$ that map d_s into $\phi := [u \ v \ w]^T$, $\{s = x, y, z\}$, are given by

$$\begin{aligned} \|\mathcal{H}_x(\omega, k_z, R)\|_{HS}^2 &= l_x(\Omega, k_z)R^2, \\ \|\mathcal{H}_y(\omega, k_z, R)\|_{HS}^2 &= l_y(\Omega, k_z)R^2 + m_y(\Omega, k_z)R^4, \\ \|\mathcal{H}_z(\omega, k_z, R)\|_{HS}^2 &= l_z(\Omega, k_z)R^2 + m_z(\Omega, k_z)R^4, \end{aligned}$$

where

$$\begin{aligned} l_x &:= l_{ux}, & l_y &:= l_{vy} + l_{wy}, & l_z &:= l_{vz} + l_{wz}, \\ m_y &:= m_{uy}, & m_z &:= m_{uz}. \end{aligned}$$

Figure 9.5 shows how the l and m functions in Corollary 8 change with Ω and k_z . Nominal-flow-dependent quantities $m_y(\Omega, k_z)$ and $m_z(\Omega, k_z)$ are determined for Couette flow.

The following corollary of Theorem 7 is obtained by exploiting the definition of operators $\mathcal{H}_r(\omega, k_z, R)$ that map $\mathbf{d} := [d_x \ d_y \ d_z]^T$ into r , $\{r = u, v, w\}$, and linearity of the trace(\cdot) operator. For example,

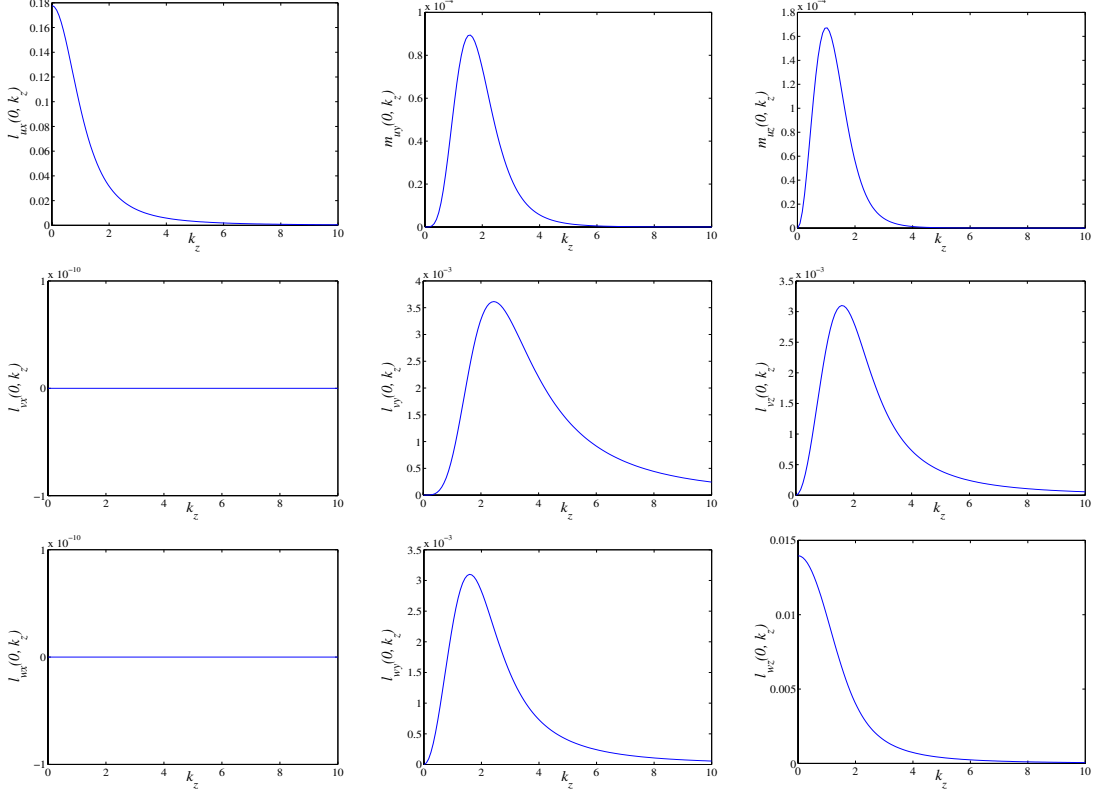


Figure 9.4: Plots of the l and m functions in Theorem 7 at $\Omega = 0$. Nominal-flow-dependent quantities $m_{uy}(0, k_z)$ and $m_{uz}(0, k_z)$ are determined for Couette flow.

$\|\mathcal{H}_u(\omega, k_z, R)\|_{HS}^2$ is determined by

$$\begin{aligned}
\|\mathcal{H}_u(\omega, k_z, R)\|_{HS}^2 &= \text{trace}(\mathcal{H}_u \mathcal{H}_u^*) = \text{trace}(\mathcal{H}_{ux} \mathcal{H}_{ux}^*) + \text{trace}(\mathcal{H}_{uy} \mathcal{H}_{uy}^*) + \text{trace}(\mathcal{H}_{uz} \mathcal{H}_{uz}^*) \\
&= \|\mathcal{H}_{ux}(\omega, k_z, R)\|_{HS}^2 + \|\mathcal{H}_{uy}(\omega, k_z, R)\|_{HS}^2 + \|\mathcal{H}_{uz}(\omega, k_z, R)\|_{HS}^2 \\
&= R^2 \|\bar{\mathcal{H}}_{ux}(\Omega, k_z)\|_{HS}^2 + R^4 \|\bar{\mathcal{H}}_{uy}(\Omega, k_z)\|_{HS}^2 + R^4 \|\bar{\mathcal{H}}_{uz}(\Omega, k_z)\|_{HS}^2 \\
&= R^2 l_{ux}(\Omega, k_z) + R^4 (m_{uy}(\Omega, k_z) + m_{uz}(\Omega, k_z)) \\
&=: R^2 l_u(\Omega, k_z) + R^4 m_u(\Omega, k_z).
\end{aligned}$$

The Hilbert–Schmidt norms of all other components of operator \mathcal{H} in (8.5) can be determined in a similar fashion.

Corollary 9 For any streamwise constant channel flow with nominal velocity $U(y)$, the Hilbert–Schmidt norms of operators $\mathcal{H}_r(\omega, k_z, R)$ that map $\mathbf{d} := [d_x \ d_y \ d_z]^T$ into r , $\{r = u, v, w\}$, are given by

$$\begin{aligned}
\|\mathcal{H}_u(\omega, k_z, R)\|_{HS}^2 &= l_u(\Omega, k_z)R^2 + m_u(\Omega, k_z)R^4, \\
\|\mathcal{H}_v(\omega, k_z, R)\|_{HS}^2 &= l_v(\Omega, k_z)R^2, \\
\|\mathcal{H}_w(\omega, k_z, R)\|_{HS}^2 &= l_w(\Omega, k_z)R^2,
\end{aligned}$$

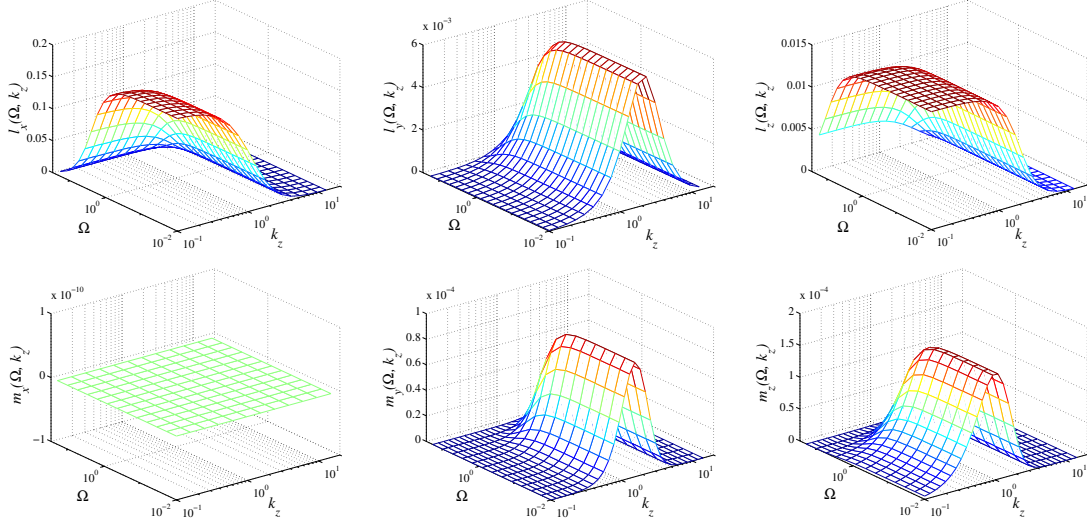


Figure 9.5: Plots of the l and m functions in Corollary 8. Nominal-flow-dependent quantities $m_y(\Omega, k_z)$ and $m_z(\Omega, k_z)$ are determined for Couette flow.

where

$$\begin{aligned} l_u &:= l_{ux}, & m_u &:= m_{uy} + m_{uz}, \\ l_v &:= l_{vy} + l_{vz}, & l_w &:= l_{wy} + l_{wz}. \end{aligned}$$

Figure 9.6 illustrates the (Ω, k_z) -parameterized plots of the l and m functions in Corollary 9. Function $m_u(\Omega, k_z)$ is determined for Couette flow.

The following corollary of Theorem 7 quantifies the aggregate effect of forces in all three spatial directions \mathbf{d} to all three velocity components ϕ . It is obtained by summing all elements in (9.4) and exploiting the square additive property of the Hilbert–Schmidt norm.

Corollary 10 *For any streamwise constant channel flow with nominal velocity $U(y)$, the Hilbert–Schmidt norm of operator $\mathcal{H}(\omega, k_z, R)$ that maps $\mathbf{d} := [d_x \ d_y \ d_z]^T$ into $\phi := [u \ v \ w]^T$, is given by*

$$\|\mathcal{H}(\omega, k_z, R)\|_{HS}^2 = l(\Omega, k_z)R^2 + m(\Omega, k_z)R^4, \quad (9.5)$$

where

$$\begin{aligned} l &:= l_{ux} + l_{vy} + l_{vz} + l_{wy} + l_{wz} = l_x + l_y + l_z = l_u + l_v + l_w, \\ m &:= m_{uy} + m_{uz} = m_y + m_z = m_u. \end{aligned}$$

Plots of $l(\Omega, k_z)$ and $m(\Omega, k_z)$ are given in Figure 9.7. Nominal-velocity-dependent quantity $m(\Omega, k_z)$ in Corollary 10 is determined for Couette flow. Both these functions achieve their largest values at $\Omega = 0$. Furthermore, $l(\Omega, k_z)$ peaks at $k_z = 0$, whereas $m(\Omega, k_z)$ peaks at $k_z = O(1)$. We also note that

$$\frac{\sup_{\Omega, k_z} m(\Omega, k_z)}{\sup_{\Omega, k_z} l(\Omega, k_z)} \approx 1.21 \times 10^{-3},$$

which implies that the peak values of the second term on the right-hand side of (9.5) are larger than the peak values of the first term on the right-hand side of (9.5) so long as (approximately) $R > 28.73$. For example, at $R = 1000$, the former quantity ($R^4 \sup_{\Omega, k_z} m(\Omega, k_z)$) dominates the latter quantity ($R^2 \sup_{\Omega, k_z} l(\Omega, k_z)$) by more than three orders of magnitude.

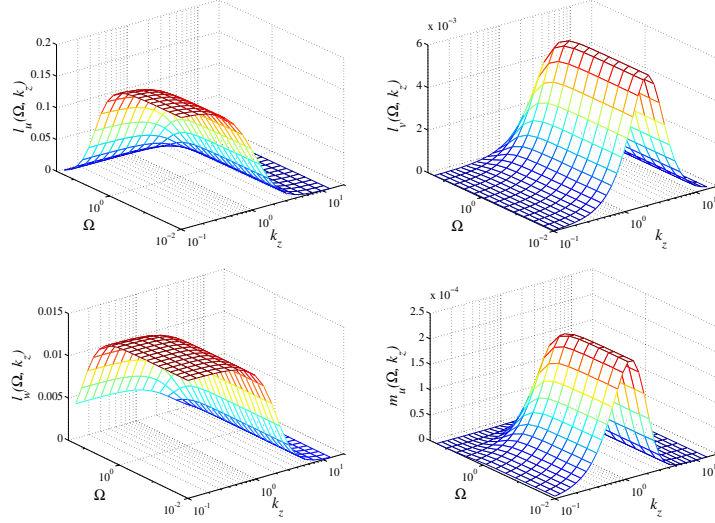


Figure 9.6: Plots of the l and m functions in Corollary 9. Nominal-flow-dependent quantity $m_u(\Omega, k_z)$ is determined for Couette flow.

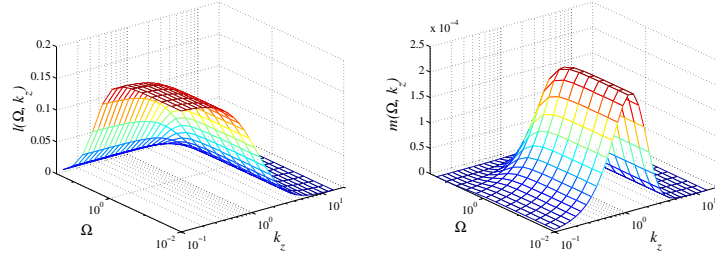


Figure 9.7: Plots of the l and m functions in Corollary 10. Nominal-flow-dependent quantity $m(\Omega, k_z)$ is determined for Couette flow.

9.3 Dependence of \mathcal{H}_∞ and \mathcal{H}_2 norms on the Reynolds number

In this section, we exploit results of § 9.1 and § 9.2 to establish the Reynolds number dependence of \mathcal{H}_∞ and \mathcal{H}_2 norms for different components of frequency response operator (8.3).

\mathcal{H}_∞ norms

We show how the \mathcal{H}_∞ norms of all nine operators in (8.3) scale with the Reynolds number. Also, we graphically illustrate the dependence of these norms on the spanwise wave-number.

The following theorem follows directly from Theorem 6 and the definition of the \mathcal{H}_∞ norm (cf. § 2.2.2). For example, the \mathcal{H}_∞ norm of operator $\mathcal{H}_{uz}(\omega, k_z, R)$ from d_z to u is determined by

$$\begin{aligned} [\|\mathcal{H}_{uz}\|_\infty](k_z) &= \sup_{\omega} \sigma_{uz,\max}(\omega, k_z, R) = R^2 \sup_{\Omega} \varsigma_{uz,\max}(\Omega, k_z) \\ &= R^2 [\|\tilde{\mathcal{H}}_{uz}\|_\infty](k_z) =: R^2 h_{uz}(k_z). \end{aligned}$$

The \mathcal{H}_∞ norms of all other components of operator \mathcal{H} in (8.3) can be determined in a similar manner. We conclude that the \mathcal{H}_∞ norms of operators from both d_y and d_z to u scale as R^2 , while the \mathcal{H}_∞ norms of all other operators in (8.3) scale as R . This is yet another way to establish the effectiveness of the wall-normal

Table 9.1: Dependence of $\sup_{k_z} [\|\mathcal{H}_{uy}\|_\infty] (k_z)$ and $\sup_{k_z} [\|\mathcal{H}_{uz}\|_\infty] (k_z)$ on R in Poiseuille and Couette flows. The values of k_z at which global maxima take place are also shown.

Flow	$\sup_{k_z} [\ \mathcal{H}_{uy}\ _\infty] (k_z)$	k_z
Poiseuille	$(R/20.29)^2$	1.95
Couette	$(R/10.29)^2$	1.55
Flow	$\sup_{k_z} [\ \mathcal{H}_{uz}\ _\infty] (k_z)$	k_z
Poiseuille	$(R/19.49)^2$	1.20
Couette	$(R/8.81)^2$	1

and spanwise forces, and the largest energy content of the streamwise velocity perturbations.

Theorem 11 *For any streamwise constant channel flow with nominal velocity $U(y)$, the \mathcal{H}_∞ norms of operators $\mathcal{H}_{rs}(\omega, k_z, R)$ that map d_s into r , $\{r = u, v, w; s = x, y, z\}$, are given by*

$$\begin{aligned} & \begin{bmatrix} [\|\mathcal{H}_{ux}\|_\infty] (k_z) & [\|\mathcal{H}_{uy}\|_\infty] (k_z) & [\|\mathcal{H}_{uz}\|_\infty] (k_z) \\ [\|\mathcal{H}_{vx}\|_\infty] (k_z) & [\|\mathcal{H}_{vy}\|_\infty] (k_z) & [\|\mathcal{H}_{vz}\|_\infty] (k_z) \\ [\|\mathcal{H}_{wx}\|_\infty] (k_z) & [\|\mathcal{H}_{wy}\|_\infty] (k_z) & [\|\mathcal{H}_{wz}\|_\infty] (k_z) \end{bmatrix} \\ &= \begin{bmatrix} h_{ux}(k_z)R & h_{uy}(k_z)R^2 & h_{uz}(k_z)R^2 \\ 0 & h_{vy}(k_z)R & h_{vz}(k_z)R \\ 0 & h_{wy}(k_z)R & h_{wz}(k_z)R \end{bmatrix}, \end{aligned}$$

where the h functions are independent of R .

We note that Kreiss, Lundbladh & Henningson showed in [10] that the \mathcal{H}_∞ norm of the resolvent $(sI - \mathcal{A})^{-1}$ of the streamwise constant LNS system (9.1) can be upper bounded by a term that grows proportionally to R^2 in the limit as $R \rightarrow \infty$. On the other hand, by considering operators from the individual forcing components to the individual velocity components, we explicitly established how the \mathcal{H}_∞ norms of these operators at $k_x = 0$ scale with the Reynolds number. This once again displays advantages of componentwise analysis over the analysis that only accounts for the aggregate effects.

Figure 9.8 graphically illustrates the k_z -dependence of functions h_{rs} , $\{r = u, v, w; s = x, y, z\}$, in Theorem 11. Clearly, the nominal-velocity dependent quantities h_{uy} and h_{uz} play the most important roles in high Reynolds number flows. Table 9.1 shows how $\sup_{k_z} [\|\mathcal{H}_{uy}\|_\infty] (k_z)$ and $\sup_{k_z} [\|\mathcal{H}_{uz}\|_\infty] (k_z)$ scale with R in both Poiseuille and Couette flows. The values of k_z at which global maxima occur are also shown.

\mathcal{H}_2 norms

We study the frequency responses (as a function of k_z) of each of the components of the transfer function (8.3). We do this using the \mathcal{H}_2 norm, that is

$$[\|\mathcal{H}_{rs}\|_2^2] (k_z) := \frac{1}{2\pi} \int_{-\infty}^{\infty} \|\mathcal{H}_{rs}(k_z, \omega)\|_{HS}^2 d\omega, \quad \text{for } r = u, v, w, \text{ and } s = x, y, z.$$

We then investigate the dependence of each of the subsystems on the Reynolds number. We conclude that amplification from both spanwise and wall-normal forcing to streamwise velocity is $O(R^3)$, while amplification for all other components is $O(R)$.

We now state the main result that follows directly from Theorem 7 using the definition of the \mathcal{H}_2 norm.

Theorem 12 *For any streamwise constant channel flow with nominal velocity $U(y)$, the \mathcal{H}_2 norms of oper-*

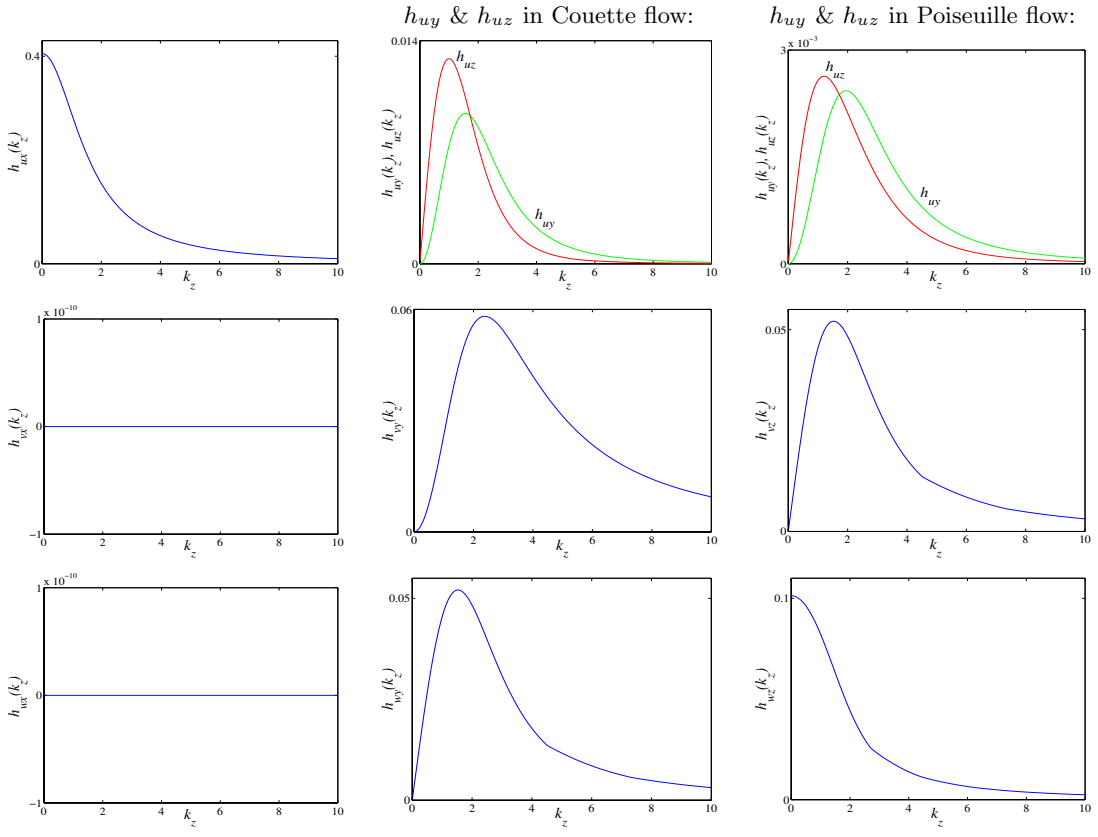


Figure 9.8: Plots of functions $h_{rs}(k_z)$, $\{r = u, v, w; s = x, y, z\}$, in Theorem 11.

ators $\mathcal{H}_{rs}(\omega, k_z, R)$ that map d_s into r , $\{r = u, v, w; s = x, y, z\}$, are given by

$$\begin{aligned}
 & \begin{bmatrix} [\|\mathcal{H}_{ux}\|_2^2](k_z) & [\|\mathcal{H}_{uy}\|_2^2](k_z) & [\|\mathcal{H}_{uz}\|_2^2](k_z) \\ [\|\mathcal{H}_{vx}\|_2^2](k_z) & [\|\mathcal{H}_{vy}\|_2^2](k_z) & [\|\mathcal{H}_{vz}\|_2^2](k_z) \\ [\|\mathcal{H}_{wx}\|_2^2](k_z) & [\|\mathcal{H}_{wy}\|_2^2](k_z) & [\|\mathcal{H}_{wz}\|_2^2](k_z) \end{bmatrix} \\
 &= \begin{bmatrix} f_{ux}(k_z)R & g_{uy}(k_z)R^3 & g_{uz}(k_z)R^3 \\ 0 & f_{vy}(k_z)R & f_{vz}(k_z)R \\ 0 & f_{wy}(k_z)R & f_{wz}(k_z)R \end{bmatrix}, \tag{9.6}
 \end{aligned}$$

where the f and g functions are independent of R .

For example, $[\|\mathcal{H}_{uy}\|_2^2](k_z)$ is determined by

$$\begin{aligned}
 [\|\mathcal{H}_{uy}\|_2^2](k_z) &:= \frac{1}{2\pi} \int_{-\infty}^{\infty} \|\mathcal{H}_{uy}(\omega, k_z, R)\|_{HS}^2 d\omega \\
 &= \frac{R^4}{2\pi} \int_{-\infty}^{\infty} \|\bar{\mathcal{H}}_{uy}(\Omega, k_z)\|_{HS}^2 d\omega \\
 &= \frac{R^3}{2\pi} \int_{-\infty}^{\infty} \|\bar{\mathcal{H}}_{uy}(\Omega, k_z)\|_{HS}^2 d\Omega \\
 &= R^3 [\|\bar{\mathcal{H}}_{uy}\|_2^2](k_z) =: R^3 g_{uy}(k_z).
 \end{aligned}$$

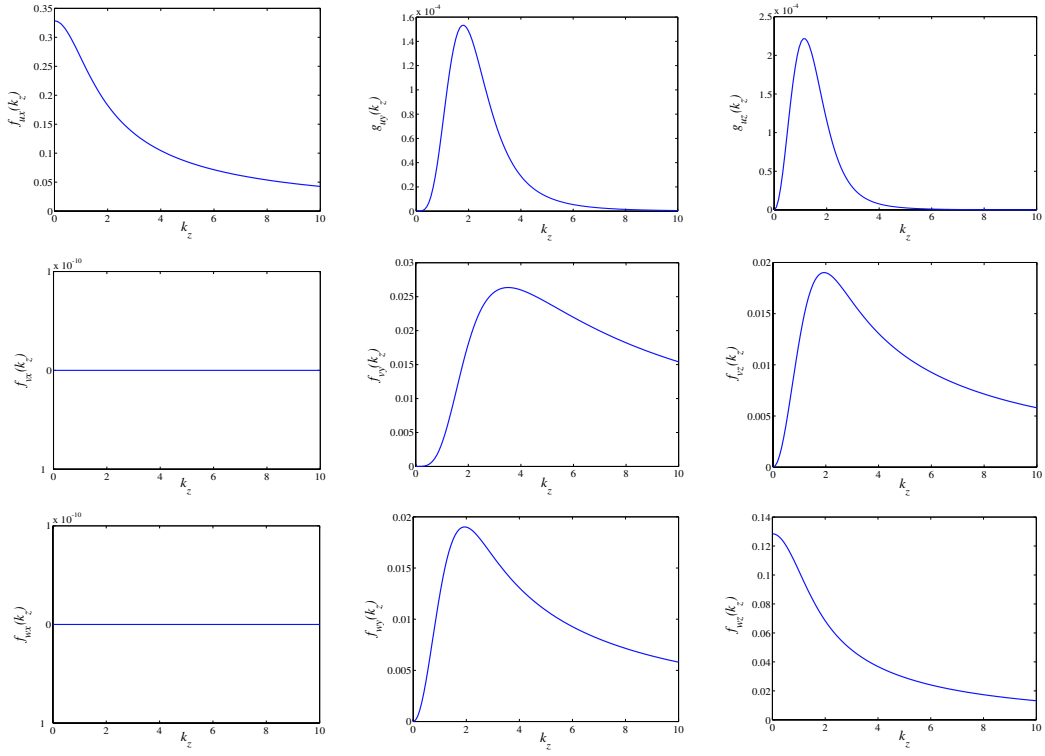


Figure 9.9: Plots of $f_{rs}(k_z)$, $\{r = u, v, w; s = x, y, z\}$, $g_{uy}(k_z)$, and $g_{uz}(k_z)$. Functions $g_{uy}(k_z)$ and $g_{uz}(k_z)$ are determined for Couette flow.

Similar procedure can be used to determine the \mathcal{H}_2 norms of all other components of operator \mathcal{H} in (8.3), which proves Theorem 12. Corollaries 13, 14, and 15 follow from Theorem 12 using the square-additivity of the \mathcal{H}_2 norm.

The energy amplification of streamwise constant perturbations scales as R^3 from the forces in the wall-normal and the spanwise directions to the streamwise velocity. In all other cases it scales as R . In particular, at $k_x = 0$ the streamwise direction forcing does not influence the wall-normal and the spanwise velocity components. This further illustrates the dominance of the streamwise velocity perturbations and the forces in the remaining two spatial directions for high Reynolds number channel flows.

The expressions for the terms that multiply R in (9.6) are the same for all channel flows. On the other hand, the expressions for g_{uy} and g_{uz} depend on the coupling operator (vortex stretching term from the NS equations) $\mathcal{C}_p := -ik_z U'(y)$, and therefore these terms are nominal-velocity dependent. Whenever either there is no mean shear or spanwise variations in the velocity perturbations, the vortex tilting mechanism is absent and the largest amplification that can be achieved is proportional to the Reynolds number.

The following corollary of Theorem 12 is obtained by summing the rows in (9.6) and exploiting the square additive property of the \mathcal{H}_2 norm.

Corollary 13 *For any streamwise constant channel flow with nominal velocity $U(y)$, the \mathcal{H}_2 norms of operators $\mathcal{H}_s(\omega, k_z, R)$ that map d_s into $\phi := [u \ v \ w]^T$, $\{s = x, y, z\}$, are given by*

$$\begin{aligned} [\|\mathcal{H}_x\|_2^2](k_z) &= f_x(k_z)R, \\ [\|\mathcal{H}_y\|_2^2](k_z) &= f_y(k_z)R + g_y(k_z)R^3, \\ [\|\mathcal{H}_z\|_2^2](k_z) &= f_z(k_z)R + g_z(k_z)R^3, \end{aligned} \tag{9.7}$$

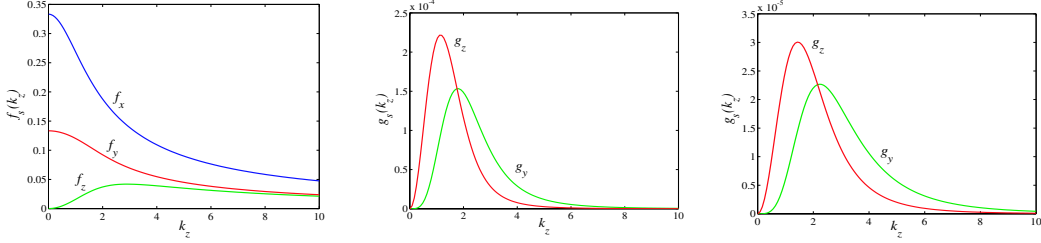


Figure 9.10: The k_z -dependence of f_x , f_y , f_z , g_y , and g_z . Expressions for f_x , f_y , and f_z are the same for all channel flows, as demonstrated in § 9.6.2. The terms responsible for the $O(R^3)$ energy amplification are shown in the middle (Couette flow) and right (Poiseuille flow) plots.

where

$$\begin{aligned} f_x &:= f_{ux}, \quad f_y := f_{vy} + f_{wy}, \quad f_z := f_{vz} + f_{wz}, \\ g_y &:= g_{uy}, \quad g_z := g_{uz}. \end{aligned}$$

Figure 9.10 graphically illustrates the k_z -dependence of functions f_x , f_y , f_z , g_y , and g_z . Expressions for f_x , f_y , and f_z are the same for all channel flows, as shown in § 9.6.2 where we derive the analytical formulae for these quantities. On the other hand, both g_y and g_z depend on the nominal velocity. In § 9.6.2, we determine the analytical expressions for these two quantities in Couette flow by doing the spectral decompositions of the Orr-Sommerfeld and Squire operators. These expressions are given in terms of rapidly convergent series and they are shown in the middle plot of Figure 9.10. The numerically computed dependence of g_y and g_z on k_z in Poiseuille flow is given in the right plot of the same figure.

Therefore, as already indicated by the numerical computations of Chapter 8, the forces in the spanwise and wall-normal directions have the strongest influence on the velocity field. We confirmed this observation by analytical derivations summarized in Corollary 13 for the streamwise constant perturbations showing that the square of the \mathcal{H}_2 norm from d_z and d_y to velocity vector ϕ scales as R^3 . On the other hand, at $k_x = 0$, the square of the \mathcal{H}_2 norm from d_x to ϕ scales as R .

The following corollary of Theorem 12 is obtained by summing the columns in (9.6) and exploiting the square additive property of the \mathcal{H}_2 norm.

Corollary 14 *For any streamwise constant channel flow with nominal velocity $U(y)$, the \mathcal{H}_2 norms of operators $\mathcal{H}_r(\omega, k_z, R)$ that map $\mathbf{d} := [d_x \ d_y \ d_z]^T$ into r , $\{r = u, v, w\}$, are given by*

$$\begin{aligned} [\|\mathcal{H}_u\|_2^2](k_z) &= f_u(k_z)R + g_u(k_z)R^3, \\ [\|\mathcal{H}_v\|_2^2](k_z) &= f_v(k_z)R, \\ [\|\mathcal{H}_w\|_2^2](k_z) &= f_w(k_z)R, \end{aligned} \tag{9.8}$$

where

$$\begin{aligned} f_u &:= f_{ux}, & g_u &:= g_{uy} + g_{uz}, \\ f_v &:= f_{vy} + f_{vz}, & f_w &:= f_{wy} + f_{wz}. \end{aligned}$$

Figure 9.11 graphically illustrates the k_z -dependence of functions f_u , f_v , f_w , and g_u . Expressions for f_u , f_v , and f_w are the same for all channel flows, as shown in § 9.6.2 where we derive the analytical formulae for these quantities. On the other hand, g_u depends on the underlying mean velocity. In § 9.6.2, we derive the analytical dependence of g_u on k_z for Couette flow. The right plot in Figure 9.11 shows the numerically computed k_z -dependence of g_u in Poiseuille flow.

Thus, the impact of the external excitations is most powerful on the streamwise velocity component. We confirmed this observation by both numerical computations of Chapter 8 and analytical derivations

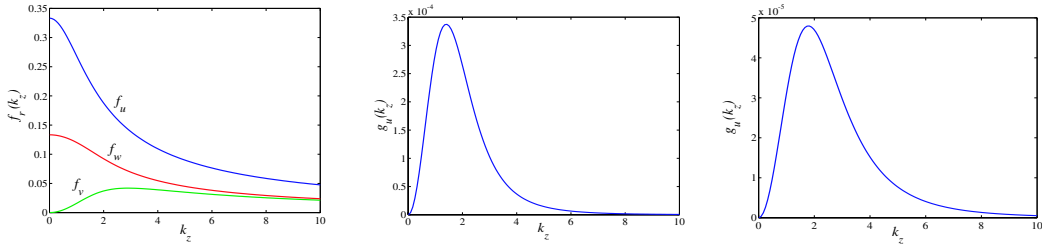


Figure 9.11: The k_z -dependence of f_u , f_v , f_w , and g_u . Expressions for f_u , f_v , and f_w are the same for all channel flows, as demonstrated in § 9.6.2. The terms responsible for the $O(R^3)$ energy amplification are shown in the middle (Couette flow) and right (Poiseuille flow) plots.

summarized in Corollary 14 for the streamwise constant perturbations showing that the square of the \mathcal{H}_2 norm from \mathbf{d} to u scales as R^3 . On the other hand, at $k_x = 0$, the square of the \mathcal{H}_2 norm from \mathbf{d} to v and w scales as R .

It is worth mentioning that Theorem 1 of [11] follows from Theorem 12 of this section. Namely, by summing all elements in (9.6) and using the square-additivity of the \mathcal{H}_2 norm the aggregate effect of all forces to all velocity components is readily obtained. For completeness, we state the main result of [11] as the following corollary.

Corollary 15 *For any streamwise constant channel flow with nominal velocity $U(y)$, the \mathcal{H}_2 norm of operator $\mathcal{H}(\omega, k_z, R)$ that maps $\mathbf{d} := [d_x \ d_y \ d_z]^T$ into $\phi := [u \ v \ w]^T$, is given by*

$$[\|\mathcal{H}\|_2^2](k_z) = f(k_z)R + g(k_z)R^3,$$

where

$$\begin{aligned} f &:= f_{ux} + f_{vy} + f_{vz} + f_{wy} + f_{wz} = f_x + f_y + f_z = f_u + f_v + f_w, \\ g &:= g_{uy} + g_{uz} = g_y + g_z = g_u. \end{aligned}$$

As shown in § 9.4, the dependence of the variance amplification on the Reynolds number at $k_x = 0$ has the same form for the ‘unstructured’ and ‘structured’ external excitations. However, the expressions for functions f and g in Theorem 12 and Corollaries 13, 14, and 15 are different in these two cases.

In § 9.4, we study the capability of the streamwise constant near-wall input components.

9.4 Energy amplification of near-wall external excitations

In this section, we study system (7.20) in the presence of streamwise constant three-dimensional perturbations. By setting $k_x = 0$ in (7.20) we obtain

$$\partial_t \begin{bmatrix} \psi_1 \\ \psi_2 \end{bmatrix} = \begin{bmatrix} \frac{1}{R} \mathcal{L} & 0 \\ \mathcal{C}_p & \frac{1}{R} \mathcal{S} \end{bmatrix} \begin{bmatrix} \psi_1 \\ \psi_2 \end{bmatrix} + \begin{bmatrix} 0 & \mathcal{B}_{y01} & \mathcal{B}_{z01} \\ \mathcal{B}_{x02} & 0 & 0 \end{bmatrix} \begin{bmatrix} d_{x0} \\ d_{y0} \\ d_{z0} \end{bmatrix}, \quad (9.9a)$$

$$\begin{bmatrix} u \\ v \\ w \end{bmatrix} = \begin{bmatrix} 0 & \mathcal{C}_{u2} \\ \mathcal{C}_{v1} & 0 \\ \mathcal{C}_{w1} & 0 \end{bmatrix} \begin{bmatrix} \psi_1 \\ \psi_2 \end{bmatrix}, \quad (9.9b)$$

with

$$\mathcal{B}_{x02} := ik_z \kappa_x(y), \quad \mathcal{B}_{y01} := -k_z^2 \Delta^{-1} \kappa_y(y), \quad \mathcal{B}_{z01} := -ik_z \Delta^{-1} (\kappa'_z(y) + \kappa_z(y) \partial_y),$$

where $\kappa_s(y)$, for every $s = x, y, z$, denote arbitrary functions of y , and $\kappa'_z(y) := d\kappa_z(y)/dy$. All other operators have the same meaning as in (9.1).

Since operators \mathcal{A} , \mathcal{B} , and \mathcal{C} in (9.1) and (9.9) have the same respective structures, we conclude that all theorems and corollaries of § 9.1, § 9.2, and § 9.3 that determine scaling with R for different measures of input-output amplification also hold for system (9.9). However, the expressions for the Reynolds number independent quantities are different for the ‘unstructured’ and ‘structured’ external excitations.

Effectiveness of near-wall external excitations

We next investigate the effectiveness of an input applied in a certain spatial direction by studying the Reynolds number dependence of $[\|\mathcal{H}_s\|_2^2](k_z)$, where

$$\mathcal{H}_s(\omega, k_z) := \mathcal{C}(k_z)(i\omega I - \mathcal{A}(k_z))^{-1}\mathcal{B}_{s0}(k_z), \quad s = x, y, z.$$

Based on the above remarks, it follows that Corollary 13 holds for both ‘unstructured’ and ‘structured’ external excitations. However, the expressions for functions f_x , f_y , f_z , g_y , and g_z are different in these two cases. This is illustrated in § 9.6.2 where we derive analytical expressions for f_x , f_y , f_z (which are the same for all channel flows) for

$$\kappa_s(y) := a(1 + \coth(a))e^{-a(y+1)} =: \kappa(y, a), \quad a > 0, \quad \forall s = x, y, z, \quad (9.10)$$

and determine the dependence of g_y and g_z on both k_z and a in terms of easily computable series in Couette flow. This particular ‘pre-modulation’ in y is chosen to analyze the effectiveness of inputs whose amplitude decays exponentially away from the lower wall. Clearly, this rate of decay (i.e., degree of localization) can be adjusted by assigning different values to parameter a . We note that functions f and g in Corollary 13 now depend on both k_z and ‘modulation parameter’ a , e.g. $f_x = f_x(k_z, a)$.

We have normalized $\kappa(y, a)$ so that

$$\int_{-1}^1 \kappa(y, a) dy = 2, \quad \forall a > 0,$$

which allows for comparison between ‘structured’ (in the limit as $a \rightarrow 0$) and ‘unstructured’ results. Clearly, in the ‘unstructured’ case there is no ‘pre-modulation’ in y , that is

$$\kappa(y) \equiv 1 \Rightarrow \int_{-1}^1 \kappa(y) dy = 2.$$

The formulae for functions $f_x(k_z, a)$, $f_y(k_z, a)$, and $f_z(k_z, a)$ are determined in § 9.6.2. Furthermore, the traces of nominal-velocity-dependent operators are determined in terms of rapidly convergent series for Couette flow in § 9.6.2.

The analytical expression for $f_x(k_z, a)$ is given by (9.35). By taking the limit of $f_x(k_z, a)$ as $a \rightarrow 0$ we obtain (9.29) which corresponds to the value of $f_x(k_z)$ for ‘unstructured’ external excitation. Furthermore, as $k_z \rightarrow \infty$, we have

$$\lim_{k_z \rightarrow \infty} f_x(k_z, a) = 0, \quad \forall a \in (0, \infty),$$

which implies that for any finite value of $a > 0$ function $f_x(k_z, a)$ decays to zero for big enough values of k_z . On the other hand, a limit of $f_x(k_z, a)$ as $a \rightarrow \infty$ is determined by

$$\lim_{a \rightarrow \infty} f_x(k_z, a) = \frac{1}{2}, \quad \forall k_z \in \mathbb{R},$$

which suggests that for external excitation that is localized in the vicinity of the lower wall (large enough values of a) and acts in the streamwise direction influence of high spanwise wave numbers becomes more and more important. This is illustrated in Figure 9.12 where we graphically illustrate the dependence of f_x on k_z for different values of a .

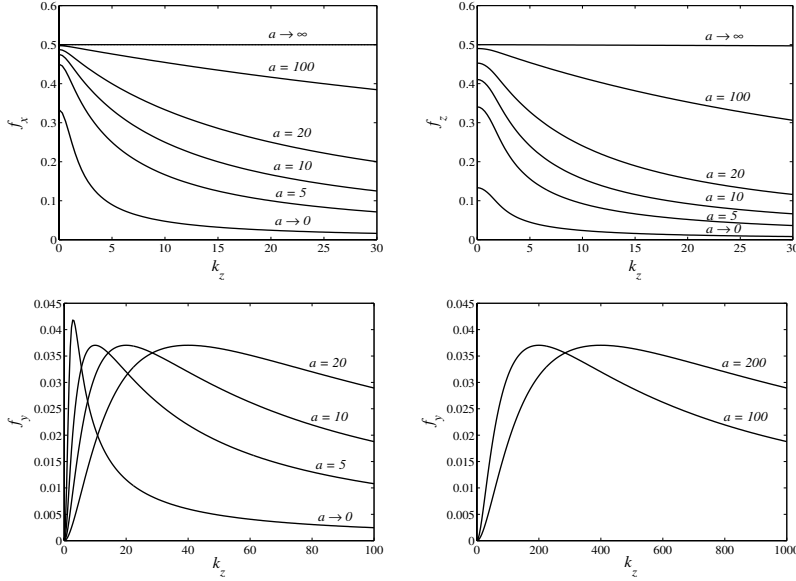


Figure 9.12: The k_z -dependence of f_x , f_y , and f_z for different values of a .

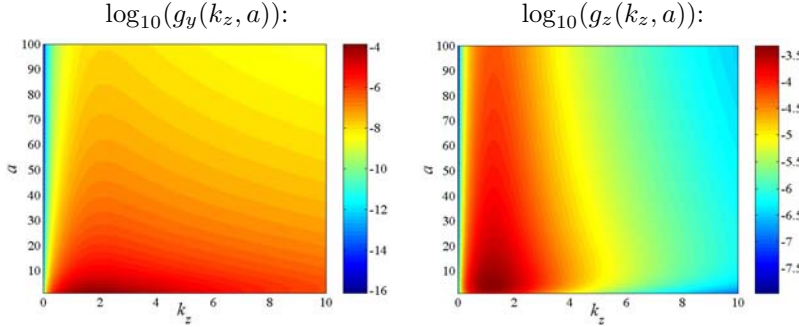


Figure 9.13: Plots of $g_y(k_z, a)$, and $g_z(k_z, a)$ in Couette flow.

The formulae for $f_y(k_z, a)$ and $f_z(k_z, a)$ are given by (9.36). The k_z -dependence of these two quantities for different values of a is shown in Figure 9.12. We note that the limits of $f_y(k_z, a)$ and $f_z(k_z, a)$ as $a \rightarrow 0$ are in agreement with the corresponding formulae (9.30) for the ‘unstructured’ excitation.

The analytical expressions for $g_y(k_z, a)$ and $g_z(k_z, a)$ in Couette flow are determined in § 9.6.2. These formulae are expressed in terms of rapidly convergent series, and they are obtained by performing the spectral decompositions of the Orr-Sommerfeld and Squire operators. Since R^3 respectively multiplies $g_y(k_z, a)$ and $g_z(k_z, a)$ in the expressions for $[\|\mathcal{H}_y\|_2^2](k_z)$ and $[\|\mathcal{H}_z\|_2^2](k_z)$ (see Corollary 13), it is relevant to analyze how $g_y(k_z, a)$ and $g_z(k_z, a)$ change with their arguments. Figure 9.13 shows the dependence of these two quantities on both k_z and a . Clearly, the magnitude of g_y decreases sharply as a increases its value. On the other hand, the value of g_z increases for a certain range of a ’s and then it starts decaying at a very slow rate. Furthermore, for any fixed value of parameter a both g_y and g_z achieve largest values at $O(1)$ values of k_z .

In Figure 9.14, we illustrate the a -dependence of the following quantities

$$\sup_{k_z} g_y(k_z, a), \quad \sup_{k_z} g_z(k_z, a), \quad \frac{\sup_{k_z} g_z(k_z, a)}{\sup_{k_z} g_y(k_z, a)},$$

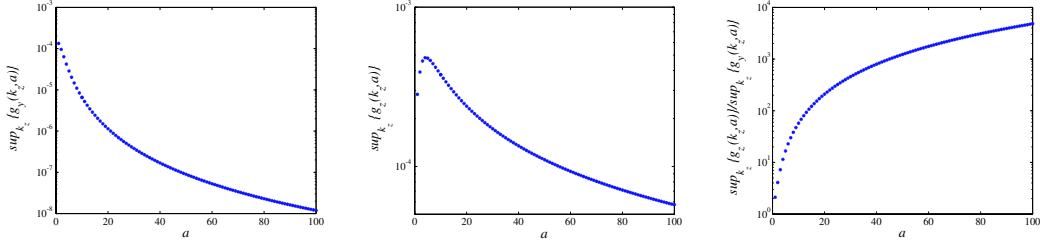


Figure 9.14: Plots of $\sup_{k_z} g_y(k_z, a)$, $\sup_{k_z} g_z(k_z, a)$, and $\sup_{k_z} g_z(k_z, a) / \sup_{k_z} g_y(k_z, a)$ in Couette flow.

in Couette flow, with the abscissa in the linear and the ordinate in the logarithmic scale. Clearly, $\sup_{k_z} g_y(k_z, a)$ decays monotonically as a function of a with a fairly sharp rate of decay, while $\sup_{k_z} g_z(k_z, a)$ peaks at a non-zero value of a and then decays slowly as a increases its value. The right plot further shows that $\sup_{k_z} g_z(k_z, a) / \sup_{k_z} g_y(k_z, a)$ is a monotonically increasing function of a and that, for example, at $a = 100$ function $\sup_{k_z} g_z(k_z, a)$ achieves almost four orders of magnitude larger value than function $\sup_{k_z} g_y(k_z, a)$. This indicates that the localized spanwise excitations have much stronger influence on the velocity field than the localized wall-normal excitations. This observation is consistent with recent numerical work on channel flow turbulence control using the Lorentz force [4–6], where it was concluded that forcing in the spanwise direction confined within the viscous sub-layer had the strongest effect in suppressing turbulence. We confirmed this observation by analytical derivations for the streamwise constant perturbations showing that the spanwise forcing localized near the lower wall has, by far, the strongest effect on the evolution of the velocity field components.

9.5 Exact determination of Hilbert–Schmidt norms

In this section, we employ the analytical procedure developed in Chapter 3 to ascertain the Hilbert–Schmidt norms of the Reynolds number independent operators $\bar{\mathcal{H}}_{rs}(\Omega, k_z)$, $\{r = u, v, w; s = x, y, z\}$. We note that $\bar{\mathcal{H}}_{ux}(\Omega, k_z)$ has a second order state-space realization, the operators $\bar{\mathcal{H}}_{rs}(\Omega, k_z)$, $\{r = v, w; s = y, z\}$, can be represented by the fourth order TPBVSR, while $\bar{\mathcal{H}}_{uy}(\Omega, k_z)$ and $\bar{\mathcal{H}}_{uz}(\Omega, k_z)$ can be described by minimal realizations with six states. These realizations can be chosen in a number of different ways. Realizations that we use are given in § 9.5.1. It is noteworthy that the Hilbert–Schmidt norms of these operators for any given pair (Ω, k_z) can be determined explicitly using the procedure of § 3.2.3 which involves only finite dimensional computations with matrices whose dimension is at most four times larger than the order of the underlying operators. Therefore, in the worst case we need to determine the state transition matrices that belong to $\mathbb{C}^{24 \times 24}$, which can be easily done, for example in MATLAB. This illustrates the power of the procedure developed in Chapter 3 and circumvents the need for numerical approximation of the underlying operators.

In Couette flow, the coupling operator simplifies to $\mathcal{C}_p = -ik_z$ and, thus, all operators in (9.1) have the constant coefficients in y . As a result, matrix A_0 in (9.13) no longer depends on the wall-normal coordinate. Hence, the nominal-flow-dependent quantities m_{uy} and m_{uz} can be determined explicitly using formula (3.19) which only requires determination of certain matrix exponentials. In other words, in streamwise constant Couette flow, each operator $\bar{\mathcal{H}}_{rs}\bar{\mathcal{H}}_{rs}^*$ can be represented by a well-posed TPBVSR with constant coefficients in y

$$\bar{\mathcal{H}}_{rs}\bar{\mathcal{H}}_{rs}^* : \begin{cases} q'(y) &= Aq(y) + B_s f_s(y), \\ \phi_r(y) &= C_r q(y), \\ 0 &= L_1 q(-1) + L_2 q(1), \quad y \in [-1, 1], \end{cases}$$

which implies that $\|\bar{\mathcal{H}}_{rs}(\Omega, k_z)\|_{HS}^2$ is determined by (cf. (3.19) in Theorem 2)

$$\|\bar{\mathcal{H}}_{rs}(\Omega, k_z)\|_{HS}^2 = -\text{tr} \left((L_1 + L_2 e^{2A})^{-1} L_2 \begin{bmatrix} 0 & I \end{bmatrix} \exp \left\{ 2 \begin{bmatrix} A & 0 \\ B_s C_r & A \end{bmatrix} \right\} \begin{bmatrix} I \\ 0 \end{bmatrix} \right).$$

9.5.1 State-space realizations of the linearized Navier-Stokes equations

Here, we describe the TPBVSR that are used for the frequency response determination of the streamwise constant LNS equations. Once the temporal Fourier transform has been applied, (9.1a) can be rewritten as

$$\psi_1 = R(i\Omega I - \mathcal{L})^{-1} (\mathcal{B}_y d_y + \mathcal{B}_z d_z), \quad (9.11a)$$

$$\psi_2 = R(i\Omega I - \mathcal{S})^{-1} (\mathcal{C}_p \psi_1 + \mathcal{B}_x d_x), \quad (9.11b)$$

with $\Omega := \omega R$. Since the Reynolds number enters conveniently into the equations, we can study (9.11) at $R = 1$, and rewrite it as

$$\psi_1^{(4)} - (2k_z^2 + i\Omega)\psi_1'' + k_z^2(k_z^2 + i\Omega)\psi_1 = \begin{bmatrix} k_z^2 & 0 \end{bmatrix} \begin{bmatrix} d_y \\ d_z \end{bmatrix} + \begin{bmatrix} 0 & ik_z \end{bmatrix} \begin{bmatrix} d'_y \\ d'_z \end{bmatrix}, \quad (9.12a)$$

$$\psi_2'' - (k_z^2 + i\Omega)\psi_2 = ik_z U'(y)\psi_1 - ik_z d_x. \quad (9.12b)$$

Equations (9.12a) and (9.12b) are ODEs in y parameterized by k_z and Ω with the boundary conditions

$$\psi_1(\pm 1) = \psi_1'(\pm 1) = \psi_2(\pm 1) = 0.$$

For notational convenience, we have suppressed the dependence of ψ_i and d_s on k_z and Ω , e.g. $\psi_i(y) := \psi_i(y, \Omega, k_z)$, $i = 1, 2$. Similarly, $\psi_i^{(r)}(y) := d^r \psi_i(y, \Omega, k_z)/dy^r$.

In particular, we choose the following realizations of (9.12a) and (9.12b)

$$(9.12a) : \begin{cases} \xi'(y) = A_1 \xi(y) + B_1 \begin{bmatrix} d_x(y) \\ d_y(y) \\ d_z(y) \end{bmatrix}, \\ \psi_1(y) = C_1 \xi(y), \\ 0 = S_1 \xi(-1) + S_2 \xi(1), \end{cases} \quad y \in [-1, 1],$$

$$(9.12b) : \begin{cases} \eta'(y) = A_2 \eta(y) + B_2 \begin{bmatrix} d_x(y) \\ d_y(y) \\ d_z(y) \end{bmatrix} + B_3(y) \psi_1(y), \\ \psi_2(y) = C_2 \eta(y), \\ 0 = T_1 \eta(-1) + T_2 \eta(1), \end{cases} \quad y \in [-1, 1],$$

where

$$A_1 := \begin{bmatrix} 0 & 1 & 0 & 0 \\ 2k_z^2 + i\Omega & 0 & 1 & 0 \\ 0 & 0 & 0 & 1 \\ -k_z^2(k_z^2 + i\Omega) & 0 & 0 & 0 \end{bmatrix}, \quad A_2 := \begin{bmatrix} 0 & 1 \\ k_z^2 + i\Omega & 0 \end{bmatrix},$$

$$B_1 := \begin{bmatrix} 0 & 0 & 0 \\ 0 & 0 & 0 \\ 0 & 0 & ik_z \\ 0 & k_z^2 & 0 \end{bmatrix}, \quad B_2 := \begin{bmatrix} 0 & 0 & 0 \\ -ik_z & 0 & 0 \end{bmatrix}, \quad B_3(y) := \begin{bmatrix} 0 \\ ik_z U'(y) \end{bmatrix},$$

$$C_1 := [1 \ 0 \ 0 \ 0], \quad C_2 := [1 \ 0],$$

$$S_1 := \begin{bmatrix} I_{2 \times 2} & 0_{2 \times 2} \\ 0_{2 \times 2} & 0_{2 \times 2} \end{bmatrix}, \quad S_2 := \begin{bmatrix} 0_{2 \times 2} & 0_{2 \times 2} \\ I_{2 \times 2} & 0_{2 \times 2} \end{bmatrix}, \quad T_1 := \begin{bmatrix} 1 & 0 \\ 0 & 0 \end{bmatrix}, \quad T_2 := \begin{bmatrix} 0 & 0 \\ 1 & 0 \end{bmatrix}.$$

We now combine these two realization with (9.1b) to obtain a TPBVSR of operator \mathcal{H} at $(k_x = 0, R = 1)$

$$(9.12, 9.1b) : \begin{cases} x'(y) = A_0(y)x(y) + B_0 \begin{bmatrix} d_x(y) \\ d_y(y) \\ d_z(y) \end{bmatrix}, \\ \begin{bmatrix} u(y) \\ v(y) \\ w(y) \\ 0 \end{bmatrix} = C_0x(y), \\ N_1x(-1) + N_2x(1), \end{cases} \quad y \in [-1, 1], \quad (9.13)$$

where $x^T(y) := [\xi^T(y) \ \eta^T(y)]$, and

$$\begin{aligned} A_0(y) &:= \begin{bmatrix} A_1 & 0 \\ B_3(y)C_1 & A_2 \end{bmatrix} = \begin{bmatrix} 0 & 1 & 0 & 0 & 0 \\ 2k_z^2 + i\Omega & 0 & 1 & 0 & 0 \\ 0 & 0 & 0 & 1 & 0 \\ -k_z^2(k_z^2 + i\Omega) & 0 & 0 & 0 & 0 \\ 0 & 0 & 0 & 0 & 1 \\ ik_z U'(y) & 0 & 0 & 0 & k_z^2 + i\Omega & 0 \end{bmatrix}, \\ B_0 &:= \begin{bmatrix} B_1 \\ B_2 \end{bmatrix} = \begin{bmatrix} 0 & 0 & 0 \\ 0 & 0 & 0 \\ 0 & 0 & ik_z \\ 0 & k_z^2 & 0 \\ 0 & 0 & 0 \\ -ik_z & 0 & 0 \end{bmatrix} =: [B_{x0} \ B_{y0} \ B_{z0}], \quad N_1 := \begin{bmatrix} S_1 & 0 \\ 0 & T_1 \end{bmatrix}, \\ C_0 &:= \begin{bmatrix} 0 & 0 & 0 & 0 & -\frac{i}{k_z} & 0 \\ 1 & 0 & 0 & 0 & 0 & 0 \\ 0 & \frac{i}{k_z} & 0 & 0 & 0 & 0 \end{bmatrix} =: \begin{bmatrix} C_{u0} \\ C_{v0} \\ C_{w0} \end{bmatrix}, \quad N_2 := \begin{bmatrix} S_2 & 0 \\ 0 & T_2 \end{bmatrix}. \end{aligned}$$

Thus, we have rendered TPBVSR of system (9.12, 9.1b) into (9.13), which is a suitable form for the application of the procedure developed in Chapter 3.

The realizations of $\bar{\mathcal{H}}_{rs}(\Omega, k_z)$ can be now easily determined for every $\{r = u, v, w; s = x, y, z\}$. For example, TPBVSR of $\bar{\mathcal{H}}_{uy}(\Omega, k_z)$ is given by

$$\bar{\mathcal{H}}_{uy} : \begin{cases} x'(y) = A_0(y)x(y) + B_{y0}d_y(y), \\ u(y) = C_{u0}x(y), \\ 0 = N_1x(-1) + N_2x(1), \end{cases} \quad y \in [-1, 1].$$

As previously mentioned, $\bar{\mathcal{H}}_{ux}(\Omega, k_z)$ and $\bar{\mathcal{H}}_{rs}(\Omega, k_z)$, for every $\{r = v, w; s = y, z\}$, are respectively the second and the fourth order operators. We note that their minimal realizations can be obtained by combining the respective realizations of (9.12b) and (9.12a) with the corresponding rows of (9.1b). For example, a

minimal realization of $\bar{\mathcal{H}}_{ux}(\Omega, k_z)$ is given by

$$\bar{\mathcal{H}}_{ux} : \begin{cases} \eta'(y) = \begin{bmatrix} 0 & 1 \\ k_z^2 + i\Omega & 0 \end{bmatrix} \eta(y) + \begin{bmatrix} 0 \\ -ik_z \end{bmatrix} d_x(y), \\ u(y) = \begin{bmatrix} -\frac{i}{k_z} & 0 \end{bmatrix} \eta(y), \\ 0 = T_1\eta(-1) + T_2\eta(1), \end{cases} \quad y \in [-1, 1].$$

Alternatively, $\|\bar{\mathcal{H}}_{ux}(\Omega, k_z)\|_{HS}^2$ can be determined from Theorem 2 using the following non-minimal realization of $\bar{\mathcal{H}}_{ux}(\Omega, k_z)$

$$\bar{\mathcal{H}}_{ux} : \begin{cases} x'(y) = A_0(y)x(y) + B_{x0}d_x(y), \\ u(y) = C_{u0}x(y), \\ 0 = N_1x(-1) + N_2x(1), \end{cases} \quad y \in [-1, 1].$$

Figure 9.3 in § 9.2 illustrates the plots of $\|\bar{\mathcal{H}}_{rs}(\Omega, k_z)\|_{HS}^2$, for every $\{r = u, v, w; s = x, y, z\}$. These computations are performed in MATLAB for any given pair (Ω, k_z) using the procedure developed in Chapter 3 with the above TPBVSR.

In § 9.5.2, we derive analytical expressions for functions $\|\bar{\mathcal{H}}_{rs}(0, k_z)\|_{HS}^2$.

9.5.2 Formulae for Hilbert–Schmidt norms at $\omega = 0$

In this subsection, we derive explicit expressions for the Hilbert–Schmidt norms of streamwise constant steady-state perturbations. As shown in § 9.2, these perturbations experience the largest amplification rates. Formulae for functions $l_{rs}(0, k_z)$ and $m_{rs}(0, k_z)$ in (9.4) are determined symbolically in MATHEMATICA using (3.19). The mean-flow-dependent quantities m_{uy} and m_{uz} are obtained for Couette flow. The analytical expressions are given by

$$\begin{cases} l_{ux}(0, k_z) = \frac{k_z (\coth(2k_z) + 2k_z \operatorname{csch}^2(2k_z)) - 1}{2k_z^4}, \\ m_{uy}(0, k_z) = \frac{c_{uy}(k_z)}{322560k_z^8(\cosh(4k_z) - 8k_z^2 - 1)^2}, \\ m_{uz}(0, k_z) = \frac{c_{uz}(k_z)}{5160960k_z^8(\cosh(4k_z) - 8k_z^2 - 1)^2}, \\ l_{vy}(0, k_z) = \frac{c_{vy}(k_z)}{1440k_z^4(\cosh(4k_z) - 8k_z^2 - 1)^2}, \\ l_{vz}(0, k_z) = \frac{c_{vz}(k_z)}{1440k_z^4(\cosh(4k_z) - 8k_z^2 - 1)^2}, \\ l_{wy}(0, k_z) = l_{vz}(0, k_z), \\ l_{wz}(0, k_z) = \frac{c_{wz}(k_z)}{1440k_z^4(\cosh(4k_z) - 8k_z^2 - 1)^2}, \end{cases}$$

where

$$\begin{aligned}
c_{uy}(k_z) &:= -297675 + 16k_z^2(-187425 + 4k_z^2(-168525 + 8k_z^2(-8337 + 2474k_z^2 + 80k_z^4))) \\
&\quad + 12(33075 + 249900k_z^2 + 42000k_z^4 + 28672k_z^6 + 768k_z^8)\cosh(4k_z) - 99225\cosh(8k_z) \\
&\quad + \frac{7}{8}k_z\csch^2(k_z)\sech^2(k_z)(3072k_z^5(45 + 16k_z^4) \\
&\quad + (14175 + 64k_z^2(2295 + 660k_z^2 - 1176k_z^4 + 1216k_z^6))\sinh(4k_z) \\
&\quad + 12(-945 + 8k_z^2(-765 + 440k_z^2 + 72k_z^4))\sinh(8k_z) + 2835\sinh(12k_z)), \\
c_{uz}(k_z) &:= +\csch^2(k_z)\sech^2(k_z)(34650 + 16k_z^2(31185 + 4k_z^2(2835 + 16k_z^2(630 + 2577k_z^2 - 592k_z^4))) \\
&\quad - (51975 + 64k_z^2(10395 + 8k_z^2(735 - 70k_z^2 + 1776k_z^4 + 160k_z^6)))\cosh(4k_z) \\
&\quad + 20790\cosh(8k_z) - 3465\cosh(12k_z) + 2k_z(8k_z(10395 + 12180k_z^2 - 2240k_z^4 - 576k_z^6)\cosh(8k_z) \\
&\quad + 224(315\cosh(2k_z)\sinh(2k_z)^5 + k_z^2(2(855 + 8k_z^2(45 + 197k_z^2 - 136k_z^4))\sinh(4k_z) \\
&\quad + (-855 + 180k_z^2 - 136k_z^4)\sinh(8k_z)))), \\
c_{vy}(k_z) &:= -1485 + 8k_z^2(-1845 + 128k_z^2(-45 + 2k_z^2(-8 + k_z^2))) - 495\cosh(8k_z) \\
&\quad + 4(495 + 3690k_z^2 + 720k_z^4 + 256k_z^6)\cosh(4k_z) \\
&\quad + 30k_z(-15 - 216k_z^2 + 128k_z^4 + 15\cosh(4k_z))\sinh(4k_z), \\
c_{vz}(k_z) &:= -135 - 8k_z^2(225 - 128k_z^4 + 256k_z^6) + 4(45 + 450k_z^2 + 720k_z^4 - 256k_z^6)\cosh(4k_z) \\
&\quad - 45\cosh(8k_z) + 90k_z(-1 - 40k_z^2 + \cosh(4k_z))\sinh(4k_z), \\
c_{wz}(k_z) &:= -135 + 8k_z^2(-225 + 16k_z^2(-5 + 4k_z^2)(3 + 4k_z^2)) - 45\cosh(8k_z) \\
&\quad + 4(45 + 450k_z^2 + 1200k_z^4 + 256k_z^6)\cosh(4k_z) \\
&\quad - 30k_z(3 + 120k_z^2 + 128k_z^4 - 3\cosh(4k_z))\sinh(4k_z).
\end{aligned}$$

Formulae for functions $\{l_x, l_y, l_z, m_y, m_z\}$, $\{l_u, l_v, l_w, m_u\}$, and $\{l, m\}$ can be readily obtained by combining their respective definitions from Corollaries 8, 9, and 10 with the above expressions.

9.6 Exact determination of \mathcal{H}_2 norms

In § 9.6.1, we derive expressions for the componentwise \mathcal{H}_2 norms of streamwise constant LNS system (9.1) in terms of solutions to the corresponding Lyapunov equations. In § 9.6.2, we utilize these relationships to determine the explicit k_z -dependence of functions f and g in Corollaries 13 and 14 for both ‘unstructured’ and ‘structured’ external excitations. The nominal-flow-dependent functions g are determined in Couette flow. The main analytical tool we use in § 9.6.2 is the formula for the trace of a class of differential operators defined by forced TPBVSR. This formula is derived in § 3.2.2.

From § 7.1.2 and § 9.1, it follows that at $k_x = 0$

$$\begin{aligned}
\mathcal{A} &= \begin{bmatrix} \frac{1}{R}\Delta^{-1}\Delta^2 & 0 \\ -ik_zU' & \frac{1}{R}\Delta \end{bmatrix} =: \begin{bmatrix} \frac{1}{R}\mathcal{L} & 0 \\ \mathcal{C}_p & \frac{1}{R}\mathcal{S} \end{bmatrix}, \\
\mathcal{A}^* &= \begin{bmatrix} \frac{1}{R}\Delta^{-1}\Delta^2 & -ik_z\Delta^{-1}U' \\ 0 & \frac{1}{R}\Delta \end{bmatrix} =: \begin{bmatrix} \frac{1}{R}\mathcal{L} & \mathcal{C}_p^* \\ 0 & \frac{1}{R}\mathcal{S} \end{bmatrix},
\end{aligned}$$

$$\mathcal{M}_x = \mathcal{N}_u = \begin{bmatrix} 0 & 0 \\ 0 & I \end{bmatrix}, \quad \mathcal{M}_y = \mathcal{N}_v = \begin{bmatrix} -k_z^2\Delta^{-1} & 0 \\ 0 & 0 \end{bmatrix}, \quad \mathcal{M}_z = \mathcal{N}_w = \begin{bmatrix} \Delta^{-1}\partial_{yy} & 0 \\ 0 & 0 \end{bmatrix},$$

where operators \mathcal{M}_s and \mathcal{N}_r are defined as $\mathcal{M}_s := \mathcal{B}_s\mathcal{B}_s^*$, for $s = x, y, z$, and $\mathcal{N}_r := \mathcal{C}_r^*\mathcal{C}_r$, for $r = u, v, w$.

The results of this section also hold for system (7.20) with ‘structured’ external excitations since operators

$$\begin{aligned}\mathcal{B}_{x0}\mathcal{B}_{x0}^* &= \begin{bmatrix} 0 & 0 \\ 0 & \kappa_u^2 \end{bmatrix}, \quad \mathcal{B}_{y0}\mathcal{B}_{y0}^* = \begin{bmatrix} -k_z^2\Delta^{-1}\kappa_v^2 & 0 \\ 0 & 0 \end{bmatrix}, \\ \mathcal{B}_{z0}\mathcal{B}_{z0}^* &= \begin{bmatrix} \Delta^{-1}(2\kappa_w\kappa'_w\partial_y + \kappa_w^2\partial_{yy}) & 0 \\ 0 & 0 \end{bmatrix},\end{aligned}$$

have the same respective structures as operators \mathcal{M}_x , \mathcal{M}_y , and \mathcal{M}_z . As remarked in § 9.4, the dependence of the variance amplification on the Reynolds number at $k_x = 0$ has the same form for the ‘unstructured’ and ‘structured’ external excitations. However, the expressions for functions f and g in Theorem 12, Corollary 13, and Corollary 14 are different in these two cases.

9.6.1 Expressions for \mathcal{H}_2 norms via Lyapunov equations

In this subsection, we provide alternative proofs of Theorem 12, Corollary 13, and Corollary 14 by exploiting the fact that the \mathcal{H}_2 norms of frequency response operators \mathcal{H}_{rs} , \mathcal{H}_s , and \mathcal{H}_r , $\{r = u, v, w; s = x, y, z\}$, can be determined based on solutions of the corresponding Lyapunov equations. The procedure outlined below is most convenient for determination of the Reynolds number independent functions f and g in (9.6), (9.7), and (9.8).

Controllability Gramians and functions f and g in Theorem 12

For each r and s , $[\|\mathcal{H}_{rs}\|_2^2](k_z)$ can be expressed in terms of the solution to an operator Lyapunov equation of the form

$$\mathcal{A}\mathcal{X}_s + \mathcal{X}_s\mathcal{A}^* = -\mathcal{M}_s \quad (9.14)$$

as $[\|\mathcal{H}_{rs}\|_2^2](k_z) = \text{trace}(\mathcal{N}_r\mathcal{X}_s)$, where \mathcal{X}_s is a 2×2 block operator whose structure we denote by

$$\mathcal{X}_s := \begin{bmatrix} \mathcal{X}_{s11} & \mathcal{X}_{s0}^* \\ \mathcal{X}_{s0} & \mathcal{X}_{s22} \end{bmatrix}.$$

Using the structure of operators \mathcal{N}_r and \mathcal{X}_s it follows that $[\|\mathcal{H}_{rs}\|_2^2](k_z)$ can be determined as

$$[\|\mathcal{H}_{rs}\|_2^2](k_z) = \text{trace}(\mathcal{N}_r\mathcal{X}_s) = \text{trace}(\mathcal{N}_{r11}\mathcal{X}_{s11}) + \text{trace}(\mathcal{N}_{r22}\mathcal{X}_{s22}).$$

The lower block triangular structure of \mathcal{A} transforms (9.14) into the set of conveniently coupled operator Sylvester equations of the form

$$\mathcal{L}\mathcal{X}_{s11} + \mathcal{X}_{s11}\mathcal{L} = -R\mathcal{M}_{s11}, \quad (9.15a)$$

$$\mathcal{S}\mathcal{X}_{s0} + \mathcal{X}_{s0}\mathcal{L} = -R\mathcal{C}_p\mathcal{X}_{s11}, \quad (9.15b)$$

$$\mathcal{S}\mathcal{X}_{s22} + \mathcal{X}_{s22}\mathcal{S} = -R(\mathcal{M}_{s22} + \mathcal{C}_p\mathcal{X}_{s0}^* + \mathcal{X}_{s0}\mathcal{C}_p^*). \quad (9.15c)$$

If the solutions of this system of equations at $R = 1$ are respectively denoted by \mathcal{P}_{s11} , \mathcal{P}_{s0} , and \mathcal{P}_{s22} , then (9.15) simplifies to

$$\mathcal{L}\mathcal{P}_{s11} + \mathcal{P}_{s11}\mathcal{L} = -\mathcal{M}_{s11}, \quad (9.16a)$$

$$\mathcal{S}\mathcal{P}_{s0} + \mathcal{P}_{s0}\mathcal{L} = -\mathcal{C}_p\mathcal{P}_{s11}, \quad (9.16b)$$

$$\mathcal{S}\mathcal{P}_{s22} + \mathcal{P}_{s22}\mathcal{S} = -(\mathcal{C}_p\mathcal{P}_{s0}^* + \mathcal{P}_{s0}\mathcal{C}_p^*), \quad (9.16c)$$

$$\mathcal{S}\mathcal{P}_{s22_1} + \mathcal{P}_{s22_1}\mathcal{S} = -\mathcal{M}_{s22}, \quad (9.16d)$$

where $\mathcal{P}_{s22} = \mathcal{P}_{s22_1} + \mathcal{P}_{s22_2}$. Clearly, equations (9.16a) and (9.16d) can be respectively solved for \mathcal{P}_{s11} and \mathcal{P}_{s22_1} . Once \mathcal{P}_{s11} is determined, (9.16b) can be solved to yield \mathcal{P}_{s0} . Finally, \mathcal{P}_{s0} can be used to determine

solution to (9.16c).

Linearity of (9.15) implies that its solutions can be expressed in terms of solutions to (9.16) as

$$\{\mathcal{X}_{s11} = R\mathcal{P}_{s11}, \mathcal{X}_{s0} = R^2\mathcal{P}_{s0}, \mathcal{X}_{s22} = R\mathcal{P}_{s22_1} + R^3\mathcal{P}_{s22_2}\},$$

which yields

$$[\|\mathcal{H}_{rs}\|_2^2](k_z) = (\text{trace}(\mathcal{N}_{r11}\mathcal{P}_{s11}) + \text{trace}(\mathcal{N}_{r22}\mathcal{P}_{s22_1}))R + \text{trace}(\mathcal{N}_{r22}\mathcal{P}_{s22_2})R^3. \quad (9.17)$$

Using the definitions of operators \mathcal{N}_r and \mathcal{M}_s , it follows that

$$\{\mathcal{N}_{u11} \equiv 0, \mathcal{N}_{v22} \equiv 0, \mathcal{N}_{w22} \equiv 0\}, \quad \left\{ \begin{array}{l} \mathcal{P}_{x11} \equiv 0, \mathcal{P}_{x22_2} \equiv 0 \\ \mathcal{P}_{y22_1} \equiv 0, \mathcal{P}_{z22_1} \equiv 0 \end{array} \right\},$$

which in combination with (9.17) gives the following expressions for functions f and g in (9.6)

$$\begin{bmatrix} f_{ux}(k_z) & g_{uy}(k_z) & g_{uz}(k_z) \\ 0 & f_{vy}(k_z) & f_{vz}(k_z) \\ 0 & f_{wy}(k_z) & f_{wz}(k_z) \end{bmatrix} = \begin{bmatrix} \text{trace}(\mathcal{N}_{u22}(k_z)\mathcal{P}_{x22_1}(k_z)) & \text{trace}(\mathcal{N}_{u22}(k_z)\mathcal{P}_{y22_2}(k_z)) & \text{trace}(\mathcal{N}_{u22}(k_z)\mathcal{P}_{z22_2}(k_z)) \\ 0 & \text{trace}(\mathcal{N}_{v11}(k_z)\mathcal{P}_{y11}(k_z)) & \text{trace}(\mathcal{N}_{v11}(k_z)\mathcal{P}_{z11}(k_z)) \\ 0 & \text{trace}(\mathcal{N}_{w11}(k_z)\mathcal{P}_{y11}(k_z)) & \text{trace}(\mathcal{N}_{w11}(k_z)\mathcal{P}_{z11}(k_z)) \end{bmatrix}. \quad (9.18)$$

These expressions are most convenient for determination of functions f and g in Corollary 13.

Observability Gramians and functions f and g in Theorem 12

Alternatively, $[\|\mathcal{H}_{rs}\|_2^2](k_z)$ can be, for every $\{r = u, v, w; s = x, y, z\}$, expressed in terms of the solution to an operator Lyapunov equation of the form

$$\mathcal{A}^*\mathcal{Y}_r + \mathcal{Y}_r\mathcal{A} = -\mathcal{N}_r \quad (9.19)$$

as $[\|\mathcal{H}_{rs}\|_2^2](k_z) = \text{trace}(\mathcal{Y}_r\mathcal{M}_s)$, where \mathcal{Y}_r is a 2×2 block operator whose structure we denote by

$$\mathcal{Y}_r := \begin{bmatrix} \mathcal{Y}_{r11} & \mathcal{Y}_{r0}^* \\ \mathcal{Y}_{r0} & \mathcal{Y}_{r22} \end{bmatrix}.$$

Using the structure of operators \mathcal{M}_s and \mathcal{Y}_r it follows that $[\|\mathcal{H}_{rs}\|_2^2](k_z)$ can be determined as

$$[\|\mathcal{H}_{rs}\|_2^2](k_z) = \text{trace}(\mathcal{Y}_r\mathcal{M}_s) = \text{trace}(\mathcal{Y}_{r11}\mathcal{M}_{s11}) + \text{trace}(\mathcal{Y}_{r22}\mathcal{M}_{s22}).$$

The lower block triangular structure of \mathcal{A} renders (9.19) into the set of conveniently coupled operator Sylvester equations of the form

$$\mathcal{S}\mathcal{Y}_{r22} + \mathcal{Y}_{r22}\mathcal{S} = -R\mathcal{N}_{r22}, \quad (9.20a)$$

$$\mathcal{S}\mathcal{Y}_{r0} + \mathcal{Y}_{r0}\mathcal{L} = -R\mathcal{Y}_{r22}\mathcal{C}_p, \quad (9.20b)$$

$$\mathcal{L}\mathcal{Y}_{r11} + \mathcal{Y}_{r11}\mathcal{L} = -R(\mathcal{N}_{r11} + \mathcal{C}_p^*\mathcal{Y}_{r0} + \mathcal{Y}_{r0}^*\mathcal{C}_p). \quad (9.20c)$$

If the solutions of this system of equations at $R = 1$ are respectively denoted by \mathcal{R}_{r22} , \mathcal{R}_{r0} , and \mathcal{R}_{r11} , then (9.20) simplifies to

$$\mathcal{S}\mathcal{R}_{r22} + \mathcal{R}_{r22}\mathcal{S} = -\mathcal{N}_{r22}, \quad (9.21a)$$

$$\mathcal{S}\mathcal{R}_{r0} + \mathcal{R}_{r0}\mathcal{L} = -\mathcal{R}_{r22}\mathcal{C}_p, \quad (9.21b)$$

$$\mathcal{L}\mathcal{R}_{r11_2} + \mathcal{R}_{r11_2}\mathcal{L} = -(\mathcal{C}_p^*\mathcal{R}_{r0} + \mathcal{R}_{r0}^*\mathcal{C}_p), \quad (9.21c)$$

$$\mathcal{L}\mathcal{R}_{r11_1} + \mathcal{R}_{r11_1}\mathcal{L} = -\mathcal{N}_{r11}, \quad (9.21d)$$

where $\mathcal{R}_{r11} = \mathcal{R}_{r11_1} + \mathcal{R}_{r11_2}$. Clearly, equations (9.21a) and (9.21d) can be respectively solved for \mathcal{R}_{r22} and \mathcal{R}_{r11_1} . Once \mathcal{R}_{r22} is determined, (9.21b) can be solved to yield \mathcal{R}_{r0} . Finally, \mathcal{R}_{r0} can be used to determine the solution to (9.21c).

Linearity of (9.20) implies that its solutions can be expressed in terms of solutions to (9.21) as

$$\{\mathcal{Y}_{r22} = R\mathcal{R}_{r22}, \mathcal{Y}_{r0} = R^2\mathcal{R}_{r0}, \mathcal{Y}_{r11} = R\mathcal{R}_{r11_1} + R^3\mathcal{R}_{r11_2}\},$$

which yields

$$[\|\mathcal{H}_{rs}\|_2^2](k_z) = (\text{trace}(\mathcal{R}_{r22}\mathcal{M}_{s22}) + \text{trace}(\mathcal{R}_{r11_1}\mathcal{M}_{s11}))R + \text{trace}(\mathcal{R}_{r11_2}\mathcal{M}_{s11})R^3. \quad (9.22)$$

Using the definitions of operators \mathcal{M}_s , and \mathcal{N}_r , it follows that

$$\begin{aligned} & \{\mathcal{M}_{x11} \equiv 0, \mathcal{M}_{y22} \equiv 0, \mathcal{M}_{z22} \equiv 0\}, \\ & \{\mathcal{R}_{u11_1} \equiv 0, \{\mathcal{R}_{v22} \equiv 0, \mathcal{R}_{v11_2} \equiv 0\}, \{\mathcal{R}_{w22} \equiv 0, \mathcal{R}_{w11_2} \equiv 0\}\}, \end{aligned}$$

which in combination with (9.22) gives the following expressions for functions f and g in (9.6)

$$\begin{bmatrix} f_{ux}(k_z) & g_{uy}(k_z) & g_{uz}(k_z) \\ 0 & f_{vy}(k_z) & f_{vz}(k_z) \\ 0 & f_{wy}(k_z) & f_{wz}(k_z) \end{bmatrix} = \begin{bmatrix} \text{trace}(\mathcal{R}_{u22}(k_z)\mathcal{M}_{x22}(k_z)) & \text{trace}(\mathcal{R}_{u11_2}(k_z)\mathcal{M}_{y11}(k_z)) & \text{trace}(\mathcal{R}_{u11_2}(k_z)\mathcal{M}_{z11}(k_z)) \\ 0 & \text{trace}(\mathcal{R}_{v11_1}(k_z)\mathcal{M}_{y11}(k_z)) & \text{trace}(\mathcal{R}_{v11_1}(k_z)\mathcal{M}_{z11}(k_z)) \\ 0 & \text{trace}(\mathcal{R}_{w11_1}(k_z)\mathcal{M}_{y11}(k_z)) & \text{trace}(\mathcal{R}_{w11_1}(k_z)\mathcal{M}_{z11}(k_z)) \end{bmatrix}. \quad (9.23)$$

These expressions are most convenient for determination of functions f and g in Corollary 14.

Expressions for functions f and g in Corollary 13 via Lyapunov equations

Corollary 13 follows from Theorem 12 and square additivity of the \mathcal{H}_2 norm. Thus, for every $s = x, y, z$, the \mathcal{H}_2 norm of operator \mathcal{H}_s from d_s to $\phi := [u \ v \ w]^T$ is given by

$$[\|\mathcal{H}_s\|_2^2](k_z) = [\|\mathcal{H}_{us}\|_2^2](k_z) + [\|\mathcal{H}_{vs}\|_2^2](k_z) + [\|\mathcal{H}_{ws}\|_2^2](k_z). \quad (9.24)$$

Therefore, combination of (9.18) and (9.24) with

$$\mathcal{N}_{u22} = \mathcal{N}_{v11} + \mathcal{N}_{w11} = I,$$

yields

$$\begin{aligned} [\|\mathcal{H}_x\|_2^2](k_z) &= \text{trace}(\mathcal{P}_{x22_1}(k_z))R &=: f_x(k_z)R, \\ [\|\mathcal{H}_y\|_2^2](k_z) &= \text{trace}(\mathcal{P}_{y11}(k_z))R + \text{trace}(\mathcal{P}_{y22_2}(k_z))R^3 &=: f_y(k_z)R + g_y(k_z)R^3, \\ [\|\mathcal{H}_z\|_2^2](k_z) &= \text{trace}(\mathcal{P}_{z11}(k_z))R + \text{trace}(\mathcal{P}_{z22_2}(k_z))R^3 &=: f_z(k_z)R + g_z(k_z)R^3, \end{aligned}$$

which provides an alternative proof of Corollary 13, and gives convenient expressions for functions f_x, f_y, f_z, g_y, g_z in terms of solutions to the corresponding Lyapunov equations. In § 9.6.2, we combine these expressions with the trace formula of § 3.2.2 to derive respective formulae for $\{f_x(k_z), f_y(k_z), f_z(k_z), g_y(k_z), g_z(k_z)\}$ for LNS systems (9.1) and (9.9) with ‘unstructured’ and ‘structured’ external excitations. Functions g_y and g_z are determined in Couette flow.

Expressions for functions f and g in Corollary 14 via Lyapunov equations

Corollary 14 follows from Theorem 12 and square additivity of the \mathcal{H}_2 norm. Thus, for every $r = u, v, w$, the \mathcal{H}_2 norm of operator \mathcal{H}_r from $\mathbf{d} := [d_x \ d_y \ d_z]^T$ to r is given by

$$[\|\mathcal{H}_r\|_2^2](k_z) = [\|\mathcal{H}_{rx}\|_2^2](k_z) + [\|\mathcal{H}_{ry}\|_2^2](k_z) + [\|\mathcal{H}_{rz}\|_2^2](k_z). \quad (9.25)$$

Therefore, combination of (9.23) and (9.25) with

$$\mathcal{M}_{x22} = \mathcal{M}_{y11} + \mathcal{M}_{z11} = I,$$

yields

$$\begin{aligned} [\|\mathcal{H}_u\|_2^2](k_z) &= \text{trace}(\mathcal{R}_{u22}(k_z))R + \text{trace}(\mathcal{R}_{u11_2}(k_z))R^3 =: f_u(k_z)R + g_u(k_z)R^3, \\ [\|\mathcal{H}_v\|_2^2](k_z) &= \text{trace}(\mathcal{R}_{v11_1}(k_z))R =: f_v(k_z)R, \\ [\|\mathcal{H}_w\|_2^2](k_z) &= \text{trace}(\mathcal{R}_{w11_1}(k_z))R =: f_w(k_z)R, \end{aligned}$$

which provides an alternative proof of Corollary 14, and gives convenient expressions for functions f_u, f_v, f_w , and g_u in terms of solutions to the corresponding Lyapunov equations. In § 9.6.2, we combine these expressions with the trace formula of § 3.2.2 to derive formulae for $\{f_u(k_z), f_v(k_z), f_w(k_z), g_u(k_z)\}$ for LNS system (9.1) with ‘unstructured’ external excitations. Function g_u is determined in Couette flow.

9.6.2 Formulae for operator traces

In this subsection, we derive analytical formulae for traces of operators that appear in the expressions for $[\|\mathcal{H}_s\|_2^2](k_z)$, $\{s = x, y, z\}$, and $[\|\mathcal{H}_r\|_2^2](k_z)$, $\{r = u, v, w\}$. The main analytical tool we use here is the formula for the trace of a class of differential operators defined by forced TPBVSR. This formula is given in § 3.2.2. In the process, we exploit the fact that some of the traces of interest have already been determined in [11].

Unstructured external excitations: determination of nominal velocity independent traces

For system (9.1) with ‘unstructured’ external excitations, the nominal velocity independent operators (whose traces we want to determine) can be represented by a well-posed TPBVSR with constant coefficients in y

$$\mathcal{F} : \begin{cases} x'(y) = Ax(y) + Bf(y), \\ g(y) = Cx(y), \\ 0 = L_1x(-1) + L_2x(1), \quad y \in [-1, 1]. \end{cases} \quad (9.26)$$

Thus, the traces of these operators can be obtained using the trace formula (3.16) of § 3.2.2 as

$$\text{trace}(\mathcal{F}) = \text{tr} \left(CB - (L_1 + L_2 e^{2A})^{-1} L_2 \begin{bmatrix} 0 & I \end{bmatrix} \exp \left\{ 2 \begin{bmatrix} A & 0 \\ BC & A \end{bmatrix} \right\} \begin{bmatrix} I \\ 0 \end{bmatrix} \right). \quad (9.27)$$

This formula is employed to determine explicit analytical expressions for functions $f_r(k_z)$, $\{r = u, v, w\}$, and $f_s(k_z)$, $\{s = x, y, z\}$ in Corollaries 13 and 14.

Formulae for $f_x(k_z)$, $f_y(k_z)$, and $f_z(k_z)$

We recall that $f_x(k_z)$, $f_y(k_z)$, and $f_z(k_z)$ are determined by $\text{trace}(\mathcal{P}_{x22_1}(k_z))$, $\text{trace}(\mathcal{P}_{y11}(k_z))$, and $\text{trace}(\mathcal{P}_{z11}(k_z))$, where operators \mathcal{P}_{x22_1} , \mathcal{P}_{y11} , and \mathcal{P}_{z11} respectively satisfy

$$\mathcal{S}\mathcal{P}_{x22_1} + \mathcal{P}_{x22_1}\mathcal{S} = -I, \quad (9.28a)$$

$$\mathcal{L}\mathcal{P}_{y11} + \mathcal{P}_{y11}\mathcal{L} = -(-k_z^2\Delta^{-1}), \quad (9.28b)$$

$$\mathcal{L}\mathcal{P}_{z11} + \mathcal{P}_{z11}\mathcal{L} = -\Delta^{-1}\partial_{yy}. \quad (9.28c)$$

The solution of (9.28a) is given by $\mathcal{P}_{x22_1} = -\frac{1}{2}\mathcal{S}^{-1}$ which in turn implies [11]¹

$$f_x(k_z) := \text{trace}(\mathcal{P}_{x22_1}(k_z)) = \frac{2k_z \coth(2k_z) - 1}{4k_z^2}. \quad (9.29)$$

On the other hand, application of Lemma 2 of [11] to equations (9.28b) and (9.28c) respectively yields

$$\begin{aligned} \text{trace}(\mathcal{P}_{y11}(k_z)) &= -\frac{1}{2}\text{trace}(\mathcal{L}^{-1}(-k_z^2\Delta^{-1})) = \frac{k_z^2}{2}\text{trace}((\Delta^2)^{-1}), \\ \text{trace}(\mathcal{P}_{z11}(k_z)) &= -\frac{1}{2}\text{trace}(\mathcal{L}^{-1}\Delta^{-1}\partial_{yy}) = -\frac{1}{2}\text{trace}((\Delta^2)^{-1}\partial_{yy}). \end{aligned}$$

Therefore, the remaining problem amounts to determination of traces of operators $(\Delta^2)^{-1}$ and $(\Delta^2)^{-1}\partial_{yy}$ whose definitions are given by

$$\begin{aligned} (\Delta^2)^{-1} : f_1 \longmapsto g_1 &\Leftrightarrow f_1 = g_1^{(4)} - 2k_z^2g_1'' + k_z^4g_1, \quad g_1(\pm 1) = g_1'(\pm 1) = 0, \\ (\Delta^2)^{-1}\partial_{yy} : f_2 \longmapsto g_2 &\Leftrightarrow f_2'' = g_2^{(4)} - 2k_z^2g_2'' + k_z^4g_2, \quad g_2(\pm 1) = g_2'(\pm 1) = 0. \end{aligned}$$

For notational convenience, we have suppressed the dependence of f_i and g_j on k_z , e.g. $f_i(y) := f_i(y, k_z)$, $i = 1, 2$. Similarly, $f_i^{(r)}(y) := d^r f_i(y, k_z)/dy^r$.

These two operators can be represented by their state-space realizations as follows

$$\begin{aligned} (\Delta^2)^{-1} : &\left\{ \begin{array}{l} x'(y) = \begin{bmatrix} 0 & 0 & 0 & -k_z^4 \\ 1 & 0 & 0 & 0 \\ 0 & 1 & 0 & 2k_z^2 \\ 0 & 0 & 1 & 0 \end{bmatrix} x(y) + \begin{bmatrix} 1 \\ 0 \\ 0 \\ 0 \end{bmatrix} f_1(y), \\ g_1(y) = \begin{bmatrix} 0 & 0 & 0 & 1 \end{bmatrix} x(y), \\ 0 = \begin{bmatrix} 0_{2 \times 2} & I_{2 \times 2} \\ 0_{2 \times 2} & 0_{2 \times 2} \end{bmatrix} x(-1) + \begin{bmatrix} 0_{2 \times 2} & 0_{2 \times 2} \\ 0_{2 \times 2} & I_{2 \times 2} \end{bmatrix} x(1), \quad y \in [-1, 1], \end{array} \right. \\ (\Delta^2)^{-1}\partial_{yy} : &\left\{ \begin{array}{l} z'(y) = \begin{bmatrix} 0 & 0 & 0 & -k_z^4 \\ 1 & 0 & 0 & 0 \\ 0 & 1 & 0 & 2k_z^2 \\ 0 & 0 & 1 & 0 \end{bmatrix} z(y) + \begin{bmatrix} 0 \\ 0 \\ 1 \\ 0 \end{bmatrix} f_2(y), \\ g_2(y) = \begin{bmatrix} 0 & 0 & 0 & 1 \end{bmatrix} z(y), \\ 0 = \begin{bmatrix} 0_{2 \times 2} & I_{2 \times 2} \\ 0_{2 \times 2} & 0_{2 \times 2} \end{bmatrix} z(-1) + \begin{bmatrix} 0_{2 \times 2} & 0_{2 \times 2} \\ 0_{2 \times 2} & I_{2 \times 2} \end{bmatrix} z(1), \quad y \in [-1, 1]. \end{array} \right. \end{aligned}$$

The realizations of both operators are in form (9.26) and thus, formula (9.27) can be used to determine their traces. Since both realizations are parameterized by spanwise wave-number, the traces of underlying operators are k_z -dependent as well. With the help of MATHEMATICA we obtain the following formulae for

¹Expression (27) in [11] should read $\frac{2k_z \coth(2k_z) - 1}{4k_z^2}$.

$\text{trace}(\mathcal{P}_{y11}(k_z))$ and $\text{trace}(\mathcal{P}_{z11}(k_z))$:

$$\begin{aligned} f_y(k_z) &= \frac{k_z^2}{2} \text{trace}((\Delta^2)^{-1}) = -\frac{16k_z^4 + 24k_z^2 + 3k_z \sinh(4k_z) - 9 \sinh^2(2k_z)}{24k_z^2(4k_z^2 - \sinh^2(2k_z))}, \\ f_z(k_z) &= -\frac{1}{2} \text{trace}((\Delta^2)^{-1} \partial_{yy}) = \frac{16k_z^4 - 3k_z \sinh(4k_z) + 3 \sinh^2(2k_z)}{24k_z^2(4k_z^2 - \sinh^2(2k_z))}. \end{aligned} \quad (9.30)$$

It worth mentioning that the above determined traces do not depend on the form of channel flow. On the other hand, the traces of operators $\mathcal{P}_{y22_2}(k_z)$ and $\mathcal{P}_{z22_2}(k_z)$ (that is, $g_y(k_z)$ and $g_z(k_z)$) are not nominal velocity independent. Rather, they depend on the underlying channel flow through its dependence on U' . The derivation of the analytical expressions for these traces in Couette flow is also given in this section.

Formulae for $f_u(k_z)$, $f_v(k_z)$, $f_w(k_z)$, and $g_u(k_z)$

We recall that $f_u(k_z)$, $f_v(k_z)$, and $f_w(k_z)$ are determined by $\text{trace}(\mathcal{R}_{u22}(k_z))$, $\text{trace}(\mathcal{R}_{v11_1}(k_z))$, and $\text{trace}(\mathcal{R}_{w11_1}(k_z))$, where operators \mathcal{R}_{u22} , \mathcal{R}_{v11_1} , and \mathcal{R}_{w11_1} respectively satisfy

$$\mathcal{S}\mathcal{R}_{u22} + \mathcal{R}_{u22}\mathcal{S} = -I, \quad (9.31a)$$

$$\mathcal{L}\mathcal{R}_{v11_1} + \mathcal{R}_{v11_1}\mathcal{L} = -(-k_z^2\Delta^{-1}), \quad (9.31b)$$

$$\mathcal{L}\mathcal{R}_{w11_1} + \mathcal{R}_{w11_1}\mathcal{L} = -\Delta^{-1}\partial_{yy}. \quad (9.31c)$$

Comparison of equations (9.28) and (9.31) implies

$$\begin{aligned} f_u(k_z) &:= \text{trace}(\mathcal{R}_{u22}(k_z)) = \text{trace}(\mathcal{P}_{x22_1}(k_z)) =: f_x(k_z), \\ f_v(k_z) &:= \text{trace}(\mathcal{R}_{v11_1}(k_z)) = \text{trace}(\mathcal{P}_{y11}(k_z)) =: f_y(k_z), \\ f_w(k_z) &:= \text{trace}(\mathcal{R}_{w11_1}(k_z)) = \text{trace}(\mathcal{P}_{z11}(k_z)) =: f_z(k_z), \end{aligned}$$

where the expressions for f_x , f_y , and f_z are given by (9.29) and (9.30). On the other hand, $g_u(k_z) := \text{trace}(\mathcal{R}_{u11_2}(k_z))$ is a function of a nominal velocity. In Couette flow, the formula for $g_u(k_z)$ can be obtained by comparing the expression for $[\|\mathcal{H}\|_2^2](k_z)$ of § 9.3 with its counterpart of [11]. By doing so, we obtain the following formula:

$$g_u(k_z) := \text{trace}(\mathcal{R}_{u11_2}(k_z)) = \begin{cases} \frac{1}{4} \sum_{n=1}^{\infty} \frac{k_z^2}{\gamma_n^4} \left\{ 1 - \frac{n^2\pi^2}{\gamma_n} \left[\frac{2k_z(\cosh(2k_z) - 1)}{\gamma_n(\sinh(2k_z) - 2k_z)} + \frac{1}{4(\alpha_n \coth(\alpha_n) - k_z \coth(k_z))} \right] \right\} & n \text{ even}, \\ \frac{1}{4} \sum_{n=1}^{\infty} \frac{k_z^2}{\gamma_n^4} \left\{ 1 - \frac{n^2\pi^2}{\gamma_n} \left[\frac{2k_z(\cosh(2k_z) + 1)}{\gamma_n(\sinh(2k_z) + 2k_z)} + \frac{1}{4(\alpha_n \tanh(\alpha_n) - k_z \tanh(k_z))} \right] \right\} & n \text{ odd}, \end{cases}$$

where

$$\gamma_n := -\left(\frac{n^2\pi^2}{4} + k_z^2\right), \quad \alpha_n := \sqrt{2k_z^2 + \frac{n^2\pi^2}{4}}, \quad n \geq 1.$$

Our current efforts are directed towards development of the formula for $g_u(k_z)$ in Poiseuille flow.

Structured external excitations: determination of nominal velocity independent traces

In this subsection, we consider streamwise constant LNS system (9.9) with ‘structured’ external excitations, and derive the explicit analytical expressions for functions f_x , f_y , and f_z in Corollary 13. This is done for ‘pre-modulation’ in the wall-normal direction defined by (9.10). In this case, the nominal velocity independent

operators (whose traces we want to determine) can be represented by a well-posed TPBVSR

$$\mathcal{F} : \begin{cases} x'(y) = Ax(y) + e^{-2a(y+1)}Bf(y), \\ g(y) = Cx(y), \\ 0 = L_1x(-1) + L_2x(1), \end{cases} \quad y \in [-1, 1], \quad (9.32)$$

where A , B , C , L_1 , and L_2 denote y -independent matrices of appropriate dimensions. Thus, the traces of these operators can be obtained using the trace formula (3.17) of § 3.2.2 with $\alpha := 2a$ and $c := 2$

$$\begin{aligned} \text{trace}(\mathcal{F}) &= \frac{1 - e^{-4a}}{4a} \text{tr}(CB) - \\ &\quad \text{tr}\left((L_1 + L_2 e^{2A})^{-1} L_2 \begin{bmatrix} 0 & I \end{bmatrix} \exp\left\{2 \begin{bmatrix} A - 2aI & 0 \\ BC & A \end{bmatrix}\right\} \begin{bmatrix} I \\ 0 \end{bmatrix}\right), \end{aligned} \quad (9.33)$$

This formula is employed to determine explicit analytical expressions for functions $f_s(k_z, a)$, for every $s = x, y, z$, in Corollary 13.

Formulae for $f_x(k_z, a)$, $f_y(k_z, a)$, and $f_z(k_z, a)$

We recall that $f_x(k_z, a)$, $f_y(k_z, a)$, and $f_z(k_z, a)$ are determined by $\text{trace}(\mathcal{P}_{x22_1}(k_z, a))$, $\text{trace}(\mathcal{P}_{y11}(k_z, a))$, and $\text{trace}(\mathcal{P}_{z11}(k_z, a))$, where operators \mathcal{P}_{x22_1} , \mathcal{P}_{y11} , and \mathcal{P}_{z11} respectively satisfy

$$\mathcal{S}\mathcal{P}_{x22_1} + \mathcal{P}_{x22_1}\mathcal{S} = -\kappa^2, \quad (9.34a)$$

$$\mathcal{L}\mathcal{P}_{y11} + \mathcal{P}_{y11}\mathcal{L} = -(-k_z^2\Delta^{-1}\kappa^2), \quad (9.34b)$$

$$\mathcal{L}\mathcal{P}_{z11} + \mathcal{P}_{z11}\mathcal{L} = -\Delta^{-1}(2\kappa\kappa'\partial_y + \kappa^2\partial_{yy}). \quad (9.34c)$$

Application of Lemma 2 of [11] to equations (9.34a), (9.34b), and (9.34c) in combination with (9.10) yields

$$\text{trace}(\mathcal{P}_{x22_1}(k_z, a)) = -\frac{1}{2}\text{trace}(\mathcal{S}^{-1}\kappa^2) = -\frac{1}{2}a^2(1 + \coth(a))^2 \text{trace}(\Delta^{-1}e^{-2a(y+1)}),$$

$$\begin{aligned} \text{trace}(\mathcal{P}_{y11}(k_z, a)) &= -\frac{1}{2}\text{trace}(\mathcal{L}^{-1}(-k_z^2\Delta^{-1}\kappa^2)) \\ &= \frac{k_z^2}{2}a^2(1 + \coth(a))^2 \text{trace}((\Delta^2)^{-1}e^{-2a(y+1)}), \end{aligned}$$

$$\begin{aligned} \text{trace}(\mathcal{P}_{z11}(k_z, a)) &= -\frac{1}{2}\text{trace}(\mathcal{L}^{-1}\Delta^{-1}(2\kappa\kappa'\partial_y + \kappa^2\partial_{yy})) \\ &= -\frac{1}{2}a^2(1 + \coth(a))^2 \text{trace}((\Delta^2)^{-1}e^{-2a(y+1)}(\partial_{yy} - 2a\partial_y)). \end{aligned}$$

Therefore, the remaining problem amounts to determination of traces of operators

$$\Delta^{-1}e^{-2a(y+1)} : f_1 \mapsto g_1 \Leftrightarrow e^{-2a(y+1)}f_1 = g_1'' - k_z^2g_1,$$

$$(\Delta^2)^{-1}e^{-2a(y+1)} : f_2 \mapsto g_2 \Leftrightarrow e^{-2a(y+1)}f_2 = g_2^{(4)} - 2k_z^2g_2'' + k_z^4g_2,$$

$$(\Delta^2)^{-1}e^{-2a(y+1)}(\partial_{yy} - 2a\partial_y) : f_3 \mapsto g_3$$

‡

$$e^{-2a(y+1)}(f_3'' - 2af_3') = g_3^{(4)} - 2k_z^2g_3'' + k_z^4g_3,$$

with boundary conditions: $g_1(\pm 1) = 0$, $g_2(\pm 1) = g_2'(\pm 1) = 0$, and $g_3(\pm 1) = g_3'(\pm 1) = 0$.

Operators $\Delta^{-1}e^{-2a(y+1)}$ and $(\Delta^2)^{-1}e^{-2a(y+1)}$ can be represented by their state-space realizations as

follows

$$\Delta^{-1}e^{-2a(y+1)} : \begin{cases} q'(y) = \begin{bmatrix} 0 & k_z^2 \\ 1 & 0 \end{bmatrix} q(y) + e^{-2a(y+1)} \begin{bmatrix} 1 \\ 0 \end{bmatrix} f_1(y), \\ g_1(y) = \begin{bmatrix} 0 & 1 \end{bmatrix} q(y), \\ 0 = \begin{bmatrix} 0 & 1 \\ 0 & 0 \end{bmatrix} q(-1) + \begin{bmatrix} 0 & 0 \\ 0 & 1 \end{bmatrix} q(1), \end{cases} \quad y \in [-1, 1],$$

$$(\Delta^2)^{-1}e^{-2a(y+1)} : \begin{cases} x'(y) = \begin{bmatrix} 0 & 2k_z^2 & 0 & -k_z^4 \\ 1 & 0 & 0 & 0 \\ 0 & 1 & 0 & 0 \\ 0 & 0 & 1 & 0 \end{bmatrix} x(y) + e^{-2a(y+1)} \begin{bmatrix} 1 \\ 0 \\ 0 \\ 0 \end{bmatrix} f_2(y), \\ g_2(y) = \begin{bmatrix} 0 & 0 & 0 & 1 \end{bmatrix} x(y), \\ 0 = \begin{bmatrix} 0_{2 \times 2} & I_{2 \times 2} \\ 0_{2 \times 2} & 0_{2 \times 2} \end{bmatrix} x(-1) + \begin{bmatrix} 0_{2 \times 2} & 0_{2 \times 2} \\ 0_{2 \times 2} & I_{2 \times 2} \end{bmatrix} x(1), \end{cases} \quad y \in [-1, 1].$$

On the other hand, a realization of operator $(\Delta^2)^{-1}e^{-2a(y+1)}(\partial_{yy} - 2a\partial_y)$ is given by

$$\begin{cases} z'(y) = \begin{bmatrix} 0 & 2k_z^2 & 0 & -k_z^4 \\ 1 & 0 & 0 & 0 \\ 0 & 1 & 0 & 0 \\ 0 & 0 & 1 & 0 \end{bmatrix} z(y) + e^{-2a(y+1)} \begin{bmatrix} 2k_z^2 \\ 2a \\ 1 \\ 0 \end{bmatrix} f_3(y), \\ g_3(y) = \begin{bmatrix} 0 & 0 & 0 & 1 \end{bmatrix} z(y), \\ 0 = \begin{bmatrix} 0_{2 \times 2} & I_{2 \times 2} \\ 0_{2 \times 2} & 0_{2 \times 2} \end{bmatrix} z(-1) + \begin{bmatrix} 0_{2 \times 2} & 0_{2 \times 2} \\ 0_{2 \times 2} & I_{2 \times 2} \end{bmatrix} z(1), \end{cases} \quad y \in [-1, 1].$$

Note that, for any given pair (k_z, a) , the realizations of all three operators are of the form (9.32). We note that since all realizations are parameterized by spanwise wave-number k_z and parameter a , the traces of underlying operators are going to depend on k_z and a as well.

Using (9.33), with the help of MATHEMATICA we obtain the following formulae for traces of operators $\mathcal{P}_{x221}(k_z, a)$, $\mathcal{P}_{y11}(k_z, a)$, and $\mathcal{P}_{z11}(k_z, a)$

$$f_x(k_z, a) = \begin{cases} \frac{a \{-a - a \coth^2(a) + 2k_z \coth(2k_z) \coth(a)\}}{4(k_z^2 - a^2)} & k_z \neq a, \\ \frac{1}{8} \{1 + \coth^2(a) - a \operatorname{csch}^3(a) \operatorname{sech}(a)\} & k_z = a, \end{cases} \quad (9.35)$$

$$f_y(k_z, a) = \begin{cases} \frac{e^{-2a} k_z^2 (1 + \coth(a))^2}{8a(a^2 - k_z^2)^3 (1 + 8k_z^2 - \cosh(4k_z))} h_y(k_z, a) & k_z \neq a, \\ \frac{\operatorname{csch}^2(a) \{(3 - 288a^2) \cosh(2a) - 3 \cosh(6a) + 8a(21 + 32a^2) \sinh(2a)\}}{384(1 + 8a^2 - \cosh(4a))} & k_z = a, \end{cases} \quad (9.36)$$

$$f_z(k_z, a) = \begin{cases} \frac{e^{-4a} (1 + \coth(a))^2}{8a(a^2 - k_z^2)^3 (1 + 8k_z^2 - \cosh(4k_z))} h_z(k_z, a) & k_z \neq a, \\ \frac{\operatorname{csch}^2(a) \{3(5 + 32a^2) \cosh(2a) - 15 \cosh(6a) + 8a(9 + 32a^2) \sinh(2a)\}}{384(1 + 8a^2 - \cosh(4a))} & k_z = a, \end{cases}$$

where

$$\begin{aligned} h_y(k_z, a) &:= a \cosh(2a) \{ a^4 + (ak_z)^2(3 + 8a^2) - 16(ak_z^2)^2 + 8k_z^6 - a^2(a^2 + 3k_z^2) \cosh(4k_z) \} + \\ &\quad k_z \sinh(2a) \{ -4(3a^4k_z - 4a^2k_z^3 + k_z^5) + a^2(3a^2 + k_z^2) \sinh(4k_z) \}, \\ h_z(k_z, a) &:= a \cosh(2a) \{ -8k_z^8 + 2a^6(1 + 8k_z^2) + a^4(k_z^2 - 40k_z^4) - a^2(2a^4 + (ak_z)^2 + k_z^4) \cosh(4k_z) + \\ &\quad a^2(k_z^4 + 32k_z^6) \} + \\ &\quad k_z \sinh(2a) \{ 4k_z(-4a^6 + 7a^4k_z^2 - 4a^2k_z^4 + k_z^6) + a^2(4a^4 - a^2k_z^2 + k_z^4) \sinh(4k_z) \}. \end{aligned}$$

Determination of nominal velocity dependent traces

Next, we determine traces of nominal-velocity-dependent operators \mathcal{P}_{s22_2} , $s = y, z$, for both ‘unstructured’ and ‘structured’ external excitations in Couette flow. While we are not able to solve for operators \mathcal{P}_{y22_2} and \mathcal{P}_{z22_2} explicitly, we are able to express their traces in terms of easily computable series. This is accomplished at the expense of doing a spectral decomposition of operators \mathcal{L} and \mathcal{S} (see § 7.1.3 for details).

Determination of $\text{trace}(\mathcal{P}_{s22_2})$

We recall that g_s , for every $s = y, z$, is determined by $\text{trace}(\mathcal{P}_{s22_2})$, where operator \mathcal{P}_{s22_2} satisfies

$$\mathcal{L}\mathcal{P}_{s11} + \mathcal{P}_{s11}\mathcal{L} = -\mathcal{M}_{s11}, \quad (9.37a)$$

$$\mathcal{S}\mathcal{P}_{s0} + \mathcal{P}_{s0}\mathcal{S} = -\mathcal{C}_p\mathcal{P}_{s11}, \quad (9.37b)$$

$$\mathcal{S}\mathcal{P}_{s22_2} + \mathcal{P}_{s22_2}\mathcal{S} = -(\mathcal{C}_p\mathcal{P}_{s0}^* + \mathcal{P}_{s0}\mathcal{C}_p^*). \quad (9.37c)$$

Solutions to (9.37a) and (9.37b) are respectively given by

$$\mathcal{P}_{s11} = \int_0^\infty e^{\mathcal{L}t} \mathcal{M}_{s11} e^{\mathcal{L}t} dt, \quad (9.38a)$$

$$\mathcal{P}_{s0} = \int_0^\infty e^{\mathcal{S}t} \mathcal{C}_p \mathcal{P}_{s11} e^{\mathcal{L}t} dt, \quad (9.38b)$$

while $\text{trace}(\mathcal{P}_{s22_2})$ can be determined as

$$g_s := \text{trace}(\mathcal{P}_{s22_2}) = -\frac{1}{2} \text{trace}(\mathcal{S}^{-1}(\mathcal{C}_p\mathcal{P}_{s0}^* + \mathcal{P}_{s0}\mathcal{C}_p^*)). \quad (9.39)$$

Combination of (9.38b) and (9.39) yields

$$\begin{aligned} g_s &= -\frac{1}{2} \text{trace}(\mathcal{S}^{-1}\mathcal{C}_p\mathcal{P}_{s11} \int_0^\infty e^{\mathcal{L}t} \mathcal{C}_p^* e^{\mathcal{S}t} dt) - \frac{1}{2} \text{trace}(\mathcal{S}^{-1}\mathcal{C}_p \int_0^\infty e^{\mathcal{L}t} \mathcal{P}_{s11} \mathcal{C}_p^* e^{\mathcal{S}t} dt) \\ &=: g_{s_1} + g_{s_2}. \end{aligned}$$

The inherent difficulty is that we cannot determine the above integrals explicitly. However, as we now show the traces can still be determined by carrying out a spectral decomposition of operators \mathcal{L} and \mathcal{S} .

In order to evaluate g_{s_1} and g_{s_2} we need the following Lemma.

Lemma 16 *Let $\{\gamma_n\}_{n \in \mathbb{N}}$, $\{\varphi_n\}_{n \in \mathbb{N}}$ be the eigenvalues and eigenfunctions of the operator \mathcal{S} , then for any trace class operators \mathcal{F} and \mathcal{G}*

$$\text{trace}(\mathcal{F} \int_0^\infty e^{\mathcal{L}t} \mathcal{G} e^{\mathcal{S}t} dt) = - \sum_{n \in \mathbb{N}} \langle \varphi_n, \mathcal{F}(\mathcal{L} + \gamma_n I)^{-1} \mathcal{G} \varphi_n \rangle.$$

Proof: Let the spectral decompositions of \mathcal{S} and \mathcal{L} be

$$\mathcal{S} = \sum_{n \in \mathbb{N}} \gamma_n E_n^{\mathcal{S}}, \quad \mathcal{L} = \sum_{m \in \mathbb{N}} \lambda_m E_m^{\mathcal{L}}$$

where $E_n^{\mathcal{S}}$ and $E_m^{\mathcal{L}}$ are the spectral projections of \mathcal{S} and \mathcal{L} respectively, that is $E_n^{\mathcal{S}} f := \langle \varphi_n, f \rangle \varphi_n$ and $E_m^{\mathcal{L}} f := \langle \sigma_m, f \rangle_{os} \sigma_m$. We can then compute

$$\begin{aligned} \int_0^\infty e^{\mathcal{L}t} \mathcal{G} e^{\mathcal{S}t} dt &= \int_0^\infty \left\{ \sum_{m \in \mathbb{N}} e^{\lambda_m t} E_m^{\mathcal{L}} \right\} \mathcal{G} \left\{ \sum_{n \in \mathbb{N}} e^{\gamma_n t} E_n^{\mathcal{S}} \right\} dt \\ &= \sum_{n \in \mathbb{N}} \sum_{m \in \mathbb{N}} \left\{ \int_0^\infty e^{(\lambda_m + \gamma_n)t} dt \right\} E_m^{\mathcal{L}} \mathcal{G} E_n^{\mathcal{S}} \\ &= - \sum_{n \in \mathbb{N}} \sum_{m \in \mathbb{N}} \frac{1}{(\lambda_m + \gamma_n)} E_m^{\mathcal{L}} \mathcal{G} E_n^{\mathcal{S}} \\ &= - \sum_{n \in \mathbb{N}} (\mathcal{L} + \gamma_n I)^{-1} \mathcal{G} E_n^{\mathcal{S}}, \end{aligned}$$

where in the last equation we made a choice to recombine the spectral decomposition of \mathcal{L} . Now, the trace of any operator \mathcal{H} can be calculated using any orthonormal basis set $\{\varphi_i\}_{i \in \mathbb{N}}$ by $\text{trace}(\mathcal{H}) = \sum_{i \in \mathbb{N}} \langle \varphi_i, \mathcal{H} \varphi_i \rangle$. Therefore

$$\begin{aligned} \text{trace}(\mathcal{F} \int_0^\infty e^{\mathcal{L}t} \mathcal{G} e^{\mathcal{S}t} dt) &= - \text{trace}(\mathcal{F} \sum_{n \in \mathbb{N}} (\mathcal{L} + \gamma_n I)^{-1} \mathcal{G} E_n^{\mathcal{S}}) \\ &= - \sum_{i \in \mathbb{N}} \left\langle \varphi_i, \mathcal{F} \sum_{n \in \mathbb{N}} (\mathcal{L} + \gamma_n I)^{-1} \mathcal{G} E_n^{\mathcal{S}} \varphi_i \right\rangle \\ &= - \sum_{n \in \mathbb{N}} \langle \varphi_n, \mathcal{F}(\mathcal{L} + \gamma_n I)^{-1} \mathcal{G} \varphi_n \rangle. \end{aligned}$$

■

Similarly, by performing a spectral decomposition of \mathcal{L} we can express \mathcal{P}_{s11} as

$$\mathcal{P}_{s11} = - \sum_{k \in \mathbb{N}} (\mathcal{L} + \lambda_k I)^{-1} \mathcal{M}_{s11} E_k^{\mathcal{L}}.$$

We are now able to express g_{s1} and g_{s2} as

$$\begin{aligned} g_{s1} &= -\frac{1}{2} \text{trace}(\mathcal{S}^{-1} \mathcal{C}_p \mathcal{P}_{s11} \int_0^\infty e^{\mathcal{L}t} \mathcal{C}_p^* e^{\mathcal{S}t} dt) \\ &= -\frac{1}{2} \sum_{n \in \mathbb{N}} \sum_{k \in \mathbb{N}} \langle \varphi_n, \mathcal{S}^{-1} \mathcal{C}_p (\mathcal{L} + \lambda_k I)^{-1} \mathcal{M}_{s11} E_k^{\mathcal{L}} (\mathcal{L} + \gamma_n I)^{-1} \mathcal{C}_p^* \varphi_n \rangle \\ &= -\frac{1}{2} \sum_{n \in \mathbb{N}} \sum_{k \in \mathbb{N}} \langle (\mathcal{L} + \lambda_k I)^{-1} \mathcal{C}_p^* \mathcal{S}^{-1} \varphi_n, \mathcal{M}_{s11} E_k^{\mathcal{L}} (\mathcal{L} + \gamma_n I)^{-1} \mathcal{C}_p^* \varphi_n \rangle_{os} \\ &= -\frac{1}{2} \sum_{n \in \mathbb{N}} \sum_{k \in \mathbb{N}} \langle (\mathcal{L} + \gamma_n I)^{-1} \sigma_k, \mathcal{C}_p^* \varphi_n \rangle_{os} \langle (\mathcal{L} + \lambda_k I)^{-1} \mathcal{C}_p^* \mathcal{S}^{-1} \varphi_n, \mathcal{M}_{s11} \sigma_k \rangle_{os}, \end{aligned}$$

and

$$\begin{aligned}
g_{s_2} &= -\frac{1}{2} \text{trace}(\mathcal{S}^{-1} \mathcal{C}_p \int_0^\infty e^{\mathcal{L}t} \mathcal{P}_{s11} \mathcal{C}_p^* e^{\mathcal{S}t} dt) \\
&= -\frac{1}{2} \sum_{n \in \mathbb{N}} \sum_{k \in \mathbb{N}} \langle \varphi_n, \mathcal{S}^{-1} \mathcal{C}_p (\mathcal{L} + \gamma_n I)^{-1} (\mathcal{L} + \lambda_k I)^{-1} \mathcal{M}_{s11} E_k^{\mathcal{L}} \mathcal{C}_p^* \varphi_n \rangle \\
&= -\frac{1}{2} \sum_{n \in \mathbb{N}} \sum_{k \in \mathbb{N}} \langle (\mathcal{L} + \lambda_k I)^{-1} (\mathcal{L} + \gamma_n I)^{-1} \mathcal{C}_p^* \mathcal{S}^{-1} \varphi_n, \mathcal{M}_{s11} E_k^{\mathcal{L}} \mathcal{C}_p^* \varphi_n \rangle_{os} \\
&= -\frac{1}{2} \sum_{n \in \mathbb{N}} \sum_{k \in \mathbb{N}} \langle \sigma_k, \mathcal{C}_p^* \varphi_n \rangle_{os} \langle (\mathcal{L} + \lambda_k I)^{-1} (\mathcal{L} + \gamma_n I)^{-1} \mathcal{C}_p^* \mathcal{S}^{-1} \varphi_n, \mathcal{M}_{s11} \sigma_k \rangle_{os}.
\end{aligned}$$

In particular, for Couette flow we have

$$\mathcal{C}_p^* = -ik_z \Delta^{-1} \Rightarrow \begin{cases} \mathcal{C}_p^* \varphi_n = -\frac{ik_z}{\gamma_n} \varphi_n, \\ \mathcal{C}_p^* \mathcal{S}^{-1} \varphi_n = -\frac{ik_z}{\gamma_n^2} \varphi_n, \end{cases}$$

which in turn implies

$$\begin{aligned}
g_{s_1} &= -\frac{1}{2} \sum_{n \in \mathbb{N}} \sum_{k \in \mathbb{N}} \frac{k_z^2}{\gamma_n^3} \langle (\mathcal{L} + \gamma_n I)^{-1} \sigma_k, \varphi_n \rangle_{os} \langle (\mathcal{L} + \lambda_k I)^{-1} \varphi_n, \mathcal{M}_{s11} \sigma_k \rangle_{os} \\
&= -\frac{1}{2} \sum_{n \in \mathbb{N}} \sum_{k \in \mathbb{N}} \frac{k_z^2}{\gamma_n^3} \frac{1}{(\lambda_k + \gamma_n)} \langle \sigma_k, \varphi_n \rangle_{os} \langle (\mathcal{L} + \lambda_k I)^{-1} \varphi_n, \mathcal{M}_{s11} \sigma_k \rangle_{os} \\
&= -\frac{1}{2} \sum_{n \in \mathbb{N}} \sum_{k \in \mathbb{N}} \sum_{m \in \mathbb{N}} \frac{k_z^2}{\gamma_n^3} \frac{1}{(\lambda_k + \gamma_n)(\lambda_m + \lambda_k)} \langle \sigma_k, \varphi_n \rangle_{os} \langle \sigma_m, \varphi_n \rangle_{os} \langle \sigma_m, \mathcal{M}_{s11} \sigma_k \rangle_{os},
\end{aligned}$$

where we arrived at the last equality by performing the spectral decomposition of operator $(\mathcal{L} + \lambda_k I)^{-1}$. Similarly,

$$\begin{aligned}
g_{s_2} &= -\frac{1}{2} \sum_{n \in \mathbb{N}} \sum_{k \in \mathbb{N}} \frac{k_z^2}{\gamma_n^3} \langle \sigma_k, \varphi_n \rangle_{os} \langle (\mathcal{L} + \lambda_k I)^{-1} (\mathcal{L} + \gamma_n I)^{-1} \varphi_n, \mathcal{M}_{s11} \sigma_k \rangle_{os} \\
&= -\frac{1}{2} \sum_{n \in \mathbb{N}} \sum_{k \in \mathbb{N}} \sum_{m \in \mathbb{N}} \frac{k_z^2}{\gamma_n^3} \frac{1}{(\lambda_m + \lambda_k)(\lambda_m + \gamma_n)} \langle \sigma_k, \varphi_n \rangle_{os} \langle \sigma_m, \varphi_n \rangle_{os} \langle \sigma_m, \mathcal{M}_{s11} \sigma_k \rangle_{os}.
\end{aligned}$$

Hence,

$$\begin{aligned}
g_s &= -\frac{1}{2} \sum_{n,k,m \in \mathbb{N}} \frac{k_z^2}{\gamma_n^3} \frac{\lambda_k + \lambda_m + 2\gamma_n}{(\lambda_m + \lambda_k)(\lambda_k + \gamma_n)(\lambda_m + \gamma_n)} \langle \sigma_k, \varphi_n \rangle_{os} \langle \sigma_m, \varphi_n \rangle_{os} \langle \sigma_m, \mathcal{M}_{s11} \sigma_k \rangle_{os} \\
&= -\frac{k_z^2}{2} \sum_{n,k,m \in \mathbb{N}} \begin{cases} \frac{\lambda_{1k} \lambda_{1m} (\lambda_{1k} + \lambda_{1m} + 2\gamma_n) A_k A_m (n\pi)^2 \cos(p_{1k}) \cos(p_{1m})}{\gamma_n^3 (\lambda_{1m} + \lambda_{1k})(\lambda_{1k}^2 - \gamma_n^2)(\lambda_{1m}^2 - \gamma_n^2)} \langle \sigma_{1m}, \mathcal{M}_{s11} \sigma_{1k} \rangle_{os} & n = \text{odd}, \\ \frac{\lambda_{2k} \lambda_{2m} (\lambda_{2k} + \lambda_{2m} + 2\gamma_n) B_k B_m (n\pi)^2 \sin(p_{2k}) \sin(p_{2m})}{\gamma_n^3 (\lambda_{2m} + \lambda_{2k})(\lambda_{2k}^2 - \gamma_n^2)(\lambda_{2m}^2 - \gamma_n^2)} \langle \sigma_{2m}, \mathcal{M}_{s11} \sigma_{2k} \rangle_{os} & n = \text{even}, \end{cases}
\end{aligned}$$

where

$$\begin{aligned} p_{1k} \tan(p_{1k}) &= -k_z \tanh(k_z), \quad \lambda_{1k} := -(p_{1k}^2 + k_z^2), \quad A_k := \left\{ (-\lambda_{1k}) \left(1 + \frac{\sin(2p_{1k})}{2p_{1k}} \right) \right\}^{-\frac{1}{2}}, \\ p_{2k} \cot(p_{2k}) &= k_z \coth(k_z), \quad \lambda_{2k} := -(p_{2k}^2 + k_z^2), \quad B_k := \left\{ (-\lambda_{2k}) \left(1 - \frac{\sin(2p_{2k})}{2p_{2k}} \right) \right\}^{-\frac{1}{2}}, \end{aligned}$$

and

$$\begin{aligned} \sigma_{1k} &:= A_k \{ \cos(p_{1k}y) - \frac{\cos(p_{1k})}{\cosh(k_z)} \cosh(k_z y) \}, \\ \sigma_{2k} &:= B_k \{ \sin(p_{2k}y) - \frac{\sin(p_{2k})}{\sinh(k_z)} \sinh(k_z y) \}. \end{aligned}$$

Therefore, the remaining task amounts to evaluation of inner products $\langle \sigma_{1m}, \mathcal{M}_{s11}\sigma_{1k} \rangle_{os}$ and $\langle \sigma_{2m}, \mathcal{M}_{s11}\sigma_{2k} \rangle_{os}$ for $s = y, z$ for both ‘unstructured’ and ‘structured’ disturbances.

Formulae for $g_y(k_z)$ and $g_z(k_z)$ in Couette flow

We recall that for ‘unstructured’ disturbances $\mathcal{M}_{y11} = -k_z^2 \Delta^{-1}$ and $\mathcal{M}_{z11} = \Delta^{-1} \partial_{yy}$. Thus,

$$\langle \sigma_{im}, \mathcal{M}_{y11}\sigma_{ik} \rangle_{os} = k_z^2 \langle \sigma_{im}, \sigma_{ik} \rangle_2, \quad \langle \sigma_{im}, \mathcal{M}_{z11}\sigma_{ik} \rangle_{os} = - \langle \sigma_{im}, \sigma''_{ik} \rangle_2, \quad \forall i = 1, 2,$$

where $\sigma''_{ik}(y) := d^2\sigma_{ik}(y)/dy^2$. We evaluate these inner products in MATHEMATICA to obtain

$$\begin{aligned} \langle \sigma_{1m}, \mathcal{M}_{y11}\sigma_{1k} \rangle_{os} &= \begin{cases} k_z^2 A_k A_m \cos(p_{1k}) \cos(p_{1m}) \left(\frac{\tanh(k_z)}{k_z} + \operatorname{sech}^2(k_z) \right) & m \neq k, \\ k_z^2 \{ A_k^2 \cos^2(p_{1k}) \left(\frac{\tanh(k_z)}{k_z} + \operatorname{sech}^2(k_z) \right) - \frac{1}{\lambda_{1k}} \} & m = k, \end{cases} \\ \langle \sigma_{2m}, \mathcal{M}_{y11}\sigma_{2k} \rangle_{os} &= \begin{cases} k_z^2 B_k B_m \sin(p_{2k}) \sin(p_{2m}) \left(\frac{\coth(k_z)}{k_z} - \operatorname{csch}^2(k_z) \right) & m \neq k, \\ k_z^2 \{ B_k^2 \sin^2(p_{2k}) \left(\frac{\coth(k_z)}{k_z} - \operatorname{csch}^2(k_z) \right) - \frac{1}{\lambda_{2k}} \} & m = k, \end{cases} \\ \langle \sigma_{1m}, \mathcal{M}_{z11}\sigma_{1k} \rangle_{os} &= \begin{cases} -k_z^2 A_k A_m \cos(p_{1k}) \cos(p_{1m}) \left(\frac{\tanh(k_z)}{k_z} + \operatorname{sech}^2(k_z) \right) & m \neq k, \\ 1 - k_z^2 \{ A_k^2 \cos^2(p_{1k}) \left(\frac{\tanh(k_z)}{k_z} + \operatorname{sech}^2(k_z) \right) - \frac{1}{\lambda_{1k}} \} & m = k, \end{cases} \\ \langle \sigma_{2m}, \mathcal{M}_{z11}\sigma_{2k} \rangle_{os} &= \begin{cases} -k_z^2 B_k B_m \sin(p_{2k}) \sin(p_{2m}) \left(\frac{\coth(k_z)}{k_z} - \operatorname{csch}^2(k_z) \right) & m \neq k, \\ 1 - k_z^2 \{ B_k^2 \sin^2(p_{2k}) \left(\frac{\coth(k_z)}{k_z} - \operatorname{csch}^2(k_z) \right) - \frac{1}{\lambda_{2k}} \} & m = k. \end{cases} \end{aligned}$$

Formulae for $g_y(k_z, a)$ and $g_z(k_z, a)$ in Couette flow

We recall that for ‘structured’ disturbances with ‘pre-modulation’ in y given by (9.10)

$$\begin{aligned} \mathcal{M}_{y11} &= -k_z^2 a^2 (1 + \coth(a))^2 \Delta^{-1} e^{-2a(y+1)}, \\ \mathcal{M}_{z11} &= a^2 (1 + \coth(a))^2 \Delta^{-1} \{ e^{-2a(y+1)} (\partial_{yy} - 2a\partial_y) \}. \end{aligned}$$

Thus,

$$\begin{aligned} \langle \sigma_{im}, \mathcal{M}_{y11}\sigma_{ik} \rangle_{os} &= k_z^2 a^2 (1 + \coth(a))^2 \langle \sigma_{im}, e^{-2a(y+1)} \sigma_{ik} \rangle_2, \quad \forall i = 1, 2, \\ \langle \sigma_{im}, \mathcal{M}_{z11}\sigma_{ik} \rangle_{os} &= -a^2 (1 + \coth(a))^2 \langle \sigma_{im}, e^{-2a(y+1)} (\sigma''_{ik} - 2a\sigma'_{ik}) \rangle_2, \quad \forall i = 1, 2, \end{aligned}$$

where $\sigma'_{ik}(y) := d\sigma_{ik}(y)/dy$. The analytical expressions for these inner products can be readily determined in MATHEMATICA.

9.7 Summary

We perform a thorough analysis of the effects of individual inputs (d_x , d_y , and d_z) to the individual outputs (u , v , and w) for the streamwise constant LNS equations. We use this componentwise analysis to derive several corollaries that quantify the aggregate effects of: a) inputs in different spatial directions d_x , d_y , and d_z to velocity vector $\phi = [u \ v \ w]^T$; b) input vector $\mathbf{d} := [d_x \ d_y \ d_z]^T$ to velocity perturbations u , v , and w ; and c) forces in all three spatial directions \mathbf{d} to all three velocity components ϕ . We analytically ascertain that for ‘channel-wide external excitations’, the spanwise and wall-normal forces have the strongest influence on the velocity field; the impact of these forces is most powerful on the streamwise velocity component. For example, we rigorously establish that the singular values of operators from d_z and d_y to u scale as R^2 . On the other hand, the singular values of operators from all other body force inputs to all other velocity outputs scale as R . Furthermore, for ‘near-wall external excitations’ we demonstrate that d_z has, by far, the strongest impact on the evolution of the velocity field. This observation is consistent with recent numerical work on channel flow turbulence control using the Lorentz force, where it was concluded that forcing in the spanwise direction confined within the viscous sub-layer had the strongest effect in suppressing turbulence. We confirm this observation by analytical derivations that quantify the \mathcal{H}_2 norms of operators from individual inputs (d_x , d_y , and d_z) to the entire velocity vector ϕ . Also, we perform a detailed analysis of the dependence of: a) maximal singular values and Hilbert–Schmidt norms on the spanwise wave-number k_z and the appropriately scaled temporal frequency $\Omega := \omega R$; and b) \mathcal{H}_∞ and \mathcal{H}_2 on the spanwise wave-number k_z . We conclude that for high Reynolds number channel flows small temporal frequency effects dominate the evolution of the velocity perturbations, and that the most amplified input-output resonances take place at $O(1)$ values of k_z .

Bibliography

- [1] W. C. Reynolds and S. C. Kassinos, “One-point modeling of rapidly deformed homogeneous turbulence,” *Proceedings: Mathematical and Physical Sciences*, vol. 451, no. 1941, pp. 87–104, 1995.
- [2] C. Henoch and J. Stace, “Experimental investigation of a salt water turbulent boundary layer modified by an applied streamwise magnetohydrodynamic body force,” *Physics of Fluids*, vol. 7, no. 6, pp. 1371–1383, 1995.
- [3] C. H. Crawford and G. E. Karniadakis, “Reynolds stress analysis of EMHD-controlled wall turbulence. Part I. Streamwise forcing,” *Physics of Fluids*, vol. 9, no. 3, pp. 788–806, 1997.
- [4] T. W. Berger, J. Kim, C. Lee, and J. Lim, “Turbulent boundary layer control utilizing the Lorentz force,” *Physics of Fluids*, vol. 12, no. 3, pp. 631–649, 2000.
- [5] Y. Du and G. E. Karniadakis, “Suppressing wall turbulence by means of a transverse traveling wave,” *Science*, vol. 288, pp. 1230–1234, 2000.
- [6] Y. Du, V. Symeonidis, and G. E. Karniadakis, “Drag reduction in wall-bounded turbulence via a transverse travelling wave,” *J. Fluid Mech.*, vol. 457, pp. 1–34, 2002.
- [7] L. H. Gustavsson, “Energy growth of three-dimensional disturbances in plane Poiseuille flow,” *J. Fluid Mech.*, vol. 98, p. 149, 1991.
- [8] M. T. Landahl, “Wave breakdown and turbulence,” *SIAM J. Appl. Math.*, vol. 28, pp. 735–756, 1975.
- [9] J. Kim and J. Lim, “A linear process in wall-bounded turbulent shear flows,” *Physics of Fluids*, vol. 12, no. 8, pp. 1885–1888, 2000.
- [10] G. Kreiss, A. Lundbladh, , and D. S. Henningson, “Bounds for threshold amplitudes in subcritical shear flows,” *J. Fluid Mech.*, vol. 270, pp. 175–198, 1994.
- [11] B. Bamieh and M. Dahleh, “Energy amplification in channel flows with stochastic excitation,” *Physics of Fluids*, vol. 13, no. 11, pp. 3258–3269, 2001.

Chapter 10

Spatio-temporal impulse responses of the linearized Navier-Stokes equations in channel flows

In this chapter, we carry input-output analysis of the LNS equations in channel flows further by investigating their spatio-temporal impulse responses. The motivation for this is twofold. First, the response to any forcing field is the superposition of shifted (spatially and temporally) family of impulse responses. Thus, the impulse responses contain qualitatively all the properties of the dynamical response. Second, these responses turn out to be closely related to numerical and experimental observations of early stages of turbulent spots. They bear remarkable qualitative resemblance to the turbulent spots, in terms of the ‘arrow-head’ shape, the streaky structures, and the cross-contamination phenomena as the spots grow. This resemblance is only qualitative, as other features of turbulent spots are not represented in the responses we compute. Our main point however is that for a full understanding of the rich dynamics of the LNS equations one must look at all of these responses. The features of the impulse responses are difficult to extract from the frequency responses (cf. chapters 8 and 9), and are certainly not obvious from the classical modal analysis of the LNS equations.

Several researchers have heretofore reported numerically determined responses of the NS and LNS equations in channel flows. Henningson & Kim [1] studied the turbulence characteristics inside the turbulent spot by performing Direct Numerical Simulations (DNS) in Poiseuille flow with $R = 1500$. The initial condition assumed a form of a double vortex. The authors found significant agreement between their results and experimental observations and concluded that the fully developed turbulent spot does not depend on the initial conditions. Henningson, Lundbladh & Johansson [2] studied the early stages of laminar-turbulent transition by analyzing the development of localized disturbances in Poiseuille and boundary layer flows. The obtained results were based on both the DNS and the analysis of the LNS equations. The Reynolds number in Poiseuille flow was set to 3000, and the flow was initialized by two pairs of counter-rotating vortices. The authors reported the dominance of streamwise elongated structures and underlined the importance of a linear three-dimensional lift-up mechanism [3, 4]. Li & Widnall [5] computed the steady-state response of the forced LNS equations in an undertaking to model the structure around turbulent spot in Poiseuille flow. The forces into the LNS equations were introduced to account for the Reynolds stresses resulting from the regions of small-scale turbulence. The authors found qualitative agreement between the oblique waves surrounding the spot and experimental results of [6]. Lundbladh & Johansson [7] performed the DNS of the plane Couette flow for various Reynolds numbers in the range between 300 and 1500. The flow was kicked off by an initial condition in the form of four pairs of counter-rotating vortices and transition was observed to take place at $R \approx 375$. This value is very close to the lowest Reynolds number for which turbulence can be experimentally maintained [8, 9].

The numerical computations that we perform in this chapter are focused on earlier stages of transition process in Poiseuille flow initiated by the linearized dynamics. One important distinction between our

results and previously published studies is in the way the flow field is computed. Most of the aforementioned references have analyzed the databases obtained as responses to favorably constructed initial conditions. We, on the other hand, study the response of the forced LNS equations to zero initial conditions. The external excitation is chosen in the form of an impulse located in the vicinity of the lower wall. This particular input shape is selected to ‘mimic’ the conditions under which the ‘natural transition’ is observed in laboratory [10]. We find that our results have some of the qualitative features of early stages of turbulent spot development observed in the previously reported experimental and numerical Poiseuille flow investigations.

Our presentation is organized as follows: in § 10.1 we briefly review the notion of the spatio-temporal impulse response of the LNS equations (see Chapter 2 for background material). In § 10.2, we study the spatio-temporal impulse responses of the LNS in subcritical Poiseuille flow with $R = 2000$. We end our presentation with some concluding remarks in § 10.3.

10.1 Preliminaries

From Chapter 7, we recall that a model of the LNS system with impulsive external excitations (7.22) is given by

$$\begin{aligned}\partial_t \psi(k_x, y, k_z, t) &= [\mathcal{A}(k_x, k_z) \psi(k_x, k_z, t)](y) + \mathbf{F}(k_x, y, k_z) \delta(t), \\ \phi(k_x, y, k_z, t) &= [\mathcal{C}(k_x, k_z) \psi(k_x, k_z, t)](y),\end{aligned}$$

where, for notational convenience, we omit the ‘caret symbol’ to denote Fourier transformed signals and operators. The temporal Dirac delta function is given by $\delta(t)$. On the other hand, for any (k_x, k_z) , $\mathbf{F}(k_x, y, k_z)$ represents a multiplication operator in y

$$\begin{aligned}\mathbf{F}(k_x, y, k_z) &:= \mathbf{F}_x(k_x, y, k_z) + \mathbf{F}_y(k_x, y, k_z) + \mathbf{F}_z(k_x, y, k_z), \\ \mathbf{F}_x &= \begin{bmatrix} -ik_x \Delta^{-1} f'_{x0} \\ ik_z f_{x0} \end{bmatrix}, \quad \mathbf{F}_y = \begin{bmatrix} -(k_x^2 + k_z^2) \Delta^{-1} f_{y0} \\ 0 \end{bmatrix}, \quad \mathbf{F}_z = \begin{bmatrix} -ik_z \Delta^{-1} f'_{z0} \\ -ik_x f_{z0} \end{bmatrix},\end{aligned}$$

and $\mathbf{f}_0(y) := [f_{x0}(y) \ f_{y0}(y) \ f_{z0}(y)]^T$ denotes an arbitrary function of the wall-normal coordinate.

The solution of system (7.22) in the presence of zero initial conditions is, for any quadruple (k_x, y, k_z, t) , determined by

$$\phi(k_x, y, k_z, t) = \phi_x(k_x, y, k_z, t) + \phi_y(k_x, y, k_z, t) + \phi_z(k_x, y, k_z, t),$$

where

$$\phi_s(k_x, y, k_z, t) := [u_s(k_x, y, k_z, t) \ v_s(k_x, y, k_z, t) \ w_s(k_x, y, k_z, t)]^T$$

represents the system’s response to the forcing applied in a certain spatial direction (for $s = x$ streamwise, for $s = y$ wall-normal, or for $s = z$ spanwise):

$$\begin{aligned}\begin{bmatrix} u_s(k_x, y, k_z, t) \\ v_s(k_x, y, k_z, t) \\ w_s(k_x, y, k_z, t) \end{bmatrix} &= [\mathcal{C}(k_x, k_z) \psi_s(k_x, k_z, t)](y) \\ &= [\mathcal{C}(k_x, k_z) e^{\mathcal{A}(k_x, k_z)t} \mathbf{F}_s(k_x, k_z)](y) =: [\mathcal{G}_s(k_x, k_z, t)](y) \\ &= \begin{bmatrix} [\mathcal{C}_u(k_x, k_z) e^{\mathcal{A}(k_x, k_z)t} \mathbf{F}_s(k_x, k_z)](y) \\ [\mathcal{C}_v(k_x, k_z) e^{\mathcal{A}(k_x, k_z)t} \mathbf{F}_s(k_x, k_z)](y) \\ [\mathcal{C}_w(k_x, k_z) e^{\mathcal{A}(k_x, k_z)t} \mathbf{F}_s(k_x, k_z)](y) \end{bmatrix} =: \begin{bmatrix} [\mathcal{G}_{us}(k_x, k_z, t)](y) \\ [\mathcal{G}_{vs}(k_x, k_z, t)](y) \\ [\mathcal{G}_{ws}(k_x, k_z, t)](y) \end{bmatrix}.\end{aligned}$$

Operators \mathcal{G}_{rs} , $\{r = u, v, w; s = x, y, z\}$, contain a large amount of information about the dynamical behavior of system (7.22). In particular, application of an inverse spatial Fourier transform yields solutions that can be visualized in the physical space. In addition to that, some intuition can be gained by analyzing

quantities that aggregate the effects of dynamics in a certain spatial and/or temporal direction. For example, the wall-normal dynamics can be comprised by computing the Hilbert–Schmidt norm of operator \mathcal{G}_s

$$\begin{aligned} [\|\mathcal{G}_s\|_{HS}^2](k_x, k_z, t) &:= \text{trace}(\mathcal{G}_s^*(k_x, k_z, t)\mathcal{G}_s(k_x, k_z, t)) = \text{trace}(\mathcal{G}_s(k_x, k_z, t)\mathcal{G}_s^*(k_x, k_z, t)) \\ &= \text{trace}(\mathbf{F}_s^*(k_x, k_z)e^{\mathcal{A}^*(k_x, k_z)t}\mathcal{C}^*(k_x, k_z)\mathcal{C}(k_x, k_z)e^{\mathcal{A}(k_x, k_z)t}\mathbf{F}_s(k_x, k_z)) \\ &= \text{trace}(\mathcal{C}(k_x, k_z)e^{\mathcal{A}(k_x, k_z)t}\mathbf{F}_s(k_x, k_z)\mathbf{F}_s^*(k_x, k_z)e^{\mathcal{A}^*(k_x, k_z)t}\mathcal{C}^*(k_x, k_z)). \end{aligned} \quad (10.2)$$

It can be shown that, for example, $[\|\mathcal{G}_s\|_{HS}^2](k_x, k_z, t)$ represents the kinetic energy density of a harmonic perturbation in the presence of the streamwise forcing. This quantity is commonly used as a measure of the velocity field perturbations [11]. The kinetic energy density can be further averaged over the remaining spatial directions or time:

$$[\|\mathcal{G}_s\|_2^2](k_x, k_z) := \int_0^\infty [\|\mathcal{G}_s\|_{HS}^2](k_x, k_z, t) dt, \quad (10.3)$$

$$[\|\mathcal{G}_s\|_2^2](k_x, t) := \frac{1}{2\pi} \int_{-\infty}^\infty [\|\mathcal{G}_s\|_{HS}^2](k_x, k_z, t) dk_z, \quad (10.4)$$

and so on. The quantity defined by (10.3) can be also interpreted as the \mathcal{H}_2 norm of system (7.22) in the presence of an external excitation applied in the spatial direction s , $\{s = x, y, z\}$ [12].

We remind the reader that, for stable systems, the \mathcal{H}_2 norm can be determined using the solutions of the operator algebraic Lyapunov equations (see Chapter 2)

$$\begin{aligned} \mathcal{A}^*(k_x, k_z)\mathcal{Y}(k_x, k_z) + \mathcal{Y}(k_x, k_z)\mathcal{A}(k_x, k_z) &= -\mathcal{C}^*(k_x, k_z)\mathcal{C}(k_x, k_z), \\ \mathcal{A}(k_x, k_z)\mathcal{X}_s(k_x, k_z) + \mathcal{X}_s(k_x, k_z)\mathcal{A}^*(k_x, k_z) &= -\mathbf{F}_s(k_x, k_z)\mathbf{F}_s^*(k_x, k_z), \end{aligned}$$

where \mathcal{A}^* , \mathbf{F}_s^* , and \mathcal{C}^* respectively represent adjoints of operators \mathcal{A} , \mathbf{F}_s , and \mathcal{C} . The \mathcal{H}_2 norm is then computed from either of the following two expressions

$$[\|\mathcal{G}_s\|_2^2](k_x, k_z) = \text{trace}\{\mathbf{F}_s^*(k_x, k_z)\mathcal{Y}(k_x, k_z)\mathbf{F}_s(k_x, k_z)\} = \text{trace}\{\mathcal{C}(k_x, k_z)\mathcal{X}_s(k_x, k_z)\mathcal{C}^*(k_x, k_z)\}.$$

The input distribution in the wall-normal direction can be chosen in a number of different ways. Since our primary objective is computation of the spatio-temporal impulse responses we would like to introduce an input that is a delta function in y as well. Because of this, we choose f_{s0} of the form

$$f_{s0}(y) = \delta(y - y_0), \quad s = x, y, z, \quad -1 < y_0 < 1.$$

However, since we have to approximate the equations in y numerically, the desired choice of f_{s0} has to be approximated with something that is similar to the Dirac function. Using an alternative definition of the delta function

$$\delta(y - y_0) := \lim_{\varepsilon \rightarrow 0^+} \frac{1}{2\sqrt{\pi\varepsilon}} e^{-\frac{(y - y_0)^2}{4\varepsilon}},$$

we propose the following choice for $f_{s0}(y)$

$$f_{s0}(y) = \frac{1}{2\sqrt{\pi\varepsilon}} e^{-\frac{(y - y_0)^2}{4\varepsilon}}, \quad \varepsilon > 0.$$

Figure 10.1 shows $f_{s0}(y)$ for $y_0 = -0.9$, and $\varepsilon = 1/2000$. Clearly, the shape of the disturbance is not an ideal impulse in the y direction, but is an approximation that is good enough to capture the phenomena we are interested in.

The mathematical considerations required for a precise description of the above operators and their adjoints are included in § 7.1.2. Section 10.2 contains the description of numerical results obtained by

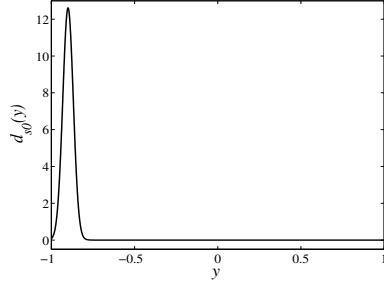


Figure 10.1: Forcing distribution in the wall-normal direction for $y_0 = -0.9$, and $\varepsilon = 1/2000$.

computing the impulse response of the LNS equations in subcritical Poiseuille flow with $R = 2000$.

10.2 Spatio-temporal impulse responses in Poiseuille flow with $R = 2000$

In this section, we study the spatio-temporal impulse responses of the LNS equations in plane Poiseuille flow with $R = 2000$. All computations are done for $R = 2000$, with 40 v and ω_y basis functions ($N = M = 39$). Both streamwise constant ($k_x = 0$) and full three-dimensional perturbations are considered. The numerical computations for these two cases are performed by gridding in the wave-number space and then applying an inverse Fourier transform to obtain the solutions in the physical space. The streamwise constant calculations are performed using 1024 linearly spaced Fourier modes in the z -direction with $\{k_{zmin} := -200, k_{zmax} := 200\}$. The number of grid points in the full three-dimensional computations was different for earlier and later time instants. For $t = \{5, 10, 15, 20\}$, computations are performed with 256×256 linearly spaced grid points in the (k_x, k_z) -plane, with $\{k_{xmin} := -20, k_{xmax} := 19.84375\}$ and $\{k_{zmin} := -30, k_{zmax} := 30\}$. For later times ($t = \{40, 80, 120, 160\}$) the wave-number plane was divided into 512×256 linearly spaced points with $\{k_{xmin} := -5, k_{xmax} := 4.98046875\}$ and $\{k_{zmin} := -18, k_{zmax} := 18\}$. Only half the number of modes in the spanwise direction are used due to symmetry properties. The ODEs for spectral coefficients are solved in MATLAB using the numerical scheme described in § 7.2.

10.2.1 Impulse responses for streamwise independent perturbations

Figure 10.2 illustrates the k_z -parameterized \mathcal{H}_2 norms of operators \mathcal{G}_s , $s = \{x, y, z\}$, for streamwise independent perturbations. The shown quantities are obtained based on solutions of the corresponding Lyapunov equations presented in § 10.1. We notice characteristic peaks in the middle and right plots. On the other hand, $[\|\mathcal{G}_x\|_2](k_z)$ decays monotonically as k_z increases, and achieves much smaller values than both $[\|\mathcal{G}_y\|_2](k_z)$ and $[\|\mathcal{G}_z\|_2](k_z)$. Also, we observe that the spanwise forcing experiences almost an order of magnitude larger amplification than the wall-normal forcing.

The kinetic energy density of streamwise constant perturbations, as a function of time, is shown in Figure 10.3. The k_z -dependence is averaged according to (10.4). Clearly, the kinetic energy density decays monotonically in the presence of d_x . On the other hand, when either d_y or d_z is introduced the kinetic energy density experiences transient amplification before eventual decay. We also observe that $[\|\mathcal{G}_y\|_2](t)$ peaks sooner than $[\|\mathcal{G}_z\|_2](t)$. Furthermore, the former quantity has much bigger rate of decay than the latter. These facts together with the results shown in Figure 10.2 imply that, at $k_x = 0$, the spatio-temporal impulsive forcing located in the vicinity of the lower wall is, by far, most effective when applied in the spanwise direction. This is in agreement with our results presented in § 9.4 where, for the streamwise constant perturbations, we analytically established that the spanwise near-wall forcing has the strongest effect on the evolution of the velocity components.

The spatio-temporal impulse response to the z -direction force at $k_x = 0$ is shown in Figure 10.4. In

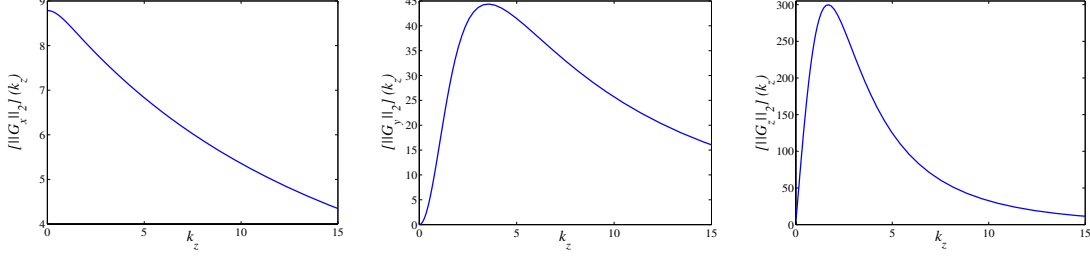


Figure 10.2: Plots of $[\|\mathcal{G}_x\|_2](k_z)$, $[\|\mathcal{G}_y\|_2](k_z)$, and $[\|\mathcal{G}_z\|_2](k_z)$ for streamwise constant perturbations. Forcing of the form $d_s = f_{s0}(y)\delta(z, t)$ is introduced, where $f_{s0}(y)$, for every $s = x, y, z$, is shown in Figure 10.1.

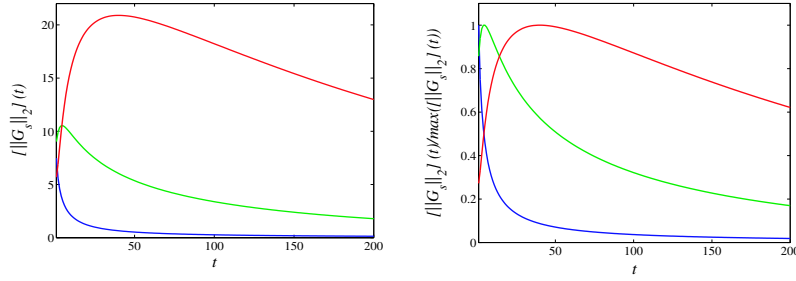


Figure 10.3: Plots of $[\|\mathcal{G}_x\|_2](t)$ (blue), $[\|\mathcal{G}_y\|_2](t)$ (green), and $[\|\mathcal{G}_z\|_2](t)$ (red) for streamwise constant perturbations. Forcing of the form $d_s = f_{s0}(y)\delta(z, t)$ is introduced, where $f_{s0}(y)$, for every $s = x, y, z$, is shown in Figure 10.1.

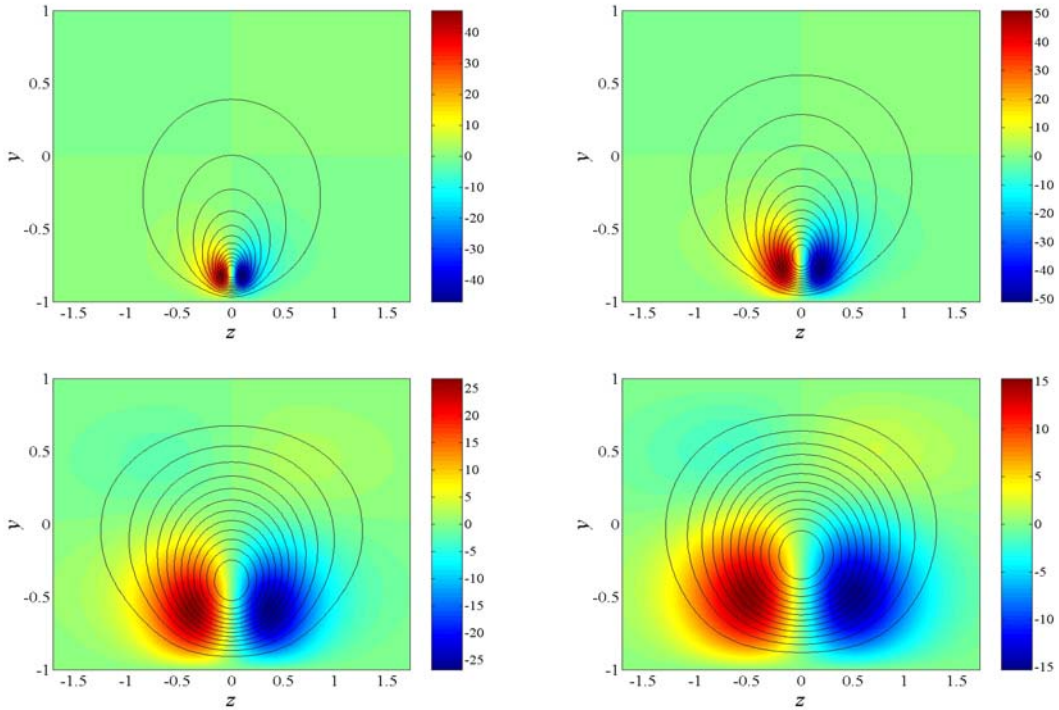


Figure 10.4: Streamwise velocity (pseudo-color plots) and stream-function (contour plots) perturbation development for streamwise constant perturbations at: $t = 5\text{ s}$ (top left), $t = 20\text{ s}$ (top right), $t = 100\text{ s}$ (bottom left), and $t = 200\text{ s}$ (bottom right). Forcing of the form $d_x = d_y \equiv 0$, $d_z = f_{z0}(y)\delta(z,t)$ is introduced, where $f_{z0}(y)$ is shown in Figure 10.1. Red color represents high speed streak, and blue color represents low speed streak. The vortex between the streaks is counter clockwise rotating.

particular, the pseudo-color plots of the streamwise velocity perturbation and contour plots of the stream-function in the (z, y) -plane are shown. These plots reveal the presence of a counter clockwise rotating vortex, a low speed streak, and a high speed streak. Clearly, the vortex is positioned between the high speed and the low speed streaks. We note that the streaks magnitude increases in the early stages of their development and afterwards it slowly decreases. The streaks also spread in both the wall-normal and the spanwise directions as time goes on. These facts explain the transient energy amplification and consequent slow rate of decay observed in Figure 10.3. Furthermore, the dominant structures are confined to the region between the lower wall and the channel's centerline, whereas a much weaker pair of streaks develops in the upper part of the channel. This can be attributed to the fact that the shape of the input in y is approximated by an impulse located near the lower wall. The full three-dimensional computations, that we discuss in § 10.2.2, reveal the existence of alternating regions of high and low velocities in the spanwise directions, the feature not observed in the computations performed at $k_x = 0$.

10.2.2 Impulse responses for full three-dimensional perturbations

Figure 10.5 shows the \mathcal{H}_2 norm of three-dimensional perturbations, as a function of both k_x and k_z . The quantities defined by (10.3) are determined based on solutions of the corresponding Lyapunov equations, with 50×90 grid points in the wave-number space (k_x, k_z) . These points are chosen in the logarithmic scale with $\{k_{xmin} := 10^{-4}, k_{xmax} := 3.02\}$ and $\{k_{zmin} := 10^{-2}, k_{zmax} := 15.84\}$. Clearly, both $\|\mathcal{G}_y\|_2(k_x, k_z)$ and $\|\mathcal{G}_z\|_2(k_x, k_z)$ achieve largest values for a relatively broad range of streamwise wave-numbers. The global maxima of these two quantities occur at $(k_x = 0, k_z = O(1))$. On the other hand, in the left plot

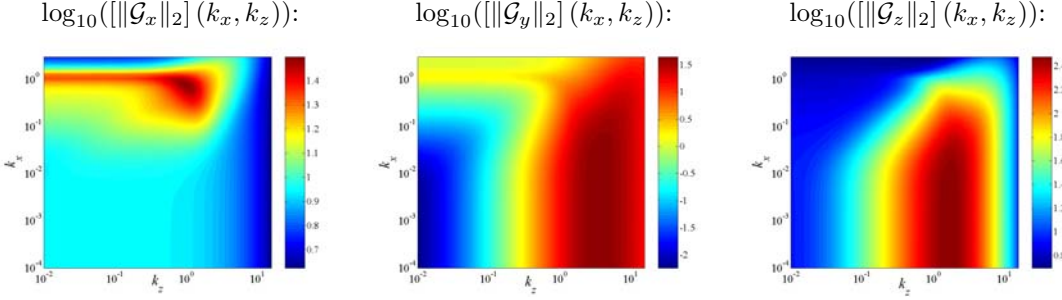


Figure 10.5: Plots of $\|\mathcal{G}_x\|_2(k_x, k_z)$, $\|\mathcal{G}_y\|_2(k_x, k_z)$, and $\|\mathcal{G}_z\|_2(k_x, k_z)$. Forcing of the form $d_s = f_{s0}(y)\delta(x, z, t)$ is introduced, where $f_{s0}(y)$, for every $s = x, y, z$, is shown in Figure 10.1.

the maximum takes place in the narrow region located in the vicinity of $(k_x \approx 1, k_z \approx 1)$. We also observe a distinct local peak at $k_z = 0$ on the same plot, which corresponds to the TS wave. Furthermore, the \mathcal{H}_2 norm achieves the largest values when d_z is introduced, which is in agreement with the previously discussed $k_x = 0$ results. This further illustrates that a forcing confined to the near-wall region is much more efficient when applied in the spanwise direction than in the other two spatial directions.

In the remainder of this section, we respectively investigate the spatio-temporal impulse responses of the LNS system for forces applied in all three spatial directions.

The three-dimensional isosurface plots of u , obtained in the presence of an impulsive spanwise forcing, are shown in Figure 10.6. Our results illustrate the propagation of the streamwise velocity perturbation as a function of both time and spatial coordinates. It seems that perturbation spreads quickly to the upper part of the channel. Further, it is noteworthy that the early stages of perturbation development are characterized by the streamwise variations in the velocity profile. These streamwise variations become less prominent as time goes on. For larger times the perturbation evolution is dominated by the structures elongated in the direction of a nominal flow. These streamwise streaky structures are usually identified in the experimental investigations related to the laminar-turbulent transition in both channel [6, 10, 13] and boundary layer flows [14, 15]. We also observe two well developed regions almost antisymmetric with respect to the horizontal plane $y = 0$ that divides the computational domain into two parts of equal size. The reason for their existence is shear, which, in Poiseuille flow, is equal to zero in the middle of the channel and grows linearly in the same fashion as one approaches either the lower or the upper wall.

Figure 10.7 shows the pseudo-color plots of the streamwise velocity perturbation profile in the horizontal plane $y \approx 0.68$ at eight different time instants. These results are obtained as a response to an impulsive spanwise forcing. The first four plots indicate the presence of streamwise varying structures in the early stages of perturbation development. On the other hand, the last four plots have the rather characteristic downstream pointing arrow-head shapes, with streamwise streaky structures ubiquitous in experimental studies of both channel [6, 10, 13] and boundary layer flows [14, 15]. We also note that the magnitude of u increases in the early stages of perturbation development and afterwards it slowly decreases. Furthermore, all plots clearly illustrate the spanwise cross-contamination and perturbation development in both x and z as time progresses. As previously mentioned, the appearance of alternating regions of high and low velocities in the spanwise direction is not a feature of the streamwise constant perturbations. Rather, it is a phenomenon that occurs only when the full three-dimensional perturbations are considered. It seems that the absence of the downstream convection at $k_x = 0$ prevents spanwise cross-contamination. Furthermore, for the streamwise constant perturbations, ω_x depends only on v (cf. (7.11)), which significantly reduces the production of the streamwise vorticity in this case. This may serve as yet another explanation with regard to why the alternating regions of high and low speed streaks are observed only in the full three-dimensional computations. However, we remark that the streaks do not propagate in the spanwise direction. The spanwise spreading of the streamwise perturbation structure is due to the creation of new weaker streaks, rather than the propagation of the existing ones [10].

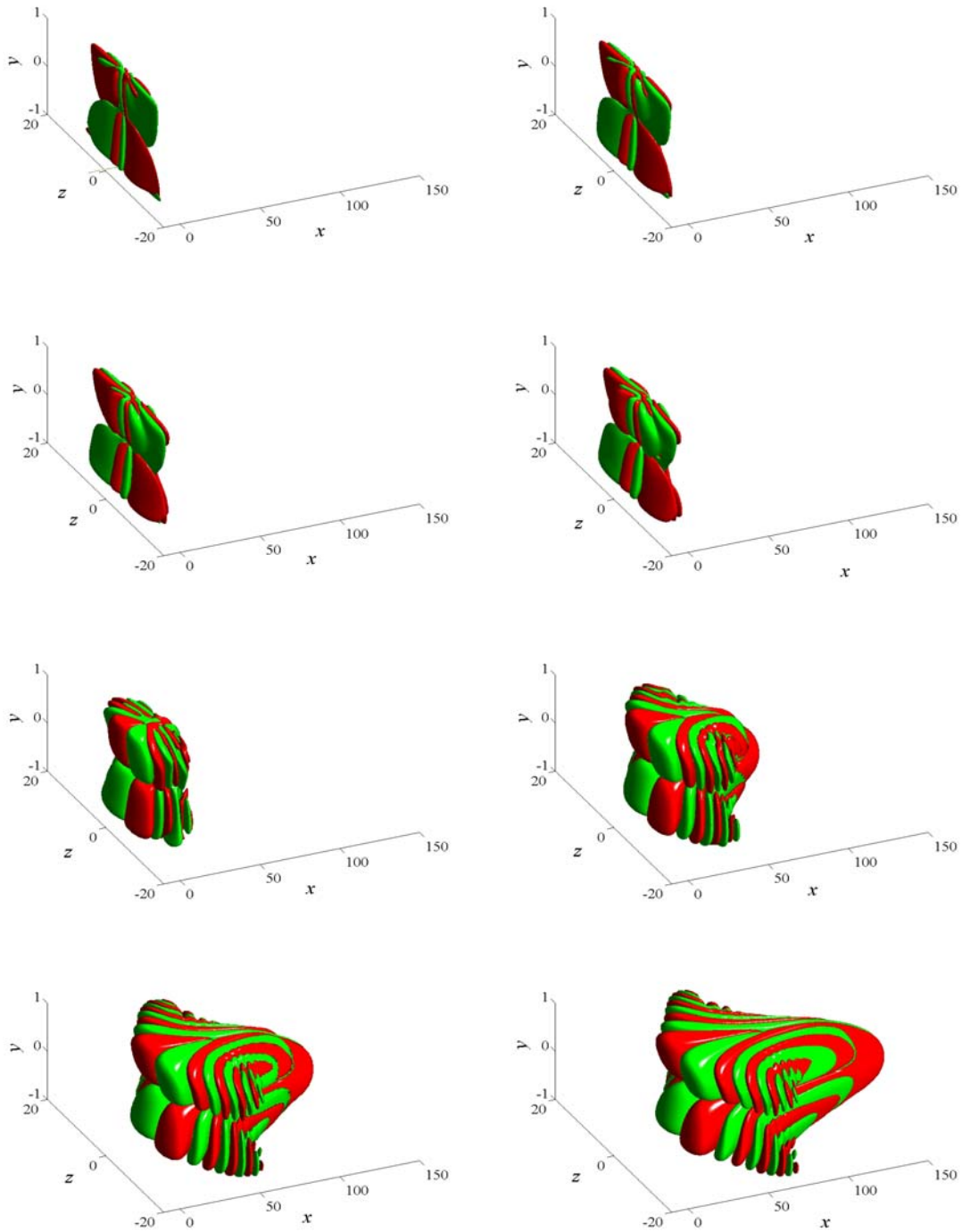


Figure 10.6: Streamwise velocity perturbation isosurface plots at: $t = 5\text{ s}$ (first row left), $t = 10\text{ s}$ (first row right), $t = 15\text{ s}$ (second row left), $t = 20\text{ s}$ (second row right), $t = 40\text{ s}$ (third row left), $t = 80\text{ s}$ (third row right), $t = 120\text{ s}$ (fourth row left), and $t = 160\text{ s}$ (fourth row right). Forcing of the form $d_x = d_y \equiv 0$, $d_z = f_{z0}(y)\delta(x, z, t)$ is introduced, where $f_{z0}(y)$ is shown in Figure 10.1. Red color represents regions of high velocity, and green color represents regions of low velocity. Isosurfaces are taken at $\pm 10^{-3}$.

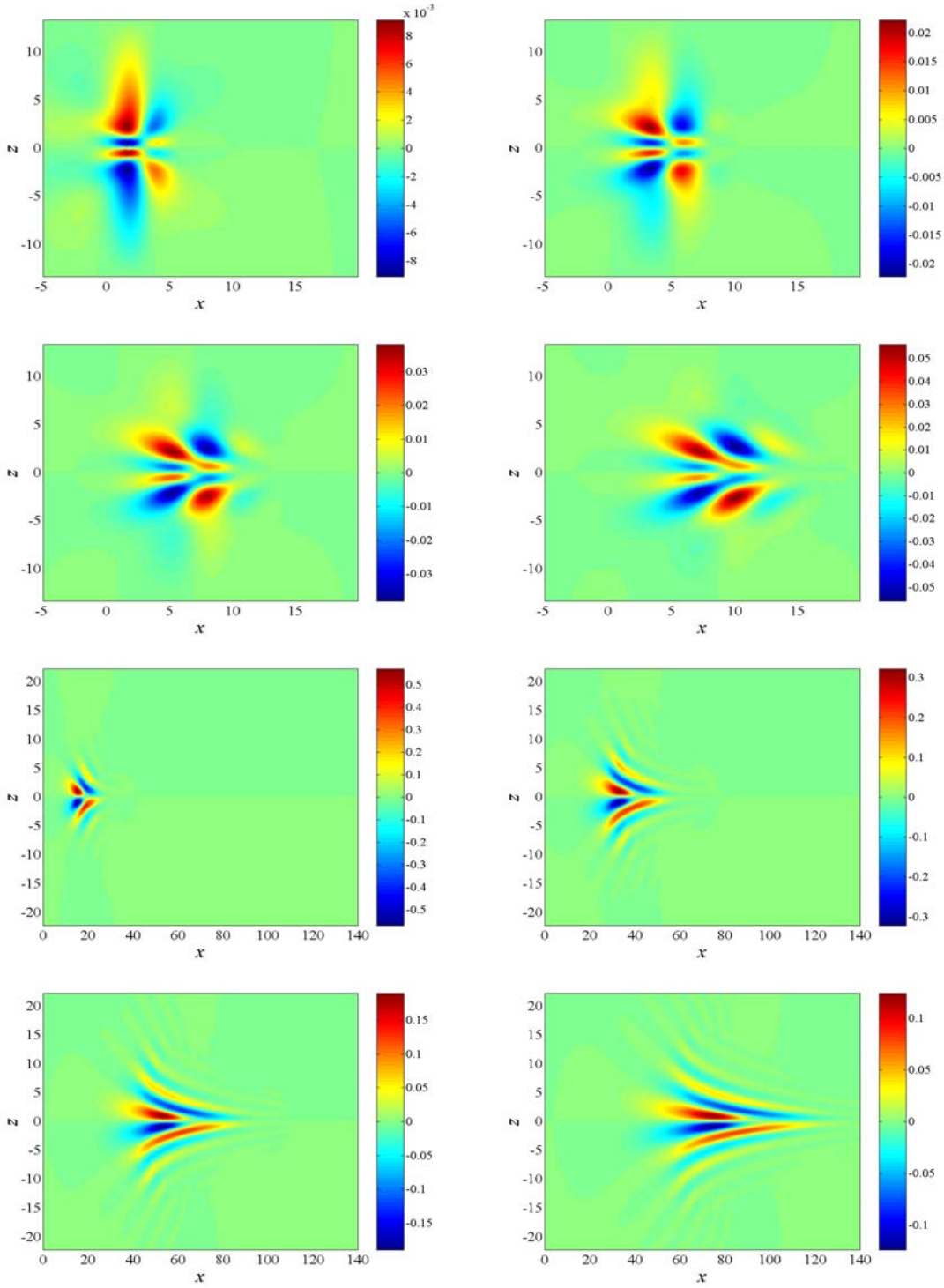


Figure 10.7: Streamwise velocity perturbation pseudo-color plots in the horizontal plane $y \approx 0.68$ at: $t = 5\text{ s}$ (first row left), $t = 10\text{ s}$ (first row right), $t = 15\text{ s}$ (second row left), $t = 20\text{ s}$ (second row right), $t = 40\text{ s}$ (third row left), $t = 80\text{ s}$ (third row right), $t = 120\text{ s}$ (fourth row left), and $t = 160\text{ s}$ (fourth row right). Forcing of the form $d_x = d_y \equiv 0$, $d_z = f_{z0}(y)\delta(x, z, t)$ is introduced, where $f_{z0}(y)$ is shown in Figure 10.1. Hot colors represent regions of high velocity, and cold colors represent regions of low velocity.

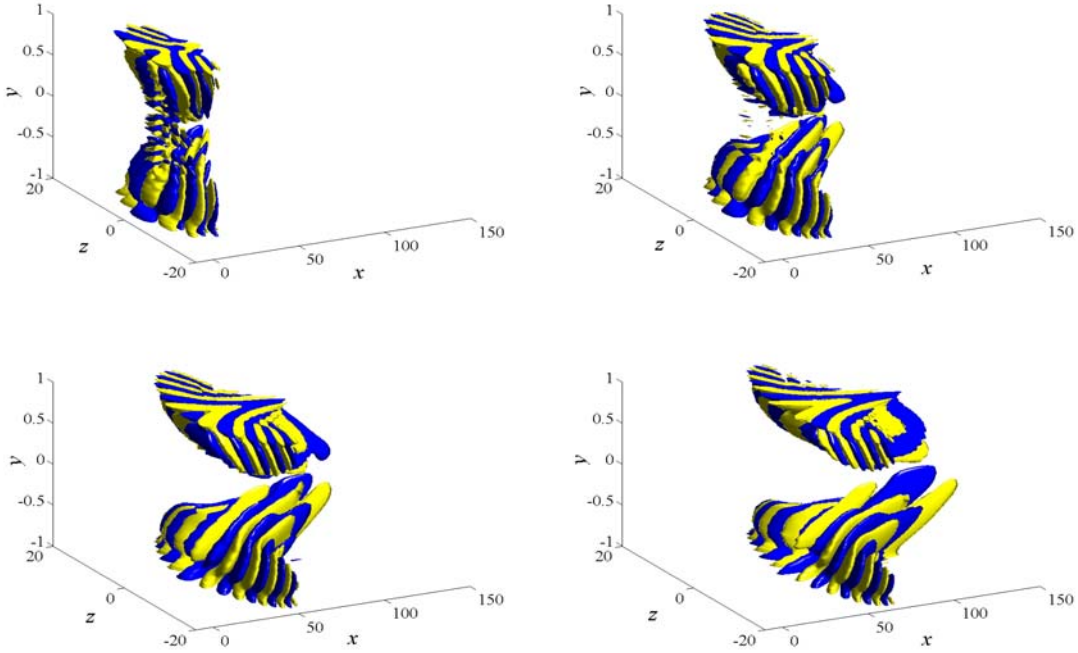


Figure 10.8: Streamwise vorticity isosurface plots at: $t = 40\text{ s}$ (top left), $t = 80\text{ s}$ (top right), $t = 120\text{ s}$ (bottom left), and $t = 160\text{ s}$ (bottom right). Forcing of the form $d_x = d_y \equiv 0$, $d_z = f_{z0}(y)\delta(x, z, t)$ is introduced, where $f_{z0}(y)$ is shown in Figure 10.1. Yellow color represents regions of high vorticity, and blue color represents regions of low vorticity. Isosurfaces are taken at $\pm 10^{-2}$.

The streamwise vorticity development in the presence of an impulsive spanwise forcing is shown in Figure 10.8. The developed structures are reminiscent of the Λ -vortices which are usually associated with the transition studies related to the secondary instability of the TS wave [17–20]. These vortices can emerge in either an aligned or a staggered pattern. Herbert [20] observed that the staggered arrangement dominates the so-called ‘natural transition’. Clearly, the spanwise impulsive forcing gives rise to the vortices that appear in the staggered configuration. It is quite remarkable that the input-output linearized model is able to generate structures traditionally thought of as being product of nonlinear interactions between two-dimensional and three-dimensional waves. The theoretical explanation of this observation is a topic of an ongoing research effort and it is outside the scope of the present study. Also, it is noteworthy that the vortex structure elongates downstream as time goes on. This is quite understandable taking into account that the perturbations further away from the walls have a higher propagation speed than their near wall analogues.

The pseudo-color plots of u and ω_x generated by an impulsive spanwise forcing are shown in Figure 10.9. A slice in a channel’s cross section is taken at $x \approx 56$ and $t = 160\text{ s}$. These plots further demonstrate the aforementioned spanwise cross-contamination and clearly show that the regions of high (warm colors) and low (cold colors) velocities occur in an alternating arrangement. We observe both wall-normal and spanwise gradients in u which indicates presence of both ω_y and ω_z . Similar observation was made by [10] in her experimental study of subcritical transition in Poiseuille flow. Furthermore, Klingmann [10] remarked that the inclination of the shear layer in the channel’s cross section may be a sign of streamwise vorticity. Indeed, our results support this assertion. Namely, it is apparent that there is a very large concentration of arrays of counter rotating streamwise vortices in the vicinity of the lower and upper walls. These streamwise vortices transport low-velocity fluid away from the walls towards the channel centerline and redistribute it in the spanwise direction.

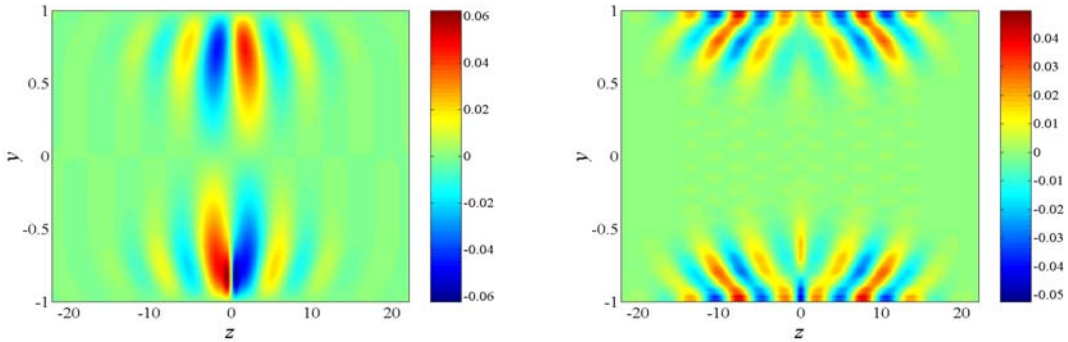


Figure 10.9: Pseudo-color plots of the streamwise velocity (left) and vorticity (right) perturbation profiles in a cross section of the channel at $x \approx 56$ and $t = 160$ s. Forcing of the form $d_x = d_y \equiv 0$, $d_z = f_{z0}(y)\delta(x, z, t)$ is introduced, where $f_{z0}(y)$ is shown in Figure 10.1.

The three-dimensional isosurface plots and the pseudo-color plots of u in the horizontal plane at $y \approx 0.68$ are respectively illustrated in Figures 10.10 and 10.11. The shown results represent a response to an impulsive wall-normal forcing. The early stages of perturbation development are dominated by the oblique waves, as for the ‘ d_z impulse response computations’. These streamwise varying structures can be also observed in the later phases of spot evolution, even though the streamwise elongated effects become dominant for larger times. The three-dimensional isosurface plots indicate the presence of two forward pointing arrowhead-shaped shear layers with ‘legs’ that extend in the upstream direction towards the walls, as in the case of the ‘ d_z impulse response results’. Remarkably, this shape of disturbance was postulated by Klingmann [10] in her analysis of the streamwise velocity perturbation contour plots in the (y, z) -plane. These contour plots were obtained experimentally by essentially determining the response of the subcritical Poiseuille flow to an impulsive y -direction forcing. A sequence of measurements was made at different time instants by traversing a single hot-wire probe in a channel’s cross section in both wall-normal and spanwise directions. Based on our two dimensional pseudo-color plots, it seems that the entire structure elongates at approximately a constant rate during its downstream propagation. Landahl [4] theoretically predicted that the streamwise extent of the disturbed region grows linearly with time for all parallel inviscid shear flows. Furthermore, the new streaks of fairly weak magnitude appear on the spanwise edges of the spot as it travels downstream.

The streamwise forcing impulse response results are shown in Figures 10.12 and 10.13, where we respectively illustrate the three-dimensional isosurface plots, and the pseudo-color plots of u in the horizontal plane at $y \approx 0.68$. The presence of oblique waves is much more prominent here than in the ‘ d_y and d_z impulse response computations’. Even though the perturbation elongates as time goes on and shapes into the characteristic arrow-head downstream-oriented structure, the streamwise variations dominate its development. From the left plot in Figure 10.5, we recall that the peaks of the \mathcal{H}_2 norm in the presence of d_x take place at $O(1)$ values of both k_x and k_z . This fact may serve as an explanation for fairly rich streamwise behavior when linearized dynamics are forced by d_x .

All results shown in this subsection illustrate the ability of the linearized model subject to external forces to generate, at least qualitatively, structures (oblique waves, streamwise vortices and streaks) usually observed in experimental laminar-turbulent transition investigation in wall-bounded shear flows [6,10,13–15].

10.3 Summary

We consider the NS equations linearized about a parallel channel flow of the form $U(y) = 1 - y^2$ in the presence of spatially distributed three-dimensional body forces. We carry out an input-output analysis to investigate the dependence of various velocity and vorticity ‘outputs’ on the various impulsive body force ‘inputs’. The spatio-temporal impulse responses of the LNS equations in channel flows, to our knowledge, have not been

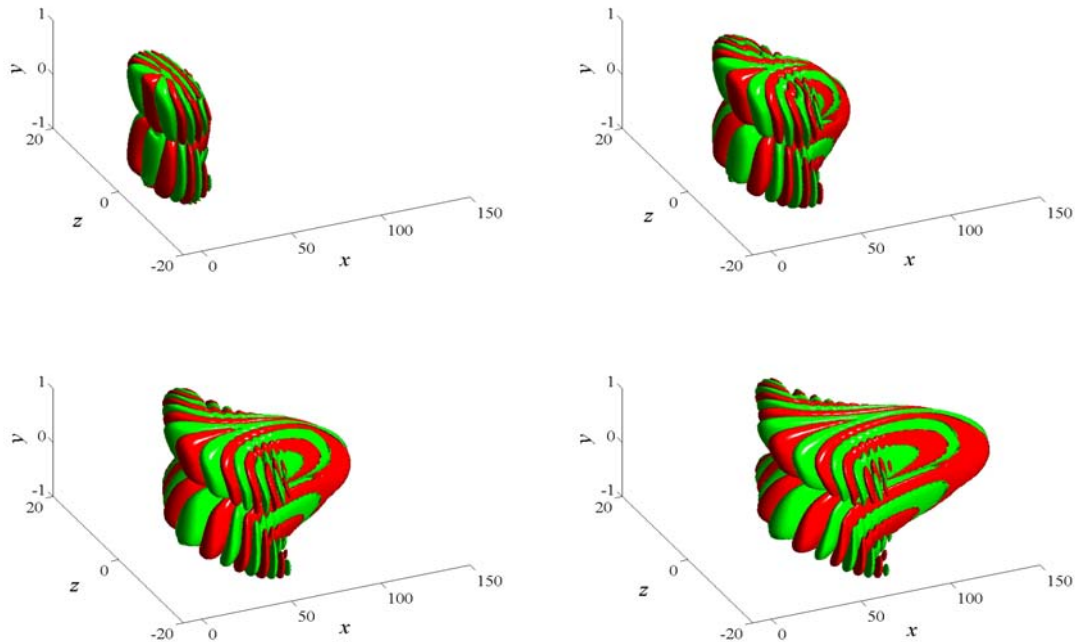


Figure 10.10: Streamwise velocity perturbation isosurface plot at: $t = 40 s$ (top left), $t = 80 s$ (top right), $t = 120 s$ (bottom left), and $t = 160 s$ (bottom right). Forcing of the form $d_x = d_z \equiv 0$, $d_y = f_{y0}(y)\delta(x, z, t)$ is introduced, where $f_{y0}(y)$ is shown in Figure 10.1. Red color represents regions of high velocity, and green color represents regions of low velocity. Isosurfaces are taken at $\pm 2 \times 10^{-4}$.

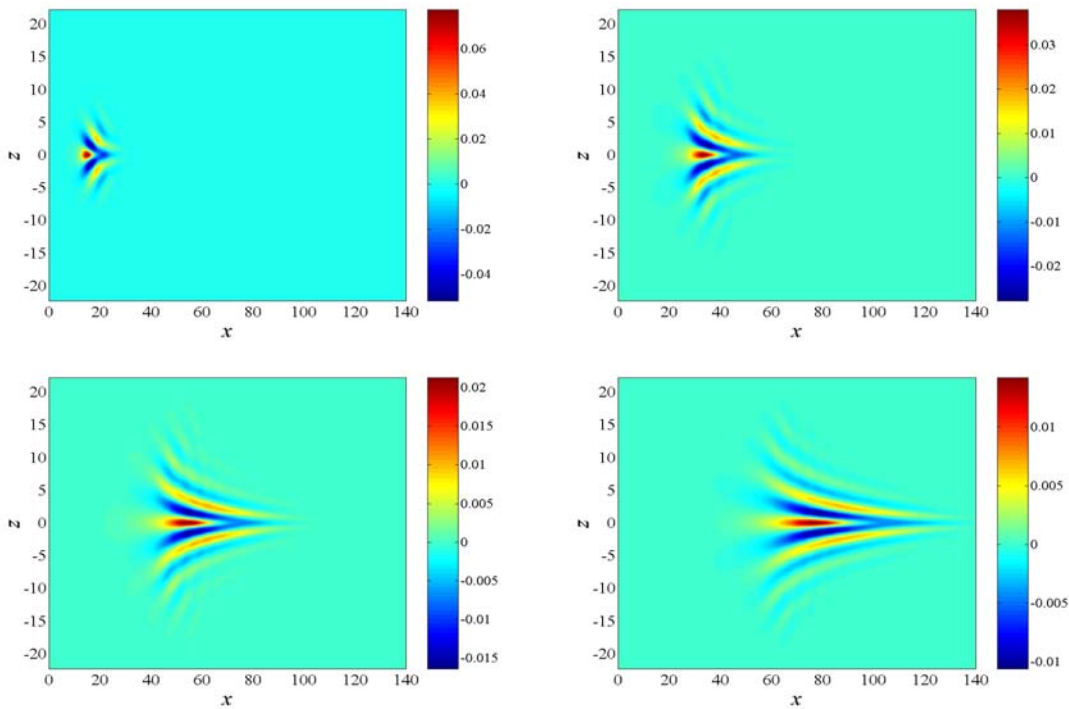


Figure 10.11: Streamwise velocity perturbation pseudo-color plots in the horizontal plane $y \approx 0.68$ at: $t = 40\text{ s}$ (top left), $t = 80\text{ s}$ (top right), $t = 120\text{ s}$ (bottom left), and $t = 160\text{ s}$ (bottom right). Forcing of the form $d_x = d_z \equiv 0$, $d_y = f_{y0}(y)\delta(x, z, t)$ is introduced, where $f_{y0}(y)$ is shown in Figure 10.1. Hot colors represent regions of high velocity, and cold colors represent regions of low velocity.

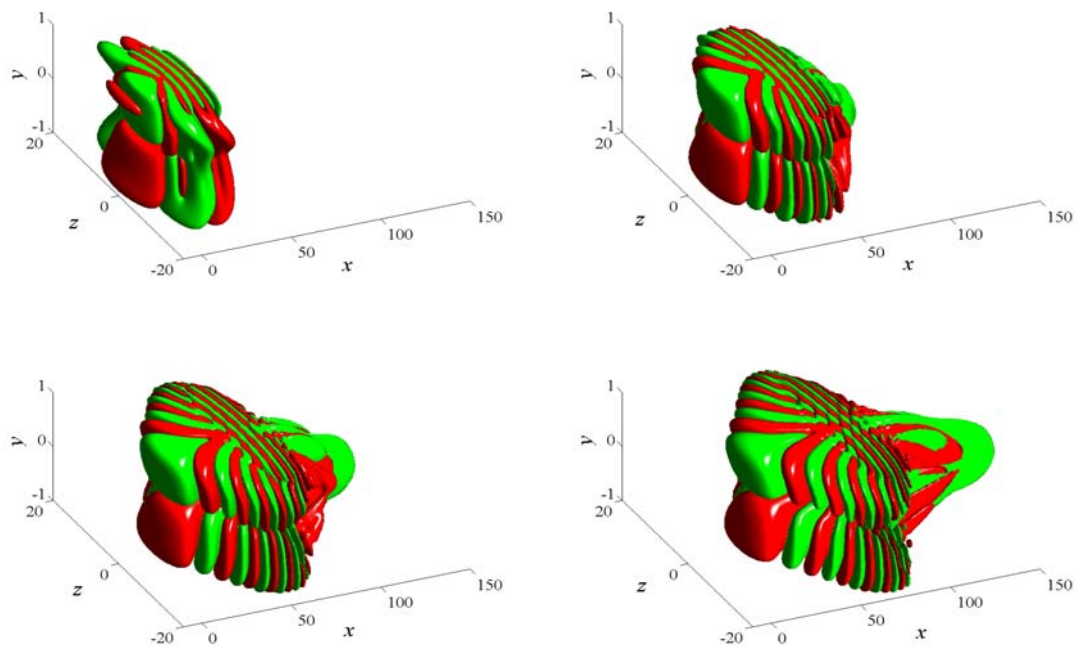


Figure 10.12: Streamwise velocity perturbation isosurface plots at: $t = 40 s$ (top left), $t = 80 s$ (top right), $t = 120 s$ (bottom left), and $t = 160 s$ (bottom right). Forcing of the form $d_y = d_z \equiv 0$, $d_x = f_{x0}(y)\delta(x, z, t)$ is introduced, where $f_{x0}(y)$ is shown in Figure 10.1. Red color represents regions of high velocity, and green color represents regions of low velocity. Isosurfaces are taken at $\pm 2 \times 10^{-4}$.

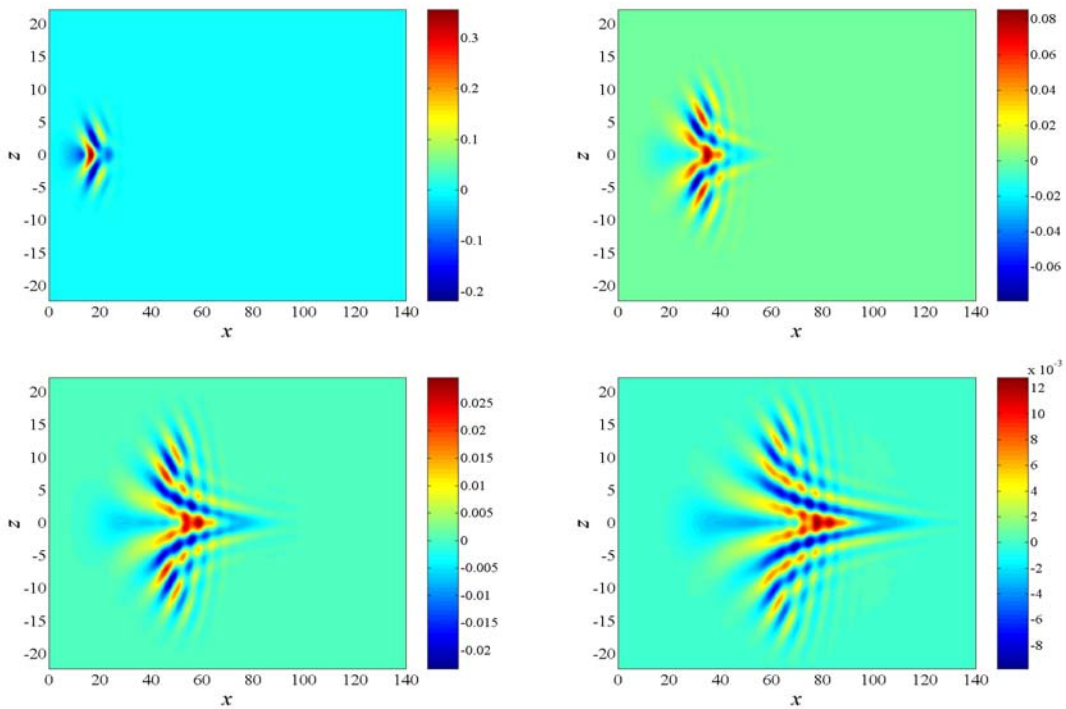


Figure 10.13: Streamwise velocity perturbation pseudo-color plots in the horizontal plane $y \approx 0.68$ at: $t = 40\text{ s}$ (top left), $t = 80\text{ s}$ (top right), $t = 120\text{ s}$ (bottom left), and $t = 160\text{ s}$ (bottom right). Forcing of the form $d_y = d_z \equiv 0$, $d_x = f_{x0}(y)\delta(x, z, t)$ is introduced, where $f_{x0}(y)$ is shown in Figure 10.1. Hot colors represent regions of high velocity, and cold colors represent regions of low velocity.

previously reported in the literature. We show that the flow response to spatio-temporal impulsive inputs forms spot-like structures with an arrow-head shape that elongates as it convects downstream. These spots are made up of alternating and staggered regions of high and low speed velocity streaks with counter-rotating vortices between them. The identified structures are inclined with respect to the wall and their inclination changes as the spot grows or decays. The spots bear a qualitative similarity to structures observed in fully nonlinear initial value simulations in channel flows, while the streaky and vortical structures within them are qualitatively similar to those observed in turbulent boundary layers. As an argument for the need for this kind of impulse response analysis of the linearized equations, we point out that such structures are practically impossible to observe from a purely modal analysis of the LNS equations.

As a final remark we point out that the LNS equations appear to have very complex dynamics that can be explored in various ways. Significantly different flow structures are induced by exciting the flow in different manners. It has long been recognized that background excitation and uncertainty significantly impact the flow structures observed in channel flow and boundary layer experiments, and that full direct numerical simulations are capable of reproducing this rich behavior. We observe here that even the linearized equations appear to contain much of that behavior.

Bibliography

- [1] D. S. Henningson and J. Kim, “On turbulent spots in plane Poiseuille flow,” *J. Fluid Mech.*, vol. 228, pp. 183–205, 1991.
- [2] D. S. Henningson, A. Lundbladh, and A. V. Johansson, “A mechanism for bypass transition from localized disturbances in wall-bounded shear flows,” *J. Fluid Mech.*, vol. 250, pp. 169–207, 1993.
- [3] M. T. Landahl, “Wave breakdown and turbulence,” *SIAM J. Appl. Math.*, vol. 28, pp. 735–756, 1975.
- [4] ——, “A note on an algebraic instability of inviscid parallel shear flows,” *J. Fluid Mech.*, vol. 98, pp. 243–251, 1980.
- [5] F. Li and S. E. Widnall, “Wave patterns in plane Poiseuille flow created by concentrated disturbances,” *J. Fluid Mech.*, vol. 208, pp. 639–656, 1989.
- [6] D. R. Carlson, S. E. Widnall, and M. F. Peeters, “A flow-visualization study of transition in plane Poiseuille flow,” *J. Fluid Mech.*, vol. 121, pp. 487–505, 1982.
- [7] A. Lundbladh and A. V. Johansson, “Direct simulation of turbulent spots in plane Couette flow,” *J. Fluid Mech.*, vol. 229, pp. 499–516, 1991.
- [8] N. Tillmark and P. H. Alfredsson, “Experiments on transition in plane Couette flow,” *J. Fluid Mech.*, vol. 235, pp. 89–102, 1992.
- [9] O. Dauchot and F. Daviaud, “Finite amplitude perturbation and spots growth mechanism in plane Couette flow,” *Physics of Fluids*, vol. 7, no. 2, pp. 335–343, 1995.
- [10] B. G. B. Klingmann, “On transition due to three-dimensional disturbances in plane Poiseuille flow,” *J. Fluid Mech.*, vol. 240, pp. 167–195, 1992.
- [11] K. M. Butler and B. F. Farrell, “Three-dimensional optimal perturbations in viscous shear flow,” *Physics of Fluids A*, vol. 4, p. 1637, 1992.
- [12] K. Zhou, J. C. Doyle, and K. Glover, *Robust and Optimal Control*. Prentice Hall, 1996.
- [13] F. Alavyoon, D. S. Henningson, and P. H. Alfredsson, “Turbulent spots in plane Poiseuille flow - flow visualization,” *Physics of Fluids*, vol. 29, no. 4, pp. 1328–1331, 1986.
- [14] F. W. Chambers and A. S. W. Thomas, “Turbulent spots, wave packets, and growth,” *Physics of Fluids*, vol. 26, no. 5, pp. 1160–1162, 1983.
- [15] M. Matsubara and P. H. Alfredsson, “Disturbance growth in boundary layers subjected to free-stream turbulence,” *J. Fluid Mech.*, vol. 430, pp. 149–168, 2001.
- [16] B. Bamieh and M. Dahleh, “Energy amplification in channel flows with stochastic excitation,” *Physics of Fluids*, vol. 13, no. 11, pp. 3258–3269, 2001.
- [17] P. S. Klebanoff, K. D. Tidstrom, and L. M. Sargent, “The three-dimensional nature of boundary-layer instability,” *J. Fluid Mech.*, vol. 12, pp. 1–34, 1962.

- [18] V. V. Kozlov and M. P. Ramazanov, “Development of finite-amplitude disturbances in Poiseuille flow,” *J. Fluid Mech.*, vol. 147, pp. 149–157, 1984.
- [19] B. J. Bayly, S. A. Orszag, and T. Herbert, “Instability mechanisms in shear flow transition,” *Ann. Rev. Fluid Mech.*, vol. 20, pp. 359–391, 1988.
- [20] T. Herbert, “Secondary instability of boundary layers,” *Ann. Rev. Fluid Mech.*, vol. 20, pp. 487–526, 1988.

Chapter 11

Conclusions and future directions

Conclusions

In contrast to the large body of work by physicists and engineers with expertise in fluid mechanics, system theoreticians have made minimal contributions to the area of flow modeling and control. As this thesis demonstrates, a number of issues in fluid mechanics can be addressed effectively using system theoretical tools. For example, we have employed input-output system analysis to:

- Unravel new mechanisms for subcritical transition.
- Compare roles of TS waves, oblique waves, and streamwise vortices and streaks in subcritical transition.
- Quantify effectiveness of forcing components.
- Quantify energy content of velocity components.
- Compare roles of unstable and ‘non-normal’ modes in supercritical flows.
- Study spatio-temporal impulse responses of the LNS equations in Poiseuille flow.

Thus, we have demonstrated that modern control theory can be very effective in advancing a classical field. On the other hand, system theoreticians can benefit tremendously from being exposed to fluid mechanical problems, because these physically relevant problems pose new theoretical challenges that traditionally have not been addressed in the control’s literature. In view of this, an interdisciplinary research effort is necessary to facilitate a transfer of knowledge from fluid mechanics to control and vice versa.

My goal is to continue development of systematic analysis and design procedures for understanding and controlling transitional and turbulent shear flows, using both system theoretical and fluid mechanical tools. Several topics for future research are given below.

Future directions

Modeling flow statistics using the LNS equations. In [1], we addressed the problem of modeling disturbances in the LNS equations by testing the validity—in *quantitative* sense—of a stochastically excited version of the linearized model. We developed a model for second order statistics of turbulent channel flow using an associated linear stochastically forced input-output system. Our results showed that certain portions of DNS-based flow statistics can be closely matched by the appropriate choice of input forcing covariance. This was done in an *ad hoc* fashion using a variety of excitation force correlations and showing the dependence of the velocity field statistics on them. We intend to develop a precise methodology for determination of external excitation statistics to guarantee matching DNS-based data in some optimal (e.g., least-squared) sense.

The motivation for this problem is twofold: a) model validation of the stochastically excited LNS equations, and b) proper weight selection in optimal control problems for drag reduction. We plan to use the input correlations determined in this way as a disturbance model in an \mathcal{H}_2 -optimal control problem. As is well known, proper weight selection can dramatically alter control performance when the controller is in feedback with the actual nonlinear system. It is therefore anticipated that an \mathcal{H}_2 controller designed using these weights will have superior performance to a controller designed without an accurate disturbance model. Furthermore, it is expected that this controller will lead to successful turbulence suppression with linear controllers in high Reynolds number flows.

Active and passive control of transition and turbulence. The use of Micro-Electro-Mechanical Systems (MEMS) devices for flow actuation and sensing is likely to revolutionize active and passive flow control in wall-bounded shear flows (e.g., boundary layer, pipe, and channel flows). This, however, would require a fully-integrated system design that accounts for the complex dynamics of flow phenomena. A work reported in this dissertation represents a step in that direction.

In this thesis, we have developed mathematical models that rigorously account for uncertain body forces. Also, we have initiated development of models that quantify the effects of both dynamical uncertainties and wall texture on flow perturbations. We plan to use these models as the basis for new control designs, including active (e.g., \mathcal{H}_2 and \mathcal{H}_∞) and passive control strategies for drag reduction.

Passive flow control is a promising technology for implementation. Examples of passive control strategies include: wall geometry deformation such as riblets and compliant walls, and flow control of conductive fluids using the Lorentz force. We are currently developing models in which wall geometry and electro-magnetic force parameters enter as coefficients and/or forcing terms in NS-type equations, and are to be used for either the suppression or enhancement of turbulence. We aim to perform a robustness analysis for these models, which will produce optimal parameters for wall geometry (e.g., spacing and height of riblets) or Lorentz force (e.g., amplitude and frequency of spatially periodic force). The new theory of input-output analysis of PDEs with periodic coefficients, developed in Chapter 4, will play a crucial role in this effort.

Analytical determination of energy amplification for full 3D LNS equations. Our ongoing research effort is directed towards development of explicit analytical expressions for the energy amplification of full three-dimensional perturbations in channel flows. This study will elucidate the relationship between TS waves, oblique waves, and streamwise vortices and streaks. It appears that convenient expressions for scaling of the \mathcal{H}_2 norm with the Reynolds number can be obtained if entire problem is parameterized by two new parameters: $\alpha := k_x^2 + k_z^2$ and $\beta := k_x R$.

Sensitivity with respect to boundary conditions. We have carried out sensitivity analysis of the LNS equations with respect to external excitations in the form of body forces. It is also relevant to study sensitivity of these equations with respect to boundary conditions. One motivation for this problem comes from observation that most active control strategies [2–6] use non-homogeneous boundary conditions in the wall-normal velocity as controls. In other words, blowing and suction on the channel walls is introduced to influence the evolution of flow perturbations. We are interested in finding out whether there are any advantages in using body forces rather than boundary conditions as feedback controls.

Bibliography

- [1] M. R. Jovanović and B. Bamieh, “Modelling flow statistics using the linearized Navier-Stokes equations,” in *Proceedings of the 40th IEEE Conference on Decision and Control*, Orlando, FL, 2001, pp. 4944–4949.
- [2] T. R. Bewley and S. Liu, “Optimal and robust control and estimation of linear paths to transition,” *J. Fluid Mech.*, vol. 365, pp. 305–349, 1998.
- [3] K. H. Lee, L. Cortelessi, J. Kim, and J. Speyer, “Application of reduced-order controller to turbulent flows for drag reduction,” *Physics of Fluids*, vol. 13, no. 5, pp. 1321–1330, 2001.
- [4] J. Kim, “Control of turbulent boundary layers,” *Physics of Fluids*, vol. 15, no. 5, pp. 1093–1105, 2003.
- [5] M. Höglberg, T. R. Bewley, and D. S. Henningson, “Linear feedback control and estimation of transition in plane channel flow,” *J. Fluid Mech.*, vol. 481, pp. 149–175, 2003.
- [6] ——, “Relaminarization of $R_{\text{et}} = 100$ turbulence using linear state-feedback control,” *Physics of Fluids*, vol. 15, no. 11, pp. 3572–3575, 2003.

Part III

Distributed control of systems on lattices

Chapter 12

Distributed backstepping control of systems on lattices

12.1 Introduction

Large arrays of spatially distributed dynamical systems are becoming prevalent in modern technological applications. These systems can range from the macroscopic—such as cross directional control in the process industry [1,2], vehicular platoons [3–9], Unmanned Aerial Vehicles (UAVs) [10–12], and satellites in formation flight [13–15]—to the microscopic, such as arrays of micro-mirrors [16] or micro-cantilevers [17]. Systems on lattices are characterized by interactions between different subsystems which often results into intricate behavioral patterns, an example of which is the so-called *string instability* [18] (or, more generally, the *spatio-temporal instability* [19]). The complex dynamical responses of these systems are caused by the aggregate effects, and they cannot be predicted by analyzing the individual plant units.

System on lattices have a special structure: each subsystem is equipped with sensing and actuating capabilities. Thus, the key design issues in the control of these systems are architectural such as the choice of localized versus centralized control. This problem has attracted a lot of attention in the last 25–30 years. A large body of literature in the area that is usually referred to as ‘decentralized control of large-scale systems’ has been created [20–28].

A framework for considering spatially distributed systems is that of a spatio-temporal system [29]. In the specific case of systems on lattices, signals of interest are functions of time and a spatial variable $n \in \mathbb{F}$, where \mathbb{F} is a discrete spatial lattice (any countable set, e.g. \mathbb{Z} or \mathbb{N}). Several authors utilized this framework in their studies of: control of vehicular platoons [3,4], control of discretized PDEs [30,31], control of ‘systems over rings’ [32–34], and control of systems with ‘dynamical symmetries’ [35,36]. In particular, Fagnani & Willems [35,36] showed that stability of linear dynamical plants with certain symmetries can be accomplished with controllers that have the same symmetry.

A particular class of spatio-temporal systems termed linear spatially invariant systems was considered in [19], where it was shown that optimal controllers (in a variety of norms) for spatially invariant plants inherit this spatially invariant structure. Furthermore, it was shown that optimal controllers with quadratic performance objectives (such as LQR, \mathcal{H}_2 , and \mathcal{H}_∞) have an inherent degree of spatial localization. These results can be used to motivate other design procedures (such as adaptive, fixed structure, etc.) for spatio-temporal systems based on certain *a priori* fixed controller structures which reflect the spatial variation and localization of the plant.

With *a priori* assumptions on the information passing structure in the distributed controller, sufficient conditions for internal stability and strict contractiveness can be expressed using Linear Matrix Inequality (LMI) conditions [37,38]. Similarly, control design for linear spatially varying distributed systems has been considered in [39], [40]. Conditions for synthesis are expressed in terms of convex operator inequalities, which in the particular cases of finite and periodic spatial domains simplify to linear matrix inequalities.

Adaptive identification and control are extensively studied for both linear (see, for example [41–44]) and

nonlinear [45] finite dimensional systems. Several researchers have also considered these problems in the infinite dimensional setting [46–52] and for spatially interconnected systems [15, 18, 20–26, 53–56]. We refer the reader to these references for a fuller discussion.

In this chapter, we study distributed control of nonlinear infinite dimensional systems on lattices. The motivation for studying this class of systems is twofold. First, we want to develop design tools for control of systems with large arrays of sensors and actuators. Several examples of systems with this property are given above. Also, our results can be used for control of discretized versions of PDEs with distributed controls and measurements. Second, infinite dimensional systems represent an insightful limit of large-scale systems: problems with, for example, stability of an infinite dimensional system indicate issues with performance of its large-scale equivalent. The latter point is illustrated in Chapter 13 where we utilize the theory for spatially invariant linear systems [19] to show that extending standard results from small to large-scale or infinite vehicular platoons has dangers.

We extend the well-known finite dimensional *integrator backstepping* design tool to a more general class of systems considered in this chapter. Backstepping approach is utilized to provide stability/regulation/asymptotic tracking of nominal systems and systems with parametric uncertainties. In the latter case, we assume that the unknown parameters are temporally constant, but are allowed to be either spatially constant or spatially varying. In both of these situations, we design adaptive Lyapunov-based estimators and controllers. As a result of our design, boundedness of all signals in the closed-loop in the presence of parametric uncertainties is guaranteed. In addition to that, the adaptive controllers provide convergence of the states of the original system to their desired values.

An important problem in the distributed control of large-scale and infinite dimensional systems on lattices is related to the choice of the appropriate controller architecture. In addition to utilizing backstepping as a tool for distributed control of systems on lattices, we also provide the answer to the following question: *what is the worst case controller architecture induced by distributed backstepping design?* We demonstrate that distributed backstepping design yields controllers that are intrinsically decentralized, with a strong similarity between plant and controller architectures. In particular, we study the ‘worst case’ control design in which all interactions are cancelled at each step of backstepping because it is convenient to describe the architectural ideas. Any other backstepping strategy yields controllers with better information transmission properties. For this ‘worst case’ situation we *quantify* the number of *control induced interactions* necessary to guarantee desired dynamical behavior. We show that this number depends on the number of interactions per plant cell and the largest number of integrators that separate interactions from control inputs. We also provide an example of systems on lattices and show how the controllers with favorable architectures can be designed.

The only situation which results in a centralized controller is for plants with temporally and spatially constant parametric uncertainties when we start our design with one parameter estimate per unknown parameter. It should be noted however that this problem can be circumvented by the ‘over-parameterization’ of the unknown constant parameters. As a result, every single control unit has its own update law of unknown parameters which avoids centralized architecture.

Backstepping is a well-studied design tool [45, 57] for finite dimensional systems. In the infinite dimensional setting, a backstepping controller was designed to suppress compression system instabilities for the nonlinear PDE Moore-Greitzer model [58]. Furthermore, a backstepping-like approach can be used to obtain stabilizing boundary feedback control laws for a class of parabolic systems (see [59, 60] for details). Backstepping boundary control can also be used as a tool for vibration suppression in flexible-link gantry robots [61]. However, backstepping has not been applied to distributed control of infinite dimensional systems on lattices to the best of our knowledge. We note that backstepping represents a recursive design scheme that can be used for systems in strict-feedback form with nonlinearities not constrained by linear bounds [45, 57]. At every step of backstepping, a new Control Lyapunov Function (CLF) is constructed by augmentation of the CLF from the previous step by a term which penalizes the error between ‘virtual control’ and its desired value (so-called ‘*stabilizing function*’). A major advantage of backstepping is the construction of a Lyapunov function whose derivative can be made negative definite by a variety of control laws rather than by a specific control law [45]. Furthermore, backstepping can be used for adaptive control of ‘parametric pure-feedback systems’ in which unknown parameters enter into equations in an affine manner [45].

Our presentation is organized as follows: in § 12.2, we introduce the notation used throughout this

chapter, give an example of systems on lattices, describe the classes of systems for which we design feedback controllers in § 12.3 (nominal state-feedback design), § 12.5 (adaptive state-feedback design), and § 12.7 (output-feedback design), discuss well-posedness of the open-loop systems, and describe different strategies that can be used for control of systems on lattices. In § 12.4, we discuss the architecture of distributed controllers induced by a nominal backstepping design, and show how controllers with less interactions can be obtained. In § 12.6, we analyze the dynamical order of distributed controllers induced by adaptive backstepping design. In § 12.8, we study in some detail the existence and uniqueness of solutions of the closed-loop systems obtained as a result of control design. In § 12.9, we discuss application of controllers developed in § 12.3, § 12.5, and § 12.7, analyze their structure, and validate their performance using computer simulations of systems containing a large number of units. We conclude by summarizing major contributions in § 12.10.

12.2 Systems on lattices

In this section an example of systems on lattices is given: we consider a mass-spring system on a line. This system is chosen because it represents a simple non-trivial example of an unstable system where the interactions between different plant units are caused by the physical connections between them. Another example of systems with this property is given by an array of microcantilevers. The interactions between different plant units may also arise because of a specific control objective that the designer wants to meet. Examples of systems on lattices with this property include: a system of cars in an infinite string (see Chapter 13), aerial vehicles and space crafts in formation flights. We also discuss the well-posedness of the unforced systems, describe the classes of systems for which we design state and output-feedback controllers in § 12.3, § 12.5, and § 12.7, and briefly outline different approaches to control of systems on lattices.

12.2.1 Notation

The sets of integers and natural numbers are denoted by \mathbb{Z} and \mathbb{N} , respectively, $\mathbb{N}_0 := \{0\} \cup \mathbb{N}$, and $\mathbb{Z}_N := \{-N, \dots, N\}$, $N \in \mathbb{N}_0$. The space of square summable sequences is denoted by l_2 , and the space of bounded sequences is denoted by l_∞ . Similarly, the space of square integrable functions is denoted by L_2 , and the space of bounded functions is denoted by L_∞ . Symbol ‘*’ is used to denote transpose of a vector (matrix), and adjoint of an operator. The state and control of the n -th subsystem (cell, unit) are respectively represented by $[\psi_{1n} \dots \psi_{mn}]^*$ and u_n , $m \in \mathbb{N}$, $n \in \mathbb{Z}$. The capital letters denote infinite vectors defined, for example, as $\Psi_k := [\dots \psi_{k,n-1} \psi_{k,n} \psi_{k,n+1} \dots]^* =: \{\psi_{kn}\}_{n \in \mathbb{Z}}$, $k \in \{1, \dots, m\}$. Operators are represented by \mathcal{A} , \mathcal{B} , etc. The n -th plant cell is denoted by G_n , and the n -th controller cell is denoted by K_n .

12.2.2 An example of systems on lattices: mass-spring system

A system consisting of an infinite number of masses and springs on a line is shown in Fig. 12.1.

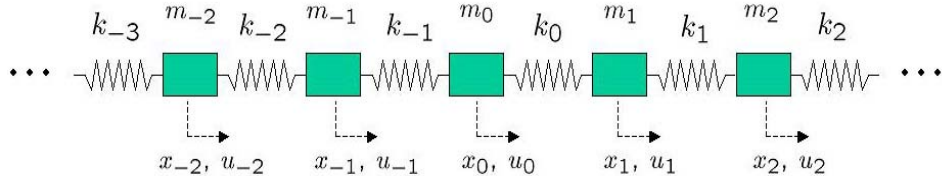


Figure 12.1: Mass-spring system.

The dynamics of the n -th mass are given by

$$m_n \ddot{x}_n = F_{n-1} + F_n + u_n, \quad n \in \mathbb{Z}, \quad (12.1)$$

where x_n represents the displacement from a reference position of the n -th mass, F_n represents the restoring force of the n -th spring, and u_n is the control applied on the n -th mass. For relatively small displacements, restoring forces can be considered as linear functions of displacements

$$F_n = k_n(x_{n+1} - x_n), \quad F_{n-1} = k_{n-1}(x_{n-1} - x_n), \quad n \in \mathbb{Z},$$

where k_n is the n -th spring constant. In this case (12.1) can be rewritten as

$$\ddot{x}_n = \frac{k_{n-1}}{m_n}(x_{n-1} - x_n) + \frac{k_n}{m_n}(x_{n+1} - x_n) + \frac{1}{m_n}u_n, \quad n \in \mathbb{Z},$$

or equivalently, in terms of its state space representation,

$$\left. \begin{aligned} \dot{\psi}_{1n} &= \psi_{2n} \\ \dot{\psi}_{2n} &= \frac{k_{n-1}}{m_n}(\psi_{1,n-1} - \psi_{1n}) + \frac{k_n}{m_n}(\psi_{1,n+1} - \psi_{1n}) + \frac{1}{m_n}u_n \end{aligned} \right\} \quad n \in \mathbb{Z}, \quad (12.2)$$

where $\psi_{1n} := x_n$ and $\psi_{2n} := \dot{x}_n$.

We also consider a situation in which the spring restoring forces depend nonlinearly on displacement. One such model is given by the so-called *hardening spring* (see, for example [57]) where, beyond a certain displacement, large force increments are obtained for small displacement increments

$$\begin{aligned} F_n &= k_n \{(x_{n+1} - x_n) + c_n^2(x_{n+1} - x_n)^3\} \\ &=: k_n(x_{n+1} - x_n) + q_n(x_{n+1} - x_n)^3, \\ F_{n-1} &= k_{n-1} \{(x_{n-1} - x_n) + c_{n-1}^2(x_{n-1} - x_n)^3\} \\ &=: k_{n-1}(x_{n-1} - x_n) + q_{n-1}(x_{n-1} - x_n)^3. \end{aligned}$$

In this case, the state space representation of (12.1) takes the following form:

$$\left. \begin{aligned} \dot{\psi}_{1n} &= \psi_{2n} \\ \dot{\psi}_{2n} &= \begin{bmatrix} \psi_{1,n-1} - \psi_{1n} \\ \psi_{1,n+1} - \psi_{1n} \\ (\psi_{1,n-1} - \psi_{1n})^3 \\ (\psi_{1,n+1} - \psi_{1n})^3 \end{bmatrix}^* \frac{1}{m_n} \begin{bmatrix} k_{n-1} \\ k_n \\ q_{n-1} \\ q_n \end{bmatrix} + \frac{1}{m_n}u_n \end{aligned} \right\} \quad n \in \mathbb{Z}. \quad (12.3)$$

When all masses and springs are homogeneous, that is,

$$m_n = m = \text{const.}, \quad k_n = k = \text{const.}, \quad c_n = c = \text{const.}, \quad \forall n \in \mathbb{Z},$$

(12.2) and (12.3) can be respectively rewritten as

$$\left. \begin{aligned} \dot{\psi}_{1n} &= \psi_{2n} \\ \dot{\psi}_{2n} &= \frac{k}{m} \{\psi_{1,n-1} - 2\psi_{1n} + \psi_{1,n+1}\} + \frac{1}{m}u_n \end{aligned} \right\} \quad n \in \mathbb{Z}, \quad (12.4)$$

and

$$\left. \begin{aligned} \dot{\psi}_{1n} &= \psi_{2n} \\ \dot{\psi}_{2n} &= \begin{bmatrix} \psi_{1,n-1} - 2\psi_{1n} + \psi_{1,n+1} \\ (\psi_{1,n-1} - \psi_{1n})^3 + (\psi_{1,n+1} - \psi_{1n})^3 \end{bmatrix}^* \frac{1}{m} \begin{bmatrix} k \\ q \end{bmatrix} + \frac{1}{m}u_n \end{aligned} \right\} \quad n \in \mathbb{Z}. \quad (12.5)$$

If the values of m and k in (12.4) are exactly known, then (12.4) represents a linear *spatially invariant* system. This implies that it can be analyzed using the tools of [19]. The other mathematical representations of a

mass-spring system are either nonlinear or spatially-varying when masses and spring constants are unknown. One of the main purposes of the present study is to design feedback controllers for this broader class of systems.

12.2.3 Classes of systems

In this subsection, we briefly summarize the classes of systems for which we design feedback controllers in § 12.3, § 12.5, and § 12.7. We consider continuous time m -th order subsystems over discrete spatial lattice \mathbb{Z} with *at most* $2N$ interactions per plant's cell (see Assumption 1). Clearly, the models presented in § 12.2.2 belong to this class of systems, as well as the model of an array of microcantilevers [17]. Also, our results can be used for control of fully actuated systems in two and three spatial dimensions.

We consider systems without parametric uncertainties of the form

$$\dot{\psi}_{1n} = f_{1n}(\Psi_1) + \psi_{2n}, \quad n \in \mathbb{Z}, \quad (12.6a)$$

$$\dot{\psi}_{2n} = f_{2n}(\Psi_1, \Psi_2) + \psi_{3n}, \quad n \in \mathbb{Z}, \quad (12.6b)$$

⋮

$$\dot{\psi}_{mn} = f_{mn}(\Psi_1, \dots, \Psi_m) + b_n u_n, \quad n \in \mathbb{Z}, \quad (12.6c)$$

where non-zero numbers b_n denote the so-called *control coefficients* [45].

If, on the other hand, we have a situation where all parameters have constant but unknown values $\forall t \in \mathbb{R}_+$ and $\forall n \in \mathbb{Z}$, it is convenient to rewrite (12.6) as

$$\dot{\psi}_{1n} = \nu_{1n}(\Psi_1) + g_{1n}^*(\Psi_1)\theta_1 + \psi_{2n}, \quad n \in \mathbb{Z}, \quad (12.7a)$$

$$\dot{\psi}_{2n} = \nu_{2n}(\Psi_1, \Psi_2) + g_{2n}^*(\Psi_1, \Psi_2)\theta_2 + \psi_{3n}, \quad n \in \mathbb{Z}, \quad (12.7b)$$

⋮

$$\dot{\psi}_{mn} = \nu_{mn}(\Psi_1, \dots, \Psi_m) + g_{mn}^*(\Psi_1, \dots, \Psi_m)\theta_m + b_n u_n, \quad n \in \mathbb{Z}, \quad (12.7c)$$

where θ_k , $k = \{1, \dots, m\}$ represent vectors of unknown parameters.

The most general case that we discuss is the one in which all parameters have unknown spatially varying values that do not depend on time. In other words, the parameters are allowed to be a function of $n \in \mathbb{Z}$ but not of $t \in \mathbb{R}_+$. In this case, it is convenient to rewrite (12.6) in the following form:

$$\dot{\psi}_{1n} = \tau_{1n}(\Psi_1) + h_{1n}^*(\Psi_1)\theta_{1n} + \psi_{2n}, \quad n \in \mathbb{Z}, \quad (12.8a)$$

$$\dot{\psi}_{2n} = \tau_{2n}(\Psi_1, \Psi_2) + h_{2n}^*(\Psi_1, \Psi_2)\theta_{2n} + \psi_{3n}, \quad n \in \mathbb{Z}, \quad (12.8b)$$

⋮

$$\dot{\psi}_{mn} = \tau_{mn}(\Psi_1, \dots, \Psi_m) + h_{mn}^*(\Psi_1, \dots, \Psi_m)\theta_{mn} + b_n u_n, \quad n \in \mathbb{Z}. \quad (12.8c)$$

A major difference between models (12.7) and (12.8) is in the number of unknown parameters. Namely, in the former the number of unknown parameters is finite, and in the latter the number of unknown parameters can be infinite.

We also consider output-feedback design for nominal systems

$$\dot{\psi}_{1n} = f_{1n}(Y) + \psi_{2n}, \quad n \in \mathbb{Z}, \quad (12.9a)$$

$$\dot{\psi}_{2n} = f_{2n}(Y) + \psi_{3n}, \quad n \in \mathbb{Z}, \quad (12.9b)$$

⋮

$$\dot{\psi}_{mn} = f_{mn}(Y) + b_n u_n, \quad n \in \mathbb{Z}, \quad (12.9c)$$

$$y_n = \psi_{1n}, \quad n \in \mathbb{Z}, \quad (12.9d)$$

and systems with parametric uncertainties

$$\dot{\psi}_{1n} = \tau_{1n}(Y) + h_{1n}^*(Y)\theta_{1n} + \psi_{2n}, \quad n \in \mathbb{Z}, \quad (12.10a)$$

$$\dot{\psi}_{2n} = \tau_{2n}(Y) + h_{2n}^*(Y)\theta_{2n} + \psi_{3n}, \quad n \in \mathbb{Z}, \quad (12.10b)$$

⋮

$$\dot{\psi}_{mn} = \tau_{mn}(Y) + h_{mn}^*(Y)\theta_{mn} + b_n u_n, \quad n \in \mathbb{Z}, \quad (12.10c)$$

$$y_n = \psi_{1n}, \quad n \in \mathbb{Z}, \quad (12.10d)$$

where $Y := \{y_n\}_{n \in \mathbb{Z}} = \{\psi_{1n}\}_{n \in \mathbb{Z}}$ denotes the distributed output of (12.9) and (12.10). Clearly, for these two systems nonlinearities are allowed to depend only on the measured output.

We introduce the following assumptions about the systems under study:

Assumption 1 *There are at most $2N$ interactions per plant cell: n -th plant cell G_n interacts only with $\{G_{n-N}, \dots, G_{n+N}\}$. In other words, functions f_{kn} , g_{kn} , h_{kn} , ν_{kn} , and τ_{kn} depend on at most $2N+1$ elements of Ψ_1, \dots, Ψ_k , $k \in \{1, \dots, m\}$, $n \in \mathbb{Z}$. For example, $f_{2n}(\Psi_1, \Psi_2) = f_{2n}(\{\psi_{1,n+j}\}_{j \in \mathbb{Z}_N}, \{\psi_{2,n+j}\}_{j \in \mathbb{Z}_N})$ (see Figure 12.2 for illustration).*

Assumption 2 *Functions f_{kn} , g_{kn} , h_{kn} , ν_{kn} , and τ_{kn} are known, continuously differentiable functions of their arguments, equal to zero at the origins of their respective systems. In addition to that, for each of these functions, infinite vectors defined as $F_k := \{f_{kn}\}_{n \in \mathbb{Z}}$ for every $k \in \{1, \dots, m\}$ satisfy:*

$$\{\Psi_1 \in l_\infty, \dots, \Psi_k \in l_\infty\} \Rightarrow F_k(\Psi_1, \dots, \Psi_k) \in l_\infty.$$

Assumption 3 *Functions g_{kn} and ν_{kn} are bounded by polynomial functions of their arguments. Furthermore, these polynomials are equal to zero at the origin.*

Assumption 4 *The sign of b in (12.7c) is known.*

Assumption 5 *The signs of b_n , $\forall n \in \mathbb{Z}$, in (12.8c) and (12.10c) are known.*

These assumptions are used in the sections related to the distributed control design and the well-posedness of both open and closed-loop systems.

Remark 4 *For notational convenience, both the well-posedness and the control design problems are solved for second order systems over discrete spatial lattice \mathbb{Z} , that is for $m = 2$.*

12.2.4 Well-posedness of open-loop systems

In this subsection we briefly analyze the well-posedness of the open-loop systems for $m = 2$. In particular, we consider the systems of § 12.2.3 as the abstract evolution equations either on a Hilbert space $\mathbb{H} := l_2 \times l_2$ or on a Banach space $\mathbb{B} := l_\infty \times l_\infty$. Either representation is convenient for addressing the questions of existence and uniqueness of solutions. With this in mind, we prove the well-posedness of the open-loop systems on \mathbb{H} and remark that similar argument can be used if the underlying state-space is \mathbb{B} rather than \mathbb{H} .

The unforced systems of § 12.2.3 can be rewritten as the abstract evolution equations of the form

$$\dot{\Psi} = \mathcal{A}\Psi + P(\Psi). \quad (12.11)$$

The state of system (12.11), a linear operator $\mathcal{A} : D(\mathcal{A}) \subset \mathbb{H} \mapsto \mathbb{H}$, and a (possibly) nonlinear mapping $P : \mathbb{H} \mapsto \mathbb{H}$ are defined as

$$\Psi := \begin{bmatrix} \Psi_1 \\ \Psi_2 \end{bmatrix} \in \mathbb{H}, \quad \mathcal{A} := \begin{bmatrix} 0 & I \\ 0 & 0 \end{bmatrix}, \quad P(\Psi) := \begin{bmatrix} P_1(\Psi_1) \\ P_2(\Psi_1, \Psi_2) \end{bmatrix},$$

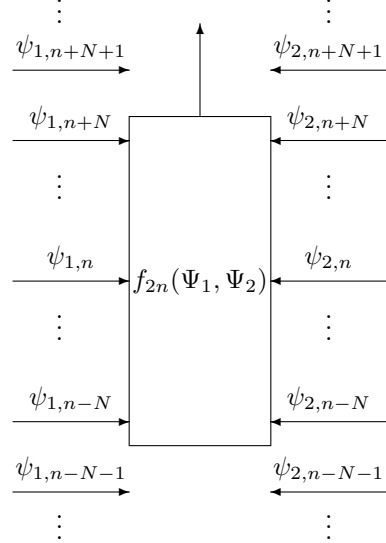


Figure 12.2: Graphical illustration of function $f_{2n}(\Psi_1, \Psi_2)$, $n \in \mathbb{Z}$.

where $D(\mathcal{A})$ represents the *domain* of \mathcal{A} , and P_k , $k = 1, 2$, denotes $\{f_{kn}\}_{n \in \mathbb{Z}}$, $\{\nu_{kn} + g_{kn}^* \theta_k\}_{n \in \mathbb{Z}}$, $\{\tau_{kn} + h_{kn}^* \theta_{kn}\}_{n \in \mathbb{Z}}$, $\{f_{kn}\}_{n \in \mathbb{Z}}$, or $\{\tau_{kn} + h_{kn}^* \theta_{kn}\}_{n \in \mathbb{Z}}$ depending on whether systems (12.6), (12.7), (12.8), (12.9), or (12.10) are considered.

One can show that \mathcal{A} is a *bounded operator* and, therefore, it generates a *uniformly continuous semigroup*. The latter property automatically implies that the semigroup generated by \mathcal{A} is *strongly continuous* (C^o)¹. If in addition to that P is locally Lipschitz then system (12.11) has a unique *mild solution* on $[0, t_{\max}]$ (see [64], Theorem 2.73). Moreover, if P is continuously (Fréchet) differentiable then (12.11) has a unique *classical solution* on $[0, t_{\max}]$ (see [64], Theorem 2.74). If $t_{\max} < \infty$ then $\lim_{t \rightarrow t_{\max}} \|\Psi(t)\| = \infty$. We remark that a function $P : \mathbb{H} \mapsto \mathbb{H}$ is Fréchet differentiable at a point $\bar{\Psi} \in \mathbb{H}$ if there exists a *bounded linear operator* $\mathcal{D} : \mathbb{H} \mapsto \mathbb{H}$ such that

$$\lim_{\|\Phi\| \rightarrow 0} \frac{\|P(\bar{\Psi} + \Phi) - P(\bar{\Psi}) - \mathcal{D}\Phi\|}{\|\Phi\|} = 0.$$

If such a linear operator exists, we denote it by $\frac{\partial P}{\partial \Psi}(\bar{\Psi})$, and refer to it as the Fréchet derivative of P .

It can be readily shown that for the systems described in § 12.2.3 that satisfy Assumption 1 and Assumption 2, P is a continuously Fréchet differentiable function of its arguments which in turn guarantees existence and uniqueness of classical solutions for these systems. To illustrate this, we consider a nonlinear mass-spring system (12.5) and determine the Fréchet derivative of P as

$$\mathcal{D} := \frac{\partial P}{\partial \Psi}(\bar{\Psi}) = \begin{bmatrix} 0 & 0 \\ \mathcal{D}_{21} & 0 \end{bmatrix},$$

¹The definitions of a bounded operator, a uniformly continuous semigroup, and a C^o -semigroup can be found, for example, in [62] and [63].

with \mathcal{D}_{21} being a tridiagonal operator determined by

$$\mathcal{D}_{21} := \begin{bmatrix} \vdots \\ \mathbf{D}_{n-1}^* \\ \mathbf{D}_n^* \\ \mathbf{D}_{n+1}^* \\ \vdots \end{bmatrix},$$

and

$$\begin{aligned} \mathbf{D}_n^* &:= [\cdots \ 0 \ d_{n,n-1} \ d_{n,n} \ d_{n,n+1} \ 0 \ \cdots], \\ d_{n,n-1} &:= \frac{k}{m} + \frac{3q}{m} (\bar{\psi}_{1,n-1} - \bar{\psi}_{1,n})^2, \\ d_{n,n} &:= -\frac{2k}{m} - \frac{3q}{m} \{(\bar{\psi}_{1,n-1} - \bar{\psi}_{1,n})^2 + (\bar{\psi}_{1,n+1} - \bar{\psi}_{1,n})^2\}, \\ d_{n,n+1} &:= \frac{k}{m} + \frac{3q}{m} (\bar{\psi}_{1,n+1} - \bar{\psi}_{1,n})^2. \end{aligned}$$

The tridiagonal structure of \mathcal{D}_{21} and the fact that

$$\bar{\Psi} \in \mathbb{H} := l_2 \times l_2 \Rightarrow \bar{\Psi} \in l_\infty \times l_\infty,$$

imply boundedness of \mathcal{D}_{21} . Therefore, it follows that \mathcal{D} is a bounded operator, that is,

$$\mathcal{D}\Phi \in \mathbb{H}, \quad \forall \Phi \in \mathbb{H}.$$

It is noteworthy that boundedness of \mathcal{D} implies that P is Fréchet differentiable on \mathbb{H} . Moreover, the continuity of \mathcal{D} (with respect to $\bar{\Psi}$) implies that P is continuously Fréchet differentiable on \mathbb{H} (see, for example, [65] for a fuller discussion).

12.2.5 Distributed controller architectures

Figure 12.3 illustrates different control strategies that can be used for distributed control of systems on lattices: centralized, localized, and fully decentralized. Centralized controllers require information from all plant cells for achieving the desired control objective. This approach usually results in best performance, but it requires excessive communication. On the other hand, in fully decentralized strategies control cell K_n uses only information from the n -th plant cell G_n on which it acts. This approach does not require any communication which often limits performance or even leads to instability. An example of a localized control architecture with nearest neighbor interactions is shown in Figure 12.3. The hope is that this approach will provide a good performance with moderate communication. We will show that Lyapunov-based design yields distributed controllers that are intrinsically decentralized with a strong similarity between plant and controller architectures.

12.3 Nominal state-feedback distributed backstepping design

In this section, we extend the well-known finite dimensional *integrator backstepping* design tool to a class of nonlinear infinite dimensional systems on lattices. We first design state-feedback distributed backstepping controllers for nominal systems (12.6) described in § 12.2.3. For notational convenience, the design problem is solved for second order subsystems over discrete spatial lattice \mathbb{Z} , that is for $m = 2$. In this case, the

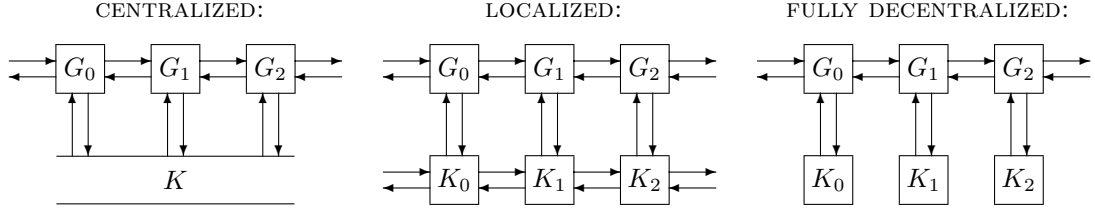


Figure 12.3: Distributed controller architectures for centralized, localized (with nearest neighbor interactions), and fully decentralized control strategies.

dynamics of the n -th cell (12.6) simplifies to

$$\dot{\psi}_{1n} = f_{1n}(\Psi_1) + \psi_{2n}, \quad n \in \mathbb{Z}, \quad (12.12a)$$

$$\dot{\psi}_{2n} = f_{2n}(\Psi_1, \Psi_2) + b_n u_n, \quad n \in \mathbb{Z}. \quad (12.12b)$$

We rewrite the dynamics of the entire system as

$$\dot{\Psi}_1 = F_1(\Psi_1) + \Psi_2, \quad (12.13a)$$

$$\dot{\Psi}_2 = F_2(\Psi_1, \Psi_2) + \mathcal{B}U, \quad (12.13b)$$

where capital letters denote infinite vectors defined in § 12.2.1, and $\mathcal{B} := \text{diag}\{b_n\}_{n \in \mathbb{Z}}$. System (12.13) represents an abstract evolution equation in the *strict-feedback form* [45] defined on either a Hilbert space $\mathbb{H} := l_2 \times l_2$ or a Banach space $\mathbb{B} := l_\infty \times l_\infty$.

In § 12.3.1, we study a situation in which the desired dynamical properties of system (12.13) are accomplished by performing a global design. Unfortunately, this is not always possible. Because of this, in § 12.3.2, we also perform design on individual cells (12.12) to guarantee the desired behavior of system (12.13). In § 12.3.3, we show how integrator backstepping can be employed as a constructive design tool for stabilization of nominal nonlinear systems on lattices.

12.3.1 Global backstepping design

Before we illustrate the global distributed backstepping design we introduce the following assumption:

Assumption 6 *The initial distributed state is such that both $\Psi_1(0) \in l_2$ and $\Psi_2(0) \in l_2$.*

The design objective is to provide global asymptotic stability of the origin of system (12.13). This is accomplished using the distributed backstepping control design. In the first step of backstepping, equation (12.13a) is stabilized by considering Ψ_2 as its control. Since Ψ_2 is not actually a control, but rather, a state variable, the error between Ψ_2 and the value which stabilizes (12.13a) must be penalized in the augmented Lyapunov function at the next step. In this way, a stabilizing control law is designed for the overall infinite dimensional system.

Step 1 The global recursive design starts with subsystem (12.13a) by considering Ψ_2 as control and proposing a radially unbounded CLF $V_1 : l_2 \mapsto \mathbb{R}$ of the form

$$V_1(\Psi_1) = \frac{1}{2} \langle \Psi_1, \Psi_1 \rangle := \frac{1}{2} \sum_{n \in \mathbb{Z}} \psi_{1n}^2.$$

The derivative of $V_1(\Psi_1)$ along the solutions of (12.13a) is given by

$$\dot{V}_1 = \langle \Psi_1, \dot{\Psi}_1 \rangle = \langle \Psi_1, F_1(\Psi_1) + \Psi_2 \rangle. \quad (12.14)$$

Assumption 7 There exist a continuously differentiable ‘stabilizing function’ $\Psi_{2d} := \Lambda(\Psi_1)$, $\Lambda(0) = 0$, such that

$$\Psi_1 \in l_2 \Rightarrow \Lambda(\Psi_1) \in l_2,$$

and

$$W_1(\Psi_1) := -\langle \Psi_1, F_1(\Psi_1) + \Lambda(\Psi_1) \rangle > 0,$$

for every $\Psi_1 \in l_2 \setminus \{0\}$.

Since Ψ_2 is not actually a control, but rather, a state variable, we introduce the change of variables

$$Z_2 := \Psi_2 - \Psi_{2d} = \Psi_2 - \Lambda(\Psi_1), \quad (12.15)$$

which adds an additional term on the right-hand side of (12.14)

$$\dot{V}_1 = -W_1(\Psi_1) + \langle \Psi_1, Z_2 \rangle. \quad (12.16)$$

The sign indefinite term in (12.16) will be taken care of at the second step of backstepping.

Step 2 Coordinate transformation (12.15) renders (12.13b) into a form suitable for the remainder of backstepping design

$$\dot{Z}_2 = F_2(\Psi_1, \Psi_2) - \frac{\partial \Lambda(\Psi_1)}{\partial \Psi_1} (F_1(\Psi_1) + \Psi_2) + \mathcal{B}U.$$

Augmentation of the CLF from Step 1 by a term which penalizes the error between Ψ_2 and Ψ_{2d} yields a function

$$V_2(\Psi_1, Z_2) := V_1(\Psi_1) + \frac{1}{2} \langle Z_2, Z_2 \rangle,$$

whose derivative along the solutions of

$$\begin{aligned} \dot{\Psi}_1 &= F_1(\Psi_1) + \Lambda(\Psi_1) + Z_2, \\ \dot{Z}_2 &= F_2(\Psi_1, \Psi_2) - \frac{\partial \Lambda(\Psi_1)}{\partial \Psi_1} (F_1(\Psi_1) + \Psi_2) + \mathcal{B}U, \end{aligned}$$

is determined by

$$\dot{V}_2 = \dot{V}_1 + \langle Z_2, \dot{Z}_2 \rangle = -W_1(\Psi_1) + \left\langle Z_2, \Psi_1 + F_2 - \frac{\partial \Lambda(\Psi_1)}{\partial \Psi_1} (F_1 + \Psi_2) + \mathcal{B}U \right\rangle.$$

In particular, the following choice of control law

$$U = -\mathcal{B}^{-1}(\Psi_1 + F_2 - \frac{\partial \Lambda(\Psi_1)}{\partial \Psi_1} (F_1 + \Psi_2) + k_2 Z_2), \quad (12.17)$$

with $k_2 > 0$ yields

$$\dot{V}_2(\Psi_1, Z_2) = -W_1(\Psi_1) - k_2 \langle Z_2, Z_2 \rangle < 0,$$

for every $\Psi_1 \in l_2 \setminus \{0\}$, $Z_2 \in l_2 \setminus \{0\}$. Therefore, control law (12.17) guarantees global asymptotic stability of the origin of system (12.13).

Results of this subsection are summarized in the following theorem.

Theorem 17 Suppose that system (12.13) satisfies Assumptions 1, 2, 6 and 7. Then, there exists a state-feedback control law $U = \Upsilon(\Psi_1, \Psi_2)$ which guarantees global asymptotic stability of the origin of system (12.13). One such control law is given by

$$U = -\mathcal{B}^{-1}(\Psi_1 + F_2(\Psi_1, \Psi_2) + k_2(\Psi_2 - \Lambda(\Psi_1)) - \frac{\partial \Lambda(\Psi_1)}{\partial \Psi_1} (F_1(\Psi_1) + \Psi_2)), \quad k_2 > 0.$$

These properties can be established with the Lyapunov function

$$V(\Psi_1, \Psi_2) := \frac{1}{2} \langle \Psi_1, \Psi_1 \rangle + \frac{1}{2} \langle \Psi_2 - \Lambda(\Psi_1), \Psi_2 - \Lambda(\Psi_1) \rangle.$$

12.3.2 Individual cell backstepping design

As already mentioned, the distributed backstepping design on the space of square summable sequences cannot always be performed. For example, if either Assumption 6 or Assumption 7 is not satisfied the construction of a quadratic CLF for system (12.13) is not possible. In this subsection, we show that global asymptotic stability of the origin of (12.13) can be achieved by performing design on each individual cell (12.12) rather than on the entire system (12.13). For a moment, let the control objective be the regulation of $\psi_{1n}(t)$ and boundedness of $\psi_{2n}(t)$, that is

$$\{\psi_{1n}(t) \rightarrow 0 \text{ as } t \rightarrow \infty; |\psi_{2n}(t)| < \infty, \forall t \geq 0\},$$

for every $n \in \mathbb{Z}$, and for all $\psi_{1n}(0) \in \mathbb{R}$, $\psi_{2n}(0) \in \mathbb{R}$. We will achieve this objective by providing the global asymptotic tracking of the following trajectory: $(\psi_{1n}, \psi_{2n}) = (0, -f_{1n}(\Psi_1)|_{\psi_{1n}=0})$. If this is accomplished for each individual cell G_n (i.e., for every $n \in \mathbb{Z}$), then by virtue of the fact that Ψ_1 is driven to zero and that $f_{1n}(\Psi_1)$ vanishes at $\Psi_1 = 0$ for every $n \in \mathbb{Z}$ (see Assumption 2), we conclude global asymptotic stability of the origin of system (12.13).

Step 1 The individual cell backstepping design starts with subsystem (12.12a) by considering ψ_{2n} as control and proposing a quadratic radially unbounded CLF $V_{1n} : \mathbb{R} \mapsto \mathbb{R}$

$$V_{1n}(\psi_{1n}) = \frac{1}{2} \psi_{1n}^2. \quad (12.18)$$

The derivative of $V_{1n}(\psi_{1n})$ along the solutions of (12.12a) is determined by

$$\dot{V}_{1n} = \psi_{1n} \dot{\psi}_{1n} = \psi_{1n} (f_{1n}(\Psi_1) + \psi_{2n}). \quad (12.19)$$

Clearly, if ψ_{2n} were a control, subsystem (12.12a) could be stabilized by cancelling nonlinearity $f_{1n}(\Psi_1)$ and adding an additional term to ensure stability

$$\psi_{2nd} := \lambda_n(\Psi_1) = -(f_{1n}(\Psi_1) + k_1 \psi_{1n}),$$

with $k_1 > 0$. Let ζ_{2n} denote the difference between ψ_{2n} and its desired value $\lambda_n(\Psi_1)$

$$\zeta_{2n} := \psi_{2n} - \lambda_n(\Psi_1) = \psi_{2n} + (f_{1n}(\Psi_1) + k_1 \psi_{1n}).$$

This transforms (12.19) into

$$\dot{V}_{1n} = -k_1 \psi_{1n}^2 + \psi_{1n} \zeta_{2n}.$$

The sign indefinite term in the last equation will be accounted for at the second step of backstepping.

Step 2 We rewrite system (12.12b) into a form suitable for the remainder of individual cell backstepping design

$$\dot{\zeta}_{2n} = f_{2n}(\Psi_1, \Psi_2) - \frac{\partial \lambda_n(\Psi_1)}{\partial \Psi_1} (\mathbf{F}_1(\Psi_1) + \Psi_2) + b_n u_n.$$

Augmentation of (12.18) by a term which penalizes the deviation of ψ_{2n} from ψ_{2nd} yields a quadratic CLF

$$V_{2n}(\psi_{1n}, \zeta_{2n}) := V_{1n}(\psi_{1n}) + \frac{1}{2} \zeta_{2n}^2,$$

whose derivative along the solutions of

$$\begin{aligned}\dot{\psi}_{1n} &= -k_1\psi_{1n} + \zeta_{2n}, \\ \dot{\zeta}_{2n} &= f_{2n}(\Psi_1, \Psi_2) - \frac{\partial\lambda_n(\Psi_1)}{\partial\Psi_1}(F_1(\Psi_1) + \Psi_2) + b_n u_n,\end{aligned}$$

is determined by

$$\dot{V}_{2n} = \dot{V}_{1n} + \zeta_{2n}\dot{\zeta}_{2n} = -k_1\psi_{1n}^2 + \zeta_{2n}(\psi_{1n} + f_{2n} - \frac{\partial\lambda_n(\Psi_1)}{\partial\Psi_1}(F_1 + \Psi_2) + b_n u_n).$$

The simplest choice of controller that provides negative definiteness of \dot{V}_{2n} is given by

$$u_n = -\frac{1}{b_n}(\psi_{1n} + f_{2n} - \frac{\partial\lambda_n(\Psi_1)}{\partial\Psi_1}(F_1 + \Psi_2) + k_2\zeta_{2n}), \quad (12.20)$$

where k_2 represents a positive design parameter. This choice of control gives

$$\dot{V}_{2n}(\psi_{1n}, \zeta_{2n}) = -k_1\psi_{1n}^2 - k_2\zeta_{2n}^2 < 0,$$

for every $(\psi_{1n}, \zeta_{2n}) \in \mathbb{R}^2 \setminus \{0\}$, and every $n \in \mathbb{Z}$. Thus, control law (12.20) warrants global asymptotic tracking of $(\psi_{1n}, \psi_{2n}) = (0, -f_{1n}(\Psi_1)|_{\psi_{1n}=0})$ of system (12.12) for every $n \in \mathbb{Z}$, which in turn implies (see Assumption 2) global asymptotic stability of the origin of system (12.13).

Results of this subsection are summarized in the following theorem.

Theorem 18 Suppose that system (12.13) satisfies Assumptions 1–2. Then, for every $n \in \mathbb{Z}$, there exists a state-feedback control law $u_n = \gamma_n(\Psi_1, \Psi_2)$ which guarantees global asymptotic stability of the origin of system (12.13). One such control law is given by

$$u_n = -\frac{1}{b_n}(\psi_{1n} + f_{2n}(\Psi_1, \Psi_2) + k_2(\psi_{2n} - \lambda_n(\Psi_1)) - \frac{\partial\lambda_n(\Psi_1)}{\partial\Psi_1}(F_1(\Psi_1) + \Psi_2)), \quad k_2 > 0,$$

where

$$\lambda_n(\Psi_1) := -(f_{1n}(\Psi_1) + k_1\psi_{1n}), \quad k_1 > 0.$$

12.3.3 Distributed integrator backstepping

In this subsection, we present results that allow for constructive design of stabilizing controllers for systems on lattices without parametric uncertainties. We show how to extend previously described nominal state-feedback controllers to a more general situation in which a system of the form

$$\dot{\psi}_n = f_n(\Psi) + g_n(\Psi)u_n, \quad f_n(0) = 0, \quad n \in \mathbb{Z}, \quad (12.21)$$

is augmented by an infinite number of integrators. We assume that f_n and g_n satisfy Assumptions 1 and 2, and respectively denote the system's state and control vectors by

$$\begin{aligned}\Psi &:= [\dots \psi_{n-1}^* \psi_n^* \psi_{n+1}^* \dots]^*, \\ U &:= [\dots u_{n-1} \quad u_n \quad u_{n+1} \quad \dots]^*,\end{aligned}$$

with $\psi_n \in \mathbb{R}^m$ and $u_n \in \mathbb{R}$ for all $n \in \mathbb{Z}$. For the purpose of global design it is convenient to rewrite (12.21)

$$\dot{\Psi} = F(\Psi) + G(\Psi)U, \quad (12.22)$$

where

$$F(\Psi) := [\cdots \ f_{n-1}^*(\Psi) \ f_n^*(\Psi) \ f_{n+1}^*(\Psi) \ \cdots]^*,$$

$$\mathcal{G}(\Psi) := \text{diag}\{g_n(\Psi)\}_{n \in \mathbb{Z}}.$$

Note that $\mathcal{G}(\Psi)$ represents an operator from l_∞ (l_2) to l_∞^m (l_2^m).

The results summarized in Lemma 19 and Lemma 20 represent natural extensions of the well known finite dimensional *integrator backstepping* design tool [45, 57], and they are respectively based on the following assumptions:

Assumption 8 *There exists a continuously differentiable state-feedback control law*

$$u_n = \lambda_n(\Psi), \quad \lambda_n(0) = 0, \quad (12.23)$$

and a smooth positive definite radially unbounded function $V_n(\psi_n)$, $V_n : \mathbb{R}^m \rightarrow \mathbb{R}$, for the n -th subsystem of (12.21) such that

$$\frac{\partial V_n(\psi_n)}{\partial \psi_n} (f_n(\Psi) + g_n(\Psi)\lambda_n(\Psi)) \leq -W_n(\psi_n) < 0, \quad \forall \psi_n \in \mathbb{R}^m \setminus \{0\}, \quad (12.24)$$

where $W_n : \mathbb{R}^m \rightarrow \mathbb{R}$ is a positive definite function for every $n \in \mathbb{Z}$.

Assumption 9 *There exists a continuously differentiable state-feedback control law*

$$U = \Lambda(\Psi), \quad \Lambda(0) = 0, \quad (12.25)$$

such that

$$\Psi \in l_2^m \Rightarrow \Lambda(\Psi) \in l_2,$$

and a smooth positive definite radially unbounded functional $V(\Psi)$, $V : l_2^m \rightarrow \mathbb{R}$, for system (12.22) such that

$$\frac{\partial V(\Psi)}{\partial \Psi} (F(\Psi) + \mathcal{G}(\Psi)\Lambda(\Psi)) \leq -W(\Psi) < 0, \quad \forall \Psi \in l_2^m \setminus \{0\}, \quad (12.26)$$

where $W : l_2^m \rightarrow \mathbb{R}$ is a positive definite functional.

Condition (12.24) guarantees global asymptotic stability of the origin of the n -th subsystem of (12.21) for every $n \in \mathbb{Z}$, which in turn guarantees global asymptotic stability of the origin of (12.22). Similarly, if the conditions of Assumption 9 are satisfied then global asymptotic stability of the origin of (12.22) can be concluded as well. Moreover, Assumption 9 guarantees existence of a CLF for infinite dimensional system (12.22). This feature can be used to obtain distributed controllers with favorable architectures, as illustrated in § 12.4.1.

In the remainder of this section, we consider system (12.21) augmented by an infinite number of integrators, that is,

$$\dot{\psi}_n = f_n(\Psi) + g_n(\Psi)\phi_n, \quad n \in \mathbb{Z}, \quad (12.27a)$$

$$\dot{\phi}_n = u_n, \quad n \in \mathbb{Z}, \quad (12.27b)$$

or equivalently

$$\dot{\Psi} = F(\Psi) + \mathcal{G}(\Psi)\Phi, \quad (12.28a)$$

$$\dot{\Phi} = U. \quad (12.28b)$$

Individual cell distributed integrator backstepping

Lemma 19 Suppose that, for every $n \in \mathbb{Z}$, the n -th subsystem of (12.27a) satisfies Assumption 8 with $\phi_n \in \mathbb{R}$ as its control. Then, the augmented function of the form

$$V_{an}(\Psi, \phi_n) := V_n(\psi_n) + \frac{1}{2}(\phi_n - \lambda_n(\Psi))^2,$$

represents a CLF for the n -th subsystem of (12.27). Therefore, there exists a state-feedback control law

$$\mathbf{U} := [\dots \lambda_{a,n-1}(\Psi, \Phi) \lambda_{an}(\Psi, \Phi) \lambda_{a,n+1}(\Psi, \Phi) \dots]^*,$$

which guarantees global asymptotic stability of the origin of system (12.28). One such control law is given by

$$\lambda_{an}(\Psi, \Phi) = -k_n(\phi_n - \lambda_n(\Psi)) + \sum_{j \in \mathbb{Z}} \frac{\partial \lambda_n}{\partial \psi_j} (f_j(\Psi) + g_j(\Psi)\phi_j) - \frac{\partial V_n(\psi_n)}{\partial \psi_n} g_n(\Psi), \quad k_n > 0.$$

Global distributed integrator backstepping

Lemma 20 Suppose that (12.28a) satisfies Assumption 9 with $\Phi \in l_2$ as its control. Then, the augmented function of the form

$$V_a(\Psi, \Phi) := V(\Psi) + \frac{1}{2} \langle \Phi - \Lambda(\Psi), \Phi - \Lambda(\Psi) \rangle,$$

represents a CLF for system (12.28). Therefore, there exists a state-feedback control law $\mathbf{U} := \Lambda_a(\Psi, \Phi)$ which guarantees global asymptotic stability of the origin of system (12.28). One such control law is given by

$$\Lambda_a(\Psi, \Phi) = -k(\Phi - \Lambda(\Psi)) + \frac{\partial \Lambda(\Psi)}{\partial \Psi} (F(\Psi) + G(\Psi)\Phi) - G^*(\Psi) \left(\frac{\partial V(\Psi)}{\partial \Psi} \right)^*, \quad k > 0.$$

Results of Lemma 19 (Lemma 20) can be also applied to a more general class of systems of the form

$$\dot{\psi}_n = f_n(\Psi) + g_n(\Psi)\phi_n, \quad n \in \mathbb{Z}, \tag{12.29a}$$

$$\dot{\phi}_n = f_{an}(\Psi, \Phi) + g_{an}(\Psi, \Phi)u_{an}, \quad n \in \mathbb{Z}, \tag{12.29b}$$

where we assume that $g_{an}(\Psi, \Phi) \neq 0$, for all $n \in \mathbb{Z}$. In this case, the input transformation

$$u_{an} := \frac{1}{g_{an}(\Psi, \Phi)} (u_n - f_{an}(\Psi, \Phi)),$$

renders (12.29) into (12.27), which allows for the application of Lemma 19 (Lemma 20).

12.4 Architecture induced by nominal distributed backstepping design

In this section, we analyze the architecture of distributed controllers induced by a backstepping design. In particular, we study a ‘worst case’ situation in which all interactions are cancelled at each step of backstepping. Any other backstepping design will result into controllers with more favorable architectures (i.e., less interactions). We show that backstepping design yields distributed controllers that are inherently decentralized, and that there is a strong similarity between plant and controller architectures. More precisely, the controller architecture is determined by two factors: the plant architecture, and the largest number of integrators that separate control from certain interactions. For example, since there are $m - 1$ integrators

between interactions $f_{1n}(\Psi_1)$ in (12.6a) and location at which control u_n enters, this largest number of integrators in system (12.6) is equal to $m - 1$.

The ‘worst case’ (i.e., the cancellation) backstepping controller for system (12.13) is given by

$$U = -\mathcal{B}^{-1}\left((1 + k_1 k_2)\Psi_1 + (k_1 + k_2)(\Psi_2 + F_1(\Psi_1)) + F_2(\Psi_1, \Psi_2) + P(\Psi_1) + Q(\Psi_1, \Psi_2)\right),$$

where

$$\begin{aligned} P(\Psi_1) &:= \frac{\partial F_1(\Psi_1)}{\partial \Psi_1} F_1(\Psi_1), \\ Q(\Psi_1, \Psi_2) &:= \frac{\partial F_1(\Psi_1)}{\partial \Psi_1} \Psi_2. \end{aligned}$$

Equivalently, the n -th cell controller is given by

$$u_n = -\frac{1}{b_n}\left((1 + k_1 k_2)\psi_{1n} + (k_1 + k_2)(\psi_{2n} + f_{1n}(\Psi_1)) + f_{2n}(\Psi_1, \Psi_2) + p_n(\Psi_1) + q_n(\Psi_1, \Psi_2)\right),$$

where $p_n(\Psi_1)$ and $q_n(\Psi_1, \Psi_2)$ respectively denote the n -th components of infinite vectors $P(\Psi_1)$ and $Q(\Psi_1, \Psi_2)$, for every $n \in \mathbb{Z}$. Based on Assumption 1 and definitions of $P(\Psi_1)$ and $Q(\Psi_1, \Psi_2)$, these two quantities are determined by

$$\begin{aligned} p_n(\Psi_1) &= \frac{\partial f_{1n}(\Psi_1)}{\partial \Psi_1} F_1(\Psi_1) = \sum_{j \in \mathbb{Z}_N} \frac{\partial f_{1n}(\Psi_1)}{\partial \psi_{1,n+j}} f_{1,n+j}(\{\psi_{1,n+j+i}\}_{i \in \mathbb{Z}_N}), \\ q_n(\Psi_1, \Psi_2) &= \frac{\partial f_{1n}(\Psi_1)}{\partial \Psi_1} \Psi_2 = \sum_{j \in \mathbb{Z}_N} \frac{\partial f_{1n}(\Psi_1)}{\partial \psi_{1,n+j}} \psi_{2,n+j}. \end{aligned}$$

The case in which no integrators separate interactions and location at which control enters is referred to as the ‘matched’ case (or equivalently, we say that the ‘matching condition’ is satisfied). If system (12.13) satisfies the matching condition then $f_{1n} = 0$ for every $n \in \mathbb{Z}$ (i.e., $F_1 \equiv 0$). Clearly, in this case both $p_n \equiv 0$ and $q_n \equiv 0$ which implies that the ‘worst case’ backstepping controller simplifies to

$$u_n = -((1 + k_1 k_2)\psi_{1n} + (k_1 + k_2)\psi_{2n} + f_{2n}(\Psi_1, \Psi_2)),$$

for every $n \in \mathbb{Z}$. Thus, when (interactions are) matched (by control) the ‘worst case’ distributed backstepping controller inherits the plant architecture. On the other hand, if the matching condition is not satisfied the additional interactions are induced by the ‘worst case’ backstepping design. This is because of cancellation of the interactions at the first step of backstepping, their propagation through an integrator, and subsequent cancellation at the second step of our recursive design. Information about these additional interactions is contained in function $p_n(\Psi_1)$. Based on the expression for $p_n(\Psi_1)$ (see Figure 12.4 for graphical illustration) we are able to explicitly quantify the number of interactions induced by a ‘worst case’ distributed backstepping design:

- For system (12.13) with at most $2N$ interactions per plant cell, the ‘worst case’ nominal distributed backstepping design induces at most $4N$ interactions per controller cell.

This statement can be generalized for system (12.6). As shown in Figure 12.5, if the n -th plant cell G_n of system (12.6) interacts with $\{G_{n-N}, \dots, G_{n+N}\}$ and if $f_{1n}(\psi_{1,n-N}, \dots, \psi_{1,n+N}) \neq 0$ for every $n \in \mathbb{Z}$, then the n -th cell K_n of the ‘worst case’ backstepping controller interacts with $\{K_{n-mN}, \dots, K_{n+mN}\}$. In other words:

- For system (12.6) with at most $2N$ interactions per plant cell, the ‘worst case’ nominal distributed backstepping design induces at most $2mN$ interactions per controller cell.

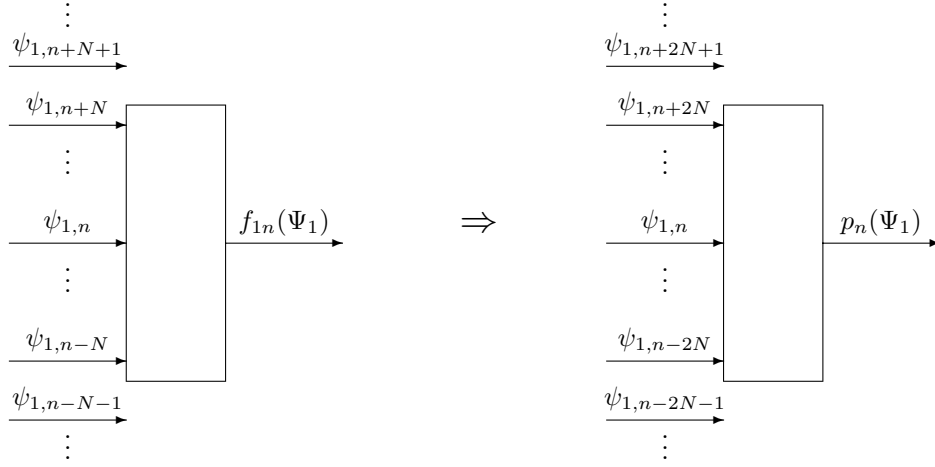


Figure 12.4: Graphical illustration of function $p_n(\Psi_1) = p_n(\{\psi_{1,n+2j}\}_{j \in \mathbb{Z}_N})$, $n \in \mathbb{Z}$. The ‘worst case’ nominal distributed backstepping design for system (12.13) with at most $2N$ interactions per plant cell induces at most $4N$ interactions per controller cell.

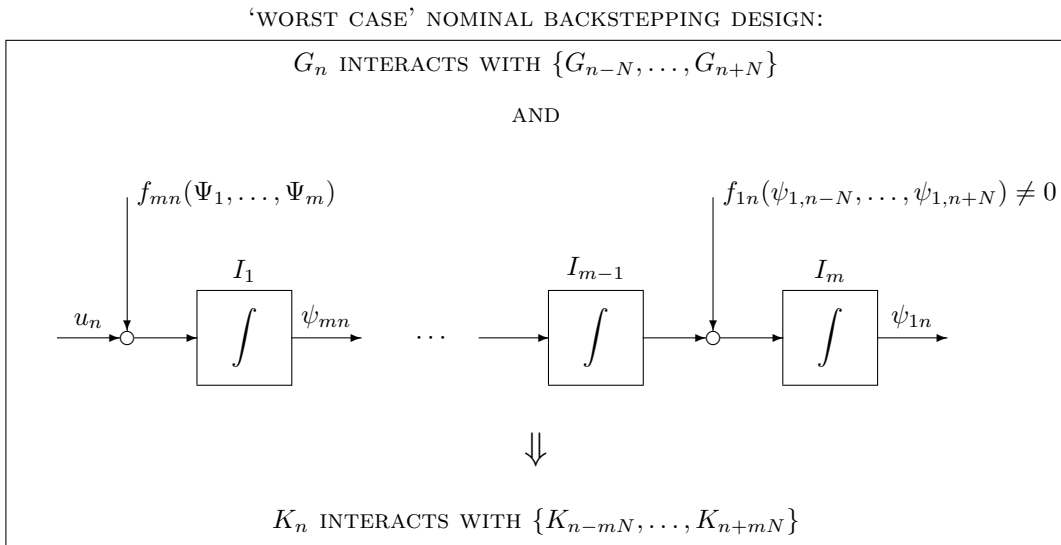


Figure 12.5: The ‘worst case’ nominal distributed backstepping design for system (12.13) with at most $2N$ interactions per plant cell induces at most $2mN$ interactions per controller cell.

Example

We consider the following, purely academic, example

$$\dot{\psi}_{1n} = \psi_{1,n-1}^2 + \psi_{1n}^2 + \psi_{1,n+1}^2 + \psi_{2n}, \quad (12.30a)$$

$$\dot{\psi}_{2n} = u_n, \quad (12.30b)$$

where $n \in \mathbb{Z}$. Clearly, system (12.30) is in form (12.12) with $f_{1n}(\Psi_1) := \psi_{1,n-1}^2 + \psi_{1n}^2 + \psi_{1,n+1}^2$, and $f_{2n} \equiv 0$. The architecture of the ‘worst case’ distributed backstepping controller for this system is illustrated in Figure 12.6. Thus, to provide global asymptotic stability of system (12.30) whose n -th cell has only the nearest neighbor interactions, the n -th cell K_n of the cancellation backstepping controller has to interact with $\{K_{n-2}, K_{n-1}, K_{n+1}, K_{n+2}\}$. In § 12.4.1, we show that domination of harmful interactions, rather than their cancellation, provides less controller interactions.

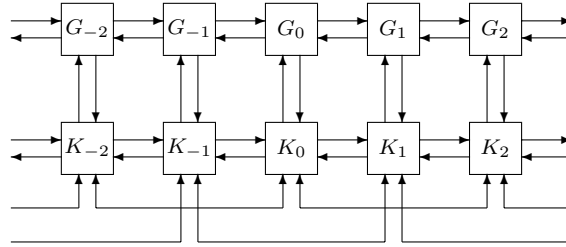


Figure 12.6: The architecture of the ‘worst case’ nominal distributed backstepping controller for system (12.30).

In applications, we clearly have to work with large-scale systems on lattices. All considerations related to infinite dimensional systems are applicable here, but with minor modifications. For example, if we consider system (12.30) with $M \in \mathbb{N}$ cells ($n = 1, \dots, M$) results of § 12.3 are still valid with the appropriate ‘boundary conditions’: $\psi_{1j} = \psi_{2j} = u_j = f_{1j} \equiv 0, \forall j \in \mathbb{Z} \setminus \{1, \dots, M\}$.

Figure 12.7 shows simulation results of uncontrolled (upper left) and controlled system (12.30) with $M = 100$ cells using the ‘worst case’ backstepping controller with $k_1 = k_2 = 1$. The initial state of the system is randomly selected. Clearly, the desired control objective is achieved with a reasonable quality of the transient response. This transient response can be further improved with a different choice of design parameters k_1 and k_2 at the expense of increasing the control effort.

12.4.1 Design of controllers with less interactions

In this subsection, we demonstrate how global backstepping design can be utilized to obtain controllers with less interactions. In particular, for system (12.30), whose initial state satisfies Assumption 6, we design a distributed controller with the nearest neighbor interactions and a fully decentralized controller. This is accomplished by a careful analysis of the interactions in system (12.30), and feedback domination rather than feedback cancellation of harmful interactions. The procedure presented here can be applied to systems in which interactions are bounded by polynomial functions of their arguments.

Nearest neighbor interaction controller

Step 1 As in § 12.3.1, the global design starts with subsystem (12.30a) by considering Ψ_2 as control and proposing a quadratic radially unbounded CLF $V_1 : l_2 \mapsto \mathbb{R}$

$$V_1(\Psi_1) = \frac{1}{2} \sum_{n \in \mathbb{Z}} \psi_{1n}^2, \quad (12.31)$$

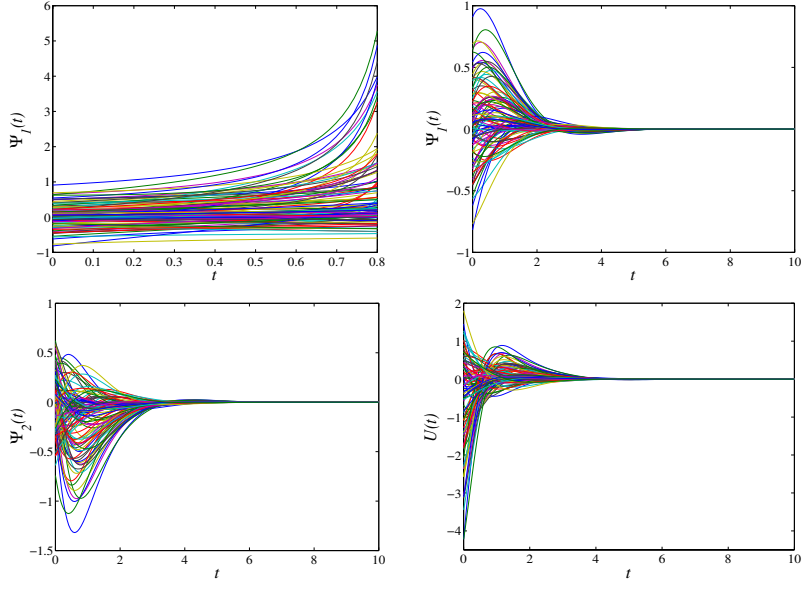


Figure 12.7: Control of system (12.30) with $M = 100$ cells using the ‘worst case’ nominal backstepping controller with $k_1 = k_2 = 1$.

whose derivative along the solutions of (12.30a) is given by

$$\dot{V}_1 = \sum_{n \in \mathbb{Z}} \psi_{1n} (\psi_{1,n-1}^2 + \psi_{1n}^2 + \psi_{1,n+1}^2 + \psi_{2n}).$$

We now use Young’s Inequality (see [45], expression (2.254)) to bound the interactions between G_n and its immediate neighbors G_{n-1} and G_{n+1} , for every $n \in \mathbb{Z}$

$$\psi_{1n} \psi_{1i}^2 \leq \kappa \psi_{1n}^2 + \frac{1}{4\kappa} \psi_{1i}^4, \quad \kappa > 0, \quad i = \{n-1, n+1\}.$$

Hence, \dot{V}_1 is upper-bounded by

$$\dot{V}_1 \leq \sum_{n \in \mathbb{Z}} \psi_{1n} (2\kappa \psi_{1n} + \psi_{1n}^2 + \frac{1}{2\kappa} \psi_{1n}^3 + \psi_{2n}). \quad (12.32)$$

Clearly, the following choice of $\psi_{2nd} := \lambda_n(\psi_{1n})$, with $k_1 > 0$,

$$\lambda_n(\psi_{1n}) = -((k_1 + 2\kappa)\psi_{1n} + \psi_{1n}^2 + \frac{1}{2\kappa}\psi_{1n}^3), \quad (12.33)$$

and a coordinate transformation

$$\zeta_{2n} := \psi_{2n} - \lambda_n(\psi_{1n}), \quad (12.34)$$

yield

$$\dot{V}_1 \leq -k_1 \sum_{n \in \mathbb{Z}} \psi_{1n}^2 + \sum_{n \in \mathbb{Z}} \psi_{1n} \zeta_{2n}.$$

The sign indefinite term in the last equation will be accounted for at the second step of backstepping.

Step 2 CLF from Step 1 is augmented by a term which penalizes the deviation of ψ_{2n} from ψ_{2nd}

$$V_2(\Psi_1, Z_2) := V_1(\Psi_1) + \frac{1}{2} \sum_{n \in \mathbb{Z}} \zeta_{2n}^2.$$

The derivative of V_2 along the solutions of

$$\begin{aligned} \dot{\psi}_{1n} &= -k_1 \psi_{1n} + \zeta_{2n}, & n \in \mathbb{Z}, \\ \dot{\zeta}_{2n} &= -\frac{\partial \lambda_n(\psi_{1n})}{\partial \psi_{1n}} (f_{1n}(\Psi_1) + \psi_{2n}) + u_n, & n \in \mathbb{Z}, \end{aligned}$$

is determined by

$$\dot{V}_2 \leq -k_1 \sum_{n \in \mathbb{Z}} \psi_{1n}^2 + \sum_{n \in \mathbb{Z}} \zeta_{2n} (\psi_{1n} - \frac{\partial \lambda_n(\psi_{1n})}{\partial \psi_{1n}} (f_{1n}(\Psi_1) + \psi_{2n}) + u_n).$$

We choose a control law of the form

$$u_n = -(\psi_{1n} - \frac{\partial \lambda_n(\psi_{1n})}{\partial \psi_{1n}} (f_{1n}(\Psi_1) + \psi_{2n}) + k_2 \zeta_{2n}), \quad (12.35)$$

with $k_2 > 0$, to obtain

$$\dot{V}_2 \leq -k_1 \sum_{n \in \mathbb{Z}} \psi_{1n}^2 - k_2 \sum_{n \in \mathbb{Z}} \zeta_{2n}^2.$$

Hence, controller (12.35) guarantees global exponential stability of the origin of the infinite dimensional system (12.30). This controller has the very same architecture as the original plant: the n -th controller cell K_n interacts only with its nearest neighbors K_{n-1} and K_{n+1} .

Figure 12.8 shows simulation results of uncontrolled (upper left) and controlled system (12.30) with $M = 100$ cells using the nearest neighbor interaction backstepping controller (12.33,12.34,12.35) with $k_1 = k_2 = 1$ and $\kappa = 0.5$. The initial state of the system is randomly selected. The desired control objective is achieved with a good quality of the transient response and a reasonable amount of control effort.

Fully decentralized controller

Step 1 We start the recursive design with subsystem (12.30a) by proposing a CLF (12.31). The derivative of $V_1(\Psi_1)$ along the solutions of (12.30a) is determined by (12.32). However, we now choose a ‘stabilizing function’ $\psi_{2nd} := \lambda_n(\psi_{1n})$ of the form

$$\lambda_n(\psi_{1n}) = -((k_1 + 2\kappa)\psi_{1n} + \psi_{1n}^2 + (k_0 + \frac{1}{2\kappa})\psi_{1n}^3), \quad (12.36)$$

with $k_0, k_1 > 0$, which clearly renders \dot{V}_1 negative definite. Coordinate transformation $\zeta_{2n} := \psi_{2n} - \lambda_n(\psi_{1n})$ yields

$$\dot{V}_1 \leq -k_1 \sum_{n \in \mathbb{Z}} \psi_{1n}^2 - k_0 \sum_{n \in \mathbb{Z}} \psi_{1n}^4 + \sum_{n \in \mathbb{Z}} \psi_{1n} \zeta_{2n}.$$

The sign indefinite term in the last equation will be taken care of at the second step of backstepping.

Step 2 The second step of our design closely follows the procedure outlined in the nearest neighbor controller design. The only difference is that we employ the Young’s inequality to upper-bound

$$\zeta_{2n} \frac{\partial \lambda_n(\psi_{1n})}{\partial \psi_{1n}} \psi_{1i}^2 \leq \kappa \left(\zeta_{2n} \frac{\partial \lambda_n(\psi_{1n})}{\partial \psi_{1n}} \right)^2 + \frac{1}{4\kappa} \psi_{1i}^4, \quad \kappa > 0, \quad \forall n \in \mathbb{Z}, \quad \forall i = \{n-1, n+1\},$$

in the expression for the temporal derivative of $V_2(\Psi_1, Z_2) := V_1(\Psi_1) + \frac{1}{2} \sum_{n \in \mathbb{Z}} \zeta_{2n}^2$. This allows us to choose

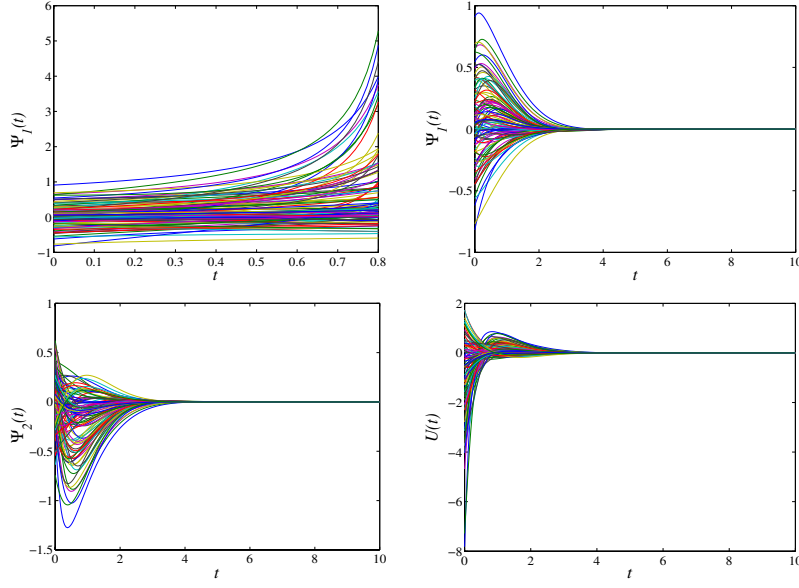


Figure 12.8: Control of system (12.30) with $M = 100$ cells using the nearest neighbor interaction backstepping controller (12.33,12.34,12.35) with $k_1 = k_2 = 1$ and $\kappa = 0.5$.

a fully decentralized controller of the form

$$u_n = - \left(\psi_{1n} - \frac{\partial \lambda_n(\psi_{1n})}{\partial \psi_{1n}} (\psi_{1n}^2 + \psi_{2n}) + (\psi_{2n} - \lambda_n(\psi_{1n})) (k_2 + 2\kappa \left(\frac{\partial \lambda_n(\psi_{1n})}{\partial \psi_{1n}} \right)^2) \right), \quad (12.37)$$

with $k_2 > 0$, to obtain

$$\dot{V}_2 \leq -k_1 \sum_{n \in \mathbb{Z}} \psi_{1n}^2 - (k_0 - \frac{1}{2\kappa}) \sum_{n \in \mathbb{Z}} \psi_{1n}^4 - k_2 \sum_{n \in \mathbb{Z}} \zeta_{2n}^2.$$

Thus, controller (12.37) with $\kappa > 0$, $k_0 \geq \frac{1}{2\kappa}$, $k_1 > 0$, and $k_2 > 0$ guarantees global asymptotic stability of the origin of the infinite dimensional system (12.30). This controller is fully decentralized: the n -th controller cell K_n interacts only with the plant cell on which it acts G_n .

Figure 12.9 shows simulation results of uncontrolled (upper left) and controlled system (12.30) with $M = 100$ cells using the fully decentralized backstepping controller (12.36,12.37) with $k_0 = k_1 = k_2 = 1$ and $\kappa = 0.5$. The initial state of the system is randomly selected. Clearly, the fully decentralized controller requires big amount of initial effort to account for the lack of information about interactions between different subsystems. We note that there is some room for improvement of these large initial excursions of control signals by the different choice of design parameters k_0 , k_1 , k_2 , and κ . However, the obtained results seem to be in agreement with our intuition:

- Higher gain is required to achieve the desired control objective when controller cells do not communicate with each other.

Remark 5 Neither a distributed controller with the nearest neighbor interactions nor a fully decentralized controller for system (12.30) can be obtained using the individual cell backstepping procedure of § 12.3.2. This is because the harmful interactions—that are dominated by feedback in the global design—are treated as the exogenous signals in the individual cell design. Thus, the ‘worst case’ backstepping controller in which K_n interacts with $\{K_{n-2}, K_{n-1}, K_{n+1}, K_{n+2}\}$ is pretty much the only controller that can come out of the individual cell backstepping design.

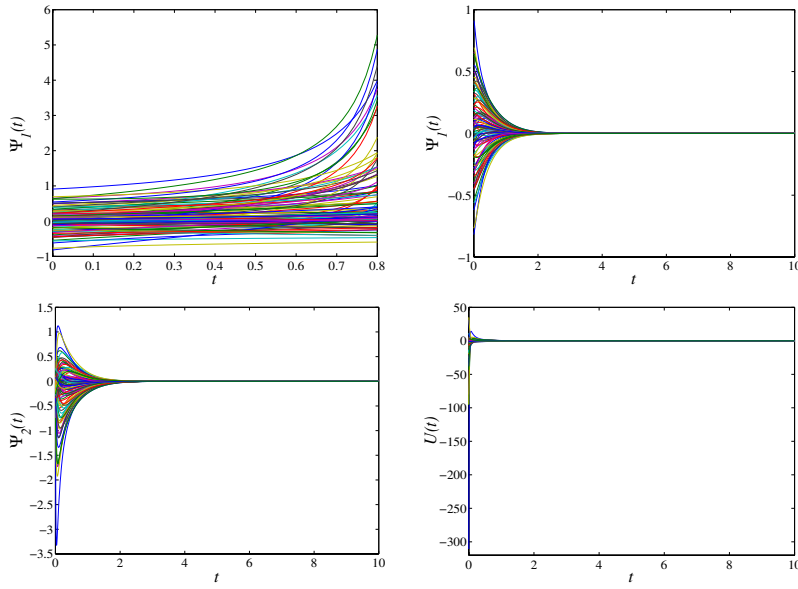


Figure 12.9: Control of system (12.30) with $M = 100$ cells using the fully decentralized backstepping controller (12.36,12.37) with $k_0 = k_1 = k_2 = 1$ and $\kappa = 0.5$.

12.5 Adaptive state-feedback distributed backstepping design

In this section, we consider adaptive state-feedback distributed design. We study systems with both spatially constant and spatially varying unknown parameters. We assume that these parametric uncertainties do not depend on time. The dynamic controllers that guarantee boundedness of all signals in the closed-loop and achieve ‘regulation’ of the plant’s state are obtained using backstepping approach.

We show that systems with constant unknown parameters are amenable to a global design. In other words, an Adaptive CLF (ACLF) can be constructed for the entire infinite dimensional system. Based on our experience with nominal backstepping this may seem advantageous, but we demonstrate that this approach yields centralized dynamical controllers, which is clearly undesirable. On the other hand, for systems with spatially varying unknown parameters global design is not possible without some *a priori* information about values of these parameters. For this class of systems we perform an individual cell adaptive backstepping design which results into distributed localized dynamical controllers. As in the nominal case, the architecture of these controllers has strong similarity with the plant architecture. Furthermore, the dynamical order of K_n depends on the number of unknown parameters in G_n , and it increases as the number of integrators between unknown parameters and the location at which control enters increases. We also note that this approach can be utilized to obtain decentralized adaptive controllers for systems with constant unknown parameters.

Remark 6 *The adaptive control design problems are solved for systems whose local dynamical order is equal to 2. For systems with $m > 2$ the appropriately modified tuning functions design [45] can be employed to guarantee desired dynamical properties.*

12.5.1 Constant unknown parameters

We first study adaptive state-feedback design for systems with constant unknown parameters (12.7). We establish that global adaptive backstepping design yields centralized distributed controllers.

For $m = 2$, (12.7) simplifies to

$$\dot{\psi}_{1n} = \nu_{1n}(\Psi_1) + g_{1n}^*(\Psi_1)\theta_1 + \psi_{2n}, \quad n \in \mathbb{Z}, \quad (12.38a)$$

$$\dot{\psi}_{2n} = \nu_{2n}(\Psi_1, \Psi_2) + g_{2n}^*(\Psi_1, \Psi_2)\theta_2 + bu_n, \quad n \in \mathbb{Z}, \quad (12.38b)$$

where $\theta_1 \in \mathbb{R}^{r_1}$, $\theta_2 \in \mathbb{R}^{r_2}$, and $b \in \mathbb{R}$ represent constant unknown parameters. We rewrite dynamics of the entire system as

$$\dot{\Psi}_1 = N_1(\Psi_1) + G_1^*(\Psi_1)\theta_1 + \Psi_2, \quad (12.39a)$$

$$\dot{\Psi}_2 = N_2(\Psi_1, \Psi_2) + G_2^*(\Psi_1, \Psi_2)\theta_2 + bU, \quad (12.39b)$$

where G_1 and G_2 are operators ($G_k : l_2 \mapsto \mathbb{R}^{r_k}$, $k = 1, 2$) defined by

$$\begin{aligned} G_1(\Psi_1) &:= [\dots \ g_{1,n-1}(\Psi_1) \ g_{1n}(\Psi_1) \ g_{1,n+1}(\Psi_1) \ \dots], \\ G_2(\Psi_1, \Psi_2) &:= [\dots \ g_{2,n-1}(\Psi_1, \Psi_2) \ g_{2n}(\Psi_1, \Psi_2) \ g_{2,n+1}(\Psi_1, \Psi_2) \ \dots]. \end{aligned}$$

Clearly, the adjoints of these two operators are respectively given by

$$G_1^*(\Psi_1) := \begin{bmatrix} \vdots \\ g_{1,n-1}^*(\Psi_1) \\ g_{1n}^*(\Psi_1) \\ g_{1,n+1}^*(\Psi_1) \\ \vdots \end{bmatrix}, \quad G_2^*(\Psi_1, \Psi_2) := \begin{bmatrix} \vdots \\ g_{2,n-1}^*(\Psi_1, \Psi_2) \\ g_{2n}^*(\Psi_1, \Psi_2) \\ g_{2,n+1}^*(\Psi_1, \Psi_2) \\ \vdots \end{bmatrix}.$$

Using Assumptions 1 and 3, we conclude boundedness of these two operators.

In the adaptive backstepping design we have to account for the lack of knowledge of parameters in (12.39). In other words, we need to estimate the values of unknown parameters θ_1 , θ_2 , and reciprocal of unknown control coefficient b , $\varrho := 1/b$, to avoid the division with an estimate of b which can occasionally assume zero value.

Step 1 We invoke Assumption 6, and start the global recursive design with subsystem (12.39a) by considering Ψ_2 as control and proposing a radially unbounded ACLF $V_{a1} : l_2 \times \mathbb{R}^{r_1} \mapsto \mathbb{R}$ of the form

$$V_{a1}(\Psi_1, \tilde{\theta}_1) = \frac{1}{2} \langle \Psi_1, \Psi_1 \rangle + \frac{1}{2} \tilde{\theta}_1^* \Gamma_1^{-1} \tilde{\theta}_1, \quad (12.40)$$

where $\tilde{\theta}_1(t) := \theta_1 - \hat{\theta}_1(t)$, and $\Gamma_1 \in \mathbb{R}^{r_1 \times r_1}$ is a positive definite matrix ($\Gamma_1 = \Gamma_1^* > 0$). ACLF (12.40) is obtained by augmenting the nominal CLF of § 12.3.1 by a term that accounts for the error between unknown parameter θ_1 and its estimate $\hat{\theta}_1$.

The derivative of $V_{a1}(\Psi_1, \tilde{\theta}_1)$ along the solutions of (12.39a) is given by

$$\dot{V}_{a1} = \left\langle \Psi_1, N_1(\Psi_1) + G_1^*(\Psi_1)\hat{\theta}_1 + \Psi_2 \right\rangle + \tilde{\theta}_1^* \left(\Gamma_1^{-1} \dot{\tilde{\theta}}_1 + G_1(\Psi_1)\Psi_1 \right).$$

With the following choice of ‘stabilizing function’ Ψ_{2d}

$$\Psi_{2d} := \Lambda(\Psi_1, \hat{\theta}_1) = - \left(N_1(\Psi_1) + G_1^*(\Psi_1)\hat{\theta}_1 + k_1 \Psi_1 \right), \quad k_1 > 0,$$

and a change of coordinates

$$Z_2 := \Psi_2 - \Lambda(\Psi_1, \hat{\theta}_1),$$

we obtain

$$\dot{V}_{a1} = -k_1 \langle \Psi_1, \Psi_1 \rangle + \langle Z_2, \Psi_1 \rangle + \tilde{\theta}_1^* \left(\Gamma_1^{-1} \dot{\tilde{\theta}}_1 + G_1(\Psi_1)\Psi_1 \right).$$

The last two terms on the right-hand side of (12.41) will be taken care of at the second step of backstepping.

Step 2 We start the second step of our design by augmenting ACLF (12.40) by three terms that account for the errors between Ψ_2 and Ψ_{2d} , and the errors between unknown parameters θ_2 and ϱ and their estimates $\hat{\theta}_2$ and $\tilde{\varrho}$

$$V_{a2}(\Psi_1, Z_2, \tilde{\theta}_1, \tilde{\theta}_2, \tilde{\varrho}) := V_{a1}(\Psi_1, \tilde{\theta}_1) + \frac{1}{2} \langle Z_2, Z_2 \rangle + \frac{1}{2} \tilde{\theta}_2^* \Gamma_2^{-1} \tilde{\theta}_2 + \frac{|b|}{2\beta} \tilde{\varrho}^2, \quad (12.41)$$

where $\tilde{\theta}_2(t) := \theta_2 - \hat{\theta}_2(t)$, $\tilde{\varrho}(t) := \varrho - \tilde{\varrho}(t)$, $\Gamma_2 \in \mathbb{R}^{r_2 \times r_2}$ is a positive definite matrix, and β is a positive constant. The derivative of V_{a2} along the solutions of

$$\begin{aligned} \dot{\Psi}_1 &= -k_1 \Psi_1 + Z_2 + \mathcal{G}_1^* \tilde{\theta}_1, \\ \dot{Z}_2 &= N_2 + \mathcal{G}_2^*(\hat{\theta}_2 + \tilde{\theta}_2) - \frac{\partial \Lambda(\Psi_1, \hat{\theta}_1)}{\partial \Psi_1} (N_1 + \mathcal{G}_1^*(\hat{\theta}_1 + \tilde{\theta}_1) + \Psi_2) - \frac{\partial \Lambda(\Psi_1, \hat{\theta}_1)}{\partial \hat{\theta}_1} \dot{\hat{\theta}}_1 + bU, \end{aligned}$$

is determined by

$$\begin{aligned} \dot{V}_{a2} &= -k_1 \langle \Psi_1, \Psi_1 \rangle + \langle Z_2, S + bU \rangle + \tilde{\theta}_2^* (\Gamma_2^{-1} \dot{\tilde{\theta}}_2 + \mathcal{G}_2 Z_2) + \frac{|b|}{\beta} \tilde{\varrho} \dot{\tilde{\varrho}} \\ &\quad + \tilde{\theta}_1^* \left(\Gamma_1^{-1} \dot{\tilde{\theta}}_1 + \mathcal{G}_1 \Psi_1 - \mathcal{G}_1 \left(\frac{\partial \Lambda(\Psi_1, \hat{\theta}_1)}{\partial \Psi_1} \right)^* Z_2 \right) \end{aligned} \quad (12.42)$$

where

$$S := \Psi_1 + N_2 + \mathcal{G}_2^* \hat{\theta}_2 - \frac{\partial \Lambda(\Psi_1, \hat{\theta}_1)}{\partial \Psi_1} (N_1 + \mathcal{G}_1^* \hat{\theta}_1 + \Psi_2) - \frac{\partial \Lambda(\Psi_1, \hat{\theta}_1)}{\partial \hat{\theta}_1} \dot{\hat{\theta}}_1$$

We can eliminate $\tilde{\theta}_1$ and $\tilde{\theta}_2$ from (12.42) with the following parameter update laws

$$\begin{aligned} \dot{\hat{\theta}}_1 &= \Gamma_1 \mathcal{G}_1(\Psi_1) \left(\Psi_1 - \left(\frac{\partial \Lambda(\Psi_1, \hat{\theta}_1)}{\partial \Psi_1} \right)^* (\Psi_2 - \Lambda(\Psi_1, \hat{\theta}_1)) \right), \\ \dot{\tilde{\theta}}_2 &= \Gamma_2 \mathcal{G}_2(\Psi_1, \Psi_2) (\Psi_2 - \Lambda(\Psi_1, \hat{\theta}_1)). \end{aligned} \quad (12.43)$$

A choice of control law of the form

$$U = -\hat{\varrho}(S + k_2 Z_2), \quad k_2 > 0,$$

together with (12.43) and the relationship

$$b\hat{\varrho} = b(\varrho - \tilde{\varrho}) = 1 - b\tilde{\varrho},$$

renders (12.42) into

$$\dot{V}_{a2} = -k_1 \langle \Psi_1, \Psi_1 \rangle - k_2 \langle Z_2, Z_2 \rangle + \frac{|b|}{\beta} \tilde{\varrho} (\dot{\tilde{\varrho}} + \beta \text{sign}(b) \langle Z_2, S + k_2 Z_2 \rangle). \quad (12.44)$$

With the following choice of update law for the estimate $\hat{\varrho}$

$$\dot{\hat{\varrho}} = \beta \text{sign}(b) \langle Z_2, S + k_2 Z_2 \rangle,$$

(12.44) simplifies to

$$\dot{V}_{a2} = -k_1 \langle \Psi_1, \Psi_1 \rangle - k_2 \langle Z_2, Z_2 \rangle =: -W(\Psi_1, Z_2) \leq 0. \quad (12.45)$$

We next establish boundedness of all signals in the closed-loop and asymptotic convergence of Ψ_1 and Ψ_2 to zero.

Establishing asymptotic convergence of Ψ_1 and Ψ_2 to zero

Negative semi-definiteness of \dot{V}_{a2} implies that V_{a2} is a non-increasing function of time. We note that properties of functions ν_{1n} and g_{1n} (see Assumptions 1–3) together with Assumption 6 guarantee boundedness of V_{a2} at $t = 0$. Hence, based on the definition of V_{a2} and its boundedness at $t = 0$, we conclude that Ψ_1 , Ψ_2 , $\hat{\theta}_1$, $\hat{\theta}_2$, and $\hat{\varrho}$ are globally uniformly bounded, that is,

$$\left. \begin{aligned} \|\Psi_k(t)\|^2 &:= \sum_{n \in \mathbb{Z}} \psi_{kn}^2(t) < \infty \\ \|\hat{\theta}_k(t)\|^2 &:= \hat{\theta}_k^*(t)\hat{\theta}_k(t) < \infty \\ \|\dot{\varrho}(t)\|^2 &:= \dot{\varrho}^2(t) < \infty \end{aligned} \right\} \quad \forall t \geq 0, \quad k = 1, 2.$$

In view of the last equation, properties of functions g_{kn} and ν_{kn} (see Assumptions 1–3), and definition of U , it follows that

$$\hat{\theta}_1 \in L_\infty, \quad \hat{\theta}_2 \in L_\infty, \quad \hat{\varrho} \in L_\infty, \quad \{\psi_{1n} \in L_\infty, \quad \psi_{2n} \in L_\infty, \quad u_n \in L_\infty, \quad \forall n \in \mathbb{Z}\},$$

which in turn implies

$$\dot{\psi}_{1n} \in L_\infty, \quad \dot{\psi}_{2n} \in L_\infty, \quad \forall n \in \mathbb{Z}.$$

Using Assumption 3 and the fact that $\{\Psi_1(t) \in l_2, \Psi_2(t) \in l_2, \forall t \geq 0\}$, we also conclude that $\{\dot{\hat{\theta}}_1(t) < \infty, \dot{\hat{\theta}}_2(t) < \infty, \dot{\hat{\varrho}}(t) < \infty, \forall t \geq 0\}$. This follows from the properties of functions ν_{kn} and g_{kn} (see Assumptions 1–3) and a simple observation that $\{\Psi(t) \in l_p \times l_q, \forall t \geq 0, \forall p, q \in (2, \infty)\}$ whenever $\{\Psi(t) \in l_2 \times l_2, \forall t \geq 0\}$. Furthermore, since $V_{a2}(\Psi_1(t), Z_2(t), \hat{\theta}_1(t), \hat{\theta}_2(t), \tilde{\varrho}(t))$ is a non-increasing non-negative function, it has a limit $V_{a2\infty}$ as $t \rightarrow \infty$. Therefore, integration of (12.45) yields

$$\begin{aligned} \int_0^\infty W(\Psi_1(t), Z_2(t)) dt &= k_1 \int_0^\infty \langle \Psi_1(t), \Psi_1(t) \rangle dt + k_2 \int_0^\infty \langle Z_2(t), Z_2(t) \rangle dt \\ &\leq V_{a2}(\Psi_1(0), Z_2(0), \tilde{\theta}_1(0), \tilde{\theta}_2(0), \tilde{\varrho}(0)) - V_{a2\infty} \\ &< \infty, \end{aligned}$$

which together with the definition of Z_2 implies

$$\psi_{1n} \in L_2, \quad \psi_{2n} \in L_2, \quad \forall n \in \mathbb{Z}.$$

Therefore, we have shown that

$$\psi_{1n}, \psi_{2n} \in L_2 \cap L_\infty, \quad \dot{\psi}_{1n}, \dot{\psi}_{2n} \in L_\infty, \quad \forall n \in \mathbb{Z}.$$

Using the Barbălat lemma (see, for example [44, 57, 66]), we conclude that both $\psi_{1n}(t)$ and $\psi_{2n}(t)$ go to zero as $t \rightarrow \infty$, for all $n \in \mathbb{Z}$. Therefore, the dynamical controller obtained as a result of our design guarantees boundedness of all signals in the closed-loop and asymptotic convergence of the state $\Psi^*(t) := [\Psi_1^*(t) \quad \Psi_2^*(t)]^*$ of (12.39) to zero.

The developments of this subsection are summarized in the following theorem.

Theorem 21 Suppose that system (12.39) satisfies Assumptions 1, 2, 3, 4, and 6. Then, the following

centralized dynamical controller

$$\begin{aligned}
U &= -\hat{\varrho}(S + k_2 Z_2), \quad k_2 > 0, \\
Z_2 &= \Psi_2 - \Lambda(\Psi_1, \hat{\theta}_1), \\
S &= \Psi_1 + N_2 + \mathcal{G}_2^* \hat{\theta}_2 - \frac{\partial \Lambda(\Psi_1, \hat{\theta}_1)}{\partial \Psi_1} (N_1 + \mathcal{G}_1^* \hat{\theta}_1 + \Psi_2) - \frac{\partial \Lambda(\Psi_1, \hat{\theta}_1)}{\partial \hat{\theta}_1} \dot{\hat{\theta}}_1, \\
\Lambda &= -(N_1(\Psi_1) + \mathcal{G}_1^*(\Psi_1) \hat{\theta}_1 + k_1 \Psi_1), \quad k_1 > 0, \\
\dot{\hat{\theta}}_1 &= \Gamma_1 \mathcal{G}_1(\Psi_1) \left(\Psi_1 - \left(\frac{\partial \Lambda(\Psi_1, \hat{\theta}_1)}{\partial \Psi_1} \right)^* Z_2 \right), \\
\dot{\hat{\theta}}_2 &= \Gamma_2 \mathcal{G}_2(\Psi_1, \Psi_2) Z_2, \\
\dot{\hat{\varrho}} &= \beta \operatorname{sign}(b) \langle Z_2, S + k_2 Z_2 \rangle,
\end{aligned} \tag{12.46}$$

guarantees boundedness of all signals in the closed-loop system (12.39, 12.46) and asymptotic convergence of the state of (12.39) to zero. These properties can be established with the Lyapunov function

$$V_{a2}(\Psi_1, Z_2, \tilde{\theta}_1, \tilde{\theta}_2, \tilde{\varrho}) := \frac{1}{2} \langle \Psi_1, \Psi_1 \rangle + \frac{1}{2} \langle Z_2, Z_2 \rangle + \frac{1}{2} \tilde{\theta}_1^* \Gamma_1^{-1} \tilde{\theta}_1 + \frac{1}{2} \tilde{\theta}_2^* \Gamma_2^{-1} \tilde{\theta}_2 + \frac{|b|}{2\beta} \tilde{\varrho}^2.$$

Remark 7 Since information from all plant cells is used to determine estimates of constant unknown parameters $\theta_1 \in \mathbb{R}^{r_1}$, $\theta_2 \in \mathbb{R}^{r_2}$, and $\varrho \in \mathbb{R}$, dynamical controller (12.46) in Theorem 21 is centralized. This controller builds one estimate per unknown parameter, and its dynamical order is equal to $r_1 + r_2 + 1$.

12.5.2 Spatially varying unknown parameters

Here we consider state-feedback design for systems with time independent spatially varying unknown parameters. An example of such a system is given by (12.8), which for $m = 2$ becomes

$$\dot{\psi}_{1n} = \tau_{1n}(\Psi_1) + h_{1n}^*(\Psi_1) \theta_{1n} + \psi_{2n}, \quad n \in \mathbb{Z}, \tag{12.47a}$$

$$\dot{\psi}_{2n} = \tau_{2n}(\Psi_1, \Psi_2) + h_{2n}^*(\Psi_1, \Psi_2) \theta_{2n} + b_n u_n, \quad n \in \mathbb{Z}. \tag{12.47b}$$

Remark 8 Even if Assumption 6 holds, the infinite number of unknown parameters in (12.47) prevents us from doing a global design. Namely, the finiteness of the global ACLF candidate for (12.47a) at $t = 0$

$$V_{a1}(\Psi_1, \{\tilde{\theta}_{1n}\}_{n \in \mathbb{Z}}) := \frac{1}{2} \langle \Psi_1, \Psi_1 \rangle + \frac{1}{2} \sum_{n \in \mathbb{Z}} \tilde{\theta}_{1n}^* \Gamma_{1n}^{-1} \tilde{\theta}_{1n},$$

would imply that most of unknown parameters are initially known, which is somewhat artificial. If we have some a priori information about values that the unknown parameters can assume we can choose a sequence of positive definite matrices $\{\Gamma_{1n}\}_{n \in \mathbb{Z}}$ such that $V_{a1}(\Psi_1(0), \{\tilde{\theta}_{1n}(0)\}_{n \in \mathbb{Z}})$ is finite. However, this would lead to parameter update laws with very large gains since elements of this sequence have to increase their values as $n \rightarrow \infty$. Clearly, this is not desirable for implementation.

In view of Remark 8, we carry out the individual cell adaptive backstepping design for system (12.47) with spatially varying parametric uncertainties. This approach can be also used for adaptive control of systems with constant unknown parameters, and we will demonstrate that it yields distributed dynamical controllers that are not centralized. Thus, individual cell adaptive design for infinite dimensional systems on lattices has advantages over global adaptive design of § 12.5.1, because the latter leads to centralized dynamical controllers.

Step 1 For the n -th cell of subsystem (12.47a) we propose an ACLF

$$V_{a1n}(\psi_{1n}, \tilde{\theta}_{1n}) = \frac{1}{2} \psi_{1n}^2 + \frac{1}{2} \tilde{\theta}_{1n}^* \Gamma_{1n}^{-1} \tilde{\theta}_{1n},$$

and choose a desired value of ‘virtual control’

$$\psi_{2nd} := \lambda_n(\Psi_1, \hat{\theta}_{1n}) = -(\tau_{1n}(\Psi_1) + h_{1n}^*(\Psi_1)\hat{\theta}_{1n} + k_{1n}\psi_{1n}), \quad k_{1n} > 0,$$

to obtain

$$\dot{V}_{a1n} = -k_{1n}\psi_{1n}^2 + \psi_{1n}\zeta_{2n} + \tilde{\theta}_{1n}^*\left(\Gamma_{1n}^{-1}\dot{\tilde{\theta}}_{1n} + \psi_{1n}h_{1n}(\Psi_1)\right),$$

where $\zeta_{2n} := \psi_{2n} - \lambda_n(\Psi_1, \hat{\theta}_{1n})$. The sign indefinite terms in \dot{V}_{a1n} will be accounted for at the second step of adaptive design.

Step 2 The derivative of ζ_{2n} is now determined by

$$\dot{\zeta}_{2n} = \tau_{2n}(\Psi_1, \Psi_2) + h_{2n}^*(\Psi_1, \Psi_2)(\hat{\theta}_{2n} + \tilde{\theta}_{2n}) + b_n u_n - \frac{\partial \lambda_n(\Psi_1, \hat{\theta}_{1n})}{\partial \Psi_1} \dot{\Psi}_1 - \frac{\partial \lambda_n(\Psi_1, \hat{\theta}_{1n})}{\partial \hat{\theta}_{1n}} \dot{\hat{\theta}}_{1n}.$$

Using Assumption 1 and the definition of $\lambda_n(\Psi_1, \hat{\theta}_{1n})$ we express $(\partial \lambda_n / \partial \Psi_1) \dot{\Psi}_1$ as

$$\begin{aligned} \frac{\partial \lambda_n}{\partial \Psi_1} \dot{\Psi}_1 &= \sum_{j \in \mathbb{Z}_N} \frac{\partial \lambda_n}{\partial \psi_{1,n+j}} \dot{\psi}_{1,n+j} = \sum_{j \in \mathbb{Z}_N} \tilde{\theta}_{1,n+j}^* h_{1,n+j}(\Psi_1) \frac{\partial \lambda_n}{\partial \psi_{1,n+j}} + \\ &\quad \sum_{j \in \mathbb{Z}_N} \frac{\partial \lambda_n}{\partial \psi_{1,n+j}} \left(\tau_{1,n+j}(\Psi_1) + h_{1,n+j}^*(\Psi_1)\hat{\theta}_{1,n+j} + \psi_{2,n+j} \right). \end{aligned}$$

Since $\{\hat{\theta}_{1,n+j}\}_{j \in \mathbb{Z}_N}$ enters into the expression for $\dot{\zeta}_{2n}$, we augment the ACLF from Step 1 as follows

$$\begin{aligned} V_{a2n}(\psi_{1n}, \zeta_{2n}, \{\tilde{\theta}_{1,n+j}\}_{j \in \mathbb{Z}_N}, \tilde{\theta}_{2n}, \tilde{\varrho}_n) &:= \\ V_{a1n}(\psi_{1n}, \hat{\theta}_{1n}) + \frac{1}{2}\zeta_{2n}^2 + \frac{1}{2} \sum_{j \in \mathbb{Z}_N \setminus \{0\}} \tilde{\theta}_{1,n+j}^* \Gamma_{1,n+j}^{-1} \tilde{\theta}_{1,n+j} + \frac{1}{2} \tilde{\theta}_{2n}^* \Gamma_{2n}^{-1} \tilde{\theta}_{2n} + \frac{1}{2} \frac{|b_n|}{\beta_n} \tilde{\varrho}_n^2, \end{aligned}$$

It is readily established that a distributed dynamical controller of the form

$$\begin{aligned} u_n &= -\hat{\varrho}_n(s_n + k_{2n}\zeta_{2n}), \\ \dot{\hat{\theta}}_{1n} &= \left(\psi_{1n} - \zeta_{2n} \frac{\partial \lambda_n}{\partial \psi_{1n}} \right) \Gamma_{1n} h_{1n}(\Psi_1), \\ \dot{\hat{\theta}}_{1,n+j} &= -\zeta_{2n} \frac{\partial \lambda_n}{\partial \psi_{1,n+j}} \Gamma_{1,n+j} h_{1,n+j}(\Psi_1), \quad j \in \mathbb{Z}_N \setminus \{0\}, \\ \dot{\hat{\theta}}_{2n} &= \zeta_{2n} \Gamma_{2n} h_{2n}(\Psi_1, \Psi_2), \\ \dot{\tilde{\varrho}}_n &= \beta_n \text{sign}(b_n) \zeta_{2n} (s_n + k_{2n}\zeta_{2n}), \\ s_n &= \psi_{1n} + \tau_{2n} + h_{2n}^* \hat{\theta}_{2n} - \frac{\partial \lambda_n}{\partial \hat{\theta}_{1n}} \dot{\hat{\theta}}_{1n} - \\ &\quad \sum_{j \in \mathbb{Z}_N} \frac{\partial \lambda_n}{\partial \psi_{1,n+j}} \left(\tau_{1,n+j} + h_{1,n+j}^* \hat{\theta}_{1,n+j} + \psi_{2,n+j} \right), \end{aligned}$$

renders \dot{V}_{a2n} into

$$\dot{V}_{a2n} = -k_{1n}\psi_{1n}^2 - k_{2n}\zeta_{2n}^2 =: -W_n(\psi_{1n}, \zeta_{2n}) \leq 0,$$

where we use the analytical expression for $\dot{\hat{\theta}}_{1n}$ in the expression for s_n .

Using similar argument as in § 12.5.1, we establish boundedness of all signals in the closed-loop and asymptotic convergence of both $\psi_{1n}(t)$ and $\psi_{2n}(t)$ to zero, for all $n \in \mathbb{Z}$.

The main result of this subsection is summarized in the following theorem.

Theorem 22 Suppose that system (12.47) satisfies Assumptions 1, 2, and 5. Then, the following distributed

dynamical controller

$$\begin{aligned}
u_n &= -\hat{\varrho}_n(s_n + k_{2n}\zeta_{2n}), \quad k_{2n} > 0, \quad \forall n \in \mathbb{Z}, \\
\zeta_{2n} &= \psi_{2n} - \lambda_n(\Psi_1, \hat{\theta}_{1n}), \\
\lambda_n &= -(\tau_{1n}(\Psi_1) + h_{1n}^*(\Psi_1)\hat{\theta}_{1n} + k_{1n}\psi_{1n}), \quad k_{1n} > 0, \quad \forall n \in \mathbb{Z}, \\
s_n &= \psi_{1n} + \tau_{2n} + h_{2n}^*\hat{\theta}_{2n} - \frac{\partial \lambda_n}{\partial \hat{\theta}_{1n}}\dot{\hat{\theta}}_{1n} - \\
&\quad \sum_{j \in \mathbb{Z}_N} \frac{\partial \lambda_n}{\partial \psi_{1,n+j}} (\tau_{1,n+j} + h_{1,n+j}^*\hat{\theta}_{1,n+j} + \psi_{2,n+j}), \\
\dot{\hat{\theta}}_{1n} &= \left(\psi_{1n} - \zeta_{2n} \frac{\partial \lambda_n}{\partial \psi_{1n}} \right) \Gamma_{1n} h_{1n}(\Psi_1), \\
\dot{\hat{\theta}}_{1,n+j} &= -\zeta_{2n} \frac{\partial \lambda_n}{\partial \psi_{1,n+j}} \Gamma_{1,n+j} h_{1,n+j}(\Psi_1), \quad j \in \mathbb{Z}_N \setminus \{0\}, \\
\dot{\hat{\theta}}_{2n} &= \zeta_{2n} \Gamma_{2n} h_{2n}(\Psi_1, \Psi_2), \\
\dot{\hat{\varrho}}_n &= \beta_n \text{sign}(b_n) \zeta_{2n} (s_n + k_{2n}\zeta_{2n}),
\end{aligned} \tag{12.48}$$

guarantees boundedness of all signals in the closed-loop system (12.47,12.48) and asymptotic convergence of the state of (12.47) to zero.

Theorem 22 can be used to derive the following corollary for localized adaptive distributed control of systems with constant parametric uncertainties.

Corollary 23 Suppose that system (12.38) satisfies Assumptions 1, 2, and 4. Then, the following distributed dynamical controller

$$\begin{aligned}
u_n &= -\hat{\varrho}_n(s_n + k_{2n}\zeta_{2n}), \quad k_{2n} > 0, \quad \forall n \in \mathbb{Z}, \\
\zeta_{2n} &= \psi_{2n} - \lambda_n(\Psi_1, \hat{\theta}_{1n}), \\
\lambda_n &= -(\nu_{1n}(\Psi_1) + g_{1n}^*(\Psi_1)\hat{\theta}_{1n} + k_{1n}\psi_{1n}), \quad k_{1n} > 0, \quad \forall n \in \mathbb{Z}, \\
s_n &= \psi_{1n} + \nu_{2n} + g_{2n}^*\hat{\theta}_{2n} - \frac{\partial \lambda_n}{\partial \hat{\theta}_{1n}}\dot{\hat{\theta}}_{1n} - \\
&\quad \sum_{j \in \mathbb{Z}_N} \frac{\partial \lambda_n}{\partial \psi_{1,n+j}} (\nu_{1,n+j} + g_{1,n+j}^*\hat{\theta}_{1n} + \psi_{2,n+j}), \\
\dot{\hat{\theta}}_{1n} &= \Gamma_{1n} \left(\psi_{1n} g_{1n}(\Psi_1) - \zeta_{2n} \sum_{j \in \mathbb{Z}_N} \frac{\partial \lambda_n}{\partial \psi_{1,n+j}} g_{1,n+j}(\Psi_1) \right), \\
\dot{\hat{\theta}}_{2n} &= \zeta_{2n} \Gamma_{2n} g_{2n}(\Psi_1, \Psi_2), \\
\dot{\hat{\varrho}}_n &= \beta_n \text{sign}(b_n) \zeta_{2n} (s_n + k_{2n}\zeta_{2n}),
\end{aligned} \tag{12.49}$$

guarantees boundedness of all signals in the closed-loop system (12.38,12.49) and asymptotic convergence of the state of (12.38) to zero.

12.6 Dynamical order induced by adaptive distributed backstepping design

As noted in Remark 7, since information from all plant cells is used to determine estimates of constant unknown parameters, the adaptive backstepping design of § 12.5.1 yields centralized dynamical controllers. On the other hand, the adaptive backstepping design of § 12.5.2 results into localized distributed dynamical controllers. The architecture of these controllers enjoys the same properties as in the nominal case:

- When matching condition is satisfied, the adaptive distributed backstepping controllers of § 12.5.2 inherit the plant architecture.
- For systems (12.38) and (12.47) with $2N$ interactions per plant cell, the adaptive distributed backstepping design § 12.5.2 induces $4N$ interactions per controller cell.

There are two important differences between nominal and adaptive backstepping designs:

- Nominal controllers are static, whereas adaptive controllers are dynamic.
- As illustrated in § 12.4, nominal controllers with less interactions can be obtained by performing a global design to identify beneficial interactions, and/or to dominate harmful interactions. On the other hand, even though the individual cell adaptive backstepping design yields localized distributed controllers, it does not seem that it lends itself easily to design of controllers with less interactions.

We next comment on the dynamical order induced by adaptive distributed backstepping design.

Constant unknown parameters

The design of § 12.5.1 yields *centralized finite dimensional* controller (12.46) in which both the dynamical order and the number of parameter estimates are equal to the number of unknown parameters. In other words, for system (12.39) with constant unknown parameters $\theta_1 \in \mathbb{R}^{r_1}$, $\theta_2 \in \mathbb{R}^{r_2}$, and $\varrho \in \mathbb{R}$, controller (12.46) has an estimate per unknown parameter (i.e., $\hat{\theta}_1$, $\hat{\theta}_2$, and $\hat{\varrho}$), and its dynamical order is equal to $r_1 + r_2 + 1$. On the other hand, controller (12.49) has different parameter update laws (for $\hat{\theta}_{1n}$, $\hat{\theta}_{2n}$, and $\hat{\varrho}_n$) in every control unit K_n , even though all unknown parameters are both spatially and temporally constant. The dynamical order of K_n , for every $n \in \mathbb{Z}$, is equal to the number of unknown parameters: $r_1 + r_2 + 1$. This ‘over-parameterization’ is advantageous in applications because it allows for implementation of *localized adaptive distributed controllers*. This useful property cannot be achieved with controller (12.46) because it requires information about entire distributed state to estimate unknown parameters. Furthermore, the design procedure described in § 12.5.2 (see Corollary 23) does not require Assumptions 3 and 6 to hold and, consequently, it can be applied to a broader class of problems.

Spatially varying unknown parameters

The individual cell adaptive backstepping design of § 12.5.1 yields localized adaptive distributed controllers. For systems with spatially varying unknown parameters, the dynamical order of these controllers is determined by two factors: the number of interactions per plant cell, and the number of unknown parameters. If, for simplicity, we assume that, for every $n \in \mathbb{Z}$, $\theta_{1n} \in \mathbb{R}^{r_1}$, $\theta_{2n} \in \mathbb{R}^{r_2}$, and $\varrho_n \in \mathbb{R}$ then the local dynamical order of controller (12.48) in Theorem 22 is equal to $(2N+1)r_1 + r_2 + 1$. Thus, for system (12.47) that does not satisfy the matching condition, the dynamical order of K_n scales linearly with the number of interactions per plant cell. Clearly, this order can become prohibitive for systems with large number of interactions per plant cell.

12.7 Output-feedback distributed backstepping design

The controllers of § 12.3 and § 12.5 provide stability/regulation/asymptotic tracking of the closed-loop systems under the assumption that the full state information is available. In this section, we study a more realistic situation in which only a distributed output is measured. We show that, as for finite dimensional systems [45], the observer backstepping can be used as a tool for fulfilling the desired control objective for systems on lattices in which nonlinearities depend only on the measured signals. The starting point of the nominal output-feedback approach is a design of an observer which guarantees the exponential convergence of the state estimates to their real values. Once this is accomplished, the combination of backstepping and nonlinear damping is used to account for the observation errors and provide closed-loop stability. In the adaptive case, filters which provide ‘virtual estimates’ of unmeasured state variables also need to be designed.

We solve output-feedback problems for systems of local dynamical order two ($m = 2$) that satisfy the matching condition. General case can be handled using similar tools. In this situation, systems (12.9) and (12.10) respectively simplify to

$$\dot{\psi}_{1n} = \psi_{2n}, \quad n \in \mathbb{Z}, \quad (12.50a)$$

$$\dot{\psi}_{2n} = f_n(Y) + b_n u_n, \quad n \in \mathbb{Z}, \quad (12.50b)$$

$$y_n = \psi_{1n}, \quad n \in \mathbb{Z}, \quad (12.50c)$$

and systems with parametric uncertainties

$$\dot{\psi}_{1n} = \psi_{2n}, \quad n \in \mathbb{Z}, \quad (12.51a)$$

$$\dot{\psi}_{2n} = \tau_n(Y) + h_n^*(Y)\theta_n + b_n u_n, \quad n \in \mathbb{Z}, \quad (12.51b)$$

$$y_n = \psi_{1n}, \quad n \in \mathbb{Z}. \quad (12.51c)$$

Both nominal and adaptive output-feedback problems are solved using individual cell backstepping design. We note that nominal output-feedback problem can be also solved using global backstepping design if the initial state of system (12.50) satisfies Assumption 6.

12.7.1 Nominal output-feedback design

We rewrite (12.50) in a form suitable for observer design

$$\dot{\psi}_n = A\psi_n + \varphi_n(Y) + b_n e_2 u_n, \quad n \in \mathbb{Z}, \quad (12.52a)$$

$$y_n = C\psi_n, \quad n \in \mathbb{Z}, \quad (12.52b)$$

where

$$\psi_n := \begin{bmatrix} \psi_{1n} \\ \psi_{2n} \end{bmatrix}, \quad \varphi_n(Y) := \begin{bmatrix} 0 \\ f_n(Y) \end{bmatrix}, \quad A := \begin{bmatrix} 0 & 1 \\ 0 & 0 \end{bmatrix}, \quad e_2 := \begin{bmatrix} 0 \\ 1 \end{bmatrix}, \quad C := [1 \ 0].$$

We proceed by designing an equivalent of *Krener-Isidori observer* (see, for example, [45, 67]) for (12.52)

$$\dot{\hat{\psi}}_n = A\hat{\psi}_n + L_n(y_n - \hat{y}_n) + \varphi_n(Y) + b_n e_2 u_n, \quad n \in \mathbb{Z}, \quad (12.53a)$$

$$\hat{y}_n = C\hat{\psi}_n, \quad n \in \mathbb{Z}, \quad (12.53b)$$

where $L_n := [l_{1n} \ l_{2n}]^*$ is chosen such that $A_{0n} := A - L_n C$ is a Hurwitz matrix for every $n \in \mathbb{Z}$. Clearly, this is going to be satisfied if and only if $l_{in} > 0, \forall i = \{1, 2\}, \forall n \in \mathbb{Z}$. In this case, an exponentially stable system of the form

$$\dot{\tilde{\psi}}_n = A_{0n}\tilde{\psi}_n, \quad n \in \mathbb{Z}, \quad (12.54)$$

is obtained by subtracting (12.53) from (12.52). The properties of A_{0n} imply the exponential convergence of $\tilde{\psi}_n := \psi_n - \hat{\psi}_n$ to zero and the existence of the positive definite matrix P_{0n} that satisfies

$$A_{0n}^* P_{0n} + P_{0n} A_{0n} = -I, \quad \forall n \in \mathbb{Z}. \quad (12.55)$$

We are now ready to design an output-feedback controller that guarantees stability of (12.50).

Step 1 The observer-backstepping design starts with subsystem (12.50a) by rewriting it as

$$\dot{\psi}_{1n} = \hat{\psi}_{2n} + \tilde{\psi}_{2n}, \quad n \in \mathbb{Z}, \quad (12.56)$$

and considering $\hat{\psi}_{2n}$ as a virtual control and $\tilde{\psi}_{2n}$ as a disturbance generated by (12.54). We propose a CLF

for the n -th subsystem of (12.56)

$$V_{1n}(\psi_{1n}, \tilde{\psi}_n) := \frac{1}{2}\psi_{1n}^2 + \frac{1}{d_{1n}}\tilde{\psi}_n^*P_{0n}\tilde{\psi}_n,$$

where P_{0n} is a positive definite matrix that satisfies (12.55), and $d_{1n} > 0$ is a design parameter. The derivative of V_{1n} along the solutions of (12.56, 12.54) for every $n \in \mathbb{Z}$ is determined by

$$\begin{aligned} \dot{V}_{1n} &= \psi_{1n}(\hat{\psi}_{2n} + \tilde{\psi}_{2n}) - \frac{1}{d_{1n}}\|\tilde{\psi}_n\|_2^2 \\ &\leq \psi_{1n}(\hat{\psi}_{2n} + d_{1n}\psi_{1n}) + \frac{1}{4d_{1n}}\tilde{\psi}_{2n}^2 - \frac{1}{d_{1n}}\|\tilde{\psi}_n\|_2^2 \\ &\leq \psi_{1n}(\hat{\psi}_{2n} + d_{1n}\psi_{1n}) - \frac{3}{4d_{1n}}\|\tilde{\psi}_n\|_2^2, \end{aligned} \quad (12.57)$$

where Young's Inequality (see [45], expression (2.254)) is used to upper bound $\psi_{1n}\tilde{\psi}_{2n}$. The following choice of a 'stabilizing function' $\hat{\psi}_{2nd}$

$$\hat{\psi}_{2nd} = -(k_{1n} + d_{1n})\psi_{1n}, \quad k_{1n} > 0, \quad \forall n \in \mathbb{Z},$$

clearly renders $\dot{V}_{1n}(\psi_{1n}, \tilde{\psi}_n)$ negative definite. Since $\hat{\psi}_{2n}$ is not actually a control, but rather, an estimate of a state variable, we introduce the change of variables

$$\zeta_{2n} := \hat{\psi}_{2n} - \hat{\psi}_{2nd} = \hat{\psi}_{2n} + (k_{1n} + d_{1n})\psi_{1n}, \quad \forall n \in \mathbb{Z},$$

which adds an additional term on the right-hand side of (12.57)

$$\dot{V}_{1n} \leq -k_{1n}\psi_{1n}^2 - \frac{3}{4d_{1n}}\|\tilde{\psi}_n\|_2^2 + \psi_{1n}\zeta_{2n}. \quad (12.58)$$

The sign indefinite term in (12.58) will be taken care of at the second step of backstepping.

Step 2 We express our system into new coordinates as

$$\dot{\psi}_{1n} = -(k_{1n} + d_{1n})\psi_{1n} + \zeta_{2n} + \tilde{\psi}_{2n}, \quad n \in \mathbb{Z}, \quad (12.59a)$$

$$\dot{\zeta}_{2n} = (k_{1n} + d_{1n})(\hat{\psi}_{2n} + \tilde{\psi}_{2n}) + l_{2n}(\psi_{1n} - \hat{\psi}_{1n}) + f_n(Y) + b_n u_n, \quad n \in \mathbb{Z}, \quad (12.59b)$$

$$\dot{\tilde{\psi}}_n = A_{0n}\tilde{\psi}_n, \quad n \in \mathbb{Z}, \quad (12.59c)$$

and propose the following CLF for its n -th subsystem

$$V_{2n}(\psi_{1n}, \zeta_{2n}, \tilde{\psi}_n) := V_{1n}(\psi_{1n}, \tilde{\psi}_n) + \frac{1}{2}\zeta_{2n}^2 + \frac{1}{d_{2n}}\tilde{\psi}_n^*P_{0n}\tilde{\psi}_n,$$

with $d_{2n} > 0$. The derivative of V_{2n} along the solutions of (12.59) for every $n \in \mathbb{Z}$ is determined by

$$\begin{aligned} \dot{V}_{2n} &= \dot{V}_{1n} + \zeta_{2n}\dot{\zeta}_{2n} - \frac{1}{d_{2n}}\|\tilde{\psi}_n\|_2^2 \leq -k_{1n}\psi_{1n}^2 - \frac{3}{4}(\frac{1}{d_{1n}} + \frac{1}{d_{2n}})\|\tilde{\psi}_n\|_2^2 + \\ &\quad \zeta_{2n}(\psi_{1n} + (k_{1n} + d_{1n})\hat{\psi}_{2n} + l_{2n}(\psi_{1n} - \hat{\psi}_{1n}) + f_n(Y) + d_{2n}(k_{1n} + d_{1n})^2\zeta_{2n} + b_n u_n). \end{aligned}$$

A control law of the form

$$u_n = -\frac{1}{b_n}(\psi_{1n} + (k_{1n} + d_{1n})\hat{\psi}_{2n} + l_{2n}(\psi_{1n} - \hat{\psi}_{1n}) + f_n(Y) + d_{2n}(k_{1n} + d_{1n})^2\zeta_{2n} + b_n u_n), \quad (12.60)$$

with $k_{2n} > 0$ for every $n \in \mathbb{Z}$, guarantees negative definiteness of \dot{V}_{2n} , that is

$$\dot{V}_{2n} \leq -k_{1n}\psi_{1n}^2 - k_{2n}\zeta_{2n}^2 - \frac{3}{4}(\frac{1}{d_{1n}} + \frac{1}{d_{2n}})\|\tilde{\psi}_n\|_2^2.$$

Hence, we conclude global asymptotic stability of the origin of closed-loop system (12.50,12.54,12.60).

12.7.2 Adaptive output-feedback design

We rewrite (12.51) in a form suitable for adaptive output-feedback design

$$\dot{\psi}_n = A\psi_n + \eta_n(Y) + \sum_{j=1}^r \theta_{jn}\varphi_{jn}(Y) + b_n e_2 u_n, \quad n \in \mathbb{Z}, \quad (12.61a)$$

$$y_n = C\psi_n, \quad n \in \mathbb{Z}, \quad (12.61b)$$

where

$$\psi_n := \begin{bmatrix} \psi_{1n} \\ \psi_{2n} \end{bmatrix}, \quad \eta_n(Y) := \begin{bmatrix} 0 \\ \tau_n(Y) \end{bmatrix}, \quad \varphi_{jn}(Y) := \begin{bmatrix} 0 \\ h_{jn}(Y) \end{bmatrix},$$

$$A := \begin{bmatrix} 0 & 1 \\ 0 & 0 \end{bmatrix}, \quad e_2 := \begin{bmatrix} 0 \\ 1 \end{bmatrix}, \quad C := [1 \ 0].$$

We proceed by designing filters which provide ‘virtual estimates’ of unmeasured state variables (see [45], § 7.3)

$$\dot{\xi}_n^{(0)} = A_{0n}\xi_n^{(0)} + L_n y_n + \eta_n(Y), \quad n \in \mathbb{Z}, \quad (12.62a)$$

$$\dot{\xi}_n^{(j)} = A_{0n}\xi_n^{(j)} + \varphi_{jn}(Y), \quad 1 \leq j \leq r, \quad n \in \mathbb{Z}, \quad (12.62b)$$

$$\dot{v}_n = A_{0n}v_n + e_2 u_n, \quad n \in \mathbb{Z}, \quad (12.62c)$$

where $L_n := [l_{1n} \ l_{2n}]^*$ is chosen such that $A_{0n} := A - L_n C$ is Hurwitz for every $n \in \mathbb{Z}$. Clearly, A_{0n} is going to be Hurwitz if and only if $l_{in} > 0$, $\forall i = \{1, 2\}$, $\forall n \in \mathbb{Z}$. In this case, an exponentially stable system of the form

$$\dot{\varepsilon}_n = A_{0n}\varepsilon_n, \quad \varepsilon_n := \psi_n - \{\xi_n^{(0)} + \sum_{j=1}^r \theta_{jn}\xi_n^{(j)} + b_n v_n\}, \quad n \in \mathbb{Z}, \quad (12.63)$$

is obtained by combining (12.61) and (12.62). The properties of A_{0n} imply the exponential convergence of ε_n to zero and the existence of the positive definite matrix P_{0n} that satisfies (12.55).

We are now ready to design an adaptive output-feedback controller for (12.51) using backstepping.

Step 1 The adaptive observer-backstepping design starts with subsystem (12.51a) by rewriting it as

$$\dot{\psi}_{1n} = \xi_{2n}^{(0)} + \sum_{j=1}^r \theta_{jn}\xi_{2n}^{(j)} + b_n v_{2n} + \varepsilon_{2n}, \quad n \in \mathbb{Z}, \quad (12.64)$$

and considering v_{2n} as a virtual control and ε_{2n} as a disturbance generated by (12.63). If v_{2n} were control, and all parameters were known, then (12.64) could be stabilized by

$$v_{2n} = -\frac{1}{b_n} \left\{ \xi_{2n}^{(0)} + (k_{1n} + d_{1n})\psi_{1n} \right\} - \sum_{j=1}^r \frac{\theta_{jn}}{b_n} \xi_{2n}^{(j)}, \quad n \in \mathbb{Z}, \quad (12.65)$$

where k_{1n} and d_{1n} are positive design parameters. To account for parametric uncertainties we add and

subtract the right-hand side of (12.65) to v_{2n} in (12.64) to obtain

$$\dot{\psi}_{1n} = - (k_{1n} + d_{1n})\psi_{1n} + b_n \left\{ v_{2n} + \omega_n^{(1)*} \hat{\vartheta}_n^{(1)} \right\} + b_n \omega_n^{(1)*} \tilde{\vartheta}_n^{(1)} + \varepsilon_{2n}, \quad n \in \mathbb{Z}, \quad (12.66)$$

where

$$\omega_n^{(1)} := \begin{bmatrix} \xi_{2n}^{(0)} + (k_{1n} + d_{1n})\psi_{1n} \\ \xi_{2n}^{(1)} \\ \vdots \\ \xi_{2n}^{(r)} \end{bmatrix}, \quad \vartheta_n^{(1)} := \begin{bmatrix} \frac{1}{b_n} \\ \frac{\theta_{1n}}{b_n} \\ \vdots \\ \frac{\theta_{rn}}{b_n} \end{bmatrix}, \quad \tilde{\vartheta}_n^{(1)} := \vartheta_n^{(1)} - \hat{\vartheta}_n^{(1)},$$

with $\vartheta_n^{(1)}$ denoting the vector of unknown parameters.

We propose a CLF of the form

$$V_{a1n}(\psi_{1n}, \tilde{\vartheta}_n^{(1)}, \varepsilon_n) := \frac{1}{2}\psi_{1n}^2 + \frac{|b_n|}{2} \tilde{\vartheta}_n^{(1)*} \Gamma_n^{-1} \tilde{\vartheta}_n^{(1)} + \frac{1}{d_{1n}} \varepsilon_n^* P_{0n} \varepsilon_n,$$

where P_{0n} is a positive definite matrix that satisfies (12.55), $d_{1n} > 0$ is a design parameter, and $\Gamma_n = \Gamma_n^* > 0$. The derivative of V_{a1n} along the solutions of (12.66, 12.63) for every $n \in \mathbb{Z}$ is determined by

$$\begin{aligned} \dot{V}_{a1n} \leq & -k_{1n}\psi_{1n}^2 + b_n\psi_{1n}(v_{2n} + \omega_n^{(1)*} \hat{\vartheta}_n^{(1)}) - \frac{3}{4d_{1n}} \|\varepsilon_n\|_2^2 + \\ & |b_n| \tilde{\vartheta}_n^{(1)*} \left(\Gamma_n^{-1} \dot{\tilde{\vartheta}}_n^{(1)} + \text{sign}(b_n)\psi_{1n} \omega_n^{(1)} \right), \end{aligned}$$

where we used Young's Inequality (see [45], expression (2.254)) to upper bound $\psi_{1n}\varepsilon_{2n}$. In particular, the following choices of a 'stabilizing function' v_{2nd} and update law for the estimate $\hat{\vartheta}_n^{(1)}$

$$\begin{aligned} v_{2nd} &= -\omega_n^{(1)*} \hat{\vartheta}_n^{(1)}, & \forall n \in \mathbb{Z}, \\ \dot{\hat{\vartheta}}_n^{(1)} &= \text{sign}(b_n)\psi_{1n} \Gamma_n \omega_n^{(1)}, & \forall n \in \mathbb{Z}, \end{aligned}$$

clearly render $\dot{V}_{a1n}(\psi_{1n}, \tilde{\vartheta}_n^{(1)}, \varepsilon_n)$ negative semi-definite. Since v_{2n} is not actually a control, we introduce the second error variable as

$$\zeta_{2n} := v_{2n} - v_{2nd} = v_{2n} + \omega_n^{(1)*} \hat{\vartheta}_n^{(1)}, \quad \forall n \in \mathbb{Z}, \quad (12.67)$$

which adds an additional term on the right-hand side of \dot{V}_{a1n}

$$\dot{V}_{a1n} \leq -k_{1n}\psi_{1n}^2 - \frac{3}{4d_{1n}} \|\varepsilon_n\|_2^2 + b_n\psi_{1n}\zeta_{2n}. \quad (12.68)$$

The sign indefinite term in the last equation will be taken care of at the second step of backstepping.

Step 2 The differentiation of ζ_{2n} with respect to time yields

$$\begin{aligned} \dot{\zeta}_{2n} &= \dot{v}_{2n} + \dot{\omega}_n^{(1)*} \hat{\vartheta}_n^{(1)} + \omega_n^{(1)*} \dot{\hat{\vartheta}}_n^{(1)} \\ &= -l_{2n}v_{1n} + u_n + \dot{\omega}_n^{(1)*} \hat{\vartheta}_n^{(1)} + \omega_n^{(1)*} \dot{\hat{\vartheta}}_n^{(1)}. \end{aligned}$$

We now use the definition of $\omega_n^{(1)}$ to rewrite $\dot{\omega}_n^{(1)*} \hat{\vartheta}_n^{(1)}$ as

$$\begin{aligned}\dot{\omega}_n^{(1)*} \hat{\vartheta}_n^{(1)} &= \mu_n^* \hat{\vartheta}_n^{(1)} + (k_{1n} + d_{1n}) \hat{\vartheta}_{1n}^{(1)} \dot{\psi}_{1n} \\ &= \mu_n^* \hat{\vartheta}_n^{(1)} + (k_{1n} + d_{1n}) \hat{\vartheta}_{1n}^{(1)} (\xi_{2n}^{(0)} + \varepsilon_{2n}) + \hat{\vartheta}_{1n}^{(1)} \omega_n^{(2)*} \hat{\vartheta}_n^{(2)},\end{aligned}$$

where $\hat{\vartheta}_{1n}^{(1)}$ represents the first element of vector $\hat{\vartheta}_n^{(1)}$ and

$$\mu_n := \begin{bmatrix} \dot{\xi}_{2n}^{(0)} \\ \dot{\xi}_{2n}^{(1)} \\ \vdots \\ \dot{\xi}_{2n}^{(r)} \end{bmatrix}, \quad \omega_n^{(2)} := (k_{1n} + d_{1n}) \begin{bmatrix} \xi_{2n}^{(1)} \\ \vdots \\ \xi_{2n}^{(r)} \\ v_{2n} \end{bmatrix}, \quad \vartheta_n^{(2)} := \begin{bmatrix} \theta_{1n} \\ \vdots \\ \theta_{rn} \\ b_n \end{bmatrix}.$$

Hence, $\dot{\zeta}_{2n}$ can be expressed as

$$\dot{\zeta}_{2n} = \sigma_n + \hat{\vartheta}_{1n}^{(1)} \omega_n^{(2)*} \hat{\vartheta}_n^{(2)} + (k_{1n} + d_{1n}) \hat{\vartheta}_{1n}^{(1)} \varepsilon_{2n} + u_n,$$

where

$$\begin{aligned}\sigma_n &:= -l_{2n} v_{1n} + \omega_n^{(1)*} \dot{\hat{\vartheta}}_n^{(1)} + \mu_n^* \hat{\vartheta}_n^{(1)} + \hat{\vartheta}_{1n}^{(1)} ((k_{1n} + d_{1n}) \xi_{2n}^{(0)} + \omega_n^{(2)*} \hat{\vartheta}_n^{(2)}), \\ \tilde{\vartheta}_n^{(2)} &:= \vartheta_n^{(2)} - \hat{\vartheta}_n^{(2)}.\end{aligned}$$

The CLF from Step 1 is augmented by the three terms that penalize ζ_{2n} , $\tilde{\vartheta}_n^{(2)}$, and ε_n , respectively, to obtain

$$V_{a2n}(\psi_{1n}, \zeta_{2n}, \tilde{\vartheta}_n^{(1)}, \tilde{\vartheta}_n^{(2)}, \varepsilon_n) := V_{a1n}(\psi_{1n}, \tilde{\vartheta}_n^{(1)}, \varepsilon_n) + \frac{1}{2} \zeta_{2n}^2 + \frac{1}{2} \tilde{\vartheta}_n^{(2)*} \Delta_n^{-1} \tilde{\vartheta}_n^{(2)} + \frac{1}{d_{2n}} \varepsilon_n^* P_{0n} \varepsilon_n,$$

where $d_{2n} > 0$ and $\Delta_n = \Delta_n^* > 0$. The derivative of V_{a2n} is determined by

$$\begin{aligned}\dot{V}_{a2n} &= \dot{V}_{a1n} + \zeta_{2n} \dot{\zeta}_{2n} + \tilde{\vartheta}_n^{(2)*} \Delta_n^{-1} \dot{\tilde{\vartheta}}_n^{(2)} - \frac{1}{d_{2n}} \|\varepsilon_n\|_2^2 \\ &\leq -k_{1n} \psi_{1n}^2 + \tilde{\vartheta}_n^{(2)*} \left(\Delta_n^{-1} \dot{\tilde{\vartheta}}_n^{(2)} + \zeta_{2n} \left(\psi_{1n} e_{r+1} + \hat{\vartheta}_{1n}^{(1)} \omega_n^{(2)} \right) \right) - \frac{3}{4} \left(\frac{1}{d_{1n}} + \frac{1}{d_{2n}} \right) \|\varepsilon_n\|_2^2 \\ &\quad + \zeta_{2n} \left(\sigma_n + \psi_{1n} e_{r+1}^* \hat{\vartheta}_n^{(2)} + d_{2n} \left((k_{1n} + d_{1n}) \hat{\vartheta}_{1n}^{(1)} \right)^2 \zeta_{2n} + u_n \right),\end{aligned}$$

with e_{r+1} being the $(r+1)$ -st coordinate vector in \mathbb{R}^{r+1} . The following choices of control law u_n and the update law for the estimate $\hat{\vartheta}_n^{(2)}$

$$\begin{aligned}u_n &= - \left(\sigma_n + \psi_{1n} e_{r+1}^* \hat{\vartheta}_n^{(2)} + d_{2n} \left((k_{1n} + d_{1n}) \hat{\vartheta}_{1n}^{(1)} \right)^2 \zeta_{2n} + b_n \zeta_{2n} \right), \quad \forall n \in \mathbb{Z}, \\ \dot{\hat{\vartheta}}_n^{(2)} &= \zeta_{2n} \Delta_n \left(\psi_{1n} e_{r+1} + \hat{\vartheta}_{1n}^{(1)} \omega_n^{(2)} \right), \quad \forall n \in \mathbb{Z},\end{aligned}$$

with $b_n > 0$, transform $\dot{V}_{a2n}(\psi_{1n}, \zeta_{2n}, \tilde{\vartheta}_n^{(1)}, \tilde{\vartheta}_n^{(2)}, \varepsilon_n)$ into a negative semi-definite function of the form

$$\dot{V}_{a2n} \leq -k_{1n} \psi_{1n}^2 - b_n \zeta_{2n}^2 - \frac{3}{4} \left(\frac{1}{d_{1n}} + \frac{1}{d_{2n}} \right) \|\varepsilon_n\|_2^2 \leq 0, \quad \forall n \in \mathbb{Z}.$$

One can establish boundedness of all signals in the closed-loop adaptive system and asymptotic convergence of ψ_{1n} , ζ_{2n} , and ε_n to zero for every $n \in \mathbb{Z}$, using similar proof technique to the one presented in § 12.5.

12.8 Well-posedness of closed-loop systems

The results established in § 12.3, § 12.5, and § 12.7 are valid only if the solution to the resulting system of equations exists. In this section, we show that the designed controllers yield the well-posed closed-loop systems.

Well-posedness of nominal closed-loop systems obtained using individual cell backstepping design

The nominal closed-loop systems obtained using individual cell backstepping design of § 12.3.2 can be considered as the abstract evolution equations on a Banach space $\mathbb{B} := l_\infty \times l_\infty$. This representation is most convenient for addressing the question of existence and uniqueness of solutions.

The closed-loop system (12.12,12.20) can be rewritten as the abstract evolution equation of the form

$$\dot{\Psi} = \mathcal{A}\Psi + P(\Psi). \quad (12.69)$$

The state of system (12.69), a linear operator \mathcal{A} , and a nonlinear mapping P are defined as

$$\Psi := \begin{bmatrix} \Psi_1 \\ \Psi_2 \end{bmatrix} \in \mathbb{B}, \quad \mathcal{A} := \begin{bmatrix} 0 & I \\ -(1+k_1k_2)I & -(k_1+k_2)I \end{bmatrix}, \quad P(\Psi) := \begin{bmatrix} P_1(\Psi_1) \\ P_2(\Psi_1, \Psi_2) \end{bmatrix},$$

where $\Psi_1 := \{\psi_{1n}\}_{n \in \mathbb{Z}}$, $\Psi_2 := \{\psi_{2n}\}_{n \in \mathbb{Z}}$, and $P_1(\Psi_1) := F_1(\Psi_1)$. On the other hand, from Assumptions 1 and 2 it follows that the elements of infinite vector $P_2(\Psi_1, \Psi_2) := \{p_{2n}(\Psi_1, \Psi_2)\}_{n \in \mathbb{Z}}$ can be expressed as

$$p_{2n}(\Psi_1, \Psi_2) := -(k_1 + k_2)f_{1n}(\Psi_1) - \sum_{j \in \mathbb{Z}_N} \frac{\partial f_{1n}(\Psi_1)}{\partial \psi_{1,n+j}} (f_{1,n+j}(\Psi_1) + \psi_{2,n+j}).$$

Clearly, $\mathcal{A} : \mathbb{B} \rightarrow \mathbb{B}$ is a bounded operator and, thus, it generates a C^0 -semigroup. Moreover, P is a continuously differentiable function of its arguments and Lyapunov analysis of § 12.3.2 guarantees boundedness of $\|\Psi(t)\|$ for all times. Therefore, we conclude that the closed-loop system (12.12,12.20) has a unique classical solution on $[0, \infty)$ (see [64], Theorem 2.74).

Remark 9 *The well-posedness of the nominal closed-loop systems obtained using global backstepping design of § 12.3.1 on $\mathbb{H} := l_2 \times l_2$ can be established using similar procedure.*

Remark 10 *The nominal output-feedback design of § 12.7.1 yields closed-loop system with infinite number of completely decoupled fourth order linear subsystems. Therefore, the existence and uniqueness of solutions is guaranteed in this case.*

Remark 11 *The well-posedness of the closed-loop systems obtained as a result of the adaptive output-feedback design of § 12.7.2 can be established using similar results. The underlying state space in this case is $\mathbb{B} := l_\infty^{4r+8}$, where $\theta_n \in \mathbb{R}^r$, for every $n \in \mathbb{Z}$.*

12.9 An example of distributed backstepping design: mass-spring system

In this section, we discuss application of controllers developed in § 12.3, § 12.5, and § 12.7 to the systems described in § 12.2.2. We further comment on the structure of these controllers and validate their performance using computer simulations of systems containing a large number of units.

12.9.1 Nominal state-feedback design

Since all systems described in § 12.2.2 satisfy the matching condition, the nominal backstepping state-feedback design leads to static distributed controllers that inherit localization properties from the original

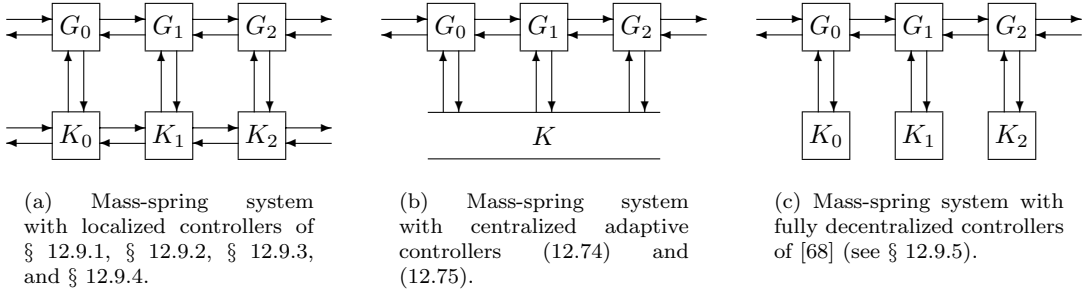


Figure 12.10: Controller architectures of mass-spring system.

plant. In other words, since n -th plant cell G_n interacts only with G_{n-1} and G_{n+1} , n -th control cell K_n communicates only with its immediate neighbors K_{n-1} and K_{n+1} , which is very convenient for implementation.

For a linear mass-spring system (12.2) without parametric uncertainties, control law (12.20), for every $n \in \mathbb{Z}$, takes the following form

$$u_{1n} = -m_n((1 + c_{1n}c_{2n} - \frac{k_{n-1} + k_n}{m_n})x_n + (c_{1n} + c_{2n})\dot{x}_n + \frac{k_{n-1}}{m_n}x_{n-1} + \frac{k_n}{m_n}x_{n+1}), \quad (12.70)$$

For a spatially invariant system (12.4) controller (12.70) simplifies to

$$u_{2n} = -m((1 + c_{1n}c_{2n} - \frac{2k}{m})x_n + (c_{1n} + c_{2n})\dot{x}_n + \frac{k}{m}(x_{n-1} + x_{n+1})), \quad n \in \mathbb{Z}. \quad (12.71)$$

For a nominal nonlinear mass-spring system (12.3), control law (12.20) can be rewritten as

$$u_{3n} = u_{1n} - q_{n-1}(x_{n-1} - x_n)^3 - q_n(x_{n+1} - x_n)^3, \quad n \in \mathbb{Z}, \quad (12.72)$$

where u_{1n} is given by (12.70). For system (12.5) controller (12.72) simplifies to

$$u_{4n} = u_{2n} - q((x_{n-1} - x_n)^3 + (x_{n+1} - x_n)^3), \quad n \in \mathbb{Z}, \quad (12.73)$$

with u_{2n} being defined by (12.71). In (12.70), (12.71), (12.72), and (12.73), c_{1n} and c_{2n} denote positive design parameters, for every $n \in \mathbb{Z}$.

Figure 12.10(a) illustrates controller architecture of mass-spring system with the aforementioned controllers. We observe that the nominal output-feedback design of § 12.9.3 and adaptive distributed designs of § 12.9.2 and § 12.9.4 result in the closed-loop systems with similar passage of information. In all these cases, backstepping design yields localized distributed controllers K_n , $\forall n \in \mathbb{Z}$, that require only measurements from the n -th plant unit G_n and its immediate neighbors G_{n-1} and G_{n+1} , to achieve desired objective.

As remarked in § 12.4, in applications we need to work with systems on lattices that contain large but finite number of units. All considerations related to infinite dimensional systems are applicable here, but with minor modifications. For example, if we consider the mass-spring system shown in Figure 12.11 with N masses ($n = 1, \dots, N$) both the equations presented in § 12.2.2 and the control laws of this section are still valid with appropriate ‘boundary conditions’ of the form $x_j = \dot{x}_j = u_j \equiv 0$, $\forall j \in \mathbb{Z} \setminus \{1, \dots, N\}$.

Simulation results of uncontrolled and controlled linear mass-spring system with $N = 100$ masses and $m = k = 1$ are shown in Figure 12.12. The initial state of the system is randomly selected. The right plot is obtained using control law (12.71) with $c_{1n} = c_{2n} = 1$, for every $n = 1, \dots, N$. Simulation results illustrate that the nominal linear localized distributed controller (12.71), which has the same architecture as the original plant, achieves desired control objective in an effective manner.

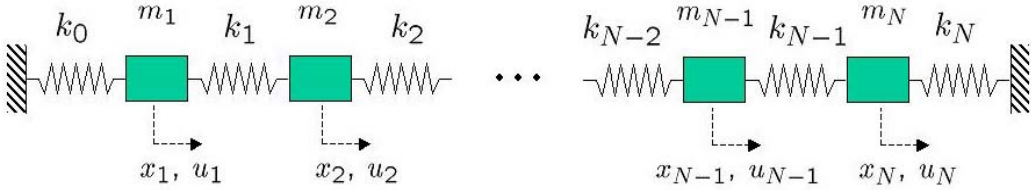


Figure 12.11: Finite dimensional mass-spring system.

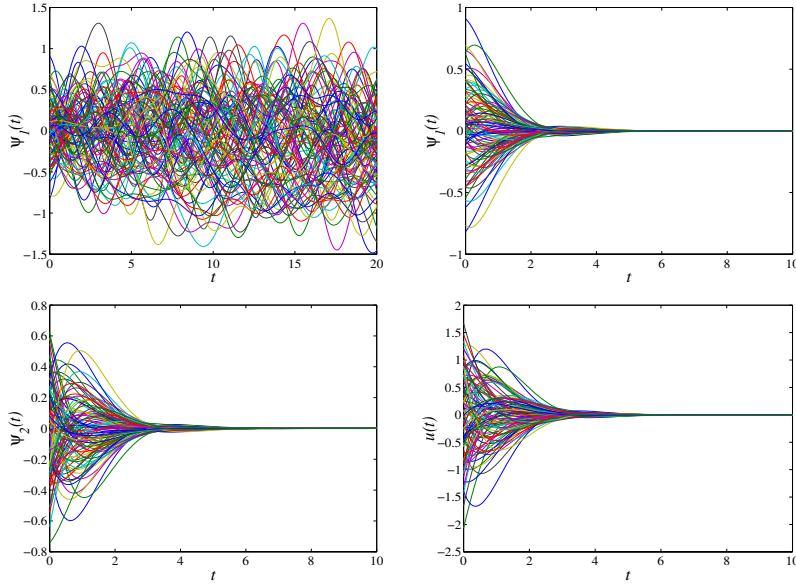


Figure 12.12: Simulation results of uncontrolled (first row left) and controlled linear mass-spring system with $N = 100$ masses and $m = k = 1$. The initial state of the system is randomly selected. Control law (12.71) is used with $c_{1n} = c_{2n} = 1, \forall n = 1, \dots, N$.

12.9.2 Adaptive state-feedback design

Constant unknown parameters: centralized control

In this section we discuss application of controllers developed in § 12.5.1 to some of systems described in § 12.2.2 with constant unknown parameters. As discussed in 12.6, since information about the entire plant's state is used in the equations for parameter update laws the adaptive backstepping design in this particular situation leads to centralized controllers. This is clearly an obstacle for practical implementations. Nevertheless, we illustrate that the designed controller achieves the desired objective successfully by performing computer simulations of systems containing a large number of units.

For a linear mass-spring system (12.4) with constant unknown parameters $\theta = \frac{k}{m}$ and $b = \frac{1}{m} > 0$,

centralized controller (12.46) takes the following form

$$\begin{aligned} u_{1n} &= -\hat{\varrho}s_n, \quad n \in \mathbb{Z}, \\ s_n &= (1 + c_{1n}c_{2n})x_n + (c_{1n} + c_{2n})\dot{x}_n + \hat{\theta}(x_{n-1} - 2x_n + x_{n+1}), \quad n \in \mathbb{Z}, \\ \dot{\hat{\theta}} &= \gamma \sum_{n \in \mathbb{Z}} (\dot{x}_n + c_{1n}x_n)(x_{n-1} - 2x_n + x_{n+1}), \\ \dot{\hat{\varrho}} &= \beta \sum_{n \in \mathbb{Z}} (\dot{x}_n + c_{1n}x_n)s_n, \end{aligned} \quad (12.74)$$

where $\beta, \gamma > 0$. For a nonlinear mass-spring system (12.5) with constant unknown parameters $\theta_1 = \frac{k}{m}$, $\theta_2 = \frac{q}{m}$, and $b = \frac{1}{m} > 0$, control law (12.46) can be rewritten as

$$\begin{aligned} u_{2n} &= -\hat{\varrho}s_n, \quad n \in \mathbb{Z}, \\ \begin{bmatrix} \dot{\hat{\theta}}_1 \\ \dot{\hat{\theta}}_2 \end{bmatrix} &= \sum_{n \in \mathbb{Z}} (\dot{x}_n + c_{1n}x_n)\Gamma \begin{bmatrix} x_{n-1} - 2x_n + x_{n+1} \\ (x_{n-1} - x_n)^3 + (x_{n+1} - x_n)^3 \end{bmatrix}, \\ \dot{\hat{\varrho}} &= \beta \sum_{n \in \mathbb{Z}} (\dot{x}_n + c_{1n}x_n)s_n, \end{aligned} \quad (12.75)$$

where $\Gamma = \Gamma^* > 0$, $\beta > 0$, and

$$s_n := (1 + c_{1n}c_{2n})x_n + (c_{1n} + c_{2n})\dot{x}_n + \left[\frac{x_{n-1} - 2x_n + x_{n+1}}{(x_{n-1} - x_n)^3 + (x_{n+1} - x_n)^3} \right]^* \begin{bmatrix} \hat{\theta}_1 \\ \hat{\theta}_2 \end{bmatrix}.$$

Clearly, both (12.74) and (12.75) are centralized controllers, as illustrated in Figure 12.10(b).

In applications, we still can use the above expressions, but with minor modifications. For example, for a mass-spring system shown in Figure 12.11 with N masses ($n = 1, \dots, N$) the appropriate formulae for controller (12.74) are given by

$$\begin{aligned} u_{1n} &= -\hat{\varrho}s_n, \quad n = 1, \dots, N, \\ s_n &= (1 + c_{1n}c_{2n})x_n + (c_{1n} + c_{2n})\dot{x}_n + \hat{\theta}(x_{n-1} - 2x_n + x_{n+1}), \quad n = 1, \dots, N, \\ \dot{\hat{\theta}} &= \gamma \sum_{n \in \mathbb{Z}} (\dot{x}_n + c_{1n}x_n)(x_{n-1} - 2x_n + x_{n+1}), \\ \dot{\hat{\varrho}} &= \beta \sum_{n \in \mathbb{Z}} (\dot{x}_n + c_{1n}x_n)s_n, \end{aligned}$$

with the ‘boundary conditions’ of the form $x_0 = \dot{x}_0 = x_{N+1} = \dot{x}_{N+1} = 0$.

Figure 12.13 shows simulation results of linear mass-spring system with $N = 100$ masses and unknown parameters $m = k = 1$, using control law (12.74) with $\gamma = \beta = c_{1n} = c_{2n} = 1$, $\forall n = 1, \dots, N$, and $\hat{\theta}(0) = \hat{\varrho}(0) = 0.5$. The initial state of the mass-spring system is randomly selected. Clearly, centralized adaptive scheme drives state of the original linear system to zero and provides boundedness of parameter estimates with a reasonable amount of control effort. On the other hand, the states of the estimators converge to constant values which do not correspond to the values of unknown parameters.

Spatially varying unknown parameters: localized control

Here we discuss application of controllers developed in § 12.5.2 to some of systems described in § 12.2.2 with time independent spatially varying unknown parameters. As illustrated in § 12.6, the adaptive backstepping in this particular situation leads to localized distributed controllers of the same architecture as the original plant. Since the design procedure yields controllers with both localized actuation and localized passage of information, there is no need for centralized computer. This feature of backstepping design is

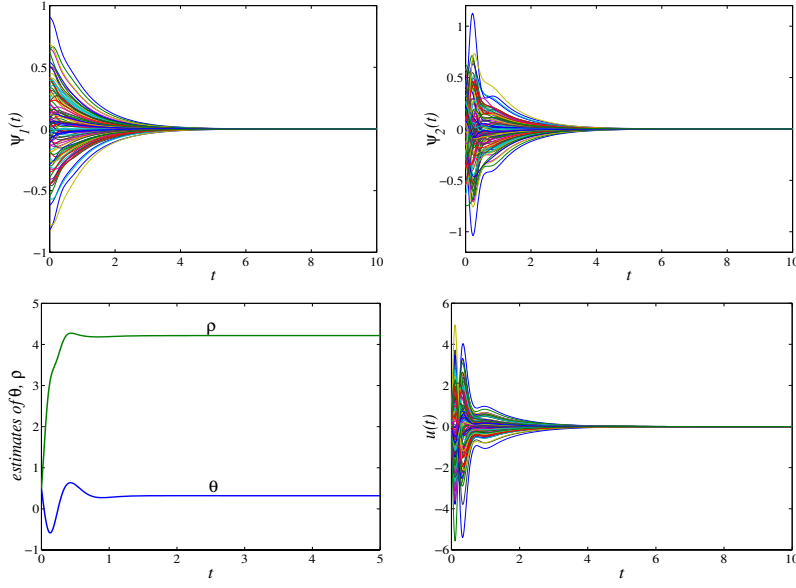


Figure 12.13: Simulation results of a linear mass-spring system with $N = 100$ masses and unknown parameters $m = k = 1$, using centralized controller (12.74) with $\gamma = \beta = c_{1n} = c_{2n} = 1$, $\forall n = 1, \dots, N$, and $\hat{\theta}(0) = \hat{\rho}(0) = 0.5$. The initial state of the mass-spring system is randomly selected.

of paramount importance for implementations. We illustrate the effectiveness of the adaptive scheme by performing computer simulations of systems containing a large number of units.

For a linear mass-spring system (12.2) with temporally constant spatially varying unknown parameters $\theta_{n1} = \frac{k_{n-1}}{m_n}$, $\theta_{n2} = \frac{k_n}{m_n}$, and $b_n = \frac{1}{m_n} > 0$, control law (12.48) takes the following form

$$\begin{aligned} u_{1n} &= -\hat{\varrho}_n s_n, \\ s_n &= (1 + c_{1n}c_{2n})x_n + (c_{1n} + c_{2n})\dot{x}_n + \begin{bmatrix} x_{n-1} - x_n \\ x_{n+1} - x_n \end{bmatrix}^* \begin{bmatrix} \hat{\theta}_{n1} \\ \hat{\theta}_{n2} \end{bmatrix} \\ \dot{\hat{\theta}}_n &= (\dot{x}_n + c_{1n}x_n)\Gamma_n \begin{bmatrix} x_{n-1} - x_n \\ x_{n+1} - x_n \end{bmatrix}, \\ \dot{\hat{\varrho}}_n &= \beta_n(\dot{x}_n + c_{1n}x_n)s_n, \end{aligned} \quad (12.76)$$

where $\Gamma_n = \Gamma_n^* > 0$ and $\beta_n > 0$ for all $n \in \mathbb{Z}$. For a nonlinear mass-spring system (12.3) with spatially varying unknown parameters, formulae for adaptive state-feedback controllers can be readily obtained from (12.3) and (12.48). In both cases the design procedure yields localized distributed controllers with the architecture shown in Figure 12.10(a).

Simulation results of linear mass-spring system with $N = 100$ masses and unknown parameters $m_n = k_n = 1$, $\forall n = 1, \dots, N$, using control law (12.76) with $\gamma_n = \beta_n = c_{1n} = c_{2n} = 1$, and $\hat{\theta}_n(0) = \hat{\varrho}_n(0) = 0.5$, $\forall n = 1, \dots, N$ are shown in Figure 12.14. The initial state of the mass-spring system is randomly selected. We observe that localized adaptive controller (12.76) provides boundedness of all parameter estimates and convergence of the state of the error system to zero.

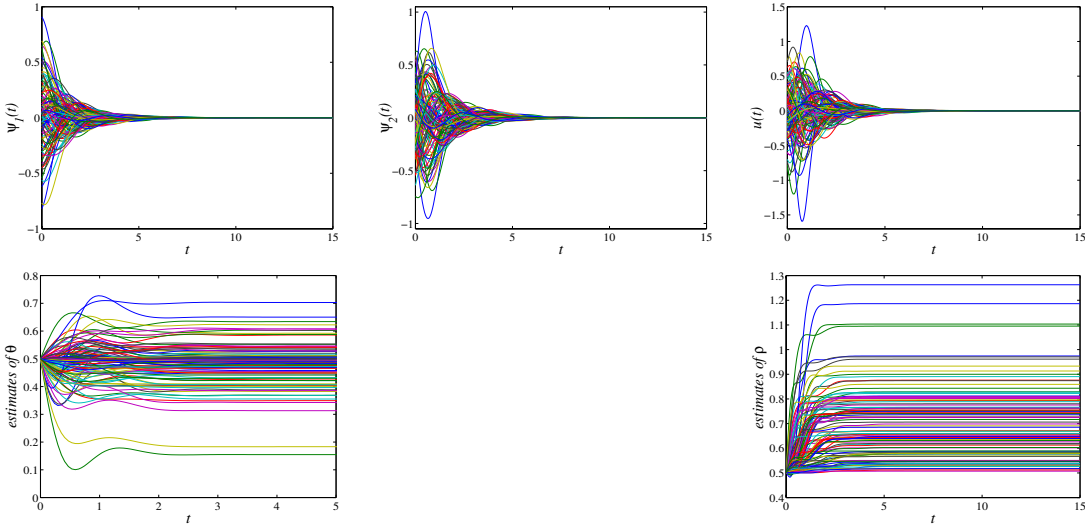


Figure 12.14: Simulation results of linear mass-spring system with $N = 100$ masses and unknown parameters $m_n = k_n = 1, \forall n = 1, \dots, N$, using control law (12.76) with $\gamma_n = \beta_n = c_{1n} = c_{2n} = 1$, and $\hat{\theta}_n(0) = \hat{p}_n(0) = 0.5, \forall n = 1, \dots, N$. The initial state of the mass-spring system is randomly selected. We remark that x and v denote states of the error system, that is, $x := \psi_1, v := \psi_2$.

12.9.3 Nominal output-feedback design

The nominal Lyapunov-based output-feedback design for mass-spring system leads to localized dynamic distributed controllers of the form

$$\left. \begin{aligned} \dot{\hat{\psi}}_{1n} &= \hat{\psi}_{2n} + l_{1n}(\psi_{1n} - \hat{\psi}_{1n}) \\ \dot{\hat{\psi}}_{2n} &= l_{2n}(\psi_{1n} - \hat{\psi}_{1n}) + f_n + b_n u_n \\ u_n &= -\frac{1}{b_n}(\psi_{1n} + (c_{1n} + d_{1n})\hat{\psi}_{2n} + l_{2n}(\psi_{1n} - \hat{\psi}_{1n}) + f_n \\ &\quad + (d_{2n}(c_{1n} + d_{1n})^2 + c_{2n})(\hat{\psi}_{2n} + (c_{1n} + d_{1n})\psi_{1n})) \end{aligned} \right\} n \in \mathbb{Z}, \quad (12.77)$$

where, for example, for system (12.5) f_n is determined by

$$f_n = \frac{k}{m}(\psi_{1,n-1} - 2\psi_{1n} + \psi_{1,n+1}) + \frac{q}{m}((\psi_{1,n-1} - \psi_{1n})^3 + (\psi_{1,n+1} - \psi_{1n})^3), \quad n \in \mathbb{Z}.$$

Architecture of (12.77) is illustrated in Figure 12.10(a).

Figure 12.15 illustrates simulation results of a linear mass-spring system using output-feedback control law (12.77). Clearly, numerical results show that the nominal output-feedback distributed controller (12.77) achieves desired control objective in an effective manner with a reasonable amount of control effort.

12.9.4 Adaptive output-feedback design

Formulae for adaptive output-feedback controllers for mass-spring systems can be readily obtained combining results of § 12.2.2 and § 12.7.2. We remark that as a result of our design we obtain localized distributed dynamic controllers whose architecture is shown in Figure 12.10(a).

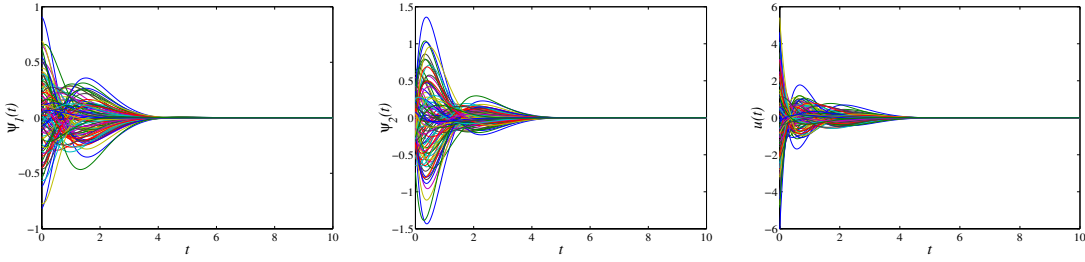


Figure 12.15: Simulation results of linear mass-spring system with $N = 100$ masses and $m_n = k_n = 1$, $\forall n = 1, \dots, N$, using output-feedback control law (12.77) with $c_{1n} = c_{2n} = 1$, $d_{1n} = d_{2n} = 0.2$, $l_{1n} = 5$, $l_{2n} = 6$, and $\hat{\psi}_{1n}(0) = \hat{\psi}_{2n}(0) = 0$, $\forall n = 1, \dots, N$. The initial state of the mass-spring system is randomly selected.

12.9.5 Fully decentralized state-feedback design

We note that fully decentralized state-feedback controllers for nominal mass-spring systems are designed in [68] using the similar procedure to the one presented in § 12.4. In other words, backstepping can be employed to obtain a sequence of controllers K_n that guarantees global asymptotic stability of the origin of the infinite dimensional mass-spring system using only measurements from the corresponding n -th plant unit G_n . This is accomplished by a careful analysis of the interactions in the underlying system, and feedback domination rather than feedback cancellation of ‘unfavorable’ interactions.

12.10 Summary

We study architectural questions in distributed control of nonlinear infinite dimensional systems on lattices. We demonstrate that nominal backstepping design always yields localized distributed controllers whose architecture can be significantly altered by different choices of stabilizing functions during the recursive design. For the ‘worst case’ situation in which all interactions are cancelled at each step of backstepping we quantify the number of control induced interactions necessary to achieve the desired design objective. This number is obtained by multiplying the number of interactions per plant cell with the largest number of integrators that separate interactions from control input. When the matching condition is satisfied the control problem can always be posed in such a way to yield controllers of the same architecture as the original plant. Furthermore, the global backstepping design can be utilized to obtain distributed controllers with less interactions. This is done by identification of beneficial interactions and feedback domination of harmful interaction.

The only situation which results in a centralized controller is for plants with constant parametric uncertainties when we start our design with one estimate per unknown parameter. We demonstrate that this can be overcome by the ‘over-parameterization’ of the unknown constant parameters. As a result, every single control unit has its own dynamical estimator of unknown parameters which avoids the centralized architecture. The order of this estimator is equal to the number of unknown parameters. Similar ideas can be also employed for adaptive control of systems with spatially varying parametric uncertainties. For this class of systems we quantify the dynamical order of each control cell induced by backstepping distributed design. In particular, for plants with interactions and unknown parameters ‘one integrator away’ from the control input, we show that this dynamical order scales linearly with the number of interactions per plant cell.

Bibliography

- [1] D. Laughlin, M. Morari, and R. D. Braatz, “Robust performance of cross-directional basis-weight control in paper machines,” *Automatica*, vol. 29, pp. 1395–1410, 1993.
- [2] E. M. Heaven, I. M. Jonsson, T. M. Kean, M. A. Manness, and R. N. Vyse, “Recent advances in cross machine profile control,” *IEEE Control Systems Magazine*, vol. 14, no. 5, October 1994.
- [3] W. S. Levine and M. Athans, “On the optimal error regulation of a string of moving vehicles,” *IEEE Transactions on Automatic Control*, vol. AC-11, no. 3, pp. 355–361, July 1966.
- [4] S. M. Melzer and B. C. Kuo, “Optimal regulation of systems described by a countably infinite number of objects,” *Automatica*, vol. 7, pp. 359–366, 1971.
- [5] K. C. Chu, “Decentralized control of high-speed vehicular strings,” *Transportation Science*, vol. 8, no. 4, pp. 361–384, November 1974.
- [6] P. Varaiya, “Smart cars on smart roads: problems of control,” *IEEE Transactions on Automatic Control*, vol. 38, no. 2, pp. 195–207, February 1993.
- [7] H. Raza and P. Ioannou, “Vehicle following control design for automated highway systems,” *IEEE Control Systems Magazine*, vol. 16, no. 6, pp. 43–60, December 1996.
- [8] D. Swaroop and J. K. Hedrick, “Constant spacing strategies for platooning in automated highway systems,” *Transactions of the ASME. Journal of Dynamic Systems, Measurement and Control*, vol. 121, no. 3, pp. 462–470, September 1999.
- [9] P. Seiler, A. Pant, and K. Hedrick, “Disturbance propagation in large interconnected systems,” in *Proceedings of the 2002 American Control Conference*, 2002, pp. 1062–1067.
- [10] D. Chichka and J. Speyer, “Solar-powered, formation-enhanced aerial vehicle systems for sustained endurance,” in *Proceedings of the 1998 American Control Conference*, 1998, pp. 684–688.
- [11] J. M. Fowler and R. D’Andrea, “Distributed control of close formation flight,” in *Proceedings of the 41st IEEE Conference on Decision and Control*, 2002, pp. 2972–2977.
- [12] ——, “A formation flight experiment,” *IEEE Control Systems Magazine*, vol. 23, no. 5, pp. 35–43, October 2003.
- [13] V. Kapila, A. G. Sparks, J. M. Buffington, and Q. Yan, “Spacecraft formation flying: dynamics and control,” *Journal of Guidance, Control, and Dynamics*, vol. 23, no. 3, pp. 561–564, May-June 2000.
- [14] R. W. Beard, J. Lawton, and F. Y. Hadaegh, “A coordination architecture for spacecraft formation control,” *IEEE Transactions on Control Systems Technology*, vol. 9, no. 6, pp. 777–790, November 2001.
- [15] H. Wong, V. Kapila, and A. G. Sparks, “Adaptive output feedback tracking control of spacecraft formation,” *International Journal of Robust and Nonlinear Control*, vol. 12, no. 2-3, pp. 117–139, February-March 2002.

- [16] D. T. Neilson, "MEMS subsystems for optical networking," in *Proceedings of 8th Microoptics Conference (MOC '01)*, Osaka, Japan, 2001.
- [17] M. Napoli, B. Bamieh, and M. Dahleh, "Optimal control of arrays of microcantilevers," *Transactions of the ASME. Journal of Dynamic Systems, Measurement and Control*, vol. 121, no. 4, pp. 686–690, December 1999.
- [18] D. Swaroop and J. K. Hedrick, "String stability of interconnected systems," *IEEE Transactions on Automatic Control*, vol. 41, no. 2, pp. 349–357, March 1996.
- [19] B. Bamieh, F. Paganini, and M. A. Dahleh, "Distributed control of spatially invariant systems," *IEEE Transactions on Automatic Control*, vol. 47, no. 7, pp. 1091–1107, July 2002.
- [20] D. D. Šiljak, *Decentralized Control of Complex Systems*. New York: Academic Press, 1991.
- [21] S. Sheikholeslam and C. A. Desoer, "Design of decentralized adaptive controllers for a class of interconnected nonlinear dynamical systems," in *Proceedings of the 31th IEEE Control and Decision Conference*, 1992, pp. 284–288.
- [22] L. Shi and S. K. Singh, "Decentralized adaptive controller design for large-scale systems with higher order interconnections," *IEEE Transactions on Automatic Control*, vol. 37, no. 8, pp. 1106–1118, August 1992.
- [23] S. Jain and F. Khorrami, "Decentralized adaptive control of a class of large-scale interconnected nonlinear systems," *IEEE Transactions on Automatic Control*, vol. 42, no. 2, pp. 136–154, February 1997.
- [24] ——, "Decentralized adaptive output feedback design for large-scale nonlinear systems," *IEEE Transactions on Automatic Control*, vol. 42, no. 5, pp. 729–735, May 1997.
- [25] C. Wen and Y. C. Soh, "Decentralized adaptive control using integrator backstepping," *Automatica*, vol. 33, no. 9, pp. 1719–1724, September 1997.
- [26] Z. P. Jiang, "Decentralized and adaptive nonlinear tracking of large-scale systems via output feedback," *IEEE Transactions on Automatic Control*, vol. 45, no. 11, pp. 2122–2128, November 2000.
- [27] Z. P. Jiang, D. W. Repperger, and D. J. Hill, "Decentralized nonlinear output-feedback stabilization with disturbance attenuation," *IEEE Transactions on Automatic Control*, vol. 46, no. 10, pp. 1623–1629, October 2001.
- [28] Z. P. Jiang, "Decentralized disturbance attenuating output-feedback trackers for large-scale nonlinear systems," *Automatica*, vol. 38, pp. 1407–1415, 2002.
- [29] E. W. Kamen, "Stabilization of linear spatially-distributed continuous-time and discrete-time systems," in *Multidimensional Systems Theory*, N. K. Bose, Ed. Hingham, MA: Kluwer, 1985.
- [30] R. W. Brockett and J. L. Willems, "Discretized partial differential equations: Examples of control systems defined on modules," *Automatica*, vol. 10, pp. 507–515, 1974.
- [31] M. L. El-Sayed and P. Krishnaprasad, "Homogeneous interconnected systems: an example," *IEEE Transactions on Automatic Control*, vol. AC-26, pp. 894–901, 1981.
- [32] P. P. Khargonekar and E. Sontag, "On the relation between stable matrix fraction factorizations and regulable realizations of linear systems over rings," *IEEE Transactions on Automatic Control*, vol. AC-27, no. 3, pp. 627–638, 1982.
- [33] E. W. Kamen and P. P. Khargonekar, "On the control of linear systems whose coefficients are functions of parameters," *IEEE Transactions on Automatic Control*, vol. AC-29, no. 1, pp. 25–33, 1984.

- [34] W. L. Green and E. W. Kamen, "Stability of linear systems over a commutative normed algebra with applications to spatially-distributed and parameter-dependent systems," *SIAM J. Control Optim.*, vol. 23, pp. 1–18, 1985.
- [35] F. Fagnani and J. C. Willems, "Representations of symmetric linear dynamical systems," *SIAM J. Control Optim.*, vol. 31, no. 5, pp. 1267–1293, 1993.
- [36] ——, "Interconnections and symmetries of linear differential systems," *Mathematics of Control Signals and Systems*, vol. 7, no. 2, pp. 167–186, 1994.
- [37] R. D'Andrea, "A linear matrix inequality approach to decentralized control of distributed parameter systems," in *Proceedings of the 1998 American Control Conference*, 1998, pp. 1350–1354.
- [38] R. D'Andrea and G. E. Dullerud, "Distributed control design for spatially interconnected systems," *IEEE Transactions on Automatic Control*, vol. 48, no. 9, pp. 1478–1495, September 2003.
- [39] G. Dullerud, R. D'Andrea, and S. Lall, "Control of spatially varying distributed systems," in *Proceedings of the 37th IEEE Control and Decision Conference*, 1998, pp. 1889–1893.
- [40] G. E. Dullerud and R. D'Andrea, "Distributed control of heterogeneous systems," *IEEE Transactions on Automatic Control*, 2002, submitted for publication.
- [41] K. S. Narendra and A. M. Annaswamy, *Stable Adaptive Systems*. Englewood Cliffs, NJ: Prentice-Hall, 1989.
- [42] S. Sastry and M. Bodson, *Adaptive Control: Stability, Convergence and Robustness*. Englewood Cliffs, NJ: Prentice-Hall, 1989.
- [43] K. J. Åström and B. Wittenmark, *Adaptive Control*. Reading, Massachusetts: Addison-Wesley, 1995.
- [44] P. A. Ioannou and J. Sun, *Robust Adaptive Control*. Upper Saddle River, NJ: Prentice-Hall, 1996.
- [45] M. Krstić, I. Kanellakopoulos, and P. Kokotović, *Nonlinear and Adaptive Control Design*. New York: John Wiley & Sons, Inc., 1995.
- [46] J. Baumeister, W. Scondo, M. A. Demetriou, and I. G. Rosen, "On-line parameter estimation for infinite dimensional dynamical systems," *SIAM J. Control Optim.*, vol. 35, no. 2, pp. 678–713, March 1997.
- [47] M. Bohm, M. A. Demetriou, S. Reich, and I. G. Rosen, "Model reference adaptive control of distributed parameter systems," *SIAM J. Control Optim.*, vol. 36, no. 1, pp. 33–81, January 1998.
- [48] M. S. de Queiroz, D. M. Dawson, M. Agarwal, and F. Zhang, "Adaptive nonlinear boundary control of a flexible link robot arm," *IEEE Transactions on Robotics and Automation*, vol. 15, no. 4, pp. 779–787, August 1999.
- [49] Y. Orlov and J. Bentsman, "Adaptive distributed parameter systems identification with enforceable identifiability conditions and reduced-order spatial differentiation," *IEEE Transactions on Automatic Control*, vol. 45, no. 2, pp. 203–216, February 2000.
- [50] J. Bentsman and Y. Orlov, "Reduced spatial order model reference adaptive control of spatially varying distributed parameter systems of parabolic and hyperbolic types," *International Journal of Adaptive Control and Signal Processing*, vol. 15, no. 6, pp. 679–696, September 2001.
- [51] W. J. Liu and M. Krstic, "Adaptive control of Burgers' equation with unknown viscosity," *International Journal of Adaptive Control and Signal Processing*, vol. 15, no. 7, pp. 745–766, November 2001.
- [52] T. Kobayashi, "Adaptive regulator design of a viscous Burgers' system by boundary control," *IMA Journal of Mathematical Control and Information*, vol. 18, no. 3, pp. 427–437, September 2001.

- [53] D. Swaroop, J. K. Hedrick, and S. B. Choi, “Direct adaptive longitudinal control of vehicle platoons,” *IEEE Transactions on Vehicular Technology*, vol. 50, no. 1, pp. 150–161, January 2001.
- [54] M. S. de Queiroz, V. Kapila, and Q. Yan, “Adaptive nonlinear control of multiple spacecraft formation flying,” *Journal of Guidance, Control, and Dynamics*, vol. 23, no. 3, pp. 385–390, May-June 2000.
- [55] H. Wong, V. Kapila, and A. G. Sparks, “Adaptive output feedback tracking control of multiple spacecraft,” in *Proceedings of the 2001 American Control Conference*, 2001, pp. 698–703.
- [56] H. Wong, H. Pan, M. S. de Queiroz, and V. Kapila, “Adaptive learning control for spacecraft formation flying,” in *Proceedings of the 40th IEEE Control and Decision Conference*, 2001, pp. 1089–1094.
- [57] H. K. Khalil, *Nonlinear Systems*. New York: Prentice Hall, 1996.
- [58] A. Banaszuk, H. A. Hauksson, and I. Mezić, “A backstepping controller for a nonlinear partial differential equation model of compression system instabilities,” *SIAM J. Control Optim.*, vol. 37, no. 5, pp. 1503–1537, 1999.
- [59] D. M. Bosković, M. Krstić, and W. Liu, “Boundary control of an unstable heat equation via measurement of domain-averaged temperature,” *IEEE Transactions on Automatic Control*, vol. 46, no. 12, pp. 2022–2028, December 2001.
- [60] A. Balogh and M. Krstić, “Infinite-dimensional backstepping-style feedback transformations for a heat equation with an arbitrary level of instability,” *European Journal of Control*, vol. 8, pp. 165–177, 2002.
- [61] C. F. Baicu, C. D. Rahn, and D. M. Dawson, “Backstepping boundary control of flexible-link electrically driven gantry robots,” *IEEE/ASME Transactions on Mechatronics*, vol. 3, no. 1, pp. 60–66, March 1998.
- [62] S. P. Banks, *State-Space and frequency-domain methods in the control of distributed parameter systems*. London, UK: Peter Peregrinus Ltd., 1983.
- [63] R. F. Curtain and H. J. Zwart, *An Introduction to Infinite-Dimensional Linear Systems Theory*. New York: Springer-Verlag, 1995.
- [64] Z. Luo, B.Z.Guo, and O.Morgul, *Stability and Stabilization of Infinite Dimensional Systems with Applications*. London: Springer-Verlag, 1999.
- [65] D. G. Luenberger, *Optimization by Vector Space Methods*. New York: John Wiley and Sons, Inc., 1969.
- [66] G. Tao, “A simple alternative to Barbălat lemma,” *IEEE Transactions on Automatic Control*, vol. 42, no. 5, p. 698, May 1997.
- [67] A. J. Krener and A. Isidori, “Linearization by output injection and nonlinear observers,” *Systems and Control Letters*, vol. 3, no. 1, pp. 47–52, June 1983.
- [68] M. R. Jovanović and B. Bamieh, “Lyapunov-based distributed control of systems on lattices,” to appear in *IEEE Transactions on Automatic Control*, 2003, available at <http://www.me.ucsb.edu/~jmihailo/publications/tac03-lattice.html>.

Chapter 13

Distributed control of vehicular platoons

Control of vehicular platoons has been an intensive area of research for almost four decades [1–9]. These systems belong to the class of systems on lattices in which the interactions between different subsystems originate because of a specific control objective that designer wants to accomplish. As already mentioned in Chapter 12, additional examples of systems on lattices with this property include formations of unmanned aerial vehicles [10–12] and constellations of satellites [13–15].

In § 13.1, we revisit the vehicular platoon control problems formulated by Levine & Athans [1] and Melzer & Kuo [2]. We show that in each case, these formulations are effectively ill-posed. Specifically, we demonstrate that in the first formulation, the system’s stabilizability degrades as the size of the platoon increases, and that the system loses stabilizability in the limit of an infinite number of vehicles. On the other hand, we illustrate that in the LQR formulation of Melzer & Kuo [2], the performance index is not detectable, leading to non-stabilizing optimal feedbacks. Effectively, these closed-loop systems do not have a uniform bound on the time constants of all vehicles. For the case of infinite platoons, these difficulties are easily exhibited using the theory of spatially invariant systems [16]. We argue that the infinite case is a useful paradigm to understand large platoons. To this end, we illustrate numerically how stabilizability and detectability degrade as functions of a finite platoon size, implying that the infinite case is a reasonable approximation to the large, but finite case. Finally, we show how to pose \mathcal{H}_2 and \mathcal{H}_∞ versions of these problems where the detectability and stabilizability issues are easily seen, and suggest a well-posed alternative formulation based on penalizing absolute positions errors in addition to relative ones.

Recent article [17] addressed some fundamental design limitations in vehicular platoons. In particular, it was shown that string stability of a finite platoon with linear dynamics cannot be achieved with any linear controller that uses only information about relative distance between the vehicle on which it acts and its immediate predecessor. A similar result was previously established for a spatially invariant infinite string of vehicles with static feedback controllers having the same information passing properties [3]. This necessitates use of distributed strategies for control of platoons and underscores the importance of developing distributed schemes with favorable architectures.

In § 13.2, we investigate some additional fundamental limitations and tradeoffs in the control of vehicular platoons. We demonstrate that in very long platoons, to avoid large position, velocity, and control amplitudes, one needs to explicitly account for the initial deviations of vehicles from their desired trajectories. We further derive explicit constraints on feedback gains—for any given set of initial conditions—to achieve desired position transients without magnitude and rate saturation. These constraints are used to generate the trajectories around which the states of the platoon system are driven towards their desired values without the excessive use of control effort.

All results of this chapter are illustrated using computer simulations of platoons containing a large number of vehicles.

13.1 On the ill-posedness of certain vehicular platoon control problems

In this section, we consider optimal control of vehicular platoons. This problem was originally studied by Levine & Athans [1], and for an infinite string of moving vehicles by Melzer & Kuo [2], both using LQR methods. We analyze the solutions to the LQR problem provided by these authors as a function of the size of the formation, and show that these control problems become effectively ill-posed as the size of the platoon increases. We investigate various ways of quantifying this ill-posedness. In § 13.1.1, we show that essentially, the resulting closed-loop systems do not have a uniform bound on the rate of convergence of the regulated states to zero. In other words, as the size of the platoon increases, the closed-loop system has eigenvalues that limit to the imaginary axis.

In § 13.1.1, we setup the problem formulations of [1, 2] and investigate the above mentioned phenomena for finite platoons numerically. In § 13.1.2, we also consider the infinite platoon case as an insightful limit which can be treated analytically. We argue that the infinite platoons capture the essence of the large-but-finite platoons. The infinite problem is also more amenable to analysis using recently developed theory for spatially invariant linear systems [16], which we utilize to show that the original solutions to this problem are not exponentially stabilizing in the case of an infinite number of vehicles. The reason for this is the lack of stabilizability or detectability of an underlying system. Thus, these control problems are inherently ill-posed even if methods other than LQR are used. In § 13.1.3, we suggest alternative problem formulations which are well-posed. The main feature of these alternative formulations is the addition of penalties on absolute position errors in the performance objective. Well-posed LQR, \mathcal{H}_2 , and \mathcal{H}_∞ problem formulations for infinite strings are proposed.

13.1.1 Optimal control of finite vehicular platoons

In this subsection, we consider the LQR problem for finite vehicular platoons. This problem was originally studied by Levine & Athans [1] and subsequently by Melzer & Kuo [2, 18]. The main point of our study is to analyze the control strategies of [1, 2], and [18] as the number of vehicles in platoon increases. We show that the solutions provided by these authors yield the non-uniform rates of convergence towards the desired formation. In other words, we demonstrate that the time constant of the closed-loop system gets larger as the platoon size increases.

A system of M identical unit mass vehicles is shown in Figure 13.1.



Figure 13.1: Finite platoon of vehicles.

The dynamics of this system can be captured by representing each vehicle as a moving mass with the second order dynamics

$$\ddot{x}_n + \kappa \dot{x}_n = u_n, \quad n \in \{1, \dots, M\}, \quad (13.1)$$

where x_n represents the position of the n -th vehicle, u_n is the control applied on the n -th vehicle, and $\kappa \geq 0$ denotes the linearized drag coefficient per unit mass.

A control objective is to provide the desired cruising velocity $v_d := \text{const.}$, and to keep the distance between the neighboring vehicles at a constant pre-specified level L . By introducing the absolute position

and velocity error variables

$$\left. \begin{array}{l} \xi_n(t) := x_n(t) - v_d t + nL \\ \zeta_n(t) := \dot{x}_n(t) - v_d \end{array} \right\} \quad n \in \{1, \dots, M\},$$

system (13.1) can be rewritten using a state-space realization of the form [2, 18]

$$\begin{bmatrix} \dot{\xi} \\ \dot{\zeta} \end{bmatrix} = \begin{bmatrix} 0 & I \\ 0 & -\kappa I \end{bmatrix} \begin{bmatrix} \xi \\ \zeta \end{bmatrix} + \begin{bmatrix} 0 \\ I \end{bmatrix} \tilde{u} =: A\psi + B\tilde{u}, \quad (13.2)$$

where $\xi := [\xi_1 \ \dots \ \xi_M]^*$, $\zeta := [\zeta_1 \ \dots \ \zeta_M]^*$, $\tilde{u} := [\tilde{u}_1 \ \dots \ \tilde{u}_M]^*$, and $\tilde{u}_n := u_n - \kappa v_d$. Alternatively, by introducing the relative position error variable

$$\eta_n(t) := x_n(t) - x_{n-1}(t) + L = \xi_n(t) - \xi_{n-1}(t), \quad n \in \{2, \dots, M\},$$

and neglecting the position dynamics of the first vehicle, the system under study can be represented by a realization with $2M - 1$ state-space variables [1]

$$\begin{bmatrix} \dot{\eta} \\ \dot{\zeta} \end{bmatrix} = \begin{bmatrix} 0 & \bar{A}_{12} \\ 0 & -\kappa I \end{bmatrix} \begin{bmatrix} \eta \\ \zeta \end{bmatrix} + \begin{bmatrix} 0 \\ I \end{bmatrix} \tilde{u} =: \bar{A}\phi + \bar{B}\tilde{u}, \quad (13.3)$$

with $\eta := [\eta_2 \ \dots \ \eta_M]^*$, and \bar{A}_{12} being an $(M - 1) \times M$ Toeplitz matrix with the elements on the main diagonal and the first upper diagonal equal to -1 and 1 , respectively.

Following [2, 18], fictitious lead and follow vehicles, respectively indexed by 0 and $M + 1$, are added to the formation (see Figure 13.2). These two vehicles are constrained to move at the desired velocity v_d and the relative distance between them is assumed to be equal to $(M + 1)L$ for all times. In other words, it is assumed that

$$\{x_0(t) = v_d t, \quad x_{M+1}(t) = v_d t - (M + 1)L, \quad \forall t \geq 0\},$$

or equivalently

$$\{\xi_0(t) = \xi_{M+1}(t) = \zeta_0(t) = \zeta_{M+1}(t) = 0, \quad \forall t \geq 0\}. \quad (13.4)$$

A performance index of the form [2, 18]

$$\begin{aligned} J &:= \frac{1}{2} \int_0^\infty \left(\sum_{n=1}^{M+1} q_1 \eta_n^2(t) + \sum_{n=1}^M (q_3 \zeta_n^2(t) + r \tilde{u}_n^2(t)) \right) dt \\ &= \frac{1}{2} \int_0^\infty \left(\sum_{n=1}^{M+1} q_1 (\xi_n(t) - \xi_{n-1}(t))^2 + \sum_{n=1}^M (q_3 \zeta_n^2(t) + r \tilde{u}_n^2(t)) \right) dt, \end{aligned} \quad (13.5)$$

is associated with system (13.2). Using (13.4), J can be equivalently rewritten as

$$J = \frac{1}{2} \int_0^\infty (\psi^*(t) Q \psi(t) + \tilde{u}^*(t) R \tilde{u}(t)) dt,$$

where matrices Q and R are determined by

$$Q := \begin{bmatrix} Q_1 & 0 \\ 0 & q_3 I \end{bmatrix}, \quad R := rI,$$

with Q_1 being an $2M \times 2M$ tridiagonal symmetric Toeplitz matrix with the first row given by

$$[2q_1 \ -q_1 \ 0 \ \dots \ 0] \in \mathbb{R}^{2M}.$$

The control problem is now in the standard LQR form.

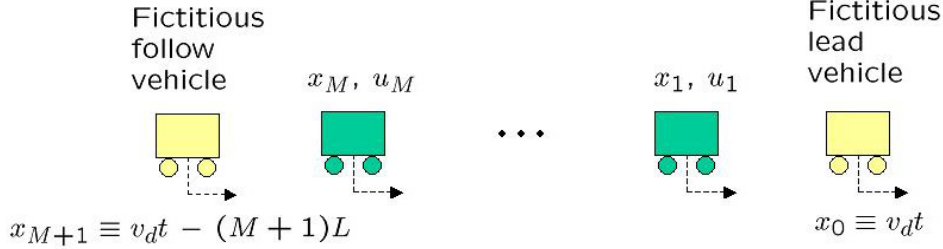


Figure 13.2: Finite platoon with fictitious lead and follow vehicles.

The left and middle plots in Figure 13.3 respectively show the dependence of the minimal and maximal eigenvalues of the solution to the LQR Algebraic Riccati Equation (ARE) P_M for system (13.2) with performance index (13.5), for $\{\kappa = 0, q_1 = q_3 = r = 1\}$. Clearly, $\lambda_{\min}\{P_M\}$ decays monotonically towards zero indicating that the pair (Q, A) gets closer to losing its detectability as the number of vehicles increases. This also follows from the PBH detectability test. Namely, as illustrated in the left plot of Figure 13.5, the minimal singular values of $D_M(\lambda) := [A^T - \lambda I \quad Q^T]^T$ at $\lambda = 0$ decrease monotonically with M . On the other hand, $\lambda_{\max}\{P_M\}$ converges towards the constant value that determines the optimal value of objective (13.5) as M goes to infinity. The right plot in Figure 13.3 illustrates the location of the dominant poles of system (13.2) connected in feedback with a controller that minimizes cost functional (13.5) for $\{\kappa = 0, q_1 = q_3 = r = 1\}$. The dotted line represents the function $-3.121/M$ which indicates that the least-stable eigenvalues of the closed-loop A matrix scale in an inversely proportional manner to the number of vehicles in platoon. Hence, the time constant of the closed-loop system gets larger as the size of platoon increases. This is further demonstrated in Figure 13.4, where the absolute and the relative position errors of an LQR controlled string (13.2,13.5) with 20 and 50 vehicles are shown. Simulation results are obtained for an initial condition of the form $\{\xi_n(0) = \zeta_n(0) = 1, \forall n = \{1, \dots, M\}\}$. These plots clearly exhibit the platoon size dependent rate of convergence towards the desired formation when a controller resulting from the LQR problem formulated by [2, 18] is implemented.

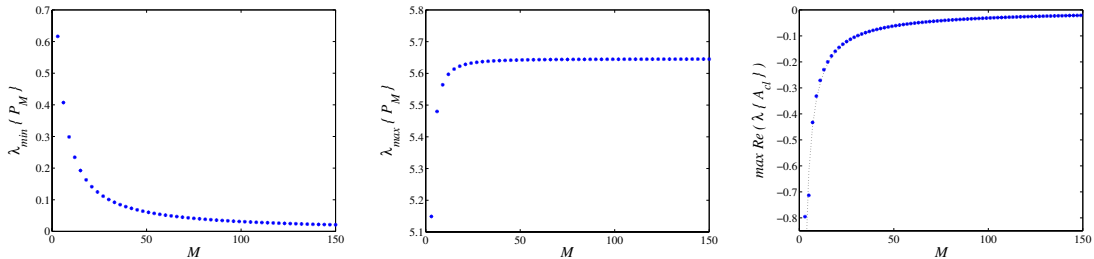


Figure 13.3: The minimal (left plot) and maximal eigenvalues (middle plot) of the ARE solution P_M for system (13.2) with performance objective (13.5), and the dominant poles of LQR controlled platoon (13.2,13.5) (right plot) as functions of the number of vehicles for $\{\kappa = 0, q_1 = q_3 = r = 1\}$.

We remark that a formulation of the LQR problem for finite platoon (13.2) without the follow fictitious vehicle and appropriately modified cost functional of the form

$$J := \frac{1}{2} \int_0^\infty \left(\sum_{n=1}^M q_1 \eta_n^2(t) + q_3 \zeta_n^2(t) + r \tilde{u}_n^2(t) \right) dt, \quad (13.6)$$

yields qualitatively similar results to the ones presented above (as can be seen from the middle plot of

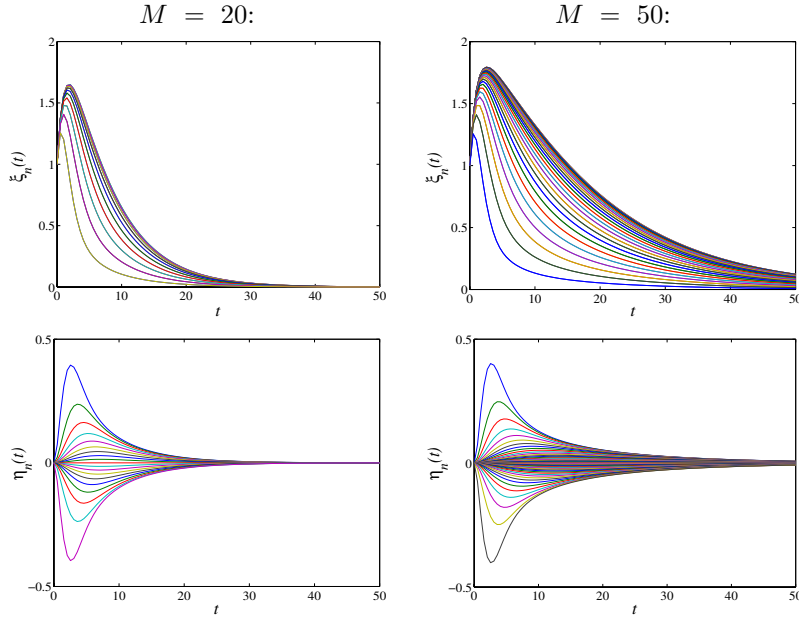


Figure 13.4: Absolute and relative position errors of an LQR controlled string (13.2,13.5) with 20 vehicles (left column) and 50 vehicles (right column), for $\{\kappa = 0, q_1 = q_3 = r = 1\}$. Simulation results are obtained for the following initial condition: $\{\xi_n(0) = \zeta_n(0) = 1, \forall n = \{1, \dots, M\}\}$.

Figure 13.5). On the other hand, for system (13.2) without both lead and follow fictitious vehicles, the appropriately modified performance objective is given by (13.7). In this case, both the first and the last elements on the main diagonal of matrix Q_1 are equal to q_1 . Based on the right plot of Figure 13.5, it follows that the pair (Q, A) for system (13.2,13.7) is practically not detectable, irrespective of the number of vehicles in formation.

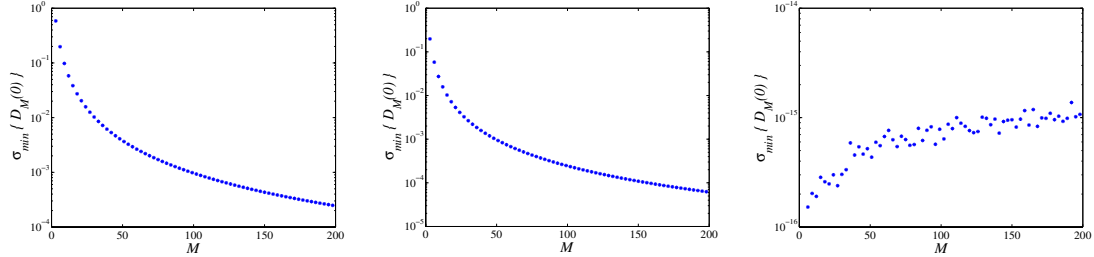


Figure 13.5: The minimal singular values of matrix $D_M(\lambda) := [A^T - \lambda I \quad Q^T]^T$ at $\lambda = 0$ for system (13.2) with performance objectives: (13.5) (left plot), (13.6) (middle plot), and (13.7) (right plot) as functions of the number of vehicles for $\{\kappa = 0, q_1 = q_3 = r = 1\}$. These singular values are given in the logarithmic scale.

Levine & Athans [1] studied the finite string of M vehicles shown in Figure 13.1, with state-space representation (13.3) expressed in terms of the relative position and absolute velocity error variables. In particular, the LQR problem with a quadratic performance objective of the form

$$J := \frac{1}{2} \int_0^\infty \left(\sum_{n=2}^M q_1 \eta_n^2(t) + \sum_{n=1}^M (q_3 \zeta_n^2(t) + r \tilde{u}_n^2(t)) \right) dt, \quad (13.7)$$

was formulated. Furthermore, the solution was provided for a platoon with $M = 3$ vehicles and $\{\kappa = r = 1, q_1 = 10, q_3 = 0\}$. We take a slightly different approach and analyze the solution to this problem as a function of the number of vehicles in platoon.

The left and middle plots in Figure 13.6 respectively show minimal and maximal eigenvalues of the solution to the ARE in LQR problem (13.3,13.7) with $\kappa = q_1 = q_3 = r = 1$. The right plot in the same figure shows the real parts of the least-stable poles of system (13.3) with a controller that minimizes (13.7). Clearly, $\lambda_{\max}\{P_M\}$ scales linearly with the number of vehicles and, thus, the optimal value of performance objective (13.7) gets larger as the size of a vehicular string grows. This is because the pair (\bar{A}, \bar{B}) gets closer to losing its stabilizability when the platoon size increases. Equivalently, this can be established by observing the monotonic decay towards zero (with M) of the minimal singular value of $[\bar{A} - \lambda I \quad \bar{B}]$ at $\lambda = 0$. In the interest of brevity, we do not show this dependence here. Furthermore, in the right plot, the dotted line represents the function $-2.222/M$, which implies the inversely proportional relationship between the dominant eigenvalues of the closed-loop A matrix and the number of vehicles in platoon. This implies again that as the number of vehicles increases, there is no uniform bound on the decay rates of regulated states to zero. This is additionally illustrated in Figure 13.7 where the relative position errors of an LQR controlled system (13.3,13.7) with 20 and 50 vehicles are shown. Simulation results are obtained for the initial condition of the form $\{\eta_n(0) = 1, \forall n = \{2, \dots, M\}; \zeta_n(0) = 1, \forall n = \{1, \dots, M\}\}$.

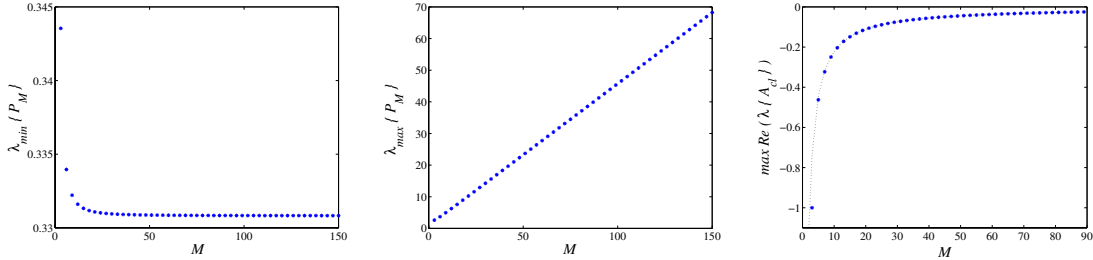


Figure 13.6: The minimal (left plot) and maximal eigenvalues (middle plot) of the ARE solution P_M for system (13.3) with performance objective (13.7), and the dominant poles of LQR controlled platoon (13.3,13.7) (right plot) as functions of the number of vehicles for $\kappa = q_1 = q_3 = r = 1$.

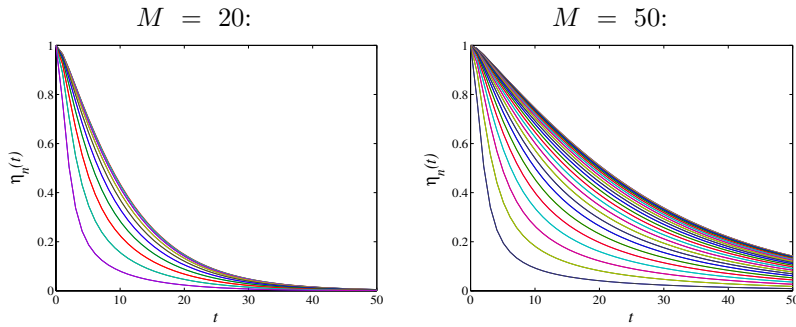


Figure 13.7: Relative position errors of LQR controlled system (13.3,13.7) with 20 vehicles (left plot) and 50 vehicles (right plot), for $\kappa = q_1 = q_3 = r = 1$. Simulation results are obtained for the following initial condition: $\{\eta_n(0) = 1, \forall n = \{2, \dots, M\}; \zeta_n(0) = 1, \forall n = \{1, \dots, M\}\}$.

The results of this subsection clearly indicate that control strategies of [1, 2, 18] lead to closed-loop systems with arbitrarily slow decay rates as the number of vehicles increases. In § 13.1.2, we show analytically that the absence of a uniform rate of convergence in finite platoons manifests itself as the absence of exponential stability in the limit of an infinite vehicular strings.

13.1.2 Optimal control of infinite vehicular platoons

In this subsection, we consider the LQR problem for infinite vehicular platoons. This problem was originally studied by Melzer & Kuo [2]. Using recently developed theory for spatially invariant linear systems [16], we show that the controller obtained by these authors does not provide exponential stability of the closed-loop system due to the lack of detectability of the pair (Q, A) in their LQR problem. We further demonstrate that the infinite platoon size limit of the problem formulation of Levine & Athans [1] yields an infinite-dimensional system which is not stabilizable.

A system of identical unit mass vehicles in an infinite string is shown in Figure 13.8. The infinite

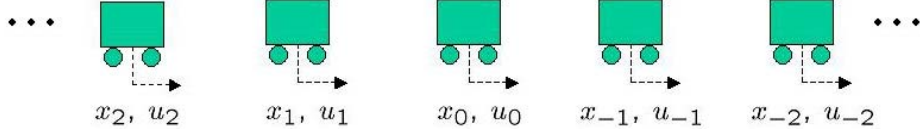


Figure 13.8: Infinite platoon of vehicles.

dimensional equivalents of (13.2) and (13.3) are respectively given by

$$\begin{bmatrix} \dot{\xi}_n \\ \dot{\zeta}_n \end{bmatrix} = \begin{bmatrix} 0 & 1 \\ 0 & -\kappa \end{bmatrix} \begin{bmatrix} \xi_n \\ \zeta_n \end{bmatrix} + \begin{bmatrix} 0 \\ 1 \end{bmatrix} \tilde{u}_n =: A_n \psi_n + B_n \tilde{u}_n, \quad n \in \mathbb{Z}, \quad (13.8)$$

and

$$\begin{bmatrix} \dot{\eta}_n \\ \dot{\zeta}_n \end{bmatrix} = \begin{bmatrix} 0 & 1 - T_{-1} \\ 0 & -\kappa \end{bmatrix} \begin{bmatrix} \eta_n \\ \zeta_n \end{bmatrix} + \begin{bmatrix} 0 \\ 1 \end{bmatrix} \tilde{u}_n =: \bar{A}_n \phi_n + \bar{B}_n \tilde{u}_n, \quad n \in \mathbb{Z}, \quad (13.9)$$

where T_{-1} is the operator of translation by -1 (in the vehicle's index). As in [2,3], we consider a quadratic cost functional of the form

$$\begin{aligned} J &:= \frac{1}{2} \int_0^\infty \sum_{n \in \mathbb{Z}} (q_1 \eta_n^2(t) + q_3 \zeta_n^2(t) + r \tilde{u}_n^2(t)) dt \\ &= \frac{1}{2} \int_0^\infty \sum_{n \in \mathbb{Z}} (q_1 (\xi_n(t) - \xi_{n-1}(t))^2 + q_3 \zeta_n^2(t) + r \tilde{u}_n^2(t)) dt, \end{aligned} \quad (13.10)$$

with q_1 , q_3 , and r being positive design parameters.

We utilize the fact that systems (13.8) and (13.9) have spatially invariant dynamics over a discrete spatial lattice \mathbb{Z} [16]. This implies that the appropriate Fourier transform (in this case the bilateral Z -transform evaluated on the unit circle) can be used to convert analysis and quadratic design problems into those for a parameterized family of finite-dimensional systems. This transform, which we refer to here as the Z_θ -transform, is defined by

$$\hat{x}_\theta := \sum_{n \in \mathbb{Z}} x_n e^{-jn\theta}.$$

Using this, system (13.8) and cost functional (13.10) transform to

$$\begin{bmatrix} \dot{\hat{\xi}}_\theta \\ \dot{\hat{\zeta}}_\theta \end{bmatrix} = \begin{bmatrix} 0 & 1 \\ 0 & -\kappa \end{bmatrix} \begin{bmatrix} \hat{\xi}_\theta \\ \hat{\zeta}_\theta \end{bmatrix} + \begin{bmatrix} 0 \\ 1 \end{bmatrix} \hat{u}_\theta =: \hat{A}_\theta \hat{\psi}_\theta + \hat{B}_\theta \hat{u}_\theta, \quad 0 \leq \theta < 2\pi, \quad (13.11)$$

and

$$J = \frac{1}{4\pi} \int_0^\infty \int_0^{2\pi} \left(\hat{\psi}_\theta^*(t) \hat{Q}_\theta \hat{\psi}_\theta(t) + \hat{u}_\theta^*(t) \hat{R}_\theta \hat{u}_\theta(t) \right) d\theta dt,$$

where

$$\hat{Q}_\theta := \begin{bmatrix} 2q_1(1 - \cos \theta) & 0 \\ 0 & q_3 \end{bmatrix}, \quad \hat{R}_\theta := r, \quad 0 \leq \theta < 2\pi.$$

Similarly, system (13.9) and cost functional (13.10) transform to

$$\begin{bmatrix} \dot{\hat{\eta}}_\theta \\ \dot{\hat{\zeta}}_\theta \end{bmatrix} = \begin{bmatrix} 0 & 1 - e^{-j\theta} \\ 0 & -\kappa \end{bmatrix} \begin{bmatrix} \hat{\eta}_\theta \\ \hat{\zeta}_\theta \end{bmatrix} + \begin{bmatrix} 0 \\ 1 \end{bmatrix} \hat{u}_\theta =: \hat{A}_\theta \hat{\phi}_\theta + \hat{B}_\theta \hat{u}_\theta, \quad 0 \leq \theta < 2\pi, \quad (13.12)$$

with

$$J = \frac{1}{4\pi} \int_0^\infty \int_0^{2\pi} \left(\hat{\phi}_\theta^*(t) \hat{Q}_\theta \hat{\phi}_\theta(t) + \hat{u}_\theta^*(t) \hat{R}_\theta \hat{u}_\theta(t) \right) d\theta dt,$$

where

$$\hat{Q}_\theta := \begin{bmatrix} q_1 & 0 \\ 0 & q_3 \end{bmatrix}, \quad \hat{R}_\theta := r, \quad 0 \leq \theta < 2\pi.$$

If $(\hat{A}_\theta, \hat{B}_\theta)$ is stabilizable and $(\hat{Q}_\theta, \hat{A}_\theta)$ is detectable for all $\theta \in [0, 2\pi]$, then the θ -parameterized ARE

$$\hat{A}_\theta^* \hat{P}_\theta + \hat{P}_\theta \hat{A}_\theta + \hat{Q}_\theta - \hat{P}_\theta \hat{B}_\theta \hat{R}_\theta^{-1} \hat{B}_\theta^* \hat{P}_\theta = 0, \quad 0 \leq \theta < 2\pi,$$

has a unique positive definite solution for every $\theta \in [0, 2\pi]$. This positive definite matrix determines the optimal stabilizing feedback for system (13.11) for every $\theta \in [0, 2\pi]$

$$\hat{u}_\theta := \hat{K}_\theta \hat{\psi}_\theta = -\hat{R}_\theta^{-1} \hat{B}_\theta^* \hat{P}_\theta \hat{\psi}_\theta, \quad 0 \leq \theta < 2\pi.$$

If this is the case, then there exist an exponentially stabilizing feedback for system (13.8) that minimizes (13.10) [16]. This optimal stabilizing feedback for (13.8) is given by

$$\tilde{u}_n = \sum_{k \in \mathbb{Z}} K_{n-k} \psi_k, \quad n \in \mathbb{Z},$$

where

$$K_n = \frac{1}{2\pi} \int_0^{2\pi} \hat{K}_\theta e^{jn\theta} d\theta, \quad n \in \mathbb{Z}.$$

It is easily shown that the pair $(\hat{A}_\theta, \hat{B}_\theta)$ is controllable for every $\theta \in [0, 2\pi]$. On the other hand, the pair $(\hat{Q}_\theta, \hat{A}_\theta)$ is not detectable at $\theta = 0$. In particular, the solution to the ARE at $\theta = 0$ is given by

$$\hat{P}_0 := \begin{bmatrix} 0 & 0 \\ 0 & r(-\kappa + \gamma) \end{bmatrix},$$

which yields a closed-loop A matrix at $\theta = 0$ of the form

$$\hat{A}_{\text{clo}} = \begin{bmatrix} 0 & 1 \\ 0 & -\gamma \end{bmatrix}, \quad (13.13)$$

with $\gamma := \frac{1}{r} \sqrt{(\kappa r)^2 + rq_3}$. Therefore, matrix \hat{A}_{clo} is not Hurwitz, which implies that the solution to the LQR problem does not provide an exponentially stabilizing feedback for the original system [16]. We remark that this fact has not been realized in [2] and [3]. The spectrum of the closed-loop generator for $\{\kappa = 0, q_1 = q_3 = r = 1\}$ is shown in Figure 13.9 to illustrate the absence of exponential stability.

It is instructive to consider the initial states that are not stabilized by this LQR feedback. Based

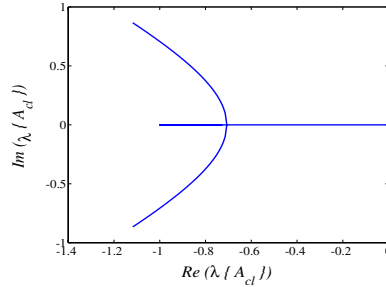


Figure 13.9: The spectrum of the closed-loop generator in an LQR controlled spatially invariant string of vehicles (13.8) with performance objective (13.10) and $\{\kappa = 0, q_1 = q_3 = r = 1\}$.

on (13.13), it follows that the solution of system (13.11) at $\theta = 0$ with the controller of [2] is determined by

$$\begin{aligned}\hat{\zeta}_0(t) &= e^{-\gamma t} \hat{\zeta}_0(0), \\ \hat{\xi}_0(t) &= \hat{\xi}_0(0) - \frac{1}{\gamma} (1 - e^{-\gamma t}) \hat{\zeta}_0(0).\end{aligned}$$

We have assumed that $\gamma \neq 0$, which can be accomplished for any $\kappa \geq 0$ by choosing $q_3 > 0$. Thus,

$$\sum_{n \in \mathbb{Z}} \xi_n(t) = \sum_{n \in \mathbb{Z}} \xi_n(0) - \frac{1}{\gamma} (1 - e^{-\gamma t}) \sum_{n \in \mathbb{Z}} \zeta_n(0),$$

which implies that $\lim_{t \rightarrow \infty} \sum_{n \in \mathbb{Z}} \xi_n(t) \neq 0$ unless

$$\sum_{n \in \mathbb{Z}} \xi_n(0) - \frac{1}{\gamma} \sum_{n \in \mathbb{Z}} \zeta_n(0) \equiv 0. \quad (13.14)$$

Therefore, if the initial condition of system (13.8) does not satisfy (13.14) than $\sum_{n \in \mathbb{Z}} \xi_n(t)$ cannot be asymptotically driven towards zero. It is not difficult to construct a physically relevant initial condition that violates (13.14). For example, this situation will be encountered if the string of vehicles at $t = 0$ cruises at the desired velocity v_d with all the vehicles being at their desired spatial locations except for a single vehicle. In other words, even for a seemingly benign initial condition of the form $\{\zeta_n(0) \equiv 0; \xi_n(0) = 0, \forall n \in \mathbb{Z} \setminus 0; \xi_0(0) = S \neq 0\}$ there exist at least one vehicle whose absolute position error does not converge to zero as time goes to infinity when the control strategy of Melzer & Kuo [2] is employed. This non-zero mean position initial condition is graphically illustrated in Figure 13.10.

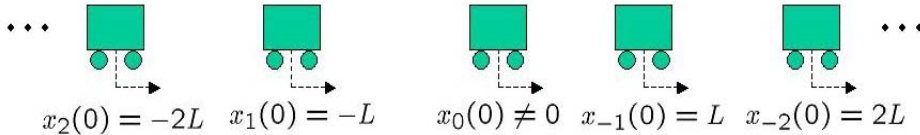


Figure 13.10: An example of a position initial condition for which there is at least one vehicle whose absolute position error does not asymptotically converge to zero when the control strategy of [2] is used.

We note that system (13.12) is not stabilizable at $\theta = 0$, which prevents system (13.9) from being stabilizable [16]. Hence, when infinite vehicular platoons are considered the formulation of design problem of Levine & Athans [1] is ill-posed (that is, unstabilizable). In particular, the solution of the ' $\hat{\eta}$ -subsystem'

of (13.12) at $\theta = 0$ does not change with time, that is $\hat{\eta}_0(t) \equiv \hat{\eta}_0(0)$, which indicates that $\sum_{n \in \mathbb{Z}} \eta_n(t) \equiv \sum_{n \in \mathbb{Z}} \eta_n(0)$. Therefore, for a non-zero mean initial condition $\{\eta_n(0)\}_{n \in \mathbb{Z}}$, the sum of all relative position errors is identically equal to a non-zero constant determined by $\sum_{n \in \mathbb{Z}} \eta_n(0)$. An example of such initial condition is given by $\{\eta_n(0) = 0, \forall n \in \mathbb{Z} \setminus 0; \eta_0(0) = S \neq 0\}$, and it is illustrated in Figure 13.11. It is quite remarkable that the control strategy of Levine & Athans [1] is not able to asymptotically steer all relative position errors towards zero in an infinite platoon with this, at first glance, innocuously looking initial condition.

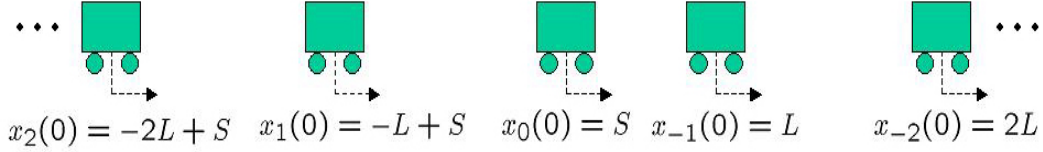


Figure 13.11: An example of a position initial condition for which there is at least a pair of vehicles whose relative distance does not asymptotically converge to the desired inter-vehicular spacing L when a control strategy of [1] is used.

Therefore, we have shown that exponential stability of an LQR controlled infinite platoon cannot be achieved due to the lack of detectability (in the case of [2, 18]) and stabilizability (in the case of [1]). These facts have very important practical implications for optimal control of large vehicular platoons. Namely, our analysis clarifies results of § 13.1.1, where we have observed that decay rates of a finite platoon with controllers of [1, 2, 18] become smaller as the platoon size increases.

In § 13.1.3, we demonstrate that exponential stability of an infinite string of vehicles can be guaranteed by accounting for position errors with respect to absolute desired trajectories in both the state-space representation and the performance criterion.

13.1.3 Alternative problem formulations

In this subsection, we propose an alternative formulation of optimal control problems for vehicular platoons. In particular, we study distributed optimal control design with respect to quadratic performance criteria (LQR, \mathcal{H}_2 , \mathcal{H}_∞), and show that the problems discussed in § 13.1.1 and § 13.1.2 can be overcome by accounting for the absolute position errors in both the state-space realization and the performance criterion. We also briefly remark on the choice of the appropriate state-space.

Alternative LQR problem formulation

In this subsection, we suggest an alternative formulation of the LQR problem in order to overcome issues raised in § 13.1.1 and § 13.1.2. Since consideration of infinite platoons is better suited for analysis, we first study the LQR problem for a spatially invariant string of vehicles, and then discuss practical implications for optimal control of finite vehicular platoons.

We represent system shown in Figure 13.8 by its state-space representation (13.8) expressed in terms of absolute position and velocity error variables, and propose the quadratic performance objective of the form

$$\begin{aligned} J &:= \frac{1}{2} \int_0^\infty \sum_{n \in \mathbb{Z}} (q_1 \eta_n^2(t) + q_2 \xi_n^2(t) + q_3 \zeta_n^2(t) + r \tilde{u}_n^2(t)) dt \\ &= \frac{1}{2} \int_0^\infty \sum_{n \in \mathbb{Z}} (q_1 (\xi_n(t) - \xi_{n-1}(t))^2 + q_2 \xi_n^2(t) + q_3 \zeta_n^2(t) + r \tilde{u}_n^2(t)) dt, \end{aligned} \quad (13.15)$$

with q_1, q_2, q_3 , and r being positive design parameters. It should be noted that in (13.15) we account for both absolute position errors ξ_n and relative position errors η_n . This is in contrast to performance index (13.10)

considered by Melzer & Kuo [2] and Chu [3], where only relative position errors are penalized in J . The main point of this subsection is to show that if one accounts for absolute position errors in the cost functional, then LQR feedback will be exponentially stabilizing.

Application of Z_θ -transform renders (13.8) into (13.11), whereas (13.15) simplifies to

$$J = \frac{1}{4\pi} \int_0^\infty \int_0^{2\pi} \left(\hat{\psi}_\theta^*(t) \hat{Q}_\theta^* \hat{\psi}_\theta(t) + \hat{u}_\theta^*(t) \hat{R}_\theta \hat{u}_\theta(t) \right) d\theta dt,$$

where

$$\hat{Q}_\theta^* := \begin{bmatrix} q_2 + 2q_1(1 - \cos \theta) & 0 \\ 0 & q_3 \end{bmatrix}, \quad \hat{R}_\theta := r, \quad 0 \leq \theta < 2\pi.$$

As shown in § 13.1.2, the pair $(\hat{A}_\theta, \hat{B}_\theta)$ is controllable for every $\theta \in [0, 2\pi]$. Furthermore, it is easily established that the pair $(\hat{Q}_\theta^*, \hat{A}_\theta)$ is detectable if and only if

$$q_2 + 2q_1(1 - \cos \theta) \neq 0, \quad \forall \theta \in [0, 2\pi].$$

Even if q_1 is set to zero, this condition is satisfied as long as $q_2 > 0$. However, in this situation the inter-vehicular spacing is not penalized in the cost functional which may result into an unsafe control strategy. Because of that, as in [2, 3], we assign a positive value to q_1 . In this case, if $q_2 = 0$, the pair $(\hat{Q}_\theta^*, \hat{A}_\theta)$ is not detectable at $\theta = 0$, which implies that accounting for the absolute position errors in the performance criterion is essential for obtaining a stabilizing solution to the LQR problem. The spectrum of the closed-loop generator shown in Figure 13.12 illustrates exponential stability of infinite string of vehicles (13.8) combined in feedback with a controller that minimizes performance objective (13.15) for $\{\kappa = 0, q_1 = q_2 = q_3 = r = 1\}$.

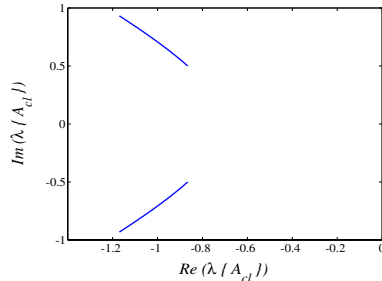


Figure 13.12: The spectrum of the closed-loop generator in an LQR controlled spatially invariant string of vehicles (13.8) with performance objective (13.15) and $\{\kappa = 0, q_1 = q_2 = q_3 = r = 1\}$.

For a finite platoon with M vehicles the appropriately modified version of (13.15) is obtained by adding an additional term that accounts for absolute position errors to the right-hand side of (13.5)

$$\begin{aligned} J &:= \frac{1}{2} \int_0^\infty \left(\sum_{n=1}^{M+1} q_1 \eta_n^2(t) + \sum_{n=1}^M (q_2 \xi_n^2(t) + q_3 \zeta_n^2(t) + r \tilde{u}_n^2(t)) \right) dt \\ &= \frac{1}{2} \int_0^\infty \left(\sum_{n=1}^{M+1} q_1 (\xi_n(t) - \xi_{n-1}(t))^2 + \sum_{n=1}^M (q_2 \xi_n^2(t) + q_3 \zeta_n^2(t) + r \tilde{u}_n^2(t)) \right) dt. \end{aligned} \tag{13.16}$$

Equivalently, (13.16) can be rewritten as

$$J = \frac{1}{2} \int_0^\infty (\psi^*(t) Q^* \psi(t) + \tilde{u}^*(t) R \tilde{u}(t)) dt,$$

where Q^* and R are $2M \times 2M$ and $M \times M$ matrices given by

$$Q^* := \begin{bmatrix} Q_1 + q_2 I & 0 \\ 0 & q_3 I \end{bmatrix}, \quad R := rI,$$

respectively. Toeplitz matrix Q_1 has the same meaning as in § 13.1.1.

The left and middle plots in Figure 13.13 respectively show the minimal and maximal eigenvalues of the ARE solution for system (13.2) with performance objective (13.16), and the right plot in the same figure shows the real parts of the least-stable poles in an LQR controlled string of vehicles (13.2,13.16) for $\{\kappa = 0, q_1 = q_2 = q_3 = r = 1\}$. Clearly, when the absolute position errors are accounted for in both the state-space realization and J , the problems addressed in § 13.1.1 are easily overcome. In particular, the least-stable closed-loop eigenvalues converge towards a non-zero value determined by the dominant pole of the spatially invariant system.

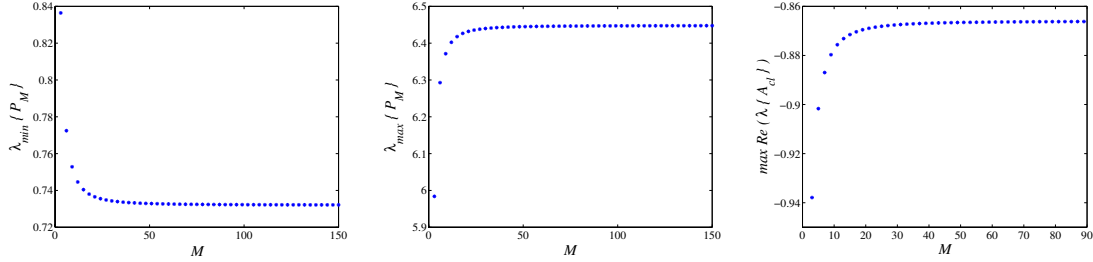


Figure 13.13: The minimal (left plot) and maximal eigenvalues (middle plot) of the ARE solution P_M for system (13.2) with performance objective (13.16), and the dominant poles of LQR controlled platoon (13.2,13.16) (right plot) as functions of the number of vehicles, for $\{\kappa = 0, q_1 = q_2 = q_3 = r = 1\}$.

Absolute position errors of an LQR controlled string (13.2,13.16) with 20 and 50 vehicles are shown in Figure 13.14. Simulation results are obtained for $\{\kappa = 0, q_1 = q_2 = q_3 = r = 1\}$ and the initial condition of the form $\{\xi_n(0) = \zeta_n(0) = 1, \forall n = \{1, \dots, M\}\}$. These plots clearly demonstrate the uniform rate of convergence towards the desired formation. This is accomplished by expressing the state-space realization in terms of the errors with respect to the absolute desired trajectories and by accounting for the absolute position errors in the performance objective.

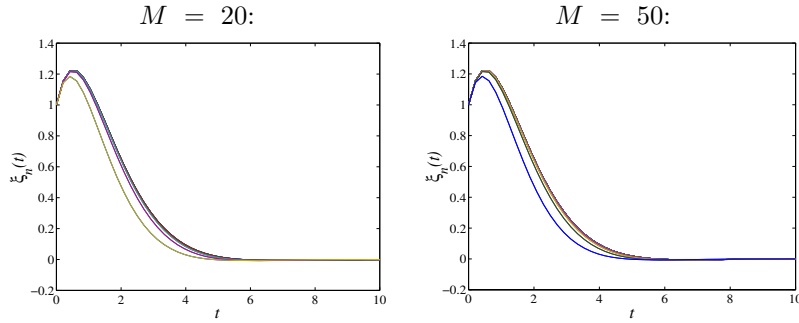


Figure 13.14: Absolute position errors of an LQR controlled string (13.2,13.16) with 20 vehicles (left plot) and 50 vehicles (right plot), for $\{\kappa = 0, q_1 = q_2 = q_3 = r = 1\}$. Simulation results are obtained for the following initial condition: $\{\xi_n(0) = \zeta_n(0) = 1, \forall n = \{1, \dots, M\}\}$.

We note that qualitatively similar results are obtained if LQR problem is formulated for system (13.2) with either functional (13.6) or functional (13.7) augmented by a term penalizing absolute position errors.

Next, we formulate the distributed \mathcal{H}_2 and \mathcal{H}_∞ design problems for a spatially invariant string of vehicles, and discuss necessary conditions for the existence of stabilizing controllers.

\mathcal{H}_2 and \mathcal{H}_∞ control of spatially invariant vehicular platoons

In this subsection, we consider a spatially invariant string of vehicles shown in Figure 13.8 in the presence of external disturbances

$$\ddot{x}_n + \kappa \dot{x}_n = u_n + d_n, \quad n \in \mathbb{Z}, \quad (13.17)$$

and formulate \mathcal{H}_2 and \mathcal{H}_∞ control problems. A disturbance acting on the n -th vehicle is denoted by d_n and it can account for the external forces such as wind gusts, rolling resistance friction, pot holes, and non-horizontal road slopes. For simplicity, we assume that there are no model uncertainties and rewrite (13.17) in the form suitable for solving a standard robust control problem [19]

$$\left. \begin{array}{l} \dot{\psi}_n = A\psi_n + B_1 w_n + B_2 \tilde{u}_n \\ z_n = C_1 \psi_n + D_{11} w_n + D_{12} \tilde{u}_n \\ y_n = C_2 \psi_n + D_{21} w_n + D_{22} \tilde{u}_n \end{array} \right\} \quad n \in \mathbb{Z}, \quad (13.18)$$

where

$$\psi_n := \begin{bmatrix} \xi_n \\ \zeta_n \end{bmatrix}, \quad \tilde{u}_n := u_n - \kappa v_d, \quad w_n := \begin{bmatrix} d_n \\ \nu_n \end{bmatrix},$$

with ν_n denoting the measurement noise for the n -th vehicle. With these choices, matrices A , B_1 , and B_2 are respectively determined by

$$A := \begin{bmatrix} 0 & 1 \\ 0 & -\kappa \end{bmatrix}, \quad B_1 := \begin{bmatrix} 0 & 0 \\ 1 & 0 \end{bmatrix}, \quad B_2 := \begin{bmatrix} 0 \\ 1 \end{bmatrix}.$$

We further assume the ‘exogenous’ and ‘sensed’ outputs for the n -th vehicle of the form

$$z_n := \begin{bmatrix} q_1(\xi_n - \xi_{n-1}) \\ q_2 \xi_n \\ q_3 \zeta_n \\ r \tilde{u}_n \end{bmatrix}, \quad y_n := \xi_n + s_1 \nu_n,$$

where q_1 , q_2 , q_3 , r , and s_1 represent positive design parameters. Thus, operators C_i and D_{ij} , for every $i, j = \{1, 2\}$ and $n \in \mathbb{Z}$, are determined by

$$\begin{aligned} C_1 &:= \begin{bmatrix} q_1(1 - T_{-1}) & 0 \\ q_2 & 0 \\ 0 & q_3 \\ 0 & 0 \end{bmatrix}, & D_{11} &:= 0, & D_{12} &:= \begin{bmatrix} 0 \\ 0 \\ 0 \\ r \end{bmatrix}, \\ C_2 &:= \begin{bmatrix} 1 & 0 \end{bmatrix}, & D_{21} &:= [0 \quad s_1], & D_{22} &:= 0. \end{aligned}$$

Application of Z_θ -transform renders (13.18) into the θ -parameterized finite dimensional family of systems of the form

$$\left. \begin{array}{l} \dot{\hat{\psi}}_\theta = \hat{A}_\theta \hat{\psi}_\theta + \hat{B}_{1\theta} \hat{w}_\theta + \hat{B}_{2\theta} \hat{\tilde{u}}_\theta \\ \dot{\hat{z}}_\theta = \hat{C}_{1\theta} \hat{\psi}_\theta + \hat{D}_{11\theta} \hat{w}_\theta + \hat{D}_{12\theta} \hat{\tilde{u}}_\theta \\ \dot{\hat{y}}_\theta = \hat{C}_{2\theta} \hat{\psi}_\theta + \hat{D}_{21\theta} \hat{w}_\theta + \hat{D}_{22\theta} \hat{\tilde{u}}_\theta \end{array} \right\} \quad \theta \in [0, 2\pi), \quad (13.19)$$

with

$$\begin{aligned}\hat{A}_\theta &= \begin{bmatrix} 0 & 1 \\ 0 & -\kappa \\ q_1(1 - e^{-j\theta}) & 0 \end{bmatrix}, & \hat{B}_{1\theta} &= \begin{bmatrix} 0 & 0 \\ 1 & 0 \end{bmatrix}, & \hat{B}_{2\theta} &= \begin{bmatrix} 0 \\ 1 \\ 0 \end{bmatrix}, \\ \hat{C}_{1\theta} &= \begin{bmatrix} q_2 & 0 \\ 0 & q_3 \\ 0 & 0 \end{bmatrix}, & \hat{D}_{11\theta} &= 0, & \hat{D}_{12\theta} &= \begin{bmatrix} 0 \\ 0 \\ r \end{bmatrix}, \\ \hat{C}_{2\theta} &= [1 \ 0], & \hat{D}_{21\theta} &= [0 \ s_1], & \hat{D}_{22\theta} &= 0.\end{aligned}$$

Solving the distributed \mathcal{H}_2 and \mathcal{H}_∞ design problems for system (13.18) amounts to solving the \mathcal{H}_2 and \mathcal{H}_∞ design problems for a parameterized family of finite dimensional LTI systems (13.19) over $\theta \in [0, 2\pi]$ [16].

The following properties of system (13.19) are readily established

1. Pairs $(\hat{A}_\theta, \hat{B}_{2\theta})$ and $(\hat{C}_{2\theta}, \hat{A}_\theta)$ are respectively stabilizable and detectable for every $\theta \in [0, 2\pi]$.
2. $\hat{D}_{12\theta}^* \hat{D}_{12\theta} = r^2 > 0$, $\forall \theta \in [0, 2\pi]$.
3. $\hat{D}_{21\theta} \hat{D}_{21\theta}^* = s_1^2 > 0$, $\forall \theta \in [0, 2\pi]$.
4. $\hat{D}_{12\theta}^* \hat{C}_{1\theta} = 0$, $\hat{B}_{1\theta} \hat{D}_{21\theta}^* = 0$, $\forall \theta \in [0, 2\pi]$.
5. Pair $(\hat{A}_\theta, \hat{B}_{1\theta})$ is stabilizable for every $\theta \in [0, 2\pi]$. Pair $(\hat{C}_{1\theta}, \hat{A}_\theta)$ is detectable for every $\theta \in [0, 2\pi]$ if and only if $q_2 \neq 0$.

If properties (4) and (5) hold than

$$\sigma_{\min} \left\{ \begin{bmatrix} \hat{A}_\theta - j\omega I & \hat{B}_{2\theta} \\ \hat{C}_{1\theta} & \hat{D}_{12\theta} \end{bmatrix} \right\} \geq \varepsilon > 0, \quad \forall \theta \in [0, 2\pi], \quad \forall \omega \in \mathbb{R}, \quad (13.20a)$$

$$\sigma_{\min} \left\{ \begin{bmatrix} \hat{A}_\theta - j\omega I & \hat{B}_{1\theta} \\ \hat{C}_{2\theta} & \hat{D}_{21\theta} \end{bmatrix} \right\} \geq \varepsilon > 0, \quad \forall \theta \in [0, 2\pi], \quad \forall \omega \in \mathbb{R}, \quad (13.20b)$$

which are necessary conditions for the existence of exponentially stabilizing solutions to these infinite dimensional \mathcal{H}_2 and \mathcal{H}_∞ control problems [16]. It is noteworthy that condition (13.20a) is going to be violated unless $q_2 \neq 0$. This further underlines the importance of incorporating the absolute position errors in the performance objective.

Next, we briefly comment on the initial conditions that cannot be dealt with the quadratically optimal controllers of this subsection.

On the choice of the appropriate state-space

In this subsection, we remark on the initial conditions that are not square summable (in a space of the absolute errors) and as such are problematic for optimal controllers involving quadratic criteria.

Motivated by example shown in Figure 13.11 we note that the initial relative position errors $\{\eta_n(0)\}_{n \in \mathbb{Z}}$ cannot be non-zero mean unless the absolute position errors at $t = 0$ sum to infinity. Namely, if $\sum_{n \in \mathbb{Z}} \xi_n(0)$ is bounded, then

$$\sum_{n \in \mathbb{Z}} \eta_n(0) := \sum_{n \in \mathbb{Z}} (\xi_n(0) - \xi_{n-1}(0)) = \sum_{n \in \mathbb{Z}} \xi_n(0) - \sum_{n \in \mathbb{Z}} \xi_{n-1}(0) = 0.$$

Clearly, for the initial condition shown in Figure 13.11, that is,

$$\{x_n(0) = -nL + S, \forall n \in \mathbb{N}_0; \quad x_n(0) = -nL, \forall n \in \mathbb{Z} \setminus \mathbb{N}_0\},$$

sequence $\{\xi_n(0)\}_{n \in \mathbb{Z}}$ sums to infinity if $S \neq 0$. In addition to that, $\{\xi_n(0)\}_{n \in \mathbb{Z}} \notin l_2$, whereas $\{\eta_n(0)\}_{n \in \mathbb{Z}} \in l_2$. Therefore, despite the fact that the inter-vehicular spacing for all but a single vehicle is kept at the desired level L , a relevant non-square summable initial condition¹ is easily constructed. It is worth noting that LQR, \mathcal{H}_2 , and \mathcal{H}_∞ controllers of § 13.1.3 are derived under the assumption of the square summable initial conditions and as such cannot be used for guarding against an entire class of physically relevant initial states. This illustrates that a Hilbert space l_2 may represent a rather restrictive choice for the underlying state-space of system (13.8). Perhaps the more appropriate state-space for this system is a Banach space l_∞ . The control design on this state-space is discussed in § 13.2.

13.2 Limitations and tradeoffs in the control of vehicular platoons

In this section, we study some fundamental limitations and tradeoffs in the control of vehicular platoons. We illustrate that in very long platoons one needs to account explicitly for the initial distances of vehicles from their desired trajectories in order to avoid large position and velocity deviations and the excessive use of control effort. We further derive an initial condition dependent set of requirements that the control gains need to satisfy to guarantee the desired quality of position transient response, and rule out saturation in both velocity and control. These requirements are used to generate the trajectories around which the states of the string of vehicles are driven to their desired values without the excessive use of control effort.

Our presentation is organized as follows: in § 13.2.1, we propose a distributed control strategy that provides stability of an infinite dimensional platoon system. In § 13.2.2, we illustrate that commanding a uniform rate of convergence for all vehicles towards their desired trajectories may require large control efforts. In § 13.2.3, we remark on some basic design limitations and tradeoffs in vehicular platoons and determine the conditions that control gains need to satisfy to provide operation within the imposed saturation limits. In § 13.2.4, we redesign the controller of § 13.2.1 to provide the desired quality of transient response and avoid large control excursions.

13.2.1 Lyapunov-based control of vehicular platoons

A system of identical unit mass vehicles in a semi-infinite string is shown in Figure 13.15.

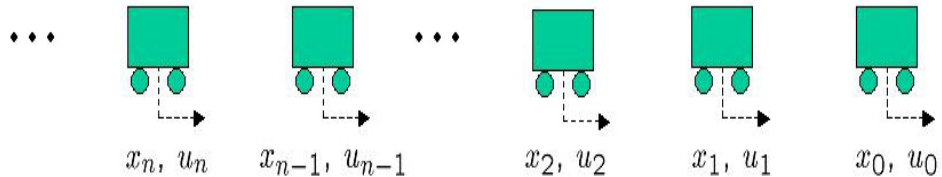


Figure 13.15: Semi-infinite platoon of vehicles. The lead vehicle is indexed by zero.

For notational convenience, we do not include the air resistance force in the model (i.e., set κ to 0 in (13.1)) which yields

$$\ddot{x}_n = u_n, \quad n \in \mathbb{N}_0, \quad (13.21)$$

where $\mathbb{N}_0 := \{0\} \cup \mathbb{N} = \{0, 1, 2, \dots\}$. A control objective the same as in § 13.1: to provide a desired constant cruising velocity v_d and to keep the inter-vehicular distance at a constant pre-specified level L . A coordinate transformation of the form

$$e_n(t) := \alpha_n \xi_n(t) + \beta_n \eta_n(t), \quad n \in \mathbb{N}_0, \quad (13.22)$$

¹In a space of the absolute position errors.

renders (13.21) into

$$\left. \begin{array}{l} \dot{\phi}_n = \psi_n \\ \dot{\psi}_n = -\beta_n u_{n-1} + (\alpha_n + \beta_n) u_n \end{array} \right\} n \in \mathbb{N}_0, \quad (13.23)$$

where α_n and β_n represent nonnegative parameters that are not simultaneously equal to zero, with $\beta_0 \equiv 0$, and $\{\phi_n := e_n, \psi_n := \dot{e}_n\}$. On the other hand, ξ_n and η_n respectively denote the previously defined (see § 13.1.1) position error variables of the n -th vehicle with respect to the absolute and relative reference frames:

$$\begin{aligned} \xi_n(t) &:= x_n(t) - v_d t + nL, & n \in \mathbb{N}_0 \\ \eta_n(t) &:= x_n(t) - x_{n-1}(t) + L, & n \in \mathbb{N}. \end{aligned}$$

By assigning different values to α_n and β_n we can adjust the relative importance of these two quantities.

The appropriate state-space for system (13.23) is a Banach space $l_\infty \times l_\infty$. This choice of the state-space implies that initially, at $t = 0$, no vehicle is infinitely far from its desired absolute position. Control design should provide boundedness of position and velocity error variables for every $t > 0$ and their asymptotic convergence to zero. In § 13.2.2, we illustrate, by means of an example, that choosing a Hilbert space $l_2 \times l_2$ rather than a Banach space $l_\infty \times l_\infty$ for the underlying state-space can be rather restrictive. Namely, this choice of the state-space can exclude an entire set of relevant initial conditions from the analysis.

In particular, a choice of control law of the form

$$u_n = \frac{\beta_n}{\alpha_n + \beta_n} u_{n-1} - \frac{1}{\alpha_n + \beta_n} (a_n \phi_n + b_n \psi_n), \quad (13.24)$$

with $\{a_n > 0, b_n > 0, \forall n \in \mathbb{N}_0\}$, yields an infinite number of stable, fully decoupled second order subsystems

$$\left. \begin{array}{l} \dot{\phi}_n = \psi_n \\ \dot{\psi}_n = -a_n \phi_n - b_n \psi_n \end{array} \right\} n \in \mathbb{N}_0. \quad (13.25)$$

Therefore, we conclude boundedness of both $e_n(t)$ and $\dot{e}_n(t)$, $\forall t \geq 0$, and their asymptotic convergence to zero, for every $n \in \mathbb{N}_0$.

In the remainder of this subsection, we assume that $\{\alpha_n := \alpha = \text{const.}, \beta_n := \beta = \text{const.}, \forall n \in \mathbb{N}; \alpha_0 \neq 0, \beta_0 \equiv 0\}$. In this case, controller (13.24) simplifies to

$$\begin{aligned} u_0 &= -\frac{1}{\alpha_0} (a_0 \phi_0 + b_0 \psi_0), \\ u_n &= \frac{\beta}{\alpha + \beta} u_{n-1} - \frac{1}{\alpha + \beta} (a_n \phi_n + b_n \psi_n), \quad n \in \mathbb{N}, \end{aligned} \quad (13.26a)$$

which in turn implies

$$u_n = \frac{\beta^n}{(\alpha + \beta)^n} u_0 - \sum_{k=1}^n \frac{\beta^{n-k}}{(\alpha + \beta)^{n-k+1}} (a_k \phi_k + b_k \psi_k), \quad (13.27)$$

for every $n \in \mathbb{N}$. If $\{\alpha \neq 0, \beta = 0\}$, controller (13.26a, 13.27) does not take information about the preceding vehicle into consideration since it only accounts for the error variable with respect to the absolute desired trajectory. Therefore, this control strategy is unsafe and because of that we choose $\beta \neq 0$. On the other hand, if $\{\alpha = 0, \beta \neq 0\}$, the information about all vehicles enters into (13.27) with the same importance which is not desirable from communication point of view. For these reasons, we consider the situation in which both α and β have positive values and rewrite (13.27) as

$$u_n = q^n u_0 - \frac{1}{\beta} \sum_{k=1}^n q^{n-k+1} (a_k \phi_k + b_k \psi_k), \quad n \in \mathbb{N}, \quad (13.28)$$

where $q := \beta/(\alpha + \beta) < 1$. With this choice of design parameters α and β the gains in (13.28) decay

geometrically as a function of spatial location. Thus, in the very long string of vehicles, the positions and velocities of vehicles in the beginning of the platoon do not have a significant influence on controls that act on vehicles in the end of the platoon. This feature is of paramount importance for practical implementations.

Using (13.28), we can establish the following bound on the infinity-norm of $u_n(t)$, for every $n \in \mathbb{N}$:

$$\|u_n\|_\infty \leq q^n \|u_0\|_\infty + \frac{1}{\beta} (\sup_k \|\phi_k\|_\infty \sup_k a_k + \sup_k \|\psi_k\|_\infty \sup_k b_k) \frac{q(1-q^n)}{1-q}, \quad (13.29)$$

which, together with the properties of system (13.25), implies boundedness of $u_n(t)$ for all $t \geq 0$, $n \in \mathbb{N}_0$. Based on (13.22), we also conclude boundedness of both $\xi_n(t)$ and $\eta_n(t)$ for all $t \geq 0$, $n \in \mathbb{N}_0$. Asymptotic convergence of these two quantities and their temporal derivatives to zero follows from the following expressions: $x_0(t) = v_d t + \frac{1}{\alpha_0} e_0(t)$, $\dot{x}_0(t) = v_d + \frac{1}{\alpha_0} \dot{e}_0(t)$, $x_n(t) = v_d t - nL + \frac{1}{\beta} \sum_{k=1}^n q^{n-k+1} e_k(t) + \frac{q^n}{\alpha_0} e_0(t)$,

$\dot{x}_n(t) = v_d + \frac{1}{\beta} \sum_{k=1}^n q^{n-k+1} \dot{e}_k(t) + \frac{q^n}{\alpha_0} \dot{e}_0(t)$, $n \in \mathbb{N}$, and the fact that $\lim_{t \rightarrow \infty} e_n(t) = 0$, $\lim_{t \rightarrow \infty} \dot{e}_n(t) = 0$, for every $n \in \mathbb{N}_0$. Therefore, controller (13.26a,13.28) provides boundedness of all signals in the closed-loop and asymptotic convergence of the platoon of vehicles to its desired cruising formation.

In § 13.2.2, we illustrate that, even though our design provides boundedness of controls for all times and all vehicles, the lack of uniform bound on $\|u_n\|_\infty$ may result in an excessive use of control effort.

13.2.2 Issues arising in control strategies with uniform convergence rates

In this subsection, we show that imposing a uniform rate of convergence for all vehicles towards their desired trajectories may generate large control magnitudes. In other words, our results indicate that in very large platoons one needs to select the control gains judiciously to avoid the excessive use of control effort. To demonstrate that these issues are not caused by the specific control strategy, we consider three different designs: a) Lyapunov-based design of § 13.2.1, b) LQR design for a platoon on a circle with M vehicles, and c) ‘controller with information of lead and preceding vehicles’, originally proposed by [20], and subsequently studied by [8,21]. In all three cases we assume that each vehicle has a limited amount of control effort at its disposal, that is $u_n(t) \in [-u_{\max}, u_{\max}]$, for all $t \geq 0$, $n \in \mathbb{N}_0$, with $u_{\max} > 0$.

Lyapunov-based design of § 13.2.1

We consider a platoon of vehicles (13.23) with controller (13.26a,13.28) and $\{a_n := a = \text{const.}, b_n := b = \text{const.}, \forall n \in \mathbb{N}_0\}$. Clearly, in this case both $e_n(t)$ and $\dot{e}_n(t)$ converge towards zero with the rates that are independent of the spatial location.

In particular, we study the situation in which at $t = 0$ the string of vehicles cruises at the desired velocity v_d with the lead vehicle being at its desired spatial location. We also assume that the distance between the vehicles indexed by n and $n - 1$, for every $n \in \{1, \dots, N\}$, $N \in \mathbb{N}$, is equal to $L + S_n$. The position initial conditions of the remaining vehicles can be chosen to ensure boundedness of $e_n(0)$ for $n > N$. For simplicity, we assume that for $n > N$ the spacing between the neighboring vehicles is at the desired level L . In other words, we consider the initial conditions of the form

$$\begin{aligned} \dot{x}_n(0) &= v_d, \quad \forall n \in \mathbb{N}_0, \\ x_n(0) &= \begin{cases} 0 & n = 0, \\ -(nL + \sum_{k=1}^n S_k) & n \in \{1, \dots, N\}, \\ -(nL + \sum_{k=1}^N S_k) & n > N, \end{cases} \end{aligned} \quad (13.30)$$

which translates into: $\{\dot{e}_n(0) = 0, \forall n \in \mathbb{N}_0\}$, and $e_n(0) = \{0, n = 0; -(nL + \sum_{k=1}^n S_k), n \in \{1, \dots, N\}; -(nL + \sum_{k=1}^N S_k), n > N\}$. Clearly, for this choice of initial condition $\{e_n(0)\}_{n \in \mathbb{N}_0} \notin l_2$, unless $\sum_{k=1}^N S_k \equiv 0$. Hence, despite the fact that the entire platoon cruises at the desired velocity v_d and the inter-vehicular spacing for most of the vehicles is kept at the desired level L , a relevant initial condition that

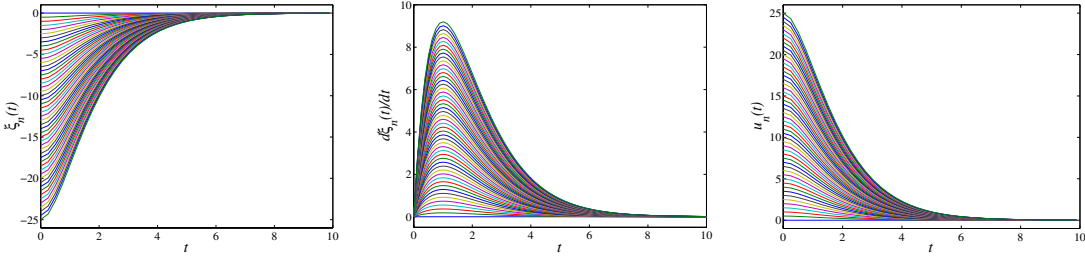


Figure 13.16: Simulation results of vehicular platoon using control law (13.26a,13.28) with $\alpha = \beta = a = 1$, and $b = 2$. The initial state of the platoon system is given by (13.31) with $N = 50$ and $S = 0.5$.

does not belong to $l_2 \times l_2$ can be easily constructed. This implies that a Hilbert space $l_2 \times l_2$ represents a rather restrictive choice for the underlying state-space of system (13.23).

The absence of uniform bound in (13.29) indicates that the large states will lead to the large control signals if the feedback gains are not appropriately selected. In particular, we observe that large initial states are readily obtained if there exists $m \in \{1, \dots, N\}$ such that $\{S_1, \dots, S_m\}$ sum to a big number. Moreover, it is not difficult to see that if $\{\text{sign } S_n = \text{const.} \neq 0, \forall n \in \{1, \dots, N\}\}$, then $|\sum_{k=1}^N S_k|$ represents a monotonically increasing function of N . Thus, for N large enough, very large initial conditions are possible if, for example, all S_n 's are either positive or negative. Because of that, we study a spatially constant non-zero sequence of S_n 's, that is we assume $\{S_n := S = \text{const.} \neq 0, \forall n \in \{1, \dots, N\}\}$. In this case, (13.30) simplifies to

$$\begin{aligned} \dot{x}_n(0) &= v_d, \quad \forall n \in \mathbb{N}_0, \\ x_n(0) &= \begin{cases} 0 & n = 0, \\ -n(L + S) & n \in \{1, \dots, N\}, \\ -(nL + NS) & n > N, \end{cases} \end{aligned} \quad (13.31)$$

or equivalently $\{\dot{e}_n(0) = 0, \forall n \in \mathbb{N}_0\}$, $e_n(0) = \{0, n = 0; -(n\alpha + \beta)S, n \in \{1, \dots, N\}; -N\alpha S, n > N\}$. For this choice of initial conditions $u_0 \equiv 0$, whereas the initial amount of control effort for the remaining vehicles is given by

$$u_n(0) = \frac{aS}{\beta} \left(n \frac{\alpha q}{1-q} + \frac{q(1-q^n)(\beta - (\alpha + \beta)q)}{(1-q)^2} \right),$$

for every $n \in \{1, \dots, N\}$, and

$$u_n(0) = \frac{aS}{\beta} \left(\frac{N\alpha q}{1-q} + \frac{q^{n-N+1}(1-q^N)(\beta - (\alpha + \beta)q)}{(1-q)^2} \right),$$

for every $n > N$, which implies that for any choice of design parameter a there exist $m \in \mathbb{N}$ such that $|u_n(0)| > u_{\max}$, for every $n > m$, provided that N is large enough. For example, if $\alpha = \beta = a = 1$, $b = 2$, $S = 0.5$, $u_{\max} = 5$, for $N = 50$, $u_{10}(0) = u_{\max} = 5$, and $|u_n(0)| > u_{\max}$, $\forall n > 10$, with $\lim_{n \rightarrow \infty} |u_n(0)| = 25$. Simulation results for this choice of design parameters and initial conditions given by (13.31), using controller (13.26a,13.28), are shown in Figure 13.16.

LQR design for a platoon on a circle

In this subsection, we consider LQR design for a platoon on a circle that consists of M vehicles. By exploiting the *spatial invariance*, we *analytically* establish that *any* LQR design leads to large control signals for the appropriately selected set of initial conditions.

The control objective is the same as in § 13.2.1: to drive the entire platoon at the constant cruising velocity v_d , and keep the distance between the neighboring vehicles at a pre-specified constant level L . Clearly, this is possible only if the radius of a circle is given by $r_M = ML/2\pi$. We rewrite system (13.21)

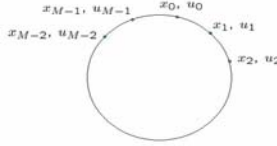


Figure 13.17: Circular platoon of M vehicles.

for $n \in \{0, \dots, M-1\}$ in terms of a state-space realization of the form

$$\begin{bmatrix} \dot{\xi}_n \\ \dot{\varsigma}_n \end{bmatrix} = \begin{bmatrix} 0 & 1 \\ 0 & 0 \end{bmatrix} \begin{bmatrix} \xi_n \\ \varsigma_n \end{bmatrix} + \begin{bmatrix} 0 \\ 1 \end{bmatrix} u_n \\ =: A_n \varphi_n + B_n u_n, \quad (13.32)$$

where $\xi_n(t) := x_n(t) - v_d t - nL$ and $\varsigma_n(t) := \dot{x}_n(t) - v_d$ denote the absolute position and velocity errors of the n -th vehicle, respectively. We propose the following cost functional

$$J := \frac{1}{2} \int_0^\infty \sum_{n=0}^{M-1} \sum_{m=0}^{M-1} (\varphi_n^*(t) Q_{n-m} \varphi_m(t) + u_n^*(t) R_{n-m} u_m(t)) dt, \quad (13.33)$$

where

$$\sum_{n=0}^{M-1} \sum_{m=0}^{M-1} \varphi_n^* Q_{n-m} \varphi_m \geq 0, \quad Q_{-n}^* = Q_n,$$

for all sequences φ_n , and

$$\sum_{n=0}^{M-1} \sum_{m=0}^{M-1} u_n^* R_{n-m} u_m > 0, \quad R_{-n}^* = R_n,$$

for all non-zero sequences u_n .

We utilize the fact that system (13.32) has spatially invariant dynamics over a circle. This implies that the Discrete Fourier Transform (DFT) can be used to convert analysis and quadratic design problems into those for a parameterized family of second order systems [16]. DFT is defined by: $\hat{x}_k := \frac{1}{\sqrt{M}} \sum_{n=0}^{M-1} x_n e^{-i \frac{2\pi n k}{M}}$, $k \in \{0, \dots, M-1\}$, and the inverse DFT is defined by: $x_n := \frac{1}{\sqrt{M}} \sum_{k=0}^{M-1} \hat{x}_k e^{i \frac{2\pi n k}{M}}$, $n \in \{0, \dots, M-1\}$. Using this, system (13.32) and quadratic performance index (13.33) transform to

$$\begin{bmatrix} \dot{\hat{\xi}}_k \\ \dot{\hat{\varsigma}}_k \end{bmatrix} = \begin{bmatrix} 0 & 1 \\ 0 & 0 \end{bmatrix} \begin{bmatrix} \hat{\xi}_k \\ \hat{\varsigma}_k \end{bmatrix} + \begin{bmatrix} 0 \\ 1 \end{bmatrix} \hat{u}_k \\ =: \hat{A}_k \hat{\varphi}_k + \hat{B}_k \hat{u}_k, \quad k \in \{0, \dots, M-1\}, \quad (13.34)$$

and

$$J = \frac{\sqrt{M}}{2} \sum_{k=0}^{M-1} \int_0^\infty (\hat{\varphi}_k^*(t) \hat{Q}_k \hat{\varphi}_k(t) + \hat{u}_k^*(t) \hat{R}_k \hat{u}_k(t)) dt,$$

where $\hat{R}_k > 0$ and

$$\hat{Q}_k := \begin{bmatrix} \hat{q}_{11k} & \hat{q}_{21k}^* \\ \hat{q}_{21k} & \hat{q}_{22k} \end{bmatrix} \geq 0,$$

for every $k \in \{0, \dots, M-1\}$. Clearly, the pair (\hat{A}_k, \hat{B}_k) is stabilizable for every $k \in \{0, \dots, M-1\}$. On the other hand, the pair (\hat{Q}_k, \hat{A}_k) is detectable if and only if $\hat{q}_{11k} > 0$ for every $k \in \{0, \dots, M-1\}$. These conditions are necessary and sufficient for the existence of a stabilizing optimal solution to the LQR problem (13.32, 13.33). For additional information about proper formulation of quadratically optimal (i.e.,

LQR, H_2 , H_∞) distributed control problems for large-scale and infinite vehicular platoons, we refer the reader to § 13.1.3..

It is readily shown that for $\dot{x}_n(0) \equiv v_d$, i.e. for $\zeta_n(0) \equiv 0$, we have:

$$\sum_{n=0}^{M-1} u_n^2(0) = \sum_{k=0}^{M-1} \frac{\hat{q}_{11k}}{\hat{R}_k} \hat{\xi}_k^*(0) \hat{\xi}_k(0),$$

which in turn implies

$$\inf_k \frac{\hat{q}_{11k}}{\hat{R}_k} \sum_{n=0}^{M-1} \xi_n^2(0) \leq \sum_{n=0}^{M-1} u_n^2(0) \leq \sup_k \frac{\hat{q}_{11k}}{\hat{R}_k} \sum_{n=0}^{M-1} \xi_n^2(0).$$

Thus, we have established the lower and upper bounds on the initial amount of control effort for a formation that cruises at the desired velocity v_d . These bounds are determined by the deviations of vehicles from their absolute desired trajectories at $t = 0$, and by the LQR design parameters \hat{q}_{11k} and \hat{R}_k . Clearly, since $\hat{q}_{11k} > 0$ (for detectability) $\inf_k \hat{q}_{11k}/\hat{R}_k$ is always greater than zero. We note that this quantity can be made smaller by increasing the control penalty. In particular, for $x_n(0) = n(L - S)$, $0 < S < L$, we have

$$\sum_{n=0}^{M-1} u_n^2(0) \geq \frac{S^2}{6} M(M-1)(2M-1) \inf_k \frac{\hat{q}_{11k}}{\hat{R}_k},$$

which illustrates an unfavorable scaling of the initial amount of control effort with the number of vehicles in formation. Hence, unless $u_{\max} \geq S^2(M-1)(2M-1) \inf_k \hat{q}_{11k}/6\hat{R}_k$, there exist at least one vehicle for which $|u_n(0)| > u_{\max}$.

Controller of [20]

In this subsection, we show that the controller of [20] faces the very same issues as the previously discussed control strategies with uniform convergence rates. We study this controller because of its superior properties compared to other ‘look-ahead vehicle following algorithms’ (see Table 1 of [8] for comparison of different constant spacing platoon strategies).

Controller of [20] for system (13.21) is, for any $n \in \mathbb{N}$, given by (see § 3.4 of [8]):

$$u_n = \frac{1}{1+q_3} (\ddot{x}_{n-1} + q_3 \ddot{x}_0 - (q_1 + \lambda) \dot{\eta}_n - q_1 \lambda \eta_n - (q_4 + \lambda q_3) (\dot{x}_n - \dot{x}_0) - \lambda q_4 (x_n - x_0 + nL)),$$

where q_1 , q_3 , q_4 , and λ represent positive design parameters, whereas the lead vehicle is indexed by 0. Equivalently, u_n is determined by the following recursive relation

$$u_n = (1 - \varrho) u_0 + \varrho u_{n-1} - \varrho f_n, \quad n \in \mathbb{N}, \quad (13.35)$$

where

$$\begin{aligned} f_n &:= (q_1 + \lambda) \dot{\eta}_n + q_1 \lambda \eta_n + (q_4 + \lambda q_3) \sum_{k=1}^n \dot{\eta}_k + \lambda q_4 \sum_{k=1}^n \eta_k \\ &= (q_1 + \lambda) (\dot{\xi}_n - \dot{\xi}_{n-1}) + q_1 \lambda (\xi_n - \xi_{n-1}) + (q_4 + \lambda q_3) (\dot{\xi}_n - \dot{\xi}_0) + \lambda q_4 (\xi_n - \xi_0), \end{aligned}$$

and $\varrho := 1/(1+q_3) < 1$. Finally, using (13.35) we express u_n as

$$u_n = u_0 - \sum_{k=1}^n \varrho^{n-k+1} f_k, \quad n \in \mathbb{N}.$$

In particular, for initial condition (13.31), or equivalently $\{\dot{\xi}_n(0) = 0, \forall n \in \mathbb{N}_0\}$, $\xi_n(0) = \{0, n = 0; -nS, n \in \{1, \dots, N\}; -NS, n > N\}$, u_0 is identically equal to 0. On the other hand, the initial amount of control

effort for the remaining vehicles is given by

$$u_n(0) = \lambda S(n \frac{q_4 \varrho}{1 - \varrho} + \frac{q_1 \varrho(1 - \varrho^n)}{1 - \varrho} - \frac{q_4 \varrho^2(1 - \varrho^n)}{(1 - \varrho)^2}),$$

for every $n \in \{1, \dots, N\}$, and

$$u_n(0) = \lambda S(N \frac{q_4 \varrho(1 + \varrho^N - \varrho^n)}{1 - \varrho} + \frac{q_1 \varrho(1 - \varrho^N)}{1 - \varrho} - \frac{q_4 \varrho^2(1 - \varrho^N)}{(1 - \varrho)^2}),$$

for every $n > N$. Thus, for any choice of design parameters q_1, q_3, q_4 , and λ there exist $m \in \mathbb{N}$ such that $|u_n(0)| > u_{\max}$, for every $n > m$, provided that N is large enough.

The results of this subsection illustrate that in very large platoons one needs to take into account the initial distance of vehicles from their desired trajectories and to adjust the control gains accordingly in order to avoid large velocity deviations and the excessive use of control effort. In the next subsection, we give conditions that the feedback gains need to satisfy to prevent saturation in both velocity and control and discuss some design limitations and tradeoffs in vehicular platoons.

13.2.3 Design limitations and tradeoffs in vehicular platoons

In this subsection, we determine the conditions that control gains need to satisfy to provide operation within the imposed saturation limits. Our analysis yields the explicit constraints on these gains—for any given set of initial conditions—to achieve desired position transients without magnitude and rate saturation. We also remark on some of the basic limitations and tradeoffs that need to be addressed in the control of vehicular platoons.

We rewrite system (13.21) as

$$\ddot{\bar{x}}_n = \bar{u}_n, \quad n \in \mathbb{N}_0. \quad (13.36)$$

The justification for the notation used in (13.36) is given in § 13.2.4. We want to drive each vehicle towards its desired absolute position $v_{dt} - nL$, and its desired velocity v_d . For the time being we are not concerned with the relative spacing between the vehicles. If we introduce the error variable $\{r_n(t) := \bar{x}_n(t) - v_{dt} + nL, n \in \mathbb{N}_0\}$, we can rewrite (13.36) as

$$\ddot{r}_n = \bar{u}_n, \quad n \in \mathbb{N}_0, \quad (13.37)$$

and choose \bar{u}_n to meet the control objective. In particular, we take \bar{u}_n of the form

$$\bar{u}_n = -p_n^2 r_n - 2p_n \dot{r}_n, \quad n \in \mathbb{N}_0, \quad (13.38)$$

where, for every $n \in \mathbb{N}_0$, p_n represents a positive design parameter. With this choice of control, the solution of system (13.37, 13.38) is for any $n \in \mathbb{N}_0$ given by

$$r_n(t) = (c_n + d_n t) e^{-p_n t}, \quad (13.39a)$$

$$\dot{r}_n(t) = (d_n - c_n p_n - d_n p_n t) e^{-p_n t}, \quad (13.39b)$$

$$\bar{u}_n(t) = (c_n p_n^2 - 2d_n p_n + d_n p_n^2 t) e^{-p_n t}, \quad (13.39c)$$

where for every $n \in \mathbb{N}_0$

$$\begin{aligned} c_n &:= r_n(0) = \bar{x}_n(0) + nL, \\ d_n &:= r_n(0)p_n + \dot{r}_n(0) \\ &= (\bar{x}_n(0) + nL)p_n + (\dot{\bar{x}}_n(0) - v_d). \end{aligned} \quad (13.40)$$

We want to determine conditions that the sequence of positive numbers $\{p_n\}_{n \in \mathbb{N}_0}$ has to satisfy to

guarantee

$$|r_n(t)| \leq r_{n,\max}, \quad \forall t \geq 0, \quad (13.41a)$$

$$|\dot{r}_n(t)| \leq v_{\max}, \quad \forall t \geq 0, \quad (13.41b)$$

$$|\bar{u}_n(t)| \leq u_{\max}, \quad \forall t \geq 0, \quad (13.41c)$$

with $\{r_{n,\max} > 0, \forall n \in \mathbb{N}_0\}$, $v_{\max} > 0$, and $u_{\max} > 0$ being the pre-specified numbers. For notational convenience, we have assumed that all vehicles have the same velocity and control saturation limits, given by v_{\max} and u_{\max} , respectively. Typically, the sequence $\{r_{n,\max}\}_{n \in \mathbb{N}_0}$ is given in terms of position initial conditions $\{r_n(0)\}_{n \in \mathbb{N}_0}$ as $\{r_{n,\max} := \gamma_n |r_n(0)|\}_{n \in \mathbb{N}_0}$, where sequence of numbers $\{\gamma_n > 1, \forall n \in \mathbb{N}_0\}$ determines the allowed overshoot with respect to the desired position trajectory of the n -th vehicle. Clearly, for this choice of $\{r_{n,\max}\}_{n \in \mathbb{N}_0}$, $\{r_n(0)\}_{n \in \mathbb{N}_0}$ satisfies (13.41a). Based on (13.39a), $r_n(t)$ asymptotically goes to zero, so we only need to determine conditions under which (13.41a) is violated for finite non-zero times. If (13.39a) achieves an extremum for some $\bar{t}_n \in (0, \infty)$, the absolute value of r_n at that point is given by:

$$|r_n(\bar{t}_n)| = \frac{|d_n|}{p_n} e^{-p_n \bar{t}_n} \leq \frac{|d_n|}{p_n} \leq \frac{|\dot{r}_n(0)|}{p_n} + |r_n(0)|.$$

Therefore, if sequence of positive numbers $\{p_n\}_{n \in \mathbb{N}_0}$ is chosen such that

$$\frac{|\dot{r}_n(0)|}{p_n} + |r_n(0)| \leq r_{n,\max}, \quad \forall n \in \mathbb{N}_0, \quad (13.42)$$

condition (13.41a) will be satisfied for every $t \geq 0$. This implies that, for good position transient response (that is, for small position overshoots), design parameters p_n have to assume large enough values determined by (13.42).

Clearly, (13.41b) is going to be violated unless $|\dot{r}_n(0)| \leq v_{\max}$, for every $n \in \mathbb{N}_0$. If \dot{r}_n has a maximum or a minimum at some non-zero finite time \bar{t}_n , the absolute value of (13.39b) at that point can be upper bounded by

$$|\dot{r}_n(\bar{t}_n)| = |d_n| e^{-p_n \bar{t}_n} \leq |d_n| \leq |r_n(0)| p_n + |\dot{r}_n(0)|.$$

Thus, to avoid velocity saturation, sequence of positive design parameters $\{p_n\}_{n \in \mathbb{N}_0}$ has to be small enough to satisfy

$$|r_n(0)| p_n + |\dot{r}_n(0)| \leq v_{\max}, \quad \forall n \in \mathbb{N}_0. \quad (13.43)$$

Finally, to rule out saturation in control we need to make sure that condition (13.41c) is satisfied for both $t = 0$ and $\bar{t}_n > 0$, where the potential extremum of \bar{u}_n takes place. The absolute values of (13.39c) at these two time instants are respectively given by $|\bar{u}_n(0)| = |-r_n(0)p_n^2 - 2\dot{r}_n(0)p_n| \leq |r_n(0)|p_n^2 + 2|\dot{r}_n(0)|p_n$, and $|\bar{u}_n(\bar{t}_n)| = |d_n| p_n e^{-p_n \bar{t}_n} \leq |d_n| p_n \leq |r_n(0)|p_n^2 + |\dot{r}_n(0)|p_n$. Since $p_n > 0$, for every $n \in \mathbb{N}_0$, condition (13.41c) is met if

$$|r_n(0)|p_n^2 + 2|\dot{r}_n(0)|p_n \leq u_{\max}, \quad \forall n \in \mathbb{N}_0. \quad (13.44)$$

Inequalities (13.42), (13.43), and (13.44) establish conditions for positive design parameters p_n to prevent saturation in velocity and control, and guarantee a good position transient response. We remark that these conditions can be somewhat conservative, but they are good enough to illustrate the major point. Clearly, for small excursions from the desired position trajectories control gains have to assume large values, determined by (13.42). On the other hand, for small velocity deviations and small control efforts these gains have to be small enough to satisfy (13.43) and (13.44). These facts illustrate some basic tradeoffs that designer faces in the control of vehicular platoons. In particular, the set of control gains that satisfies (13.43) and (13.44) determines the maximal position deviations and the rates of convergence towards the desired trajectories. In other words, the position overshoots and settling times can be significantly increased in the presence of stringent requirements on velocity and control saturation limits.

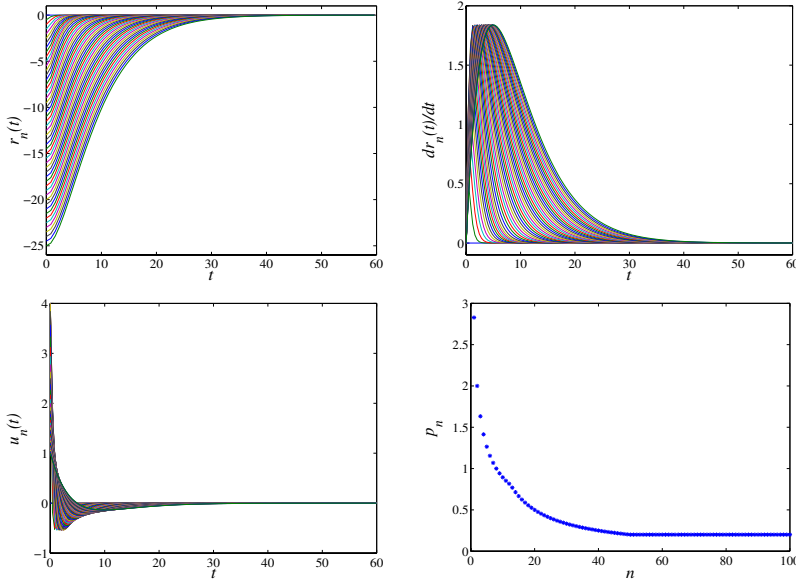


Figure 13.18: Solution of system (13.37,13.38) for initial conditions determined by (13.45) with $N = 50$ and $S_n = 0.5$, for every $n \in \{1, \dots, N\}$. The control gains are determined using (13.46) with $v_{\max} = u_{\max} = 5$, and $\{\varrho_n = 1, \sigma_n = 0.8, \forall n \in \mathbb{N}\}$.

For the example considered in § 13.2.2 with the initial conditions of the form

$$\begin{aligned} \dot{x}_n(0) &= v_d, \quad \forall n \in \mathbb{N}_0, \\ \bar{x}_n(0) &= \begin{cases} 0 & n = 0, \\ -(nL + \sum_{k=1}^n S_k) & n \in \{1, \dots, N\}, \\ -(nL + \sum_{k=1}^N S_k) & n > N, \end{cases} \end{aligned} \quad (13.45)$$

condition (13.42) is always satisfied, which implies that the largest deviation for all vehicles from their desired absolute positions takes place at $t = 0$. Therefore, the chosen initial conditions do not impose any lower bounds on the control gains. On the other hand, whereas conditions (13.43) and (13.44) do not put any constraints on p_0 , they respectively dictate the following upper bounds on $\{p_n\}_{n \in \mathbb{N}}$: $p_n \leq \{v_{\max}/|\sum_{k=1}^n S_k|, n \in \{1, \dots, N\}; v_{\max}/|\sum_{k=1}^N S_k|, n > N\}$, and $p_n \leq \{\sqrt{u_{\max}/|\sum_{k=1}^n S_k|}, n \in \{1, \dots, N\}; \sqrt{u_{\max}/|\sum_{k=1}^N S_k|}, n > N\}$. In particular, the following choice of $\{p_n\}_{n \in \mathbb{N}}$

$$p_n = \begin{cases} \min \left\{ \frac{\varrho_n v_{\max}}{|\sum_{k=1}^n S_k|}, \sqrt{\frac{\sigma_n u_{\max}}{|\sum_{k=1}^n S_k|}} \right\} & n < N, \\ \min \left\{ \frac{\varrho_n v_{\max}}{|\sum_{k=1}^N S_k|}, \sqrt{\frac{\sigma_n u_{\max}}{|\sum_{k=1}^N S_k|}} \right\} & n \geq N, \end{cases} \quad (13.46)$$

with $\{0 < \varrho_n \leq 1, 0 < \sigma_n \leq 1, \forall n \in \mathbb{N}\}$, clearly satisfies the above requirements. Figure 13.18 illustrates the solution of system (13.37,13.38) for initial conditions determined by (13.45) with $N = 50$ and $S_n = 0.5$, for every $n \in \{1, \dots, N\}$. The control gains are chosen using (13.46) with $v_{\max} = u_{\max} = 5$, $\{\varrho_n = 1, \sigma_n = 0.8, \forall n \in \mathbb{N}\}$, to prevent reaching imposed velocity and control saturation limits. The dependence of these gains on discrete spatial variable n is also illustrated in Figure 13.18.

Thus we have shown that controller (13.38) with the gains satisfying (13.42), (13.43), and (13.44) pre-

cludes saturation in both velocity and control and takes into account the desired quality of position transient response. However, this control strategy is unsafe, since it does not account for the inter-vehicular spacings. Because of that, in § 13.2.4 we redesign controller (13.26a,13.27) by incorporating the constraints imposed by (13.41) in the synthesis.

13.2.4 Control without reaching saturation

We again consider system (13.21), and introduce an error variable of the form

$$\varepsilon_n(t) := \alpha_n \zeta_n(t) + \beta_n \chi_n(t), \quad n \in \mathbb{N}_0, \quad (13.47)$$

where: $\{\zeta_n(t) := x_n(t) - v_d t + nL - r_n(t) = \xi_n(t) - r_n(t), n \in \mathbb{N}_0\}$, $\{\chi_n(t) := \zeta_n(t) - \zeta_{n-1}(t) = x_n(t) - x_{n-1}(t) + L - r_n(t) + r_{n-1}(t), n \in \mathbb{N}\}$, with $r_n(t)$ being defined by (13.39a,13.40), $\{p_n\}_{n \in \mathbb{N}_0}$ satisfying (13.42), (13.43), and (13.44), and parameters $\{\alpha_n\}_{n \in \mathbb{N}_0}$ and $\{\beta_n\}_{n \in \mathbb{N}_0}$ having the properties discussed in § 13.2.1. The initial conditions on these two variables and their first derivatives are given by: $\{\zeta_n(0) = x_n(0) - \bar{x}_n(0) =: \mu_n, n \in \mathbb{N}_0\}$, $\{\dot{\zeta}_n(0) = \dot{x}_n(0) - \dot{\bar{x}}_n(0) =: \nu_n, n \in \mathbb{N}_0\}$, $\{\chi_n(0) = \zeta_n(0) - \zeta_{n-1}(0) = \mu_n - \mu_{n-1}, n \in \mathbb{N}\}$, $\{\dot{\chi}_n(0) = \dot{\zeta}_n(0) - \dot{\zeta}_{n-1}(0) = \nu_n - \nu_{n-1}, n \in \mathbb{N}\}$, where $\{x_n(0), \dot{x}_n(0)\}_{n \in \mathbb{N}_0}$ and $\{\bar{x}_n(0), \dot{\bar{x}}_n(0)\}_{n \in \mathbb{N}_0}$ represent the actual and the measured initial conditions, respectively. If perfect information about the initial positions and velocities is available, then clearly $\{\mu_n = \nu_n = 0, \forall n \in \mathbb{N}_0\}$. However, since initial condition uncertainties are always present we want to design a controller to guard against them.

Double differentiation of (13.47) with respect to time yields

$$\begin{aligned} \ddot{\varepsilon}_n &= (\alpha_n + \beta_n)(u_n - \bar{u}_n) - \beta_n(u_{n-1} - \bar{u}_{n-1}) \\ &=: (\alpha_n + \beta_n)\tilde{u}_n - \beta_n\tilde{u}_{n-1}, \quad n \in \mathbb{N}_0, \end{aligned} \quad (13.48)$$

where \bar{u}_n is given by (13.38). System (13.48) can be represented in terms of its state-space realization of the form

$$\left. \begin{aligned} \dot{\vartheta}_n &= v_n \\ \dot{v}_n &= -\beta_n\tilde{u}_{n-1} + (\alpha_n + \beta_n)\tilde{u}_n \end{aligned} \right\} \quad n \in \mathbb{N}_0, \quad (13.49)$$

where $\{\vartheta_n := \varepsilon_n, v_n := \dot{\varepsilon}_n\}$. In particular, this system can be stabilized by the following feedback

$$\tilde{u}_0 = -\frac{1}{\alpha_0}(a_0\vartheta_0 + b_0v_0), \quad (13.50a)$$

$$\tilde{u}_n = \tilde{u}_0 \prod_{k=1}^n q_k - \sum_{k=1}^n \frac{1}{\beta_k}(a_k\vartheta_k + b_kv_k) \prod_{i=k}^n q_i, \quad (13.50b)$$

with $q_k := \beta_k/(\alpha_k + \beta_k)$, provided that $\{\beta_n \neq 0, \forall n \in \mathbb{N}\}$. It is noteworthy that, if parameters α_n and β_n are such that $\{\alpha_n := \alpha = \text{const.}, \beta_n := \beta = \text{const.}, \forall n \in \mathbb{N}\}$, then controller (13.50) has the same properties as controller (13.26a,13.27). For the same choices of design parameters $\{a_n\}_{n \in \mathbb{N}_0}$ and $\{b_n\}_{n \in \mathbb{N}_0}$, these two control strategies are only distinguished by the regions from where the states of systems (13.23) and (13.49) have to be brought to the origin. Namely, due to different formulations of control objectives, the initial states of system (13.23) may occupy a portion of the state-space that is significantly larger than a region to which the initial conditions of system (13.49) belong. In the former case, this region is determined by the maximal deviations from the desired absolute trajectories at $t = 0$, whereas, in the latter case, it is determined by the precision of measurement devices, that is their ability to yield an accurate information about the initial positions and velocities. As illustrated in § 13.2.2, the initial conditions may have an unfavorable scaling with discrete spatial variable n , which may result in the very large initial position deviations (and consequently, a large amount of the initial control effort) for large n 's, unless the size of the initial conditions is explicitly accounted for. We have shown in § 13.2.3 how to generate the initial condition dependent trajectories around which the states of vehicular platoon can be driven to zero without extensive use of control effort and large position and velocity overshoots.

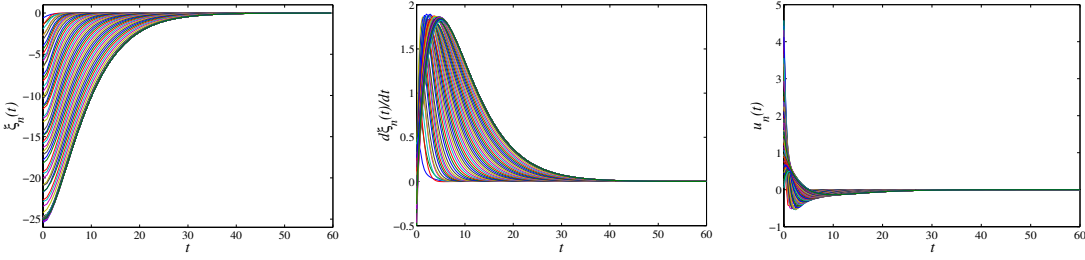


Figure 13.19: Simulation results of platoon with 101 vehicles ($M = 100$) using controller (13.51) with $\alpha_0 = 1$, $\{\alpha_n = \beta_n = 1, \forall n \in \{1, \dots, M\}\}$, $\{a_n = 1, b_n = 2, \forall n \in \{0, \dots, M\}\}$. The measured initial condition is given by (13.45) with $N = 50$ and $S_n = 0.5$, for every $n \in \{1, \dots, N\}$, whereas the numbers μ_n and ν_n that determine the actual initial condition are randomly selected.

Using the definition of \tilde{u}_n , we finally give the expressions for $\{u_n\}_{n \in \mathbb{N}_0}$

$$u_n = \bar{u}_n + \tilde{u}_n, \quad (13.51)$$

where \bar{u}_n and \tilde{u}_n are respectively given by (13.38) and (13.50). We remark that $\{u_n \equiv \bar{u}_n, \forall n \in \mathbb{N}_0\}$ if perfect information about the initial conditions is available. The only role of $\{\tilde{u}_n\}_{n \in \mathbb{N}_0}$ is to account for the discrepancies in the initial conditions due to measurement imperfections.

Asymptotic convergence of ζ_n , χ_n , $\dot{\zeta}_n$, and $\dot{\chi}_n$ to the origin for every $n \in \mathbb{N}_0$ can be easily established. Therefore, controller (13.51) provides operation within the imposed saturation bounds and asymptotic convergence of the platoon of vehicles to its desired cruising formation.

Simulation results of the platoon system with 101 vehicles ($M = 100$) using controller (13.51) with $\{\alpha_0 = 1, \alpha_n = \beta_n = 1, \forall n \in \{1, \dots, M\}\}$, $\{a_n = 1, b_n = 2, \forall n \in \{0, \dots, M\}\}$ are shown in Figure 13.19. The measured initial condition is given by (13.45) with $N = 50$ and $S_n = 0.5$, for every $n \in \{1, \dots, N\}$, whereas the numbers μ_n and ν_n that determine the actual positions and velocities at $t = 0$ are randomly selected. The rates of convergence towards the origin are chosen using (13.46) with $v_{\max} = u_{\max} = 5$, $\{\varrho_n = 1, \sigma_n = 0.8, \forall n \in \{1, \dots, M\}\}$, to prevent reaching imposed velocity and control saturation limits, and p_0 is set to 1. These convergence rates are shown in the far right plot in Figure 13.18. Clearly, the desired control objective is successfully accomplished with the quality of the transient response determined by the prescribed saturation bounds.

13.3 Summary

In this chapter, we have illustrated potential difficulties in the control of large or infinite vehicular platoons. In particular, shortcomings of previously reported solutions to the LQR problem have been exhibited. By considering the case of infinite platoons as the limit of the large-but-finite case, we have shown *analytically* how the aforementioned formulations lack stabilizability or detectability. We have argued that the infinite case is a useful abstraction of the large-but-finite case, in that it explains the almost loss of stabilizability or detectability in the large-but-finite case, and the arbitrarily slowing rate of convergence towards desired formation observed in numerical studies of finite platoons of increasing sizes. Finally, using the infinite platoon formulation, we have shown how incorporating absolute position errors in the cost functional alleviates these difficulties and provides uniformly bounded rates of convergence. It is noteworthy that the early work of [1–3, 18] is very widely cited, but to our knowledge these serious difficulties with their methods have not been previously pointed out in the literature.

We have further shown that imposing a uniform rate of convergence for all vehicles towards their desired trajectories may generate large control magnitudes for certain physically realistic initial conditions. Therefore, even though the formulation of an optimal control problem suggested in § 13.1.3 circumvents the weak points of [1–3, 18], additional care should be exercised in control of vehicular platoons (as illustrated

in § 13.2). Namely, we have demonstrated that in very large platoons the designer needs to pay attention to the initial deviations of vehicles from their desired trajectories when selecting control gains. We have also established explicit constraints on these gains—for any given set of initial conditions—to assure the desired quality of position transients without magnitude and rate saturation. These requirements have been used to generate the trajectories around which the states of the platoon system are driven towards their desired values without the excessive use of control effort.

Bibliography

- [1] W. S. Levine and M. Athans, "On the optimal error regulation of a string of moving vehicles," *IEEE Transactions on Automatic Control*, vol. AC-11, no. 3, pp. 355–361, July 1966.
- [2] S. M. Melzer and B. C. Kuo, "Optimal regulation of systems described by a countably infinite number of objects," *Automatica*, vol. 7, pp. 359–366, 1971.
- [3] K. C. Chu, "Decentralized control of high-speed vehicular strings," *Transportation Science*, vol. 8, no. 4, pp. 361–384, November 1974.
- [4] S. Shladover, C. Desoer, J. Hedrick, M. Tomizuka, J. Walrand, W.-B. Zhang, D. McMahon, H. Peng, S. Sheikholeslam, and N. McKeown, "Automated vehicle control developments in the path program," *IEEE Transactions on Vehicular Technology*, vol. 40, no. 1, pp. 114–130, February 1991.
- [5] P. Varaiya, "Smart cars on smart roads: problems of control," *IEEE Transactions on Automatic Control*, vol. 38, no. 2, pp. 195–207, February 1993.
- [6] H. Raza and P. Ioannou, "Vehicle following control design for automated highway systems," *IEEE Control Systems Magazine*, vol. 16, no. 6, pp. 43–60, December 1996.
- [7] D. Swaroop and J. K. Hedrick, "String stability of interconnected systems," *IEEE Transactions on Automatic Control*, vol. 41, no. 2, pp. 349–357, March 1996.
- [8] ——, "Constant spacing strategies for platooning in automated highway systems," *Transactions of the ASME. Journal of Dynamic Systems, Measurement and Control*, vol. 121, no. 3, pp. 462–470, September 1999.
- [9] D. Swaroop, J. K. Hedrick, and S. B. Choi, "Direct adaptive longitudinal control of vehicle platoons," *IEEE Transactions on Vehicular Technology*, vol. 50, no. 1, pp. 150–161, January 2001.
- [10] D. Chichka and J. Speyer, "Solar-powered, formation-enhanced aerial vehicle systems for sustained endurance," in *Proceedings of the 1998 American Control Conference*, 1998, pp. 684–688.
- [11] J. M. Fowler and R. D'Andrea, "Distributed control of close formation flight," in *Proceedings of the 41st IEEE Conference on Decision and Control*, 2002, pp. 2972–2977.
- [12] ——, "A formation flight experiment," *IEEE Control Systems Magazine*, vol. 23, no. 5, pp. 35–43, October 2003.
- [13] V. Kapila, A. G. Sparks, J. M. Buffington, and Q. Yan, "Spacecraft formation flying: dynamics and control," *Journal of Guidance, Control, and Dynamics*, vol. 23, no. 3, pp. 561–564, May-June 2000.
- [14] R. W. Beard, J. Lawton, and F. Y. Hadaegh, "A coordination architecture for spacecraft formation control," *IEEE Transactions on Control Systems Technology*, vol. 9, no. 6, pp. 777–790, November 2001.
- [15] H. Wong, V. Kapila, and A. G. Sparks, "Adaptive output feedback tracking control of spacecraft formation," *International Journal of Robust and Nonlinear Control*, vol. 12, no. 2-3, pp. 117–139, February-March 2002.

- [16] B. Bamieh, F. Paganini, and M. A. Dahleh, “Distributed control of spatially invariant systems,” *IEEE Transactions on Automatic Control*, vol. 47, no. 7, pp. 1091–1107, July 2002.
- [17] P. Seiler, A. Pant, and K. Hedrick, “Disturbance propagation in large interconnected systems,” in *Proceedings of the 2002 American Control Conference*, 2002, pp. 1062–1067.
- [18] S. M. Melzer and B. C. Kuo, “A closed-form solution for the optimal error regulation of a string of moving vehicles,” *IEEE Transactions on Automatic Control*, vol. AC-16, no. 1, pp. 50–52, February 1971.
- [19] K. Zhou, J. C. Doyle, and K. Glover, *Robust and Optimal Control*. Prentice Hall, 1996.
- [20] J. K. Hedrick, D. McMahon, V. Narendran, and D. Swaroop, “Longitudinal vehicle controller design for IVHS system,” in *Proceedings of the 1991 American Control Conference*, 1991, pp. 3107–3112.
- [21] D. Swaroop and J. K. Hedrick, “Direct adaptive longitudinal control of vehicle platoons,” in *Proceedings of the 33th IEEE Control and Decision Conference*, 1994, pp. 684–689.

Chapter 14

Conclusions and future directions

Conclusions

We have presented constructive design tools for distributed control of systems on lattices. All results for infinite dimensional systems are readily accommodated to finite dimensions. We have illustrated that distributed backstepping can be successfully used to obtain state and output-feedback controllers for both nominal systems and systems with unknown parameters. These parametric uncertainties are assumed to be temporally constant, but are allowed to vary spatially. Furthermore, within the Lyapunov framework desired control objectives can be achieved irrespective of whether the plant dynamics is linear or nonlinear, spatially invariant or spatially varying. We have also shown that the design problem can always be posed in such a way to yield controllers with an intrinsic degree of localization. This degree of localization is determined by the number of interactions per plant cell, and the largest number of integrators that separate interactions from control inputs. If all interactions are to be cancelled at each step of backstepping, then each control cell has to communicate with larger number of its neighbors. For systems that satisfy matching condition (i.e., no integrators separate interactions from control inputs) desired properties can be achieved with a controller that has the same architecture as the original plant. Also, by judicious choice of stabilizing functions during the recursive design (identify beneficial interactions; dominate harmful interactions) controllers with less interactions can be obtained.

We have also discussed potential difficulties in the control of large scale vehicular platoons by exhibiting shortcomings of several widely cited solutions to the LQR problem. This has been done by considering infinite platoons as an insightful limit of large-but-finite platoons. Spatially invariant theory has been utilized to show how to avoid ill-posedness and provide uniform convergence rates. It has also been demonstrated that control strategies with uniformly bounded rates of convergence could introduce the peaking in control effort. This problem is solved by trajectory generation: for any given set of initial conditions, explicit constraints on convergence rates have been derived to avoid peaking in velocity and control and guarantee the desired quality of position transient response.

The control of vehicular platoons illustrates that a lot of intuition about behavior of large scale systems can be gained by considering their infinite dimensional analogues with dynamical symmetries. The main messages that we want to send across are:

- **Care should be exercised when extending standard results from small to large scale systems.**
- **Infinite dimensional systems represent useful abstractions of large-but-finite systems.** For example, problems with stability of infinite dimensional systems indicate problems with performance of their large scale counterparts.
- **Large-but-finite systems require large scale computations. Spatially invariant infinite dimensional abstractions of these systems lead to almost analytical results.** For example, an optimal control problem for a large-but-finite platoon of vehicles amounts to solving a large scale Riccati equation, which is computationally prohibitive. On the other hand, the same problem for

spatially invariant platoon of vehicles amounts to finding a solution to a parameterized family of second order Riccati equations, which can be done analytically (as illustrated in Chapter 13). Thus, there is a lot to be gained by considering infinite dimensional systems with dynamical symmetries as a limit of large scale systems on lattices.

Several topics for future research are given below.

Future directions

Architectural issues in distributed and networked control design. Several important distributed control problems that are not addressed in this thesis are outlined below: a) *a priori* assignment of localization constraints in non-conservative ways for spatially invariant systems, b) robust and optimal distributed control of finite or spatially varying systems with edge and spatial variation effects, c) identification of spatially varying parameters, d) nonlinear robust and adaptive distributed control of PDEs, e) spatio-temporal model reduction, and f) distributed design in the presence of spatial unmodelled dynamics.

Design of inversely optimal localized controllers. Design of optimal controllers with pre-specified localization constraints is a difficult problem. Optimality of a closed-loop system is desirable because it guarantees, among other things, favorable gain and phase margins. These margins provide robustness to different types of uncertainty. Alternatively, one can ask a following question: given a localized stabilizing controller, is it inversely optimal with respect to some physically meaningful performance objective? For example, it is relevant to study whether distributed backstepping controllers of Chapter 12 are inversely optimal, and if not whether they could be appropriately modified such that inverse optimality is guaranteed. Our initial investigations indicate that the answer to this question is positive. We plan to first study this problem for spatially invariant linear systems because they are amenable to a thorough analysis. These results will be used to motivate design of both optimal and inversely optimal controllers for other classes of problems.

Modular adaptive distributed design. Our current efforts are directed towards development of modular adaptive schemes in which parameter update laws and controllers are designed separately. The major advantage of using this approach rather than the Lyapunov-based design is the versatility that it offers. Namely, adaptive controllers of Chapter 12 are limited to Lyapunov-based estimators. From a practical point of view it may be advantageous to use the appropriately modified standard gradient or least-squares type identifiers.

Limitations and tradeoffs in the control of vehicular formations. Research interest in controlling vehicular formations (UAVs, spacecrafsts, satellites) is experiencing rapid growth. The interactions between different UAVs arise due to both aerodynamic coupling and feedback control. We plan to study fundamental limitations and tradeoffs in controlling large formations of UAVs and satellites, and to design efficient control strategies with favorable architectures for this increasingly relevant class of systems.

Input-output analysis of peaking in vehicular platoons. We have demonstrated that certain physically relevant initial conditions in combination with fast convergence rates can lead to peaking in both velocity and control. Faster rates of convergence towards the desired formation cause larger peaks. We intend to study this phenomenon using input-output tools. In particular, we plan to determine how the L_∞ induced gain (that is, the L_1 norm) of externally excited platoon, with a controller that provides uniform rate of convergence, scales with the number of vehicles in formation. If this norm scales badly with the platoon size, then the L_1 control would be an appropriate framework for avoiding peaking in vehicular platoons.